N° d'ordre: 40418

Habilitation à diriger des recherches

présentée

devant l'université de Lille 1

par

Olivier Lafon

Équipe d'accueil : Verre et méthodologie RMN
Laboratoire d'accueil : Unité de Catalyse et de Chimie du Solide, UMR CNRS 8181
École doctorale : Molécules et matière condensée

Titre du mémoire :

Développement de la spectroscopie de Résonance Magnétique Nucléaire pour les solides et la matière molle

À soutenir le 10 Décembre 2010 devant la commission d'examen

MM. :	Christian	Bonhomme	Rapporteurs
	Anne	Lesage	
	Dominique	Massiot	
MM. :	Geoffrey	Bodenhausen	Examinateurs
	Guy	Lippens	
	Lionel	Montagne	
	Hervé	Vezin	
	Jean-Paul	Amoureux	

« I wol yow telle, as was me taught also,
The foure spirites and the bodies sevene,
By ordre, as ofte I herde my lord hem nevene. »

Geoffrey Chaucer, *The Canon's Yeoman's Tale* in *The Canterbury Tales*

« Je vais vous dire, comme on l'on a appris,
Les corps volatils et les corps solides,
Dans l'ordre où mon maître souvent les nommait. »

Geoffrey Chaucer, traduction d'André Crépin, *Conte de l'Assistant* dans *Les contes de Canterbury*

Remerciements

Il est généralement d'usage de remercier dans un ouvrage l'ensemble des personnes ayant contribué à sa réalisation. Pour une habilitation à diriger des recherches, ce nombre est relativement élevé. J'espère pouvoir remercier oralement ceux que j'ai omis ici faute de place.

Suivant l'ordre chronologique, je tiens tout d'abord à remercier vivement Lyndon Emsley de l'École Normale Supérieure de Lyon. Ses cours de RMN m'ont donné l'envie d'en savoir plus. Sur ses conseils bibliographiques, je lus « Quantum Description of High-Resolution NMR in Liquids » de Maurice Goldman. Cet ouvrage me donna l'impression que la spectroscopie RMN était une technique compliquée, donc intéressante. *I thank also Robert V. Law from Imperial College.* L'étude dans son laboratoire du polymorphisme des molécules amphiphiles par RMN des solides (et d'autres formes de mousses lors des *pub crawls*) acheva de me convaincre que les spectroscopistes RMN étaient des gens fréquentables et qu'il me fallait entrer dans leur *club*.

Je voudrais remercier aussi chaleureusement Philippe Lesot et Jacques Courtieu, qui ont dirigé mon DEA et ma thèse. Ils m'ont formé à la recherche scientifique et m'ont donné l'envie d'en faire mon metier. Par dessus tout, je retiendrai leur disponibilité et les nombreuses discussions scientifiques que nous avons eu pendant ma thèse. Elles m'ont permis d'apprendre que la recherche scientifique était aussi un art de la conservation, où les idées naissent et murissent des échanges entre collègues.

Mes sincères remerciements vont aussi à Thibault Charpentier et Dimitrios Sakellariou, qui m'ont fait passé du cristal liquide au solide. Au cours de mon post-doc, je n'ai pas appris à être patient mais j'ai réalisé que le démarrage de projets innovants nécessite de la tenacité.

Je tiens à exprimer ma profonde gratitude à Jean-Paul Amoureux, qui m'a accueilli à Lille en tant que maître de conférences. Je le remercie en particulier pour son dynamisme et son goût de la nouveauté. À son contact, j'ai aussi réalisé combien l'émulation internationale était importante pour la recherche scientifique.

Je voudrais également exprimer ma reconnaissance à Julien Trébosc, ingénieur de recherche en RMN des solides à Lille. J'ai énormément appris sur les aspects expérimentaux de la RMN des solides en travaillant avec lui. Mes remerciements vont aussi à mes collègues lillois Laurent Delevoye et Grégory Tricot, qui sont à l'interface entre la méthodologie et les applications de la RMN des solides. Cela a toujours été un plaisir de travailler avec eux et je suis sûr que nous aurons bientôt d'autres projets communs. J'adresse aussi mes remerciements à Rose-Noël Vannier et Lionel Montagne, qui dirigent respectivement l'axe chimie du solide et du l'Unité Catalyse et Chimie du Solide. Je sais combien la gestion, le pilotage et l'animation sont indispensables au fonctionnement des laboratoires.

Je remercie aussi vivement Hervé Vezin, avec qui j'ai initié l'activité DNP à Lille. Son optimisme et son soutien ont été essentiels pour le démarrage du projet.

Une bonne partie des travaux présentés dans cette habilitation n'auraient tout simplement pas pu être obtenus sans l'enthousiasme et le travail des étudiants du groupe. Je tiens à les remercier tous. Bingwen Hu m'a marqué par sa créativité et sa vivacité d'esprit. Il est actuellement chercheur à l'université Normal de Shanghai. J'ai apprecié chez Qiang Wang sa rigueur et sa méthode. Nous avons avec lui réellement pu faire le point sur certains sujets en dépit de ses allers-retours entre la Chine et la France. Il a aussi été à l'origine du recouplage entre noyaux quadripolaires. Qiang Wang devrait soutenir sa thèse fin octobre et enchaîner ensuite avec un poste de chercheur au centre de résonance magnétique de Wuhan. Xingyu Lu a démarré sa thèse en janvier dernier. J'espère qu'il tirera parti de sa formation à Lille.

Je remercie aussi sincèrement Anne Lesage, Christian Bonhomme et Dominique Massiot, qui ont accepté d'être rapporteurs de cette habilitation. Mes sincères remerciements vont aussi autres membres du jury, Geoffrey Bodenhausen, Guy Lippens, Lionel Montagne, Hervé Vezin et Jean-Paul Amoureux.

Finalement, je remercie aussi mes amis et ma famille, qui m'ont soutenu et encouragé dans cette carrière passionnante mais accaparante d'enseignant-chercheur. J'ai ici une pensée particulière pour ma compagne Aurélie, qu'elle soit ici remerciée pour sa compréhension et ses conseils.

Table des matières

Introduction

Quelques problèmes de chimie au début du XXI^{e} siècle

À l'issue du XX^{e} siècle, grand siècle de la mécanique quantique et de la biologie moléculaire, certains pourraient remettre en cause l'intérêt de la chimie comme champ disciplinaire. Elle est toutefois une science indispensable, puisqu'elle est le lieu de création de nouvelles formes de matière et de l'élucidation des relations entre les propriétés de la matière et sa structure, du micromètre aux dimensions atomiques. Les développements de la chimie sont inspirés par ses motivations internes, les défis scientifiques rencontrés dans d'autres disciplines (physique, biologie, géoscience) et les enjeux socio-économiques, tels que le progrès technologique (électronique, santé. . .) ou les préoccupations de la société en matière d'environnement, de santé ou de sécurité.

Les questions non encore résolues, mais accessibles aux chimistes d'aujourd'hui, sont innombrables. Quelques-unes sont données ci-dessous :

i. Jusqu'où pouvons-nous pousser la synthèse en chimie ? Les composés chimiques synthétiques sont encore loin d'atteindre la complexité de l'agencement de la matière au sein des êtres vivants (cellules, foraminifères. . .). L'accroissement du degré de complexité passera notamment par la maîtrise de l'auto-assemblage intra- et inter-moléculaire. L'auto-assemblage au sein des êtres vivants n'est possible que grâce aux systèmes moléculaires de réparation, tels que les protéines chaperonnes ou les enzymes de réparation de l'ADN. Il pourrait être intéressant de développer des systèmes synthétiques analogues afin de contrôler l'élaboration de nouveaux matériaux nano- et micro-structurés.

ii. Est-il possible de concevoir des systèmes synthétiques auto-réplicants ? D'un point de vue fondamental, ceci permettrait d'envisager d'autres formes moléculaires pour la vie. D'un point de vue pratique, ces systèmes pourraient être utiles pour la production de composés chimiques complexes en quantité suffisante.

iii. La miniaturisation ultime des outils techniques relève aussi du champ de la chimie. Pouvons-nous concevoir des composants électroniques, des capteurs, des moteurs ou des robots dont les dimensions soient de l'ordre de quelques nanomètres ? L'utilisation de tels dispositifs impliquera aussi l'élaboration de chaîne fonctionnelle depuis l'échelle moléculaire jusqu'à l'échelle macroscopique.

iv. Dans le domaine de la théorie de l'information, pouvons-nous concevoir des ordinateurs qui, à l'image du cerveau, seraient capables de créer les interconnexions dont ils ont besoin au lieu d'utiliser celles préétablies ?

v. Dans le domaine de la santé, pouvons-nous prédire la structure tertiaire d'une protéine et éventuellement sa fonction à partir de sa séquence ? À l'inverse, sommes-nous capables de proposer une séquence d'acides aminés ayant une structure et une fonction voulues ?

vi. Est-il possible de prévoir les structures cristallines que peut adopter une petite molécule et son diagramme de phase ? Ceci a des conséquences importantes dans le domaine de la pharmacie.

vii. La caractérisation et la modélisation de la matière amorphe demeurent aussi une question centrale en chimie. Ainsi, les propriétés structurales et dynamiques des verres, des catalyseurs hétérogènes, des matériaux polymères, des gels ou des pâtes sont encore loin d'être comprises. Le vieillissement des matériaux amorphes (plastiques, bétons, verres, adhésifs) a pourtant des conséquences économiques importantes. Les solides amorphes sont aussi utilisés en pharmacie, où ils permettent d'obtenir des vitesses de dissolution plus élevées et conduisent ainsi à une meilleure biodisponibilité des substances actives.

viii. Un enjeu économique majeur est celui de l'énergie. Au cours du XX^{e} siècle, la consommation mondiale d'énergie a été multipliée par 40, pendant que la population mondiale quadruplait. Aujourd'hui, cette consommation mondiale augmente de 1 % par an. Cet accroissement des besoins énergétiques est, cependant, confronté à deux problèmes : l'épuisement des combustibles fossiles (charbon, gaz, pétrole), qui représentent environ 75 % de la consommation énergétique mondiale, et les conséquences sur le climat de la combustion des matières carbonées fossiles. Assurer à la population de la planète un avenir énergétique, à la fois confortable et sûr, soulève de nombreux problèmes scientifiques et techniques. En particulier, un effort important en chimie des matériaux est nécessaire pour optimiser la production de l'énergie, les conditions de son stockage et de son utilisation. Il s'agit par exemple de développer des matériaux haute performance, résistants à l'irradiation, pour le conditionnement à long terme des déchets fortement radioactifs, les réacteurs de 4ème génération ou les futurs réacteurs de fusion. L'hydrogène apparaît comme une solution technologique pérenne pour le stockage et le transport de l'énergie. Cependant, les différentes étapes (production, stockage, utilisation) de cette filière énergétique impliquent l'emploi de matériaux nouveaux, tels que, par exemple, les membranes et les électrolytes solides pour les électrolyseurs haute-température et les piles à combustible.

Solutions apportées par la spectroscopie RMN

Pour pouvoir répondre à ces différentes questions, les chimistes devront être capables de contrôler la structure et la dynamique depuis l'échelle atomique jusqu'à l'échelle macroscopique. Ce contrôle nécessite l'utilisation de techniques avancées de caractérisations. En particulier, la RMN s'est révélée être un outil indispensable en chimie. En effet, elle présente plusieurs avantages :

i. Elle sonde l'environnement local des noyaux et ne nécessite pas d'ordre à longues distances. Elle constitue donc une méthode de choix pour l'étude des liquides (petites molécules organiques et macromolécules biologiques en solution. . .), de la matière molle (gels, pâtes, cristaux liquides. . .) et des solides amorphes (verres, polymères. . .), hétérogènes (nanomatériaux, matériaux hybrides, catalyseurs. . .), désordonnés (matériaux pour batterie et piles à combustible, fibres amyloïdes. . .) ;

ii. Il s'agit d'une méthode non destructive. En outre, comme elle met en jeu des faibles énergies, l'échantillon est peu perturbé par la mesure ;

iii. La RMN est une technique sensible à la dynamique. Elle permet de sonder des mouvements atomiques ayant des constantes de temps comprises entre 10 ns et quelques secondes ;

iv. La RMN bénéficie en général d'une grande sélectivité. En effet, les interactions entre les spins nucléaires et les champs magnétiques extérieurs sont souvent beaucoup plus importantes que celles exercées sur les spins nucléaires avec les champs magnétiques locaux, produits par les atomes voisins. De ce fait, les champs magnétiques extérieurs permettent de manipuler les spins nucléaires et de sélectionner les interactions internes contenant les informations chimiques pertinentes.

Cependant, son utilisation est limitée dans un certains nombres de domaines (chimie des interfaces, composés paramagnétiques, observation des noyaux peu sensibles ou possédant un fort moment quadripolaire électrique, échantillons de faible volume, tels que les biopsies, les molécules biologiques marquées isotopiquement, les matériaux avancés. . .) par son manque de sensibilité ou sa sélectivité encore insuffisante. D'importantes activités de recherche sont menées actuellement pour surmonter ces limitations.

Thématiques de recherche

Mes thématiques de recherche s'inscrivent dans le cadre de ces développements méthodologiques, l'objectif étant de faire de la spectroscopie RMN une méthode efficace et de routine, pour l'analyse des solides et de la matière molle.

Mon travail de recherche a, dans un premier temps, porté sur le développement de la RMN en milieu orienté chiral comme méthode d'analyse stéréochimique. La motivation de ces recherches est l'essor considérable de la synthèse asymétrique depuis une trentaine d'années et son utilisation dans de multiples domaines, depuis les matériaux (tacticité des polymères) jusqu'à la pharmacologie. Cependant, les techniques d'analyse stéréochimique existantes (pouvoir rotatoire, HPLC chirale, RMN isotrope. . .) ne sont pas toujours efficaces et générales. Dans ce contexte, la RMN en milieu orienté chiral constitue une alternative crédible [1–3]. Elle a notamment permis de différencier une grande variété d'énantiomères, y compris ceux dépourvus de groupement fonctionnel, tels que les hydrocarbures saturés [4], ou les énantiomères chiraux par substitution isotopique [5]. Mon travail a permis de mieux comprendre l'origine des discriminations chirales observées pour ces énantiomères flexibles de chiralité isotopique [6–10]. La RMN en milieu orienté chiral s'est aussi révélée une méthode de choix pour l'étude de la dynamique conformationnelle. Elle a notamment permis d'observer des changements de conformations invisibles en milieu achiral, tels que l'interconversion entre des conformères énantiomères [11,12]. Ces applications de la RMN en milieu orienté chiral sont souvent rendues possibles par l'utilisation de la RMN du ^{2}H et plus précisément de la sensibilité de l'interaction quadripolaire de ce noyau à l'orientation moléculaire. Cependant, les spectres ^{2}H de molécules polydeutérées ou en abondance naturelle sont souvent complexes à interpréter. Pour résoudre ce problème, différentes approches ont été introduites : les expériences d'autocorrélation ^{2}H [13–15], les expériences de corrélations ^{2}H–^{13}C [16,17] et les expériences de corrélation ^{2}H–^{2}H [18–20].

Ma seconde thématique de recherche est le développement de la spectroscopie RMN pour les solides micro-cristallins, non-cristallins ou hétérogènes. Si l'utilité de la spectroscopie RMN dans ce domaine a d'ores et déjà été démontrée, son utilisation est encore limitée par un manque de sensibilité et de sélectivité. Le but de nos recherches au sein de l'équipe « Verres et méthodologie RMN » est de lever ces verrous méthodologiques et d'étendre le domaine d'application de la RMN des solides.

À l'état solide, les mouvements atomiques sont limités et souvent anisotropes. Par conséquent, si aucune précaution n'est prise, les interactions RMN anisotropes, telles que l'interaction dipolaire, l'anisotropie de déplacement chimique (CSA) et l'interaction quadripolaire, ne sont pas moyennées à zéro. Ces interactions conduisent alors à des spectres larges sans signature détaillée, desquels il est difficile d'extraire une information chimique pertinente. La sélectivité de la RMN peut néanmoins être fortement améliorée en conjuguant l'utilisation de champs magnétiques stationnaires, $\boldsymbol{B}^0$, intenses, la rotation à l'angle magique (MAS) et la manipulation des moments magnétiques nucléaires par des champs radiofréquences. Les champs $\boldsymbol{B}^0$ intenses permettent d'augmenter la sensibilité et la résolution spectrale, notamment pour les noyaux quadripolaires. La méthode MAS tend à réduire, voire à éliminer, les interactions RMN anisotropes et contribue donc à accroître la résolution et la sensibilité. Les séquences d'impulsions de champ radiofréquence (rf) ont différentes finalités. Elles peuvent servir à réintroduire sélectivement une interaction RMN anisotrope dans les conditions MAS (nous parlons alors de *recouplage*) ou à l'inverse, contribuer à l'élimination des couplages dipolaires élevés, qui limitent la résolution spectrale (nous parlons alors de *découplage*). Mon travail de recherche a notamment porté sur le développement de méthodes de recouplage dipolaire entre noyaux identiques (recouplage homonucléaire) [21–27] ou dissemblables (recouplage hétéronucléaire) [28–32], ainsi que sur l'introduction de techniques de découplages dipolaires homonucléaires [33–35].

Ma contribution au domaine du recouplage dipolaire a recouvert plusieurs aspects. Tout d'abord, mon sujet de post-doctorat a été l'application de méthodes de recouplage existantes pour la mesure de ^{3}H–^{3}H [27]. Cette technique de RMN des solides est actuellement celle qui permet de mesurer les distances internucléaires les plus élevées (jusqu'à 14,4 Å). À Lille, nous avons développé de nouvelles séquences de recouplage dipolaire compatibles avec les hauts champs et les hautes fréquences MAS (jusqu'à $\nu_r = 80$ kHz). L'utilisation de haut champ est, en effet, cruciale pour l'accroissement de la sensibilité et de la résolution. Cependant, plus le champ $\boldsymbol{B}^0$ est élevé, plus les méthodes de recouplage se doivent d'être robustes au déplacement chimique isotrope et au CSA.

Ces vitesses de rotation élevées présentent deux avantages principaux. Premièrement, elles améliorent la résolution et la sensibilité des spectres RMN ^{1}H et ^{19}F. Deuxièmement, elles éliminent les bandes de rotation dues au CSA pour les expériences ^{13}C et ^{31}P à haut champ. Par conséquent, les méthodes de recouplage utilisées pour les noyaux ^{1}H, ^{19}F, ^{13}C ou ^{31}P se doivent d'être compatibles avec la très haute vitesse. Nous avons introduit, à la fois, des méthodes de recouplage homo- et hétéro-nucléaire. Les méthodes de recouplage dipolaire ont été appliquées pour observer diverses proximités interatomiques, ^{1}H–^{1}H [22], ^{13}C–^{13}C, ^{19}F–^{19}F [23, 26], ^{31}P–^{31}P [21] et ^{27}Al–^{27}Al [25]. Les recouplages hétéronucléaires ont été employés pour mesurer des distances ^{13}C–^{14}N [30], ^{13}C–^{17}O [31], ainsi que pour mettre en évidence les proximités ^{1}H–^{23}Na et ^{23}Na–^{31}P [29, 32].

Une autre problématique est le développement de séquences de découplage homonucléaire dipolaire capables d'augmenter, à la fois, la résolution des spectres ^{1}H et les temps de vie des cohérences transverses ^{1}H lors d'expériences multi-impulsions. En effet, pour des réseaux bi- ou tri-dimensionnels de protons, les interactions dipolaires entre les différentes paires ^{1}H–^{1}H ne commutent pas entre elles [36] et les largeurs de raie ^{1}H décroissent comme l'inverse de la fréquence MAS [37–39]. Même à des fréquences MAS atteignant 80 kHz, les résonances ^{1}H sont encore élargies par les couplages dipolaires ^{1}H–^{1}H résiduels [40]. Pour éliminer ces couplages dipolaires élevés, une solution consiste à utiliser des champs rf, qui peuvent, eux, moduler les interactions RMN avec des fréquences de 200 kHz. Des méthodes de découplage dipolaire ^{1}H–^{1}H combinant rotation de l'échantillon et séquences multi-impulsions (CRAMPS) avaient été développées pour des fréquences MAS modérées (jusqu'à 25 kHz). Notre travail a consisté à développer des méthodes CRAMPS compatibles avec des fréquences MAS élevées (supérieures à 30 kHz) [33, 34, 41]. Deux approches ont été explorées : une méthode synchronisée sur la période de rotor et une méthode non-synchronisée.

Outre l'accroissement de la résolution et de la sélectivité, un autre défi important est l'augmentation de la sensibilité de la RMN et la diminution des temps d'expérience. La stratégie la plus répandue consiste à utiliser des champs $\boldsymbol{B}^0$ élevés. C'est dans cette optique que nous avons développé des séquences adaptées aux hauts champs. Cependant, cette stratégie se heurte au gain limité de sensibilité par augmentation du champ et à la difficulté de construire des aimants produisant des champs $\boldsymbol{B}^0$ très intenses, stationnaires et uniformes. Dans ce contexte, une approche prometteuse consiste à utiliser le phénomène de polarisation dynamique nucléaire (DNP) et à transférer une partie de l'aimantation des électrons non-appariés vers les noyaux de l'échantillon. Récemment, l'équipe de R. G. Griffin au MIT a montré que la DNP conduisait à des gains de sensibilité de un à deux ordres de grandeur pour des solutions gelées à haut champ (jusqu'à 9.4 T) en rotation à l'angle magique [42, 43]. La DNP n'est sûrement pas une méthode aussi générale que l'utilisation des hauts-champs, puisqu'elle nécessite la présence, au sein de l'échantillon, d'agents paramagnétiques. Cependant, elle devrait se révéler utile pour de nombreux systèmes ayant des applications importantes (biomolécules, nanomatériaux, électrodes, matériaux poreux et catalyseurs) qui contiennent déjà des centres paramagnétiques ou au sein desquels il est possible d'introduire des radicaux organiques. La DNP/RMN haut-champ a été appliquée, jusqu'ici, essentiellement pour les noyaux ^{13}C et ^{15}N de molécules organiques ou biologiques au sein de solutions gelées. Un de nos projets de recherche vise donc à explorer les potentialités de la DNP/RMN pour les matériaux et les catalyseurs. Une demande ANR Jeunes chercheurs a été déposé pour cette thématique.

En parallèle au développement de la DNP, il est pertinent de développer des méthodes rapides d'acquisition des spectres RMN multi-dimensionnels. En effet, avec le développement de méthodes RMN de plus en plus sensibles telles que la DNP, le facteur limitant pour l'enregistrement des spectres multi-dimensionnels n'est souvent plus le rapport signal-sur-bruit, mais la nécessité d'un échantillonnage complet du signal à la fréquence de Nyquist dans les différentes dimensions spectrales. Ce type d'échantillonnage est nécessaire pour éviter les repliements et les artefacts de troncature lors du traitement par transformée de Fourier (TF). Pour dépasser cette limite, il est nécessaire d'utiliser des méthodes de traitement autres que la TF, telles que la covariance, les méthodes de décomposition ou de maximisation d'entropie, qui peuvent bénéficier d'échantillonnage non uniforme dans le domaine temporel [44–49]. Ces méthodes ont été introduites et testées essentiellement en RMN des liquides. Nous nous proposons de les adapter et d'évaluer leur efficacité dans le cas de la RMN des solides.

Chapitre 1

RMN en milieu anisotrope chiral

La préparation et la caractérisation de stéréoisomères purs constituent aujourd'hui un thème de recherche important en chimie. Une des motivations de ces recherches est l'importance de la synthèse asymétrique en pharmacologie. Suite à l'exemple tragique de la thalidomide, le cahier des charges imposé à l'industrie pharmaceutique est aujourd'hui des plus stricts : l'activité biologique de chaque énantiomère d'un principe actif doit être connue et testée. Mais l'importance de la synthèse asymétrique et de l'analyse stéréochimique ne se limite pas à la pharmacologie. Elles sont aujourd'hui utilisées dans de nombreux domaines de la chimie, depuis les arômes jusqu'à la chimie des matériaux (propriété optique, tacticité des polymères), en passant par l'agrochimie (herbicides, insecticides). D'un point de vue plus fondamental, l'analyse stéréochimique et la synthèse asymétrique jouent un rôle clef dans l'identification des mécanismes réactionnels chimiques et biochimiques.

Cependant, les méthodes d'analyse stéréochimique existantes (mesure de pouvoir rotatoire, HPLC chirale, RMN isotrope) ne sont pas toujours efficaces et générales. Les méthodes chiroptiques peuvent être faussées par la présence d'impuretés chirales. La séparation d'énantiomères par HPLC utilisant une phase stationnaire chirale est parfois relativement longue à mettre au point. Enfin, les méthodes de dosage énantiomérique par RMN isotrope nécessitent d'adapter l'agent énantiopur aux fonctionnalités de la molécule étudiée et sont peu efficaces pour les molécules dépourvues de groupement polaire. En outre, en milieu isotrope, les discriminations chirales observées par RMN sont souvent faibles par rapport aux largeurs de raies.

1.1 Analyse stéréochimique dans les cristaux liquides polypeptidiques

Dans ce contexte, l'équipe de RMN en milieu orienté de l'université Paris-Sud a développé une technique originale d'analyse stéréochimique utilisant la RMN en milieu anisotrope chiral [1]. Le principe de cette méthode est le suivant. Dans un milieu orienté chiral, deux énantiomères adoptent, en moyenne, des orientations différentes. La spectroscopie RMN permet de mettre en évidence cette différence d'orientation par l'intermédiaire des observables RMN anisotropes, telles que le CSA, l'interaction dipolaire et l'interaction quadripolaire pour les noyaux de spin $I \geq 1$.

Cette idée fut proposée pour la première fois en 1968 par Snyder *et coll.* [2]. Cependant, la phase cholestérique utilisée à l'époque présentait de nombreux inconvénients (peu homogène, mauvais solvant organique, énantiosélectivité…) et cette méthode fut rapidement abandonnée. Au début des années 1990, l'équipe de RMN en milieu orienté a repris les travaux de Snyder en testant d'autres phases liquides-cristallines chirales [50, 51]. À ce jour, les meilleurs résultats ont été obtenus avec les solutions organiques d'homopolypeptides de synthèse : le poly-(γ-benzyl-L-glutamate) (PBLG), le poly-(γ-ethyl-L-glutamate) (PELG), le poly-(ϵ-carbo-benzyloxy-L-lysine) (PCBLL) et le poly-(N-methyl-N'-(R-1-phenylethyl)) guanidine ((R)-PPEMG) [1, 52–54]. Ces polymères chiraux forment sur une large gamme de température une phase liquide-cristalline faiblement orientante avec un grand nombre de solvants organiques usuels ($CHCl_3$, CH_2Cl_2, DMF, THF, pyridine…). Ces phases présentent plusieurs propriétés avantageuses pour l'analyse stéréochimique :

1. Les paramètres d'ordre des solutés dissous à l'intérieur de ces phases sont faibles (de l'ordre de 10^{-5} à 10^{-2}). Ainsi, l'amplitude des interactions RMN anisotropes ne dépasse pas quelques milliers de hertz et est comparable à l'amplitude des interactions RMN isotropes, ce qui permet d'obtenir des spectres haute-résolution ;
2. La phase ainsi formée supporte une grande quantité de soluté (10-200 mg) sans perdre ses propriétés anisotropes ;
3. Ces cristaux liquides chiraux permettent de discriminer un grand nombre d'énantiomères, y compris ceux qui ne possèdent pas de groupement fonctionnel, tels que les hydrocarbures saturés [4]. En effet, contrairement aux méthodes de dosages énantiomériques par RMN isotrope, la RMN en milieu anisotrope chiral ne nécessite pas la formation de complexes diastéréoisomères entre les énantiomères étudiés et l'agent énantiopur (ici, le polymère). La chiralité du polymère conduit uniquement à une différence d'orientation entre énantiomères.

Au cours de ma thèse, la RMN dans les cristaux liquides polypeptidiques a, par exemple, été utilisée pour discriminer les énantiomères M et P de composés de type cyclotrivératrylène sous leur forme couronne [7]. Elle a aussi été utilisée pour déterminer la pureté énantiomérique de complexes (arène)chrome obtenus par une nouvelle réaction de couplage asymétrique [55].

1.2 Énantiomères de chiralité isotopique et prochiralité

La substitution d'un atome par son isotope peut suffire à rendre une molécule chirale. Nous parlons alors de chiralité isotopique. Les énantiomères de chiralité isotopique ont des structures très proches, mais ils peuvent présenter des réactivités distinctes en présence d'une substance énantiopure. Ainsi, des synthèses énantiosélectives et des résolutions cinétiques ont été réalisées pour des molécules chirales par substitution $^1H/^2H$ [56–58] ou même $^{12}C/^{13}C$ [59]. En outre, les réactions enzymatiques et les voies biosynthétiques sont connues pour leur énantiosélectivité dans le cas des molécules de chiralité isotopique [60]. Ainsi, la plupart des substances naturelles considérées habituellement comme prochirales comprennent en réalité des énantiomères de chiralité isotopique et il existe très souvent, dans les substances naturelles, un enrichissement en faveur de l'un des énantiomères de chiralité isotopique.

La discrimination des énantiomères de chiralité isotopique est cruciale pour l'étude stéréochimique des mécanismes réactionnels et des voies biosynthétiques [60, 61]. Les rapports isotopiques $^1H/^2H$ et les excès énantiomériques pour les molécules de chiralité isotopique représentent aussi une signature du mode voire du lieu de production des molécules organiques. Ainsi, la discrimination des énantiomères de chiralité isotopique pourrait permettre de perfectionner les méthodes d'authentification des substances organiques, telles que la méthode d'analyse SNIF-NMR [62–64]. Cette méthode permet déjà d'obtenir des informations fiables sur le mode de production synthétique ou naturel d'un composé et les traitements technologiques, qu'il a pu subir. Pour des composés naturels, il est possible d'identifier l'organisme qu'il l'a produit et l'origine géographique de cet organisme [65, 66]. Cependant, pour les composés de chiralité isotopique, la méthode SNIF-NMR actuelle repose uniquement sur la mesure des rapports isotopiques moyens pour les deux énantiomères. La mesure de la pureté énantiomèrique pour ces composés permettra sans aucun doute d'accroître la sélectivité et la fiabilité de la méthode SNIF-NMR.

La discrimination des énantiomères de chiralité isotopique est, cependant, difficile. Les méthodes de HPLC chirale ne sont efficaces que pour un petit nombre de composés [67]. Les méthodes chiroptiques sont généralement difficiles à appliquer en raison de la faible différence de pouvoir rotatoire entre ces énantiomères et de la faible intensité du dichroïsme circulaire [68]. La méthode standard utilisée par les chimistes organiciens pour différencier des énantiomères de chiralité isotopique consiste à utiliser des agents chiraux de dérivation, ce qui nécessite de faire réagir le mélange d'énantiomères avec un réactif énantiopur [68, 69]. Cependant, les discriminations chirales observées sont faibles. À l'inverse, la RMN en milieu anisotrope chiral conduit à des discriminations spectrales importantes entre énantiomères de chiralité isotopique et ne nécessite pas la présence de fonction chimique particulière [5].

Il a été montré, par RMN du ^{2}H, que ces discriminations entre énantiomères de chiralité isotopique sont identiques à celles observées entre directions énantiotopes au sein des molécules prochirales analogues perdeutérées [5]. Ceci a été confirmé, au cours de ma thèse, par l'utilisation de la RMN du ^{13}C [6].

Pour comprendre les discriminations entre énantiomères de chiralité isotopique, il est donc nécessaire d'élucider l'origine des discriminations entre directions énantiotopes au sein des molécules prochirales. Des directions énantiotopes sont des directions interatomiques échangeables par une rotation impropre de symétrie (S_n) mais pas par une rotation propre. Dans une phase anisotrope chirale, des énantiotopes d'une molécule adoptent *a priori* des orientations moyennes différentes. Cependant, cette différence d'orientation n'est pas toujours visible par RMN.

Les discriminations énantiotopiques observables par RMN dans les cristaux liquides chiraux n'ont pas exactement la même origine dans le cas des molécules rigides et flexibles. Par molécule rigide, nous entendons un composé qui adopte une conformation unique à l'échelle de temps de la RMN. Dans ce cas, la différence d'orientation entre discriminations énantiotopiques est observable par RMN, uniquement si le nombre de paramètres d'ordre moléculaire indépendants diffère entre les phases orientées chirales et achirales. Il a été montré que cette condition n'était satisfaite que pour les solutés prochiraux, non-plans, de symétrie C_s, $C_{2\mathrm{v}}$, $D_{2\mathrm{d}}$ et S_4 [70–72]. En revanche, aucune discrimination énantiotopique n'est observable pour les molécules rigides appartenant à d'autres groupes de symétrie [73].

Pour les molécules prochirales flexibles, qui adoptent des conformations énantiomères à l'échelle de temps de la RMN, l'origine des discriminations énantiotopiques est différente. Tout d'abord, ces discriminations n'ont pas pour origine une différence de population entre conformères énantiomères. En effet, il a été montré expérimentalement que les faibles interactions entre la phase liquide-cristalline chirale et le soluté ne suffisent pas à déplacer l'équilibre entre énantiomères [11,74]. Les discriminations énantiotopiques observées résultent en réalité d'une différence d'orientation entre conformères énantiomères. Dans le cas où le nombre d'observables RMN est suffisant, il est possible de calculer l'ensemble des paramètres d'ordre des conformères énantiomères [7]. Néanmoins, nous avons montré que les discriminations énantiotopes pour les composés flexibles peuvent être prédites de façon qualitative en invoquant une structure moyenne. Nous avons introduit une définition rigoureuse de cette structure moyenne et avons montré comment elle peut être calculée de façon exacte à partir de la structure et de la population des différents conformères [10]. Cette structure moyenne appartient à un groupe de symétrie ponctuel, qui peut être déterminé à partir de la symétrie des différents conformères et des changements de conformations [7, 8]. Dans de nombreux cas, cette symétrie moyenne, alliée à des raisonnements intuitifs, permet de prédire la structure moyenne et le nombre de discriminations énantiotopiques observables. Ces différentes avancées permettent aujourd'hui de proposer une description qualitative satisfaisante des phénomènes de discriminations entre les directions énantiotopes ou les énantiomères de chiralité isotopique au sein des milieux anisotropes chiraux.

1.3 Analyse de la dynamique conformationnelle

Nous avons démontré les potentialités de la RMN en milieu anisotrope chiral pour l'étude de la dynamique conformationnelle [11, 12]. Nous avons montré que cette méthode permet d'observer l'interconversion entre énantiomères, énantiomères de chiralité isotopique ou directions énantiotopes de molécules prochirales, ce qui est impossible en milieu achiral. En outre, l'analyse des spectres ^{2}H a permis de déterminer les constantes de vitesse associées à la rotation intramoléculaire autour de liaison simple entre atomes de carbone hybridés sp^2. Comme les phases liquides-cristallines polypeptidiques utilisées sont stables sur une large gamme de températures (de 210 à 355 K pour les phases PBLG/CHCl$_3$), il est possible de déterminer les paramètres d'activation associés à ces changements de conformation. L'excellent accord entre les enthalpies d'activation déterminées par RMN dans les cristaux liquides chiraux et par modélisation démontre que les interactions entre la phase et le soluté dans les milieux faiblement orientants ne sont pas suffisantes pour affecter la dynamique conformationnelle.

Ces expériences illustrent aussi, de façon éclatante, comment les concepts de stéréochimie, tels que l'isomérie, la chiralité ou l'énantiotopicité, impliquent le choix d'une vitesse limite d'interconversion entre les structures isomères ou les éléments énantiotopes. Ainsi, nous avons étudié des molécules, qui peuvent être considérées, du point de vue de la RMN, comme chirales en dessous de la température de coalescence et achirale au dessus de cette température. Cette nécessité du choix d'une vitesse limite a notamment été discutée par Eliel [75].

1.4 Attribution des spectres ^{2}H en milieu anisotrope

La RMN du ^{2}H constitue une des meilleures sondes locales de l'orientation et de la dynamique dans la matière molle et les solides. En effet, cette méthode bénéficie de plusieurs avantages :

i. Les atomes d'hydrogène sont présents sur de nombreux sites des molécules organiques. La RMN du ^{2}H permet donc de sonder a priori différents groupements d'une molécule organique ;
ii. L'amplitude de la constante de couplage quadripolaire ^{2}H (de l'ordre de 170 kHz) est plus élevée que celles des principales interactions RMN anisotropes rencontrées dans les composés organiques (couplages dipolaires ^{1}H–^{1}H, ^{1}H–^{13}C ou CSA ^{13}C). Par conséquent, l'interaction quadripolaire ^{2}H est une des observables RMN anisotropes les plus sensibles aux paramètres d'ordre moléculaire ;
iii. Cette interaction est suffisamment faible pour que les vitesses de relaxation et les largeurs de raies soient très inférieures aux différences d'éclatements quadripolaires. Ainsi, il est possible en général de résoudre les signaux associés aux différents sites ^{2}H présents dans l'échantillon ;
iv. Le faible rapport gyromagnétique de ce noyau conduit à des couplages dipolaires ^{2}H–^{2}H faibles, ce qui simplifie l'allure des spectres.

Dans le cas des milieux anisotropes chiraux, la RMN du ^{2}H est généralement la méthode qui permet de mettre en évidence les différences d'orientation les plus faibles entre énantiomères ou directions énantiotopes. En outre, en dépit du faible rapport gyromagnétique de cet isotope et de sa faible abondance isotopique naturelle ($1,15 \times 10^{-2}$ %), il est possible aujourd'hui d'enregistrer des expériences ^{2}H en abondance naturelle [76, 77].

L'utilisation de la RMN du ^{2}H dans les milieux faiblement orientant est, cependant, limitée par la complexité des spectres ^{2}H pour les molécules polydeutérées ou en abondance naturelle. Pour surmonter ce problème d'attribution, différentes techniques RMN multidimensionnelles ont été développées. Elles peuvent être classées en trois catégories :

- les expériences d'autocorrélation 2D et 3D ^{2}H,
- les expériences de corrélation 2D ^{2}H–^{13}C,
- les expériences de corrélation 2D ^{2}H–^{2}H.

1.4.1 Autocorrélation 2D et 3D ^{2}H

Nous avons tout d'abord introduit de nouvelles expériences RMN 2D et 3D d'autocorrélation ^{2}H. Ces méthodes permettent d'apparier les deux composantes de chaque doublet quadripolaire et d'attribuer les signaux deutérium sur la base d'une différence de déplacement chimique. Ces expériences RMN multidimensionnelles ont l'avantage d'être utilisables en abondance naturelle ^{2}H. Cependant, les séquences 2D d'autocorrélation Q-résolue et Q-COSY présentaient un défaut majeur : elles ne pouvaient pas être phasées, ce qui limitait la résolution spectrale [78]. Pour surmonter ce problème, nous avons montré qu'il suffit d'ajouter un filtre gradient-z aux séquences existantes, ce qui permet d'obtenir des spectres 2D d'autocorrélation ^{2}H phasés [13]. Ces expériences ont été utilisées pour l'attribution des spectres ^{2}H en abondance naturelle [7, 9]. Pour simplifier encore d'avantage l'attribution des spectres RMN ^{2}H, nous avons introduit ensuite des expériences RMN 3D d'autocorrélation ^{2}H [14]. En particulier, nous avons proposé une version 3D des expériences 2D double-quantum ^{2}H [78]. Cette variante 3D de la séquence INADEQUATE a l'avantage, contrairement aux spectres 2D correspondants, d'être quantitative et de permettre la mesure de la pureté énantiomérique d'un composé chiral. Cette séquence a été appliquée en abondance naturelle ^{2}H [77].

1.4.2 Corrélation ^{2}H–^{13}C

Si les expériences d'autocorrélation ^{2}H ont l'avantage d'être utilisables en abondance naturelle, leur résolution est limitée par la faible gamme des déplacements chimiques ^{2}H. Il est alors tentant d'explorer d'autres stratégies pour l'attribution des signaux ^{2}H.

Une possibilité consiste à corréler les éclatements quadripolaires ^{2}H aux déplacements chimiques ^{13}C. En effet, les spectres ^{13}C sont plus faciles à analyser que les spectres ^{2}H et ce pour deux raisons :

i. La gamme de déplacements chimiques ^{13}C ($\approx$ 200 ppm) est 100 fois plus importante que celle des noyaux ^{2}H ($\approx$ 20 ppm) ;

ii. Dans les cristaux liquides chiraux, les discriminations chirales ^{13}C sont généralement inférieures aux différences de déplacement chimique entre sites ^{13}C.

Différentes expériences de corrélation hétéronucléaire (HETCOR) ^{2}H–^{13}C ont été proposées pour les solides et la matière molle. Une première possibilité consiste à utiliser un transfert par polarisation croisée des noyaux ^{2}H vers les noyaux ^{13}C [79, 80]. Cependant, ce type de transfert est difficile à réaliser techniquement pour des solutés faiblement orientés, au sein desquels les couplages ^{2}H–^{13}C sont faibles. En effet, pour le transfert de polarisation croisée, l'écart à la condition de Hartmann-Hahn doit être inférieur au couplage dipolaire hétéronucléaire.

Une autre possibilité consiste à utiliser des transferts de type INEPT [10,16,17] ou HMQC [81, 82] via les couplages J et dipolaires. Dans le cas des expériences

HETCOR ^{2}H–^{13}C pour les solutés faiblement orientées, le transfert INEPT avec détection ^{13}C s'est révélé être la méthode la plus sensible [16]. Les expériences HETCOR ^{2}H–^{13}C avec transfert INEPT ont ainsi permis de faciliter l'attribution des spectres ^{2}H de molécules polydeutérées [10,16,17]. Dans les phases anisotropes chirales, elles permettent aussi d'apparier les signaux ^{13}C et ^{2}H associés à un même énantiomère ou à un même élément énantiotope, ce qui facilite le calcul des paramètres d'ordre moléculaire. Cependant, compte tenu de la sensibilité des spectromètres RMN actuels, il n'est pas possible d'appliquer ces méthodes pour des composés en abondance isotopique naturelle.

1.4.3 Corrélation ^{2}H–^{2}H

Les expériences de corrélation homonucléaire (HOMCOR) ^{2}H–^{2}H permettent de corréler les éclatements quadripolaires de noyaux deutérium couplés ou au moins reliés par une chaîne ininterrompue de couplage. Cette stratégie fournit des informations supplémentaires par rapport aux expériences d'autocorrélation ^{2}H ou de corrélation ^{2}H–^{13}C. En particulier, elle permet, pour un mélange de plusieurs molécules, d'apparier les signaux ^{2}H associés aux différents constituants. Dans les milieux anisotropes chiraux, cette méthode permet de séparer les signaux ^{2}H associés à chaque énantiomère [16] ou de distinguer les stéréoisomères *like* et *unlike* [18]. Compte tenu de la sensibilité actuelle des spectromètres RMN, ces expériences HOMCOR ^{2}H ne sont réalisables que pour des molécules enrichies en deutérium.

Les expériences HOMCOR ^{2}H les plus simples consistent à corréler les noyaux ^{2}H via les couplages dipolaires ^{2}H–^{2}H [16, 18, 83]. Cependant, dans les milieux anisotropes faiblement orientants, les couplages dipolaires ^{2}H–^{2}H sont souvent nuls ou trop faibles pour donner lieu à des pics de corrélation sur les cartes 2D COSY ^{2}H–^{2}H. Pour pallier à la faible efficacité des transferts directs ^{2}H–^{2}H, nous avons proposé des séquences HOMCOR ^{2}H utilisant des relais par les noyaux ^{13}C ou ^{1}H [19, 20]. Cela a nécessité le calcul de l'évolution de la matrice-densité pour une paire de spin IS avec $I = 1$ et $S = 1/2$ sous l'effet des couplages scalaires et dipolaires hétéronucléaires. Dans ce but, nous avons décomposé la matrice-densité sur une base d'opérateurs-produits adaptés et nous avons déterminé les règles d'évolution de l'ensemble de ces opérateurs sous l'effet des couplages [19]. La possibilité de corréler des noyaux ^{2}H par des relais ^{13}C et ^{1}H a été démontré experimentalement pour des molécules polydeutérées en abondance naturelle ^{13}C. Le temps d'expérience nécessaire est inférieur à 15 heures.

1.5 Perspectives

La RMN dans les cristaux liquides polypeptidiques constitue aujourd'hui une des méthodes d'analyse énantiomérique et énantiotopique parmi les plus générales et les plus efficaces. Plusieurs développements dans ce domaine sont attendus. Certains sont discutés ci-dessous, même si cette thématique n'est plus aujourd'hui au coeur de mes activités de recherche.

Une première limitation de la RMN dans les milieux anisotropes chiraux est l'impossibilité d'utiliser les cristaux liquides polypeptidiques à base de solvants organiques pour l'analyse stéréochimique des composés hydrosolubles. Il est donc souhaitable de trouver des milieux anisotropes faiblement orientants, capables de dissoudre et de discriminer un grand nombre d'énantiomères hydrosolubles. Les études réalisées jusqu'ici sur les milieux anisotropes chiraux tendent à montrer qu'il est nécessaire d'utiliser des polymères de structure hélicoïdal pour observer des discriminations chirales importantes. Les gels étirés de gélatine [84] ou de carraghénane [85] ainsi que les cristaux liquides d'ADN [86] possèdent les caractéristiques recherchées et ont déjà permis de discriminer les énantiomères de l'alanine. Il reste à tester la généralité de cette technique en l'appliquant à différentes classes de molécules chirales et prochirales hydrosolubles (acides, polyalcools, amines, sulfates, carbamates. . .).

La RMN du ^{2}H est actuellement la méthode conduisant aux discriminations spectrales les plus grandes entre énantiomères ou directions énantiotopes. Cependant, elle souffre de deux limitations majeures : une faible sensibilité en abondance naturelle et une faible gamme de déplacement chimique, ce qui rend plus difficile la résolution des différents sites deutérium. Différentes alternatives peuvent être envisagées. La solution la plus simple consiste à utiliser la RMN ^{13}C découplé des protons. Dans ce cas, les énantiodiscriminations observées correspondent à des différences de CSA ^{13}C [87]. Cependant, l'emploi de cette méthode est limitée par les faibles énantiodiscriminations observées, en particulier pour les atomes ^{13}C hybridés sp^{3} et pour des champs magnétiques modérés. Une autre possibilité consiste à observer des énantiodiscriminations sur la base d'une différence de couplages dipolaires ^{1}H–^{1}H [88]. Si cette méthode bénéficie d'une sensibilité élevée, la faible gamme des déplacements chimiques ^{1}H et les couplages multiples ^{1}H–^{1}H limitent la résolution spectrale et peuvent masquer les énantiodiscriminations. Des séquences permettant de sélectionner certains couplages ^{1}H–^{1}H ont été proposées. Cependant, comme elles utilisent des impulsions sélectives, elles ne sont applicables que lorsqu'un signal ^{1}H est suffisamment isolé pour pouvoir être excité sélectivement [89, 90]. La mesure des couplages dipolaires ^{1}H–^{13}C est l'alternative la plus prometteuse à la RMN du ^{2}H en abondance naturelle. Premièrement, cette interaction RMN est sensible à l'ordre orientationnel, puisque la constante de couplage dipolaire pour une liaison covalente ^{1}H–^{13}C est de l'ordre de 110 kHz, soit 65 % de la constante de couplage quadripolaire ^{2}H (170 kHz). Deuxièmement, les expériences permettant de mesurer les couplages ^{1}H–^{13}C sont au moins 100 fois plus sensibles, en terme de rapport signal sur bruit, que la RMN du ^{2}H en abondance naturelle. Néanmoins, l'utilisation des couplages dipolaires ^{1}H–^{13}C à une liaison, $^{1}D_{HC}$, est encore limitée par deux difficultés :

i. Les couplages dipolaires ^{1}H–^{13}C à longue distance peuvent masquer les discriminations chirales ;

ii. L'ordre orientationnel dans les cristaux liquides chiraux correspond à une situation intermédiaire où l'amplitude des $^{1}D_{HC}$ est comparable à celle des couplages $^{1}J_{HC}$. Par conséquent, l'amplitude du couplage total $^{1}T_{HC} = {}^{1}J_{HC} + {}^{1}D_{HC}$ varie entre 0 et quelques centaines de Hz, ce qui complique l'observation sélective des couplages ^{1}H–^{13}C à une liaison.

Des méthodes utilisant des impulsions sélectives ont été proposées [91] mais elles ne sont applicables que s'il existe au moins un signal ^{1}H isolé. Ainsi, il n'y a pas actuellement de méthode générale pour la mesure des couplages ^{1}H–^{13}C dans les cristaux liquides polypeptidiques.

Un autre défi important est la détermination de la configuration absolue en utilisant la RMN dans les milieux anisotropes chiraux. La solution de ce problème nécessite la prédiction des spectres RMN de chaque énantiomère dans le milieu anisotrope chiral. Une première possibilité est bien sûr d'utiliser une méthode de corrélation chimique et d'enregistrer les spectres de composés chiraux analogues, dont la configuration absolue est connue [92]. Cette méthode est, cependant, relativement exigeante car elle requiert la synthèse de nouveaux composés. En outre, le choix des analogues n'est pas toujours simple car de faibles modifications structurales peuvent influer sur l'orientation moléculaire. Une voie prometteuse consiste à utiliser des méthodes de simulation moléculaire pour prédire les orientations des deux énantiomères au sein de la mésophase [93]. Comme l'ordre orientationnel est une propriété à l'équilibre, il est possible d'employer soit des méthodes de type Monte-Carlo ou de dynamique moléculaire. Les paramètres utilisés pour les simulations pourront être optimisés sur des petites molécules de soluté. En particulier, l'hydrogène moléculaire et ses isotopomères se sont révélés être des composés de choix pour sonder le champ électrostatique au sein des mésophases [94].

Si la détermination de la configuration absolue par RMN en milieu anisotrope chiral en est encore à ses balbutiements, la mesure des couplages dipolaires en milieu anisotrope est aujourd'hui largement utilisée pour déterminer la structure tridimensionnelle des petites molécules organiques rigides [95] et des macromolécules [96]. Les couplages dipolaires en milieu orienté fournissent des informations sur l'orientation des directions interatomiques par rapport au directeur de la phase. Ainsi, pour les molécules rigides, il est possible de déterminer l'orientation relative de paires éloignées d'atomes au sein de la molécule. Ces contraintes à longue distance sont complémentaires des informations structurales à courte distance obtenues par RMN en milieu isotrope à partir des couplages ^3J [97], des corrélations par l'effet Overhauser nucléaire (NOE) [98] et des informations angulaires obtenues par relaxation croisée [99]. En particulier, la mesure des couplages dipolaires permet de préciser la configuration relative d'éléments stéréogènes présents au sein d'une même molécule [100, 101]. Si cette approche a été validée pour plusieurs molécules rigides, son utilisation reste plus limitée pour les molécules flexibles. En effet, il s'agit alors souvent d'un problème sous-déterminé, où le nombre d'observables RMN est inférieur au nombre de paramètres nécessaires pour décrire le système (paramètres d'ordre des différents conformères [102] ou des différentes parties rigides de la molécule [103, 104]). Devant ce constat, il pourrait être intéressant de supplémenter les couplages dipolaires par la mesure des éclatements quadripolaires ^{2}H, qui sont plus sensibles à l'ordre orientationnel. Ceci nécessitera le calcul des constantes de couplages quadripolaires par DFT au sein de la mésophase.

Il est aussi intéressant de s'interroger sur les possibilités offertes par la RMN des solides pour l'analyse stéréochimique. La détermination de la configuration relative bénéficiera sûrement des développements récents en cristallographie RMN [105, 106]. En effet, en phase solide, les changements de conformations sont considérablement ralentis, voire empêchés, ce qui permet de corréler plus facilement la configuration d'un site à celle d'un autre site distant. En outre, la RMN des solides bénéficie de deux avantages supplémentaires. Premièrement, elle permet de s'affranchir des problèmes de solubilité. Deuxièmement, le produit chiral étudié peut être réutilisé facilement pour des opérations ultérieures d'analyse ou de synthèse. La cristallographie RMN constitue aussi une méthode possible pour la mesure de la pureté énantiomérique. En effet, pour les racémiques vrais, qui représentent 90 % des composés chiraux connus [107], le composé racémique et les énantiomères purs cristallisent selon des mailles de symétries distinctes. Cette différence de symétrie peut être observée par RMN des solides à travers de différence de déplacement chimique [108] ou de couplages dipolaires [109]. Là encore, l'utilisation des nouvelles méthodes de cristallographie RMN en abondance naturelle pourra permettre de généraliser cette approche.

1.6 Articles

J|A|C|S
JOURNAL OF THE AMERICAN CHEMICAL SOCIETY

Article

Enantiodiscrimination in Deuterium NMR Spectra of Flexible Chiral Molecules with Average Axial Symmetry Dissolved in Chiral Liquid Crystals: The Case of Tridioxyethylenetriphenylene

Philippe Lesot, Olivier Lafon, Herbert Zimmermann, and Zeev Luz

J. Am. Chem. Soc., **2008**, 130 (27), 8754-8761• DOI: 10.1021/ja800957a • Publication Date (Web): 11 June 2008

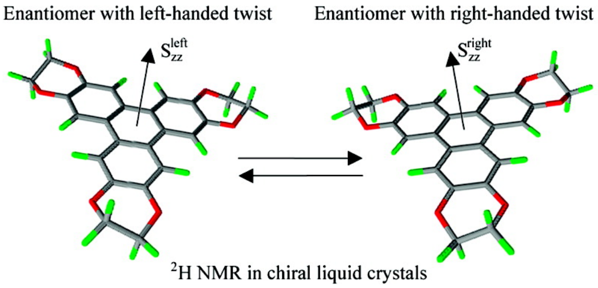

J|A|C|S
ARTICLES

Enantiodiscrimination in Deuterium NMR Spectra of Flexible Chiral Molecules with Average Axial Symmetry Dissolved in Chiral Liquid Crystals: The Case of Tridioxyethylenetriphenylene

Philippe Lesot,*,† Olivier Lafon,†,‖ Herbert Zimmermann,‡ and Zeev Luz*,§

Université de Paris-Sud (XI), Laboratoire de Chimie Structurale Organique, RMN en Milieu Orienté, ICMMO, CNRS UMR 8182, Bât. 410, 91405 Orsay cedex, France, Max-Planck-Institut für Medizinische Forschung, Abteilung Biophysik, Jahnstrasse 29, 69120 Heidelberg, Germany, and Weizmann Institute of Science, Department of Chemical Physics, Rehovot 76100, Israel

Received February 7, 2008; E-mail: philesot@icmo.u-psud.fr; zeev.luz@weizmann.ac.il

Abstract: Flexible chiral molecules undergoing fast interconversion (on the NMR time scale) between different conformational enantiomers may yield "average" axial species with enantiotopically related sites. Contrary to the situation observed for rigid axial molecules, signals from these enantiotopic sites in NMR spectra recorded in chiral liquid-crystalline solvents can be resolved. In the present work, we studied the deuterium NMR spectra of tridioxyethylenetriphenylene (compound **4**) statistically deuterated to 10% in the flexible side chains and dissolved in chiral and achiral lyotropic liquid crystals based on poly(γ-benzylglutamate). The fast chair–chair flipping of the side chains in **4** on average renders the molecule axially symmetric (D_{3h}) with pairs of enantiotopic ethylene deuterons. These deuterons exhibit unusually large enantiodiscrimination. To explain this observation, we first describe how the average symmetry of flexible molecules can be derived from the symmetry of the "frozen" conformers and the nature of the averaging process. The procedure is then applied to **4** and used to analyze the NMR results. It is shown that the large enantiodiscrimination in the present case reflects a large difference in the orientational ordering of the conformational enantiomers participating in the interconversion processes as well as a large geometrical factor due to the special shape of the dioxyethylene side groups. ^{1}H and ^{13}C NMR spectra of **4** in the same lyotropic liquid crystalline solvent are analyzed to determine its ordering characteristics. Several related cases are also discussed.

Introduction

It is well-known that enantiodiscrimination in the NMR spectra of chiral or prochiral solutes is observed more often and is much more pronounced in chiral liquid-crystalline (CLC) solvents[1,2] than in chiral isotropic solvents, in which such discrimination is relatively rare.[3] By the general term spectral enantiodiscrimination we mean the doubling of the NMR spectra of racemic mixtures (*enantiomeric* discrimination) or the splitting of signals corresponding to enantiotopic sites in prochiral molecules (*enantiotopic* discrimination). In chiral isotropic solvents, enantiomeric discrimination usually results from differences in the isotropic NMR observables of the enantiomers. In the absence of very specific forces, solute–solvent interactions are too weak to significantly affect chemical shifts and J couplings, so spectral enantiodiscrimination is very small or absent. For the same reasons, only a few examples of enantiotopic discrimination in isotropic NMR have been reported in the literature.[3] In a CLC solvent, an additional factor affects the discrimination, namely, the different orientational orderings of the different enantiomers of the solute. This ordering modifies the NMR spectrum of the solute by affecting anisotropic terms in the spin Hamiltonian, such as chemical-shift anisotropy (CSA), quadrupolar interactions (for nuclei with $I \geq 1$), and intramolecular dipole–dipole interactions.[4] In practice, the numerous dipolar interactions of protons with other protons or with carbon-13 nuclei often result in spectra that are too complex to analyze, even if simplifying two-dimensional (2D) NMR methods are used.[5] For this reason, one commonly uses ^{2}H-{^{1}H} and ^{13}C-{^{1}H} NMR techniques, which exhibit simple spectra with discrimination due to dispersion in the quadrupolar interaction ($I = 1$ for ^{2}H) and the CSA, respectively. Likewise, the reduction of the effective symmetries of prochiral solutes

---

† Université de Paris-Sud (XI).
‡ Max-Planck-Institut für Medizinische Forschung.
§ Weizmann Institute of Science.
‖ Present address: Université de Lille 1, ENSCL, UCCS, CNRS UMR 8181, 59652 Villeneuve d'Ascq, France.

(1) Sarfati, M.; Lesot, P.; Merlet, D.; Courtieu, J. *Chem. Commun.* **2000**, 2069.
(2) Aroulanda, C.; Sarfati, S.; Courtieu, J.; Lesot, P. *Enantiomer* **2001**, *6*, 2081.
(3) Bilz, A.; Stork, T.; Helmchen, G. *Tetrahedron: Asymmetry* **1997**, *8*, 3999.
(4) (a) Emsley J. W. In *NMR of Liquid Crystals*; Emsley, J. W., Ed.; Reidel: Dordrecht, The Netherlands, 1985; (b) Emsley, J. W. In *Encyclopedia of NMR*; Grant, D. M., Harris, R. K., Eds.; John Wiley & Sons: Chichester, U.K.: 1995; p 2781.
(5) (a) Farjon, J.; Merlet, D.; Lesot, P.; Courtieu, J. *J. Magn. Reson.* **2002**, *158*, 169. (b) Farjon, J.; Baltaze, J.-P.; Lesot, P.; Merlet, D.; Courtieu, J. *Magn. Reson. Chem.* **2004**, *42*, 594. (c) Ziani, L.; Courtieu, J.; Merlet, D. *J. Magn. Reson.* **2006**, *183*, 60. (d) Uday, R. P.; Bikash, B.; Suryaprakash, N. *J. Phys. Chem. B* **2007**, *111*, 12403.

10.1021/ja800957a CCC: $40.75

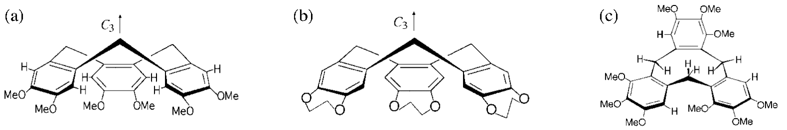

(1) (2) (3)

Figure 1. Structural formulas of (a) hexamethoxytribenzocyclononatriene (**1**), commonly called cyclotriveratrylene (CTV), which is the parent compound of the CTV series; (b) the tridioxyethylene derivative of CTV (**2**), in which the flexible dioxyethylene groups undergo fast chair−chair switches (see Figure 2b); and (c) the saddle isomer of nonamethoxy-CTV (**3**), which is a flexible molecule that undergoes rapid pseudorotation involving six isodynamic conformers.

when they are dissolved in CLC solvents renders the enantiotopically related sites nonequivalent.[6–8] Both types of spectral discrimination have been amply studied, particularly in lyotropic liquid crystals based on solutions of poly(γ-benzyl-L-glutamate) (PBLG) in suitable organic cosolvents (chloroform, DMF, etc.).[1] These chiral nematic-phase solvents proved extremely useful in studying enantiodiscrimination of a large range of chiral solutes, including chiral hydrocarbons.[9]

A common feature of these studies is that rigid prochiral compounds having a C_n symmetry axis with $n \geq 3$ do not exhibit enantiotopic discrimination, even though such discrimination is consistent with the general principles of chirality.[6] For example, in CLC solutions of the rigid-crown isomer of cyclotriveratrylene (CTV, compound **1** in Figure 1a), no splittings are observed in the $^{13}\text{C-}\{^1\text{H}\}$ or $^2\text{H-}\{^1\text{H}\}$ NMR spectra for nuclei which are related by the molecular vertical symmetry planes.[10] When such axial molecules are dissolved in achiral nematic liquid crystals, their ordering is characterized by a single independent order parameter, S_{zz}, which corresponds to the degree of alignment of the molecular C_n axis in the mesophase. This situation remains unchanged when such a solute is dissolved in a CLC solvent, since C_n (a symmetry element of the first kind) remains a symmetry axis in a chiral environment.[6] Consequently, sites that are enantiotopically related remain degenerate in CLC solution unless the chiral environment exerts forces that are sufficiently strong to twist the solute's geometrical or electronic structure, thereby selectively modifying the magnetic parameters of the enantiotopic sites. As indicated above, such effects have not been observed experimentally to date.

The situation is different for flexible molecules that on average possess axial symmetry (C_n with $n \geq 3$). By "flexible" we mean that the molecule rapidly (on the NMR time scale) interconverts between two or more conformations having similar energies. Below we shall define in a precise way what we mean by "average" symmetry, but for now we will simply say that this term refers to the symmetry of the spin Hamiltonian that describes the NMR spectrum in the fast-exchange regime. In contrast to rigid axial molecules, there are several known examples of flexible molecules having average axial symmetry that exhibit enantiodiscrimination of sites that on average are enantiotopically related. Two such previously studied examples are compounds **2** and **3**, whose structures are shown in panels b and c, respectively, of Figure 1. In tridioxyethylene-CTV (**2**), the rapid flipping of the dioxyethylene groups results in an average C_{3v} symmetry for the molecule and renders the ethylene hydrogens pairwise-enantiotopic, as explained in the section entitled Comparison with Related Systems (see below) and in ref 10. In the $^2\text{H-}\{^1\text{H}\}$ NMR spectra of **2**, these ethylene deuterons indeed exhibit two doublets in achiral liquid-crystalline solutions but four doublets in CLC solutions.[10] Similarly, the saddle form of nonamethoxy-CTV (**3**) undergoes rapid pseudorotation, resulting in an average C_{3h} symmetry with the methylene hydrogens related pairwise-enantiotopically. In the deuterium NMR spectra of **3** in achiral liquid crystals, the methylene deuterons exhibit a single doublet, while two doublets are observed in CLC solutions.[11] The origin of the enantioseparation in these compounds stems from the fact that the interconverting species comprises different enantiomeric conformers that experience different orientational orderings in the chiral mesophases. As a result, sites that in the average molecule are enantiotopically related actually experience different "histories", and when the bookkeeping is complete, they yield different average quadrupolar interactions.

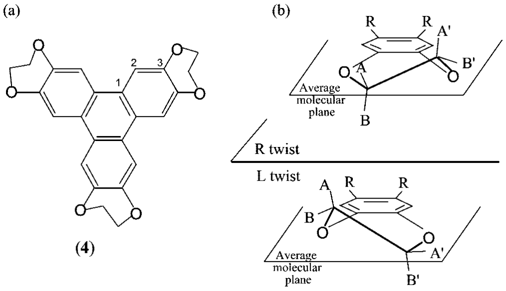

(4)

Figure 2. (a) Structural formula of tridioxyethylenetriphenylene (**4**), showing the numbering used for the aromatic carbon atoms. (b) The two interconverting chair conformations of the dioxyethylene side groups and the labeling of their hydrogens. The "average molecular plane" is the plane of the triphenylene core.

In this paper, we generalize the discussion of the origin of enantiotopic discrimination in flexible molecules with average axial symmetry. We first discuss how the average symmetry can be derived from the symmetry of the individual conformers and the nature of the dynamic process. New experimental results for tridioxyethylenetriphenylene (**4**) (see Figure 2a) are then presented and analyzed in terms of these symmetry considerations. In this example, the spectral discrimination of the

---

(6) Merlet, D.; Emsley, J. W.; Lesot, P.; Courtieu, J. *J. Chem. Phys.* **1999**, *111*, 6890.

(7) Aroulanda, A.; Merlet, D.; Courtieu, J.; Lesot, P. *J. Am. Chem. Soc.* **2001**, *123*, 12059.

(8) Merlet, D.; Loewenstein, A.; Smadja, W.; Courtieu, J.; Lesot, P. *J. Am. Chem. Soc.* **1998**, *120*, 963.

(9) Lesot, P.; Sarfati, M.; Courtieu, J. *Chem.—Eur. J.* **2003**, *9*, 1724.

(10) Lesot, P.; Merlet, D.; Sarfati, M.; Courtieu, J.; Zimmermann, H.; Luz, Z. *J. Am. Chem. Soc.* **2002**, *124*, 10071. Note that in this paper, there is a printing mistake in the labels of hydrogens A and B in the sentence just below eq 10.

(11) Lafon, O.; Lesot, P.; Zimmermann, H.; Poupko, R.; Luz, Z. *J. Chem. Phys. B.* **2007**, *111*, 9453.

enantiotopic sites of the average molecule is exceptionally large. This apparently results from the relatively large difference in the ordering characteristics of interchanging enantiomers as well as from the special chair geometry of their side groups.

Symmetry of Chiral Flexible Molecules

To identify the symmetry of the spin Hamiltonian of a rapidly interconverting molecular species, or more generally, the average symmetry of such a flexible molecule, it is usually sufficient to use intuition or apply simple inspection methods. However, it is useful to support such assignments by means of a more formal procedure. The symmetry of flexible molecules was extensively discussed in the 1960s,[12] mainly in connection with vibrational−rotational spectroscopy but also for NMR.[13,14] To date, however, no special attention has been paid to the family of processes in which rapidly interconverting chiral conformers yield on-average achiral (but possibly prochiral) species. Here we are particularly interested in processes where the average structures have axial symmetry. In such cases, the symmetries of the fixed (frozen) conformers are limited to (proper) point groups lacking symmetry elements of the second kind, while some of the dynamic processes are isomorphic with just such operations. For our present discussion, it is convenient to use the formalism developed by Altmann.[15] Although this formalism met with some criticism, it is still adequate (and useful) for the specific examples treated here.[16–18]

We consider a set of two or more equivalent chiral conformers that are rapidly interconverting on the NMR time scale. The symmetry group of the frozen conformers, G, is called the Schrödinger group. Since we are interested in chiral molecules, G is a proper group in all of our cases. By "equivalent conformers" we mean conformers having identical structures, namely, identical numbers of A−B-type bonds with the same lengths (where A and B represent atoms). In an achiral environment, all of the conformers therefore have identical energies and are termed isodynamic. For reasons discussed in the Introduction, we shall assume that this equivalence also holds for enantiomers in chiral environments, even though in principle they may have slightly different geometries and energies in such solvents. The operations that permute one isodynamic conformer into another are called isodynamic operations. The set of all such permutations form a group that is called the isodynamic group, I. Except for the identity element, this group has no elements in common with G. In simple cases, isodynamic groups are often isomorphic with symmetry point groups. Altmann's method is particularly convenient to apply in such cases. For chiral molecules undergoing racemization, these groups clearly contain elements that are isomorphic with improper symmetry operations, since they represent interconversions between enantiomers.

To discuss the situation in the fast-exchange regime, it is convenient to introduce the Schrödinger supergroup, S. According to Altmann,[15] S is the semidirect product of I and G:

$$S = I \wedge G \tag{1}$$

If the isodynamic operations are feasible, as is clearly the case in the fast-NMR regime, then S reflects the effective symmetry of the average molecule. In particular, it is isomorphic with the symmetry of the spin Hamiltonian of the rapidly interconverting molecule. In all of the examples discussed below, I and G commute, so instead of the semidirect product, we can in fact define S using the direct product:

$$S = I \otimes \mathrm{G} \tag{2}$$

Finally, in a chiral environment such as a CLC solution, the effective symmetry of the average molecule is reduced to S', the proper subgroup of S, since the improper operations are eliminated in a chiral environment. Enantiotopically related sites in S become inequivalent in S' and may exhibit enantiodiscrimination in their NMR spectra.

Experimental Section

Compound **4** was prepared by one-step oxidative trimerization of benzo-1,2-dioxyethylene.[19] To a stirred solution of $MoCl_5$ (2.8 g) in 10 mL of dry CH_2Cl_2, 1.36 g of benzo-1,2-dioxyethylene was added slowly (over 30 min) at room temperature. The dark-green reaction product was poured into 40 mL of a 1/1 water/methanol mixture. The yellow precipitate was treated with 150 mL of *n*-hexane and stirred for 30 min. The desired crystalline product was filtered, washed with water, methanol, and *n*-hexane, and dried. Yield: 720 mg (5%). TLC (silica/CH_2Cl_2): one spot, $M = 402$. For the deuterium NMR measurements, an isotopologue of **4** that was statistically enriched to 10% deuterium in the ethylene groups was prepared by trimerization of the correspondingly deuterated benzo-1,2-dioxyethylene. The latter was prepared by alkylation of benzocatechin with 10% statistically deuterated 1,2-dibromoethylene, which in turn was prepared as described in ref 10.

Two types of lyotropic oriented solvents based on poly(γ-benzylglutamate) were employed: chiral solvents consisting of PBLG dissolved in CH_2Cl_2 and achiral solvents (denoted PBG) consisting of mixtures of equal masses of PBLG and poly(γ-benzyl-D-glutamate) (PBDG) dissolved in CH_2Cl_2. The samples were prepared as described previously.[10,11] A typical solution consisted of 15 wt % PBLG (or PBLG + PBDG) and ~0.3 wt % solute in CH_2Cl_2. More information on sample preparation can be found in ref 1. Detailed compositions of the solutions used in the present work are given in the figure captions of the relevant spectra.

The ^{2}H-{^{1}H} NMR spectra shown here were recorded near room temperature (302 K) at 92.1 MHz using a 14.1 T Bruker Avance II spectrometer equipped with a selective ^{2}H cryoprobe. ^{2}H−^{1}H scalar and dipolar couplings were removed using the WALTZ-16 decoupling sequence. The ^{1}H and ^{13}C spectra were recorded at 9.4 T. Additional experimental details are given in the figure captions.

Results and Discussion

^{1}H and ^{13}C NMR Spectra of 4 in Achiral Isotropic Solutions. The proton NMR spectrum of **4** in CD_2Cl_2 is a simple two-line spectrum due to the aromatic (δ_{ar}) and oxyethylene aliphatic (δ_{al}) hydrogens, while the ^{13}C-{^{1}H} spectrum consists of a single aliphatic resonance and three aromatic peaks. In the absence of proton decoupling, the ^{13}C signals of the aromatic C2−H and aliphatic CH_2 carbons exhibit splittings due to $^1J_{C-H}$ couplings. The data derived from these spectra are summarized in Table 1.

Analysis of Deuterium NMR Spectra of 4 in Liquid-Crystalline Solutions. The structure of **4** is shown in Figure 2a. There are three half-chair dioxyethylene groups bonded at the periphery of the triphenylene plane; at room temperature, these groups undergo fast chair−chair interconversions between the

---

(12) Longuet-Higgins, H. C. *Mol. Phys.* **1963**, *6*, 445.
(13) Luz, Z.; Naor, R. *Mol. Phys.* **1982**, *46*, 891.
(14) Woodman, C. M. *Mol. Phys.* **1966**, *11*, 109.
(15) Altmann, S. L. *Proc. R. Soc. London* **1967**, *A298*, 184.
(16) Woodman, C. M. *Mol. Phys.* **1970**, *19*, 753.
(17) Watson, J. K. G. *Mol. Phys.* **1971**, *21*, 577.
(18) Altmann, S. L. *Mol. Phys.* **1971**, *21*, 587.
(19) Kumar, S.; Manickam, M. *Chem. Commun.* **1997**, 1615.

Table 1. Chemical Shifts and *J* Couplings for a Solution of **4** in CD_2Cl_2[a]

	^1H spectrum		^{13}C spectrum			
parameter	aromatic	aliphatic	Ar-1	Ar-2	Ar-3	aliphatic
δ (ppm)[b]	7.87	4.46	123.1	109.4	142.7	64.0
$^2J_{H-H}$ (Hz)	–	−11.1[c]	–	–	–	–
$^1J_{C-H}$ (Hz)	–	–	–	+155.4[c]	–	+148.5[c]

[a] A $^1J_{C\text{-}D}$ value of 27.0 Hz was measured for the solvent. [b] The carbon and proton chemical shifts were measured relative to the natural-abundance ^{13}C and residual ^1H signals in the CD_2Cl_2 solvent, respectively, for which the respective values on the δ scale were 5.32 and 53.8 ppm. [c] The signs of the *J* couplings are based on data in ref 8.

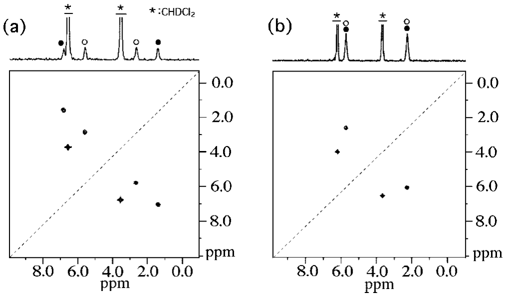

Figure 3. Deuterium *Q*-COSY Fz 2D spectra (at 92.1 MHz with proton decoupling) of solutions of compound **4** (statistically deuterated to 10% in the dioxyethylene side chains) in (a) the chiral solvent PBLG/CH_2Cl_2 and (b) the achiral solvent PBG/CH_2Cl_2 at 302 K. 1D projection spectra are shown at the top of each 2D map. The truncated doublet (∗) is due to natural-abundance deuterium in the CH_2Cl_2 solvent. Experimental details: 1024 (t_2) × 400 (t_1) data points with 8 scans per FID, LB = 0. Sample compositions: (a) PBLG (100 mg), CH_2Cl_2 (560 mg), **4** (1.7 mg); (b) PBLG (51 mg), PBDG (50 mg), CH_2Cl_2 (562 mg), **4** (1.5 mg).

left (L) and right (R) conformations shown in Figure 2b. The fast flipping is clearly demonstrated by the single aliphatic proton signal of **4** observed in isotropic liquids. The ^2H-{^1H} *Q*-COSY Fz 2D spectra of **4** dissolved in chiral and achiral polypeptide liquid-crystalline solutions are shown in Figure 3a,b, respectively. The compound was 10% statistically deuterated in the ethylene hydrogens, and the spectra were recorded under broadband proton decoupling. Both spectra exhibit a strong (truncated) doublet due to natural-abundance deuterons in the CH_2Cl_2 cosolvent. In addition, one or two doublets due to the dioxyethylene deuterons of the solute molecules are observed in the achiral or chiral solvent, respectively. The measured quadrupolar splittings in the two mesophases are summarized in Table 2.

The single doublet observed for the ethylene deuterons in the achiral solvent is consistent with fast flipping of the dioxyethylene groups that renders all of the ethylene hydrogens equivalent. On the other hand, the doubling of the spectrum in the chiral solvent reflects the enantiotopic relation within the various oxyethylene groups in the average molecule. In order to determine the symmetry of the average molecule and trace the origin of this chiral splitting, we need to consider the nature of the averaging process and the symmetries of the frozen conformers. Actually, as shown in Figure 4, there are two types of frozen conformers associated with compound **4**. The first consists of two enantiomers in which the twists of the three dioxyethylene groups are cyclic, i.e., either anticlockwise (RRR) or clockwise (LLL), where the R and L twists are defined in Figure 2b. The point group symmetry of these conformers (their Schrödinger group) is $G = D_3$, with the C_3 axis perpendicular to the triphenylene plane and the three C_2 axes lying within this plane (Figure 4a). If the chair−chair switching proceeds in concert, the isodynamic group, *I*, is isomorphous with $C_s = \{E, \sigma_h\}$, where σ_h corresponds to reflection with respect to the triphenylene plane. Consequently, the average symmetry of the molecule (the Schrödinger supergroup) becomes $S = C_s \otimes D_3 \approx D_{3h}$. A similar result is obtained for the second conformer, which consists of a set of six isodynamic conformations. In this set, the twists of the dioxyethylene groups result in three homomers of the form RLL, LLR, and LRL and their corresponding antipodes, in which R and L are interchanged. The symmetry group of these frozen conformers is $C_2 = \{E, C_2\}$, where the C_2 axis lies in the molecular plane (Figure 4b). The isodynamic group of this set of conformers consists of two types of operations: interchanges between homomers, which correspond to C_3 operations, and interchanges between enantiomers, which correspond to σ_h (reflection in the triphenylene plane). Hence, the isodynamic group is $I = C_3 \otimes C_s \approx C_{3h}$, and the symmetry in the fast-exchange limit becomes $S = C_{3h} \otimes C_2 \approx D_{3h}$, which is identical to that for the cyclically twisted set of conformers. Clearly, exchange between the two sets of conformers leads to the same average symmetry.

Table 2. Absolute Values of Quadrupolar Splittings ($\Delta\nu_Q$) Observed in Solutions of **4** in Poly(γ-benzylglutamate)-Based Liquid-Crystalline Solvents

	$\lvert\Delta\nu_Q\rvert$ (Hz)	
solvent[a]	$CHDCl_2$[b]	**4**
PBG/CH_2Cl_2	232 ± 2	318 ± 8
PBLG/CH_2Cl_2	278 ± 2	271 ± 8 / 499 ± 8[c]
ratio[d]	1.20	1.21

[a] The compositions of the solutions are given in the caption of Figure 3. [b] Splitting observed for the natural-abundance deuterons in the cosolvent. [c] Splittings observed for the inner/outer doublets of the ethylene deuterons in **4**. [d] Ratio of the average splitting in the PBLG solvent to the splitting in the PBG solvent.

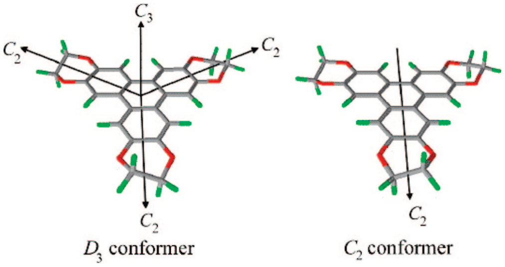

Figure 4. Structures of the conformers of compound **4**: (a) the LLL conformer with D_3 symmetry; (b) the LRR conformer with C_2 symmetry. Carbon, hydrogen, and oxygen atoms are shown in gray, lime, and red respectively. The elements of the associated symmetry point groups are displayed.

The symmetry operations in the D_{3h} group consist of all of the proper rotations of the D_3 subgroup plus three vertical and one horizontal reflection as well as a pair of improper rotations. Thus, in a chiral environment where the latter operations are eliminated, the effective symmetry of the average molecule is reduced to $S' = D_3$. Referring to Figure 2b, we note that atoms in the pairs AB′ and BA′ are related by C_2 rotations and are thus completely equivalent, while those in the AA′ and BB′ pairs and the AB and A′B′ pairs in the average molecule are related by vertical and horizontal reflections, respectively, and therefore are enantiotopically related. These relations are reflected in the NMR results shown in Figure 3. In the achiral solvent (Figure 3b), a single doublet due to all of ethylene deuterons is observed, while in the CLC solvent (Figure 3a), there are two doublets, one for the AB′ pair and one for the BA′ pair.

Origin of the Enantiodiscrimination in Compound 4. In this section we analyze the spectral enantiodiscrimination described in the previous paragraph. We first consider only the conformers with D_3 symmetry. Qualitatively similar results are expected if the other conformers are included in the analysis. We label the two enantiomers R and L, as shown in Figure 2b. In these conformers, the three dioxyethylene groups are equivalent, and within each group in the fast exchange limit, sites A and B′ as well as sites B and A′ are related by C_2 symmetry; hence, $\langle \Delta\nu_Q{}^{A} \rangle = \langle \Delta\nu_Q{}^{B'} \rangle$ and $\langle \Delta\nu_Q{}^{A'} \rangle = \langle \Delta\nu_Q{}^{B} \rangle$. It is therefore sufficient to consider one deuterium of type A and one of type B. Their average quadrupolar splittings are given by eqs 3 and 4, respectively:

$$\langle \Delta\nu_Q{}^{A} \rangle = P^{R} S_{zz}{}^{R} (\Delta\nu_Q{}^{A})^{R} + P^{L} S_{zz}{}^{L} (\Delta\nu_Q{}^{A})^{L} \tag{3}$$

$$\langle \Delta\nu_Q{}^{B} \rangle = P^{R} S_{zz}{}^{R} (\Delta\nu_Q{}^{B})^{R} + P^{L} S_{zz}{}^{L} (\Delta\nu_Q{}^{B})^{L} \tag{4}$$

where P^{J} and $S_{zz}{}^{J}$ are the relative population and axial order parameter of enantiomer J, respectively, and $(\Delta\nu_Q{}^{N})^{J}$ is the quadrupole splitting of a deuteron at site N in enantiomer J:

$$(\Delta\nu_Q{}^{N})^{J} = \frac{3}{4} Q_{C-D} (3 \cos^2 \beta^{NJ} - 1) \tag{5}$$

In eq 5, Q_{C-D} is the deuterium quadrupolar interaction constant of the C−D bond (~170 kHz for aliphatic deuterons) and β^{NJ} is the angle between the molecular C_3 axis and the C−D bond of site N in enantiomer J. From the structure of the oxyethylene group, it follows that $\beta^{AR} = \pi - \beta^{BL}$ and $\beta^{BR} = \pi - \beta^{AL}$, so $(\Delta\nu_Q{}^{A})^{R} = (\Delta\nu_Q{}^{B})^{L}$ and $(\Delta\nu_Q{}^{B})^{R} = (\Delta\nu_Q{}^{A})^{L}$.

In an achiral solvent, $P^{R} = P^{L} = {}^{1}/_{2}$ and $S_{zz}{}^{R} = S_{zz}{}^{L} \equiv S_{zz}$, resulting in identical splittings for the two deuterons:

$$\begin{aligned} \langle \Delta\nu_Q{}^{A} \rangle &= \langle \Delta\nu_Q{}^{B} \rangle \equiv \langle \Delta\nu_Q \rangle \\ &= \frac{S_{zz}}{2} [(\Delta\nu_Q{}^{A})^{R} + (\Delta\nu_Q{}^{B})^{R}] \\ &= \frac{S_{zz}}{2} [(\Delta\nu_Q{}^{A})^{L} + (\Delta\nu_Q{}^{B})^{L}] \end{aligned} \tag{6}$$

The geometry of the dioxyethylenebenzene moiety was calculated previously using DFT,[10] and values of 8.6 and 105.0° for β^{AL} and β^{BL}, respectively, were obtained. Thus, from eq 5, we obtain $(\Delta\nu_Q{}^{A})^{L} = 246.4$ kHz and $(\Delta\nu_Q{}^{B})^{L} = -101.9$ kHz; use of these values and $|\langle \Delta\nu_Q \rangle| = 318$ Hz (from Table 2) in eq 6 yields an estimate of 4.4×10^{-3} for the order parameter $|S_{zz}|$. It is shown below that the sign of S_{zz} is in fact negative, indicating that the solute molecules are oriented with their C_3 axes perpendicular to the director. This is common for disklike molecules in nematic solvents.

The situation is different in CLC solutions. In this case, the values of the order parameters $S_{zz}{}^{L}$ and $S_{zz}{}^{R}$ will in general be different, resulting in different average splittings of the A and B deuterons. However, we expect the average of the splittings observed in the chiral solvent to be similar to the splitting in the achiral one. Assuming that the splittings of the enantiomers in the chiral solvent have identical signs gives an average value of 384 Hz, which is a factor of 1.21 larger than the value of 318 Hz measured in the achiral solvent (see Table 2). The difference is most likely due to the different composition of the two solutions. This is supported by the observation that the same ratio is observed for the splittings of the solvent deuterons in the two solutions: 278/232 = 1.20 (Table 2). The similarity of the two ratios also provides support for the assumption of identical signs (negative) for the splittings observed for the two enantiotopic deuterons. The enantiodiscrimination, $\Delta(\Delta\nu_Q) \equiv \langle \Delta\nu_Q{}^{A} \rangle - \langle \Delta\nu_Q{}^{B} \rangle$, can now be calculated from the structure of the oxyethylene chains in the enantiomers. Neglecting any effects of the chiral environment on their geometries and using the equalities indicated after eq 5, we obtain:

$$\begin{aligned} \Delta(\Delta\nu_Q) &\equiv \langle \Delta\nu_Q{}^{A} \rangle - \langle \Delta\nu_Q{}^{B} \rangle \\ &= (P^{L} S_{zz}{}^{L} - P^{R} S_{zz}{}^{R})[(\Delta\nu_Q{}^{A})^{L} - (\Delta\nu_Q{}^{B})^{L}] \end{aligned} \tag{7}$$

The discussion of the conformers with C_2 symmetry is more involved; since these conformers are not axial, several order parameters are required for calculating the enantiodiscrimination. Although the relevant equations can in principle be written down, they cannot be solved because the number of required parameters exceeds the number of NMR observables.[11] Also, the relative abundance of the C_2 and D_3 conformers, which is required for the calculation of the overall enantiodiscrimination, is not known. On the basis of the overall shape of the molecule (Figure 2a), however, it is safe to assume that the dominant ordering parameter for all of the conformers is S_{zz}, where the z axis is perpendicular to the triphenylene plane. In order to make the calculations tractable and obtain an estimate for the overall enantiodiscrimination, we shall assume that the flipping processes of the R and L dioxyethylene groups (Figure 2b) are uncorrelated[20] and that associated with each conformer is a single order parameter ($S_{zz}{}^{R}$ or $S_{zz}{}^{L}$, respectively) that reflects the net effect of all of the side groups. We shall also assume that the probabilities for R and L twists are equal ($P^{R} = P^{L} = {}^{1}/_{2}$). A significant population preference is energetically highly unlikely. In fact, no such preferences have been experimentally observed to date in case of mixtures of interconverting enantiomers dissolved in polypeptide CLC solvents.[21,22] When this assumption is made, an equation similar to eq 7 is obtained, in which the $S_{zz}{}^{J}$ parameters reflect some kind of average ordering for enantiomers which are predominantly R or L twisted:

$$\begin{aligned} \Delta(\Delta\nu_Q) &= \frac{1}{2}(S_{zz}{}^{L} - S_{zz}{}^{R})[(\Delta\nu_Q{}^{A})^{L} - (\Delta\nu_Q{}^{B})^{L}] \\ &= (174.2\ \text{kHz})\Delta S_{zz} \end{aligned} \tag{8}$$

where $\Delta S_{zz} = S_{zz}{}^{L} - S_{zz}{}^{R}$ and we have used the quadrupolar splitting values given after eq 6. Likewise, the average splitting of the two doublets is:

$$\begin{aligned} \langle \Delta\nu_Q \rangle &= \frac{1}{2}[\langle \Delta\nu_Q{}^{A} \rangle + \langle \Delta\nu_Q{}^{B} \rangle] \\ &= \frac{1}{4}(S_{zz}{}^{L} + S_{zz}{}^{R})[(\Delta\nu_Q{}^{A})^{L} + (\Delta\nu_Q{}^{B})^{L}] \\ &= (72.2\ \text{kHz})\langle S_{zz} \rangle \end{aligned} \tag{9}$$

---

(20) This assumption is equivalent to neglecting intramolecular interactions between side groups, which is amply justified in view of the large (>10 Å) distance between them.

(21) Emsley, J. W.; Lesot, P.; Courtieu, J.; Merlet, D. *Phys. Chem. Chem. Phys.* **2004**, *6*, 5331.

(22) Lafon, O.; Lesot, P.; Fan, C.-A.; Kagan, H. B. *Chem.—Eur. J.* **2007**, *13*, 3772.

where $\langle S_{zz}\rangle = (S_{zz}{}^{L} + S_{zz}{}^{R})/2$. Thus, from Table 2, an average value of $|\langle S_{zz}\rangle| = 5.3 \times 10^{-3}$ is estimated in the CLC solution. Moreover, the ratio of the enantiodiscrimination to the average splitting of the enantiotopic deuterons is given by:

$$\frac{\Delta(\Delta\nu_Q)}{\langle\Delta\nu_Q\rangle} = 2.4\frac{\Delta S_{zz}}{\langle S_{zz}\rangle} \tag{10}$$

From Table 2, we obtain $|\Delta(\Delta\nu_Q)/\langle\Delta\nu_Q\rangle| = 0.6$, so from eq 10, $|\Delta S_{zz}/\langle S_{zz}\rangle| = 0.25$. Only the magnitudes of these ratios can be given, since we have no way to correlate the two deuterium doublets observed in the CLC solution with the AB′ and BA′ pairs in **4**. The spectral discrimination of the enantiotopic sites in this compound is especially large. This is mainly due to a large intrinsic discrimination in the ordering of the two enantiomers induced by interaction with the chiral solvent, which is augmented by the relatively large geometrical coefficient (2.4) in eq 10. This coefficient reflects the difference in the splittings of a particular deuteron in the two enantiomers or of the two exchanging deuterons in the same enantiomer, i.e., $[(\Delta\nu_Q{}^{A})^{L} - (\Delta\nu_Q{}^{B})^{L}] = [(\Delta\nu_Q{}^{B})^{R} - (\Delta\nu_Q{}^{A})^{R}]$. The value of the coefficient is particularly large in the present case because one of the exchanging C−D bonds is nearly parallel to the molecular C_3 axis whereas the other is nearly perpendicular to it. From the results following eq 10, a value of 1.29 or 0.78 (depending on the sign of $\Delta S_{zz}/\langle S_{zz}\rangle$) is calculated for the ratio $S_{zz}{}^{L}/S_{zz}{}^{R}$. This corresponds to a very effective discrimination, probably reflecting the screw shape of the half-chair dioxyethylene groups at the periphery of the triphenylene plane.

Ordering of 4 in the PBLG-Based Liquid Crystals. In the above discussion, it was indicated that S_{zz} of **4** in the PBG solutions is negative, i.e., that the solute molecules have a preference for being aligned with their z axes perpendicular to the director. Here we briefly provide experimental evidence for this statement obtained from analysis of additional ^{1}H and ^{13}C spectra (with and without proton decoupling) of isotopically normal **4** in PBLG/CD$_2$Cl$_2$ solution at 302 K. The composition of this sample was similar to that given in the caption of Figure 3a.

The ^{1}H spectrum of **4** exhibits two doublets with broad components associated with the aromatic (with a splitting of ~130 Hz) and aliphatic (~105 Hz) hydrogens, respectively. The splitting of the aromatic signal reflects the through-space dipolar coupling between nearby hydrogens on adjacent benzene rings of the triphenylene core. Assuming threefold symmetry for the latter yields a calculated interhydrogen distance of ~1.72 Å. We recall that the dipolar splitting for a pair of equivalent hydrogens is $T_{H-H} = 3D_{H-H}$,[23] where for an axially symmetric molecule, D_{H-H} is given by the general formula:

$$D_{X-Y} = -S_{zz}[K_{X-Y}/(r_{X-Y})^3][(3\cos^2\beta_{X-Y} - 1)/2] \tag{11}$$

where β_{X-Y} is the angle between the r_{X-Y} direction and the molecular symmetry axis and K_{X-Y} is a constant proportional to the magnetic moments of the X and Y nuclei ($K_{H-H} = 1.20 \times 10^5$ Hz/Å^3 and $K_{C-H} = 3.02 \times 10^4$ Hz/Å^3). Inserting the measured splitting ($|T_{H-H}| = 3|D_{H-H}| = 130$ Hz) in eq 11 yields $|S_{zz}| \approx 3.7 \times 10^{-3}$. This result is similar to that derived above for the quadrupole splitting of the methylene deuterons (5.3×10^{-3}), but the sign of S_{zz} remains undetermined.

The doublet due to the aliphatic protons predominantly reflects the dipolar interaction between hydrogens belonging to the same methylene group (A and B or A′ and B′). The components of this doublet exhibit some unresolved structure that is partly attributable to their (slight) enantiotopic nonequivalence and perhaps also due to dipolar interactions with hydrogens of nearby methylene groups. The measured splitting, $T_{H-H'}$, can nevertheless provide a rough estimate for the magnitude of the intramethylene dipolar interaction ($|D_{H-H'}| \approx |T_{H-H'}|/3 = 35$ Hz) and will be used below in the analysis of the ^{13}C methylene spectrum.

The proton-coupled ^{13}C spectrum of **4** in the PBLG/CH$_2$Cl$_2$ solution (not shown) exhibits a single peak for the aromatic C−H carbon and a symmetric five-line pattern for the oxyethylene carbons. The ^{13}C spectrum of a C−H pair is expected to yield a doublet with a total splitting, T_{C-H}, equal to $^{1}J_{C-H} + 2D_{C-H}$. The lack of such a splitting for the aromatic carbon indicates that the scalar and dipolar couplings fortuitously cancel each other. Hence, $D_{C-H} \approx -{}^{1}J_{C-H}/2 = -78$ Hz, and use of eq 11 with $\beta_{C-H} = \pi/2$ and $r_{C-H} = 1.09$ Å yields $S_{zz} = -6.7 \times 10^{-3}$. The result is somewhat larger in magnitude than the previous values, but now the sign of the order parameter is clearly determined.

Finally, we confirm the above conclusion by analyzing the ^{13}C spectrum of the oxyethylene group. Its symmetric five-line pattern consists of a strong central peak, a weak doublet with components at ±42 Hz relative to the central peak, and an outer doublet with components at ±208 Hz that are about half as intense as the central line. Schematic examples of such as spectral pattern are reported in ref 8. The spectrum corresponds to AA′X spin, where A and A′ represent the nonequivalent enantiotopic hydrogens and X the ^{13}C nucleus. If differences in the chemical shifts of A and A′ and any interactions between hydrogens on neighboring methylene groups are neglected, the spin Hamiltonian for this system becomes:

$$\begin{aligned}\hat{H} = -\nu_0{}^{C}\hat{S}_z - \nu_0{}^{H}(\hat{I}_z{}^{H} + \hat{I}_z{}^{H'}) + ({}^{1}J_{C-H} + 2D_{C-H})\hat{S}_z\hat{I}_z{}^{H} + \\ ({}^{1}J_{C-H'} + 2D_{C-H'})\hat{S}_z\hat{I}_z{}^{H'} + ({}^{2}J_{H-H'} + 2D_{H-H'})\hat{I}_z{}^{H}\hat{I}_z{}^{H'} + \\ {}^{1}\!/_{2}({}^{2}J_{H-H'} - D_{H-H'})(\hat{I}_+{}^{H}\hat{I}_-{}^{H'} + \hat{I}_-{}^{H}\hat{I}_+{}^{H'})\end{aligned} \tag{12}$$

where the first two terms are the Zeeman energies of the ^{13}C and ^{1}H nuclei, respectively, the third and fourth terms correspond to the ^{13}C−^{1}H scalar and dipolar couplings, respectively (with the latter assumed to be different for the two hydrogens), and the last two terms correspond to the scalar and dipolar interactions, respectively, between the methylene hydrogens. A straightforward exact solution of eq 12 indeed yields a symmetric five-line spectrum with peak positions and relative intensities given by the formulas in Table 3.

The formulas in Table 3 show that the combined relative intensity of the central line and the two components of the inner doublet is exactly equal to 2, as is the combined intensity of the two outer-doublet components. Hence, the latter could readily be identified by comparison with the peak intensities in the spectrum. The signs and magnitudes of D_{C-H} and $D_{C-H'}$ could then be determined from the measured splitting of this doublet and the corresponding deuterium quadrupole interactions given in Table 2. Recalling that $|\Delta\nu_Q|/|D_{C-H}| \approx 12$,[10] we expect the dipolar interactions to have magnitudes of $|D_{C-H}| \approx 22.6$ Hz and $|D_{C-H'}| \approx 41.6$ Hz and identical signs (since the $\Delta\nu_Q$'s have identical signs). Since $^{1}J_{C-H} = +148.5$ Hz (Table 1), it follows from the formula for the outer-doublet positions in Table 3 that only a positive sign for the D_{C-H} values is consistent with the measured positions of the outer-doublet components

---

[23] Emsley, J. W.; Lindon, J. C. *NMR Spectroscopy Using Liquid Crystal Solvents*; Pergamon Press: Oxford, U.K., 1975; Chapter 2.

Table 3. Peak Positions and Relative Intensities of the Five-Line Pattern in the ^{13}C Spectrum of a Methylene Group Calculated Using the Hamiltonian of eq 12

spectral feature	position	relative intensity[a]
central peak	ν_o	$2(^2J_{H-H'} - D_{H-H'})^2[(D_{C-H} - D_{C-H'})^2 + (^2J_{H-H'} - D_{H-H'})^2]^{-1}$
inner doublet (weak)	$\nu_o \pm [(D_{C-H} - D_{C-H'})^2 + (^2J_{H-H'} - D_{H-H'})^2]^{1/2}$	$(D_{C-H} - D_{C-H'})^2[(D_{C-H} - D_{C-H'})^2 + (^2J_{H-H'} - D_{H-H'})^2]^{-1}$
outer doublet (strong)	$\nu_o \pm [^1J_{C-H} + D_{C-H} + D_{C-H'}]$	1

[a] For the inner and outer doublets, the entries give the relative intensity of each doublet component.

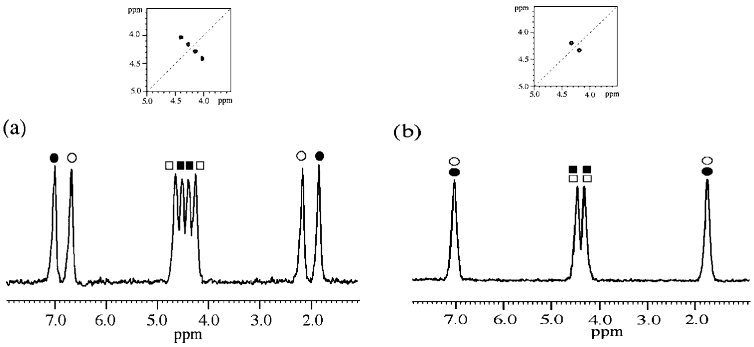

Figure 5. Columns extracted from the 92.1 MHz tilted deuterium *Q*-COSY Fz 2D spectra (with proton decoupling) of **2** (statistically deuterated to 10% in the dioxyethylene side chains) at 302 K in (a) the chiral solvent PBLG/CH$_2$Cl$_2$ and (b) the achiral solvent PBG/CH$_2$Cl$_2$. The central parts of the respective *Q*-COSY maps are shown as insets. Experimental details: 1500 (t_2) × 512 (t_1) data points with 16 scans per FID, LB = 1 Hz. Sample compositions: (a) PBLG (101 mg), CH$_2$Cl$_2$ (581 mg), **2** (2 mg); (b) PBLG (51 mg), PBDG (50 mg), CH$_2$Cl$_2$ (584 mg), **2** (1.5 mg).

(±208 Hz). An exact calculation assuming $D_{C-H}/D_{C-H'} = \Delta\nu_Q(H)/\Delta\nu_Q(H')$ yields $D_{C-H} = +20.9$ Hz and $D_{C-H'} = +38.6$ Hz. All of the parameters in Eq. 12, are now determined except for the sign of $D_{H-H'}$. To determine this sign, we can calculate $D_{H-H'}$ from the outer-doublet position formula in Table 3 using the just-derived D_{C-H} values, $^2J_{H-H} = -10$ Hz (see Table 1), and the observed positions of the inner-doublet components (±42 Hz). The calculation yields two values for $D_{H-H'}$, +28 and −48 Hz. These values must be compared with the approximate result obtained above from the proton spectrum ($|D_{H-H'}| \approx 35$ Hz). Neither of the ^{13}C results fits exactly with the latter one, but the positive one is somewhat closer, so we tentatively assign the value of +28 Hz to $D_{H-H'}$ and explore the validity of the chosen sign in the next paragraph.

We first note that the $D_{H-H'}$ interaction is not modulated by the chair−chair flipping of the oxyethylene groups. This follows from the symmetry of the two conformations in Figure 2b; the polar angle $\beta_{H-H'}$ between the vector $r_{H-H'}$ and the symmetry axis of the triphenylene core in the R-twist conformation (upper diagram) becomes $\pi - \beta_{H-H'}$ in the L-twist conformation (lower diagram). Hence, the $D_{H-H'}$ value is identical in the two conformations and of course identical to that in the dynamically averaged molecule. The value of $\beta_{H-H'}$ can be estimated from the geometrical parameters of the frozen oxyethylene group (given in Table 3 of ref 10) to be 40°. Substituting this value into eq 11 along with $D_{H-H'} = +28$ Hz yields $S_{zz} = -3.4 \times 10^{-3}$, thus confirming the positive sign for $D_{H-H'}$. We note that whenever the sign of S_{zz} could be determined, it consistently came out negative, but the estimates of the magnitude of S_{zz} (5.3, 3.7, 6.7, and 3.4 in units of 10^{-3}) varied by almost a factor of 2. The large dispersion in these values is partly due to uncertainty in the measurements (broad doublets in the ^{1}H spectra) and partly due to lack of exact knowledge of the molecular geometry.

Comparison with Related Systems. It is interesting to compare the above results with those for the cone-shaped molecule **2** (Figure 1b).[10] Here too, flexible dioxyethylene groups are linked to the periphery of a rigid axial moiety, but in the frozen state of **2**, unlike the case in **4**, all four hydrogens in an oxyethylene group are nonequivalent, with the A (B) hydrogens pointing outward from (inward to) the CTV core (see Figure 2b). This compound, like **4**, exhibits two types of frozen conformers having different symmetries. One of these conformers consists of the two isodynamic enantiomers RRR and LLL having symmetry $G = C_3$. A correlated chair−chair interconversion corresponds to a vertical reflection; thus, the isodynamic group is $I = \{E, \sigma_v\} = C_s$, and the average symmetry in the fast-exchange regime becomes $S = C_s \otimes C_3 = C_{3v}$. A similar result is obtained for the second type of conformer, which consists of the three isodynamic homomers RLL, LRL, and LLR and their corresponding antipodes, with $G = C_1$. In this case, there are two types of chair−chair flips: those interchanging between enantiomers ($C_s = \{E, \sigma_v\}$) and those interchanging between homomers ($C_3 = \{E, C_3\}$). Hence, the isodynamic group is $I = C_3 \otimes C_s = C_{3v}$, and the Schrödinger supergroup is again $S = C_1 \otimes C_{3v} = C_{3v}$. Exchange between the two types of conformers clearly retains the C_{3v} symmetry. In achiral media, hydrogens A and A′ (Figure 2b) are equivalent but enantiotopically related, and so are B and B′. However, A and B (A′ and B′) remain nonequivalent. In CLC media, the effective symmetry of the average molecule reduces to $S' = C_3$, and enantiodiscrimination of the A and A′ as well as the B and B′ sites is expected. These relations were well-demonstrated in the deuterium spectrum of compound **2** (10% statistically deuterated in the dioxyethylene side chains) dissolved in PBLG/CHCl$_3$.[10] We have now obtained somewhat better resolved spectra of this compound using CH$_2$Cl$_2$ as cosolvent. The spectra are shown in Figure 5, and the measured splittings are summarized in Table 4.

Table 4. Absolute Values of Quadrupolar Splittings ($\Delta\nu_Q$) Observed in Oriented Solutions of **2**

	$|\Delta\nu_Q|$ (Hz)		
solvent[a]	$CHDCl_2$[b]	**2**A	**2**B
PBG/CH_2Cl_2	236 ± 3	16 ± 7	500 ± 8
$PBLG/CH_2Cl_2$	213 ± 3	34 ± 6 / 12 ± 6[c]	472 ± 7 / 416 ± 7[c]
ratio[d]	1.11	1.45[e]	1.13

[a] The compositions of the solutions are given in the caption of Figure 5. [b] Splitting observed for the natural-abundance deuterons in the cosolvent. [c] Splittings observed for the inner/outer doublets. [d] Ratio of the splitting in the PBG solvent to the average splitting in the PBLG solvent. [e] This value is obtained if opposite signs for the two splittings in the chiral solvent are assumed.

In the achiral solvent, two doublets are observed for the oxyethylene deuterons, which split into pairs of doublets in the chiral solvent. A geometrical analysis shows that the outer one corresponds to the BB′ pair and the inner one to the AA′ pair.[11] An analysis similar to the one described above for **4** applied to the outer pairs of doublets (**2**B in Table 4) yields the following results for the order parameters in the chiral solvent: $|\langle S_{zz}\rangle| \approx 5.7 \times 10^{-3}$, $|\Delta S_{zz}/\langle S_{zz}\rangle| \approx 0.13$, and $S_{zz}^{L}/S_{zz}^{R} \approx 1.13$ or 0.89. Apparently the dominant factor in the alignment of compound **2** is the cone-shaped structure of the rigid part of the molecule. Consequently, the value of the order parameter is somewhat larger than for compound **4**, but the enantioseparation is smaller. It is difficult to make a similar analysis on the inner doublets due to the A deuterons, for which the splittings are very small as a result of almost complete cancellation of large geometrical factors. The remaining splittings are then very sensitive to the approximations made in deriving the equations relating the splittings and the axial order parameter. In particular, neglect of small distortions of the chiral solutes and of even minor nonaxial order parameters for the nonaxial conformers have a relatively strong effect on the final results. The data in Table 4 even suggest that the two doublets arising from the A deuterons in the chiral solvent may have opposite signs. This follows from the comparison of the splittings in the chiral and achiral oriented solvents. In order for the average splitting ratio of the A deuterons to be similar to that of the natural-abundance deuterons in the solvent (as is that for the B deuterons), such an assumption must be made.

The saddle form of nonamethoxy-CTV, compound **3**, is another example of a flexible molecule that averages to an axial species with enantiotopically related sites. As in the above examples, enantiodiscrimination was observed in the deuterium NMR spectra of these sites. However, the symmetry of the six interconverting chiral conformers is far from axial, allowing only qualitative analysis of the results.[11] Another case worth mentioning in this connection is the ring inversion of *cis*-decalin.[24,25] However, the symmetry of the average molecule is not axial in that case, so the above considerations do not apply.

Conclusions

Rigid axial molecules with a C_n ($n \geq 3$) symmetry axis possessing enantiotopically related sites do usually not exhibit NMR spectral enantiotopic discrimination when dissolved in CLC solvents. Exhibition of such discrimination would require significant distortions[26–28] of the geometrical and/or electronic structure that renders the enantiotopic sites nonequivalent. The solute−solvent interactions in PBG-based lyotropic solvents are apparently not strong enough to cause such distortions. In contrast, chiral flexible molecules with average axial symmetries do exhibit such spectral enantiodiscrimination. The discrimination could stem from selective preferences in the population and/or ordering of one of the interconverting enantiomers. We have argued that the dominant discrimination originates from the latter effect. Discrimination in the ordering of conformational enantiomers is associated with only weak solute−solvent interactions and is commonly observed for racemic mixtures dissolved in CLC solvents. Furthermore, deviation from the equilibrium population of racemic mixtures is neither observed nor energetically expected in the case of interconverting enantiomers. Here we have demonstrated such an effect on the deuterium NMR spectra of partially deuterated tridioxyethylenetriphenylene (**4**). In its frozen state, this molecule is chiral and axially symmetric (or nearly so). Fast chair−chair flipping of the dioxyethylene side chains renders the molecule fully axial with pairs of enantiotopic sites. These sites exhibit large enantiodiscrimination in the deuterium NMR spectrum of **4** in a CLC solvent, which could be explained in terms of large selective ordering of the different conformational enantiomers.

Acknowledgment. P.L. acknowledges the Weizmann Institute of Science and the Technion Institute of Technology of Haifa for their invitation and financial support during his visit in Israel. O.L. is grateful to the MNESR for a Ph.D. grant. This research was made possible, in part, by the historic generosity of the Harold Perlman family.

JA800957A

---

(24) Boeffel, C.; Luz, Z.; Poupko, R.; Zimmermann, H. *J. Am. Chem. Soc.* **1990**, *112*, 7158.

(25) Sarfati, M.; Aroulanda, C.; Courtieu, J.; Lesot, P. *Tetrahedron: Asymmetry* **2001**, *12*, 737.

(26) Such selective distortions may be induced by special chiral agents that form adducts with the solute molecules, such as dirhodium complexes. The latter method was very recently shown to induce significant chiral discrimination in the NMR spectra of chiral CTV derivatives.

(27) Gomez, E. D.; Brotin, T.; Duddeck, H. *Tetrahedron: Asymmetry* **2007**, *18*, 2155.

(28) Duddeck, H. *Chem. Rec.* **2005**, *5*, 396.

CHEMISTRY
A EUROPEAN JOURNAL

DOI: 10.1002/chem.200601284

Analysis of Intramolecular Dynamic Processes in Enantiomeric Diaryl Atropisomers and Related Derivatives by ^{2}H NMR Spectroscopy in Polypeptide Liquid Crystals

Olivier Lafon,[a] Philippe Lesot,*[a] Chun-An Fan,[b] and Henri B. Kagan[b]

Abstract: We demonstrate the analytical potential of ^{2}H-{^{1}H} NMR spectroscopy in weakly ordering, chiral lyotropic liquid crystals made of poly(γ-benzyl-L-glutamate) (PBLG) dissolved in chloroform or dichloromethane for investigating the intramolecular dynamic processes of four deuterated diaryls (derivatives of 1-(4′-methylphenyl)-naphthalene). When the rotation of the aryl groups about the sp^{2}–sp^{2} bond is sufficiently slow relative to the NMR timescale, the method allows the spectral discrimination of enantiomeric atropisomers or enantiotopic directions in the prochiral derivatives. The effect of the position of substituents on the phenyl group on the conformational dynamics of these compounds has been examined as well as the nature of the organic co-solvent. When coalescence phenomena are observed, simulation of the experimental ^{2}H-{^{1}H} lineshapes using a formalism tailored for two deuterons undergoing mutual exchange allows the rate constants and the activation parameters for the internal rotation processes to be calculated. Experimental values of $\Delta H^{\ddagger}$ have been compared with data evaluated by molecular modelling calculations and the activation parameters are discussed for the various compounds. It is shown that these polypeptide mesophases have no significant impact on the interconversion dynamics of these compounds. In contrast with the nematic thermotropic phases, Haller's equation cannot be used to predict the evolution of the quadrupolar splittings ($\Delta\nu_{Q}$ values), and hence the order parameters, versus T in the PBLG mesophases. For these particular lyotropic systems, it is shown that an exponential function of the form $\Delta\nu_{Q}[\text{Hz}] = C \times \exp(-E/RT[\text{K}])$ provides excellent agreement between the experimental and expected $\Delta\nu_{Q}$ values. Analysis of the results reported in this work suggests that orientation and chiral discrimination phenomena in these lyotropic solvents could be treated separately because they would involve different interaction mechanisms.

Keywords: atropisomerism · chirality · conformational analysis · exchange processes · kinetic and activation parameters · liquid crystals · NMR spectroscopy

Introduction

The use of chiral atropisomers in asymmetric synthesis has successfully been investigated during the last two decades.[1,2] Atropisomerism is a particular class of stereoisomerism involving molecular structures in which internal rotation about a single covalent bond is sufficiently hindered such that different stereoisomers can be isolated.[1–3] Typical examples are tetra-*ortho*-substituted diaryls. In these compounds, the bulkiness of the substituents determines the height of the barrier to the rotation about the sp^{2}–sp^{2} single bond that corresponds to the activation energy for the interconversion between the enantiomeric or diastereoisomeric atropisomers. The ability to separate their signals using chromatographic techniques (HPLC, GC) or NMR spectroscopy is directly related to the exchange rate constant, that itself depends on the magnitude of the barrier to rotation, $\Delta H^{\ddagger}$, and the sample temperature, T.

NMR spectroscopy is exquisitely well-suited to the analysis of dynamic phenomena (tautomerism, hindered rotation, etc.). The method relies on the fact that dynamic processes modify the resonance lineshapes when the exchange or interconversion rate constant, k, is comparable to the magni-

---

[a] Dr. O. Lafon, Dr. P. Lesot
Laboratoire de Chimie Structurale Organique
ICMMO UMR CNRS 8182
Bât. 410, Université de Paris-Sud, 91405 Orsay (France)
Fax: (+33) 169-15-81-05
E-mail: philesot@icmo.u-psud.fr

[b] Dr. C.-A. Fan, Prof. H. B. Kagan
Laboratoire de Catalyse Moléculaire, ICMMO UMR CNRS 8182
Bât. 420, Université de Paris-Sud, 91405 Orsay (France)

Supporting information for this article is available on the WWW under http://www.chemeurj.org/ or from the author.

tude of the NMR interactions (in frequency units).[4,5] In isotropic NMR methods, only the isotropic part of the chemical shift or scalar coupling provides information on the dynamic processes,[4,5] even though original approaches involving diffusion NMR experiments (DOSY spectroscopy) have recently been explored.[6] This restriction can limit the efficiency of the method if the dynamic process does not sufficiently affect NMR interactions and thereby modify the NMR spectra. To overcome this problem, the use of NMR spectroscopy in magnetically aligned media was proposed in the early seventies.[7–9] In particular, proton-decoupled deuterium NMR (^{2}H-{^{1}H} NMR) spectroscopy of isotopically enriched compounds embedded in liquid crystals (LCs) was successfully applied to the analysis of various types of dynamic processes.[7,8]

Although the molecules under investigation have to be isotopically labelled, the analysis of molecular interconversion processes using ^{2}H-{^{1}H} NMR spectroscopy of deuterated molecules in liquid crystals possesses several practical advantages.[7,8] Firstly, the spectra are free of background signals originating from the LC. Secondly, the dynamic effects on the NMR lineshapes and the coalescence phenomena can be readily interpreted because the spectra are only dominated by residual quadrupolar interactions. Thirdly, the spectral separations between exchanging ^{2}H anisotropic signals can be much larger than those observed in isotropic ^{1}H or ^{13}C NMR spectra, thus allowing a much wider range of dynamic processes to be studied.[7,8] Fourthly, the simulation of dynamic ^{2}H-{^{1}H} NMR spectra requires only the solution of Bloch–McConnell-type equations rather than the full density matrix[9] and so calculations of the kinetic rate constants and activation parameters are facilitated.

Until now such investigations were restricted to molecules dissolved in achiral thermotropic nematics such as EBBA, phase V or ZLI 2452.[9–12] In particular, the method was used to study the ring inversion of perdeuterated (halo)cyclohexanes,[9,11] *p*-dioxane,[12] and *cis*-decalin.[10] However, this approach should basically be irrelevant in the analysis of interconversions between enantiomers or enantiotopic directions because their spectral discrimination is impossible in an achiral LC. To overcome this problem, it is necessary to record ^{2}H NMR spectra using chiral liquid crystals (CLCs), such as those made of poly(γ-benzyl-L-glutamate) (PBLG) dissolved in chloroform or dichloromethane.[13–17] In these chiral LCs, enantiomers or enantiotopic directions in prochiral molecules are on average oriented differently and hence their residual anisotropic magnetic interactions are likely to be different.[15,16,18]

Very recently, we reported the first example of the analysis of rotational isomerism phenomena using NMR spectroscopy in CLCs.[19] In this work, we extensively explore the analytical potential of ^{2}H NMR spectroscopy in polypeptide mesophases for the investigation of the intramolecular dynamic process of four deuterated diaryls derived from 1-(4′-methylphenyl)naphthalene and denoted **1**–**4**. The structures and the numbering are given in Figure 1. From a stereochemical point of view, the monobromide aromatic derivatives, **1** and **2**, are chiral compounds for non-planar conformations. On the other hand, the non-planar, di- and monodeuterated derivatives, **3** and **4**, can be defined as prochiral and chiral by virtue of the isotopic substitution H/D, respectively.

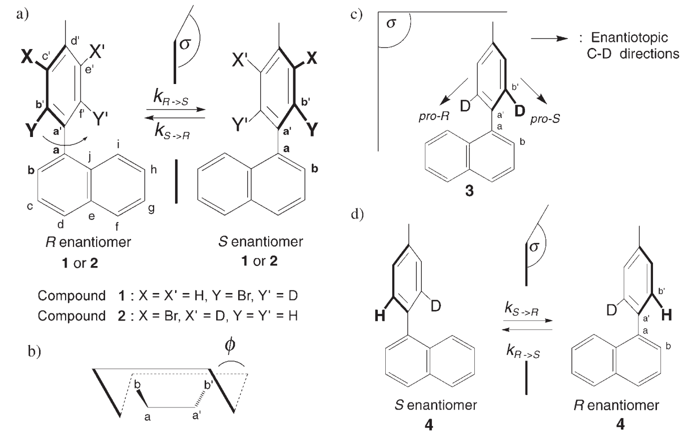

Figure 1. a) Enantiomeric conformers associated with the 1-bromo-3-deuterio-5-methyl-2-(1′-naphthyl)benzene (**1**) and the 1-bromo-3-deuterio-2-methyl-5-(1′-naphthyl)benzene (**2**). The absolute configuration of each enantiomer is defined by application of the Cahn–Ingold–Prelog priority rules.[3] The notation (a–j and a′–g′) applies to all compounds. b) Definition of the inter-ring torsion angle (b-a-a′-b′), ϕ, used to calculate the potential energy profiles. c) Elements of symmetry for 1-(2′,6′-dideuterio-4′-methylphenyl)naphthalene (**3**) when the dihedral angle, ϕ, is equal to 90°. In this case, the C–D directions are enantiotopic. d) Enantiomeric rotamers associated with 1-(2′-deuterio-4′-methylphenyl)naphthalene (**4**).

In an introductory part, we will briefly present some aspects of dynamic ^{2}H NMR spectroscopy in CLCs. Then the discussion will be divided into three subsections. Firstly, we will analyse the conformational behaviour of compounds **1**–**4** using molecular modelling calculations (MMCs). Secondly, the ^{2}H NMR results in PBLG mesophases will be presented. In particular, we will examine the influence of the position of bromine and deuterium atoms on the barrier to rotation. Thirdly, we will investigate the effect of organic co-solvents on the conformational dynamics of these biaryls. For all compounds, the activation parameters ($\Delta H^{\neq}$, $\Delta S^{\neq}$ and

$\Delta G^{\neq}(T)$) will be determined by ^{2}H NMR spectroscopy in CLCs or by other methods such as HPLC and subsequently compared with those predicted by MMCs.

Theoretical Aspects

Enantiodiscrimination using ^{2}H NMR in chiral liquid crystals: In deuterium (spin $I=1$) NMR spectroscopy using liquid crystals as solvent, the partially averaged magnetic interactions are dominated by the quadrupolar interaction.[20,21] The ^{2}H-{^{1}H} NMR spectra of deuterated solutes or of solutes at the natural abundance level consist of the sum of quadrupolar doublets in accord with the number of non-equivalent deuterons.[16] In CLCs, the existence of enantioselective interactions leads enantiomers or enantiotopic directions (for instance C–D bonds) in prochiral molecules to be oriented differently on average, and hence $S^{R \text{ or } pro\text{-}R} \neq S^{S \text{ or } pro\text{-}S}$, where S is an order parameter [see Eq. (2)].[13,16] Clearly, NMR analysis of these systems provides information that is not accessible by NMR analysis in achiral LCs. Enantiodifferentiation observed in ^{2}H-{^{1}H} NMR spectra is based on differences between the quadrupolar splittings, $|\Delta\nu_Q^A - \Delta\nu_Q^B|$, expressed in Hz, where the subscripts A and B correspond to the stereochemical descriptors R and S for enantiomers and *pro-R* and *pro-S* for enantiotopic directions. In both cases, the quadrupolar splittings are given by Equation (1),[14,15,21] where K_D is the ^{2}H quadrupolar coupling, $S_{C-D}^{A \text{ or } B}$ is the internuclear order parameter associated with the C–D bond, given by Equation (2), and $\theta_{C-D}^{A \text{ or } B}$ is the angle between the C–D axis and the magnetic field axis.[14,15] In practice, when S_{C-D}^A differs from S_{C-D}^B, then two sharp quadrupolar doublets centred generally on the same chemical shift (small ^{2}H chemical shift anisotropy) are observed (Figure 2).[14,15] The relatively large magnitude of the K_D parameter (160–185 kHz) contributes to the success of the method.

$$\Delta\nu_Q^{A \text{ or } B} = \frac{3}{2} K_D S_{C-D}^{A \text{ or } B} \tag{1}$$

$$S_{C-D}^{A \text{ or } B} = \left\langle \frac{3\cos^2(\theta_{C-D}^{A \text{ or } B}) - 1}{2} \right\rangle \tag{2}$$

Dynamic NMR spectroscopy of spin $I=1$ nuclei and activation parameters: The theory of dynamic ^{2}H NMR spectroscopy in oriented solvents has been described by various authors.[7,22] For our purpose, we restricted the framework to two non-coupled, non-equivalent deuterons in mutual interconversion (denoted A and B) and undergoing only Zeeman and quadrupolar interactions. In our case the two sites will correspond to either enantiomers (A, $B \equiv R$ or S) or enantiotopic directions (A, $B \equiv$ *pro-R* or *pro-S*) and an exchange process between two "equally populated sites" only is considered.[23] Owing to the absence of a difference in the chemical shift between the exchanging sites ($\omega_0^A = \omega_o^B = \omega_o$), the positions of the two transitions ($\omega_{0,1}$ and $\omega_{-1,0}$) are located symmetrically relative to the offset resonance frequency, ω_o, irrespective of the sign of the quadrupolar splittings, as shown in Figure 2. Readers interested in the theoretical formalism used in this work can refer to the Supporting Information.

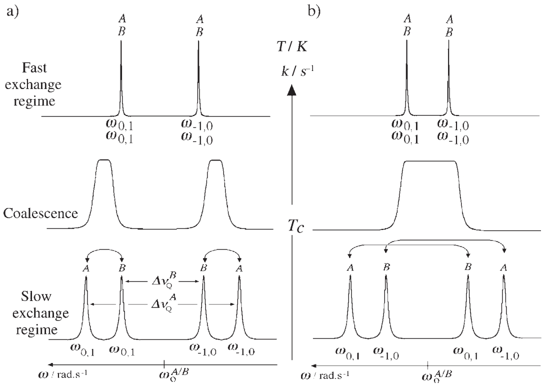

Figure 2. a) Schematic structures of 1D ^{2}H NMR spectra of two deuterons (A and B) undergoing mutual exchange in the three possible exchange regimes. We assume that the signs of $\Delta\nu_Q^A$ and $\Delta\nu_Q^B$ are positive, $|\Delta\nu_Q^A| > |\Delta\nu_Q^B|$, and $|\Delta\nu_Q^A| - |\Delta\nu_Q^B|$ is smaller than $|\Delta\nu_Q^A|$ and $|\Delta\nu_Q^B|$. b) Identical to a) but for $\Delta\nu_Q^A > 0$ and $\Delta\nu_Q^B < 0$. The arrows indicate the mutually exchanged transitions. The reduction of both $\Delta\nu_Q$ values and linewidths at high temperature mimics the decrease in orientational order when T is increased.

Computer simulation of the ^{2}H NMR spectral lineshapes and their fits with experimental resonances allow the kinetic constant, k, at the various temperatures explored to be determined. However, as the kinetic rate constant, the quadrupolar splittings and the relaxation time of deuterons are temperature-dependent, an accurate determination of k from simulations requires a good assessment of the parameters $\Delta\omega = 2\pi(\Delta\nu_Q^A/2 - \Delta\nu_Q^B/2)$ and $1/T_2^*$ at each temperature (see the Supporting Information).[7–9,24] Nevertheless, sufficiently accurate values of $1/T_2^*$ can be inferred from the linewidths of analogous samples (at the same T) in which exchange is not observed (achiral mesophase). If the difference, $\Delta\omega$, is directly measured from ^{2}H NMR spectra in the slow exchange regime, the $\Delta\omega$ values in the fast exchange regime will be obtained by extrapolation of the evolution of $\Delta\nu_Q$ values in the slow exchange regime, as we will describe in the discussion below.[12,24]

In a second step, the set of k parameters extracted from simulated ^{2}H NMR spectra is analysed by plotting an Eyring's plot, namely the natural logarithm of kNh/RT against $1/T$, before and after the coalescence temperature (see Figure 6b).[5a] Indeed, the dependence of $k(T)$ on temperature is theoretically described by Eyring's Equation (3),[25,26] where $\Delta G^{\neq}$ is defined by Equation (4), $R = 8.31$ J K^{-1} mol^{-1}, $N = 6.02 \times 10^{23}$ mol^{-1} and $h = 6.62 \times 10^{-34}$ J s.

$$k(T) = \frac{RT}{Nh} \exp\left(-\frac{\Delta G^{\neq}}{RT}\right) \quad (3)$$

$$\Delta G^{\neq}(\mathrm{T}) = \Delta H^{\neq} - T\Delta S^{\neq} \quad (4)$$

Interestingly, the rate constant, $k(T_c)$ (in s^{-1}), and the free energy of activation at the coalescence temperature T_c, $\Delta G^{\neq}(T_c)$ (in $kJ\,mol^{-1}$), can be rapidly deduced from the measurement of the half-difference of values of $|\Delta\nu_Q|$ ($|\Delta\Delta\nu_Q/2| = |\Delta\nu_Q^A/2 - \Delta\nu_Q^B/2|$) in the ^2H NMR spectra below T_c.[27] Indeed, at this particular temperature and assuming identical T_2^* for both exchanging deuterons, we can write Equations (5) and (6).[2,3,5a,25]

$$k(T_c) = \frac{2\pi \times |\Delta\nu_Q^A/2 - \Delta\nu_Q^B/2|}{2\sqrt{2}} \quad (5)$$

$$\Delta G^{\neq}(T_c) = RT_c \times \ln\left(\frac{RT_c}{Nh} \times \frac{\sqrt{2}}{\pi \times |\Delta\nu_Q^A/2 - \Delta\nu_Q^B/2|}\right) \quad (6)$$

Results and Discussion

Conformational analysis of diaryl derivatives 1–4 by MMCs: We have determined the evolution of the potential energy, E_{pot}, of **1**–**4** as a function of the inter-ring dihedral angle, ϕ(b-a-a′-b′), by MMCs (see Figure 1b). The calculations were carried out with the Hyperchem 5.0 software package using the semi-empirical AM1 force field.[28,29] More sophisticated approaches such as ab initio (STO-3 G) or DFT methods[30] were not used because the relative energies obtained with the AM1 and STO-3G methods for some specific values of ϕ differed by less than 3%. Hence it was pertinent to plot $E_{pot} = f(\phi)$ by using the less time-consuming method. Owing to the Born–Oppenheimer's approximation, the classical quantum-chemical software packages are not able to take into consideration isotope effects and hence they cannot distinguish between hydrogen and deuterium atoms. To mimic the decrease in the average distance of a C–D bond, we have artificially shortened the C–H distance to 107.3 pm at the site of isotopic substitution.[31]

The results of the MMCs are discussed in two parts. First, we compare the potential energy profiles of diaryl bromide derivatives **1** and **2**, which are both chiral with non-planar geometries (see Figure 1a) but differ from each other by virtue of the position of the bromine atom in the methylphenyl group. The different positions of the bromine atom in **1** and **2** should affect the height of the barrier to internal rotation about the a–a′ bond. Hence, the characteristics of the ^2H NMR spectra in chiral LCs should be significantly modified in terms of chiral discrimination at a given temperature, for instance, at room temperature. Secondly, we discuss the case of di- and monodeuterated derivatives **3** and **4** to analyse the effect of isotopic (H/D) substitution on conformational exchange.

The evolution of E_{pot} for **1** and **2** between 0 and 360° is displayed in Figure 3. For a simple comparison of data, the maximum for each curve has been set to 0. Data relative to these plots are listed in Table 1. For **1** and **2**, the curves are symmetrical about $\phi = 180°$ and the regions of the curve to the two sides of the maximum correspond to the enantiomeric conformers which may or may not be isolable, depending on the energy difference, $\Delta H^{\neq}$, between the minimum and the maximum potential energy. In the case of **1**, steric hindrance to rotation produces the highest energy rotamer for $\phi = 180°$, when the bromide interacts with the aromatic hydrogen atom denoted as i (see Figure 1). Quantitatively, the difference in E_{pot} between the maximum-energy planar rotamers obtained at $\phi = 0$ and 180° is equal to $-9.4\,kJ\,mol^{-1}$. Hence, the enantiomeric interconversion process is energetically favoured when the bromine atom interacts with the aromatic hydrogen atom b ($\phi = 0°$). Consequently, $\Delta H^{\neq}(\mathbf{1})$ is defined as the difference between the energy of the conformer at $\phi = 0°$ and the minimum of E_{pot}.

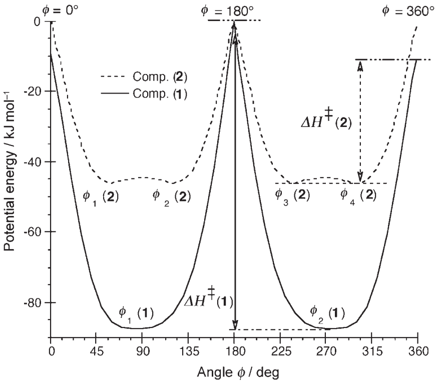

Figure 3. Potential energy profiles of **1** and **2** versus the dihedral angle ϕ (0–360°). The maximum for each curve was set to 0.

Table 1. Data extracted from the potential energy profile analysis of compounds **1**–**4**.

Compound	ϕ_{min}[a] [°]	$E_{pot}(0°)$[b] [$kJ\,mol^{-1}$]	$E_{pot}(\phi_{min})$[a] [$kJ\,mol^{-1}$]	$E_{pot}(180°)$[b] [$kJ\,mol^{-1}$]	$\Delta H^{\neq}$[c] [$kJ\,mol^{-1}$]
1	83.1	−9.4	−87.5	0	+78.1
2	57.5/ 122.5	< −0.05	−46.3	0	+46.3
3	57.5/ 122.5	< −0.05	−45.9	0	+45.9
4	57.5/ 122.5	< −0.05	−45.9	0	+45.9

[a] The minimal energy conformer was calculated by using a convergence criterion equal to $0.012\,kJ\,mol^{-1}$. [b] Each point of the curve was calculated with a convergence criterion equal to $0.04\,kJ\,mol^{-1}$. [c] Here, we define $\Delta H^{\neq}$ as being equal to $E_{pot}(0°) - E_{pot}(\phi_{min})$.

In the case of **2**, the energies of the rotamers at $\phi=0$ (or 360°) and 180° can be considered to be equal ($<0.05\,\mathrm{kJ\,mol^{-1}}$) and hence no preferential planar conformer exists. This behaviour indicates that the steric hindrance due to the bromine atom in the *meta* position is negligible compared with the steric hindrance of a bromine atom in the *ortho* position and does not affect the barrier to rotation compared with a non-substituted derivative.

The inter-ring torsion angle corresponding to the lowest energy conformation (ϕ_{min}) results from the balance between the steric repulsion due to the *ortho* substituents and the π-orbital overlap that produces maximum resonance stabilisation when the aromatic rings are co-planar.[3] The E_{pot} curve for **1** is quite flat in the angular regions around 90 and 270°, with two minima located at $\phi_1(\mathbf{1})=83.1°$ and $\phi_2(\mathbf{1})=276.9°$. This pattern of behaviour is generally observed when strong steric repulsion exists between bulky *ortho* substituents.[3] For **2**, the evolution of E_{pot} shows four local minima ($\phi_1(\mathbf{2})$, $\phi_2(\mathbf{2})$, $\phi_3(\mathbf{2})$ and $\phi_4(\mathbf{2})$) at $\phi=57.5$ and 122.5° and the complementary angles 302.5 and 237.5°. The presence of two local minima located symmetrically about 90° is due to the effect of resonance stabilisation by π orbital overlap at these four angles. This effect is measured at around $2\,\mathrm{kJ\,mol^{-1}}$. Finally, the large difference in activation energy, $\Delta H^{\neq}$, between **1** and **2** ($\approx 32\,\mathrm{kJ\,mol^{-1}}$) originates from the difference in steric hindrance due to the bulkiness of the bromine atom (vdW radius = 185 pm) relative to the hydrogen atom (vdW radius = 120 pm).

Compared with **1** and **2**, the dideuterated compound **3** is symmetrical with two small-volume substituents on the phenyl ring (two deuterons). From a chemical point of view, this molecule can be defined as prochiral because if we are able to dissymmetrise the phenyl ring through an appropriate chemical reaction, we obtain a chiral compound for all the dihedral angles ϕ differing from 0 and 180° (planar structure).[3] From a stereochemical point of view, this molecule is characterised by a plane of symmetry (σ) when $\phi=90°$ (see Figure 1c).

Depending on the constant k, which is related to the magnitude of $\Delta H^{\neq}$ and T, the stereochemical relationship between the two C–D directions in **3** is not the same and so gives different ^{2}H-{^{1}H} anisotropic spectra. Theoretically, three stereochemical situations exist. Firstly, if the rotation around the aryl–aryl bond is fast, no spectral discrimination between the C–D directions is possible and so a single doublet is expected. Secondly, if the rotation is sufficiently hindered, the C–D directions should be distinguished if their orientational order parameters are sufficiently different in the PBLG chiral phase. As the average conformation of **3** is of C_s symmetry, the C–D directions can be considered as enantiotopic.[3,16] In principle, two quadrupolar doublets are expected in the ^{2}H-{^{1}H} spectrum if $S^{pro\text{-}R}_{\mathrm{C-D_i}} \neq S^{pro\text{-}S}_{\mathrm{C-D_i}}$. Thirdly, if the rotation is impossible and if the dihedral angle ϕ is not 90° the molecule should adopt C_1 symmetry and then two enantiomeric forms exist in which the C–D directions are now diastereotopic. In this particular situation, four quadrupolar doublets should be observed. As the substituents at the b′ and f′ positions are identical, the evolution of E_{pot} for **3** versus ϕ is symmetrical about $\phi=90°$ and very similar to the evolution of E_{pot} for **2** (see Figure SI-2 in the Supporting Information). In fact the regions to each side of this angle correspond to enantiomeric pairs. In this particular case, it should be emphasised that the conformers at ϕ and $360-\phi$ are also mirror images and so the evolution of E_{pot} between 0 and 360° is also symmetrical about $\phi=180°$. Once again, the regions to the two sides of the absolute maximum correspond to enantiomeric pairs. Steric hindrance produces the highest energy rotational conformers for $\phi=0$ (360) and 180°. Owing to the absence of stabilisation by π orbital overlap when the phenyl and naphthyl rings are orthogonal, the lowest energy conformers are not found at 90° (see Table 1).[3] The barrier to rotation, $\Delta H^{\neq}$, is evaluated as $+45.9\,\mathrm{kJ\,mol^{-1}}$, while the barrier to interconversion between the enantiomeric conformer pairs, ϕ_1/ϕ_2 or ϕ_3/ϕ_4, is less than $+2\,\mathrm{kJ\,mol^{-1}}$. The slightly smaller value of $\Delta H^{\neq}$ for **3** relative to **2** ($0.4\,\mathrm{kJ\,mol^{-1}}$) indicates that the bromine atom in the *meta* position has only a very small effect on the height of the barrier to rotation.

As a result of dissymmetrisation of the phenyl ring, the diaryl **4** does not possess a plane of symmetry for the conformation $\phi=90°$ and it can be defined as a chiral derivative by virtue of the isotopic substitution (H/D). This molecule presents enantiomeric forms when ϕ is different to 0 and 180°. In the past, some rigid and flexible chiral molecules due to isotopic substitution have been investigated by ^{2}H NMR spectroscopy in polypeptide LCs, but derivatives exhibiting a conformational exchange detectable by NMR spectroscopy have not yet been explored.[32,33] In addition, it is worthwhile comparing the results obtained for **3** and **4** in order to analyse possible steric isotope effects on ^{2}H NMR spectra.[34] The MMCs carried out on **4** show that the potential energy profiles for **3** and **4** are identical. No deviation of the ϕ angles or of the $\Delta H^{\neq}$ values for **3** and **4** occurs when one of two C–D bonds is replaced by a C–H bond in the structure.

NMR study of 1-bromo-3-deuterio-5-methyl-2-(1′-naphthyl)-benzene (1): The ^{2}H-{^{1}H} NMR spectrum of compound **1** dissolved in PBLG/CHCl$_3$ at room temperature shows two quadrupolar doublets with a difference in quadrupolar splittings, $|\Delta\nu_Q^A-\Delta\nu_Q^B|$, equal to 257 Hz (Figure 4a). As the absolute configuration of each doublet is unknown, the stereodescriptors R and S were replaced by the arbitrary notations A and B. The presence of two doublets suggests a priori a difference in the orientation of the C–D direction in each enantiomer. To confirm this, we recorded the ^{2}H-{^{1}H} NMR spectrum of **1** dissolved in an achiral polypeptide oriented phase made of an equimassic mixture of PBLG and PBDG (enantiomer of PBLG), both dissolved in CHCl$_3$ (see Table 4 below). In this mixture, denoted "PBG", the spectral discrimination of the enantiomers or enantiotopic directions was eliminated.[35] Experimentally, the two doublets collapse into a single doublet. This second step therefore shows unambiguously that the enantiomers of **1** are spectrally dis-

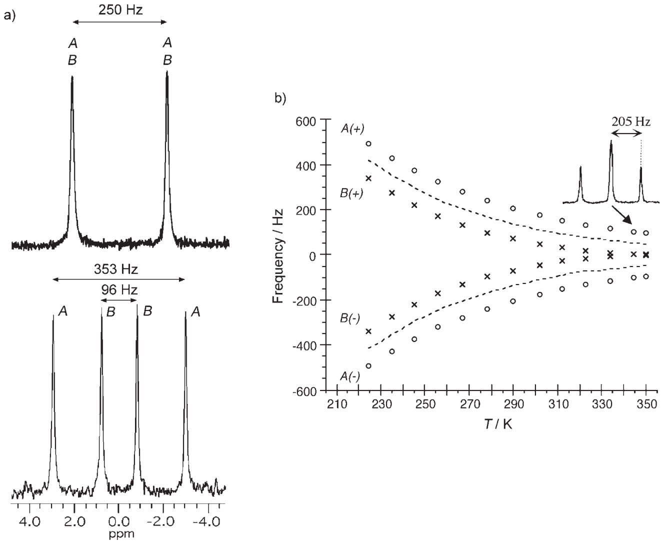

Figure 4. a) 61.4 MHz ^{2}H-{^{1}H} NMR spectra of **1** recorded at $T=302$ K in the PBG/CHCl$_3$ achiral phase (top) and in the PBLG/CHCl$_3$ chiral phase (bottom). b) Graphical evolution of positive and negative components of doublets A (outer) and B (inner) of **1** in the PBLG/CHCl$_3$ phase versus T. The dashed line corresponds to an experimental value of $\Delta\nu_Q^{average}$, namely the evolution that should be observed in the achiral mesophase assuming the same sign for values of $\Delta\nu_Q$. The insert shows the spectrum recorded at 345 K.

criminated. If this was not the case, two doublets would still be observed in PBG and then the NMR spectra in the two mesophases would be accounted for by other reasons (molecular conformational effects or mesophase-related phenomena). The magnitude of the doublet splitting in the PBG mesophase ($|\Delta\nu_Q^{PBG}|=250$ Hz) implies that the sign of the quadrupolar splittings in PBLG are identical, either positive or negative. Opposite signs would have led to a value of around 130 Hz. Ideally, the anticipated value should be equal to 225 Hz, but differences in the sample preparation can yield these small differences (see below). Finally, note that enantiomers of **1** have also been discriminated by proton-decoupled ^{13}C NMR spectroscopy.[14,36] Remarkably, this example illustrates that NMR spectroscopy in CLCs can be used to analyse chiral molecules without any stereogenic centre and devoid of conventional reactive functionality for which classical NMR tools are rather limited.[15]

From a conformational analysis point of view, we show here that the interconversion between enantiomers of **1** is sufficiently slow on the ^{2}H NMR timescale to allow separation of their deuterium signals at room temperature. This result is consistent with the $\Delta H^{\neq}$ value calculated by MMCs. Within experimental error, integration of the peak areas of A and B leads to identical values, thus indicating that the mixture is still racemic in the chiral LC phase. This implies that $K=k_{R\rightarrow S}/k_{S\rightarrow R}=1$ and thus shows that the mesophase does not modify the equilibrium constant in favour of one of the two enantiomers.

In a second series of NMR experiments, we recorded the ^{2}H-{1H} NMR spectra of **1** versus T (224–350 K) to check if the coalescence phenomenon could be observed (see Figure 4b). The evolution of the difference in quadrupolar splittings, $|\Delta\nu_Q^A-\Delta\nu_Q^B|$, the average linewidth (measured on the four components) and the average quadrupolar splitting, $\Delta\nu_Q^{average}=|\Delta\nu_Q^A+\Delta\nu_Q^B|/2$, is provided in the Supporting Information (see Figure SI-3). Analysis of the spectra shows that enantiomers are differentiated over the entire range of T. This result also includes the case in which one singlet and one doublet are simultaneously observed, as in the spectrum recorded at $T=345$ K (see the inset in Figure 4b). This situation arises when the C–D internuclear axis of one of the two enantiomers is aligned on average along the magic angle ($\theta=54.7°$) direction [Eq. (2)]. As a consequence, even at very high temperatures, the coalescence phenomenon was not observed.

As expected for any solute in a LC, the quadrupolar splittings increase monotonically as T decreases. This is a consequence of the reduction in the mobility of molecules in the mesophase as T is lowered. For a simple quantitative evaluation of the evolution of $|\Delta\nu_Q^{average}|$, $|\Delta\nu_Q^A|$, $|\Delta\nu_Q^B|$ or $|\Delta\nu_Q^A-\Delta\nu_Q^B|$ versus T, we can calculate the relative spectral variation, $\Delta X/\bar{X}$, expressed in %, of these quantities between T_{min} and T_{max} by using Equation (7), where X represents $|\Delta\nu_Q^{average}|$, $|\Delta\nu_Q^A|$, $|\Delta\nu_Q^B|$ or $|\Delta\nu_Q^A-\Delta\nu_Q^B|$. From this simple evaluation, we find that the relative spectral variations of $|\Delta\nu_Q^A-\Delta\nu_Q^B|$ and $|\Delta\nu_Q^{average}|$ between T_{min} and T_{max} are equal to 38 and 160%, respectively. This large difference in the relative variation of these quantities suggests that chiral discrimination and orientation mechanisms are two separate phenomena. This assumption is supported by other results reported in this paper.

$$\frac{\Delta X}{\bar{X}}[\%] = 100\times\frac{X^{T_{max}}-X^{T_{min}}}{(X^{T_{max}}+X^{T_{min}})/2} \qquad (7)$$

The evolution of $|\Delta\nu_Q^{average}|$ (and associated order parameters) as well as $|\Delta\nu_Q^A|$ and $|\Delta\nu_Q^B|$ versus T (in K) over a range of around 130 K can be fitted using an exponential function of the form given by Equation (8), where $R = 8.314\,\mathrm{J\,K^{-1}\,mol^{-1}}$ and the constants C and E are the parameters to be evaluated. Values of C and E are expressed in Hz and $\mathrm{J\,mol^{-1}}$, respectively, and are listed in Table 2.

$$\Delta\nu_Q[\mathrm{Hz}] = C \times \exp\left(-\frac{E}{RT[\mathrm{K}]}\right) \qquad (8)$$

Table 2. C and E parameters for fitting the evolution of $|\Delta\nu_Q^{\mathrm{average}}|$, $|\Delta\nu_Q^A|$ and $|\Delta\nu_Q^B|$ using Equation (8).

Entry	Compd	Polypeptide/ co-solvent	C prefactor [Hz] $|\Delta\nu_Q^{\mathrm{average}}|$ $|\Delta\nu_Q^A|/|\Delta\nu_Q^B|$	E factor [$\mathrm{kJ\,mol^{-1}}$] $|\Delta\nu_Q^{\mathrm{average}}|$ $|\Delta\nu_Q^A|/|\Delta\nu_Q^B|$	Average E factor [$\mathrm{kJ\,mol^{-1}}$][a]	χ parameter $|\Delta\nu_Q^{\mathrm{average}}|$ $|\Delta\nu_Q^A|/|\Delta\nu_Q^B|$
1	**1**	PBLG/$CHCl_3$	4.43	−9.866	−10.758	0.992
			15.1/0.49	−7.881/−13.635		0.981/0.995
2	**1**	PBLG/CH_2Cl_2	9.43	−8.253	−8.709	0.999
			21.2/2.1	−7.347/−10.071		0.999/0.995
3	**2**	PBLG/$CHCl_3$	128.3	−3.583	−3.585	0.999
			204.4/77.6	−3.063/−4.108		0.997/0.999
4	**3**	PBLG/$CHCl_3$	81.7	−4.337	−4.081	0.998
			143.6/59.6	−3.493/−4.668		0.997/0.996
5	**3**	PBG/$CHCl_3$	82.3	−4.442	–	0.998
6	**3**	PBLG/CH_2Cl_2	121.9	−2.272	−1.299	0.996
			177.0/197.0	−2.275/−0.323		0.993/0.954
7	**4**	PBLG/$CHCl_3$	69.4	−4.585	−3.986	0.998
			135.8/66.4	−3.543/−4.429		0.992/0.999
8	**4**	PBLG/$CHCl_3$	84.3[b]	−4.259[b]	–	0.999[b]

[a] Average E factor for $|\Delta\nu_Q^A|$ and $|\Delta\nu_Q^B|$. [b] Corrected values for $|\Delta\nu_Q^{\mathrm{average}}|$ [see Eq. (9)].

The factor E is the same for fitting the evolution of $|\Delta\nu_Q^A|$, $|\Delta\nu_Q^B|$ or the positive, $A(+)$ or $B(+)$, and negative, $A(-)$ or $B(-)$, resonances. In contrast, the prefactor C associated with the positive and negative resonances is obtained by dividing the value of C obtained for $\Delta\nu_Q^A$ or $\Delta\nu_Q^B$ by a factor of +2 and −2, respectively. Except in one case (Table 2, entry 6), we observe that the outer doublet, $\Delta\nu_Q^A$, is characterised by a higher C and a lower E than the inner doublet. This situation is expected if the variations in $\Delta\nu_Q^A$ and $\Delta\nu_Q^B$ are rather similar between $T_{\min}$ and $T_{\max}$. Equation (8) differs from Haller's equation, $S = S_o(1-T/T^*)^{\alpha}$, which is classically used to fit the evolution of the order parameters versus T for nematic liquid crystals.[37] In fact, this equation cannot be used to fit anisotropic parameters in the case of organic solutions of PBLG because the nematic–isotropic transition temperature (N→I) cannot be determined (due to the evaporation of co-solvent). As we will see below, this kind of evolution has been ascertained using two liquid-crystalline phases irrespective of the compound (**1**–**4**) (see Table 2). For all of them, the factor E relative to the evolution of $|\Delta\nu_Q^{\mathrm{average}}|$ is approximately the average of factors E determined for $|\Delta\nu_Q^A|$ and $|\Delta\nu_Q^B|$. Thus, the discrepancy between the factors E obtained for **1** is less than 10%. This behaviour suggests that the enantiomeric discrimination in the CLC may be described as a deviation from the average order existing in the achiral oriented phase.

Remarkably, Equation (8) is similar to the Boltzmann's relation. In fact, we can infer that the evolution of the magnitude of $\Delta\nu_Q$ for a given C–D bond, and consequently the associated $S_{\mathrm{C-D}}$ order parameter, versus T can be related to the "strength" of the interaction potential (van der Waals) between this molecular direction and its environment. The negative sign for E indicates an attractive potential between the PBLG helices and the C–D bond. In addition, the E values (in $\mathrm{kJ\,mol^{-1}}$) obtained are comparable to energies associated with van der Waals interactions and are very close to the thermal energies (RT), which vary from 1.771 (213 K) to 2.910 $\mathrm{kJ\,mol^{-1}}$ (350 K) in this study.[38] To confirm these results, further investigations on a wide range of solutes are underway.

In contrast to $|\Delta\nu_Q^{\mathrm{average}}|$, the variation in $|\Delta\nu_Q^A - \Delta\nu_Q^B|$ versus T is relatively small and its evolution can be fitted using a linear function. In this example, we found that $|\Delta\nu_Q^A - \Delta\nu_Q^B|\,[\mathrm{Hz}] = -0.934T[\mathrm{K}] + 542.2$, with $\chi = 0.989$. The existence of distinct evolutions for $|\Delta\nu_Q^{\mathrm{average}}|$ and $|\Delta\nu_Q^A - \Delta\nu_Q^B|$ is somewhat consistent with the large differences in the relative variations of these quantities. Again, these facts are new arguments in favour of the separation of the mechanisms for orientation and chiral discrimination, which can be seen as distinct phenomena and so treated separately.

The absence of coalescence signals at 350 K implies that T_c is at a higher temperature and hence the activation parameters cannot be calculated using 1D ^{2}H NMR spectra in the PBLG/$CHCl_3$ solvent. Another co-solvent with a higher boiling point, such as DMF, could be used in order to record ^{2}H NMR spectrum above $T = 350$ K, but this change has not been explored because the magnitude of $|\Delta\nu_Q^A/2 - \Delta\nu_Q^B/2|$ in this new oriented solvent is a priori unknown. To estimate the exchange rates, we have explored the use of 2D exchange spectroscopy (EXSY 2D experiments).[22,39] However, irrespective of the mixing time used, no exchange cross-peaks between the two quadrupolar doublets were observed experimentally on the 2D map, very likely because the activation barrier is too high to be determined by this approach. In fact, because Equations (4) and (6) are equal at T_c, we may predict T_c of **1** by making some reasonable assumptions. By using the hypothesis in which the quantities $|\Delta\nu_Q^A/2 - \Delta\nu_Q^B/2|$ at $T > 350$ K, $\Delta H^{\neq}$ and $\Delta S^{\neq}$ are known, we can graphically resolve this equality to determine T_c and $\Delta G^{\neq}(T_c)$.[40] The magnitude of $|\Delta\nu_Q^A/2 - \Delta\nu_Q^B/2|$ above 350 K can be extrapolated from the exponential fit of the entities $\Delta\nu_Q^A$ and $\Delta\nu_Q^B$ (see Table 2, entry 1). If the $\Delta H^{\neq}$ value can be set to the value determined by the MMCs (+78.1 $\mathrm{kJ\,mol^{-1}}$), we ignore the $\Delta S^{\neq}$ value for **1**. However, we can assume that $\Delta S^{\neq}$ is close to the data obtained for analogous com-

Table 3. Comparison of the data evaluated by molecular modelling calculations and experimental parameters for compounds **2**, **3** and **4**.

	Data evaluated from molecular modelling		Data determined from NMR experiment in CLC							
Compd.	ϕ [°]	$\Delta H^{\neq}$ [kJ mol^{-1}]	Polypeptide/ co-solvent	T_c [K]	$\lvert\Delta\Delta\nu_Q/2\rvert$ [Hz]	$k(T_c)$[a] [s^{-1}]	$\Delta G^{\neq}(T_c)$[b] [kJ mol^{-1}]	$\Delta H^{\neq}$[c] [kJ mol^{-1}]	$\Delta S^{\neq}$[c] [J mol^{-1} K^{-1}]	$\Delta G^{\neq}(T_c)$[c] [kJ mol^{-1}]
2	57.5/122.5	46.3	PBLG/$CHCl_3$	250±2	175±5	389±12	48.5±0.5	44.7±0.5	−18±2	49.0±0.5
3	57.4/122.6	45.9	PBLG/$CHCl_3$	245±2	102±5	226±11	48.6±0.5	44.2±0.5	−19±2	48.9±0.5
3	57.4/122.6	45.9	PBLG/CH_2Cl_2	245±2	106±5	235±11	48.5±0.5	43.6±0.5	−16±2	47.6±0.5
4	57.4/122.6	45.9	PBLG/$CHCl_3$	245±2	98±5	218±11	48.7±0.5	44.3±0.5	−20±2	49.2±0.5

[a] Values calculated from Equation (5). [b] Values calculated from Equation (6). [c] Values derived from the Eyring's plot.

pounds (such as **2**). By using this argument, the $\Delta S^{\neq}$ value was set to $-19\,\mathrm{J\,mol^{-1}\,K^{-1}}$ (see Table 3). This approach leads to a value for T_c of 415.5 K and $\Delta G^{\neq}(T_c)$ of $+86.0\,\mathrm{kJ\,mol^{-1}}$.[41]

As an alternative to the NMR approach, we explored the analytical potential of chiral HPLC. Thus it was possible to separate the enantiomers of **1** by using a chiral stationary phase (Chiralcel ODH column) at 298 K with hexane as eluent (flow $0.5\,\mathrm{mL\,min^{-1}}$). The chromatogram (not shown) displays two sharp peaks (with retention time = 35.3 and 46.6 min) separated by a rather flat "plateau". These particular chromatograms are generally recorded for molecules undergoing an interconversion between enantiomers during their elution on a resolving enantiopure stationary phase. The effect is referred to as "peak coalescence of the second type".[42] By using the technique developed by Schurig and co-workers, it is possible to simulate the chromatogram of **1** in order to evaluate $\Delta G^{\neq}(298\,\mathrm{K}) = +91.4 \pm 0.6\,\mathrm{kJ\,mol^{-1}}$.[43] By assuming that $\Delta S^{\neq} = -19\,\mathrm{J\,mol^{-1}\,K^{-1}}$, we can estimate $\Delta H^{\neq}$ to be $+85.7\,\mathrm{kJ\,mol^{-1}}$ from Equation (4). The difference between the data determined by this approach and that deduced by MMCs is about 10%. Although the $\Delta S^{\neq}$ term is generally small for intramolecular exchanges in small molecules, the discrepancy in $\Delta H^{\neq}$ can mainly be attributed to the approximation made for $\Delta S^{\neq}$. Here we probably underestimate $\Delta S^{\neq}$ because **1** exhibits a much greater steric hindrance than other compounds. However, the relatively good agreement between the two results is satisfactory. Another approach would involve evaluating $\Delta S^{\neq}$ by combining the value of $\Delta H^{\neq}$ determined by MMCs and $\Delta G^{\neq}$ value derived by HPLC at 298 K. By using Equation (4) we found $\Delta S^{\neq} = -45\,\mathrm{J\,mol^{-1}\,K^{-1}}$. This value is two times higher than those determined by NMR analysis for **2** or **3**. By using this new value, we can evaluate T_c for compound **1** to be 473 K and $\Delta G^{\neq}(T_c)$ to be $+99.4\,\mathrm{kJ\,mol^{-1}}$. Reasonably, the correct value of $\Delta S^{\neq}$ is intermediate between the two values given above. By using the average value ($-32\,\mathrm{J\,mol^{-1}\,K^{-1}}$), $T_c = 442.5$ K and $\Delta G^{\neq}(T_c) = +92.3\,\mathrm{kJ\,mol^{-1}}$ are obtained.

NMR study of the 1-bromo-3-deuterio-2-methyl-5-(1′-naphthyl)benzene (2): In contrast to compound **1**, the ^{2}H-{^{1}H} NMR spectrum of **2** recorded at room temperature (302 K) shows a single quadrupolar doublet with a splitting of 538 Hz (see Figure 5a). Consequently the interconversion between the enantiomeric forms of **2** is sufficiently fast on the NMR timescale to prevent spectral enantiodiscrimination in PBLG at room temperature. This result is in agreement with the smaller barrier to internal rotation in **2** relative to **1**, as evaluated by MMCs (see Table 1). Spectrally, this single quadrupolar doublet corresponds to the average of the quadrupolar splittings arising from the *R* and *S* isomers. In fact, this ^{2}H NMR spectrum is identical to that expected in the achiral oriented solvent, PBG. This conclusion will be illustrated for diaryl **3**.

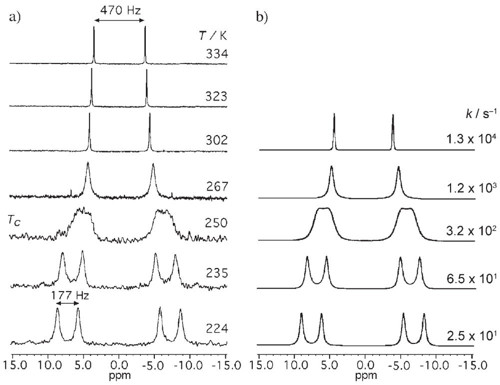

Figure 5. a) Experimental 61.4 MHz ^{2}H-{^{1}H} NMR spectra of **2** dissolved in the PBLG/$CHCl_3$ phase recorded at different temperatures as indicated on the right side. b) Simulated spectra computed with the specific rate constant, *k*, indicated on the right side.

To observe the coalescence phenomenon for **2**, we have to reduce the interconversion rate by lowering the temperature. Figure 5a shows the experimental evolution of the anisotropic ^{2}H-{^{1}H} NMR spectra of **2** versus *T*. For a better visualisation, the evolution of $\Delta\nu_Q$ values over the temperature range 224–350 K is shown in Figure 6a (see also Figure SI-3b in the Supporting Information). While significant line-broadening is observed below 270 K, the coalescence phenomenon occurs at $T_c = 250 \pm 2$ K. Here, the phenomenon can be clearly identified because a single doublet with very broad components (≈130 Hz linewidth) is recorded. This spectral lineshape indicates that the signs of the $\Delta\nu_Q$ values are the same for both enantiomers (as for **1**) at low temperatures (see Figure 2a). Thus it is possible to determine the

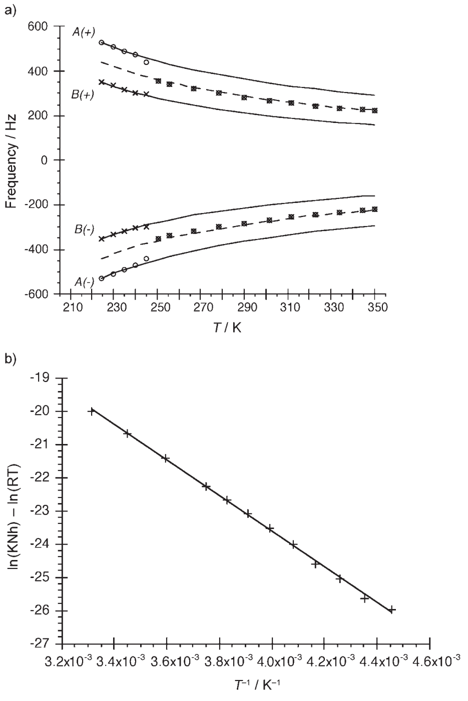

Figure 6. a) Graphical evolution of the positive and negative components of the doublets *A* (outer) and *B* (inner) of **2** dissolved in the PBLG/$CHCl_3$ phase versus *T*. The continuous lines represent the predicted evolution of the components for both doublets versus *T* if no coalescence phenomenon exists (see text). The dashed lines simulate the average evolution of $\Delta\nu_Q$ (derived from the predicted evolution) that should be ideally observed in the achiral oriented phase, assuming identical signs for the values of $\Delta\nu_Q$. b) Eyring's plot obtained for **2**. The full line corresponds to the linear fit of data ($\chi = 0.999$).

relative sign of the $\Delta\nu_Q$ values without recording data in the PBG mesophase. Below T_c, two resolved quadrupolar doublets, the linewidths of which decrease with *T* (until 224 K), are observed, thus demonstrating that 1) the average orientation of each enantiomer is different in the mesophase and 2) their lifetime is now sufficiently long on the NMR timescale to observe their respective NMR signal. This notable result highlights the ability of the polypeptide helices to distinguish between enantiomers of axially chiral derivatives even if the barrier to rotation is not enough to discriminate them at room temperature.

Although the half-difference of the $\Delta\nu_Q$ values is temperature-dependent, its evolution is very weak below T_c. Consequently, by adopting an average value for $|\Delta\nu_Q^A/2 - \Delta\nu_Q^B/2|$ equal to (175 ± 5) Hz, we can evaluate $k(T_c)$ to be $(389 \pm 12)\ s^{-1}$ and $\Delta G^{\neq}(T_c)$ to be $(+48.5 \pm 0.5)\ kJ\,mol^{-1}$ for **2** using Equations (5) and (6) and $T_c = (250 \pm 2)$ K. The analysis of Eyring's plot over a sufficient temperature range around T_c allows $\Delta G^{\neq}(T_c)$ as well as other activation parameters to be calculated more accurately from NMR results. This supposes, however, that we are able to determine the rate constants for each temperature by fitting the experimental ^2H NMR signals to the theoretical lineshapes [see Equations (SI-4) and (SI-5) in the Supporting Information]. Below T_c, the quantity $|\Delta\nu_Q^A/2 - \Delta\nu_Q^B/2|$ is directly measured from the experimental spectra (see Figure 5a). Above T_c, this quantity has to be extrapolated from the evolution of the *A* and *B* doublets observed in the slow exchange regime, as if the coalescence phenomenon did not exist.[12,24] In this hypothetical case, two doublets are expected owing to chiral discrimination. Regarding the previous results obtained for **1**, we have assumed that the four transitions, $\omega^A_{-1,0}$, $\omega^B_{-1,0}$, $\omega^A_{0,1}$ and $\omega^B_{0,1}$, follow an exponential evolution over the entire temperature range. Thus, it is possible to predict the frequency evolution of these transitions versus *T* using Equation (8) and data extracted from the slow exchange regime. The parameters *C* and *E* associated with $\Delta\nu_Q^A$ and $\Delta\nu_Q^B$ values are listed in Table 2 (entry 3). As an illustration, the hypothetical evolution of the four components above T_c is shown in Figure 6a (continuous lines). Thus, these extrapolations permit the term $|\Delta\nu_Q^A/2 - \Delta\nu_Q^B/2|$ to be calculated in the fast exchange regime.[24] By assuming that sufficiently accurate values of $1/T_2^*$ can be extracted from the linewidths of analogous samples for which no exchange process is observed (PBG phase), this strategy allows the variables of Equations (SI-4) and (SI-5) in the Supporting Information, which are actually kept constant during the fitting procedure, to be predicted.

As expected, the points on the Eyring's plot (Figure 6b) form a straight line, the slope and *y* intercept of which permit $\Delta H^{\neq}$ and $\Delta S^{\neq}$, respectively, to be determined.[5] Parameters derived from the Eyring's plot are $\Delta H^{\neq} = (+44.7 \pm 0.5)\ kJ\,mol^{-1}$, $\Delta S^{\neq} = (-18.0 \pm 0.5)\ J\,mol^{-1}\,K^{-1}$ and finally $\Delta G^{\neq} = (+49.0 \pm 0.5)\ kJ\,mol^{-1}$ at T_c. The discrepancy between $\Delta G^{\neq}(T_c)$ deduced from the Eyring's plot and calculated using Equation (6) mainly arises from the uncertainty in T_c. The experimental $\Delta H^{\neq}$ value differs by less than 2 $kJ\,mol^{-1}$ (<4%) from the theoretical value determined by MMCs (see Table 3), thus indicating the reliability of the two methods. The small magnitude of $\Delta S^{\neq}$ is reasonable because the transition state of small-to-medium-sized molecules undergoing an intramolecular exchange is not more significantly ordered (from the entropic point of view) than the ground state.[5a] Under these conditions, the entropy change, $\Delta S^{\neq}$, between the ground state (the lowest energy rotamer) and the transition state (the highest energy rotamer) is rather small or even close to zero.[5a] Also we found that the rotation rate is around $1.3 \times 10^4\ s^{-1}$ at 302 K, thus implying that spectral enantiodiscrimination could be observed at this temperature only if $|\Delta\nu_Q^A/2 - \Delta\nu_Q^B/2|$ was much larger than 5850 Hz [Eq. (5)]! Finally, the excellent agreement between the predicted and experimental $\Delta H^{\neq}$ values indicates that the intermolecular forces between the solute and the PBLG phase do not significantly influence the conformational interconversion process of **2** (compared with an isolated molecule). This new study confirms other recent results involving complex calculations.[44]

From the point of view of orientational behaviour, the comparison between the evolution of the spectral data versus T for **1** and **2** is noteworthy (see Figure 4b and Figure 6a). Indeed, as the main directions of electrical field gradient (EFG) tensor for the C–D bonds in **1** and **2** are almost parallel, they provide the same information in terms of order parameters relative to the magnetic field axis and hence it is possible to interpret the differences observed. Over the temperature range explored (224–350 K), the global evolution of $|\Delta\nu_Q^{\text{average}}|$ and $|\Delta\nu_Q^A/2-\Delta\nu_Q^B/2|$ (partly obtained by extrapolation) for **2** is similar to the evolution observed for **1**, but differences in their respective variations exist. If the relative variation of $|\Delta\nu_Q^A-\Delta\nu_Q^B|$ for **2** and **1** is similar (29 instead of 38 %), the relative variation of $|\Delta\nu_Q^{\text{average}}|$ is very different (67 instead of 160 %). From a theoretical point of view, these results suggest that the chiral discrimination mechanisms for **2** and **1** are similar over a large temperature range and lead to spectral separation of similar magnitude. Thus the values of $|\Delta\nu_Q^A-\Delta\nu_Q^B|$ for **2** and **1** are equal to 314 and 353 Hz, respectively, at 213 K, and 204 and 266 Hz at 350 K. In other words, the position of the bromine atom has only a small effect on the spectral separation, thus suggesting that the discrimination mechanisms are more sensitive to a global shape recognition rather than to local changes in the molecular structure. This conclusion confirms recent work on the discrimination of chiral hydrocarbons that indicated that shape recognition plays a crucial role in the chiral discrimination mechanisms of apolar enantiomers.[15] In contrast, the molecular orientation mechanisms seem to be more sensitive to the global geometry of the solute since the position of the bromide on the phenyl ring significantly affects the magnitude of $|\Delta\nu_Q^{\text{average}}|$. This result could be related to the fact that these mechanisms are more sensitive to electrostatic intermolecular interactions, for which the position of the bromine atom plays an important role. This analysis of the results supports again the idea that the chiral discrimination and orientation phenomena do not follow the same laws and could be treated using different interaction mechanisms.

NMR study of 1-(2′,6′-dideuterio-4′-methylphenyl)naphthalene (3): With regard to the MMC results, the spectral behaviour of **3** should be a priori very similar to that of **2** in spite of their stereochemical differences. Figure 7a shows some anisotropic ^{2}H-{^{1}H} NMR spectra of **3** recorded in the PBLG phase between 213 and 350 K (see also Figure SI-4 and SI-5a in the Supporting Information). Similarly to **2**, we observe a sharp quadrupolar doublet (linewidth < 5 Hz) at 302 K and above, while the coalescence phenomenon is reached at $T_c = (245 \pm 2)$ K. This T_c value is slightly lower than that for **2** because the difference in $\Delta\nu_Q$ values for the C–D directions is now equal to 204 instead of 348 Hz. As before, the coalescence lineshape corresponds to the case in which the quadrupolar doublets have identical signs at low temperatures. The presence of two resolved doublets below T_c indicates two distinct averages for the orientation of the C–D directions ($S_{\text{C-D}}^{pro\text{-}R} \neq S_{\text{C-D}}^{pro\text{-}S}$). To confirm this result, we recorded the ^{2}H-{^{1}H} NMR spectra of **3** in the achiral phase PBG/CHCl$_3$ over the same temperature range (see Figure 7b and SI-5b in the Supporting Information). A single doublet ($S_{\text{C-D}}^{pro\text{-}R} = S_{\text{C-D}}^{pro\text{-}S}$) was observed irrespective of the temperature. This last result shows that the two doublets observed at low T in PBLG do not originate from a particular reorientation phenomenon of the solute, but arise from the orientational non-equivalence of the C–D directions in the chiral mesophase. Thus we assess experimentally the enantiotopic character of these directions when the rotation is slow relative to the NMR timescale and so demonstrate that the molecular structure resulting from averaging of all rotamers has C_s symmetry.

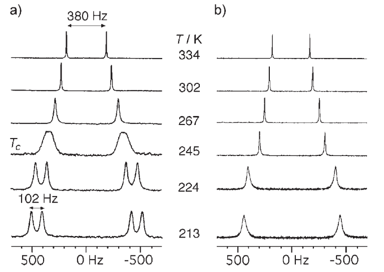

Figure 7. Experimental 61.4 MHz ^{2}H-{^{1}H} NMR spectra of **3** dissolved in a) the PBLG/CHCl$_3$ phase and b) the PBG/CHCl$_3$ phase at different temperatures as indicated. Note the difference in linewidth at 245 K.

By using an averaged value of $|\Delta\Delta\nu_Q/2| = 102 \pm 5$ Hz, we calculated $k(T_c) = (226 \pm 11)\ \text{s}^{-1}$ and $\Delta G^{\neq}(T_c) = (+48.6 \pm 0.5)\ \text{kJ mol}^{-1}$ from Equations (5) and (6). By applying the procedure described above for **2**, the k values extracted from each simulated ^{2}H-{^{1}H} NMR spectrum were analysed using the Eyring's plot. The evolution of the average of the $\Delta\nu_Q$ values (dashed lines) extrapolated from data measured in the slow regime correctly fits the evolution of $|\Delta\nu_Q^{\text{average}}|$ (measured below and above T_c) from 213 to 305 K, but diverges slightly at higher temperatures (see Figure SI-4 in the Supporting Information). The discrepancy measured at 350 K is 38 Hz, that is, an error of around 10 %. This effect is mainly related to the small number of points used for fitting data during the slow exchange regime (five points). As the temperature range used to evaluate k varies from 224 to 302 K, this divergence has only a small impact on the accuracy of k. Parameters derived from the Eyring's plot are given in Table 3. Once again the experimental $\Delta H^{\neq}$ value differs by less than $2\ \text{kJ mol}^{-1}$ (< 4 %) from the value obtained by MMCs. The rotation rate calculated at 302 K ($k = 1.2 \times 10^4\ \text{s}^{-1}$) is very similar to the value found for **2**, thus confirming that the bromine atom in the *meta* position does not hinder rotation about the sp^2–sp^2 bond.

As in preceding examples, the evolution of $|\Delta\nu_Q^{\text{average}}|$ for **3** dissolved in the PBLG and PBG phases can be fitted with good agreement by using Equation (8) ($\chi > 0.997$). Comparison of the results obtained in the two phases indicates that parameters C and E differ by less than 1 and 3 %, respectively (see Table 2, entries 4 and 5). These minor discrepancies arise mainly from small differences in the sample preparation (slight changes in the composition) as well as in differences in the average degree of polymerisation (DP) of the polypeptides used (see Table 4). As in the case of **1**, the evolution of the difference of $\Delta\nu_Q$ values is linear below T_c. Again, we confirm the assumption that mechanisms for orientation and discrimination are not the same. In addition, it appears that the discrimination phenomenon could be seen as a simple perturbation of the orientation phenomenon. If this was not the case, the E fitting factors associated with the evolution of $|\Delta\nu_Q^A|$, $|\Delta\nu_Q^B|$ and $|\Delta\nu_Q^{\text{average}}|$ (in the PBG or PBLG phase) versus T should be very different. Except for the cases in which the angular terms $\theta^A_{\text{C-D}_i}$ and $\theta^B_{\text{C-D}_i}$ are rather close to the magic angle, the above statements could explain why the signs of the quadrupolar splittings for monodeuterated enantiomers or C–D enantiotopic directions are generally identical.

Experimentally, spectral discrimination of the enantiomeric rotamers (ϕ_1/ϕ_2 and ϕ_3/ϕ_4) was not observed in the spectra at low temperatures, even by recording the ^{2}H NMR spectrum at 200 K (not shown). Below this temperature, the sample starts to form a gel phase, thus preventing the use of PBLG as a weakly ordering liquid crystal with a low viscosity. This result is in accord with the MMCs since the height of the barrier between the most populated enantiomeric conformers, ϕ_1/ϕ_2 or ϕ_3/ϕ_4, is only around 2 kJ mol^{-1}. Thus, if we assume that $|\Delta\Delta\nu_Q/2|$ could vary between 50 and 110 Hz, we can predict that the second coalescence phenomenon should be observed between 11.2 and 11.6 K! These temperatures are technically impossible to reach with current NMR probes and is evidently not applicable to a PBLG sample. Finally, note that the evolution of the spectra could also be explained by assuming a potential energy profile with only just two minima set at 90 and 270°, corresponding to a prochiral conformer of C_s symmetry.

NMR study of 1-(2′-deuterio-4′-methylphenyl)naphthalene (4): The evolution of the ^{2}H-{^{1}H} NMR spectra (quadrupolar splitting, linewidths) for compound **4** versus T is very similar to that observed for **3** (see Figure SI-6 in the Supporting Information). The coalescence phenomenon is observed at (245 ± 2) K and the average value of $|\Delta\Delta\nu_Q/2|$ measured below T_c (on three points) is equal to (98 ± 5) Hz (instead of 102 Hz). This small deviation can be attributed to small differences in the sample composition, but also to the linewidths measured at T_c (around 25 Hz). By using these values, we obtain $k(T_c) = (218 \pm 10)\ \text{s}^{-1}$ and $\Delta G^{\neq}(T_c) = (+48.4 \pm 0.5)\ \text{kJ mol}^{-1}$. The activation parameters derived from the Eyring's plot analysis are listed in Table 3. Within experimental error, we can conclude that the activation parameters for **3** and **4** are identical. This means that the conformational dynamics are the same, or at least, the replacement of deuterium by the hydrogen atom does not modify the conformational behaviour of **4** compared with **3** sufficiently to induce differences in the activation parameters larger than experimental error. The evolution of $|\Delta\nu_Q^{\text{average}}|$ versus T for **4** (dashed line) and **3** (continuous line) is plotted in Figure 8. As can be seen, small differences exist, in particular, at high temperatures. This effect primarily results from minor differences in the sample preparation or the macroscopic homogeneity of the phase. To correct these effects and obtain a more reliable comparison, a correction to $|\Delta\nu_Q^{\text{average}}(\mathbf{4})|$ can be applied by weighting each value with a parameter that is directly related to the liquid-crystalline phase. With this aim, we used the ^{13}C–^{1}H dipolar coupling, $^1D_{\text{CH}}$, of the organic co-solvent (here, chloroform), which can be measured from the signals from ^{13}C satellites in the ^{1}H NMR spectra.[15] The correction applied to $|\Delta\nu_Q^{\text{average}}(\mathbf{4})|$ is given by Equation (9).

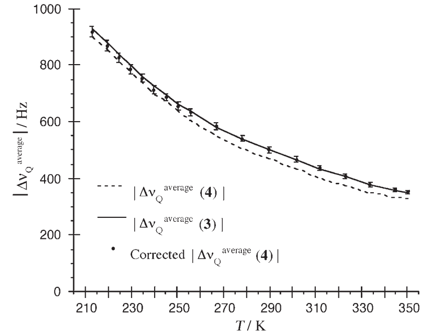

Figure 8. Comparison of $|\Delta\nu_Q^{\text{average}}(\mathbf{3})|$ and $|\Delta\nu_Q^{\text{average}}(\mathbf{4})|$ with and without corrections. Note the excellent fit between values of **4** (after correction) and **3**.

$$|\Delta\nu_Q^{\text{corrected average}}(\mathbf{4})| = |\Delta\nu_Q^{\text{average}}(\mathbf{4})| \times \left|\frac{^1D_{\text{CH}}(\mathbf{3})}{^1D_{\text{CH}}(\mathbf{4})}\right| \tag{9}$$

Applying this correction harmonises the two sets of data. Quantitatively, differences of 3 and 2 % in the C and E parameters, respectively, are found when the evolution of $|\Delta\nu_Q^{\text{average}}(\mathbf{3})|$ and $|\Delta\nu_Q^{\text{average}}(\mathbf{4})|$, after corrections, are fitted using Equation (8) (see Table 2, entries 4 and 8). From an orientational point of view, we have thus demonstrated that the origin of the discrimination of enantiomers of chiral molecules by virtue of isotopic substitution (H/D) is a consequence of the discrimination of enantiotopic C–D directions in related, prochiral molecules.

Influence of the co-solvent on the conformational dynamics: As an extension of this study, we investigated the influence of the nature of the organic co-solvent on the orientational behaviour and the intramolecular dynamic processes of compounds **1** and **3**. For this purpose, we replaced chloroform by dichloromethane and recorded the ^{2}H NMR spectra over the maximal temperature range 213–344 K. It is difficult to heat the PBLG sample in dichloromethane above 345 K owing to the boiling point of this co-solvent. Figure 9a and 9b show the spectral evolution of the positive and negative components of the quadrupolar doublets of **1** and **3** as a function of temperature. In both cases, the global evolution of the $\Delta\nu_Q$ values is identical to that obtained when chloroform was employed as co-solvent. Thus for **3**, the coalescence effect is visible at (245 ± 2) K, while no effect is observed for **1** in the temperature range explored. By using the same procedure as described above for evaluating T_c for **1** dissolved in the PBLG/CHCl$_3$ phase and by setting $\Delta S^{\neq}$ to $(-32\pm2)\,\mathrm{J\,mol^{-1}\,K^{-1}}$, we evaluate T_c and $\Delta G^{\neq}(T_c)$ to be 442.5 K and $+92.3\,\mathrm{kJ\,mol^{-1}}$, respectively. These data are similar to those obtained in PBLG/CHCl$_3$, thus reflecting the fact that the values of $|\Delta\Delta\nu_Q/2|$ are small and similar in both media at high temperatures. Similarly to preceding examples, the coalescence phenomenon for **3** is characterised by a single doublet with broad components and then by two quadrupolar doublets below T_c. By using an average value of $|\Delta\Delta\nu_Q/2| = (106\pm5)$ Hz, we obtain $k(T_c) = (235\pm11)\,\mathrm{s^{-1}}$ and $\Delta G^{\neq}(T_c) = (+48.5\pm0.5)\,\mathrm{kJ\,mol^{-1}}$. As before, the evolution of the average of the $\Delta\nu_Q$ values extrapolated from data recorded in the slow exchange regime (dashed line) fits the evolution of $|\Delta\nu_Q^{\mathrm{average}}|$ (measured below and above T_c) with an error <5 % between 213 and 305 K, but starts to diverge for temperatures above 305 K. At 340 K, the discrepancy is less than 40 Hz, that is, an error of 14 %. The activation parameters derived from the Eyring's analysis are included in Table 3. Although the $\Delta G^{\neq}(T_c)$ value is slightly smaller than other $\Delta G^{\neq}(T_c)$ values, we estimate that the deviation between the activation parameters obtained in the PBLG/CHCl$_3$ and PBLG/CH$_2$Cl$_2$ phases is not sufficient to confirm that the nature of the co-solvent affects the dynamics of the compounds investigated here.

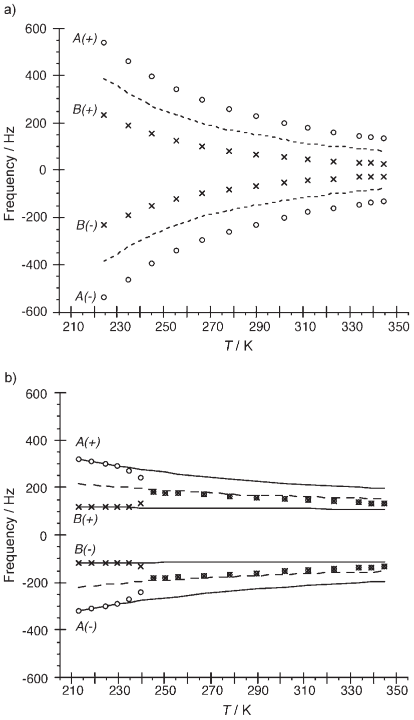

Figure 9. a) Evolution of the positive and negative components of doublets *A* (outer) and *B* (inner) of **1** in the PBLG/CH$_2$Cl$_2$ phase versus *T*. b) As for a), but for compound **3**. See the caption to Figure 6a for a definition of the curves and graphical points.

As before, the evolution of $|\Delta\nu_Q^{\mathrm{average}}|$ for both compounds can be fitted using Equation (8). The *C* and *E* factors are listed in Table 2 (entries 2 and 6). The *E* factor, which reflects the decrease in the exponential function, is globally reduced by around 17 % for **1** and 48 % for **3** compared with values in the PBLG/CHCl$_3$ mesophase. These findings are consistent with the relative variations in $|\Delta\nu_Q^{\mathrm{average}}|$, which are equal to 131 % for **1** and 44 % for **3** between $T_{\mathrm{min}} = 224$ K and $T_{\mathrm{max}} = 344$ K instead of 156 and 83 % measured in the PBLG/CHCl$_3$ phase. Note also that there is only a small variation in $\Delta\nu_Q^B$ (Figure 9b), but it can still be fitted with an exponential function with a very small *E* factor, while the evolution of $\Delta\nu_Q^A$ shows a significant variation between T_{min} and T_{max}. The differential spectral evolution between the inner and outer doublets results from a different evolution of orientational behaviour between the enantiotopic C–D directions. This evolution, not observed for the other samples, is rather difficult to interpret because we probe only two directions of the five independent internuclear directions required to determine correctly Saupe's matrix.[20,21] Put simply, we can assume that the C–D direction associated with $\Delta\nu_Q^B$ tends to reorient towards the magnetic field axis as *T* increases, thus balancing the global decrease in the molecular order parameters due to faster molecular motions.

Conclusion

Herein, we have demonstrated the robustness of ^{2}H NMR spectroscopy in weakly ordering, chiral LCs for the investigation of the intramolecular dynamic processes of new diaryl atropisomers and related prochiral derivatives. This approach is a powerful method for calculating the kinetic and activation parameters of enantiomers or enantiotopic directions undergoing intramolecular conformational exchange because their spectral discrimination is much more efficient in an oriented polypeptide solvent compared with isotropic NMR methods dedicated to chiral analysis.

Beyond the advantages offered by this analytical method, the interpretation of these new experimental results has enhanced our understanding of the orientation and chiral discrimination mechanisms in polypeptide LCs. First, we have demonstrated the excellent agreement between the theoretical evaluation of ΔH^{+} and experimental values extracted by NMR analysis using two different organic co-solvents. This result explicitly indicates that the intermolecular forces between the solute and the polypeptide oriented phase do not significantly influence the conformational interconversion process of molecules undergoing an intramolecular dynamic process (compared with an isolated molecule). The study of a possible deviation of activation parameters by changing the nature of polypeptide used (poly(γ-ethyl-L-glutamate) or poly(ε-carbobenzyloxy-L-lysine)) is currently underway. Secondly, in the temperature range explored, it appears that the evolution of $\Delta\nu_Q$ values (in Hz) versus T (in K) can be fitted using an exponential function of the form $\Delta\nu_Q = C \times \exp(-E/RT)$, whereas the evolution of the difference in $\Delta\nu_Q$ values between enantiomers or two enantiotopic directions is linear. This situation suggests (at least for the compounds investigated here) that the mechanisms of orientation and discrimination could be treated separately because the contributions of shape recognition and purely electrostatic interactions differ in both mechanisms. Hence they can be seen as uncorrelated phenomena. With regard to these results, it seems that chiral discrimination might be seen as a simple perturbation of the orientation mechanism. This assessment is important for a better modelling of the PBLG system. It is also important to establish if the exponential function used for predicting the evolution of $\Delta\nu_Q$ values versus T can be applied to a wide range of solutes. The question is now open.

Finally, this work points out a recurrent semantic problem between the communities of organic chemists and spectroscopists about the definition of the intrinsic stereoisomeric nature (chiral, prochiral)[3] of a chemical species and how a molecule should be considered. This problem (already pointed out by several authors in various contexts[16,45–47]) arises with the compounds investigated here, for which the stereoisomeric nature of the molecules can be discussed as a function of the temperature of the experiment. It raises the basic question as to whether the classical definition of stereoisomerism or pro-stereoisomerism should be imposed by the reality of synthetic chemistry, based either on the possibility of isolating a molecule[3,45,46] or disposing of a chemical reaction able to synthesise enantiomers from a prochiral molecule,[16,47] or the reality of the spectroscopic methods, which depend on the experimental conditions or the observational technique itself.[46] With regard to these two points of view, the definition introduced by Eliel[46] in which "a chemical species" is defined "as a molecule at or very near a minimum in a potential energy hypersurface" seems a priori to be more satisfactory because this concept is independent of the method of observation and experimental conditions as far as possible. Under this condition, two chemical species are identical when the interconverting energy barrier is less than RT and (stereo)isomeric when the barrier is higher. This definition offers the advantage of involving no practical methodologies used in chemical laboratories, but to be related only to the stability scale of the various possible isomers of a given compound.

Experimental Section

Synthesis of deuterated compounds: Scheme 1a and 1b show the synthetic strategies leading to compounds **1**–**4**. The detailed description of the syntheses is reported in the Supporting Information.

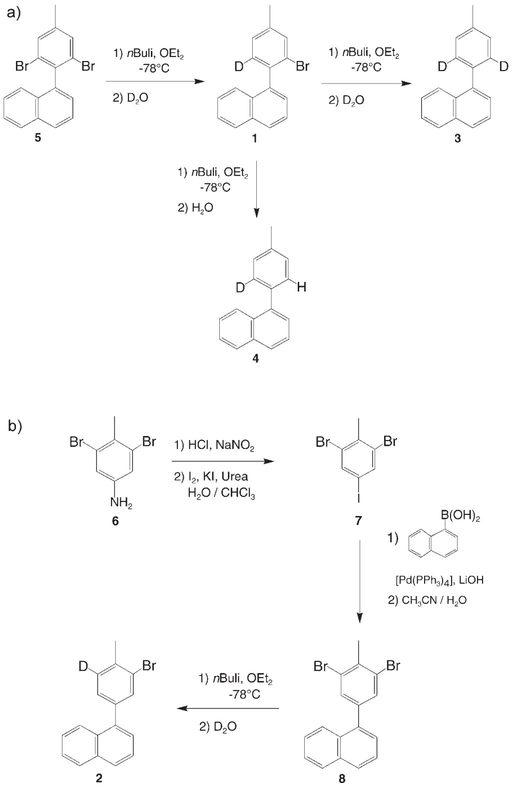

Scheme 1. a) Synthesis of compounds **1**, **3** and **4**. b) Synthesis of compound **2**.

Practical aspects of NMR spectroscopy in oriented solvents: The PBLG and PBDG polymers are commercially available from Sigma Corp. The preparation of fire-sealed oriented samples can be found in references [14] and [15]. The samples were made by mixing the solute (ca. 15 mg), polypeptide (ca. 100 mg) and co-solvent (ca. 440 mg). The exact composition of each sample is listed in Table 4. The $^{2}H-\{^{1}H\}$ NMR spectra were recorded on a 400 MHz Bruker Avance spectrometer equipped with a 5 mm QXO probe. The temperature was controlled by a BVT 3200 variable-temperature controller over the range of 200 (−73 °C) to 350 K (+77 °C). Note that the sample homogeneity is destroyed by boil-

Table 4. Composition of the liquid-crystalline NMR samples investigated.

NMR sample	Solute	Polymer	DP[a]	Co-solvent	Solute [mg][b]	Polymer [mg][b]	Co-solvent [mg][b]	Amount of polymer [wt %]
1	**1**	PBLG	782	$CHCl_3$	15	101	440	18.2
2	**1**	PBLG/PBDG	782/914	$CHCl_3$	12	51+53	440	18.7
3	**1**	PBLG	782	CH_2Cl_2	10	107	442	19.1
4	**2**	PBLG	782	$CHCl_3$	12	101	440	18.3
5	**3**	PBLG	782	$CHCl_3$	11	101	441	18.3
6	**3**	PBLG/PBDG	782/914	$CHCl_3$	10	50+51	439	18.4
7	**3**	PBLG	782	CH_2Cl_2	10	99	441	18.0
8	**4**	PBLG	782	$CHCl_3$	11	99	442	18.0

[a] DP: average degree of polymerisation of the polypeptide used (PBLG and PBDG). [b] To an accuracy of ±1 mg.

ing the co-solvent above 350 K for $CHCl_3$ and above 344 K for CH_2Cl_2. The temperature was calibrated using standard procedures. Mixtures were left for 10–15 min to equilibrate at the sample temperature before recording spectra. All 1D ^{2}H NMR spectra were recorded with 1024 scans of 2048 data points. The tuning and matching of the deuterium coil were optimised at each temperature. The classical WALTZ-16 sequence was used to decouple protons (< 0.4 W of power).

Acknowledgements

The authors are grateful to Prof. Dr. V. Schurig and Dr. O. Trapp for calculating the free energy of activation from the HPLC study. Also they cordially thank Dr. R. Paugam for stimulating discussions. O.L. and C.-A.F. acknowledge MNESER for a Ph.D. grant and the CNRS of Gif-sur-Yvette for their financial support, respectively.

---

[1] P. Llyod-Williams, E. Giralt, *Chem. Soc. Rev.* **2001**, *30*, 145–157, and references therein.

[2] M. Oki, *Top. Stereochem.* **1983**, *14*, 1–82, and references therein.

[3] A. L. Eliel, A. H. Wilen, *Stereochemistry of Organic Compounds*, Wiley, New York, **1994**.

[4] H. S. Gutowsky, D. W. McCall, C. P. Slichter, *J. Chem. Phys.* **1953**, *21*, 279–292.

[5] a) A. D. Bain, *Prog. Nucl. Magn. Reson. Spectrosc.* **2003**, *39*, 63–103, and references therein; b) S. Grilli, L. Lunazzi, A. Mazzanti, M. Pinamonti, *Tetrahedron* **2004**, *60*, 4451–4458; c) D. Casarini, C. Coluccini, L. Lunazzi, A. Mazzanti, *J. Org. Chem.* **2005**, *70*, 5098–5102.

[6] a) C. S. Johnson, *J. Magn. Reson., Ser. A* **1993**, 102, 214–218; b) E. J. Cabrita, S. Berger, P. Bräuer, J. Kärger, *J. Magn. Reson.* **2002**, 157, 124–131; c) P. Thureau, B. Ancian, S. Viel, A. Thévand, *Chem. Commun.* **2006**, 200–202.

[7] R. Poupko, Z. Luz in *Encyclopedia of Nuclear Magnetic Resonance* (Eds.: G. M. Grant, R. K. Harris), Wiley, Chichester, **1996**, pp. 1783–1797, and references therein.

[8] Z. Luz in *Nuclear Magnetic Resonance of Liquid Crystals* (Ed.: J. W. Emsley), NATO, Dordrecht, **1985**, pp. 315–340.

[9] R. Poupko, Z. Luz, *J. Chem. Phys.* **1981**, *75*, 1675–1681.

[10] C. Boeffel, Z. Luz, R. Poupko, H. Zimmermann, *J. Am. Chem. Soc.* **1990**, *112*, 7158–7163.

[11] a) S. Ternieden, D. Muller, K. Muller, *Liquid Crystals* **1999**, *26*, 759–769; b) S. Ternieden, D. Zauser, K. Muller, *Liquid Crystals* **2000**, *27*, 1171–1182.

[12] M. E. Moseley, R. Poupko, Z. Luz, *J. Magn. Reson.* **1982**, *48*, 354–360.

[13] I. Canet, J. Courtieu, A. Loewenstein, A. Meddour, J.-M. Péchiné, *J. Am. Chem. Soc.* **1995**, *117*, 6520–6526.

[14] M. Sarfati, P. Lesot, D. Merlet, J. Courtieu, *Chem. Commun.* **2000**, 2069–2081.

[15] P. Lesot, M. Sarfati, J. Courtieu, *Chem. Eur. J.* **2003**, *9*, 1724–1745.

[16] a) C. Aroulanda, D. Merlet, J. Courtieu, P. Lesot, *J. Am. Chem. Soc.* **2001**, *123*, 12059—12066; b) P. Lesot, D. Merlet, M. Sarfati, J. Courtieu, H. Zimmermann, Z. Luz, *J. Am. Chem. Soc.* **2002**, *124*, 10071–10082.

[17] C. Aroulanda, M. Sarfati, J. Courtieu, P. Lesot, *Enantiomer* **2001**, *6*, 281–287.

[18] Note that the case of chiral, substituted cyclohexanes is very peculiar because the exchange rate between enantiomers can be determined without discriminating the enantiomeric forms. Indeed for these compounds, the interconversion between enantiomers also leads to the interconversion of diastereotopic directions (axial and equatorial bonds) that are nonequivalent in achiral LCs.

[19] P. Lesot, O. Lafon, C.-A. Fan, H. B. Kagan, *Chem. Commun.* **2006**, 389–391.

[20] C. Zannoni in *Nuclear Magnetic Resonance of Liquid Crystals* (Ed.: J. W. Emsley), NATO, Dordrecht, **1985**, pp. 1–31.

[21] J. W. Emsley, J. C. Lindon, *NMR Spectroscopy Using Liquid Crystal Solvents*, Pergamon Press, Oxford, **1975**.

[22] a) B. Halle, *Prog. Nucl. Magn. Reson. Spectrosc.* **1996**, *32*, 137–159; b) Z. Luz in *NMR of Ordered Liquids* (Eds.: E. E. Burnell, C. A. de Lange), Kluwer, Dordrecht, **2002**, pp. 419–448.

[23] M. H. Levitt, *Spin Dynamics*, Wiley, **2005**, Chichester, pp. 492–494.

[24] E. Gelerinter, Z. Luz, R. Poupko, H. Zimmermann, *J. Chem. Phys.* **1990**, *92–93*, 8845–8850.

[25] a) J. A. Pople, W. G. Schneider, H. J. Bernstein, *High Resolution NMR*, McGraw-Hill, New York, **1959**, pp. 218–230; b) G. Binsch, *Top. Stereochem.* **1968**, *3*, 97–192.

[26] H. Eyring, *Chem. Rev.* **1935**, *35*, 65–77.

[27] This approach is called the "coalescence temperature method".

[28] M. J. S. Dewar, K. M. Dieter, *J. Am. Chem. Soc.* **1986**, *108*, 8075–8086.

[29] HyperchemTM, Professional 6.1, Hypercube, Inc, 1115 NN 4th street, Gainsville, Florida, 32601 (USA).

[30] a) R. F. Stewart, *J. Chem. Phys.* **1970**, *52*, 431–438; b) L. J. Sham, W. Kohn, *Phys. Rev.* **1965**, *140*, 1697–1705.

[31] a) K. L. Servis, R. L. Domenick, *J. Am. Chem. Soc.* **1986**, *108*, 2211–2214; b) S. Berger, H. Künzer, *Tetrahedron* **1983**, *39*, 1327–1329; c) G. S. Pawley, E. A. Yeats, *Acta Crystallogr. Sect. B* **1969**, *25*, 2009–2013.

[32] A. Meddour, I. Canet, A. Loewenstein, J.-M. Péchiné, J. Courtieu, *J. Am. Chem. Soc.* **1994**, *116*, 9652–9656.

[33] P. Lesot, O. Lafon, J. Courtieu, P. Berdagué, *Chem. Eur. J.* **2004**, *10*, 3741–3746.

[34] L. S. Bartell, *J. Am. Chem. Soc.* **1961**, *83*, 3567–3571.

[35] C. Canlet, D. Merlet, P. Lesot, A. Meddour, A. Loewenstein, J. Courtieu, *Tetrahedron: Asymmetry* **2000**, *11*, 1911–1918.

[36] a) P. Lesot, D. Merlet, A. Meddour, A. Loewenstein, J. Courtieu, *J. Chem. Soc., Faraday Trans.* **1995**, *91*, 1371–1375; b) A. Meddour, P. Berdagué, A. Hedli, J. Courtieu, P. Lesot, *J. Am. Chem. Soc.* **1997**, *119*, 4502–4508.

[37] a) I. Haller, *Prog. Solid State Chem.* **1975**, *10*, 103–118; b) H. Kneppe, V. Reiffenrath, *Chem. Phys. Lett.* **1982**, *87*, 59–62; c) M. L. Magnuson, B. M. Fung, J.-P. Bayle, *Liquid crystals* **1995**, *19*, 823–832.

[38] J. Israelachvili, *Intermolecular and Surface Forces*, Academic Press, San Diego, **1991**.

[39] a) J. Jeener, B. H. Meier, P. Bachmann, R. R. Ernst, *J. Chem. Phys.* **1979**, *71*, 4546–4553; b) C. Boeffel, Z. Luz, R. Poupko, A. J. Vega, *Isr. J. Chem.* **1989**, *29*, 283–296.

[40] In practice, we plot the two right sides of Equations (4) and (6) versus T_c and then determine the intersection point of the two plots.

[41] This implies that the coalescence phenomenon cannot be reached at 350 K and hence the data derived from the MMCs are consistent with the NMR results. At 350 K, the value of $\Delta G^{\ddagger}$ determined from Equation (4) ($\Delta G^{\ddagger} = +84.7\,\mathrm{kJ\,mol^{-1}}$) is too high compared with the value calculated with Equation (6) ($\Delta G^{\ddagger} = +70.9\,\mathrm{kJ\,mol^{-1}}$).

[42] a) V. Schurig, W. Bürkle, *J. Am. Chem. Soc.* **1982**, *104*, 7573–7580; b) F. Gasparrini, D. Misiti, M. Pierini, C. Villani, *Tetrahedron: Asymmetry* **1997**, *8*, 2069–2073; c) M. Jung, V. Schurig, *J. Am. Chem. Soc.* **1992**, *114*, 529–534.

[43] W. Bürkle, H. Karfunkel, V. Schurig, *J. Chromatogr.* A **1984**, *288*, 1–14.

[44] a) J. W. Emsley, P. Lesot, D. Merlet, *Phys. Chem. Chem. Phys.* **2004**, *6*, 522–530; b) J. W. Emsley, P. Lesot, J. Courtieu, D. Merlet, *Phys. Chem. Chem. Phys.* **2004**, *6*, 5331–5337.

[45] K. Mislow, P. Bickart, *Isr. J. Chem.* **1977**, *17*, 1–6.

[46] E. L. Eliel, *Isr. J. Chem.* **1977**, *17*, 7–11.

[47] a) S. Fujita, *J. Am. Chem. Soc.* **1990**, *112*, 3390–3397; b) S. Fujita, *Tetrahedron* **2000**, *56*, 735–740.

Received: September 6, 2006

ELSEVIER

Available online at www.sciencedirect.com

SCIENCE @ DIRECT®

Journal of Magnetic Resonance 174 (2005) 254–264

JMR
Journal of
Magnetic Resonance

www.elsevier.com/locate/jmr

Theoretical and experimental investigation of ^{13}C relayed ^{2}H–^{2}H-COSY 2D experiments: Application to the analysis of weakly aligned solutes

Olivier Lafon, Philippe Lesot *

Laboratoire de Chimie Structurale Organique, CNRS UMR 8074, ICMMO, Bât. 410, Université de Paris-Sud, 91405 Orsay, France

Received 8 December 2004; revised 8 December 2004
Available online 12 March 2005

Abstract

We describe new NMR 2D experiments denoted DECADENCY for DEuterium CArbon DEuterium Nuclear Correlation spectroscopY dedicated to the analysis of anisotropic deuterium spectra. They belong to the class of X-relayed Y,Y-COSY 2D experiments that was initially explored in the case of a ^{1}H–X–^{1}H fragment ($I_X = 1/2$) in isotropic medium. DECADENCY 2D experiments permit to correlate the quadrupolar doublets associated with two inequivalent deuterium nuclei in an oriented CD_2 fragment through heteronuclear polarization transfers. Two kinds of pulse sequences are described here using either a double INEPT-type or DEPT-type process. DECADENCY 2D experiments provide an interesting alternative to ^{2}H–^{2}H COSY experiments when the geminal ^{2}H–^{2}H total coupling (scalar and dipolar) is null or too small to provide visible cross-correlation peaks. Such a situation is typically observed for geminal deuteriums in prochiral or chiral molecules dissolved in chiral liquid crystals. The efficiency of these techniques is illustrated using dideuterated prochiral molecules, the phenyl[$^{2}H_2$]methanol and the 1-chloro[1-$^{2}H_2$]nonane, both dissolved in organic solutions of poly-γ-benzyl-L-glutamate. The advantages of each sequence are presented and discussed. It is shown that the relative sign of the quadrupolar doublets can be determined.

Keywords: ^{2}H NMR spectroscopy; Quadrupolar splittings; Chiral liquid crystals; C–D polarization transfers

1. Introduction

NMR spectroscopy in chiral polypeptide oriented solvents is now a well-established technique [1–4]. It provides efficient and original solutions to organic chemists for investigating enantiomeric purity of a mixture, analyzing stereochemistry or answering to a specific analytical problem.

As a typical example, we have recently studied the mechanism of SmI_2 mediated cyclization of δ-iodo-α,β-unsaturated esters using proton-decoupled deuterium NMR (^{2}H–{^{1}H}) in PBLG solvents as spectral tool [5]. Actually in the course of this work, we have developed an interesting strategy for distinguishing *meso* from *d,l* stereoisomers in a mixture, and then for safely assessing diastereoisomeric and enantiomeric purity. In a first step, a "CD_2" probe was introduced in the molecules under studied, thus leading to a 1D ^{2}H–{^{1}H} spectrum made of six resolved quadrupolar doublets centered approximately on the same chemical shift, two associated with the *meso* compound, four associated with the enantiomers. In a second step, proton-decoupled deuterium COSY 2D experiments in chiral and achiral anisotropic phases were performed and allowed to pair up and assign quadrupolar doublets belonging to *meso* and *d,l* stereoisomers on the basis of ^{2}H–^{2}H correlation peaks in the 2D map [5].

---

* Corresponding author. Fax: +33 01 69 15 81 05.
E-mail address: philesot@icmo.u-psud.fr (P. Lesot).

doi:10.1016/j.jmr.2005.02.011

It can be argued here that deuterium–carbon correlation experiments could be used for pairing up the quadrupolar doublets of *meso* and *d,l* isomers [6,7]. This solution is pertinent but was not applicable because the difference of carbon-13 chemical shifts for the carbon atom in the CD_2 probe in the *meso* and *d,l* isomers was too small to provide separated resonances (at least at 9.4 T).

In this approach, the pairing up and subsequently the assignment of doublets using COSY 2D experiments is only possible when the ^2H–^2H total coupling (scalar and dipolar) between geminal deuterium nuclei is sufficiently large in magnitude to produce cross-correlation peaks visible on the 2D map. As organic solutions of polypeptide orient any solutes rather weakly, this condition could be not always fulfilled.

A priori, such a problem should not exist anymore if we are able to correlate deuterium nuclei in the CD_2 probe, transferring the polarization stepwise from ^2H to ^{13}C and back to ^2H. In this scheme, cross-correlations should be governed by one-bond carbon–deuterium total couplings, $^1T_{CD}$ with $^1T_{CD} = {}^1J_{CD} + 2\ {}^1D_{CD}$. Disregarding the spurious cases where $^1T_{CD}$ is small ($^1J_{CD} \approx -2\ {}^1D_{CD}$) or null ($^1J_{CD} = -2\ {}^1D_{CD}$), the magnitude of $^1T_{CD}$ is generally distributed around the value of scalar couplings $^1J_{CD}$, namely about 20–30 Hz. Consequently, cross-correlations between geminal deuterons should be always detected whatever the magnitude of the homonuclear ^2H–^2H couplings.

In the first part of this work, we theoretically describe new 2D experiments, called DECADENCY (DEuterium CArbon DEuterium Nuclear Correlation spectroscopY), that allow the correlation between the quadrupolar doublets of inequivalent deuterons bonded to the same carbon-13 atom without the need of ^2H–^2H dipolar couplings. Two pulse sequences using two consecutive polarization transfers (PT) are proposed. They use either an INEPT-type or a DEPT-type transfer mechanism. In the second part, the efficiency of these sequences is studied using prochiral molecules of C_s symmetry: the phenyl[$^2H_2$]methanol and an equimolar mixture of this molecule and 1-chloro[1-$^2H_2$]nonane. Both samples are dissolved in an oriented organic solution of poly-γ-benzyl-L-glutamate (PBLG) in chloroform. The experimental results obtained using both 2D sequences are reported and discussed.

2. Theoretical analysis

DECADENCY 2D experiments are homonuclear experiments based on a relayed heteronuclear transfer mechanism. They belongs to the class of X-relayed Y,Y-COSY 2D experiments that was pioneered by Lallemand and next by Wüthrich in the case of a ^1H–X–^1H fragment [8,9]. To the best of our knowledge, such a concept was only applied to spin-1/2 nuclei in isotropic phase, and was never explored in case of a D-X-D fragment ($I_X = 1/2$) aligned in a liquid crystal, so far. The main difference between a ^1H–X–^1H and ^2H–X–^2H fragment arises from the presence of the quadrupolar interaction associated with spin-1 nuclei in oriented solvent.

After a double Fourier transformation, the 2D map of DECADENCY experiments must be formally equivalent to the ^2H–^2H COSY 2D map. It contains the same kind of spectral information [5], namely diagonal peaks (DP), autocorrelation peaks (AP), and cross-correlation peaks (CP) for a $^{13}CD_2$ spin (see Fig. 2A). However in DECADENCY experiments, all signals result from two consecutive PT's via the one-bond ^{13}C–^2H total couplings. In this scheme, CP's correspond to the case where polarization is transferred from deuterium to carbon-13 nucleus, and then transferred back to the second deuterium ($D^i \rightarrow {}^{13}C \rightarrow D^j$) in a CD_2 group. On the other hand, DP's and AP's correspond to the case where polarization is transferred from deuterium to carbon-13 nucleus and then returns to the same deuterium ($D^i \rightarrow {}^{13}C \rightarrow D^i$). In this aim, two mechanisms of C–D polarization transfers involving either a double INEPT-type or a DEPT-type process can be considered [10–12]. Both of schemes present advantages and limits, and hence they will be examined below.

To determine analytical expressions for the different signals in the DECADENCY 2D experiments, we used the product-operator formalism developed for two non-equivalent deuterium nuclei denoted D^i and D^j, coupled to the same carbon via $^1T_{CD}$. For our purpose, we have considered the simplest relevant case where the geminal ^2H–^2H coupling is disregarded. A brief description of various product operators associated to this system and their evolution under the influence of ^{13}C–^2H coupling are given in Appendix A. In according with previously reported approaches for spin-1/2 [13,14], the evolution of product operators during the sequences was calculated with *Mathematica* [15]. As a result of the large number of terms involved, only the evolutions contributing to the final signal are considered. Note also that the geminal deuterium nuclei, D^i and D^j, behave identically and have an interchangeable role. Consequently for the clarity, the spin labels 'i,j' and 'j,i' used in the product operators or in equations, mean 'i or j' and 'j or i', respectively. The superscript notation 'C' will be relative to the carbon-13 nucleus.

2.1. Double INEPT polarization transfer

The standard DECADENCY sequence based on two consecutive INEPT-type polarization transfers, simply derives from the well-known HETCOR pulse sequence that was recently used to correlate deuterium to carbon in weakly orienting media (CDCOM 2D experiment)

[6,7]. Actually, compared against the CDCOM experiment, a further INEPT transfer of polarization from the carbon-13 to deuterium nucleus is introduced just before the acquisition period of signal. The pulse scheme of the sequence (denoted DECADENCY-INEPT) is given in Fig. 1A. During the variable evolution period t_1, deuterium single quantum coherences evolve under the influence of chemical shift and quadrupolar interaction, while the ^{13}C–^{2}H total couplings, T_{CD}, are refocussed by the ^{13}C π pulse at the midpoint of t_1.

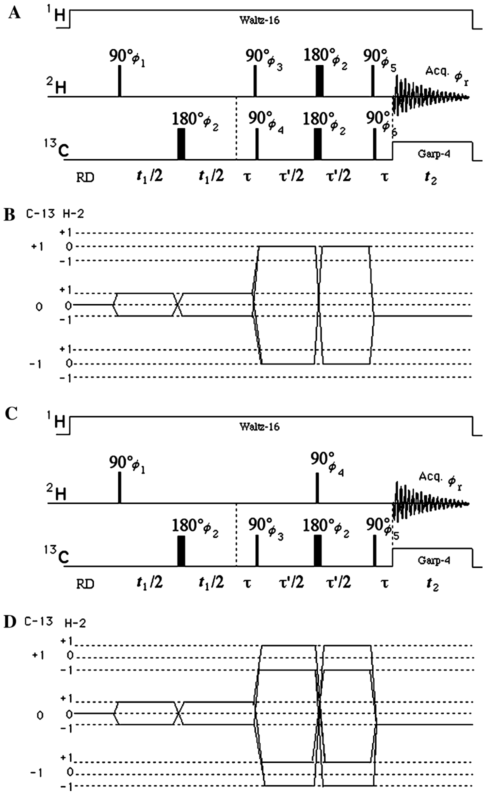

Fig. 1. Pulse scheme and coherence transfer pathway diagram for correlation peaks in DECADENCY experiments based on either two consecutive INEPT-type PTs (A and B) or DEPT-type PTs (C and D). The basic 4-step phase cycling is: $\phi_1 = 2(x), 2(-x)$; $\phi_2 = \phi_3 = \phi_5 = \phi_6 = 4(x)$; $\phi_4 = 2(x, -x)$; $\phi_r = x, -x, -x, x$ and $\phi_1 = 2(x), 2(-x)$; $\phi_2 = \phi_4 = \phi_5 = 4(x)$; $\phi_3 = 2(x, -x)$; $\phi_r = x, -x, -x, x$, respectively. Quadrature detection in F_1 dimension uses TPPI method (π/2 phase increment of the first pulse). The choice of values for the τ and τ′ delays is discussed in the text. In both experiments, the proton nuclei are decoupled by applying the Waltz-16 sequence whilst the Garp-4 sequence suppresses ^{13}C–D couplings during the aquisition period. A 180° composite pulse in the middle of t_1 can be implemented to improve the refocussing of ^{13}C–D couplings.

The removal of heteronuclear couplings by refocussing has the advantage of requiring much less average power than broadband decoupling. The C–D coupling evolves during the first delay τ, leading to an antiphase magnetization of deuterium with respect to ^{13}C–^{2}H coupling, and corresponding to the product operator $2I_x^{i,j}S_z^{C}E^{j,i}$. In the following, the identity operator, E, will be omitted. Deuterium coherences are then converted into ^{13}C coherences during the first step of polarization transfer ($D^{i,j} \rightarrow {}^{13}C$) that is made by the simultaneous application of ^{2}H and ^{13}C π/2 pulses.

At this step of the sequence and after four-step phase cycle, the density operator contains the terms: $2I_z^{i,j}S_y^{C}$, $2I_x^{i,j}S_y^{C}$, $2K_y^{i,j}S_y^{C}$, and $2D_y^{i,j}S_y^{C}$. The term, $2I_z^{i,j}S_y^{C}$, is representative of antiphase *y*-magnetization of ^{13}C with respect to ^{13}C–^{2}H coupling. The second and third term, $2I_x^{i,j}S_y^{C}$ and $2K_y^{i,j}S_y^{C}$, correspond to the ^{13}C–^{2}H heteronuclear zero- and double-quantum coherence, in-phase and antiphase, respectively, with respect to quadrupolar doublet. Finally, the fourth one, $2D_y^{i,j}S_y^{C}$, corresponds to the ^{13}C–^{2}H heteronuclear single- and triple-quantum coherence. Note that the terms, $2I_z^{i,j}S_y^{C}$ and $2I_x^{i,j}S_y^{C}$, are "formally analogous" to that obtain in the case of a PT between two spin-1/2 nuclei while $2K_y^{i,j}S_y^{C}$ and $2D_y^{i,j}S_y^{C}$ are specific of the polarization transfer from spin-1 to spin-1/2 nucleus [10]. However, the final evolution of the four previous operators indicates that the antiphase ^{13}C magnetization (associated to a single coherence) contributes to the signal of CP's, DP's, and AP's, while the other terms contribute to DP's and AP's only. Note here that the two first steps of the phase cycle restrict the observed signal during t_2 to the terms directly deriving from the four previous product operators, thus eliminating the undesired signals of deuterium nuclei bound to ^{12}C. The remaining two steps remove axial peaks arising from pure longitudinal ^{13}C magnetization during t_1. A more sophisticated phase cycle or pulse field gradients could be proposed to strictly select ^{13}C 1Q-coherence, $2I_z^{i,j}S_y^{C}$, during τ′ period. Nevertheless the use of pulse field gradients produce loss of sensitivity, while the increase of step number in phase cycle can generate unuseful artifacts [16]. On the other hand, the presence of $2D_y^{i,j}S_y^{C}$ term is not cumbersome while heteronuclear two-spin zero- and double-quantum coherences also contribute (weakly) to the signal of CP's when the deuterium–deuterium coupling is not null.

In DECADENCY 2D experiments, only cross-correlation peaks provide the relevant information, consequently we focus our attention on the evolution of the antiphase ^{13}C magnetization. During the τ′ period, only ^{13}C chemical shifts are refocused by applying two simultaneous ^{2}H and ^{13}C π pulses at the middle point. The antiphase ^{13}C magnetization is then converted into antiphase ^{2}H magnetization with respect to ^{13}C–^{2}H coupling ($C \rightarrow D^{j,i}$) by applying again two simultaneous ^{2}H and ^{13}C π/2 pulses. At this step of the sequence, the deuterium magnetization contains the terms $2I_y^{i,j}S_z$, $I_y^{i,j}S_z^CQ_z^{j,i}$, $2S_z^CI_y^{j,i}$, and $Q_z^{i,j}S_z^CI_y^{j,i}$. Among these four product operators, only the first and third operator products will give rise to observable signals during t_2 if $^2T_{DD}$ is null. If the first term finally contributes to signal of DP's and AP's, the third one contributes to the CP signals. During the second delay τ, the evolution of antiphase ^2H magnetization under the influence of $^1T_{CD}$ coupling leads to an in-phase ^2H magnetization with respect to ^{13}C–^2H coupling, which is observable during acquisition when the broad-band carbon decoupling sequence is turned on. Finally, after a four-step phase cycle and disregarding all relaxation terms and phase factors, the expression of cross-correlation signals is:

$$S_{CP}(t_1,t_2) \propto \frac{2}{3}\mathrm{i}\{\sin[\omega_{D^{i,j}}(t_1+\tau)]\cos\lfloor\omega_{Q^{i,j}}(t_1+\tau)\rfloor\} \times \left\{\begin{array}{l} \sin[\omega_{CD^{i,j}}(\tau)]\sin[2\omega_{CD^{i,j}}(\tau')] \\ \times\sin[2\omega_{CD^{j,i}}(\tau')]\sin[\omega_{CD^{j,i}}(\tau)] \end{array}\right\} \times \left\{\begin{array}{l} e^{\mathrm{i}[\omega_{D^{j,i}}(\tau+t_2)]-\omega_{Q^{j,i}}(\tau+t_2)]} \\ +e^{\mathrm{i}[\omega_{D^{j,i}}(\tau+t_2)]+\omega_{Q^{j,i}}(\tau+t_2)]} \end{array}\right\}. \tag{1}$$

In this equation $\omega_D = 2\pi\nu_D$, $\omega_Q = \pi\Delta\nu_Q$ and $\omega_{CD} = \pi\, ^1T_{CD}$, where $^1T_{CD}$ is the one-bond ^{13}C–^2H total coupling. The position of terms in the equation allows a better presentation of the evolution of signal during the periods t_1, τ, τ', and t_2.

After a four-step phase cycle and disregarding all relaxation terms and phase factors, the expression of diagonal and autocorrelation signals following the same coherence order (1Q) than for cross-correlation signals during τ' is:

$$S_{DP\ \mathrm{and}\ AP}(t_1,t_2) \propto \frac{1}{3}\mathrm{i}\{\sin[\omega_{D^{i,j}}(t_1+\tau)]\cos[\omega_{Q^{i,j}}(t_1+\tau)]\} \times \left\{\begin{array}{l} \sin^2[\omega_{CD^{i,j}}(\tau)]\cos[2\omega_{CD^{i,j}}(\tau')] \\ \times(1+2\cos[2\omega_{CD^{j,i}}(\tau')]) \end{array}\right\} \times \left\{\begin{array}{l} e^{\mathrm{i}[\omega_{D^{i,j}}(\tau+t_2)-\omega_{Q^{i,j}}(\tau+t_2)]} \\ +e^{\mathrm{i}[\omega_{D^{i,j}}(\tau+t_2)+\omega_{Q^{i,j}}(\tau+t_2)]} \end{array}\right\}. \tag{2}$$

As it can be seen from the Eqs. (1) and (2), the efficiency of the two consecutive PTs strongly depends on the value of τ and τ' delays. Disregarding relaxation effects, the intensity of CP's (I_{CP}) varies with τ as $\sin[\omega_{CD^{i,j}}(\tau)]\sin[\omega_{CD^{j,i}}(\tau)]$ while intensities of DP's and AP's (I_{DP} and I_{AP}) vary as $\sin^2[\omega_{CD^{i,j}}(\tau)]$ (the chemical shift and the quadrupolar interaction only modulate the peak phase). In the ideal case, where $^1T_{CD^i} = {}^1T_{CD^j} = T_{CD}$, I_{DP}, I_{AP}, and I_{CP} would be maximized when $\tau = 1/(2|T_{CD}|)$. With regard to the dependence with τ' (disregarding relaxation terms), the intensity of CP's is modulated as $\sin[2\omega_{CD^{i,j}}(\tau')]\sin[2\omega_{CD^{j,i}}(\tau')]$ while intensities of DP's and AP's are modulated as $(1+2\cos[2\omega_{CD^{j,i}}(\tau')])$. Here again, the choice of τ' affects the relative intensity of AP's and DP's compared to CP's. Thus, in the ideal case where $^1T_{CD^1} = {}^1T_{CD^2} = T_{CD}$, we can demonstrate that I_{CP} is maximum (I_{CPmax}) when $\tau' = 1/(4|T_{CD}|)$. In contrast when $\tau' = 1/(3|T_{CD}|)$, I_{DP} and I_{AP} are equal to zero and $I_{CP} = 3/4(I_{CPmax})$. This case is simulated in Fig. 2B. Finally, when $\tau' = 1/(2|T_{CD}|)$, $I_{CP} = 0$, and only the DP's and AP's are observed in the 2D spectrum. Actually, when $\Delta\nu_{Q^1} \neq \Delta\nu_{Q^2}$, the ideal case where $^1T_{CD^1} = {}^1T_{CD^2}$ does not exist, and hence in practice, DP's, AP's, and CP's are never totally suppressed as expected theoretically.

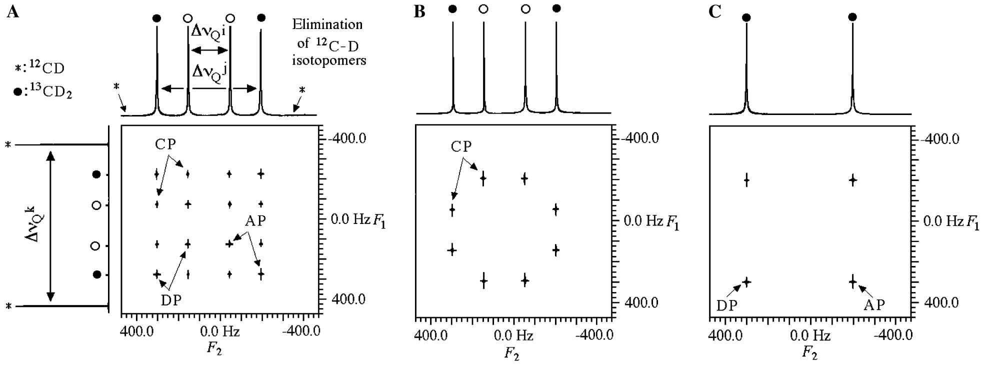

Fig. 2. Numerical simulations of the DECADENCY-INEPT 2D experiment (magnitude mode) on a fictitious ^{12}CD (98.9%) spin system and $^{13}CD_2$ spin system (1.1%) with two non-equivalent deuterium nuclei ($\delta_{D^i} = \delta_{D^j} = \delta_{D^k} = 1$ ppm, $\Delta\nu_{Q^i} = 200$ Hz, $\Delta\nu_{Q^j} = 500$ Hz, and $\Delta\nu_{Q^k} = 800$ Hz) in $^2T_{D^iD^j}$ is assumed to be zero. In the simulations (A and B), $^1T_{CD^i} = {}^1T_{CD^j} = 30$ Hz (ideal case but non realistic if $\Delta\nu_{Q^i} \neq \Delta\nu_{Q^j}$) and (C) $^1T_{CD^i} = 0$, $^1T_{CD^j} = 30$ Hz. The delay τ is set to 16.7 ms (1/[2T$_{CD}$]) whereas the delay τ' is equal to 8.3 ms (1/[4T$_{CD}$]) for simulation (A and C) and 11.1 ms (1/[3T$_{CD}$]) for (B). In F_1 dimension of the contour plot (A), the 1D spectrum showing the signal of ^{12}CD and $^{13}CD_2$ spin system is displayed. In F_2 dimension is given the projection of the 2D map. Note the elimination of undesired signals of deuteriums bound to ^{12}C by the phase cycling. The diagonal, autocorrelation and cross-correlation peaks are denoted DP, AP, and CP. On the third simulation (C), only the DP's and AP's associated with deuterium j are visible ($^1T_{CD^j} \neq 0$).

As a result of the low dispersion of $^1T_{CD}$'s for weakly aligned solutes, the average of $^1T_{CD}$'s gives in general good results, but this point will be examined further during the discussion of experimental results.

From Eqs. (1) and (2), it clearly appears that CP's disappear if one of the two $^1T_{CD}$s is equal to zero. This particular spectral situation is illustrated in Fig. 2C. In this last example, only DP's and AP's associated with the quadrupolar doublet of the deuterium (here D^j) sharing a non-zero coupling with the carbon-13 atom ($^1T_{CD^j} \neq 0$) is visible on the 2D map. These peaks originate from a double C–D polarization transfer involving the same deuterium, namely $D^{i,j} \rightarrow {}^{13}C \rightarrow D^{i,j}$.

2.2. Double DEPT polarization transfer

An alternative to the C–D INEPT-type PT is provided by the C–D DEPT-type PT that involved heteronuclear multiple-quantum (0 and 2) coherences [17]. This type of transfer can be implemented in the DECADENCY 2D experiment. The pulse scheme and the coherence transfer pathway diagram for cross-correlation signals of this second experiment (denoted DECADENCY-DEPT) are given in Figs. 1C and D. The pulse block yielding two consecutive PT's is simpler compared to the previous one. It is only made of two single carbon-13 $\pi/2$ pulses separated by two simultaneous deuterium $\pi/2$ pulses and carbon-13 π pulse at the midpoint of the refocussing delay τ'. Note that phase cycle of DECADENCY-INEPT and DECADENCY-DEPT experiments removes the same coherence transfer pathways.

Compared with the DECADENCY-INEPT sequence, the time evolution of the density operator of the DECADENCY-DEPT sequence is identical up to the first carbon-13 $\pi/2$ pulse. This last pulse converts antiphase ^{2}H magnetization with respect to ^{2}H–^{13}C coupling into heteronuclear zero- and double-quantum coherences. After a four-step phase cycle, the density operator at the beginning of the τ' period contains the terms, $2I_x^{i,j}S_y^C$, $2I_y^{i,j}S_y^C$, $2K_x^{i,j}S_y^C$, and $2K_y^{i,j}S_y^C$, that are associated to the ^{13}C–^{2}H heteronuclear zero- and double-quantum coherences (see Appendix A). Contrarily to the DECADENCY-INEPT 2D sequence, these four product operators evolving during τ' finally lead to CP's as shown in the coherence pathway diagram. Actually, in this scheme, the coherence pathways contributing to signal of DP's and AP's are the same than for CP's. During the interval τ', the coherences evolve under the influence of the ^{13}C–^{2}H coupling, the ^{2}H chemical shifts and ^{2}H quadrupolar interactions while ^{13}C chemical shift is refocused by the ^{13}C π pulse. The ^{2}H $\pi/2$ pulse at the midpoint of τ' permits to transfer heteronuclear coherences from one geminal deuterium nucleus toward the other one. The last ^{13}C $\pi/2$ pulse converts heteronuclear multi-quantum coherences into detectable ^{2}H magnetization. After a four-step phase cycle and disregarding all relaxation terms and phase factors, the expression of CP's is:

$$S_{CP}(t_1,t_2) \propto -\frac{1}{3}\left\{\begin{array}{c} \sin[\omega_{CD^{i,j}}(\tau)]\sin[2\omega_{CD^{i,j}}(\tau'/2)] \\ \times\sin[2\omega_{CD^{j,i}}(\tau'/2)]\sin[\omega_{CD^{j,i}}(\tau)] \end{array}\right\} \times\left\{\begin{array}{l} e^{i[(\omega_{D^{j,i}}+\omega_{Q^{j,i}})(\tau'/2+\tau+t_2)]} \\ \times\left(\begin{array}{l} \cos[(\omega_{CD^{i,j}}+\omega_{CD^{j,i}})(\tau'/2)]\sin[(\omega_{D^{i,j}}-\omega_{Q^{i,j}})(t_1+\tau+\tau'/2)] \\ +\cos[(\omega_{CD^{i,j}}-\omega_{CD^{j,i}})(\tau'/2)]\sin[(\omega_{D^{i,j}}+\omega_{Q^{i,j}})(t_1+\tau+\tau'/2)] \end{array}\right) \\ +e^{i[(\omega_{D^{j,i}}-\omega_{Q^{j,i}})(\tau'/2+\tau+t_2)]} \\ \times\left(\begin{array}{l} \cos[(\omega_{CD^{i,j}}+\omega_{CD^{j,i}})(\tau'/2)]\sin[(\omega_{D^{i,j}}+\omega_{Q^{i,j}})(t_1+\tau+\tau'/2)] \\ +\cos[(\omega_{CD^{i,j}}-\omega_{CD^{j,i}})(\tau'/2)]\sin[(\omega_{D^{i,j}}-\omega_{Q^{i,j}})(t_1+\tau+\tau'/2)] \end{array}\right) \end{array}\right\}. \tag{3}$$

Under the same conditions, the expressions of signal for DP's and AP's are, respectively:

$$S_{DP}(t_1,t_2) \propto -\frac{1}{6}\{\cos[\omega_{D^{i,j}}(t_1+\tau+\tau'/2)]\} \times\left\{\begin{array}{l} \sin^2[\omega_{CD^{i,j}}(\tau)]\cos^2[\omega_{CD^{i,j}}(\tau'/2)] \\ \times(1+4\cos[2\omega_{CD^{j,i}}(\tau'/2)]+\cos[4\omega_{CD^{j,i}}(\tau'/2)]) \end{array}\right\} \times\left\{\begin{array}{l} e^{i[\omega_{Q^{i,j}}(t_1+\tau+\tau'/2)+(\omega_{D^{i,j}}-\omega_{Q^{i,j}})(\tau'/2+\tau+t_2)]} \\ +e^{i[-\omega_{Q^{i,j}}(t_1+\tau+\tau'/2)+(\omega_{D^{i,j}}+\omega_{Q^{i,j}})(\tau'/2+\tau+t_2)]} \end{array}\right\} \tag{4}$$

and

$$S_{AP}(t_1,t_2) \propto -\frac{1}{6}i\{\sin[\omega_{D^{i,j}}(t_1+\tau+\tau'/2)]\} \times\left\{\begin{array}{l} \times(1+4\cos[2\omega_{CD^{j,i}}(\tau'/2)]+\cos[4\omega_{CD^{j,i}}(\tau'/2)]) \\ \times\sin^2[\omega_{CD^{i,j}}(\tau)]\sin^2[\omega_{CD^{i,j}}(\tau'/2)] \end{array}\right\} \times\left\{\begin{array}{l} e^{i[-\omega_{Q^{i,j}}(t_1+\tau+\tau'/2)+(\omega_{D^{i,j}}-\omega_{Q^{i,j}})(\tau'/2+\tau+t_2)]} \\ +e^{i[\omega_{Q^{i,j}}(t_1+\tau+\tau'/2)+(\omega_{D^{i,j}}+\omega_{Q^{i,j}})(\tau'/2+\tau+t_2)]} \end{array}\right\}. \tag{5}$$

As previously, the choice of delays τ and τ' is important and affects the relative intensity of CP's, AP's, and DP's. As in case of the DECADENCY-INEPT experiment, the defocusing and refocusing intervals τ must be set as close as possible to $1/(2\,|T_{CD}|)$. On the contrary the evolution of intensities with τ' significantly differs from that calculated before. In the ideal case where $^1T_{CD^i} = {}^1T_{CD^j} = T_{CD}$, the value $\tau' = 1/(2|T_{CD}|)$ cancels DP's and AP's, and CP's would be exclusively observed on the 2D map. In contrast when $\tau' = 1/(|T_{CD}|)$, $I_{DP} = I_{CP} = 0$ and only AC's are detected.

Fig. 3A shows an example of simulated DECADENCY-DEPT 2D experiment when $\tau' = 1/(2|T_{CD}|)$. Surprisingly, the number of CP's is divided by a factor of two, and only two pairs of cross-correlations instead of four (see Fig. 2B), appear on the 2D map. This occurrence is rather interesting compared to the DECADENCY-INEPT 2D experiment, because the relative sign of quadrupolar splittings can be reliable determined. If we assume that the geminal C–D total couplings, $^1T_{CD^i}$ and $^1T_{CD^j}$, have the same sign, which is usually the case for weakly aligned solutes, the analysis of Eq. (3) compared with Eq. (1) indicates that the frequency position of CP's

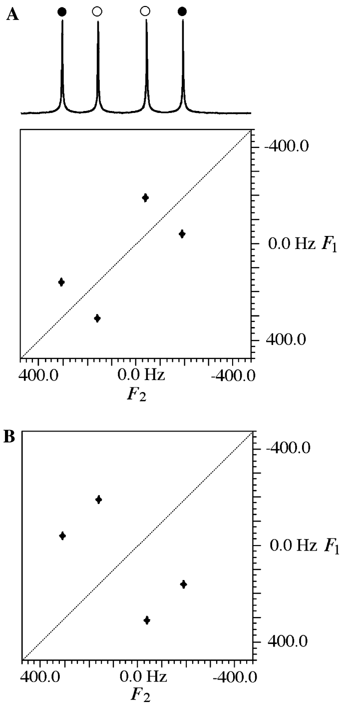

Fig. 3. Numerical simulation (magnitude mode) of the DECADENCY 2D experiment using a double DEPT-type transfer on a fictitious $^{13}CD_2$ spin system with two non-equivalent deuteriums (apart from the sign of quadrupolar splittings, the spin-system parameters are identical to those given in caption of Fig. 2) in an oriented medium. In both experiments, the delays τ are τ' are set to $1/(2|T_{CD}|)$. The signs of quadrupolar splittings are identical (positive or negative) in the simulation (A) and opposite in the simulation (B). Note the change of localization of CP's on the 2D map.

on the 2D map depends on the relative sign of quadrupolar doublets. In contrast, the position of CP's is independent on the sign of $^1T_{CD}$'s. As illustration, Fig. 3B presents an example of simulated 2D map where the CP's are distributed perpendicularly to the main diagonal, corresponding to the case where the signs of quadrupolar splittings are opposite.

3. Experimental section

3.1. Sample preparation

The NMR sample of phenyl[$^2H_2$]methanol (**1**) was prepared using 50 mg solute, 100 mg PBLG with a DP = 562, MW ≈ 120,000, (purchased from Sigma), and 350 mg of dry chloroform. The NMR sample of equimolar mixture of **1** and 1-chloro[1-$^2H_2$]nonane (**2**) was made by adding 76.7 and 50.1 mg of these solutes dissolved in 100 mg PBLG and 350 mg chloroform. The components of the mixture were weighed into a 5 mm o.d. NMR tube which was sealed to avoid solvent evaporation. Other experimental details can be found in [3].

3.2. NMR spectroscopy

The 2D experiments were performed at 9.4 T on a Bruker DRX 400 high-resolution spectrometer equipped with a 5 mm four-channel probe (QXO) operating at 61.4 MHz for deuterium and 100.6 MHz for carbon. This probe allows the matching and tuning of deuterium channel (outer coil), but the deuterium channel (lock) of any probes (dual or broadband) can be used to perform such experiments. The temperature of the sample was maintained at 300 K by the standard variable temperature unit of spectrometer (BVT 3200) and the experiments were performed without sample spinning. All 2D matrices were zero-filled to 1k $(t_1) \times 2k$ (t_2) data points prior to the double Fourier transformation. Unless otherwise specified, 2D contour plots are displayed in magnitude mode. Other experimental NMR parameters or details are given in the figure captions.

4. Results and discussion

To experimentally explore and illustrate the potentialities of the DECADENCY 2D experiments, we investigate the case of **1** dissolved in the PBLG/CHCl$_3$ phase at 300 K. In a chiral oriented medium, the C–D enantiotopic directions of this prochiral molecule of C_s symmetry in average are non-equivalent and exhibit two quadrupolar doublets (and distinct C–D total couplings) corresponding to the *pro-R and pro-S* deuterium atoms [18]. As it is not possible to assign these splittings by NMR spectroscopy, the labels A and B are used. In this example, the splittings measured for D^A and D^B are equal to $|\Delta\nu_{Q^A}| = 215$ Hz and $|\Delta\nu_{Q^B}| = 330$ Hz. The exact values of $|^1T_{CD}|$'s determined from the analysis of ^{13}C–$\{^1H\}$ 1D spectrum are 27 and 31 Hz.

Fig. 4A presents the DECADENCY-INEPT 2D map of **1** displayed at low contour plot level when $\tau = 1/(2T_{CD})$ and $\tau' = 1/(4T_{CD})$ with T_{CD} set to the average value of $|^1T_{CD}|$'s, i.e., 29 Hz. As expected, 16 peaks (4 × 4) corresponding to the various types of peaks generated by the sequence are observed. The presence of CP's allows the correlation between geminal deuterium nuclei D^A and D^B bonded to the prostereogenic carbon of the molecule. Contrarily to the simulations, the intensities of four DP's and AP's are not equal. Disregarding effects due to pulse imperfections (that can be reduced by using composite pulses), this situation arises because experimentally $^1T_{CD^i} \neq {}^1T_{CD^j}$. If the average value of $|^1T_{CD}|$'s provides a suitable compromise for calculating the τ

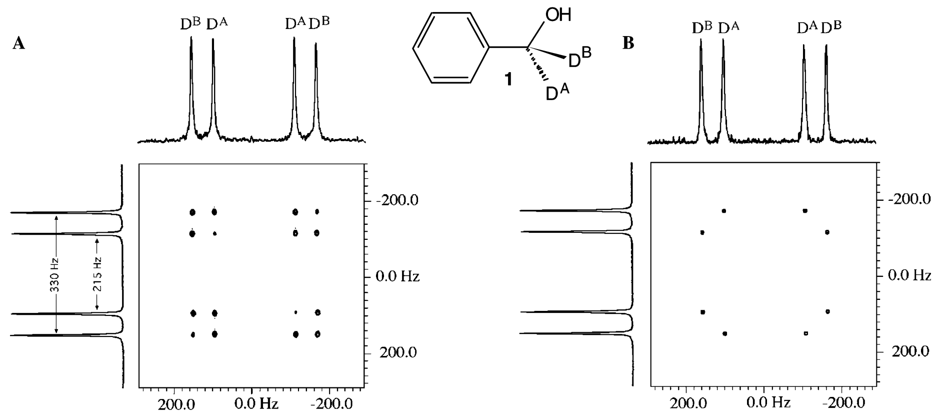

Fig. 4. DECADENCY-INEPT 2D spectra of **1** obtained when (A) $\tau = 1/(2T_{CD})$, $\tau' = 1/(4T_{CD})$ and (B) $\tau = 1/(2T_{CD})$, $\tau' = 1/(3T_{CD})$ with $T_{CD} = 29$ Hz. Both spectra have been recorded in the same conditions, using 128 (t_1) × 478 (t_2) data points and 320 scans per t_1 increment. No filtering and no symmetrization were applied here. In F_1 dimension is displayed the ^{2}H–{^{1}H} 1D spectrum of **1** while in F_2 dimension is given the projection of the 2D map. The assignment of quadrupolar splittings (A and B) relative to the molecular numbering is arbitrary.

delay, the difference between the ideal and the set value generates variations in peak intensity. This effect is, however, not really cumbersome for analyzing of the 2D map.

Fig. 4B shows the DECADENCY-INEPT 2D experiment of **1** when $\tau = 1/(2T_{CD})$ and $\tau' = 1/(3T_{CD})$. On the 2D map plotted and with high level contour plot, only CP's are visible, but DP's and AP's are not totally suppressed as expected by theory and they can be seen at lower contour plot levels. The reasons given previously explain also the origin of the presence of residual DP's and AP's in the 2D map. The same phenomenon was observed for the DECADENCY-DEPT 2D experiments.

Actually, another phenomenon involving ^{2}H–^{2}H couplings participates to the intensity variations observed on the 2D maps. To simplify the theoretical part, we have disregarded the contribution of the homonuclear couplings to the signal, but the experimental situation is more complex. Indeed if coupling patterns originating from ^{2}H–^{2}H couplings are not visible on the 1D spectrum (generally included in linewidth), dipolar interactions between deuterium geminal exist and can participate to the signals. Here again, their contributions are not cumbersome for the analysis of spectra data, because whatever the manner, the aim of these sequences is to correlate the signal of non-equivalent geminal deuterium nuclei in oriented medium. Consequently, no modification of both 2D sequences was explored to remove them.

Finally, it was found experimentally an example of CD_2 system for which one of two deuterium–carbon total couplings is null. This rare case was observed at 300 K for solute **1** (50 mg) dissolved in an oriented solution of poly-ε-carbobenzyloxy-L-lysine (100 mg) and chloroform (350 mg). As expected by theory, the DECADENCY-INEPT 2D map (not reported here) shows exclusively diagonal and autocorrelation peaks associated with the deuterium nucleus coupled to the carbon atom.

4.1. Separation of NMR signals in a mixture

Encouraged by these results, we have investigated the case of a mixture of two dideuterated prochiral solutes. For our purpose we have prepared an equimolar mixture of **1** and 1-chloro[1-$^2H_2$]nonane (**2**) dissolved in the PBLG/$CHCl_3$ phase.

The ^{2}H–{^{1}H} 1D spectrum of the mixture is shown in Fig. 5A. The difference in intensity of pairs of doublets for **1** and **2** is a direct consequence of a significant ^{2}H–^{2}H homonuclear coupling for solute **1** that increases the linewidth, and so reduces the intensity of corresponding doublets. A gaussian filtering allows the measurement of the ^{2}H–^{2}H homonuclear coupling, i.e., 1.5 Hz. Figs. 5B and C present the DECADENCY-INEPT and DECADENCY-DEPT 2D maps obtained for the mixture. For both experiments, the delay τ is set to $1/(2T_{CD})$ while $\tau' = 1/(4T_{CD})$ and $\tau' = 1/(2T_{CD})$ were used for the INEPT-type and DEPT-type transfer, respectively. Considering the magnitude of ^{2}H–^{13}C total couplings for solute **1** (27 and 31 Hz), and **2** (around 34 Hz), the constant T_{CD} was kept to 29 Hz, which is close to the optimum value for the different deuterium nuclei.

As expected in both 2D experiments, the CP's are the dominant peaks on the 2D maps, and allow the correlation between the two pairs of quadrupolar doublets associated with geminal deuterium nuclei in solute **1** and **2**. However the dispersion of C–D couplings around T_{CD} prevents the total cancellation of peaks, which would be suppressed in the ideal case. As a result, residual peaks associated with DP's and AP's are more or less

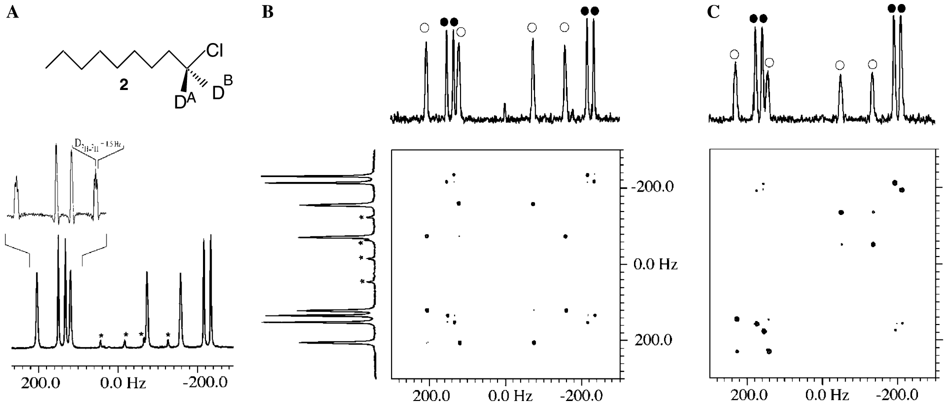

Fig. 5. (A) Structure of solute **2** and ^{2}H–{^{1}H} 1D spectrum of the mixture (**1** + **2**) in PBLG/CHCl$_3$ recorded with 64 scans and 2048 data points. In inset is shown the coupling pattern when a gaussian filtering (LB = −3 Hz, GB = 60%) is applied. (B) DECADENCY-INEPT 2D map of the mixture obtained when $\tau = 1/(2T_{CD})$, $\tau' = 1/(4T_{CD})$, with T_{CD} equals to 29 Hz. (C) DECADENCY-DEPT 2D map of the mixture obtained when $\tau = \tau' = 1/(2T_{CD})$. Both 2D spectra have been recorded using the same experimental conditions, using 128 (t_1) × 512 (t_2) data points and 320 scans per t_1. Filtering in both dimensions ($LB_{1,2} = 1$ Hz) and symmetrization were applied here. In F_1 dimension is displayed the 1D spectrum while in F_2 dimension is given the projection of the 2D map. Resonances marked by a star are associated with deuterated impurities. The quadrupolar splittings are equal to 193 and 361 Hz for solute **1** (labelled with open circles) and equal to 347 and 383 Hz for solute **2** (labelled with solid circles).

visible at lower level. Same reasons explain the presence of two pairs of CP's with low intensity perpendicular to the main diagonal in the case of DECADENCY-DEPT.

The position of the most intense CP's on the DECADENCY-DEPT 2D map indicates that the quadrupolar doublets have the same sign, positive or negative. To check this point we have recorded the ^{2}H–{^{1}H} 1D spectrum of the equimolar mixture of **1** and **2** dissolved in a racemic mixture of PBLG and PBDG (the enantiomer of PBLG) in chloroform. In such a solvent, noted hereafter PBG, spectral enantiodiscriminations are cancelled [19], and the quadrupolar splittings measured, $(\Delta\nu_Q)^{PBG}$, correspond to the algebraic average of splittings measured for D^{A} and D^{B} in the PBLG mesophase. In this example, the experimental values for solute **1** and **2** in PBG are equal to 292 and 368 Hz, while expected values would be equal to 277 and 365 Hz. As the compositions of the PBLG and PBG samples are identical, the observed discrepancies only reflect the difference of DP between PBLG (DP = 512) and PBDG (DP = 914, MW ≈ 200,000). This result proves that the signs of quadrupolar doublets are the same.

4.2. Phase sensitive experiment

As it is not possible to phase all resonances in pure absorption mode, the 2D maps of DECADENCY experiments are displayed in magnitude mode. The reason is that the signal is modulated by the quadrupolar splittings during the evolution τ delays (see in Eqs. (1) and (2)), thus leading to a phase modulation in F_1 and F_2 dimensions after the double Fourier transform.

The implementation of 90° pulses to refocus quadrupolar interaction during the fixed delays could be considered, but this solution generates several "irrelevant" terms in the density operators, thus leading to an important loss of sensitivity [20]. In the case of DECADENCY-INEPT 2D experiment, a possible alternative consists of simply removing the τ delays from the initial sequence and allowing the ^{13}C–^{2}H couplings to evolve during t_1 and t_2 periods. In practice, the ^{13}C π pulse in the midpoint of t_1 and the two τ intervals were removed while the deuterium decoupling is turned off during the acquisition. After a double Fourier transformation, a phased 2D map is expected with the same spectral information (δ_D, $^{1}T_{CD}$, and $\Delta\nu_Q$) in both dimensions. Note here that this solution is not applicable for the DECADENCY-DEPT 2D experiment because the signal evolves under the effect of the quadrupolar splittings during the $\tau'/2$ intervals as we can see in Eqs. (3)–(5).

To illustrate our purpose, we have recorded the phased DECADENCY-INEPT 2D experiment of **1** using $\tau' = 1/(4\,T)$ in order to maximize the intensity of CP's. As a result of the evolution of ^{13}C–^{2}H couplings during t_1 and t_2, 32 CP's (4 × 8) in pure absorption mode (16 positive peaks and 16 negatives) are now observed on the 2D spectrum shown in Fig. 6A. Actually the signals of quadrupolar doublets are in-phase while the two components resulting from the ^{13}C–^{2}H coupling are antiphase due to the absence of the delays τ. As a consequence of the non-equivalence of $^{1}T_{CD}$ for *pro-R* and *pro-S* deuteriums, the eight correlation sub-patterns between the two quadrupolar splittings do not form a square (see the inset). As previously residual DP's and

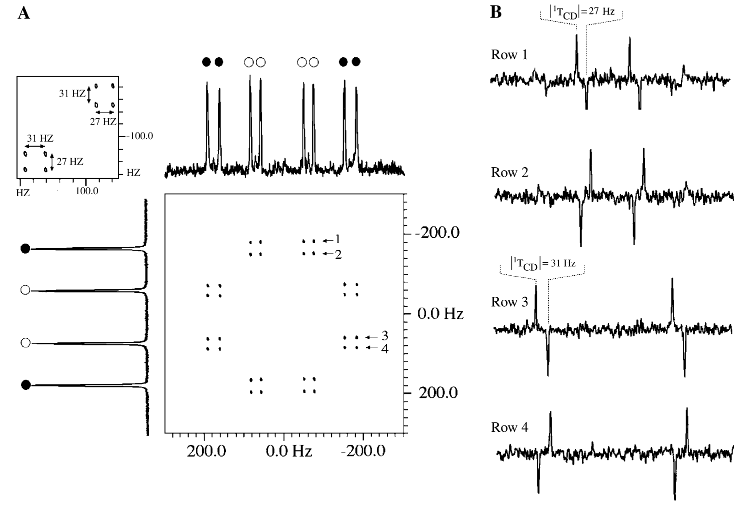

Fig. 6. (A) Phased variant of DECADENCY-INEPT 2D map of **1** obtained with no ^{13}C decoupling in F_2 and F_1 dimensions and using $\tau' = 1/(4T)$, with T_{CD} equal to 29 Hz. (B) Four rows extracted from the 2D map showing the phase of resonances. In inset is displayed a zoom of the 2D map. The 2D spectrum have been recorded using 128 (t_1) × 512 (t_2) data points and 320 scans per t_1. Filtering in both dimensions ($LB_{1,2} = 1$ Hz) was applied. In F_1 dimension is displayed the ^{2}H–{^{1}H} 1D spectrum of **1**, while in F_2 dimension is given the positive projection of the 2D map. The phase cycling of the phased DECADENCY-INEPT 2D experiment is identical to that of DECADENCY-INEPT 2D experiment. TPPI sampling scheme is used in F_1 dimension.

AP's are observed at very low level (not shown), however the 32 components (8 × 4) present a phase-twist lineshape. Calculations and computer simulations have confirmed this result.

Although possible, the application of the phased DECADENCY-INEPT experiments to analyse congested deuterium 1D spectra seems to be rather limited due to the substantial increase of peak numbers on the 2D map and the magnitude of the ^{13}C–^{2}H couplings.

5. Conclusion

We have theoretically and experimentally shown that it is possible to produce correlation between quadrupolar doublets of non-equivalent deuterium nuclei bonded to the same carbon in aligned solutes, using a double C–D polarization transfer of INEPT-type or DEPT-type. DECADENCY experiments exhibit no analytical complexity and under some conditions of timing ratio, the 2D maps are formally equivalent to ^{2}H–^{2}H COSY maps. In this work, the efficiency of these 2D experiments were illustrated using geminal deuteriums in prochiral molecules dissolved in a chiral liquid crystal. Obviously, these experiments could be successfully carried on for correlating any type of diastereotopic deuterium nuclei bonded to the same carbon atom, as in case of enantiomer solutes in chiral and non-chiral oriented solvents.

Acknowledgments

The authors thank Profs. J. Courtieu and B. Ancian for their helpful discussion.

Appendix A

To investigate theoretically the ^{13}C relayed ^{2}H–^{2}H-COSY 2D experiment, it is necessary to calculate analytically the time evolution of the density operator for a $^{13}CD_2$ group with two non-equivalent deuterium nuclei. For such spin system, there are 18 eigenvectors and the density operator is represented by a 18 × 18 dimension matrix. Assuming that the coupling between deuterium geminal nuclei are disregarded, analytical calculations can be greatly simplified by expressing the Hamiltonian and the density operator in a suitable orthogonal basis such as tensor operator product basis [21] or product operator basis [10,22]. We opted for the last one because it is more intuitive and provides much better physical insight. The 324 product operators for a $^{13}CD_2$ group are built from the product of the individual operators associated to a single carbon nucleus and two deuterons. For the carbon-13 nucleus, the usual Cartesian operators for spin-1/2, $\{E^C, S_x^C, S_y^C$, and $S_z^C\}$ are retained [21]. For deuterium nuclei, the Cartesian operators for spin-1 recently reported were used [23]. This basis-set consists of the unit matrix E, the angular moment operators for spin-1, I_x, I_y, and I_z, and five other operators denoted K_x, K_y, D_x, D_y, and Q_z.

The operators, K_x and K_y, defined as

$$K_x = I_xI_z + I_zI_x \text{ and } K_y = I_yI_z + I_zI_y, \tag{6}$$

represent the antiphase single-quantum magnetization of the quadrupolar doublet along the x and y axes, respectively. The operators, D_x and D_y, defined as

$$D_x = I_x^2 - I_y^2 \text{ and } D_y = I_xI_y + I_yI_x, \tag{7}$$

are the pure real and the pure imaginary spin-1 double quantum coherences. Finally, Q_z is the operator associated with the quadrupolar order and is equal to:

$$Q_z = 3I_z^2 - I^2. \tag{8}$$

This basis is advantageous because it provides a concise and relevant representation of Hamiltonians, coherences and polarization states in deuterium NMR spectroscopy in weakly oriented media. The rules describing the time evolution of individual spin-1/2 operators under radiofrequency pulses and chemical shifts are familiar [10,22]. The effect of radiofrequency

Table A
Evolution of product operators under the effect of heteronuclear IS coupling where S = 1/2 and I = 1

Coherence orders		$\hat{O}(0)$[a]	$\exp[-i(\omega t)2I_zS_z^C]\hat{O}(0)\exp[i(\omega t)2I_zS_z^C]$ with $\omega = \pi T$
p_S	p_I		
0	0	I_z	I_z
		Q_z	Q_z
		S_z^C	S_z^C
		$2I_zS_z^C$	$2I_zS_z^C$
		$2Q_zS_z^C$	$2Q_zS_z^C$
0	±1	I_x	$I_x\cos(\omega t) + 2I_yS_z^C\sin(\omega t)$
		I_y	$I_y\cos(\omega t) - 2I_xS_z^C\sin(\omega t)$
		K_x	$K_x\cos(\omega t) + 2K_yS_z^C\sin(\omega t)$
		K_y	$K_y\cos(\omega t) - 2K_xS_z^C\sin(\omega t)$
		$2I_xS_z^C$	$2I_xS_z^C\cos(\omega t) + I_y\sin(\omega t)$
		$2I_yS_z^C$	$2I_yS_z^C\cos(\omega t) - I_x\sin(\omega t)$
		$2K_xS_z^C$	$2K_xS_z^C\cos(\omega t) + K_y\sin(\omega t)$
		$2K_yS_z^C$	$2K_yS_z^C\cos(\omega t) - K_x\sin(\omega t)$
±1	0	S_x^C	$S_x^C\{2\cos(2\omega t) + 1\}/3 + Q_zS_x^C\{\cos(2\omega t) - 1\}/3 + I_zS_y^C\sin(2\omega t)$
		S_y^C	$S_y^C\{2\cos(2\omega t) + 1\}/3 + Q_zS_y^C\{\cos(2\omega t) - 1\}/3 - I_zS_x^C\sin(2\omega t)$
		$I_zS_x^C$	$I_zS_x^C\cos(2\omega t) + \{2S_y^C + Q_zS_y^C\}\sin(2\omega t)/3$
		$I_zS_y^C$	$I_zS_y^C\cos(2\omega t) - \{2S_x^C + Q_zS_x^C\}\sin(2\omega t)/3$
		$Q_zS_x^C$	$S_x^C\{2\cos(2\omega t) - 2\}/3 + Q_zS_x^C\{\cos(2\omega t) + 2\}/3 + I_zS_y^C\sin(2\omega t)$
		$Q_zS_y^C$	$S_y^C\{2\cos(2\omega t) - 2\}/3 + Q_zS_y^C\{\cos(2\omega t) + 2\}/3 - I_zS_x^C\sin(2\omega t)$
±1	±1	$I_xS_x^C$	$I_xS_x^C\cos(\omega t) + K_xS_y^C\sin(\omega t)$
		$I_xS_y^C$	$I_xS_y^C\cos(\omega t) - K_xS_x^C\sin(\omega t)$
		$I_yS_x^C$	$I_yS_x^C\cos(\omega t) + K_yS_y^C\sin(\omega t)$
		$I_yS_y^C$	$I_yS_y^C\cos(\omega t) - K_yS_x^C\sin(\omega t)$
		$K_xS_x^C$	$K_xS_x^C\cos(\omega t) + I_xS_y^C\sin(\omega t)$
		$K_xS_y^C$	$K_xS_y^C\cos(\omega t) - I_xS_x^C\sin(\omega t)$
		$K_yS_x^C$	$K_yS_x^C\cos(\omega t) + I_yS_y^C\sin(\omega t)$
		$K_yS_y^C$	$K_yS_y^C\cos(\omega t) - I_yS_x^C\sin(\omega t)$
0	±2	D_x	$D_x\cos(2\omega t) + 2D_yS_x^C\sin(2\omega t)$
		D_y	$D_y\cos(2\omega t) - 2D_xS_z^C\sin(2\omega t)$
		$2D_xS_z^C$	$2D_xS_z^C\cos(2\omega t) + D_y\sin(2\omega t)$
		$2D_yS_z^C$	$2D_yS_z^C\cos(2\omega t) - D_x\sin(2\omega t)$
±1	±2	$D_xS_x^C$	$D_xS_x^C$
		$D_xS_y^C$	$D_xS_y^C$
		$D_yS_x^C$	$D_yS_x^C$
		$D_yS_y^C$	$D_yS_y^C$

[a] The identity operators for I = 1/2 and S = 1 are omitted. $\hat{O}(0)$ corresponds to the initial operator at time $t = 0$.

pulses, chemical shifts, and quadrupolar couplings on the spin-1 operators were reported in [23]. In contrast, if some evolution rules of product operators or tensor product operators under coupling between spin-1 and spin-1/2 have been reported previously [10,22,24,25], they are not exhaustive.

To the best of our knowledge, the evolution of the antiphase single-quantum magnetizations of the quadrupolar doublet and those of the spin-1 double quantum coherences under the coupling have never been presented so far. To investigate thoroughly ^{13}C relayed ^{2}H–^{2}H-COSY 2D experiment, we have to conveniently determine the rules describing the evolution of the 36 relevant product operators corresponding to an IS system, where $S = 1/2$ and $I = 1$, under the effect of heteronuclear coupling Hamiltonian. For our purpose, we used the basis-sets mentioned above and the algebraic density matrix calculations were computed using the software *Mathematica* [15]. The explicit results are presented in Table A.

References

[1] I. Canet, J. Courtieu, A. Loewenstein, A. Meddour, J.-M. Péchiné, Enantiomeric analysis in a polypeptide lyotropic liquid crystal by deuterium NMR, J. Am. Chem. Soc. 117 (1995) 6520–6526.

[2] P. Lesot, M. Sarfati, J. Courtieu, Natural abundance deuterium NMR spectroscopy in polypeptide liquid crystals as a new and incisive means for enantiodifferentiation of chiral hydrocarbons, Chem. Eur. J. 9 (2003) 1724–1745.

[3] M. Sarfati, P. Lesot, D. Merlet, J. Courtieu, Theoretical and experimental aspects of enantiomeric differentiation using natural abundance multinuclear NMR spectroscopy in polypeptide liquid crystals, Chem. Commun. (2000) 2069–2081, and references therein.

[4] C. Aroulanda, M. Sarfati, J. Courtieu, P. Lesot, Investigation of enantioselectivity of three polypeptide liquid-crystalline solvents using NMR spectroscopy, Enantiomer 6 (2001) 281–287.

[5] H. Villar, F. Guibe, C. Aroulanda, P. Lesot, Investigation of SmI_2 mediated cyclisation process of δ-iodo-α, β-unsaturated esters by deuterium 2D NMR in oriented solvents, Tetrahedron: Asymmetry 13 (2002) 1465–1475.

[6] P. Lesot, M. Sarfati, D. Merlet, B. Ancian, J.W. Emsley, B.A. Timimi, 2D-NMR strategy dedicated to the analysis of perdeuterated enantiomer solutes in weakly ordered chiral liquid crystals, J. Am. Chem. Soc. 125 (2003) 7689–7695.

[7] O. Lafon, P. Berdagué, P. Lesot, Use of two-dimensional correlation between ^{2}H quadrupolar splittings and ^{13}C CSA's for assignment of NMR spectra in chiral nematics, Phys. Chem. Chem. Phys. 6 (2004) 1080–1084.

[8] M.A. Delsuc, E. Guittet, N. Trotin, J.-Y. Lallemand, Two-dimensional correlation spectroscopy with heteronuclear relay, J. Magn. Reson. 56 (1984) 163–166.

[9] D. Neuhaus, G. Wider, K. Wagner, K. Wüthrich, X-relayed ^{1}H–^{1}H correlated spectroscopy, J. Magn. Reson. 57 (1984) 164–168.

[10] R.R. Ernst, G. Bodenhausen, A. Wokaun, Principles of Nuclear Magnetic Resonance in One and Two Dimensions, Clarendon Press, Oxford, 1987.

[11] G.A. Morris, R. Freeman, Enhancement of nuclear magnetic resonances signals by polarization transfer, J. Am. Chem. Soc. 101 (1979) 760–762.

[12] D.M. Doddrell, D.T. Pegg, M.R. Bendall, Distortionless enhancement of NMR signals by polarization transfer, J. Magn. Reson. 48 (1982) 323–327.

[13] J. Shriver, NMR product-operator calculations in mathematica, J. Magn. Reson. 94 (1991) 612–616.

[14] P. Güntert, N. Schaeffer, G. Otting, K. Wüthrich, POMA: a complete mathematica implementation of the NMR product-operator formalism, J. Magn. Reson. Ser. A 101 (1993) 103–105.

[15] Wolfram Inc., Mathematica, Version 4.2, Champaign, IL, 2002.

[16] J. Keller, R.T. Clowes, A.L. Daies, E.D. Laue, Pulsed-field gradients: theory and practice, Methods Enzymol. 239 (1994) 145–207.

[17] T.T. Nakashima, R.E.D. McClung, B.K. John, Experimental and theoretical investigation of ^{2}D–^{13}C DEPT spectra on CD_n systems, J. Magn. Reson. 58 (1984) 27–36.

[18] C. Aroulanda, D. Merlet, J. Courtieu, P. Lesot, NMR experimental evidence of the differentiation of enantiotopic directions in C_s and C_{2v} molecules using partially oriented, chiral media, J. Am. Chem. Soc. 123 (2001) 12059–12066.

[19] C. Canlet, D. Merlet, P. Lesot, A. Meddour, A. Loewenstein, J. Courtieu, Deuterium NMR Stereochemical Analysis of *threo-erythro* isomers bearing remote chiral centres in racemic and non-racemic liquid crystalline solvents, Tetrahedron: Asymmetry 11 (2000) 1911–1918.

[20] S. Antonijevic, S. Wimperis, Refocussing of chemical and paramagnetic shift anisotropies in ^{2}H NMR using the quadrupolar–echo experiment, J. Magn. Reson. 164 (2003) 343–350.

[21] N. Müller, G. Bodenhausen, R.R. Ernst, Relaxation-induced violation of coherence transfer selection rules in nuclear magnetic resonance, J. Magn. Reson. 75 (1987) 297–334.

[22] O.W. Sorensen, G.W. Eich, M.H. Levitt, G. Bodenhausen, R.R. Ernst, Relaxation-induced violation of coherence transfer selection rules in nuclear magnetic resonance, Prog. NMR Spectrosc. 16 (1983) 163–192.

[23] D. Merlet, M. Sarfati, B. Ancian, J. Courtieu, P. Lesot, 2D-NMR strategy dedicated to the analysis of perdeuterated enantiomer solutes in weakly ordered chiral liquid crystals, Phys. Chem. Chem. Phys. 2 (2000) 2283–2290.

[24] N. Chandrakumar, Polarization transfer between spin-1 and spin-1/2 Nuclei, J. Magn. Reson. 60 (1984) 28–36.

[25] R. Kemp-Harper, D.J. Philip, P.W. Kuchel, Nuclear magnetic resonance of *J*-coupled quadrupolar nuclei: use of the tensor operator product basis, J. Chem. Phys. 115 (2001) 2908–2916.

Chapitre 2

Recouplage dipolaire homonucléaire

Les couplages dipolaires entre noyaux dépendent des distances interatomiques. De ce fait, la caractérisation structurale par RMN des solides est souvent basée sur la mesure des couplages dipolaires. En particulier, les séquences de recouplage dipolaire homonucléaire réintroduisent les couplages dipolaires entre des isotopes identiques dans les conditions MAS [110, 111]. Les séquences de recouplage peuvent être classées en fonction du rang des opérateurs de spin dans l'expression de l'hamiltonien dipolaire recouplé. Notre travail de recherche a porté sur les séquences de recouplage double-quantum (2Q), qui génèrent un hamiltonien dipolaire de rang 2 dans l'espace de spin et convertissent l'aimantation longitudinale en cohérence 2Q. En effet, ces recouplages 2Q sont utilisés dans de nombreuses expériences de RMN des solides, telles que :

- le filtrage 2Q qui vise à observer sélectivement les systèmes de spins comportant au moins deux noyaux identiques voisins [112, 113],
- la spectroscopie de corrélation bidimensionnelle (2D) 2Q-simple–quantum (1Q) [114] ou 1Q–1Q avec filtrage 2Q [115], qui permet de mettre en évidence les proximités entre atomes et ainsi d'attribuer les signaux RMN de solides,
- la mesure de distances interatomiques homonucléaires [111],
- la mesure d'angles entre liaisons ou de torsion [116, 117].

Parmi ces différentes applications, notre activité de recherche a essentiellement porté sur la mesure de distances ^{3}H–^{3}H, et le développement de la spectroscopie de corrélation 2Q–1Q à haut champ et haute fréquence MAS.

2.1 Mesures de longues distances homonucléaires

La mesure précise de quelques distances interatomiques élevées est cruciale pour l'étude des interactions intermoléculaires et la détermination de structure d'édifices supramoléculaires. Cette mesure est, par exemple, nécessaire pour déterminer la conformation d'une petite molécule liée à une protéine membranaire ou insoluble. La connaissance de la conformation d'une molécule d'intérêt thérapeutique, en interaction avec sa cible, permet la synthèse d'analogues plus efficaces, plus sélectifs et plus simples.

Différentes techniques d'analyse permettent de déterminer des distances interatomiques élevées. Citons notamment les techniques de diffraction, le transfert d'énergie entre molécules fluorescentes (FRET), la RMN des solutions et des solides. Cependant, ces méthodes ne sont pas toujours applicables. Les méthodes de diffraction nécessitent la préparation d'échantillons cristallins et ne permettent pas toujours d'observer les ligands, qui peuvent être mobiles. La technique FRET nécessite l'introduction de fluorophores, ce qui peut modifier la conformation du ligand. La RMN des solutions n'est applicable que pour des systèmes solubles dont la masse molaire est inférieure à 35 kg.mol^{-1}. La RMN des solides a l'avantage, elle, d'être applicable pour des systèmes insolubles, non cristallins et mobiles et nous disposons aujourd'hui de plusieurs méthodes pour mesurer des distances élevées par RMN des solides. Une première possibilité consiste à utiliser l'interaction de pseudo-contact entre les noyaux et une balise paramagnétique, qui peut être présente dans la protéine ou introduite chimiquement [118–120]. Cette méthode permet de mesurer des distances jusqu'à 20 Å. Une seconde possibilité consiste à mesurer des couplages dipolaires internucléaires. Par exemple, la mesure de couplages homo- ou hétéronucléaires avec une balise fluor-19 permet de déterminer des distances jusqu'à 11 Å [121–124]. Cependant, l'introduction d'une balise paramagnétique ou d'un atome ^{19}F est susceptible de modifier la conformation du ligand ou de la macro-molécule.

Il est donc hautement souhaitable de disposer, en RMN des solides, de méthodes de mesure de distances qui ne perturbent pas la structure du système étudié. La mesure de distances homonucléaires élevées impliquent l'observation de couplages dipolaires entre noyaux de rapport gyromagnétique élevé. En effet, la mesure de couplage dipolaire ^{13}C–^{13}C ou ^{13}C–^{15}N entre des sites sélectivement marqués permet de mesurer des distances au plus égales à 5–6 Å, ce qui est insuffisant pour détecter le changement de conformation d'un ligand [124]. Dans ce contexte, la RMN du ^{3}H offre plusieurs avantages. Premièrement, la substitution ^{1}H/^{3}H correspond à une faible modification structurale. Deuxièmement, ce noyau de spin-1/2 possède un rapport gyromagnétique élevé ($\gamma(^{3}\mathrm{H}) = 1.07\gamma(^{1}\mathrm{H})$). Troisièmement, l'abondance naturelle du ^{3}H est négligeable (3×10^{-16} %), ce qui assure l'absence de signaux parasites et la possibilité de marquage sélectif par une paire ^{3}H–^{3}H. En effet, en raison du phénomène de troncature dipolaire [125–127], il n'est possible de mesurer, de façon précise, des couplages dipolaires homonucléaires que pour des paires isolées.

Une des limitations à l'utilisation de la RMN ^{3}H est la radioactivité de cet isotope. Cependant, la dangerosité associée à la manipulation de ces échantillons ne doit pas être exagérée. En effet, le noyau ^{3}H est un émetteur β^- peu énergétique et le parcours maximal (6 μm) des électrons émis est de l'ordre de grandeur des dimensions cellulaires. Par conséquent, les électrons émis par le tritium sont bloqués par la couche de peau morte qui recouvre l'épiderme. En outre, le temps de demi-vie du ^{3}H est de 12,4 années, ce qui laisse le temps de réaliser des expériences RMN reproductibles. Du fait de sa faible radioactivité, le tritium est aujourd'hui utilisé comme traceur par de nombreux laboratoires de biochimie et de biologie, et des composés marqués en ^{3}H sont disponibles commercialement. La RMN de composés tritiés en solution a été largement employée pour l'étude de la stéréochimie et des mécanismes réactionnels [128–131]. En revanche, les seules études par RMN des solides concernaient les solides statiques $^3H_2$ et ^{2}H–^{3}H à des températures inférieures à 10 K [132]. Pour les solides, l'utilisation de la RMN du tritium a aussi été freinée par le faible écart (de l'ordre de 7 %) entre les fréquences de Larmor ^{1}H et ^{3}H, ce qui rend plus difficile le découplage hétéronucléaire ^{1}H–^{3}H.

Notre projet a consisté à démontrer la faisabilité de la mesure de longues distances ^{3}H–^{3}H par RMN des solides. La méthode a été testée pour des composés organiques ditritiés au sein desquels la distance ^{3}H–^{3}H est fixe. L'activité des échantillons était inférieure à 50 mCi. Les composés organiques ditritiés sont dilués dans le même composé chimique isotopiquement non modifié, afin de n'observer que les couplages dipolaires intramoléculaires. La fraction molaire en composé ditritié est de l'ordre de 0,4 %. Les mesures RMN solides ont été réalisées avec une sonde commerciale DOTY 4 mm ^{3}H/^{1}H/X spécialement conçue pour ce projet. En particulier, la chambre MAS est étanche aux particules, tandis que les gaz servant à la rotation de l'échantillon sont envoyés vers un détecteur de radioactivité.

Les couplages dipolaires ^{3}H–^{3}H ont été mesurés à l'aide d'une séquence de recouplage homonucléaire HORROR [133]. En effet, la gamme de fréquences des signaux ^{3}H observés est faible, de l'ordre de 1 kHz. Il n'était donc pas nécessaire d'utiliser une séquence très robuste au déplacement chimique isotrope. En outre, la séquence HORROR a l'avantage d'employer un faible champ rf ^{3}H, qui peut être combiné avec un découplage ^{1}H suffisant. En effet, la sonde utilisée n'était pas capable de délivrer des champs rf élevés en ^{1}H et en ^{3}H. Enfin, la méthode HORROR étant γ-encodée, les oscillations dipolaires observées sont plus grandes, ce qui permet de déterminer les distances interatomiques avec une plus grande précision. Ce protocole a permis de mesurer des distances ^{3}H–^{3}H de 9,4 Åavec une précision de 2 % et de 14,4 Åavec une précision de 15 %. La distance de 14,4 Åest la distance la plus élevée mesurée jusqu'ici par RMN des solides.

2.2 Observations de proximités homonucléaires

Les techniques de recouplage dipolaire permettent de déterminer, avec précision, des distances interatomiques uniquement pour des paires isolées de noyaux. Cette méthode est donc utile, principalement, lorsque la mesure d'une ou deux distances suffit à déterminer la structure du système. Elle est, par exemple, indiquée pour des systèmes ligand/cible, où les structures de la cible et du ligand non liés sont bien connues et où la seule inconnue est la conformation du ligand en interaction avec la cible. En revanche, cette méthode n'est pas utilisable pour la mesure d'un grand nombre de distances.

À l'inverse, les séquences de corrélation homonucléaire (HOMCOR) 2Q–1Q utilisant des recouplages dipolaires (D-HOMCOR) permettent de détecter, en une expérience sur un échantillon unique, un grand nombre de proximités homonucléaires. Cependant, il n'est pas possible, pour le moment, d'estimer les distances interatomiques à partir de ces expériences. Les expériences D-HOMCOR sont particulièrement utiles pour l'attribution des signaux RMN des solides, lorsque les corrélations via les couplages J ne sont pas envisageables. C'est notamment le cas pour les noyaux quadripolaires et les noyaux de spin-1/2 soumis à des couplages dipolaires élevés (^{1}H, ^{19}F). Par rapport aux expériences D-HOMCOR 1Q–1Q, la variante 2Q–1Q a l'avantage de permettre de sonder les proximités entre sites ayant des fréquences de résonances proches ou identiques [134].

2.2.1 Description des méthodes de recouplage

Pour les expériences D-HOMCOR 2Q-1Q, une séquence de recouplage idéale doit satisfaire aux conditions suivantes :

i. Son efficacité 2Q doit être aussi grande que possible ;

ii. Elle doit être robuste au déplacement chimique isotrope et au CSA. Cette condition est particulièrement critique à haut champ pour des noyaux soumis à de forts écrantages électroniques, tels que le ^{13}C, le ^{19}F et le ^{31}P ;

iii. Elle doit être robuste aux inhomogénéités de champ rf ;

iv. Elle doit être utilisable à haute-vitesse ($\nu_r > 30$ kHz), en particulier pour des utilisations en ^{1}H, ^{19}F, ^{13}C et ^{31}P. Cette spécification implique que la demande en puissance rf ne croîsse pas trop rapidement avec la vitesse de rotation.

v. Elle ne doit pas être sensible aux possibles désynchronisations entre les recouplages qui encadrent la période d'évolution, t_1. Ces désynchronisations peuvent être provoquées par les fluctuations de vitesse du rotor ;

vi. Elle doit être γ-encodée [133, 135]. Ceci signifie que l'hamiltonien dipolaire recouplé est modulé, en phase, par l'angle d'Euler, γ_{MR}, qui relie le repère de la molécule à celui du rotor. Cette modulation de phase a plusieurs avantages. Elle permet un gain en sensibilité de 20 % pour les poudres et conduit à des oscillations dipolaires plus importantes. De plus, la durée entre l'excitation et la reconversion des cohérences 2Q peut être variée librement, ce qui permet d'adapter au mieux la largeur spectrale en dimension indirecte pour les expériences D-HOMCOR 2Q–1Q, et conduit à une plus grande robustesse à la désynchronisation entre la séquence rf et la rotation de l'échantillon ;

vii. La période de la séquence de recouplage ne doit pas être trop grande, afin de pouvoir échantillonner correctement le maximum de la courbe de création des cohérences 2Q.

Aucune des séquences de recouplage dipolaire existantes ne remplit l'ensemble de ces critères. Les séquences basées sur la symétrie $\mathrm{C}N_n^\nu$ ou $\mathrm{R}N_n^\nu$ nécessitent, pour la plupart, des champs radiofréquences incompatibles avec la haute-vitesse [135–138]. Par exemple, la séquence POST-C7 nécessite un champ rf, $\nu_{rf} = 7\nu_r$ [137]. La séquence BAck-to-BAck (BABA) est l'un des recouplages les plus utilisés à haute vitesse, mais elle est sensible aux différences de déplacements chimiques et au CSA [139, 140]. En outre, elle présente deux défauts supplémentaires dans le cas des ^{1}H et ^{19}F. Premièrement, l'amplitude de l'interaction dipolaire recouplée est grande par rapport à la fréquence d'échantillonnage du BABA et de ce fait, le maximum d'efficacité 2Q ne peut très souvent pas être échantillonné correctement. Deuxièmement, la séquence BABA comprend des fenêtres, où aucun champ rf n'est appliqué. Or pour les noyaux ^{1}H ou ^{19}F, la relaxation $T_{1\rho}$ durant le verrouillage de l'aimantation est généralement plus longue qu'en l'absence d'irradiation. Les séquences comportant des fenêtres sont donc moins efficaces que celles dépourvues de fenêtres. Une autre séquence de recouplage 2Q est la méthode [fpRFDR] [141], dans laquelle le recouplage zéro-quantum, fpRFDR [142], est encadré par des impulsions $\pi/2$. Cette technique est plus robuste que la séquence BABA. Cependant, elle comporte aussi des fenêtres et n'est donc pas adaptée au recouplage des noyaux ^{1}H ou ^{19}F.

Confrontés à cette absence de méthodes de recouplage 2Q adaptées aux hautes vitesses, nous avons été amenés à rechercher de nouvelles stratégies. Nous avons utilisé les symétries $\mathrm{R}N_n^\nu$, qui sont généralement plus robustes que les symétries $\mathrm{C}N_n^\nu$ de par leurs règles de sélection plus strictes. En outre, nous avons exploré, à la fois, des recouplages non-γ-encodés et γ-encodés. En effet, les séquences non-γ-encodés sont moins efficaces que les séquences γ-encodés, mais elles sont, en général, plus robustes pour une puissance rf donnée, car elles sont compatibles avec l'utilisation d'un supercyclage.

Les séquences non-γ-encodées introduites sont basées sur la symétrie $\mathrm{R}2_2^1$. L'application d'un déphasage de 180° à partir du milieu du recouplage permet d'accroître la robustesse de la séquence au déplacement chimique isotrope et au

CSA. Deux séquences utilisant cette symétrie et ce supercyclage se sont révélées intéressantes : la séquence SPIP basée sur l'inversion $\mathcal{R} = \theta_0 180_0 \theta_{180}$ et la séquence $BR2_2^1$ basée sur $\mathcal{R} = \tau - 180_0 - \tau$. En raison de son absence de fenêtre, la séquence SPIP est plus adaptée au cas du recouplage ^{1}H ou ^{19}F, tandis que le temps de recouplage plus court de la séquence $BR2_2^1$ est favorable pour les noyaux ^{13}C ou ^{31}P. Les recouplages non-γ-encodés peuvent conduire à des repliements dans la dimension indirecte du spectre 2Q–1Q lorsque la gamme, $\Delta\nu_{\text{iso}}$, des déplacements chimiques isotropes est supérieure à la fréquence MAS. Néanmoins, différentes techniques peuvent être employées pour contourner ce problème.

Plusieurs séquences γ-encodés compatibles avec la haute-vitesse ont été testées. Elles ont été construites à partir de différentes symétries et d'inversions $\mathcal{R}$, consistant en des impulsions 180° simples ou des impulsions composites. Nous avons, en particulier, employé la séquence $R12_2^5$ proposée récemment pour le recouplage ^{1}H–^{1}H à $\nu_r = 67$ kHz [143].

2.2.2 Applications pour les noyaux de spin-1/2

Les séquences de recouplages ont été testées pour les noyaux ^{1}H, ^{19}F, ^{13}C et ^{31}P. Les séquences qui ont donné les meilleurs résultats sont les recouplages SPIP, $BR2_2^1$ et $R12_2^5$. Notre étude a permis de dégager trois critères principaux pour le choix des séquences de recouplages.

i. Le premier critère est l'amplitude des couplages dipolaires : pour les noyaux soumis à des couplages dipolaires homonucléaires élevés (^{1}H, ^{19}F), il faut utiliser des séquences sans fenêtre (SPIP ou $R12_2^5$), tandis que pour les noyaux (^{13}Cet ^{31}P), il est préférable d'employer la séquence $BR2_2^1$.

ii. Il convient ensuite de comparer $\Delta\nu_{\text{iso}}$ à la largeur d'excitation du recouplage. À $\nu_r = 30$ kHz, la largeur d'excitation du $R12_2^5$ est de 25 kHz, tandis que celle du $BR2_2^1$ et du SPIP sont respectivement égales à 70 et 90 kHz. Les séquences $BR2_2^1$ et SPIP sont donc particulièrement adaptées pour les noyaux présentant une large gamme de déplacements chimiques (^{19}F, ^{13}C et ^{31}P).

iii. Un dernier critère est la sensibilité de l'échantillon à une élévation de température. Cette élévation résulte des pertes diélectriques et par effet Joule [144]. En effet, le courant électrique circulant dans la bobine engendre, non seulement, un champ magnétique rf mais aussi un champ électrique rf à l'origine des pertes diélectriques. Ces pertes sont particulièrement importantes à haut-champ et augmentent avec le carré de la fréquence de nutation rf. Si les échantillons sont sensibles à une élévation de température (échantillons biologiques en solution aqueuse ionique) et si la sonde n'est pas spécialement conçue pour limiter le champ électrique rf [145], il n'est pas envisageable d'utiliser la séquence $R12_2^5$, qui nécessite une fréquence de nutation

TAB. 2.1 – Critères de choix pour le recouplage.

Isotope	$\Delta\nu_{\text{iso}} < 25$ kHz et non sensible à la température	$\Delta\nu_{\text{iso}} > 25$ kHz ou sensible à la température
^{1}H	$R12_2^5$	SPIP
^{19}F	$R12_2^5$	SPIP
^{13}C et ^{31}P	$R12_2^5$	$BR2_2^1$

rf, $\nu_1 = 3\nu_r$. En revanche, les séquences SPIP et $BR2_2^1$ emploient des valeurs de ν_1 plus faibles (environ 100 kHz pour le SPIP à $\nu_r = 65$ kHz).

Les critères de choix des séquences de recouplage sont donnés dans le tableau 2.1.

La large gamme d'excitation de la séquence SPIP a, en particulier, permis d'attribuer l'ensemble des signaux RMN ^{19}F du composé $Ba_3Al_2F_{12}$, qui sont distribués sur plus de 90 kHz à 18,8 T.

2.2.3 Applications pour les noyaux quadripolaires

Le recouplage homonucléaire des noyaux quadripolaires est particulièrement difficile car l'interaction quadripolaire est largement supérieure aux champs rf, ce qui rend difficile la manipulation des moments magnétiques nucléaires. Pour cette raison, les premières expériences de recouplage dipolaires entre les noyaux quadripolaires ont été réalisées en l'absence de champ rf. En effet, la diffusion de spin entre noyaux quadripolaires est activée par les interférences entre le couplage dipolaire homonucléaire et l'interaction quadripolaire [146] ou par celles entre les couplages dipolaires homonucléaires et les couplages dipolaires hétéronucléaires avec les protons [147]. Le phénomène de résonance rotationnelle R^2 a aussi été appliqué [148]. Cependant, ces méthodes ne sont efficaces que dans un certain domaine de fréquence MAS, et pour une gamme limitée de fréquence de résonance [149].

Pour les noyaux quadripolaires demi-entiers, une autre solution consiste à utiliser de faibles champs rf, dits sélectifs, pour manipuler la transition centrale entre les niveaux d'énergie $+1/2$ et $-1/2$, de façon à réintroduire l'interaction dipolaire [125, 150]. En particulier, la condition HORROR [133] permet de réintroduire sélectivement l'interaction dipolaire homonucléaire [151]. Récemment, il a été montré que l'utilisation des symétries permet d'augmenter la robustesse des séquences de recouplage aux inhomogénéités de champ rf [152]. Cependant, les recouplages existants entre noyaux quadripolaires n'étaient capables d'exciter qu'une gamme de fréquence d'au plus 5 kHz à $\nu_r = 15$ kHz. De ce fait, ces méthodes ne permettaient pas de corréler les sites aluminium octaédriques et tétraédriques à haut champ, puisque la différence de fréquence de résonance entre ces sites est de l'ordre de 10 kHz.

Pour remédier à cette situation, nous avons proposé une séquence de symétrie $BR2_2^1$ utilisant un champ rf correspondant à la condition HORROR [24, 25]. En outre, nous avons limité le nombre d'impulsions rf dans la séquence. Cette nouvelle méthode bénéficie d'une efficacité (de l'ordre de 5 %) deux fois plus grande que celles des méthodes existantes. En outre, elle permet d'exciter une gamme de fréquences de 10 kHz à $\nu_r = 15$ kHz, et est plus robuste aux inhomogénéités de champ rf. Il a, ainsi, été possible d'observer les corrélations entre aluminium octaédriques et tétraédriques à haut champ pour des différents composés aluminophosphate [25, 153].

2.3 Perspectives

Concernant la RMN du ^{3}H, la prochaine étape consistera à appliquer cette méthode pour déterminer la conformation bioactive du paclitaxel (nom commercial : taxol), un anti-cancéreux, en interaction avec la protéine tubuline. D'autres problématiques peuvent être envisagées, telles que l'étude de la structure des oligomères de la protéine H-NS en interaction avec l'ADN. Cette protéine, associée à l'ADN, joue à la fois un rôle dans le repliement des chromosomes et la régulation des gènes.

Pour la séquence de recouplage SPIP, il est important aujourd'hui de mieux comprendre l'origine de la robustesse de cette séquence. En particulier, l'effet du supercyclage doit être élucidé.

Un problème plus général est celui de la troncature dipolaire pour les systèmes contenant plus de deux noyaux identiques couplés et non alignés [125–127]. Dans ce cas, le couplage dipolaire entre plus proches voisins moyenne, partiellement ou complètement, les couplages dipolaires avec les noyaux plus lointains. Ceci empêche la mesure de distances multiples pour des échantillons uniformément marqués. Face à ce constat, deux questions se posent :

i. Quelles informations structurales est-il possible d'obtenir à partir des expériences *D*-HOMCOR 2Q–1Q ;

ii. Est-il possible de concevoir des séquences de recouplage homonucléaire qui ne soient pas affectées par la troncature dipolaire et qui permettent de mesurer des distances élevées de façon précise ?

À la première question, nous pourrions répondre que pour une fréquence 1Q donnée, l'intensité la plus grande est observée pour la fréquence 2Q correspondant à la plus courte distance homonucléaire [154]. Ainsi, les expériences *D*-HOMCOR 2Q–1Q permettent d'identifier les plus proches voisins, comme les expériences *J*-HOMCOR. Certes, elles sont moins sélectives, mais elles bénéficient, en contrepartie, d'une efficacité plus grande. Elles sont particulièrement utiles pour l'attribution des signaux RMN. Cependant, elles ne permettent pas, pour le moment, d'obtenir des contraintes précises sur les distances interatomiques. En particulier, le temps de recouplage correspondant à une intensité maximale pour un pic 2Q–1Q ne dépend pas uniquement de la distance entre plus proches voisins, mais aussi de la taille du système de spin [21,154]. Seules des simulations pour un grand nombre de noyaux [39, 155] permettront d'extraire des informations structurales quantitatives des spectres D-HOMCOR 2Q-1Q obtenus pour différents temps de recouplage.

Pour la deuxième question, la façon la plus simple de contourner le problème de la troncature dipolaire consiste à utiliser des séquences de recouplage dipolaire sélectives en fréquence. Citons, parmi ces techniques, la résonance rotationnelle [156] ou la méthode SEASHORE [157,158]. Cependant, ces méthodes sélectives ne permettent de déterminer qu'un petit nombre de distances à la fois, et le nombre d'expériences requises pour déterminer l'ensemble des distances interatomiques peut alors être prohibitif. Une solution consiste à utiliser une version stochastique de SEASHORE [159]. Il reste à tester ces méthodes pour des noyaux autres que ^{13}C et à voir, s'il est possible de les implémenter dans des expériences 2D D-HOMCOR.

2.4 Articles

J|A|C|S
COMMUNICATIONS

Measurement of Long-Range Interatomic Distances by Solid-State Tritium-NMR Spectroscopy

Alexander K. L. Yuen,[†] Olivier Lafon,[§] Thibault Charpentier,*[,§] Myriam Roy,[†] Francine Brunet,[§]
Patrick Berthault,[§] Dimitrios Sakellariou,[§] Bruno Robert,[‡] Sylvie Rimsky,[||] Florence Pillon,[†]
Jean-Christophe Cintrat,[†] and Bernard Rousseau*[,†]

CEA, iBiTecS, Service de Chimie Bioorganique et de Marquage, F-91191 Gif sur Yvette, France, CEA, iBiTecS, Service de Bioénergétique, Biologie Structurale et Mécanismes, F-91191 Gif sur Yvette, France, CEA, IRAMIS, SIS2M, Laboratoire Structure et Dynamique par Résonance Magnétique, F-91191 Gif sur Yvette, France, and LBPA, CNRS, ENS de Cachan, 61, avenue du Président Wilson, F-94235 Cachan, France

Received January 29, 2009; Revised Manuscript Received October 19, 2009; E-mail: thibault.charpentier@cea.fr; bernard.rousseau@cea.fr

Solid-state NMR has clearly proven to be valuable for probing molecular structure, owing to its ability to measure accurate interatomic distances.[1] In the absence of high-resolution X-ray data, such measurements are mandatory for determining the conformation of a small molecule bound to an insoluble or membrane protein. Knowledge of this conformation is of key importance in drug design.[2] Long-range distances can be determined using either beacons such as ^{19}F (distances up to 8 Å)[3] or paramagnetic spin labels (up to 20 Å).[4] In both of these cases, however, modification of the ligand structure is an unwanted consequence. Isotopic labeling using ^{13}C−^{13}C or ^{13}C−^{15}N does not lead to structural modifications, but only short distances can be measured (5−6 Å).[1] Most of the conformational changes when a ligand binds its receptor involve variation of long-range interatomic distances. For instance, the bioactive conformation of paclitaxel requires the determination of a key distance greater than 10 Å.[5] To gain access to such distances without structural modifications, we speculated that tritium would be an attractive label owing to the fact that it has a spin of $^1/_2$ and the highest gyromagnetic ratio of any nucleus (1.07 times that of proton). As the natural abundance of tritium is negligible (3×10^{-16}%), no background signal would be observed. Furthermore, modern synthetic protocols can furnish a variety of selectively labeled materials with tritium atoms at precise locations.[6] Tritiated compounds can be purchased from commercial companies at a price in the same range as that for a ^{13}C- or ^{15}N-labeled compound. Their safe handling is well-known, and countless biochemistry and biology laboratories routinely use them. In addition, tritium has already proven useful in liquid-state NMR where it has helped elucidate stereochemical and mechanistic aspects of small-molecule chemistry over the past few decades.[7]

In this Communication, we show that solid-state ^{3}H NMR is a powerful tool for accurately determining long-range interatomic distances without modification of molecular structure. The largest NMR distance ever measured between two nuclei was obtained using a model compound.

To assess the potential of solid-state tritium-NMR, we designed small molecules rigid enough to obtain nonfluctuating ^{3}H−^{3}H distances. Compounds **1**−**4** (Figure 1) incorporating two tritium atoms separated by 4.31, 6.0, 9.4, and 13.8 Å, respectively, were synthesized by catalytic hydrogenolysis of their brominated precursors using tritium gas and Pd/C.[8] For each NMR analysis, a powder mixture of 50 mCi (∼ 0.15 to 0.3 mg) of the tritiated compound, 40 mg of its unlabeled form, and 0.2 wt % of paramagnetic salt Cu(NO$_3$)$_2$ was prepared (the latter being added to shorten relaxation times).

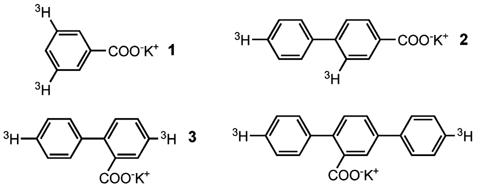

Figure 1. Model compounds for distance measurement.

The ^{3}H spectra of compound **1** obtained in 8 scans are displayed in Figure 2. They prove that a high signal-to-noise ratio can be obtained with small quantities of tritiated material. The use of ^{1}H−^{3}H cross-polarization significantly increases the sensitivity, mostly as a consequence of the shorter proton relaxation time. For compounds **1**−**4** the proton T_1 was determined to be approximately 10 times shorter than that of tritium (e.g., $T_1 > 360$ s for ^{3}H and $T_1 = 26$ s for ^{1}H in compound **1**).

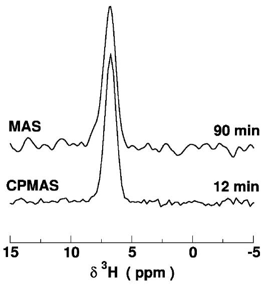

Figure 2. Comparison between ^{3}H spectra of compound **1** obtained by direct acquisition (top) and ^{1}H−^{3}H cross-polarization (bottom) in eight scans. Total experiment times are indicated on the right; MAS = magic angle spinning; CP = cross-polarization.

For interatomic distance measurements, numerous NMR recoupling techniques have been reported in the literature and their improvement is still the subject of intensive research. Among the several common pulse sequences we investigated, the best results

---

[†] CEA, iBiTecS, Service de Chimie Bioorganique et de Marquage.
[§] CEA, IRAMIS.
[‡] CEA, iBiTecS, Service de Bioénergétique, Biologie Structurale et Mécanismes.
[||] LBPA, CNRS.

10.1021/ja908915v

were obtained with HORROR.[9] This sequence offered the advantage of requiring only a moderate ^{3}H rf-field amplitude (matched at half the spinning frequency) so that a high ^{1}H-decoupling rf-field (here 80 kHz) could be applied, keeping the total power reasonable on two channels very close in frequency.

As shown in Figure 3, remarkably long dipolar oscillations are observed for compound **1**, allowing precise ^{3}H−^{3}H distance measurement. From these oscillations, the interatomic distance was extracted, accounting for the damped signal arising from the simultaneous response of the ^{3}H−^{3}H spin pair and that of isolated ^{3}H spins. For **1**, the discrepancy between the measured and the expected values is less than 1% (Table 1). Even for longer distances such as those found in compounds **2** and **3**, the accuracy remained excellent, with a discrepancy in the range of 2%. To the best of our knowledge, this constitutes unprecedented accuracy for such long-range interatomic distances.

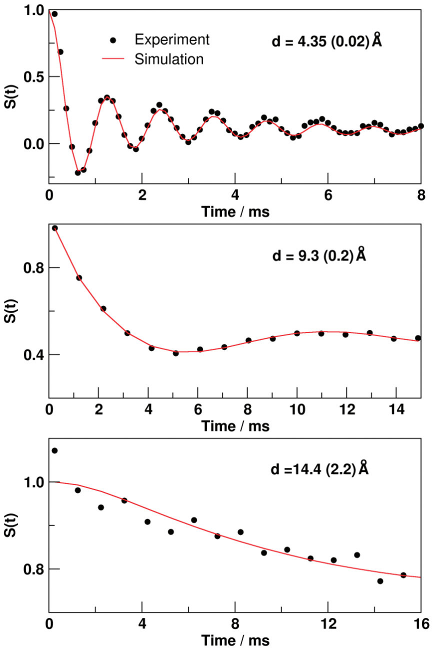

Figure 3. Variation of the ^{3}H-signal intensity $S(t)$ (in arbitrary units) for compounds **1**, **3**, and **4** (from top to bottom) with the ^{3}H rf-irradiation time under HORROR conditions (here 4 kHz). The experimental data were fitted using an advanced theoretical framework to perform the spin pair dynamics simulations.[10] Experimental details in Supporting Information.

The case of compound **4** revealed that, even in the absence of an observable dipolar oscillation, it was possible to extract a 14.4 Å distance with a precision of approximately ±15%. Such results were obtained due to high tritium dilution (less than 1 tritium for every 1000 hydrogen atoms), avoiding problems associated with the dipolar truncation effect.[11] Furthermore, the use of ^{1}H−^{3}H decoupling, which is more efficient than ^{1}H−^{1}H decoupling, contributes to the precision of the method.[12] Finally, this method relies upon direct measurement of the dipolar oscillation, which is more precise than using diffusion measurements.

Table 1. Predicted vs Measured ^{3}H−^{3}H Distances in Å for Compounds **1**−**4**

compound	1	2	3	4
predicted distance[a]	4.31	6.0	9.4	13.8
measured distance	4.35 ± 0.02	5.9 ± 0.1	9.3 ± 0.2	14.4 ± 2.2

[a] Distances predicted for molecules **1**−**4** using DFT relaxed molecular structures with the PWSCF package.[13]

In summary, we have described a simple, sensitive, and accurate approach for the determination of short- to long-range interatomic distances using standard probe electronics and sample holders and have successfully applied it to model compounds. The measured distance of 14.4 ± 2.2 Å reported here is the highest ever obtained using NMR. To generalize this approach to samples with a larger ^{3}H chemical shift distribution or shorter $T_{1\rho}$ values, modifications of the experimental conditions such as use of higher spinning frequency, sample volume reduction, or design of new pulse sequences would be beneficial.

This novel method will allow the study of drugs at their binding sites in insoluble or membrane proteins. Application of this approach to the study of biological questions such as the bioactive conformation of microtubule-bound paclitaxel is underway in our laboratories.

Acknowledgment. This work was supported by an ANR grant from the French Ministry of Research (Program MASTRIT NT05-2_42116). Nathalie Thromat is warmly acknowledged for her help in addressing safety issues.

Supporting Information Available: Experimental details, spectroscopic data, and safety procedures. This material is available free of charge via the Internet at http://pubs.acs.org.

References

(1) Griffin, R. G. *Nat. Struct. Biol.* **1998**, *5*, 508–512.
(2) Watts, A. *Nat. Rev. Drug Discovery* **2005**, *4*, 555–568.
(3) Watts, J. A.; Watts, A.; Middleton, D. A. *J. Biol. Chem.* **2001**, *276*, 43197–43204.
(4) Balogh, E.; Wu, D.; Zhou, G.; Gochin, M. *J. Am. Chem. Soc.* **2009**, *131*, 2821–2823.
(5) Paik, Y.; Yang, C.; Metaferia, B.; Tang, S.; Bane, S.; Ravindra, R.; Shanker, N.; Alcaraz, A. A.; Johnson, S. A.; Schaefer, J.; O'Connor, R. D.; Cegelski, L.; Snyder, J. P.; Kingston, D. G. I. *J. Am. Chem. Soc.* **2007**, *129*, 361–370.
(6) (a) O'Connell, T. M.; Gerig, J. T.; Williams, P. G. *J. Am. Chem. Soc.* **1993**, *115*, 3048–3055. (b) Faucher, N.; Cintrat, J. C.; Berthault, P.; Rousseau, B. *Angew. Chem., Int. Ed.* **2002**, *41*, 497–498.
(7) Valentine, A. M.; Wilkinson, B.; Liu, K. E.; Komar-Panicucci, S.; Priestley, N. D.; Williams, P. G.; Morimoto, H.; Floss, H. G.; Lippard, S. J. *J. Am. Chem. Soc.* **1997**, *119*, 1818–1827.
(8) Faucher, N.; Ambroise, Y.; Cintrat, J. C.; Doris, E.; Pillon, F.; Rousseau, B. *J. Org. Chem.* **2002**, *67*, 932–934.
(9) Nielsen, N. C.; Bildsoe, H.; Jakobsen, H. J.; Levitt, M. H. *J. Chem. Phys.* **1994**, *101*, 1805–1812.
(10) Charpentier, T.; Fermon, C.; Virlet, J. *J. Magn. Reson.* **1998**, *132*, 181–190.
(11) Bayro, M. J.; Huber, M.; Ramachandran, R.; Davenport, T. C.; Meier, B. H.; Ernst, M.; Griffin, R. G. *J. Chem. Phys.* **2009**, *130*, 114506.
(12) Brown, S. P.; Lesage, A.; Elena, B.; Emsley, L. *J. Am. Chem. Soc.* **2004**, *126*, 13230–13231.
(13) The PwSCF code is implemented in the Quantum-ESPRESSO suite of programs. Giannozzi, P. et al., http://www.quantum-espresso.org.

JA908915V

Journal of Magnetic Resonance 203 (2010) 113–128

Contents lists available at ScienceDirect

Journal of Magnetic Resonance

journal homepage: www.elsevier.com/locate/jmr

Homonuclear dipolar recoupling under ultra-fast magic-angle spinning: Probing $^{19}F-^{19}F$ proximities by solid-state NMR

Qiang Wang [a,b,c], Bingwen Hu [a], Olivier Lafon [a], Julien Trébosc [a], Feng Deng [b,*], Jean-Paul Amoureux [a,*]

[a] UCCS, CNRS-8181, Lille-University, 59652, Villeneuve d'Ascq, France
[b] State Key Laboratory of Magnetic Resonance and Atomic and Molecular Physics, Wuhan Center for Magnetic Resonance, WIPM, Chinese Academy of Sciences, Wuhan 430071, China
[c] Graduate School of the Chinese Academy of Sciences, Beijing, China

ARTICLE INFO

Article history:
Received 5 November 2009
Revised 9 December 2009
Available online 14 December 2009

Keywords:
Solid-state NMR
Double quanta
Ultra-fast MAS
^1H and ^{19}F
High field magnet

ABSTRACT

We describe dipolar recoupling methods that accomplish, at high magic-angle spinning (MAS) frequencies, the excitation of double-quantum (DQ) coherences between spin-1/2 nuclei. We employ rotor-synchronized symmetry-based pulse sequences which are either γ-encoded or non-γ-encoded. The sensitivity and the robustness to both chemical-shift anisotropy and offset are examined. We also compare different techniques to avoid signal folding in the indirect dimension of two-dimensional double-quantum ↔ single-quantum (DQ–SQ) spectra. This comprehensive analysis results in the identification of satisfactory conditions for dipolar $^{19}F-^{19}F$ recoupling at high magnetic fields and high MAS frequencies. The utility of these recoupling methods is demonstrated with high-resolution DQ–SQ NMR spectra, which allow probing $^{19}F-^{19}F$ proximities in powered fluoroaluminates.

1. Introduction

One of the frontiers in solid-state NMR is the development of recoupling and decoupling methods, compatible with high magic-angle spinning (MAS) frequencies of 30 kHz and greater. Recently, the reduction of rotor diameter has led to a considerable increase of sample spinning frequency. For instance, ultra-fast MAS frequencies, larger than 60 kHz, can now be reached easily by employing commercial rotors with outer diameters (o.d.) of 1.2–1.3 mm.

One of the key advantages of high MAS frequencies is the better average of large dipolar interactions. This leads to a gain in resolution, sensitivity per spin and transverse relaxation time, especially in the case of ^1H and ^{19}F nuclei, which are submitted to large dipolar interactions [1–3]. Furthermore, ultra-fast MAS (i) minimizes spinning sidebands arising from chemical-shift anisotropy (CSA), (ii) allows low-power radio frequency (rf) decoupling schemes, and (iii) increases the spectral width (SW_1) in the indirect dimension of rotor-synchronized experiments. Last, small rotor o.d. leads to the ability of generating very high rf magnetic fields. These specifications are advantageous for isotopes, such as ^{19}F, which exhibit large CSA and extended ranges of isotropic chemical shifts ($\Delta\nu_{iso}$).

In the presence of MAS, dipolar recoupling sequences are required to reintroduce the dipole–dipole couplings, which are averaged out by MAS. These methods allow probing the inter-nuclear proximities [4–22]. In particular, they are essential when efficient coherence transfers through the *J*-couplings are precluded, as in the case of ^1H, ^{19}F and quadrupolar nuclei [19,21,22]. In the following, we will focus on double-quantum (DQ) homonuclear dipolar recoupling sequences, which allow the excitation of DQ coherences (DQC) between isotopes with the same atomic number. These recoupling methods can be incorporated into two-dimensional (2D) NMR experiments, which correlate DQC with single-quantum coherences (SQC) within each homonuclear spin pair. Compared to SQ–SQ homonuclear correlation (HOMCOR) experiments, DQ–SQ HOMCOR spectroscopy benefits from the possibility to probe proximities between sites with identical or close resonance frequencies [23].

However, at high spinning frequencies, the use of well-established homonuclear dipolar recoupling methods, such as symmetry-based pulse sequences [11–13,15–18], is limited by the requirement of high-power rf field, which is proportional to the MAS frequency, ν_R. The Back-to-Back (BABA) scheme, which emerged in the mid-1990s [8,9], is presently one of the most popular DQ homonuclear dipolar recoupling sequences under fast and ultra-fast MAS ($\nu_R > 30$ kHz). This technique has been used mainly to observe $^1H-^1H$ and $^{19}F-^{19}F$ correlations [8,9,24–26]. Nevertheless, it suffers from two major drawbacks. First, it is not robust to CSA and to large differences in resonance frequencies ($\Delta\nu_{iso}$). Second, it does not display the property called "γ-encoding" since the recoupled dipolar Hamiltonian is amplitude-modulated by the Euler angle, γ_{MR}, which is one of the three angles defining the orientation of the molecule in the rotor-fixed frame [10,15,17]. The presence of "γ-encoding" leads (i) to a ≈20% increase of theoretical maximum efficiency of DQ-filtered (DQF) experiments

---

* Corresponding authors.
E-mail addresses: dengf@wipm.ac.cn (F. Deng), jean-paul.amoureux@univ-lille1.fr (J.-P. Amoureux).

1090-7807/$ - see front matter © 2009 Elsevier Inc. All rights reserved.
doi:10.1016/j.jmr.2009.12.009

in powder samples, and (ii) to larger oscillations of this DQF signal as function of the recoupling periods, which allows determining inter-nuclei distances with greater accuracy [10,15,17]. Furthermore, for non-γ-encoded recoupling sequences, the interval between the excitation and reconversion parts has to be an integer multiple of the rotor period. Therefore, in usual DQ–SQ NMR experiments, the spectral width in the indirect dimension (SW_1) is restricted to submultiples of ν_R.

Recently we have proposed an alternative to BABA recoupling by introducing the Sandwiched PI pulse (SPIP) scheme [19,22] The SPIP method is a super-cycled version of the $R2_2^1$ symmetry-based pulse sequence. We have demonstrated that this sequence is compatible with ultra-fast MAS. Furthermore, it displays higher robustness to CSA and offset than BABA. This allows the observation of $^{19}F-^{19}F$ proximities, although these nuclei are submitted to large magnetic shielding. Yet the SPIP recoupling is not γ-encoded. In the meantime, it was shown that $R12_2^5$ and $R14_4^5$ symmetry-based sequences accomplish $^1H-^1H$ dipolar recoupling at $\nu_R = 67$ kHz [18]. These γ-encoded methods provide higher DQF efficiency than BABA but their robustness to offset and CSA has not been investigated so far.

The present article provides a comprehensive comparison of γ-encoded and non-γ-encoded DQ homonuclear dipolar recoupling methods at high MAS frequencies. In particular, we analyze their DQF efficiency as well as their robustness to offset and CSA. Robust γ-encoded recoupling sequences compatible with ultra-fast MAS are introduced by combining symmetry principles and appropriate composite pulses. These novel recoupling methods are employed to obtain high-resolution $^{19}F-^{19}F$ DQ–SQ spectra of inorganic fluoroaluminates. Different techniques to avoid signal folding in the DQ indirect dimension are also examined.

2. Pulse sequences

2.1. Symmetry-based DQ dipolar recoupling sequences

A DQ dipolar recoupling sequence compatible with high MAS frequencies should ideally possess the following properties: (i) the rf-power requirements are below the usual probe specifications, (ii) the sequence provides the highest achievable DQF efficiency, (iii) it is robust to offset, CSA and rf imperfections and (iv) the magnitude of the recoupled dipolar interaction is much lower than the inverse of the recoupling cycle time, i.e. the maximal sampling frequency of the DQC build-up curve. In particular the criterion (iii) is critical when the recoupling sequence is applied to nuclei exhibiting large CSA as well as a large spread of resonance frequencies. This will be illustrated in the present article by dipolar $^{19}F-^{19}F$ recoupling in inorganic fluoroaluminates. In that case, the CSA is typically in the order of 100 ppm, while the isotropic chemical shifts (δ_{iso}) can span over more than 100 ppm [22]. Therefore, at large static magnetic fields, e.g. $B_0 = 18.8$ T, the magnitude of CSA and offset interactions can reach at least 75 kHz, whereas the largest $^{19}F-^{19}F$ dipolar coupling constants are about $b_{jk}/(2\pi) = -7$ kHz ($d_{jk} = 250$ pm).

The interferences of unwanted interactions can be limited by employing symmetry arguments for the design of the recoupling sequences [11–13,15–18]. These symmetry-based methods comprise both CN_n^ν and RN_n^ν classes. We will only consider, in this article, recoupling sequences deriving from RN_n^ν symmetries, which benefit from more restrictive selection rules than CN_n^ν sequences and hence are usually more robust [12]. The RN_n^ν pulse sequences, depicted in Fig. 1f, are composed of $N/2$ $R_{\pi\nu/N}R'_{-\pi\nu/N}$ inversion cycle pairs, spanning n rotor periods. The prime indicates a change in the sign of all phases internal to the basic inversion element R. The R_0 element rotates the resonant nuclear spins by an odd multiple of π about the x-axis of the rotating frame. It may be a single or a composite π pulse or a suitable amplitude, phase and/or frequency modulation scheme, lasting nT_R/N.

The spin dynamics during RN_n^ν pulse sequences can be described in the framework of average Hamiltonian theory (AHT) [15]. For a homonuclear spin pair, I_j and I_k, the first-order average Hamiltonian of homonuclear dipolar DQ recoupling must contain terms proportional to the DQ operators $I_j^\pm I_k^\pm$. The magnitude of these DQ recoupled dipolar interactions governs the optimal recoupling time. The choice of the RN_n^ν symmetry and of the basic element affects the magnitude of the recoupled dipolar interactions by

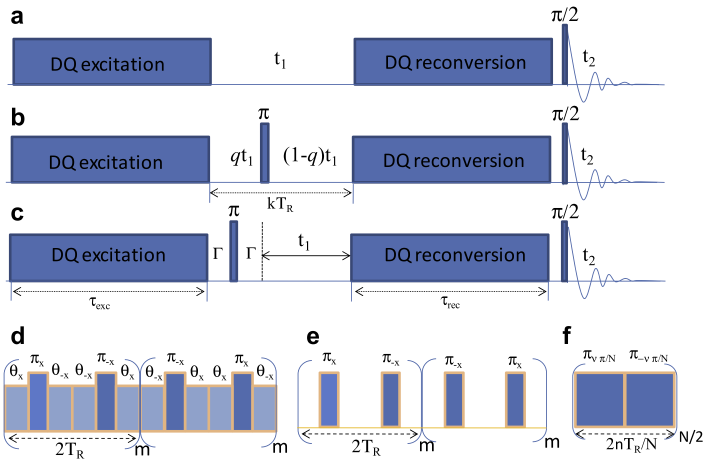

Fig. 1. (a–c) General DQ–SQ pulse schemes. (a) This scheme can be used either for γ-encoded sequences or non-γ-encoded sequences if the evolution time is rotor-synchronized: $t_1 = kT_R$. In the present article, the excitation and reconversion delays are identical, $\tau_{exc} = \tau_{rec} = \tau$. (b and c) Schemes that can be used with non-γ-encoded sequences if the F_1 spectral width is insufficient to avoid foldings. In both cases, the delay between the excitation and reconversion periods must be rotor-synchronized (kT_R), and a π pulse has been added. There are either (b) two evolution periods qt_1 and $(1-q)t_1$, or (c) only one evolution period t_1 and two short delays Γ sandwiching the π pulse and calculated according to Eq. (6). (d–f) Homonuclear recoupling sequences: (d) SPIP, (e) $BR2_2^1$, and (f) RN_n^ν .

modifying the scaling factors $\kappa_{lm\lambda\mu}$ of symmetry-allowed terms [15]. For homonuclear dipolar DQ recoupling, the quantum numbers $\{l, m, \lambda, \mu\}$ are restricted to $\{2, m, 2, \pm 2\}$ with $m = \pm 1$ and ± 2. The strength of the recoupled DQ interaction can be assessed by calculating the root mean square (rms) of the scaling factors:

$$\kappa^{rms}_{\mathrm{DD2Q}} = \left(\sum_m \left[|\kappa_{2m22}|^2 + |\kappa_{2m2-2}|^2 \right] \right)^{1/2} \tag{1}$$

where the sum is taken over $m = \pm 1$ and ± 2. Formulae for scaling factors are given in Ref. [27]. They were determined by employing the 'C and R symmetries' Mathematica package which takes into account the possible super-cycle [12,13,27–29]. The optimal recoupling time, leading to maximal DQF efficiency, decreases with increasing $\kappa^{rms}_{\mathrm{DD2Q}}$ scaling factor (see Eq. (5)). Therefore, large $\kappa^{rms}_{\mathrm{DD2Q}}$ values allow reducing the irreversible losses during the recoupling times and hence enhance the DQF efficiency, provided the recoupled dipolar interaction remains lower than the sampling frequency of the DQC build-up curve.

2.2. Non-γ-encoded recoupling sequences

Two non-γ-encoded recoupling methods were employed, SPIP and BR2_2^1 [19,20]. Both of these methods, depicted in Fig. 1d and e, respectively, derive from R2_2^1 symmetry. The basic R2_2^1 scheme spanning two rotor periods, accomplishes both 0Q and 2Q dipolar recoupling [30]. However, it does not eliminate the unwanted CSA and offset terms in the first-order average Hamiltonian. We have shown that the robustness to CSA and offset is increased by applying an overall phase shift of 180° from the middle of the recoupling sequence [19,20]. These block-super-cycled methods spanning 4p rotor periods may be written explicitly as follows:

$$\left(\mathrm{R}2_2^1\right)^p \left(\mathrm{R}2_2^{-1}\right)^p = \mathrm{R}2P_{2p}^{p}\mathrm{R}2P_{2p}^{-p} \tag{2}$$

The only difference between SPIP and BR2_2^1 schemes lies in the basic inversion element, R. SPIP and BR2_2^1 sequences are based on R = $\theta_0 180_0 \theta_{180}$ and τ–180_0–τ, respectively. Here, ξ_φ indicates a rectangular, resonant rf pulse with flip angle ξ and phase φ, and τ is a window delay during which no rf field is applied [15]. In the SPIP sequence, the use of spin-lock periods with flip-angles θ allows decreasing the irreversible losses, when the $T_{1\rho}$ relaxation time is much larger than the T_2' constant time [19]. The performances of SPIP and BR2_2^1 depend on the relative durations of the π pulse, τ_π, and the rotor period, T_R, i.e. the pulse fraction $f = \tau_\pi/T_\mathrm{R}$. Globally, the use of low f fraction, i.e. strong π pulses, increases the robustness to offset and CSA, but decreases the $\kappa^{rms}_{\mathrm{DD2Q}}$ scaling factor [20]. Therefore, the optimal pulse fraction ($f \approx 0.2$–0.3) results from a compromise between the irreversible losses and the CSA and offset interferences. Typical values of $\kappa^{rms}_{\mathrm{DD2Q}}$ parameters for SPIP and BR2_2^1 schemes are reported in Table 1.

2.3. γ-Encoded recoupling sequences and composite π pulses

For ideal γ-encoded DQ recoupling sequences, if the homonuclear J-coupling is disregarded, the first-order average Hamiltonian of an isolated spin pair I_j and I_k must contain only pure DQ terms

$$\overline{H}^{(1)} = \overline{\varpi}^{jk}_{2m22} I_j^+ I_k^+ + \overline{\varpi}^{jk*}_{2m22} I_j^- I_k^- \tag{3}$$

where $m = \pm 1$ or ± 2, depending on the pulse sequence symmetry. For γ-encoded recoupling, the complex amplitudes, $\overline{\varpi}^{jk}_{2m22}$ and $\overline{\varpi}^{jk*}_{2m22}$, depend on the Euler angle, γ_MR, through their arguments (called phases) but not through their amplitudes.

A large number of RN$_n^\nu$ sequences achieve γ-encoded DQ recoupling. A selection of RN$_n^\nu$ symmetries with $n \leqslant 10$ and $N \leqslant 30$ was given in Ref. [31]. However, not all the types of symmetry can be employed at high MAS frequencies owing to the limited probe performances in terms of rf field. For instance, an o.d. 2.5 and 1.2–1.3 mm MAS probe can reasonably deliver, during the recoupling interval, ^{19}F nutation frequencies, ν_1, up to 160 and 230 kHz, respectively. Therefore, when the rotor with o.d. 2.5 mm (resp. 1.2–1.3 mm) spins at $\nu_\mathrm{R} \approx 32$ (resp. 65 kHz), only recoupling schemes requiring ν_1/ν_R ratios lower than 5 (resp. 3.5) can be employed. The ν_1 parameter depends upon the RN$_n^\nu$ symmetry and the basic element, R. For instance, for RN$_n^\nu$ sequences based on the element R = 180_0, the required rf nutation frequency is equal to $\nu_1(180) = N\nu_R/(2n)$. Recently, it was demonstrated that R12_2^5 and R14_4^5 pulse sequences using R = 180_0 achieve efficient ^{1}H–^{1}H DQ recoupling at ν_R = 67 kHz [18]. However, we show below that the DQF efficiencies of these sequences are greatly affected by offsets larger than 5 kHz. Therefore, R12_2^5 and R14_4^5 schemes may not be suitable for isotopes, such as ^{19}F, ^{13}C or ^{31}P, which exhibit a large range of shifts.

Table 1
Properties of the homonuclear dipolar DQ recoupling sequences employed in this article.

Scheme	ν_1 (kHz)[a]	$\kappa^{rms}_{\mathrm{DD2Q}}$	τ^{opt} (μs)[b]
SPIP	73[c]	0.047	
	103[d]	0.028	
BR2_2^1	37.5[c]	0.080	
	60[d]	0.114	
R12_2^5[e]	$3\nu_\mathrm{R}$	0.246	126
R14_4^5[e]	$1.75\nu_\mathrm{R}$	0.237	131
R14_4^5c[f]	$4.1\nu_\mathrm{R}$	0.173	180
R10_4^2c[f]	$2.9\nu_\mathrm{R}$	0.158	197
R14_8^3c[f]	$2.0\nu_\mathrm{R}$	0.127	244
R18_8^5c[f]	$2.6\nu_\mathrm{R}$	0.150	207
R18_{10}^4c[f]	$2.1\nu_\mathrm{R}$	0.126	246

[a] The ν_1 nutation frequency is defined as $\nu_1^2 = (\tau_E)^{-1}\int_0^{\tau_E} \nu_1^2(t)\mathrm{d}t$, where $\tau_\mathrm{E} = \mathrm{n}T_\mathrm{R}/N$ is the duration of a basic element.

[b] The τ_{opt} values are calculated according to Eq. (5) using $b_{\mathrm{jk}}/(2\pi) = -9135$ Hz.

[c] ν_R = 33 kHz. For SPIP and BR2_2^1, the nutation frequency of π pulses is $\nu_{1\pi}$ = 85 kHz, and for SPIP, that of spin-lock is $\nu_{1\mathrm{SL}}$ = 70 kHz.

[d] ν_R = 66 kHz. For SPIP and BR2_2^1: $\nu_{1\pi}$ = 111 kHz, and for SPIP: $\nu_{1\mathrm{SL}}$ = 100 kHz. These parameters are those employed for the numerical simulations of Fig. 2a and b (ν_R = 33 kHz) or Fig. 2c and d (ν_R = 66 kHz).

[e] These sequences use a 180_0 pulse as basic element.

[f] These sequences use a R$_4$ = $60_0 300_{180} 60_0$ pulse as basic element.

The robustness to offset of γ-encoded recoupling sequences can be improved by the use of broadband composite pulse as basic element [15,32]. The gain in robustness is achieved at the cost of a larger rf-power requirement. The increase in rf nutation frequency between R = 180_0 and a composite pulse is

$$\frac{\nu_1(R)}{\nu_1(180)} = \frac{\sum \xi_j}{180} \tag{4}$$

where ξ_j is the flip angle of the jth pulse of the composite pulse and the sum is over all the pulses constituting the R element. The seven tested composite R$_p$ (p = 1–7) elements and their ν_1(R)/ν_1(180) ratios are listed in Table 2. These composite elements cannot be incorporated into R12_2^5 and R14_4^5 schemes at ν_R = 65 kHz owing to the limited rf field delivered by the probe. At such high MAS frequencies, the only solution consists in combining these composite pulses with RN$_n^\nu$ symmetries displaying lower $\nu_1(180)/\nu_R$ rf requirements, i.e. lower $N/(2n)$ ratios. In the present article, we concentrate on the use of R14_8^3, R18_8^5 and R18_{10}^4 symmetries, which correspond to $\nu_1(180)/\nu_R$ ratios of 0.875, 1.125 and 0.9, respectively. Given the rf-power limitation, at ν_R = 65 kHz composite pulses R$_1$ to R$_6$ can be combined with these three symmetries, whereas R$_7$ element is only compatible with R14_8^3 and R18_{10}^4 .

In order to identify good γ-encoded recoupling sequences, we performed analytical AH calculations up to the second-order. For

Table 2
Selection of composite pulses employed in this article.

Notation	Composite pulse	$\nu_1(\mathrm{R})/\nu_1(180)$[a]
R1	$90_0 270_{180}$	2
R2	$90_{90} 180_0 90_{90}$	2
R3	$180_{120} 180_{240} 180_{120}$	3
R4	$60_0 300_{180} 60_0$	2.3
R5	$90_0 240_{90} 90_0$	2.3
R6	$90_{45} 90_{135} 90_{45}$	1.5
R7	$90_0 225_{180} 315_0$	3.5

[a] The ratio is calculated according to Eq. (4).

γ-encoded DQ recoupling sequences, the first-order AH is given by Eq. (3), and Eq. (1) becomes $\kappa_{\mathrm{DD2Q}}^{rms} = \sqrt{2}|\kappa_{2m22}|$, where m = 1 or 2. The calculation of first-order $\kappa_{\mathrm{DD2Q}}^{rms}$ scaling factors allows assessing the optimum recoupling time. If the irreversible losses, the homonuclear J-coupling and the interferences arising from offset and CSA are disregarded, the maximal DQF efficiency for an isolated spin pair is reached for an excitation and reconversion intervals equal to [17]:

$$\tau^{opt} = \tau_{\mathrm{exc}}^{\mathrm{opt}} = \tau_{\mathrm{rec}}^{\mathrm{opt}} = \frac{1.26}{|\kappa_{2m22}|b_{jk}} = \frac{1.26\sqrt{2}}{\kappa_{\mathrm{DD2Q}}^{\mathrm{rms}} b_{jk}} \qquad (5)$$

where b_{jk} is the dipolar coupling constant in rad s^{-1}. Furthermore, in the frame of AHT, the interferences of offset (resp. CSA) for ^{19}F nuclei mainly result from $\delta_{\mathrm{iso}} \times \delta_{\mathrm{iso}}$ (resp. CSA × CSA) cross-terms in the second-order AH. Therefore, we also determined the rms scaling factors of $\delta_{\mathrm{iso}} \times \delta_{\mathrm{iso}}$ and CSA × CSA terms [33]. A comparison of first- and second-order scaling factors for various γ-encoded DQ recoupling is given in the Supplementary Information (SI, Fig. S1). This AHT approach predicts that R_1, R_4 and R_7 composite pulses provide the highest robustness to offset and CSA, especially when compared with that provided by the R = 180 element.

RN_n^{ν} symmetries, such as $\mathrm{R}10_4^2$, which achieve a simultaneous γ-encoded SQ *and* DQ recoupling, were also investigated. Compared to ideal γ-encoded DQ-only recoupling sequences, they display similar robustness to offset and CSA but slightly smaller on-resonance DQF efficiency. The results obtained for $\mathrm{R}10_4^2$ are also presented in the article. This symmetry corresponds to a $\nu_1(180)/\nu_R$ ratio of 1.25.

2.4. 1D DQF and 2D DQ–SQ NMR experiments

The typical scheme of DQ–SQ dipolar homonuclear correlation (D-HOMCOR) experiments is described in Fig. 1a. A first *excitation* sequence is applied for an interval τ_{exc} in order to transform the longitudinal magnetization into DQC. A second *reconversion* period of duration τ_{rec}, followed by a $\pi/2$ pulse, transforms the DQC into SQC corresponding to observable transverse magnetization. Signals passing through DQC are selected by a four-step phase cycle of the pulses used for exciting or reconverting the DQC. In this article, we use equal excitation and reconversion intervals: $\tau = \tau_{\mathrm{exc}} = \tau_{\mathrm{rec}}$. For one-dimensional (1D) DQF sequences, there is no evolution period, $t_1 = 0$, whereas for 2D DQ–SQ experiments, the t_1 delay is incremented. Hence, the evolution of DQC during t_1 is correlated with that of SQC during t_2 and the resulting 2D spectra display DQ–SQ correlations.

γ-Encoded and non-γ-encoded homonuclear dipolar recoupling sequences can be applied during τ periods. When using γ-encoded DQ recoupling, the phase modulation of DQF signal by the angle $2\pi\nu_{\mathrm{R}}t_1$ can be compensated by adjusting the overall rf phase of reconversion sequence [15,34]. This procedure allows varying freely the t_1 period in DQ–SQ experiments and hence the spectral width SW_1 in the indirectly-detected dimension. If the recoupling sequence is non-γ-encoded, a shift in the rf phase does not eliminate the amplitude modulation of the DQF signal by $2\pi\nu_{\mathrm{R}}t_1$. Therefore, the reconversion period must start mandatory an integer number of rotor periods after the end of excitation period. The excitation and reconversion intervals are then said to be rotor-synchronized. As a consequence, in typical 2D DQ–SQ experiments, SW_1 is thus limited to ν_{R}.

Nevertheless, different methods allow avoiding the signal folding in the F_1 dimension. A first possibility is the use of a shearing transformation with a factor of two in order to convert the DQ–SQ spectrum into a SQ–SQ representation. This shearing transformation reduces the spread in resonance frequencies by a factor of two in the F_1 dimension. In addition, it is possible to scale down along F_1 the isotropic chemical shifts by introducing a π pulse during the evolution of DQC. This variant of DQ–SQ experiment is depicted in Fig. 1b [35]. The π pulse is bracketed by two unequal incremented time periods, qt_1 and $(1-q)t_1$. Therefore, the scaled DQC frequency is $(1–2q)(\nu_{\mathrm{j}} + \nu_{\mathrm{k}})$, where ν_{j} and ν_{k} are the SQ frequencies of the dipolar coupled nuclei, j and k. For instance, when q = 1/3, this method allows reducing the range of ν_{iso} shifts by a factor of 3. The last technique is depicted in Fig. 1c. Prior to the t_1 period, a π pulse refocuses DQC evolution under ν_{iso} shifts during the adjustable delay, 2Γ. The Δt_1 increment time is chosen freely according to the desired spectral width and for each t_1 step, the Γ value is calculated so as to maintain rotor-synchronization of the excitation and reconversion recoupling. In other words, Γ delay is chosen in such way that

$$\tau_\pi + 2\Gamma + t_1 = kT_R \quad \text{with} \quad 0 < \tau_\pi + 2\Gamma \leqslant T_R \qquad (6)$$

where τ_π is the length of the π pulse and k is an integer. The method described above is derived from that introduced for DQ–SQ experiment using zero-quantum dipolar recoupling [36]. We show that it can be employed for all DQ–SQ sequences incorporating non-γ-encoded recoupling. The pros and the cons of these different techniques to avoid signal folding in the F_1 dimension are discussed in Section 4.

3. Numerical simulations

Numerical simulations were performed to assess the efficiency and the robustness of γ-encoded and non-γ-encoded recoupling sequences at high MAS frequency. These simulations were performed using SIMPSON [37] software for an isolated pair of ^{19}F nuclei denoted I_j and I_k. The inter-nuclear distance was fixed to d_{jk} = 226 pm, which corresponds to a dipolar coupling constant $b_{jk}/(2\pi) = -9135$ Hz. We consider two nuclei with either identical chemical shift (Fig. 2a and c) or with two symmetrical chemical shifts with respect to the irradiation frequency ($\nu_{\mathrm{offset}} = \Delta\nu_{\mathrm{iso}}/2$, Fig. 2b and d). The powder averages were calculated using 320 (α, β) orientations, selected according to the REPULSION algorithm with 15 γ-angles [38]. We detected the magnetization transferred from I_j to I_k during the DQF experiment. It corresponds to one of the two cross-peaks between I_j and I_k transitions on the 2D DQ–SQ spectrum. These simulations were done starting from I_j longitudinal magnetization, i.e. the operator I_{jz}, and detecting only the -1Q coherence of spin I_k, which corresponds to the operator I_k^-. The transferred magnetization was normalized to that of I_k spin after a $\pi/2$ pulse in order to calculate the DQF efficiency. For a spin pair, the above definition results in DQF efficiencies, which are twice smaller than those given by Levitt et al. [16,17].

We performed numerical simulations at various magnetic field strengths and MAS frequencies. In order to simplify the comparison between simulations, the ratio between B_0 and ν_{R} was kept constant, and the range of ν_{offset} was proportional to B_0. The numerical simulations were thus performed either for (B_0, ν_{R}) = (9.4 T, 33 kHz) or (18.8 T, 66 kHz).

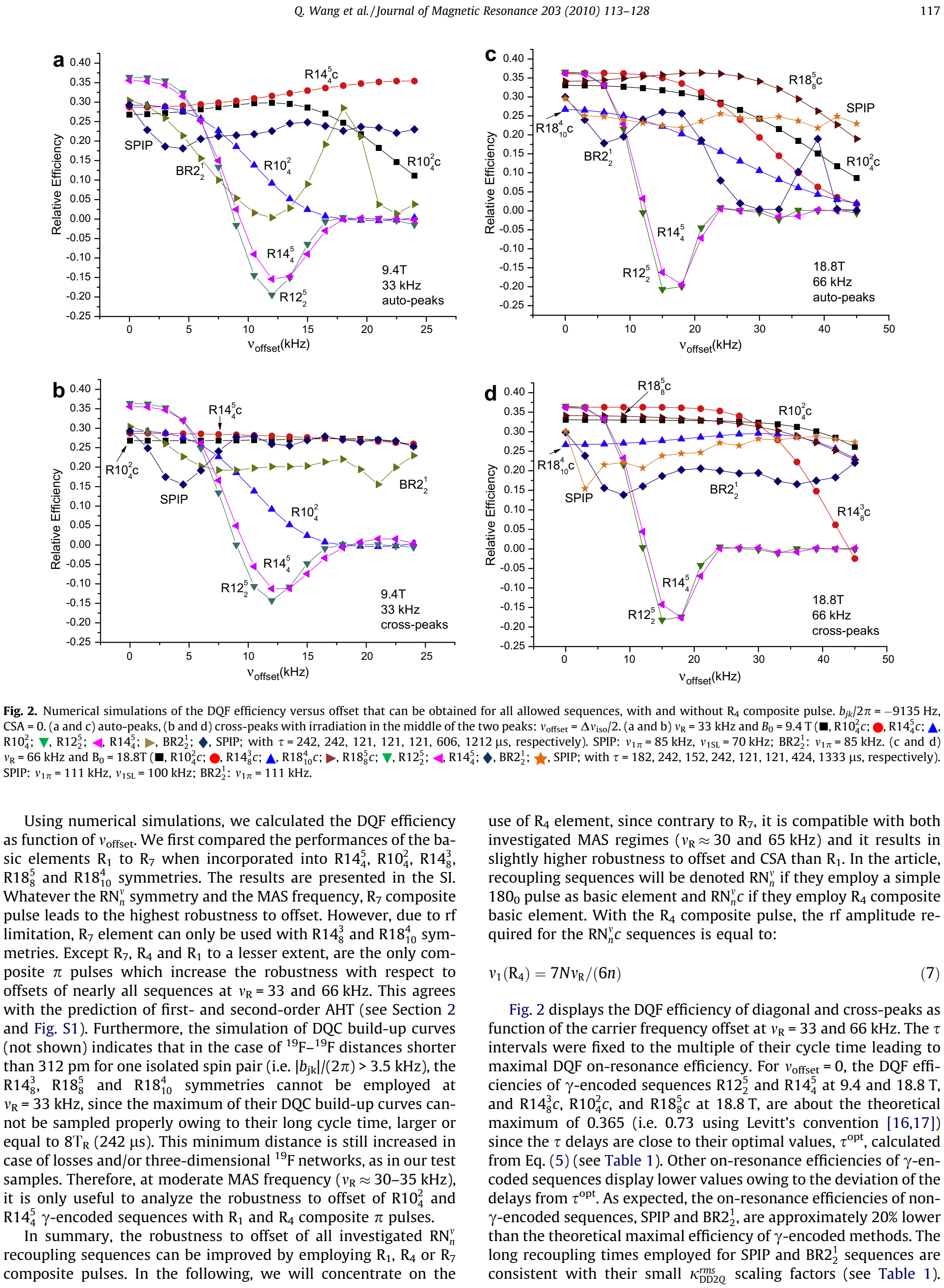

Fig. 2. Numerical simulations of the DQF efficiency versus offset that can be obtained for all allowed sequences, with and without R_4 composite pulse. $b_{jk}/2\pi = -9135$ Hz, CSA = 0. (a and c) auto-peaks, (b and d) cross-peaks with irradiation in the middle of the two peaks: $\nu_{offset} = \Delta\nu_{iso}/2$. (a and b) $\nu_R = 33$ kHz and $B_0 = 9.4$ T (■, R10$_4^2c$; ●, R14$_4^5c$; ▲, R10$_4^2$; ▼, R12$_2^5$; ◀, R14$_4^5$; ▶, BR2$_2^1$; ◆, SPIP; with τ = 242, 242, 121, 121, 121, 606, 1212 µs, respectively). SPIP: $\nu_{1\pi} = 85$ kHz, $\nu_{1SL} = 70$ kHz; BR2$_2^1$: $\nu_{1\pi} = 85$ kHz. (c and d) $\nu_R = 66$ kHz and $B_0 = 18.8$T (■, R10$_4^2c$; ●, R14$_8^3c$; ▲, R18$_{10}^4c$; ▶, R18$_8^5c$; ▼, R12$_2^5$; ◀, R14$_4^5$; ◆, BR2$_2^1$; ★, SPIP; with τ = 182, 242, 152, 242, 121, 121, 424, 1333 µs, respectively). SPIP: $\nu_{1\pi} = 111$ kHz, $\nu_{1SL} = 100$ kHz; BR2$_2^1$: $\nu_{1\pi} = 111$ kHz.

Using numerical simulations, we calculated the DQF efficiency as function of ν_{offset}. We first compared the performances of the basic elements R_1 to R_7 when incorporated into R14$_4^5$, R10$_4^2$, R14$_8^3$, R18$_8^5$ and R18$_{10}^4$ symmetries. The results are presented in the SI. Whatever the RN$_n^\nu$ symmetry and the MAS frequency, R_7 composite pulse leads to the highest robustness to offset. However, due to rf limitation, R_7 element can only be used with R14$_8^3$ and R18$_{10}^4$ symmetries. Except R_7, R_4 and R_1 to a lesser extent, are the only composite π pulses which increase the robustness with respect to offsets of nearly all sequences at $\nu_R = 33$ and 66 kHz. This agrees with the prediction of first- and second-order AHT (see Section 2 and Fig. S1). Furthermore, the simulation of DQC build-up curves (not shown) indicates that in the case of ^{19}F–^{19}F distances shorter than 312 pm for one isolated spin pair (i.e. $|b_{jk}|/(2\pi) > 3.5$ kHz), the R14$_8^3$, R18$_8^5$ and R18$_{10}^4$ symmetries cannot be employed at $\nu_R = 33$ kHz, since the maximum of their DQC build-up curves cannot be sampled properly owing to their long cycle time, larger or equal to $8T_R$ (242 µs). This minimum distance is still increased in case of losses and/or three-dimensional ^{19}F networks, as in our test samples. Therefore, at moderate MAS frequency ($\nu_R \approx 30$–35 kHz), it is only useful to analyze the robustness to offset of R10$_4^2$ and R14$_4^5$ γ-encoded sequences with R_1 and R_4 composite π pulses.

In summary, the robustness to offset of all investigated RN$_n^\nu$ recoupling sequences can be improved by employing R_1, R_4 or R_7 composite pulses. In the following, we will concentrate on the use of R_4 element, since contrary to R_7, it is compatible with both investigated MAS regimes ($\nu_R \approx 30$ and 65 kHz) and it results in slightly higher robustness to offset and CSA than R_1. In the article, recoupling sequences will be denoted RN$_n^\nu$ if they employ a simple 180_0 pulse as basic element and RN$_n^\nu c$ if they employ R_4 composite basic element. With the R_4 composite pulse, the rf amplitude required for the RN$_n^\nu c$ sequences is equal to:

$$\nu_1(R_4) = 7N\nu_R/(6n) \tag{7}$$

Fig. 2 displays the DQF efficiency of diagonal and cross-peaks as function of the carrier frequency offset at $\nu_R = 33$ and 66 kHz. The τ intervals were fixed to the multiple of their cycle time leading to maximal DQF on-resonance efficiency. For $\nu_{offset} = 0$, the DQF efficiencies of γ-encoded sequences R12$_2^5$ and R14$_4^5$ at 9.4 and 18.8 T, and R14$_8^3c$, R10$_4^2c$, and R18$_8^5c$ at 18.8 T, are about the theoretical maximum of 0.365 (i.e. 0.73 using Levitt's convention [16,17]) since the τ delays are close to their optimal values, τ^{opt}, calculated from Eq. (5) (see Table 1). Other on-resonance efficiencies of γ-encoded sequences display lower values owing to the deviation of the delays from τ^{opt}. As expected, the on-resonance efficiencies of non-γ-encoded sequences, SPIP and BR2$_2^1$, are approximately 20% lower than the theoretical maximal efficiency of γ-encoded methods. The long recoupling times employed for SPIP and BR2$_2^1$ sequences are consistent with their small κ_{DD2Q}^{rms} scaling factors (see Table 1).

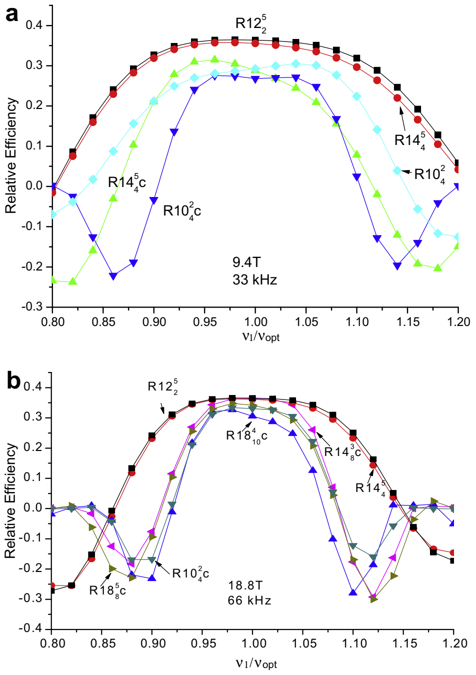

Fig. 3. Numerical simulations of the DQF efficiency versus the deviation in rf nutation frequency for on-resonance auto-peak, for all investigated DQ recoupling sequences, with and without R_4 composite pulse. The nominal rf nutation frequencies are given in Table 1. (a) $\nu_R = 33$ kHz and $B_0 = 9.4$T (■, R12$_2^5$; ●, R14$_4^5$; ▲, R14$_4^5c$; ▼; R10$_4^2c$; ◀, R10$_4^2$; with τ = 121, 121, 121, 242, 121 µs, respectively), (b) $\nu_R = 66$ kHz and $B_0 = 18.8$T (■, R12$_2^5$; ●, R14$_4^5$; ▲, R18$_{10}^4c$; ▶, R18$_8^5c$; ◀, R14$_8^3c$; ▼, R10$_4^2c$; with τ = 121, 121, 304, 242, 242, 182 µs, respectively). $b_{jk}/2\pi = -9135$ Hz. CSA = 0.

These small scaling factors allow sampling properly the maximum of their DQC build-up curves.

Furthermore, the numerical simulations of Fig. 2 permit to assess the robustness to offset of the investigated recoupling methods. The most robust sequences are R14$_4^5c$ and SPIP at $\nu_R = 33$ kHz and R18$_8^5c$ and SPIP at $\nu_R = 66$ kHz. SPIP sequence suppresses offset interferences without the use of composite pulses and hence it benefits from much lower rf-power requirements, especially at $\nu_R = 66$ kHz (Table 1). It must be reminded that none of the composite pulses can be used with R12$_2^5$, which is too much rf demanding.

The improved robustness to offset introduced by the use of composite pulses is partly counter-balanced by the increased sensitivity of these methods to rf-inhomogeneity (Fig. 3). This sensitivity to rf-inhomogeneity can be largely avoided by using restricted samples, at the expense of a decreased signal to noise ratio. This means that composite π pulses, which require larger rf fields than single π pulses, should be used preferentially with samples presenting large chemical-shift ranges.

4. Experimental results

4.1. Samples and experimental conditions

The investigated broadband DQ dipolar recoupling sequences, were tested for three different samples (α-CaAlF$_5$, β-BaAlF$_5$ and Ba$_3$Al$_2$F$_{12}$) corresponding to small, moderate and large spreads in ^{19}F chemical shifts, respectively. For ^{19}F sites in these three samples, the magnitudes of anisotropic chemical de-shielding constants ($|\delta_{\text{aniso}}|$), determined from spinning sideband patterns, are comprised between 75 and 110 ppm. In this article, the lines (noted L) are numbered starting from the right side of the spectra, and the peaks are described in the figures according to this line notation. We have used the same notation as that used in Ref. [26] to define the fluorine species (noted F). The assignment of the lines has been done for the three samples by simultaneous NMR experiments and DFT calculations [22,26,39]. All inter-nuclear fluorine-fluorine distances up to 375, 473 and 466 pm have been

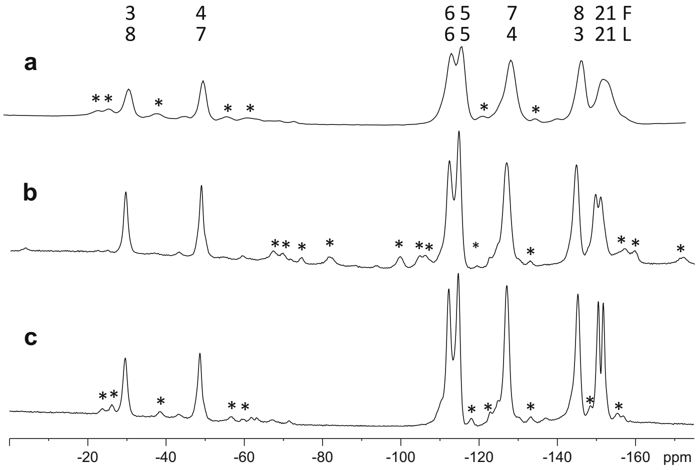

Fig. 4. Ba$_3$Al$_2$F$_{12}$. ^{19}F MAS spectra recorded at: (a) 9.4 T and $\nu_R = 30$ kHz, (b) 18.8 T and $\nu_R = 30$ kHz, (c) 18.8 T and $\nu_R = 67$ kHz. The most important spinning sidebands are indicated with $*$.

given for α-$CaAlF_5$, β-$BaAlF_5$ and $Ba_3Al_2F_{12}$, respectively, in the SI of Ref [22].

The structure of α-$CaAlF_5$ is built-up from isolated infinite chains of AlF_6^{3-} octahedra sharing opposite corners [40]. It involves three inequivalent fluorine sites: one shared F1 and two unshared F2 and F3, of multiplicity 4, 8 and 8, respectively. The ^{19}F MAS spectrum exhibits three lines in the small chemical-shift range of $\Delta\delta_{iso} = 18$ ppm, at −164, −154 and −146 ppm, for L1, L2 and L3, respectively (Fig. S9), with relative intensities 1:2:2. The structure of β-$BaAlF_5$ is built-up from isolated infinite chains of octahedra sharing adjacent corners [41]. This structure involves ten inequivalent sites (two shared F1 and F5, and eight unshared) of same multiplicity. The ^{19}F chemical-shift range of the 10 resonances is moderate: $\Delta\delta_{iso} = 55.6$ ppm, which means a moderate frequency spread of $\Delta\nu_{iso} = 21$ kHz at 9.4 T (Fig. 9, Fig. S10). The most difficult sample is $Ba_3Al_2F_{12}$, for which the chemical-shift range is very large and equal to $\Delta\delta_{iso} = 122.8$ ppm, which represents a large frequency spread of $\Delta\nu_{iso} = 46.25$ kHz at 9.4 T. The structure of $Ba_3Al_2F_{12}$ is built-up from rings formed by four AlF_6^{3-} octahedra sharing adjacent corners [42]; which involve eight inequivalent F sites: two shared (F1, F2), two free (F3, F4) and four unshared (F5–F8) of multiplicity 4, 4 and 8, respectively (Fig. 4).

All NMR experiments have been performed on Bruker Avance-II spectrometers using wide-bore 9.4 T and narrow-bore 18.8 T magnets. We have employed double resonance MAS probes with rotor o.d. of 1.3 mm at 18.8 T and double or triple resonance MAS probes with o.d. of 2.5 mm at 9.4 T. For all 2D experiments, phase sensitive detection in the indirect dimension was obtained using the States procedure [43]. The ^{19}F chemical shifts were referenced to $CFCl_3$.

The relevance of high magnetic field and high MAS frequency for ^{19}F solid-state NMR is illustrated by Fig. 4. Increases in magnetic field and MAS frequency both contribute to enhance spectral resolution. Large strength of magnetic field spreads the resonance frequencies, when the sample is well crystallized and does not display a continuous distribution of surrounding. High MAS frequencies better average out homogeneous $^{19}F-^{19}F$ dipolar couplings. For instance, at 18.8 T and $\nu_R = 67$ kHz, the L1 and L2 lines are resolved in the ^{19}F MAS spectrum of $Ba_3Al_2F_{12}$ (see Fig. 4c), whereas

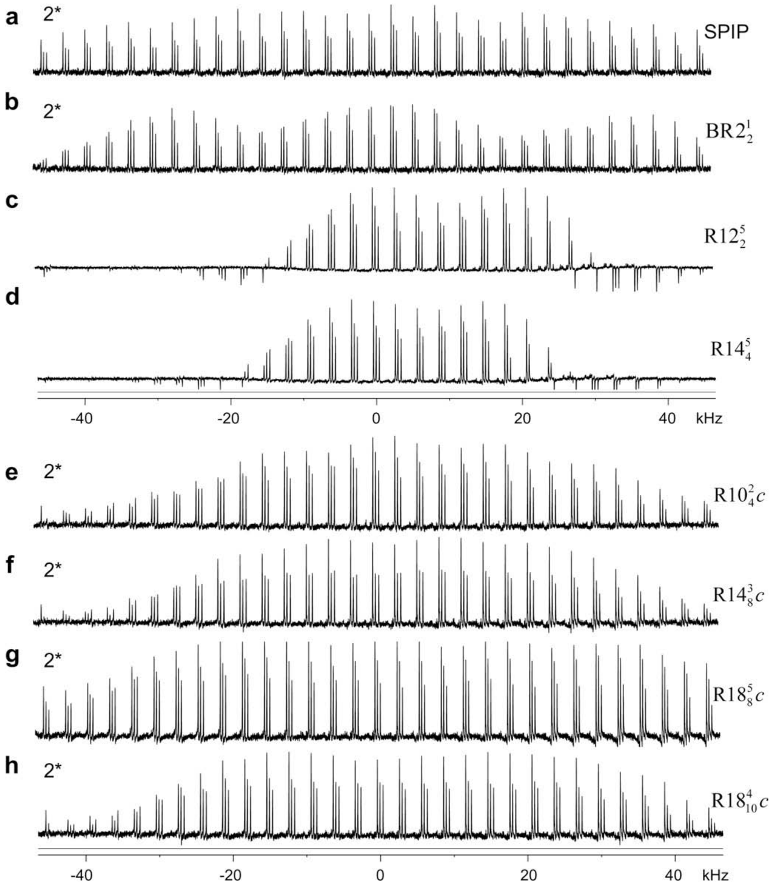

Fig. 5. α-$CaAlF_5$. Experimental DQF spectra versus offset irradiation, recorded at 18.8T and $\nu_R = 67$ kHz. (a) SPIP, (b) $BR2_2^1$, (c) $R12_2^5$, (d) $R14_4^5$, (e) $R10_4^2c$, (f) $R14_8^3c$, (g) $R18_8^5c$, and (h) $R18_{10}^4c$, with τ = 240, 120, 60, 60, 60, 120, 120, 150 µs, respectively. In (e–h) the R_4 composite pulse has been used. All spectra, except those in (c and d) have been scaled up by the factor 2. SPIP: $\nu_{1\pi} = 111$ kHz, $\nu_{1SL} = 100$ kHz; $BR2_2^1$: $\nu_{1\pi} = 111$ kHz.

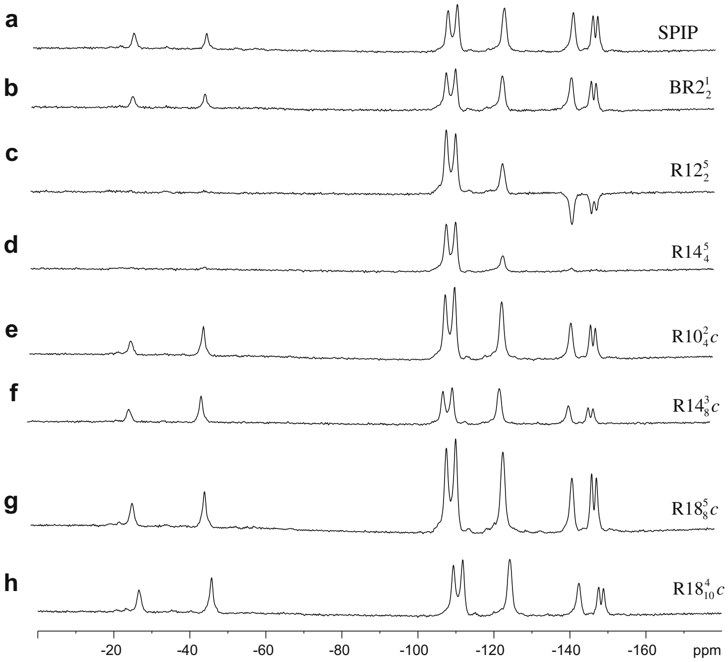

Fig. 6. $Ba_3Al_2F_{12}$. Experimental DQF RN_n^ν spectra recorded at 18.8 T and $\nu_R = 67$ kHz. (a) SPIP, (b) BR2$^1_2$, (c) R12$^5_2$, (d) R14$^5_4$, (e) R10^2_4c, (f) R14^3_8c, (g) R18^5_8c, and (h) R18$^4_{10}c$, with $\tau = 240$, 120, 60, 60, 60, 120, 120, 150 μs, respectively. In (e–h) the R_4 composite pulse has been used. The rf-irradiation was done at −93 ppm. SPIP: $\nu_{1\pi} = 111$ kHz, $\nu_{1SL} = 100$ kHz; BR2$^1_2$: $\nu_{1\pi} = 111$ kHz.

they are not at 9.4 T and $\nu_R = 30$ kHz (see Fig. 4a). A still more advanced solution would be to combine ultra-fast rotation and multiple pulse sequences. This type of homonuclear dipolar decoupling techniques has been developed for protons, which are submitted to small shielding [44–46]. However, the existing decoupling sequences cannot cope with the large shielding of nuclei, such as ^{19}F.

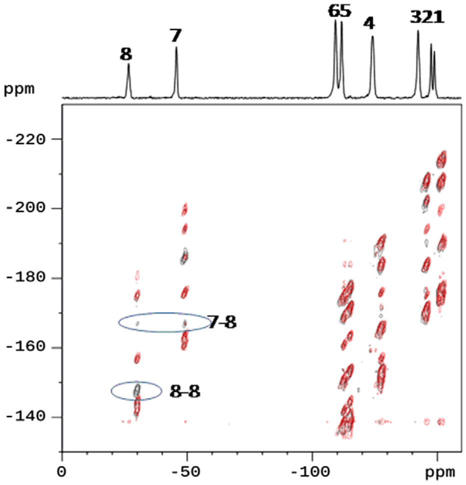

Fig. 7. $Ba_3Al_2F_{12}$. Rotor-synchronized DQ–SQ spectra recorded at 18.8 T and $\nu_R = 66.6$ kHz, with sequence of Fig. 1a. Two recoupling sequences were used: R18^5_8c with R_4 and $\tau = 120$ μs (red) and SPIP with $\nu_{1\pi} = 113$ kHz, $\nu_{1SL} = 100$ kHz and $\tau = 180$ μs (black). The rf-irradiation was done at −86 ppm. (For interpretation of the references to color in this figure legend, the reader is referred to the web version of this article.)

Besides enhancement in spectral resolution, high MAS frequencies result in longer T_2 transverse relaxation times [3], larger spectral width in F_1 dimension of rotor-synchronized 2D experiments and larger sampling frequency for the DQC build-up curves. The enhanced resolution observed with high magnetic field and ultra-fast MAS frequency is still emphasized in 2D experiments, and for example it allowed observing relayed negative peaks in the DQ–SQ spectrum of α-$CaAlF_5$ (Fig. S9).

In practice, NMR experiments were performed either at $(B_0, \nu_R) = (9.4$ T, 30–32 kHz) or (18.8 T, 65–67 kHz). For both experimental conditions, the ratio between CSA magnitude and MAS frequency is approximately constant and identical numbers of CSA spinning sidebands are observed in the NMR spectra. The only difference between the two series of experiments lies in the magnitude of offset and effective homonuclear dipolar couplings.

4.2. DQF efficiency and robustness to offset

In Fig. 5 are represented the DQF signals of α-$CaAlF_5$ recorded versus offset (−45 to 45 kHz) at $B_0 = 18.8$ T and $\nu_R = 67$ kHz. At this field, the chemical frequency range of this sample is moderate ($\Delta\nu_{iso} = 13.6$ kHz) and the behaviors of the three lines are globally identical. Fig. 5 allows assessing the robustness to offset of the different investigated recoupling sequences compatible with $\nu_R = 67$ kHz. In agreement with numerical simulations, the γ-encoded R12$^5_2$ and R14$^5_4$ sequences result in the largest on-resonance sensitivity. The other γ-encoded recoupling methods, R10^2_4c, R14^3_8c, R18^5_8c and R18$^4_{10}c$,

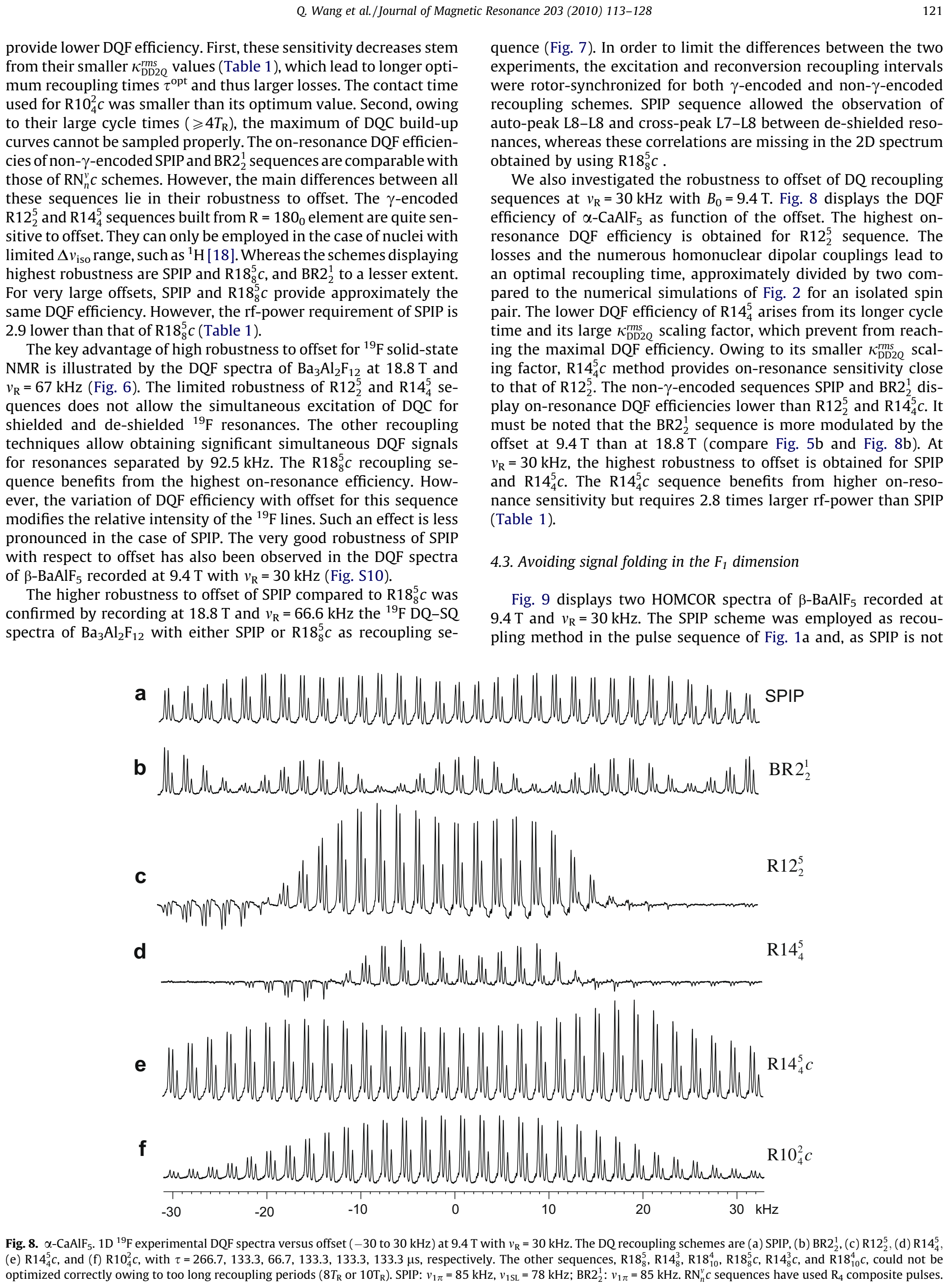

provide lower DQF efficiency. First, these sensitivity decreases stem from their smaller κ^{rms}_{DD2Q} values (Table 1), which lead to longer optimum recoupling times τ^{opt} and thus larger losses. The contact time used for $R10_4^2c$ was smaller than its optimum value. Second, owing to their large cycle times ($\geqslant 4T_R$), the maximum of DQC build-up curves cannot be sampled properly. The on-resonance DQF efficiencies of non-γ-encoded SPIP and $BR2_2^1$ sequences are comparable with those of $RN_n^\nu c$ schemes. However, the main differences between all these sequences lie in their robustness to offset. The γ-encoded $R12_2^5$ and $R14_4^5$ sequences built from R = 180_0 element are quite sensitive to offset. They can only be employed in the case of nuclei with limited $\Delta\nu_{iso}$ range, such as ^{1}H [18]. Whereas the schemes displaying highest robustness are SPIP and $R18_8^5c$, and $BR2_2^1$ to a lesser extent. For very large offsets, SPIP and $R18_8^5c$ provide approximately the same DQF efficiency. However, the rf-power requirement of SPIP is 2.9 lower than that of $R18_8^5c$ (Table 1).

The key advantage of high robustness to offset for ^{19}F solid-state NMR is illustrated by the DQF spectra of $Ba_3Al_2F_{12}$ at 18.8 T and ν_R = 67 kHz (Fig. 6). The limited robustness of $R12_2^5$ and $R14_4^5$ sequences does not allow the simultaneous excitation of DQC for shielded and de-shielded ^{19}F resonances. The other recoupling techniques allow obtaining significant simultaneous DQF signals for resonances separated by 92.5 kHz. The $R18_8^5c$ recoupling sequence benefits from the highest on-resonance efficiency. However, the variation of DQF efficiency with offset for this sequence modifies the relative intensity of the ^{19}F lines. Such an effect is less pronounced in the case of SPIP. The very good robustness of SPIP with respect to offset has also been observed in the DQF spectra of β-$BaAlF_5$ recorded at 9.4 T with ν_R = 30 kHz (Fig. S10).

The higher robustness to offset of SPIP compared to $R18_8^5c$ was confirmed by recording at 18.8 T and ν_R = 66.6 kHz the ^{19}F DQ–SQ spectra of $Ba_3Al_2F_{12}$ with either SPIP or $R18_8^5c$ as recoupling sequence (Fig. 7). In order to limit the differences between the two experiments, the excitation and reconversion recoupling intervals were rotor-synchronized for both γ-encoded and non-γ-encoded recoupling schemes. SPIP sequence allowed the observation of auto-peak L8–L8 and cross-peak L7–L8 between de-shielded resonances, whereas these correlations are missing in the 2D spectrum obtained by using $R18_8^5c$.

We also investigated the robustness to offset of DQ recoupling sequences at ν_R = 30 kHz with B_0 = 9.4 T. Fig. 8 displays the DQF efficiency of α-$CaAlF_5$ as function of the offset. The highest on-resonance DQF efficiency is obtained for $R12_2^5$ sequence. The losses and the numerous homonuclear dipolar couplings lead to an optimal recoupling time, approximately divided by two compared to the numerical simulations of Fig. 2 for an isolated spin pair. The lower DQF efficiency of $R14_4^5$ arises from its longer cycle time and its large κ^{rms}_{DD2Q} scaling factor, which prevent from reaching the maximal DQF efficiency. Owing to its smaller κ^{rms}_{DD2Q} scaling factor, $R14_4^5c$ method provides on-resonance sensitivity close to that of $R12_2^5$. The non-γ-encoded sequences SPIP and $BR2_2^1$ display on-resonance DQF efficiencies lower than $R12_2^5$ and $R14_4^5c$. It must be noted that the $BR2_2^1$ sequence is more modulated by the offset at 9.4 T than at 18.8 T (compare Fig. 5b and Fig. 8b). At ν_R = 30 kHz, the highest robustness to offset is obtained for SPIP and $R14_4^5c$. The $R14_4^5c$ sequence benefits from higher on-resonance sensitivity but requires 2.8 times larger rf-power than SPIP (Table 1).

4.3. Avoiding signal folding in the F_1 dimension

Fig. 9 displays two HOMCOR spectra of β-$BaAlF_5$ recorded at 9.4 T and ν_R = 30 kHz. The SPIP scheme was employed as recoupling method in the pulse sequence of Fig. 1a and, as SPIP is not

Fig. 8. α-$CaAlF_5$. 1D ^{19}F experimental DQF spectra versus offset (−30 to 30 kHz) at 9.4 T with ν_R = 30 kHz. The DQ recoupling schemes are (a) SPIP, (b) $BR2_2^1$, (c) $R12_2^5$, (d) $R14_4^5$, (e) $R14_4^5c$, and (f) $R10_4^2c$, with τ = 266.7, 133.3, 66.7, 133.3, 133.3, 133.3 μs, respectively. The other sequences, $R18_8^5$, $R14_8^3$, $R18_{10}^4$, $R18_8^5c$, $R14_8^3c$, and $R18_{10}^4c$, could not be optimized correctly owing to too long recoupling periods ($8T_R$ or $10T_R$). SPIP: $\nu_{1\pi}$ = 85 kHz, ν_{1SL} = 78 kHz; $BR2_2^1$: $\nu_{1\pi}$ = 85 kHz. $RN_n^\nu c$ sequences have used R_4 composite pulses.

γ-encoded, the excitation and reconversion intervals were rotor-synchronized. Therefore, the spectral width in the F_1 dimension is limited to $SW_1 = \nu_R$. Even if the chemical-shift range $\Delta\delta_{iso}$ = 55.6 ppm, and the strength of magnetic field are moderate, the spread in resonance frequencies of DQC reaches 42 kHz and thus exceeds $SW_1 = \nu_R$. Consequently, in the usual DQ–SQ representation (shown in Fig. 9a), six peaks are folded along F_1: L1–L1, L1–L2, L1–L3, L2–L3, L9–L10, and L10–L10. However, as in that case the spread in resonance frequencies of SQC, $\Delta\nu_{iso}$ = 21 kHz is lower than ν_R, this signal folding can be avoided by doing a shearing processing with a factor of two. After such a shearing, the slope of the auto-peaks becomes equal to one, and the spectrum is then presented in a symmetrical way (Fig. 9b), as a SQ–SQ spectrum. However, this shearing is useless when $\Delta\nu_{iso}$ is larger than ν_R. This is illustrated by the 2D ^{19}F–^{19}F HOMCOR spectra of $Ba_3Al_2F_{12}$ at 9.4 T, for which the frequency spread ($\Delta\nu_{iso}$ = 46.25 kHz) is larger

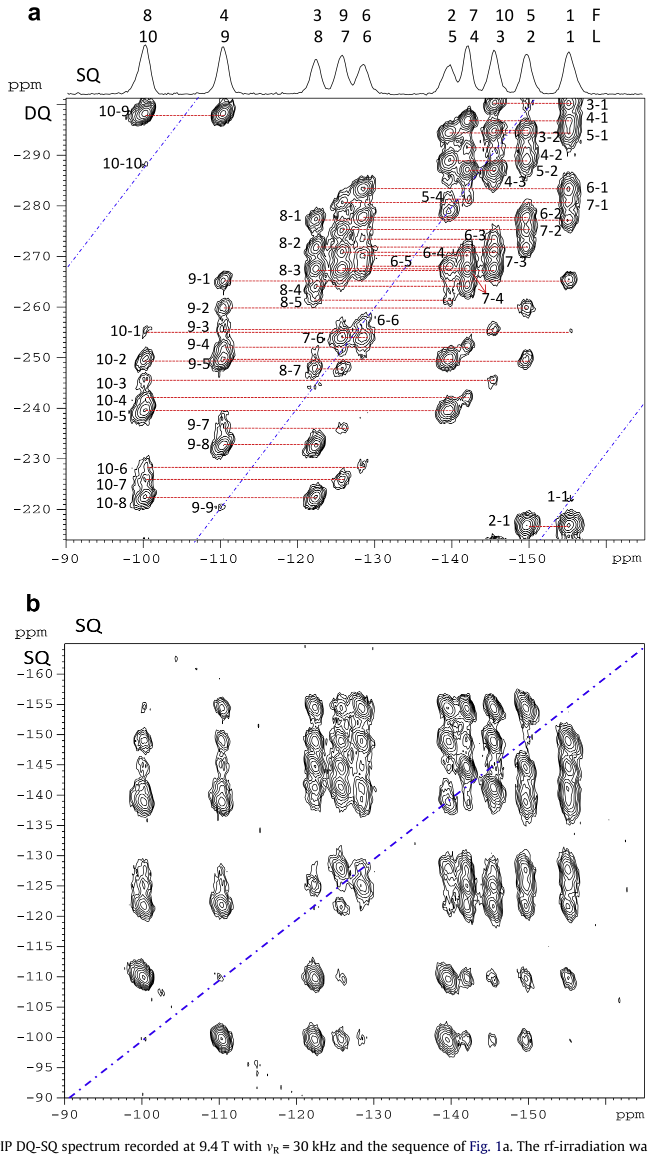

Fig. 9. β-BaAlF$_5$. Experimental SPIP DQ-SQ spectrum recorded at 9.4 T with ν_R = 30 kHz and the sequence of Fig. 1a. The rf-irradiation was done at −129 ppm. The nutation frequencies of SPIP were: $\nu_{1\pi}$ = 85 kHz, ν_{1SL} = 78 kHz, and τ = 267 μs. (a) Un-sheared spectrum. Due to the folding along F_1, the vertical scaling is only correct for the central part of the resonances. For the four other resonances, the correct F_1 value can be obtained by adding either + 80 ppm for (10, 10) and (10, 9), or −80 ppm for (2, 1) and (1, 1) correlation peaks (80 ppm = ν_R/ν_0). (b) Sheared spectrum; the vertical scaling is correct for all peaks.

than ν_R = 30 kHz (Fig. 10). Indeed, the sheared spectrum shown in Fig. 10b is much more difficult to interpret than that shown in Fig. 10a. The only difference with respect to the un-sheared spectrum recorded with a sufficient spinning speed ($\nu_R > 2\Delta\nu_{iso}$) is that the auto-correlation line is parted in several pieces of lines in Fig. 10a.

For samples with large spread in resonance frequencies ($\Delta\nu_{iso} > \nu_R$), the signal folding in F_1 dimension for non-γ-encoded recoupling schemes can be avoided by inserting a π pulse during the evolution period of DQC (Fig. 1b and c). However, when the delays between central π pulse and the recoupling intervals are not multiple of the rotor period, this π pulse reintroduces the CSA during one rotor period at the maximum. This unwanted dephasing may be non negligible in case of large CSA, as with ^{19}F nuclei. Fig. 11 shows that the non-refocused CSA affects the sensitivity of DQF experiments. The variation in DQF efficiency with the de-synchronization delay Γ differs

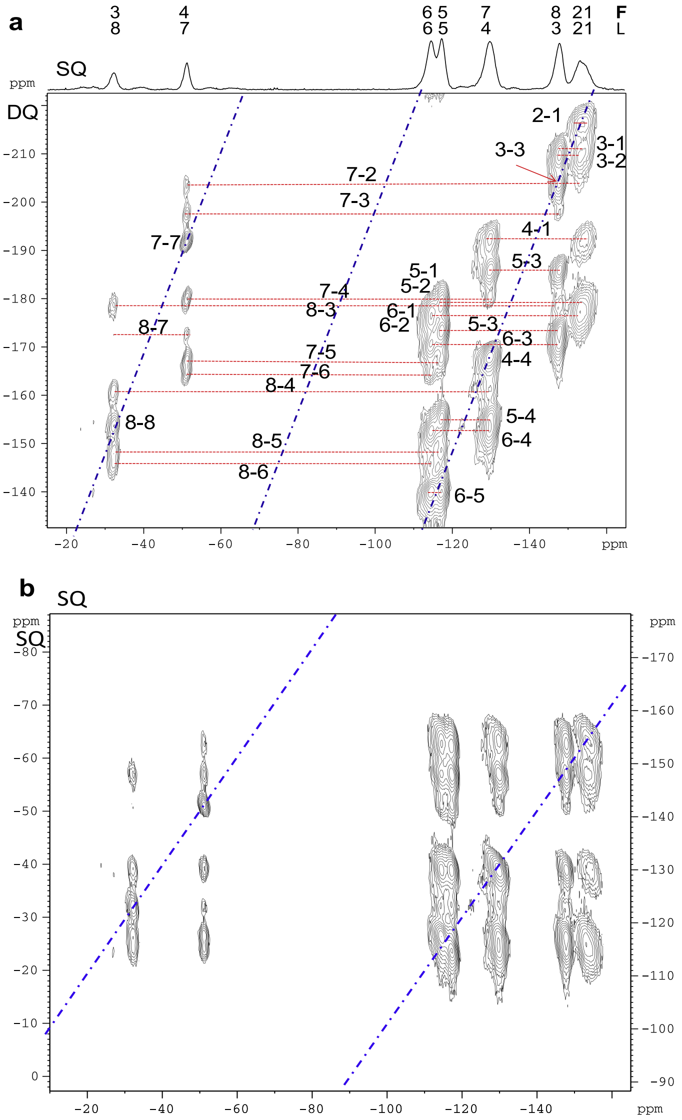

Fig. 10. $Ba_3Al_2F_{12}$. Experimental 2D SPIP DQ–SQ spectrum recorded at 9.4 T with ν_R = 30 kHz and the sequence of Fig. 1a. The nutation frequencies of SPIP were: $\nu_{1\pi}$ = 85 kHz, ν_{1SL} = 78 kHz, and τ = 267 µs. The rf-irradiation was done at −93 ppm. (a) Un-sheared spectrum. Due to the folding along F_1, the vertical scaling is only correct for the central part of the resonances. For the other resonances, the correct F_1 value can be obtained by adding ±80 ppm (80 ppm = ν_R/ν_0). (b) Sheared spectrum. The right (resp. left) vertical scaling concerns the right (resp. left) peaks.

between $BR2_2^1$ and SPIP. As the spin dynamics created by first-order AH terms is identical with $BR2_2^1$ and SPIP recoupling, the discrepancy in DQF efficiencies for de-synchronized π pulse must arise from different recoupled CSA terms in the second-order AH. This is supported by the fact that $BR2_2^1$ sequence is more robust to CSA than SPIP [20]. Fig. 11 demonstrates that practically $BR2_2^1$ scheme has to be preferred over SPIP for the pulse sequences of Fig. 1b and c.

The DQ–SQ experiments of Fig. 1b and c were compared with $SW_1 = 3\nu_R$ in the case of $Ba_3Al_2F_{12}$ at 9.4 T and $\nu_R = 30$ kHz (Fig. 12). Both methods allow avoiding signal folding in F_1 dimension. The method of Fig. 1b scales the chemical shifts along F_1 by the factor $(1 - 2q)$. The total evolution time on DQC must thus be $(1 - 2q)$ times longer than that related to methods described in Fig. 1a and c, to observe the same resolution. However, the homogeneous line broadening is not affected by the central π pulse and this longer evolution time on DQC thus leads to a decreased resolution. This effect can be observed by comparing spectra shown in Fig. 12a and b and recorded with methods described in Fig. 1b and c, respectively.

An alternative to the method of Fig. 1c consists in incorporating γ-encoded recoupling schemes in the pulse sequence of Fig. 1a. For instance, the $R14_4^5c$ sequence was used at $\nu_R = 30$ kHz to acquire the DQ–SQ spectrum of $Ba_3Al_2F_{12}$ (Fig. 12c). The increment $\Delta t_1 = T_R/3$ allowed avoiding the signal folding along the F_1 dimension and the spectral resolution was similar to that of Fig. 12b. However, spinning sidebands along F_1 dimension appeared. These sidebands always exist in case of large CSA and non rotor-synchronized excitation and reconversion recoupling. Their intensities depend on the recoupling sequence, and as an example, they are larger with the $R14_4^5c$ sequence than with the $BR2_2^1$ sequence (compare Fig. 12b and c).

Experiments similar to those of Fig. 12b and c were performed at 18.8 T and $\nu_R = 65$ kHz, with $SW_1 = 3\nu_R$. The γ-encoded and non-γ-encoded recoupling schemes were $R18_8^5c$ and $BR2_2^1$, with the pulse sequences of Fig. 1a and c, respectively. The corresponding 2D spectra, presented in Fig. 13a and b, show that DQ–SQ spectra without any signal folding can be acquired even if the spread in resonance frequencies of DQC covers 185 kHz. Compared to Fig. 12c, the spectrum of Fig. 13a displays a larger number of CSA spinning sidebands owing to the different recoupling sequence. These spinning sidebands complicate the spectrum analysis. The intensity of these sidebands is much lower when using $BR2_2^1$ recoupling (compare Fig. 13a and b-1). The spectrum of Fig. 13b can be compared with that of Fig. 13c, which was obtained by using SPIP recoupling incorporated into the pulse sequence of Fig. 1a. The spectrum of Fig. 13b benefits from the absence of signal folding along the F_1 dimension. However, the rotor-synchronized SPIP sequence is more robust to offset than the non-rotor-synchronized $BR2_2^1$. Consequently, the L1–L1, L8–L3 and L4–L2 correlations can be easily observed in Fig. 13c but not in Fig. 13b. Furthermore, the 2D spectrum of Fig. 13c was acquired in three-times less experimental time than that of Fig. 13b.

5. Conclusions

We have presented, analyzed and compared several homonuclear dipolar double-quantum recoupling methods for nuclei submitted to large homonuclear dipolar interactions, such as ^1H and ^{19}F. These rotor-synchronized and symmetry-based methods are the non-γ-encoded SPIP and $BR2_2^1$ sequences, and several γ-encoded RN_n^ν sequences. The main criteria of choice are related to: (1) the spinning speed, (2) the rf-power limitation of the probe,

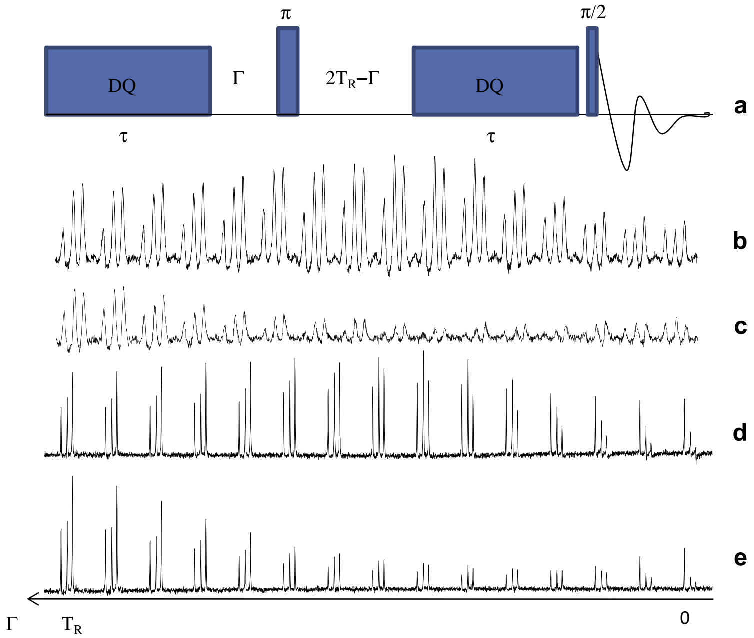

Fig. 11. Effect of an additional π pulse on 1D DQF spectra of α-$CaAlF_5$ at: (b and c) $B_0 = 9.4$ T and $\nu_R = 32$ kHz or (d and e) $B_0 = 18.8$ T and $\nu_R = 60$ kHz. The DQF signals were acquired by employing the pulse sequence depicted in (a) using non-γ-encoded schemes: $BR2_2^1$ in (b and d) and SPIP in (c and e). The delay Γ was varied from 0 to T_R. At $\Gamma = T_R$, the CSA is refocused. SPIP: $\nu_{1\pi} = 105$ kHz, $\nu_{1SL} = 97$ kHz, $\tau = 266.7$ µs; $BR2_2^1$: $\nu_{1\pi} = 105$ kHz, $\tau = 133.3$ µs.

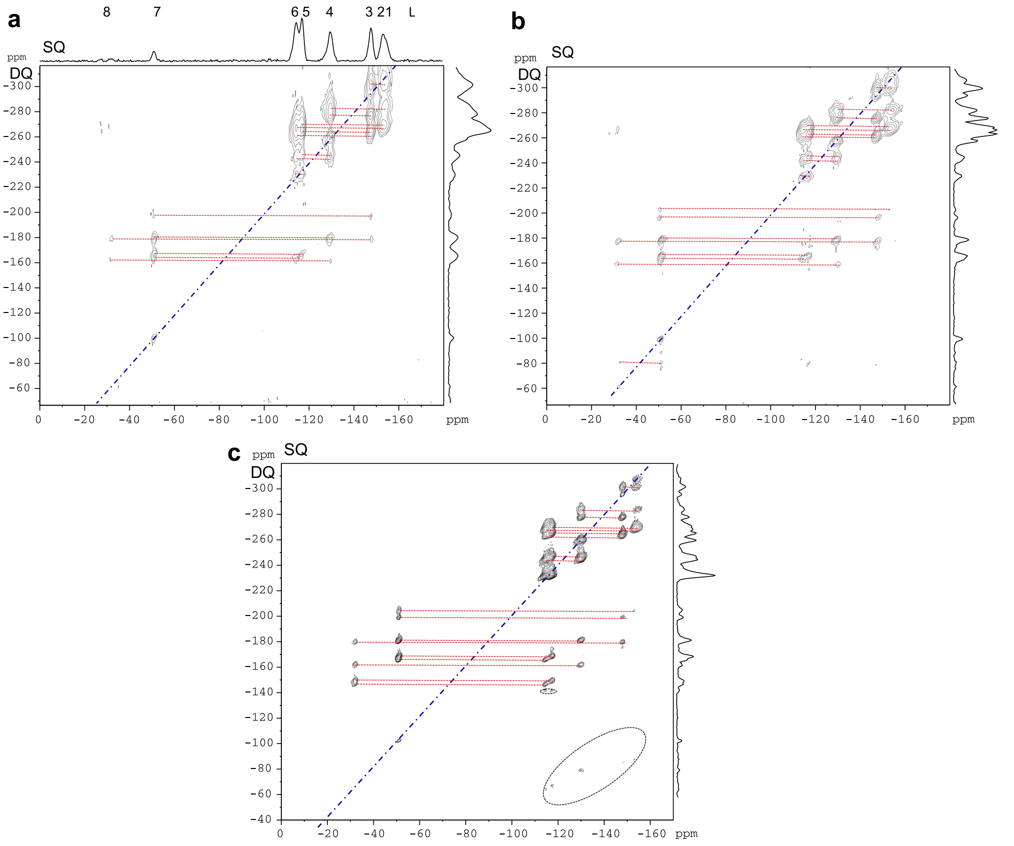

Fig. 12. $Ba_3Al_2F_{12}$. Experimental DQ–SQ un-sheared spectra recorded at 9.4 T with $\nu_R = 30$ kHz and the same spectral width of $SW_1 = 3\nu_R$. (a and b) Spectra obtained with $BR2_2^1$ and the pulse sequence described either: (a) in Fig. 1b with $\Delta t_1 = T_R$ and $q = 1/3$; the spectrum has been re-scaled along F_1 or (b) in Fig. 1c with $\Delta t_1 = T_R/3$. (c) Spectrum recorded with $R14_4^5c$ sequence with R_4 and the pulse sequence described in Fig. 1a and $\Delta t_1 = T_R/3$. Regions which are circled in (c) are small sidebands along F_1 of the cross-peaks. They are hardly observable in (a and b). $BR2_2^1$: $\nu_{1\pi} = 85$ kHz, $\tau = 133.3$ µs. $R14_4^5c$: $\tau = 133.3$ µs.

(3) the spread in resonance frequency $\Delta\nu_{iso}$, (4) the optimum recoupling time (for loss reasons) and (5) the requirement of high sensitivity. It must be noted that ^1H and ^{19}F are two very NMR sensitive nuclei, and that the on-resonance sensitivity of the methods is thus generally not the main criterion of choice.

When the frequency range is small, $\Delta\nu_{iso} < 0.5\nu_R$, such as ^{19}F in α-$CaAlF_5$ or ^1H in general, there is no offset limitation. The criteria of choice in between SPIP, $BR2_2^1$, $R12_2^5$, $R14_4^5$, $R10_4^2$, $R14_8^3$, $R18_8^5$, and $R18_{10}^4$ sequences are thus only related to the required rf field and the optimum recoupling time. $R12_2^5$, which benefits from a small cycle ($2T_R$) and a short optimum recoupling time, thus leading to easy sampling of the built-up curve and weak losses, is the sequence of choice if the probe can provide a sufficient rf field, especially at ultra-fast MAS ($\nu_1 = 3\nu_R$). Furthermore, it benefits from larger DQF efficiency than SPIP. If $R12_2^5$ is not compatible with the rf-power limitation of the probe, alternatives consist in using SPIP or $R14_4^5$. However, SPIP should then be preferred owing to its shorter cycle time ($2T_R$) and smaller required rf-field, especially at ultra-fast MAS.

When the frequency range is moderate, $0.5\nu_R < \Delta\nu_{iso} < \nu_R$, such as ^{19}F in β-$BaAlF_5$, the sequence must be selected according to the same previous criteria, but a shearing processing by a factor of two may be used to avoid the folding of the resonances along F_1.

When the frequency range is large, $\Delta\nu_{iso} > \nu_R$, such as ^{19}F in $Ba_3Al_2F_{12}$, γ-encoded sequences, such as $R12_2^5$, built from single 180_0 pulse have a too limited offset robustness. A possible solution consists in employing broadband composite π pulses (e.g. R_4: $60_0300_{180}60_0$) as basic element. This method enhances the robustness to offsets of RN_n^ν sequences but also their rf requirement. We show that $R14_4^5c$ and $R18_8^5c$ recoupling methods allow acquiring DQ–SQ spectra of $Ba_3Al_2F_{12}$ at $\nu_R \approx 30$ and 65 kHz, respectively. If these γ-encoded methods allow avoiding the signal folding, they create significant spinning sidebands along F_1 dimension. The DQ–SQ spectra of $Ba_3Al_2F_{12}$ can also be obtained by using non-γ-encoded methods, such as SPIP and $BR2_2^1$. The introduction of a π pulse during the evolution period of DQC allows avoiding the signal folding. In that case, we show that $BR2_2^1$ has to be employed. The 2D spectra acquired by this method display small spinning sidebands, which simplify the spectral interpretation. Finally the super-cycled SPIP sequence benefits from the highest robustness to offset and allows the observation of homonuclear correlation between sites displaying large differences in isotropic chemical shifts.

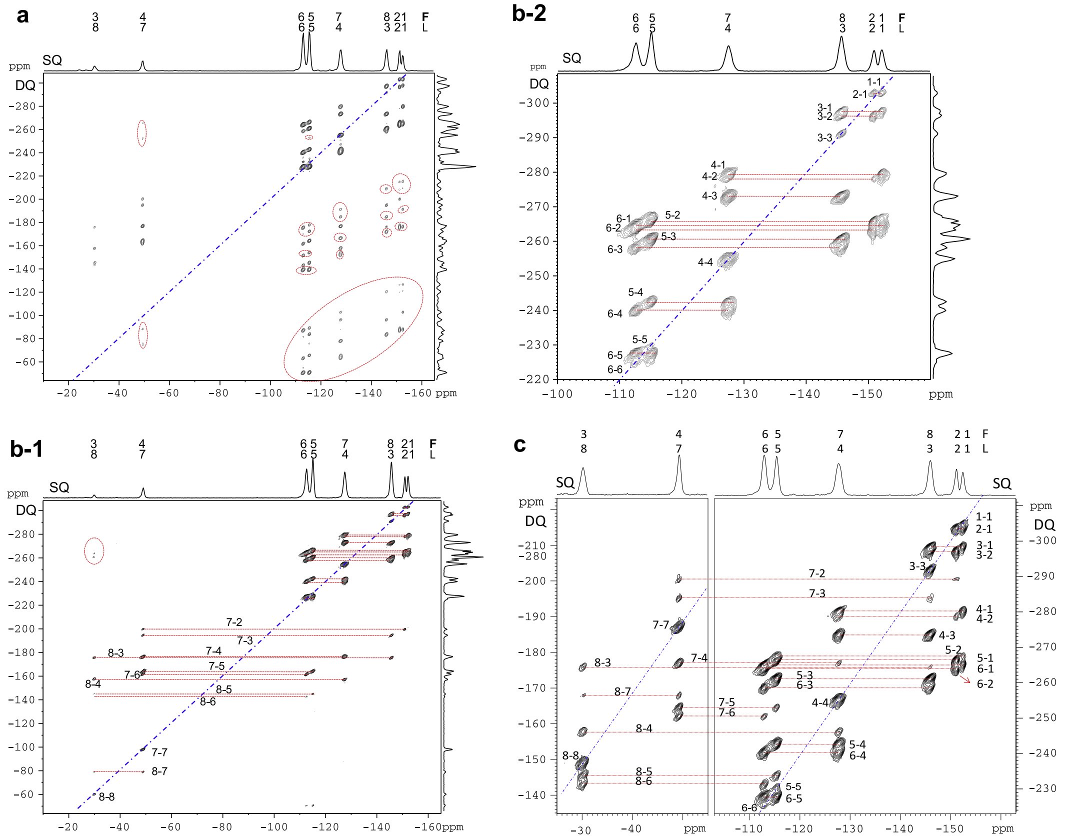

Fig. 13. $Ba_3Al_2F_{12}$. DQ–SQ spectra recorded at 18.8 T with $\nu_R = 65$ kHz and the rf-irradiation at −93 ppm. Two recoupling schemes were used with same $SW_1 = 3\nu_R$ ($\Delta t_1 = T_R/3$): (a) R18^5_8c with R_4 and sequence of Fig. 1a ($\tau = 120$ μs), and (b-1) BR2^1_2 with sequence of Fig. 1c ($\tau = 120$ μs and $\nu_{1\pi} = 120$ kHz). (b-2) Expansion of the right upper part of (b-1), in order to obtain the same spectral widths as the right part of (c). (c) Rotor-synchronized ($SW_1 = \nu_R$) SPIP spectrum with: $\nu_{1\pi} = 120$ kHz, $\nu_{1SL} = 100$ kHz, and $\tau = 240$ μs. The full spectrum has been acquired in a single experiment but for the sake of readability, only the spectral regions displaying correlation peaks are presented. Due to the folding along F_1, the vertical scaling on the right is only correct for the pairs of correlation peaks both situated in the right square of the spectrum. The vertical scaling on the left, which is correct for the pairs of correlation peaks with one peak in the left part and one peak in the right part, has been obtained by adding 86.3 ppm (ν_R/ν_0) to the right vertical scaling. For the three other peaks ((8, 8), (8, 7), (7, 7)), the correct F_1 value can be obtained by adding 86.3 ppm to this left vertical scaling.

As SPIP scheme is not compatible with the introduction of a central π pulse, the absence of signal folding has to be sacrificed for the sake of greater robustness. In summary, in the case of very large frequency spread for the resonances, our preferred choice is to introduce rotor-synchronized SPIP recoupling into the usual DQ–SQ experiment (Fig. 1a). This method provides the highest robustness to offset, requires low rf field, minimizes the experimental time and eliminates sidebands along the F_1 dimension. If the interpretation of the SPIP DQ–SQ spectrum with folded peaks appears difficult to the scientist, our second choice is then the non-rotor-synchronized BR2^1_2 scheme with a π pulse during the evolution period. Folded resonances along F_1 are avoided, but the sensitivity is largely decreased with respect to rotor-synchronized SPIP.

It must be noted that experimental relative efficiencies of the various sequences do not always correspond to those obtained with simulations. These differences of relative efficiencies are related to the sparse sampling of the built-up curves and to the irreversible losses. Practically, the best way to sample correctly the built-up curves may thus be: first to find with a fast spinning speed the best number of recoupling cycles, and second to optimize the spinning speed, while keeping the same number of cycles. Obviously, these problems of sparse sampling and irreversible losses decrease with increasing field and spinning speed.

It is also very important to note the great advantage of using the highest available spinning speed and magnetic field for resolution purpose. The use of small sample volumes for ultra-fast spinning speed is indeed most of the time not a problem for these very sensitive nuclei.

Last, it must be reminded that all double- and zero-quantum dipolar recoupling sequences intrinsically suffer from dipolar truncation effects [47,48] meaning that medium- or long-range spatial proximities between two nuclei cannot be directly probed when one of these is also involved in a short-range correlation with a third nucleus. However, this important limitation may be now partly overcome by some new advanced recoupling methods [49,50].

Acknowledgments

Authors are grateful for funding provided by Region Nord/Pas de Calais, Europe (FEDER), CNRS, French Minister of Science, USTL, ENSCL and Bruker BIOSPIN. They also thank Drs. F. Fayon and F. Aussenac for helpful discussions and Drs. A. Le Bail, A.M. Mercier, and M. Body, who supplied the samples. Financial support from the TGE RMN THC (FR-3050) for conducting the research is gratefully acknowledged. They also would like to thank Prof. Malcolm H. Levitt and Dr. Andreas Brinkmann for providing the 'C and R symmetries' Mathematica package. F.D. thanks the National Natural Science Foundation of China (20773159, 20673139, 20933009) and the National Basic Research Program of China (2009CB918600) for financial support.

Appendix A. Supplementary data

Supplementary data associated with this article can be found, in the online version, at doi:10.1016/j.jmr.2009.12.009.

References

[1] A. Samoson, Extended magic-angle spinning, in: D.M. Grant, R.K. Harris (Eds.), Encyclopedia of Nuclear Magnetic Resonance, vol. 9, John Wiley & Sons, Chichester, 2002, pp. 59–64.

[2] L.S. Du, A. Samoson, T. Tuherm, C.P. Grey, ^{19}F/^{23}Na double resonance MAS NMR study of oxygen/fluorine ordering in the oxyfluoride $Na_5W_3O_9F_5$, Chem. Mater. 12 (2000) 3611–3616.

[3] [a] K. Mao, J.W. Wiench, V.S.Y. Lin, M. Pruski, Indirectly detected through-bond chemical shift correlation NMR spectroscopy in solids under fast MAS: studies of organic-inorganic hybrid materials, J. Magn. Reson. 196 (2009) 92–95;
[b] K. Mao, M. Pruski, Directly and indirectly detected through-bond heteronuclear correlation solid-state NMR spectroscopy under fast MAS, J. Magn. Reson. 201 (2009) 165–174.

[4] T. Guillon, J. Schaefer, Rotational-echo double-resonance NMR, J. Magn. Reson. 81 (1988) 196–200.

[5] B.H. Meier, W.L. Earl, Excitation of multiple quantum transitions under magic-angle conditions: adamantine, J. Chem. Phys. 85 (1986) 4905–4911.

[6] T.G. Oas, R.G. Griffin, M.H. Levitt, Rotary resonance recoupling of dipolar interactions in solid-state nuclear magnetic resonance spectroscopy, J. Chem. Phys. 89 (1988) 692–695.

[7] R. Tycko, G. Dabbagh, Measurement of nuclear magnetic dipole–dipole couplings in magic-angle spinning NMR, Chem. Phys. Lett. 173 (1990) 461–465.

[8] W. Sommer, J. Gottwald, D.E. Demco, H.W. Spiess, Dipolar heteronuclear multiple-quantum NMR spectroscopy in rotating solids, J. Magn. Reson. A 113 (1995) 131–134.

[9] M. Feike, D.E. Demco, R. Graf, J. Gottwald, S. Hafner, H.W. Spiess, Broadband multiple-quantum NMR spectroscopy, J. Magn. Reson. A 122 (1996) 214–221.

[10] N.C. Nielsen, H. Bildsoe, H.J. Jakobsen, M.H. Levitt, Double-quantum homonuclear rotary resonance: efficient dipolar recovery in magic angle spinning, J. Chem. Phys. 101 (1994) 1805–1812.

[11] Y.K. Lee, N.D. Kurur, M. Helmle, O.G. Johannessen, N.C. Nielsen, M.H. Levitt, Efficient dipolar recoupling in the NMR of rotating solids: a seven-fold symmetric radiofrequency pulse sequence, Chem. Phys. Lett. 242 (1995) 304–309.

[12] M. Carravetta, M. Edén, X. Zhao, A. Brinkmann, M.H. Levitt, Symmetry principles for the design of radiofrequency pulse sequences in the nuclear magnetic resonance of rotating solids, Chem. Phys. Lett. 321 (2000) 205–215.

[13] A. Brinkmann, M. Edén, M.H. Levitt, Synchronous helical pulse sequences in magic-angle spinning nuclear magnetic resonance: double quantum recoupling of multiple-spin systems, J. Chem. Phys. 112 (2000) 8539–8554.

[14] Y. Ishii, ^{13}C–^{13}C dipolar recoupling under very fast magic angle spinning in solid state nuclear magnetic resonance: applications to distance measurements, spectral assignments and high-throughput secondary-structure determination, J. Chem. Phys. 114 (19) (2001) 8473–8483.

[15] M.H. Levitt, Symmetry-based pulse sequences in magic-angle spinning NMR, in: D.M. Grant, R.K. Harris (Eds.), Encyclopedia of nuclear magnetic resonance, vol. 9, John Wiley & sons, Chichester, 2002.

[16] P.E. Kristiansen, M. Carravetta, J.D. van Beek, W.C. Lai, M.H. Levitt, Theory and applications of super-cycled symmetry-based recoupling sequences in solid-state NMR, J. Chem. Phys. 12 (2006) 234510–234519.

[17] G. Pileio, M. Concistrè, N. McLean, A. Gansmüller, R.C.D. Brown, M.H. Levitt, Analytical theory of γ-encoded double-quantum recoupling sequences in solid-state nuclear magnetic resonance, J. Magn. Reson. 186 (2007) 65–74.

[18] L. Mafra, R. Siegel, C. Fernandez, D. Schneider, F. Aussenac, J. Rocha, High-resolution ^{1}H homonuclear dipolar recoupling NMR spectra of biological solids at MAS rates up to 67 kHz, J. Magn. Reson. 199 (2009) 111–114.

[19] B. Hu, Q. Wang, O. Lafon, J. Trébosc, F. Deng, J.P. Amoureux, Robust and efficient spin-locked symmetry-based double-quantum homonuclear dipolar recoupling for probing ^{1}H–^{1}H proximity in the solid state, J. Magn. Reson. 198 (2009) 41–48.

[20] B. Hu, L. Delevoye, O. Lafon, J. Trébosc, J.P. Amoureux, Double-quantum NMR spectroscopy of ^{31}P species submitted to very large CSAs, J. Magn. Reson. 200 (2009) 178–188.

[21] Q. Wang, B. Hu, O. Lafon, J. Trébosc, F. Deng, J.P. Amoureux, Double-quantum homonuclear NMR correlation spectroscopy of quadrupolar nuclei subjected to magic-angle spinning and high magnetic field, J. Magn. Reson. 200 (2009) 251–260.

[22] Q. Wang, B. Hu, F. Fayon, J. Trébosc, C. Legein, O. Lafon, F. Deng, J.P. Amoureux, Double-quantum ^{19}F–^{19}F dipolar recoupling at ultra-fast magic angle spinning NMR: application to the assignment of ^{19}F NMR spectra of inorganic fluorides, Phys. Chem. Chem. Phys. 11 (2009) 10391–10395.

[23] I. Schnell, Dipolar recoupling in fast MAS solid-state NMR spectroscopy, Prog. Nucl. Magn. Reson. Spectrosc. 45 (2004) 145–207.

[24] S.P. Brown, Probing proton–proton proximities in the solid state, Prog. Nucl. Magn. Reson. Spectrosc. 50 (2007) 199–251.

[25] C.D. Martin, S. Chaudhuri, C.P. Grey, J.B. Parise, Effect of A-site cation radius on ordering of BX6 octahedra in (K, Na)MgF3 perovskite, Am. Mineral. 90 (2005) 1522–1533.

[26] C. Martineau, C. Legein, J.Y. Buzaré, F. Fayon, On the assignment of ^{19}F MAS NMR spectra of fluoroaluminates using through-space spectral edition of ^{19}F–^{27}Al and ^{19}F–^{19}F connectivities, Phys. Chem. Chem. Phys. 11 (2009) 950–957.

[27] A. Brinkmann, M.H. Levitt, Symmetry principles in the nuclear magnetic resonance of spinning solids: hetero-nuclear recoupling by generalized Hartmann–Hahn sequences, J. Chem. Phys. 115 (2001) 357–384.

[28] M. Edén, M.H. Levitt, Pulse sequence symmetries in the NMR of spinning solids. Application to heteronuclear decoupling, J. Chem. Phys. 111 (1999) 1511–1519.

[29] [a] Wolfram Research Inc., Champaign, Illinois, USA, 2007. Mathematica 6. Available from: <http://reference.wolfram.com/mathematica/ref>.;
[b] 'C and R symmetries' Mathematica package written by M.H. Levitt and A. Brinkmann. Available from: <http://www.mhl.soton.ac.uk/public/Main/software/CandRsymmetries/index.html> and <http://www.mhl.soton.ac.uk/public/Main/software/mPackages/UpdateInformation.html>.

[30] M. Edén, D. Zhou, J. Yu, Improved double-quantum NMR correlation spectroscopy of dipolar-coupled quadrupolar spins, Chem. Phys. Lett. 431 (2006) 397–403.

[31] M. Carravetta, M. Eden, O.G. Johannessen, H. Luthman, P.J.E. Verdegem, J. Lugtenburg, A. Sebald, M.H. Levitt, Estimation of carbon–carbon bond lengths and medium-range inter-nuclear distances by solid-state nuclear magnetic resonance, J. Am. Chem. Soc. 123 (2001) 10628–10638.

[32] (a) M.H. Levitt, Composite pulses, Prog. NMR Spectrosc. 18 (1986);
(b) M.H. Levitt, Composite pulses, in: D.M. Grant, R.K. Harris (Eds.), Encyclopedia of Nuclear Magnetic Resonance, John Wiley & sons, Chichester, 2002, pp. 1396–1410.

[33] A. Brinkmann, M. Eden, Second order average Hamiltonian theory of symmetry-based pulse schemes in the nuclear magnetic resonance of rotating solids: application to triple-quantum dipolar recoupling, J. Chem. Phys. 120 (2004) 11726.

[34] T. Karlsson, A. Brinkmann, P.J.E. Verdegem, J. Lugtenburg, M.H. Levitt, Multiple-quantum relaxation in the magic-angle-spinning NMR of ^{13}C spin pairs, Solid State Nucl. Magn. Reson. 14 (1999) 43–58.

[35] G. Mali, G. Fink, F. Taulelle, Double-quantum homonuclear correlation magic-angle sample spinning nuclear magnetic resonance spectroscopy of dipolar-coupled quadrupolar nuclei, J. Chem. Phys. 120 (2004) 2835–2845.

[36] K. Riedel, C. Herbst, J. Leppert, O. Ohlenschläger, M. Görlach, R. Ramachandran, Broadband homonuclear double-quantum NMR/filtering via zero-quantum dipolar recoupling in rotating solids, Chem. Phys. Lett. 424 (2006) 178–183.

[37] M. Bak, J.T. Rasmussen, N.C. Nielsen, SIMPSON: a general simulation program for solid-state NMR spectroscopy, J. Magn. Reson. 147 (2000) 296–330.

[38] M. Bak, N.C. Nielsen, REPULSION: a novel approach to efficient powder averaging in solid-state NMR, J. Magn. Reson. 125 (1997) 132–139.

[39] A. Zheng, S.B. Liu, F. Deng, ^{19}F chemical shift of crystalline metal fluorides: theoretical predictions based on periodic structure models, J. Phys. Chem. C 113 (33) (2009) 15018–15023.

[40] A. Hémon, G. Courbion, Refinement of the room temperature structure of α-$CaAlF_5$, Acta. Crystallogr. C47 (1991) 1302–1303.

[41] A. Le Bail, G. Férey, A.M. Mercier, A. de Kozak, M. Samouël, Structure determination of β and γ-$BaAlF_5$ by X-ray and neutron powder diffraction. A model for the $\alpha \to \beta \to \gamma$ transitions, J. Solid State Chem. 89 (1990) 282–291.

[42] V. Kaiser, D. Babel, Crystal structure of $Ba_3Al_2F_{12}$, Z. Anorg. Allg. Chem. 630 (2004) 794–798.

[43] D. States, R. Haberkorn, D. Rubens, A two-dimensional Nuclear Overhauser Experiment with pure absorption phase in four quadrants, J. Magn. Reson. 48 (1982) 286–292.

[44] M. Leskes, P.K. Madhu, S. Vega, Super-cycled homo-nuclear dipolar decoupling in solid state NMR: toward cleaner ^{1}H spectrum and higher spinning rates, J. Chem. Phys. 128 (2008) 052309.

[45] E. Salager, R.S. Stein, S. Steuernagel, A. Lesage, B. Elena, L. Emsley, Enhanced sensitivity in high-resolution ^{1}H solid-state NMR spectroscopy with DUMBO dipolar decoupling under ultra-fast MAS, Chem. Phys. Lett. 469 (2009) 336–341.

[46] J.P. Amoureux, B. Hu, J. Trebosc, Enhanced resolution in proton solid-state NMR with very-fast MAS experiments, J. Magn. Reson. 193 (2008) 305–307.

[47] M.J. Bayro, M. Huber, R. Ramachandran, T.C. Davenport, B.H. Meier, M. Ernst, R.G. Griffin, Dipolar truncation in magic-angle spinning NMR recoupling experiments, J. Chem. Phys. 130 (2009) 114506.

[48] V. Ladizhansky, Homonuclear dipolar recoupling techniques for structure determination in uniformly ^{13}C-labeled proteins, Solid State NMR 36 (2009) 119–128.

[49] (a) N. Khaneja, N.C. Nielsen, Triple oscillating field technique for accurate distance measurements by solid-state NMR, J. Chem. Phys. 128 (2008) 015103; (b) L.A. Straasø, M. Bjerring, N. Khaneja, N.C. Nielsen, Multiple-oscillating-field techniques for accurate distance measurements by solid-state NMR, J. Chem. Phys. 130 (2009) 225103.

[50] A.K. Paravastu, R. Tycko, Frequency-selective homonuclear dipolar recoupling in solid state NMR, J. Chem. Phys. 124 (2006) 194303.

Journal of Magnetic Resonance 200 (2009) 251–260

Contents lists available at ScienceDirect

Journal of Magnetic Resonance

journal homepage: www.elsevier.com/locate/jmr

Double-quantum homonuclear NMR correlation spectroscopy of quadrupolar nuclei subjected to magic-angle spinning and high magnetic field

Q. Wang [a,b,c], B. Hu [a], O. Lafon [a], J. Trébosc [a], F. Deng [b,*], J.P. Amoureux [a,*]

[a] UCCS, CNRS-8181, Lille University, Fr-59652, Villeneuve d'Ascq, France
[b] State Key Laboratory of Magnetic Resonance and Atomic and Molecular Physics, Wuhan Center for Magnetic Resonance, Wuhan Institute of Physics and Mathematics, Chinese Academy of Sciences, Wuhan 430071, China
[c] Graduate School of the Chinese Academy of Sciences, Beijing, China

ARTICLE INFO

Article history:
Received 27 April 2009
Revised 6 July 2009
Available online 14 July 2009

Keywords:
Solid-state NMR
Half-integer quadrupolar nuclei
Fast MAS
Double-quanta spectroscopy

ABSTRACT

We present a new application of the $R2_2^1$ symmetry-based dipolar recoupling scheme, for exciting directly double-quantum (2Q) coherences between the central transition of homonuclear half-integer quadrupolar nuclei. With respect to previously published 2Q-recoupling methods (M. Eden, D. Zhou, J. Yu, Chem. Phys. Lett. 431 (2006) 397), the $R2_2^1$ sequence is used without $\pi/2$ bracketing pulses and with an original super-cycling. This leads to an improved efficiency (a factor of two for spin-5/2) and to a much higher robustness to radio-frequency field inhomogeneity and resonance offset. The 2Q-coherence excitation performances are demonstrated experimentally by ^{27}Al NMR experiments on the aluminophosphates berlinite, VPI5, AlPO$_4$-14, and AlPO$_4$-CJ3. The two-dimensional 2Q–1Q correlation experiments incorporating these recoupling sequences allow the observation of 2Q cross-peaks between central transitions, even at high magnetic field where the difference in offset between octahedral and tetrahedral ^{27}Al sites exceeds 10 kHz.

1. Introduction

Solid-state nuclear magnetic resonance (SS NMR) spectroscopy is a powerful tool for the investigation of materials. Magic-angle spinning (MAS) enhances spectral resolution by largely removing the effects of anisotropic spin interactions, such as chemical shift anisotropy (CSA) and dipolar couplings. However, the through-space dipolar couplings encode important information on the spatial proximity of atoms through their inverse cubic dependence on the inter-nuclear distance. Therefore, dedicated radio-frequency (rf) pulse sequences have been developed to specifically reintroduce these interactions under the MAS conditions [1,2]. In particular, homonuclear recoupling sequences restore dipolar interactions between nuclei of the same isotopic type. Nevertheless, most of homonuclear recoupling schemes are dedicated to the case of spin-1/2 nuclei, whereas about two thirds of NMR active, stable nuclei have larger half-integer spin values (e.g. $S = 3/2$: ^{11}B, ^{23}Na; $S = 5/2$: ^{17}O, ^{27}Al).

Homonuclear dipolar recoupling of quadrupolar nuclei under MAS is difficult because of the intricate nuclear spin dynamics of the quadrupolar nuclei in the presence of rf fields and sample rotation. Therefore, dipolar recoupling in quadrupolar systems was first achieved without the application of rf-field. Indeed, the MAS averaging of homonuclear couplings can be prevented by interferences between homonuclear dipolar couplings and another anisotropic interaction, such as heteronuclear dipolar coupling with protons [3,4] or quadrupolar interactions [5–12]. Rotational resonance (R^2) has also been demonstrated [13]. However, these recoupling phenomena under the absence of the rf-field occur only in a limited range of MAS frequency and their efficiencies are low for an extended range of resonance frequencies [7,9]. Off-magic-angle spinning prevents the averaging of dipolar interactions but entails resolution decrease, except when employing dynamic angle spinning (DAS) methods [14,15].

In case of half-integer nuclei, the application of weak (selective) rf pulses allows rotating the central transition (CT) coherence between energy levels $-1/2$ and $1/2$ in the same fashion as for fictitious spin-1/2 nuclei [16]. For rf amplitudes much smaller than the quadrupolar coupling, the CT nutation frequency of spin-S is $\nu_{\mathrm{nut}}^{\mathrm{CT}} = (S + 1/2)\nu_1$. Even if the fictitious spin-1/2 approximation may not be fulfilled at all times for all crystallite orientations in a powder, the dipolar recoupling techniques employing rf fields that were originally introduced for spins-1/2 were transposed to the case of half-integer quadrupolar nuclei. Rotary resonance recoupling (R^3) techniques and especially the HORROR condition [17,18] have been demonstrated for recoupling of quadrupolar nuclei [19–23]. The HORROR condition, which selectively

---

* Corresponding authors. Tel.: +33 3 20 43 41 43; fax: +33 3 20 43 68 14 (J.P. Amoureux).

E-mail addresses: dengf@wipm.ac.cn (F. Deng), jean-paul.amoureux@univ-lille1.fr (J.P. Amoureux).

1090-7807/$ - see front matter © 2009 Elsevier Inc. All rights reserved.
doi:10.1016/j.jmr.2009.07.009

reintroduces the homonuclear dipolar interaction, is obtained for a spin-S when the rf amplitude ν_1 fulfills:

$$\nu_1 = \nu_R/(2S+1) \tag{1}$$

where ν_R is the MAS frequency. Recently, it was shown that symmetry-based pulse sequences display superior rf error tolerance than the HORROR recoupling [24–27]. These symmetry-based pulse sequences were incorporated into 2D experiments, which correlate 2Q-coherences (2QCs) with the respective CT single-quantum (1Q) coherences within each spin-pair [25]. Compared to 1Q–1Q correlation experiments, the 2Q–1Q correlation spectroscopy benefits from the increased frequency dispersion of 2QCs and the possibility to probe correlation between equivalent sites. These symmetry-based recoupling methods have been integrated into 1D 2Q filtering (2QF) experiments in order to measure inter-nuclear distances and to analyze the relative orientations of quadrupolar and dipolar tensors [28], and it was concluded that 'analysis of 2Q filtered curves of quadrupolar nuclei is feasible if some prior knowledge on dipolar and/or quadrupolar interactions is available'. Very recently [57], it has also been shown that these two relative orientations could been obtained directly by fitting the line-shapes observed in 2D 2Q–1Q spectra, even with powder samples. The symmetry-based pulse sequences were also used in case of double-rotation (DOR) experiments by synchronizing the rf pulses with the outer rotation of the sample and this allowed obtaining 2D 2Q–1Q spectra with high-resolution in both dimensions for ^{23}Na and ^{27}Al nuclei [29].

However, all existing 2Q-recoupling sequences suffer from a large sensitivity to offsets and to rf-field missetting and inhomogeneity. This is a direct consequence of the low rf amplitudes required to minimize CT signal losses during the recoupling and the requirement that the rf amplitude satisfies Eq. (1). The restricted bandwidths set practical limitations on uniform 2QC excitation of samples exhibiting large frequency dispersion (e.g. ^{27}Al), because of chemical or quadrupolar shifts. The chemical shift dispersion is especially critical for NMR studies in high magnetic fields. The low tolerance to rf errors requires the use of volume-restricted rotors, thus decreasing the achievable sensitivity. The purpose of this article is to propose a new application of the $R2_2^1$ symmetry-based sequence, which reduces both limitations for homonuclear dipolar 2Q-excitation and reconversion.

2. Pulse sequence

2.1. 1D 2QF experiment and 2D 2Q–1Q spectroscopy

Fig. 1a depicts the pulse scheme, which has been mainly employed so far to record 2D 2Q–1Q correlation spectra on half-integer quadrupolar nuclei [22,25,27]. Homonuclear 2QCs were excited by partly zero-quantum (0Q) recoupling sequences that were bracketed by two CT-selective $\pi/2$ pulses. These bracketing $\pi/2$ pulses achieve the conversion of the 0Q recoupling sequences into 2Q schemes. The bracketed recoupling methods allow the excitation of 2QCs from longitudinal magnetization. The excited 2QCs are subjected to a CT-selective π-pulse, which is phase-cycled to eliminate all 2QC involving a single nucleus through its satellite transitions (Fig. 1c) [22]. The 2QCs are reconverted into longitudinal CT polarization by repeating the excitation pulse sequence with a phase-shift of $\pi/2$ [2]. Finally the CT-selective $\pi/2$ read-pulse creates observable 1Q coherences. Maximal sensitivity is obtained when the excitation and reconversion delays are equal. These delays are denoted τ in the following.

For 1D 2QF experiment (see numerical simulations of Figs. 2–5 and experimental results of Fig. 6 and 7), the CT-selective π-pulse is inserted between two equal short delays [25]. For 2D 2Q–1Q spectra (see Figs. 8–10), the delays around the central pulse are replaced by unequal incremented time periods, qt_1 and $(1-q)t_1$. [22]. The position of the CT-selective π-pulse allows scaling the chemical and quadrupolar shifts in the indirect dimension F_1, such that the scaled CT 2QC frequency is $(1-2q)(\nu_j+\nu_k)$, where ν_j and ν_k are the CT 1Q frequencies of the connected two species.

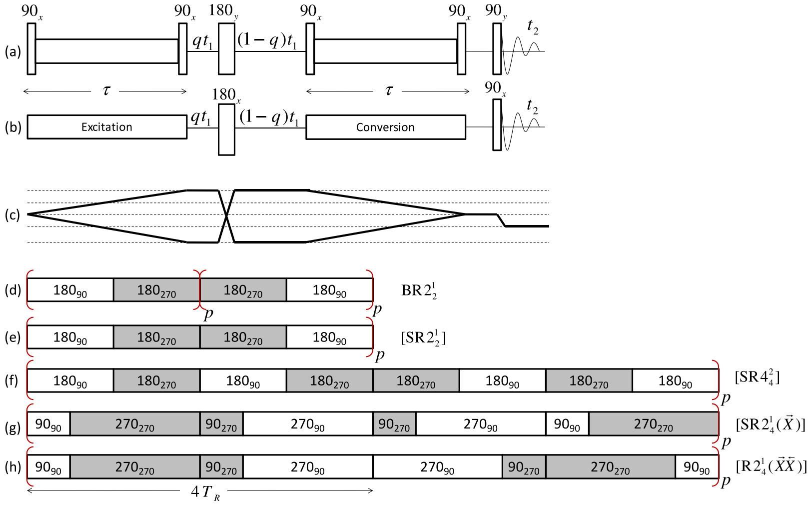

Fig. 1. 2Q–1Q pulse sequences using bracketed (a) or unbracketed (b) homonuclear dipolar recoupling schemes. All rf pulses depicted in the figure are CT-selective. The selected coherence transfer pathway is shown in (c). The DQ single-spin signal is cancelled by the CT-selective π-pulse and only spin-pair DQ coherences result in observable signal. The q parameter is used to scale *all* interactions in order to avoid folding of the resonances along the F_1 dimension. Recoupling schemes used in this article with either sequence (b): $BR2_2^1$ (π) (d), or sequence (a): [$SR2_2^1$ (π)] (e), [$SR4_4^2$ (π)] (f), [$SR2_4^1$ ($\vec{X}$)] (g) or [$R2_4^1$ ($\vec{X}\,\overleftarrow{X}$)] (h). They use either simple (d–f), or composite (g and h) π-pulses. Phases are equal to 90 or 270°, according to the pulse is shown in white or grey. The recoupling schemes use two types of super-cycling: (d) an overall phase shift from the middle of τ delay, or (e–h) a succession of $SRN_n^{N/2}$ blocks that last either $4T_R$ (e) or $8T_R$ (f–h).

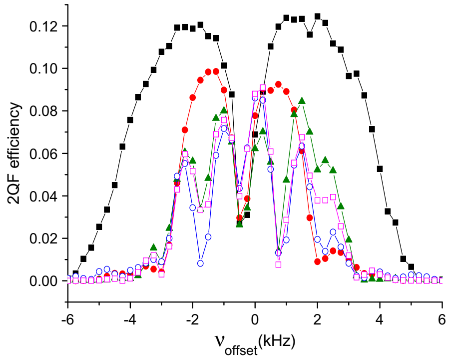

Fig. 2. Simulations of 2QF efficiency of the 'diagonal' peak ($\Delta = 0$) with $F_1 = 2(1-2q)F_2$, versus resonance offset, ν_{offset}, at Larmor frequency $\nu_0 = 208.6$ MHz and a MAS frequency $\nu_R = 15$ kHz. The spin system consists of two ^{27}Al nuclei ($S = 5/2$) with quadrupolar parameters, $C_Q = 4.07$ MHz and $\eta_Q = 0.43$. The dipolar coupling between them was $b_{12} = -95$ Hz. The rf nutation frequency for the recoupling sequence was fixed to $\nu_1 = 2.5$ kHz. The pulse lengths for the central π and the four bracketing $\pi/2$ pulses are 25 and 12.5 µs, respectively. Different homonuclear recoupling sequences were employed: black full squares (■): BR2_2^1 (π) with $\tau = 2933$ µs, red full dots (●): [SR2_2^1 (π)] with $\tau = 2133$ µs, green full triangles (▲): [SR4_4^2 (π)] with $\tau = 2666$ µs, red empty squares (□) [R2_4^1 ($\overrightarrow{X}\,\overleftarrow{X}$)] with $\tau = 2133$ µs, and blue empty dots (○) [SR2_4^1 ($\overrightarrow{X}$)] with $\tau = 2133$ µs (For interpretation of color mentioned in this figure, the reader is referred to the web version of this article.).

Furthermore, as the homonuclear recoupling sequences are not γ-encoded [2,18], the t_1 evolution period must be incremented in steps of integer number of rotor period, τ_R, thus leading to a limited spectral width in F_1 [25]. However, any folding in F_1 can be avoided by using an appropriate scaling, i.e. an appropriate q value.

However, an important limitation of the application of rf pulse sequences to half-integer quadrupolar nuclei is the difficulty to selectively control the central-transition polarization. Hence, in the design of pulse sequences dedicated to half-integer quadrupolar nuclei, we must endeavor to limit the number of rf pulses in order to increase the sensitivity. Following this general principle, we employ sequences that achieve 2Q-recoupling but does not require any bracketing $\pi/2$-pulse [25]. This possibility was first demonstrated by Edén and co-workers when introducing R2_2^1 recoupling methods but was not further exploited [25]. To the best of our knowledge, only one 2QF 1D spectrum of α-Al$_2$O$_3$ recorded without bracketing $\pi/2$-pulse has been presented in the literature [25]. In the present article, we further investigate the potentialities of this unbracketed recoupling method. The corresponding pulse scheme for 2D 2Q–1Q spectroscopy of half-integer spin nuclei is depicted in Fig. 1b. Timing and phase-cycling are identical to those used for the sequence of Fig. 1a. Hence the coherence transfer pathways are still those displayed in Fig. 1c. The main differences between the methods introduced in Ref. [25] and in the present article lye in the absence of bracketing $\pi/2$ pulses and in the super-cycle of the recoupling sequences. The super-cycle we use is similar to that described by Mali et al. [22] and corresponds to a global phase-reversal at the midpoint of the τ intervals. These two simultaneous differences yield higher efficiency and robustness than previous methods. The design and the super-cycle of the employed recoupling methods are presented in the next subsection.

2.2. Homonuclear dipolar recoupling

In this work, RN_n^ν-based [2,30] recoupling schemes are employed. They are composed of N/2 R$_\varphi$R$_{-\varphi}$ inversion cycle pairs, where R is an inversion element of duration nT_R/N and φ indicates an overall phase-shift of $\nu\pi/N$. Here, R either represents a simple π_0-pulse (Fig. 1d–f) or the composite inversion pulses $\overrightarrow{X} = (\pi/2)_0(3\pi/2)_\pi$ (Fig. 1g and h) and $\overleftarrow{X} = (3\pi/2)_\pi(\pi/2)_0$. (Fig. 1h), which are both internally compensated to resonance offsets and rf errors. The RN_n^ν sequences built from the basic elements are denoted R$N_n^\nu(\pi)$ and R$N_n^\nu(\overrightarrow{X})$ in the following.

Several RN_n^ν symmetries were tested for the dipolar recoupling of half-integer quadrupolar nuclei. R4_4^1 and R6_6^2 symmetries achieve zero-quantum (0Q) dipolar recoupling and suppress all other dipolar and shielding terms [2,24,25]. Therefore, they must be bracketed by CT-selective $\pi/2$ pulses in order to excite 2QC and they can only be employed with the pulse sequence of Fig. 1a [25]. In contrast, R$N_N^{N/2}$ (π or $\overrightarrow{X}$) and R2_4^1 (π or $\overrightarrow{X}$) pulse sequences (Fig. 1d–h) generate a dipolar average Hamiltonian (AH) between homonuclear spins j and k, which comprises both 0Q and 2Q operators [25]. The expression of the AH corresponding to the different sequences described in this article (Eq. (2) and (3)) has been given in ref [25], and it is only introduced here for the reader convenience. The recoupling sequences described in Fig. 1d–h provide both 0Q and 2Q-recoupling and the corresponding AH is equal to:

$$H = b_{jk} f(\beta_R, \gamma_R)\{S_j^+ S_k^+ + S_j^- S_k^- - 4S_{jz}S_{kz} + S_j^+ S_k^- + S_j^- S_k^+\} \tag{2}$$

In the above equation, b_{jk} is the dipolar coupling constant and $f(\beta_R, \gamma_R) = 3\sin(2\beta_R) \cdot \cos\gamma_R /(16\sqrt{2})$ is a function of Euler angles (β_R, γ_R) describing the orientation of the inter-nuclear vector in the rotor-fixed frame. Eq. (2) shows that R$N_N^{N/2}$ and R2_4^1 schemes can be incorporated in the pulse sequences of Fig. 1b, since the 2Q terms, $S_j^+ S_k^+ + S_j^- S_k^-$, enable direct excitation of 2QC from longitudinal magnetization. R$N_N^{N/2}$ and R2_4^1 symmetries do not suppress all shielding terms [25,27]. However, these undesirable AH terms can be suppressed by the $\text{SRN}_n^\nu = \text{RN}_n^\nu \text{RN}_n^{-\nu}$ phase inversion super-cycle, while the average dipolar Hamiltonian is not affected and hence Eq. (2) remains valid [2,31,32]. As discussed in Ref. [25] and [27], the super-cycled sequences SR$N_N^{N/2}$ and SR2_4^1 can also be incorporated in the pulse sequence of Fig. 1a in order to convert the 0Q operators in Eq. (2) into pure 2Q operators. These $\pi/2$-bracketed sequences are denoted [SR$N_N^{N/2}$] and [SR2_4^1] in the following. Their AH is equal to:

$$[\mathrm{H}] = 2b_{jk} f(\beta_R, \gamma_R)\left\{S_j^+ S_k^+ + S_j^- S_k^-\right\} \tag{3}$$

disregarding the quadrupolar interaction.

The performances of $\pi/2$-bracketed recoupling schemes have already been compared by Edén and co-workers in the context of ^{23}Na ($S = 3/2$) and ^{27}Al ($S = 5/2$) homonuclear correlations [25,27]. In Ref. [25], they showed that the [SR2_2^1 (π)] sequence (Fig. 1a and e) is more efficient and more robust to offsets and rf-field inhomogeneity than [SR4_4^1 (π)], [SR6_6^2 (π)] and [HORROR] sequences. Very recently, they demonstrated that [SR4_4^2 (π)] scheme outperforms [SR2_2^1 (π)], [SR2_4^1 ($\overrightarrow{X}$)] and [R2_4^1 ($\overrightarrow{X}\,\overleftarrow{X}$)] (a short name for [R$2_4^1(\overrightarrow{X})$ R$2_4^1(\overleftarrow{X})$]) sequences in terms of optimum 2QF efficiencies for ^{23}Na and ^{27}Al nuclei, whereas [SR2_4^1 ($\overrightarrow{X}$)] and [R2_4^1 ($\overrightarrow{X}\,\overleftarrow{X}$)] sequences manifest higher robustness to both resonance offsets and rf-field inhomogeneity.

However, it was noticed that the 2QF efficiency drops significantly versus offsets, even for small differences in the CT frequencies. This prevents the observation of cross-peaks between sites exhibiting large differences in isotropic chemical shifts. To reduce this problem, we explore here an unbracketed R2_2^1 -based recoupling scheme employing a simple π_0-pulse as basic element. Edén and co-workers showed the possibility of 2QC excitation of quadrupolar spins by using unbracketed SR2_2^1 (π) recoupling method. However, they obtained a lower 2QF efficiency for the unbracketed sequence than for the bracketed version [SR2_2^1 (π)] [25]. This

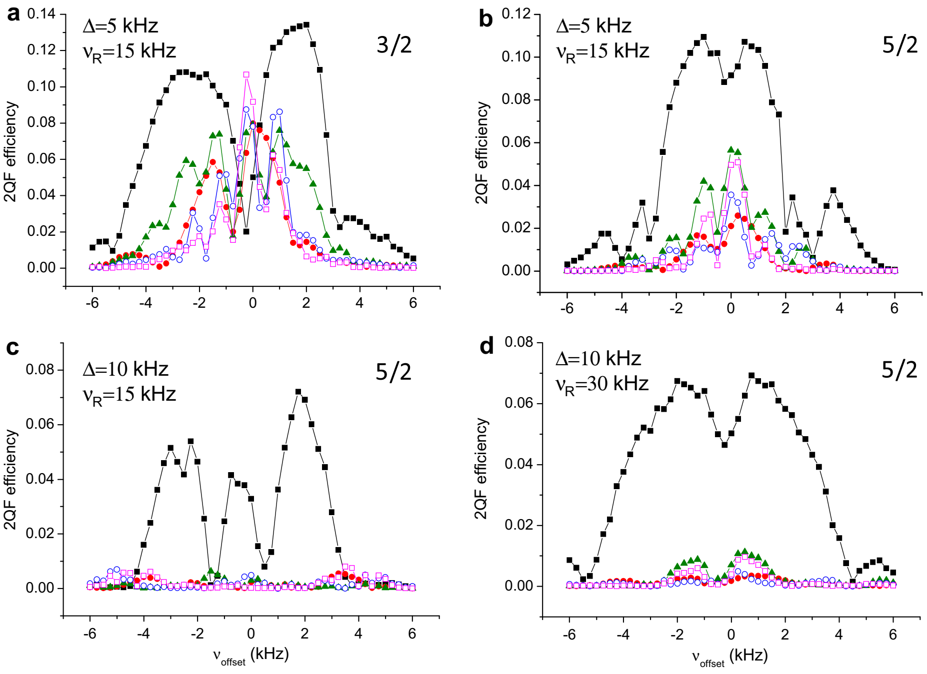

Fig. 3. Simulations of 2QF efficiency of cross-peaks ($\varDelta \neq 0$) versus resonance offset, ν_{offset}. (a) The spin system consists of two ^{23}Na nuclei ($S = 3/2$) with quadrupolar parameters $C_Q = 2.6$ MHz, $\eta_Q = 0.6$, and a dipolar coupling constant $b_{12} = -259$ Hz. The Larmor frequency was $\nu_0 = 105.8$ MHz and the MAS frequency $\nu_R = 15$ kHz. The frequency separation between the two sites was $\varDelta = 5$ kHz. The rf nutation frequency for the recoupling sequence was $\nu_1 = 3.75$ kHz. (b–d) The spin system consists of two ^{27}Al nuclei ($S = 5/2$), and its parameters are identical to those of Fig. 2, except the frequency separation, the MAS frequency and the rf nutation frequency, which are as follows: (b) $\varDelta = 5$ kHz, $\nu_R = 15$ kHz, $\nu_1 = 2.5$ kHz, (c) $\varDelta = 10$ kHz, $\nu_R = 15$ kHz, $\nu_1 = 2.5$ kHz, (d) $\varDelta = 10$ kHz, $\nu_R = 30$ kHz, $\nu_1 = 5$ kHz. Symbols for the different recoupling schemes are identical to those defined for Fig. 2.

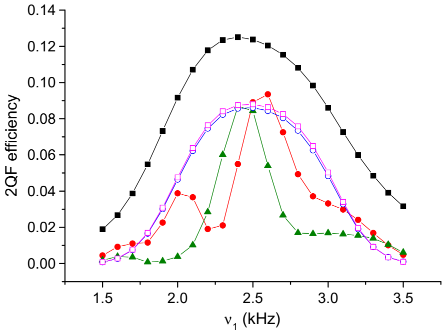

Fig. 4. Simulations of 2QF efficiency of the 'diagonal' peak ($\varDelta = 0$), versus the rf nutation frequency, ν_1. The spin system consists of two ^{27}Al nuclei ($S = 5/2$). The carrier frequency is optimized for maximum nominal ($\nu_1 = 2.5$ kHz) sensitivity: $\nu_{\text{offset}} = 0$ for [$\mathrm{R2}_4^1(\vec{X}\,\overleftarrow{X})$] and [$\mathrm{SR2}_4^1\ (\vec{X})$] sequence, 1 kHz for $\mathrm{BR2}_2^1\ (\pi)$ and [$\mathrm{SR2}_2^1\ (\pi)$] sequences, 1.5 kHz for [$\mathrm{SR4}_4^2\ (\pi)$] sequence. All other parameters and symbols are identical to those employed in Fig. 2.

can result from the super-cycle as well as the recoupling time, which was optimized for the unbracketed version. In this article, we investigate the unbracketed $\mathrm{R2}_2^1$ sequence employing a super-cycle, which consists in a phase inversion from the middle of the τ delay. This original super-cyle, depicted in Fig. 1d, better eliminates the offset and rf error dependence than the usual phase inversion super-cycle, $\mathrm{SR2}_2^1 = \mathrm{R2}_2^1\mathrm{R2}_2^{-1}$. It will be denoted $\mathrm{BR2}_2^1$ in the following. When the excitation and reconversion intervals span 4p rotor periods, the $\mathrm{BR2}_2^1\ (\pi)$ sequence corresponds to $(\mathrm{R2}_2^1)_\mathrm{p}(\mathrm{R2}_2^{-1})_\mathrm{p} = \mathrm{R2p}_{2\mathrm{p}}^{\mathrm{p}}\mathrm{R2p}_{2\mathrm{p}}^{-\mathrm{p}}$ symmetry. The better performances of $\mathrm{BR2}_2^1$ super-cycling compared to phase inversion super-cycling cannot be explained by the selection rules on the zero- and first-order AH and are not yet fully understood [31]. In this article, we compare the performances of $\mathrm{BR2}_2^1\ (\pi)$ recoupling sequence with those of previously reported sequences, [$\mathrm{SR2}_2^1\ (\pi)$], [$\mathrm{SR4}_4^2\ (\pi)$], [$\mathrm{SR2}_4^1\ (\vec{X})$] and [$\mathrm{R2}_4^1(\vec{X}\,\overleftarrow{X})$].

3. Simulations

In preparation for the experiments, we performed simulations with the SIMPSON software [33], and the powder averaging was performed using 168 crystallites following the REPULSION algorithm [34]. The computing time is approximately proportional to the cube of the size of the density matrix describing the spin system. Therefore, to limit the computing time to a few days for each figure, we have restricted our spin-system to only two interacting nuclei of spin-3/2 or -5/2. We have chosen to use two identical sites with the same quadrupolar parameters, and hence the same powder line-shapes, but with symmetrical isotropic chemical shifts of ±$\varDelta/2$ with respect to the reference frequency. The gravity

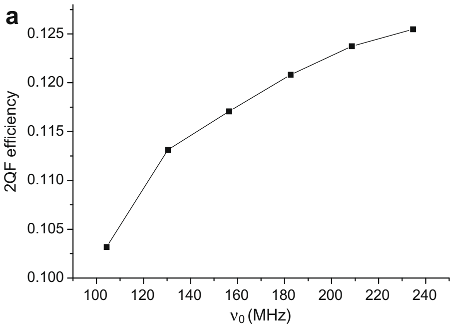

Fig. 5. Simulations of BR2_2^1 (π) 2QF efficiency of the 'diagonal' peak ($\Delta = 0$), versus (a) the Larmor frequency ν_0 ($C_Q = 4.07$ MHz) and (b) the C_Q value ($\nu_0 = 208.6$ MHz). The carrier frequency is fixed at $\nu_{\text{offset}} = 1$ kHz, $\nu_R = 15$ kHz, $\eta_Q = 0.43$.

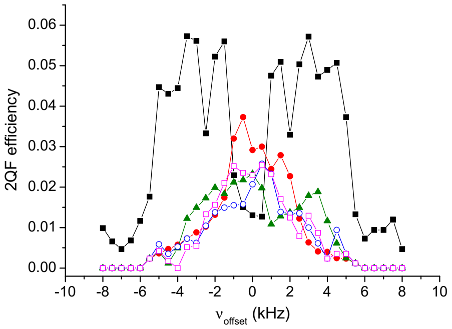

Fig. 6. Experimental ^{27}Al 2QF efficiency of the 'diagonal' peak ($\Delta = 0$) versus the resonance offset. The experiments were performed at $\nu_0 = 208.6$ MHz and $\nu_R = 15$ kHz on berlinite powder. The rf nutation frequency for the homonuclear recoupling sequence was $\nu_1 \approx 2.5$ kHz. The rf-power for the central π and the four bracketing π/2 pulses is 7.9 kHz. The excitation time τ for BR2_2^1 (π), [SR2_2^1 (π)], [SR4_4^2 (π)], [R2_4^1 ($X\bar{X}$)] and [SR2_4^1 ($\bar{X}$)] are 1866, 1333, 1066, 1066 and 1066 µs. All other parameters and symbols are identical to those employed in Fig. 2.

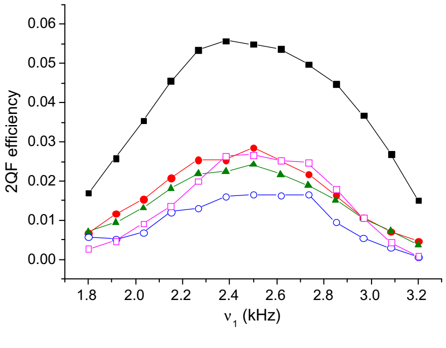

Fig. 7. Experimental ^{27}Al 2QF efficiency of the 'diagonal' peak ($\Delta = 0$) versus the rf nutation frequency. The experiments were performed at $\nu_0 = 208.6$ MHz and $\nu_R = 15$ kHz on berlinite powder. The employed resonance offsets, ν_{offset}, were fixed to the values that for each recoupling sequence provided the optimum 2QF efficiency in Fig. 6. All other parameters and symbols are identical to those employed in Fig. 6.

centers of these line-shapes are shifted from the isotropic chemical shift values by the quadrupolar induced shifts ($\nu_{\text{QIS}} < 0$), and they thus appear at $\pm\Delta/2 + \nu_{\text{QIS}}$. The rf-carrier is defined with respect to the reference frequency through the off-resonance frequency (ν_{offset}), which means that the frequency differences between the rf irradiation and the isotropic chemical shifts (or the line-shape gravity centers) are equal to $\pm\Delta/2 - \nu_{\text{offset}}$ (or to $\pm\Delta/2 - \nu_{\text{offset}} + \nu_{\text{QIS}}$). The spinning speed was always fixed to $\nu_R = 15$ kHz (except in Fig. 3d), and the quadrupolar and dipolar parameters of the two-spin system are those of ^{23}Na in Na_2SO_4 for spin-3/2 nuclei ($C_Q = 2.6$ MHz, $\eta_Q = 0.6$, $d_{12} = 318$ pm, $b_{12} = -259$ Hz) and of ^{27}Al in $AlPO_4$ berlinite for spin-5/2 nuclei ($C_Q = 4.07$ MHz, $\eta_Q = 0.43$, $d_{12} = 440$ pm, $b_{12} = -95$ Hz) (except in Fig. 5b). In both cases, the inter-nuclear vector was assumed aligned with the z principal axis of the quadrupolar tensor.

We ran simulations on a two-spin system, denoted S_1 and S_2 in the following. We detected the magnetization transferred from S_1 to S_2 during the 2QF experiment. It corresponds to one of the two cross-peaks between S_1 and S_2 CT transitions on the 2D 2Q–1Q spectrum. These simulations were done starting from S_1 longitudinal magnetization, i.e. the operator S_{1z}, and detecting only the −1Q coherence of spin-S_2, which corresponds to the operator S_2^-. The transfer efficiency was then calculated in comparison to the signal from a CT-selective 90° pulse on S_2.

3.1. 'Diagonal'-peak, with $F_1 = 2(1 - 2q)F_2$, of two similar nuclei ($\Delta = 0$)

We have first investigated the case of two nuclei with identical chemical shifts, $\Delta = 0$. The 2QF efficiency was calculated by numerical simulations as function of the offset, ν_{offset}, for all sequences described in Fig. 1, and at two different static magnetic fields 9.4 and 18.8 T. The obtained efficiencies correspond to those of auto-peaks situated on the diagonal of the 2D 2Q–1Q spectrum, which has a slope of 2(1 − 2q). For spin-3/2 nuclei (results not shown), all recoupling sequences are equivalent in terms of efficiency (around 16% for on-resonance irradiation, $\nu_{\text{offset}} = 0$) and robustness to offset. However, the efficiency of diagonal peaks is slightly less sensitive to offsets for BR2_2^1 (π) method. In contrast, for spin-5/2 nuclei, the BR2_2^1 method displays a higher efficiency and robustness to offset compared to the bracketed sequences. The results obtained at 9.4 (not shown) and 18.8 T (Fig. 2) are very similar. The larger 2QF efficiency for the unbracketed method partly stems from the inability of the bracketing pulses to selectively rotate the central-transition polarization, since the rf pulses do not operate in the CT-selective regime for all crystallites and time

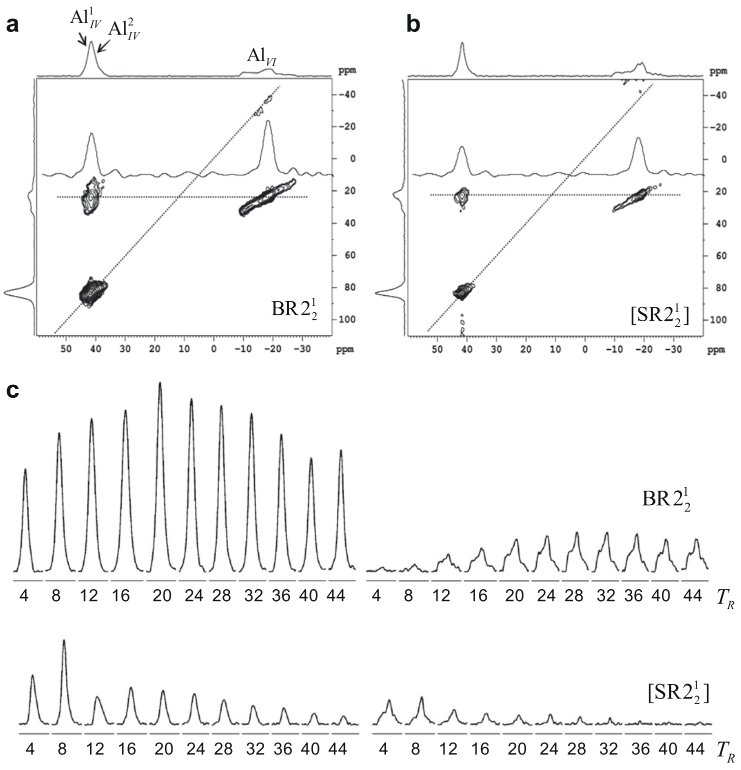

Fig. 8. Experimental 2Q–1Q ^{27}Al correlation spectra of AlPO$_4$-VPI5 at 9.4 T (ν_0 = 104.3 MHz) and ν_R = 13.5 kHz, using (a) BR2_2^1 (π) and (b) [SR2_2^1 (π)] for 2QC excitation. The parameter q has been fixed to 0.2, and the 2D spectra have been re-scaled along F_1 to restore the actual chemical shift values. The relaxation delay was 0.5 s and the indirect dimension of each spectrum was acquired with 120 points each obtained with 64 scans. The total experimental time for each 2D spectrum was 64 min. The rf nutation frequencies were $\nu_1 \approx 2.25$ kHz for the homonuclear recoupling sequence and 4.17 kHz for the CT-selective π and $\pi/2$ pulses. The excitation and reconversion intervals τ were equal to 2070 µs and 592 µs for BR2_2^1 (π) and [SR2_2^1 (π)] sequences, respectively. Slices along the cross-peaks ($F_1 \approx 24$ ppm) are also represented. (c) F_1 projections versus τ expressed in number of rotor periods. The left part corresponds to tetrahedral auto-peak ($F_1 \approx 90$ ppm), while the right part corresponds to cross-peaks ($F_1 \approx 24$ ppm).

points. An interesting phenomenon can also be observed in Fig. 2: all sensitivity curves present a narrow dip for on-resonance irradiation. This dip is always observed, whatever may be the relative orientations of the two quadrupolar tensors and the inter-nuclear vector. We do not have presently any explanation for this effect. This dip entails that the carrier frequency must be set up in a frequency region devoid of resonance.

3.2. Cross-peaks of two different nuclei ($\Delta \neq 0$)

We then simulated the case of two nuclei resonating at Δ = 5 kHz from each other. The simulations were performed for spin-3/2 at 9.4 T (Fig. 3a) and spin-5/2 at 18.8 T (Fig. 3b). By comparing Figs. 2 and 3b, we observe that for spin-5/2 nuclei the maximum efficiency of bracketed sequences is roughly divided by a factor of two when increasing the chemical difference from Δ = 0 to 5 kHz, whereas that of BR2_2^1 (π) is only slightly decreased. All experiments present one or several dips of sensitivity, which means that for sensitivity reasons, the carrier frequency must be carefully optimized. However, globally, the BR2_2^1 sensitivity is much larger and much more robust to offset than bracketed sequences, especially for spin-5/2 nuclei. For spin-3/2 nuclei this chemical shift difference, Δ = 5 kHz, is often an upper limit for most nuclei (e.g. ^{23}Na or ^{11}B), even at high magnetic fields, but this value can be much larger for spin-5/2 nuclei. For example, it can amount to Δ = 10 kHz for the cross-peaks between tetrahedral and octahedral ^{27}Al sites at 18.8 T. Thus we performed the same simulations, with the same spinning speed ν_R = 15 kHz, but we doubled the chemical shift difference: Δ = 10 kHz (Fig. 3c). It can be observed in this figure that the efficiencies obtained for bracketed sequences then become negligible. This is not the case with the BR2_2^1 sequence, and even if there are two large dips at $\nu_{\text{offset}} \approx 0.5$ and -1.5 kHz, it always remains possible to get a reasonable efficiency ($\approx$ 6–8%) by optimizing the carrier frequency. These two dips disappear when increasing the spinning speed and thus the rf-field. In Fig. 3d, simulated with Δ = 10 kHz and ν_R = 30 kHz, one observes for the BR2_2^1 sequence the same maximum efficiency as in Fig. 3c, without the two dips. The spectral width is larger than in Fig. 3b but the increase of isotropic chemical shift difference leads to a 30% decrease in the maximal 2QF efficiency. Simultaneously, the efficiency for the bracketed sequences remains very weak. The observation of 2Q–1Q cross-peaks of half-integer quadrupolar nuclei with large frequency separation thus requires the use of the BR2_2^1 sequence under fast MAS.

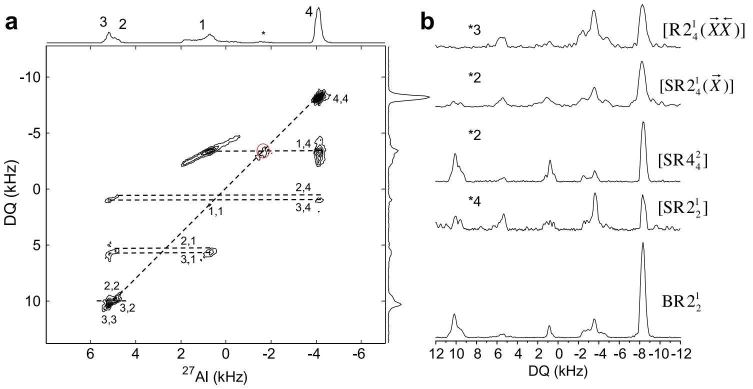

Fig. 9. Experimental ^{27}Al correlation spectra of AlPO$_4$-14 at 18.8 T (ν_0 = 208.6 MHz) and ν_R = 16 kHz. (a) 2Q–1Q 2D spectrum using BR2_2^1 (π) for 2QC excitation. The parameter q has been fixed to 0.2, and the spectrum has been re-scaled in the F_1 dimension. The relaxation delay was 0.6s and the indirect dimension of each spectrum was acquired with 140 points each obtained with 192 scans. The total experimental time for each 2D spectrum was 4.5 h. It can be decreased to 2 h, without loss in *S*/*N* ratio, by using an initial hyper-secant CT enhancing. The impurity at c.a. −2 kHz is indicated by a star and its auto-peak is circled. The rf nutation frequencies were $\nu_1 \approx 2.67$ kHz for the homonuclear recoupling sequence and 6.67 kHz for the CT-selective π and $\pi/2$ pulses. (b) Comparison of F_1 projections for the five homonuclear recoupling sequences described in Fig. 1. The excitation time τ for BR2_2^1 (π), [SR2_2^1 (π)], [SR4_4^2 (π)], [R2_4^1 ($\vec{X}\overleftarrow{X}$)] and [SR2_4^1 ($\vec{X}$)] are 1250, 750, 1000, 1000 and 1000 µs.

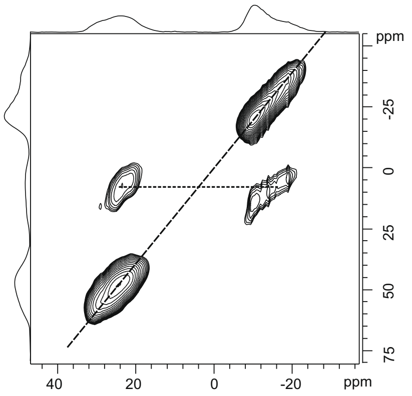

Fig. 10. Experimental 2Q–1Q ^{27}Al correlation spectrum of AlPO$_4$-CJ3 at ν_0 = 78.16 MHz and ν_R = 12.5 kHz, using BR2_2^1 (π) for 2QC excitation. The relaxation delay was 0.5s and the indirect dimension of each spectrum was acquired with 56 points each obtained with 704 scans. The total experimental time was 5.5 h. The rf nutation frequencies were $\nu_1 \approx 2.08$ kHz for the homonuclear recoupling sequence and 4.76 kHz for the CT-selective π and $\pi/2$ pulses. The excitation and reconversion intervals τ were equal to τ = 1280 µs. For the FAM/RAPT sequence, the rf nutation frequency was ν_1 = 60 kHz, the duration of x and ($\bar{x}$)-rf pulse was τ_{pulse} = 0.85 µs and the delay between the pulse train was τ_{interval} = 0.85 µs. 30 x-($\bar{x}$) cycles were used in the FAM/RAPT sequence.

3.3. Sensitivity to rf-inhomogeneity, C_Q and B_0 values

Another important experimental parameter is the robustness to rf-field missetting, i.e. the deviation of rf-field from the HORROR condition given by Eq. (1). The simulations were performed for the diagonal auto-peaks (Δ = 0) of the spins-5/2 system, at 18.8 T and ν_R = 15 kHz. For each recoupling sequence, the offset was fixed to the optimal value that provided the maximal sensitivity in Fig. 2. The rf-field was varied between 1.5 and 3.5 kHz in 100 Hz steps. It can be observed in Fig. 4 that the full-width at half-maximum corresponding to BR2_2^1 (π), is approximately 25% larger than that of [SR2_4^1 ($\vec{X}$)] or [R2_4^1($\vec{X}\overleftarrow{X}$)] and much larger than that of [SR2_2^1 (π)] or [SR4_4^2 (π)]. Moreover, as stated above, the unbracketed sequence provides much higher sensitivity than the bracketed ones. With a full rotor sample, this lower sensitivity to rf-inhomogeneity still increases the sensitivity advantage of BR2_2^1 (π) over the bracketed sequences.

In Fig. 5 the 2QF efficiency of the diagonal peaks (Δ = 0), obtained for the BR2_2^1 (π) sequence is plotted as function of the magnetic field (Fig. 5a) and the C_Q value (Fig. 5b). In both cases, one observes an increase of efficiency with a decrease of the second-order quadrupole interaction (except for weak C_Qs in Fig. 5b, because weak rf pulses then do not rotate correctly the CT coherences).

4. Experimental verifications

As shown before, the differences between the bracketed and unbracketed sequences are more pronounced for spin-5/2 nuclei than for spin-3/2 nuclei. Aluminum-27 is a very important quadrupolar nucleus, which it is the subject of numerous publications in SS NMR. For our purpose of 2Q–1Q experiments, it has the advantage of presenting a large chemical shift difference between the tetrahedral and octahedral species, whose cross-peaks are thus difficult to excite, especially at large magnetic fields. For this reason, we have decided to focus our experimental verifications on aluminum nuclei in four different well-known AlPO$_4$ samples, namely berlinite, VPI5, AlPO$_4$-14 and CJ3. The coherence transfer pathway depicted in Fig. 1c was selected by a 64-step nested phase-cycling incrementing in $\pi/2$ steps the 2Q-excitation block, the selective π-pulse and the read-pulse, respectively [22]. We have used the States procedure for frequency sign discrimination in the 2Q indirect dimension. Other experimental parameters are indicated in the figure captions. ^{27}Al shifts in ppm are referenced to Al^{3+} (aq).

4.1. Sensitivity versus offset in berlinite

The sensitivity versus offset of the diagonal peak (Δ = 0) has been measured in a volume-restricted sample of berlinite at 18.8 T and ν_R = 15 kHz for the five selected sequences shown in Fig. 1. This compound presents a single species [35], and the 2Q–1Q spectrum thus only displays a single diagonal auto-peak. The closest distance between two aluminum nuclei is equal to 440 pm [36], which corresponds to $b_{12} = -95$ Hz. The experimental (Fig. 6) and simulated (Fig. 2) results have very similar behavior with respect to ν_{offset}. However, experimental intensities are roughly two times smaller than simulated ones, and optimum transfer times are shorter than those predicted from numerical simulations: $\tau_{\text{exp}} \approx 1.1/1.75$ ms instead of $\tau_{\text{sim}} \approx 1.9/2.5$ ms, for bracketed/unbracketed sequences, respectively. This scaling down of intensities has been observed previously [22,25,27–29] It may be partly related to pulse transients, but it is certainly mainly related to the irreversible losses occurring during excitation and conversion periods, which also explains the shortening of the experimental transfer delays.

4.2. Sensitivity versus rf-field in berlinite

On the same restricted sample of berlinite, we have also measured the 2QF signal that can be obtained at $\nu_R = 15$ kHz for the diagonal peak ($\Delta = 0$), versus the rf-field amplitude. The relative rf-field amplitude was varied by a factor between 0.7 and 1.3 with respect to its optimal value (Fig. 7). The most robust method with respect to rf-inhomogeneity, is the unbracketed $BR2_2^1$ (π) sequence, as already shown by simulations (Fig. 4). For this method, the full-width at half-maximum ($\approx$ 1.2 kHz, $\approx \nu_{1\text{opt}}/2$) is approximately equal to its calculated value ($\approx$ 1.3 kHz: Fig. 4).

4.3. Dynamics of 0Q ↔ 2Q transfers in AlPO$_4$-VPI5

In Fig. 8 we have represented the two 2Q–1Q 2D spectra of AlPO$_4$-VPI5 recorded at 9.4T and $\nu_R = 13.5$ kHz with the same $R2_2^1$ basic recoupling scheme in its unbracketed (Fig. 8a) or bracketed (Fig. 8b) version. There are three different aluminum species in this compound: two overlapping tetrahedral sites (Al_{IV}^1 - $Al_{IV}^2 \approx 40$ ppm) and one octahedral site ($Al_{VI} \approx$ -20 ppm). The quadrupolar parameters C_Q (MHz)/η_Q of the octahedral species are 3.5/0.91 [37], and those of the tetrahedral species 1.1/0.3 (Al_{IV}^1) and 2.4/0.8 (Al_{IV}^2) [38]. The closest Al–Al distances (below 500 pm) involve pairs of distinct aluminum sites: Al_{VI}–Al_{IV}^1 (437 and 484 pm), Al_{VI}–Al_{IV}^2 (448 and 471 pm), Al_{IV}^1–Al_{IV}^2 (470 and 479 pm). The contacts between identical species are Al_{IV}^1–Al_{IV}^1 (498 pm), Al_{IV}^2–Al_{IV}^2 (521 pm) and Al_{VI}–Al_{VI} (594 pm) [39,40]. All Al–Al dipolar interactions are thus smaller than 100 Hz in absolute value. The $BR2_2^1$ sequence yields sensitivity enhancement for all peaks of 2D NMR spectra, and especially for the two cross-peaks in spite of their moderate chemical shift difference ($\Delta \approx 6$ kHz). Moreover, it can also be observed on the F_1 projection displayed versus the half-recoupling time τ (Fig. 8c) that the optimum 2Q–1Q signal is observed for a recoupling time that is c.a. three times longer when omitting the bracketing $\pi/2$ pulses. This effect, which results from the ratio of two between the scaling factors of double-quantum terms in the dipolar average Hamiltonian (see Eqs. (2) and (3)), has also been observed on berlinite. It has two opposite effects. On one hand, losses are increased during this longer transfer time. However, on the other hand it allows a fine adjustment of the recoupling time, even in case of large homonuclear dipolar interactions and/or slow spinning speeds. Indeed, the 2Q–1Q methods applied to half-integer quadrupolar nuclei accelerate by a factor of c.a. $S + 1/2$ the recoupling effect, relative that observed for spin-1/2 nuclei [25,28]. A large scaling factor can lead to a too fast build up of 2QC compared to the minimal sampling period ($4T_R$) of the recoupling intervals, and hence may reduce the 2QF signal amplitude. It should be pointed out that no cross-peaks were observed at 18.8 T and $\nu_R = 15$ kHz for the [$SR2_2^1$ (π)] sequence, whereas the $BR2_2^1$ sequence allows observing cross-peaks in such experimental conditions (not shown).

4.4. 2D 2Q–1Q spectra of AlPO$_4$-14

In Fig. 9a we have represented the 2Q–1Q 2D spectrum of as synthesized AlPO$_4$-14 recorded at 18.8 T and $\nu_R = 16$ kHz, and using $BR2_2^1$ (π) for 2QC excitation and reconversion. This compound presents four different aluminum species [41]: two tetrahedral sites (Al_3: $\delta_{cs} = 42.7$ ppm, $C_Q = 1.72$ MHz, $\eta_Q = 0.57$; Al_2: $\delta_{cs} = 43.5$ ppm, $C_Q = 3.90$ MHz, $\eta_Q = 0.83$), one pentavalent aluminum atom (Al_1: $\delta_{cs} = 27.1$ ppm, $C_Q = 5.61$ MHz, $\eta_Q = 0.93$) and one octahedral site (Al_4: $\delta_{cs} = -1.3$ ppm, $C_Q = 2.55$ MHz, $\eta_Q = 0.67$), and in addition, our sample also presents an extra-framework impurity at -2 kHz. Along with Al–O–P–O–Al connectivities, which are common for all aluminophosphate molecular sieves, in AlPO$_4$-14 there are also some Al–O–Al connectivities due to edge sharing between AlO$_6$ octahedra and vertex sharing between AlO$_5$ and AlO$_6$ polyhedra. The corresponding distances are 290 pm for Al_4–O–Al_4 connectivity ($b_{44} = -333$ Hz) and 360 pm for Al_1–O–Al_4 connectivity ($b_{14} = -174$ Hz) [42]. All other distances are much larger, and as an example they range over 430–480 pm ($b_{23} = -73$ to -102 Hz) between Al_2 and Al_3 nuclei.

All peaks are easily distinguishable in this figure, even the cross-peaks between tetrahedral and octahedral sites ($Al_{2,3}$–Al_4), even if they are 540 pm apart ($b_{24} = b_{34} = -52$ Hz) and display a large difference in isotropic chemical shift ($\Delta \approx 10$ kHz). The F_1 projections of the five sequences described in Fig. 1 are compared in Fig. 9b. This comparison points out the fact that the unbracketed $BR2_2^1$ (π) method gives at least a two-fold sensitivity gain over all bracketed sequences. According to simulations, this sensitivity gain would increase at $\nu_R = 30$–35 kHz (see Fig. 3d). The Al_1 auto-peak is hardly visible as it corresponds to long distances (670 pm and $b_{11} = -27$ Hz) and is certainly submitted to dipolar truncation with respect to the much larger dipolar interaction ($b_{14} = -174$ Hz) between the Al_1 and Al_4 sites. This dipolar truncation, which occurs in all 2Q–1Q and 1Q–1Q homonuclear dipolar methods, is one of the most important limitations of these methods.

4.5. 2Q–1Q spectrum of AlPO$_4$-CJ3

To demonstrate the ability of the 2Q–1Q $BR2_2^1$ method to be applied even at low magnetic field, we have recorded the 2D spectrum of AlPO$_4$-CJ3, [$Al_2P_2O_8$][$OCH_2CH_2NH_3$], at 7.1 T. There are two different ways of enhancing the initial ±1/2 Zeeman populations: either by saturating all populations (FAM/RAPT) [43,44] or by inverting sequentially the populations from the outer STs to the CT (DFS [45], HS [46], WURST [47]). These initial rf manipulations of the populations are not described in Fig. 1a–c. We have used the FAM/RAPT sequence, which is less efficient than the inversion methods, but more robust and which is the only method that can be used with old consoles. We obtained a signal gain of c.a. 2 on AlPO$_4$-CJ3. This sample presents two different species: one octahedral (Al_1: $C_Q(1 + \eta_Q{}^2/3) \approx 2.6$ MHz) and one tetrahedral site (Al_2: $C_Q(1 + \eta_Q{}^2/3) \approx 3.0$ MHz). The shortest Al–Al distance is between Al_1 nuclei (289 pm, $b_{11} = -336$ Hz), whereas all other distances are larger than 420 pm ($|b| < 110$ Hz) [48]. In Fig. 10 we have represented the 2Q–1Q spectrum recorded with initial FAM/RAPT and the $BR2_2^1$ sequence (Fig. 1a and d), which displays all auto- and cross-peaks with a large S/N ratio. The $BR2_2^1$ sequences gave a S/N ratio at least twice that observed with the four bracketed sequences (not shown). Moreover, in agreement with Eq. (2) and (3) its optimum contact time (1280 μs) was twice that of all bracketed sequences (640 μs).

5. Conclusions

We have demonstrated 2Q–1Q homonuclear correlation 2D experiments among the central transition of half-integer quadrupolar spins with an unbracketed dipolar recoupling sequence based on the $R2_2^1$ rotor-synchronized and symmetry-based scheme initially developed for spin-1/2 nuclei. It must be noted that the super-cycling of this sequence differs from that used previously in the literature and yields higher efficiency and more robustness to rf-inhomogeneity and to offsets for auto- and cross-peaks. It allows the observation of cross-peaks that are separated by more than 10 kHz, provided the spinning speed is fast enough.

In addition to the initial enhancement of the ±1/2 Zeeman populations [43–47] three other tools can be applied to increase the signal: recycled or full echo acquisition, and slightly off-magic-angle spinning. Final recycling of the signal with CPMG train [49,50] is mostly useful when the constant time (T'_2) describing irreversible losses is large enough to be able to observe at least four or five echoes. Increasing the T'_2 value can be obtained by using fast MAS [51], which also increases the indirect spectral width of rotor-synchronized methods. As an example, by using simultaneously an initial FAM/RAPT saturation and a final CPMG recycling of the signal, a signal enhancement by a factor of c.a. 6 has been demonstrated on ^{23}Na spectra of Na_2SO_4 [23]. Another way to increase the T'_2 value is by spinning slightly off magic-angle ($\approx 0.5°$) [52]. Indeed, it has recently been shown that a signal gain of c.a. 3 could be obtained without any noticeable broadening on the second-order quadrupolar CT line-shapes [53]. When, in spite of these tools, the T'_2 value remains too small to record a sufficient number of echoes, a full echo acquisition may allow to increase the S/N ratio by a factor up to $\sqrt{2}$ [53]. Sequences described in Fig. 1a and b have then to be slightly changed for this purpose with an additional CT-selective π-pulse at the end, and the phase-cycling must be changed to select at the end the $0 \rightarrow +1 \rightarrow -1$ levels instead of the $0 \rightarrow -1$ levels as described in Fig. 1c.

When the signal is sufficient, e.g. by using the $BR2_2^1$ method with these additional tools, a high-resolution double-quantum dimension can be achieved by using high-resolution filters for half-integer quadrupolar nuclei [23]: MQMAS [54] or STMAS [55,56].

One limitation of all these sequences applied to half-integer quadrupolar nuclei is related to the fact their sensitivity curves always present one or several narrow dips, which means a careful optimization of the carrier frequency. More importantly, another limitation concerns the dipolar truncation. This means that long-range correlations between two nuclei are not visible when one of these is also involved in a short-range correlation with a third nucleus. A third limitation of all dipolar-based through-space methods is that they do not allow distinguishing between through-bond connectivity and through-space proximities. However, short recoupling times allow exciting 2QCs between the nearest-neighbor nuclei. Therefore, through-space experiments allow generally obtaining the same results as with through-bond methods, at the expense of lower S/N ratio. It must be noted that recently, several methods [58], though explicitly dealing with spin-1/2 nuclei for biological samples, are definitely exploring the same avenues than our method for quadrupolar nuclei.

Acknowledgments

Authors are grateful for funding provided by Region Nord/Pas de Calais, Europe (FEDER), CNRS, French Minister of Science, FR-3050, USTL, ENSCL, and Bruker BIOSPIN. F.D. thanks the National Natural Science Foundation of China (20773159 and 20673139) and the National Basic Research Program of China (2009CB918600) for financial support.

References

[1] S. Dusold, A. Sebald, Dipolar recoupling under magic-angle-spinning conditions, Annu. Rep. NMR Spectrosc. 41 (2000) 185–264.
[2] M.H. Levitt, in: D.M. Grant, R.K. Harris (Eds.), Symmetry-Based Pulse Sequences in Magic-Angle Spinning Solid-State NMR in Encyclopedia of Nuclear Magnetic Resonance, vol. 9, Wiley, Chichester, 2002.
[3] S. Ding, C.A. McDowell, Spectral spin diffusion of a spin-3/2 system in rotating solids, Mol. Phys. 85 (1995) 283–298.
[4] N.G. Dowell, S.E. Ashbrook, S. Wimperis, Relative orientation of quadrupole tensors from high-resolution NMR of powdered solids, J. Phys. Chem. A 106 (2002) 9470–9478.
[5] M.J. Duer, Determination of structural data from multiple-quantum magic-angle spinning NMR experiments, Chem. Phys. Lett. 277 (1997) 167–174.
[6] M.J. Duer, A.J. Painter, Correlating quadrupolar nuclear spins: a multiple-quantum NMR approach, Chem. Phys. Lett. 313 (1999) 763–770.
[7] M. Eden, L. Frydman, Quadrupolar-driven recoupling of homonuclear dipolar interactions in the nuclear magnetic resonance of rotating solids, J. Chem. Phys. 114 (2001) 4116–4123.
[8] M. Eden, J. Grinshtein, L. Frydman, High-resolution 3D exchange NMR spectroscopy and the mapping of connectivities between half-integer quadrupolar nuclei, J. Am. Chem. Soc. 124 (2002) 9708–9709.
[9] M. Eden, L. Frydman, Homonuclear NMR correlations between half-integer quadrupolar nuclei undergoing magic-angle spinning, J. Phys. Chem. B 107 (2003) 14598–14611.
[10] A.P.M. Kentgens, E.R.H. van Eck, T.G. Ajithkumar, T. Anupold, J. Past, A. Reinhold, A. Samoson, New opportunities for double rotation NMR of half-integer quadrupolar nuclei, J. Magn. Reson. 178 (2006) 212–219.
[11] I. Hung, A.P. Howes, T. Anupold, A. Samoson, D. Massiot, M.E. Smith, S.P. Brown, R. Dupree, ^{27}Al double rotation two-dimensional spin diffusion NMR: complete unambiguous assignment of aluminum sites in $9Al_2O_3{\cdot}2B_2O_3$, Chem. Phys. Lett. 432 (2006) 152–156.
[12] A. Vinu, K. Ariga, T. Mori, K. Takegoshi, Two dimensional ^{11}B–^{11}B exchange NMR study in mesoporous boron carbon nitride at 21.8 T, Solid State Nucl. Magn. Reson. 31 (2007) 193–196.
[13] M. Nijman, M. Ernst, A.P.M. Kentgens, B.H. Meier, Rotational-resonance NMR experiments in half-integer quadrupolar spin-systems, Mol. Phys. 98 (2000) 161–178.
[14] P. Hartmann, C. Jäger, J.W. Zwanziger, Off-angle correlation spectroscopy applied to spin-1/2 and quadrupolar nuclei, Solid State Nucl. Magn. Reson. 13 (1999) 245–254.
[15] T.G. Ajithkumar, A.P.M. Kentgens, Homonuclear correlation experiments of half-integer quadrupolar nuclei using multiple-quantum techniques spinning at a P_4 magic angle, J. Am. Chem. Soc. 125 (2003) 2398–2399.
[16] S. Vega, Fictitious spin-1/2 operator formalism for multiple quantum NMR, J. Chem. Phys. 68 (1978) 5518–5527.
[17] T.G. Oas, R.G. Griffin, M.H. Levitt, Rotary resonance recoupling of dipolar interactions in solid-state nuclear magnetic resonance spectroscopy, J. Chem. Phys. 89 (1988) 692–695.
[18] N.C. Nielsen, H. Bildsoe, H.J. Jakobsen, M.H. Levitt, Double-quantum homonuclear rotary resonance: efficient dipolar recovery in magic-angle spinning nuclear magnetic resonance, J. Chem. Phys. 101 (1994) 1805–1812.
[19] M. Baldus, D. Rovnyak, R.G. Griffin, Radio-frequency-mediated dipolar recoupling among half-integer quadrupolar spins, J. Chem. Phys. 112 (2000) 5902–5909.
[20] S. Wi, J.W. Logan, D. Sakellariou, J.D. Walls, A. Pines, Rotary resonance recoupling for half-integer quadrupolar nuclei in solid-state nuclear magnetic resonance spectroscopy, J. Chem. Phys. 117 (2002) 7024–7033.
[21] J. Painter, M.J. Duer, Double-quantum-filtered nuclear magnetic resonance spectroscopy applied to quadrupolar nuclei in solids, J. Chem. Phys. 116 (2002) 710–722.
[22] G. Mali, G. Fink, F. Taulelle, Double-quantum homonuclear correlation magic-angle sample spinning nuclear magnetic resonance spectroscopy of dipolar-coupled quadrupolar nuclei, J. Chem. Phys. 120 (2004) 2835–2845.
[23] G. Mali, V. Kaucic, Enhancing sensitivity or resolution of homonuclear correlation experiment for half-integer quadrupolar nuclei, J. Magn. Reson. 171 (2004) 48–56.
[24] M. Eden, H. Annersten, A. Zazzi, Pulse-assisted homonuclear dipolar recoupling of half-integer quadrupolar spins in magic-angle spinning NMR, Chem. Phys. Lett. 410 (2005) 24–30.
[25] M. Eden, D. Zhou, J. Yu, Improved double-quantum NMR correlation spectroscopy of dipolar-coupled quadrupolar spins, Chem. Phys. Lett. 431 (2006) 397–403.
[26] M.R. Hansen, H.J. Jakobsen, J. Skibsted, Structural environments for boron and aluminum in alumina-boria catalysts and their precursors from ^{11}B and ^{27}Al single- and double-resonance MAS NMR experiments, J. Phys. Chem. C112 (2008) 7210–7222.
[27] A.Y.H. Lo, M. Eden, Efficient symmetry-based homonuclear dipolar recoupling of quadrupolar spins: double-quantum NMR correlations in amorphous solids, Phys. Chem. Chem. Phys. 10 (2008) 6635–6644.
[28] G. Mali, V. Kaucic, F. Taulelle, Measuring distances between half-integer quadrupolar nuclei and detecting relative orientations of quadrupolar and dipolar tensors by double-quantum homonuclear dipolar recoupling nuclear magnetic resonance experiments, J. Chem. Phys. 128 (2008) 204503.
[29] A. Brinkmann, A.P.M. Kentgens, T. Anupold, A. Samoson, Symmetry-based recoupling in double-rotation NMR spectroscopy, J. Chem. Phys. 129 (2008) 174507.
[30] M. Carravetta, M. Edén, X. Zhao, A. Brinkmann, M.H. Levitt, Symmetry principles for the design of radiofrequency pulse sequences in the nuclear magnetic resonance of rotating solids, Chem. Phys. Lett. 321 (2000) 205–215.

[31] A. Brinkmann, M. Eden, Second order average Hamiltonian theory of symmetry-based pulse schemes in the nuclear magnetic resonance of rotating solids: application to triple-quantum dipolar recoupling, J. Chem. Phys. 120 (2004) 11726–11745.

[32] A. Brinkmann, J. Schmedt auf der Günne, M.H. Levitt, Homonuclear zero-quantum recoupling in fast magic-angle spinning nuclear magnetic resonance, J. Magn. Reson. 156 (2002) 79–96.

[33] M. Bak, J.T. Rasmussen, N.C. Nielsen, SIMPSON: a general simulation program for solid-state NMR spectroscopy, J. Magn. Reson. 147 (2000) 296–330.

[34] M. Bak, N.C. Nielsen, REPULSION: a novel approach to efficient powder averaging in solid-state NMR, J. Magn. Reson. 125 (1997) 132–139.

[35] D. Massiot, F. Fayon, B. Alonso, J. Trebosc, J.P. Amoureux, Chemical bonding differences evidenced from *J*-coupling in solid-state NMR experiments involving quadrupolar nuclei, J. Magn. Reson. 164 (2003) 160–164.

[36] A. Goiffon, J.C. Jumas, M.M. Aurin, E. Philippot, J. Solid State Chem. 61 (1986) 384–396.

[37] J. Rocha, W. Kolodziejski, H. He, J. Klinowski, Solid state NMR studies of hydrated porous aluminophosphate VPI-5, J. Am. Chem. Soc. 114 (1992) 4884–4888.

[38] J. Rocha, A.P. Esculcas, C. Fernandez, J.P. Amoureux, 2D triple-quantum ^{27}Al MAS NMR spectroscopy study of the high-temperature phase transformation of microporous VPI-5, J. Phys. Chem. 100 (1996) 17889.

[39] L.B. McCusker, Ch. Barlocher, E. Jahn, M. Bulow, Zeolites 11 (1991) 308.

[40] E.G. Derouane, H. He, S.B. Derouane-Abd Hamid, I.I. Ivanova, In situ MAS NMR investigations of molecular sieves and zeolite-catalyzed reactions, Catal. Lett. 58 (1999) 1–19.

[41] C. Fernandez, J.P. Amoureux, C. Chezeau, L. Delmotte, A. Kessler, Al-MAS NMR characterization of $AlPO_4$-14. Enhanced resolution and information by MQMAS, Microporous Mater. 6 (1996) 331–340.

[42] R.W. Broach, S.T. Wilson, R.M. Kirchner, Corrected crystallographic tables and figure for as-synthesized $AlPO_4$-14, Microporous Mesoporous Mater. 57 (2003) 211–214.

[43] P.K. Madhu, A. Golbourt, L. Frydman, S. Vega, Sensitivity enhancement of the MQMAS NMR experiment by fast amplitude modulation of the pulses, Chem. Phys. Lett. 307 (1999) 41–47.

[44] Z. Yao, H.T. Kwak, D. Sakellariou, L. Emsley, P.J. Grandinetti, Sensitivity enhancement of the central transition NMR signal of quadrupolar nuclei under magic-angle spinning, Chem. Phys. Lett. 327 (2001) 85–90.

[45] A.P.M. Kentgens, R. Verhagen, Advantages of double-frequency sweeps in static, MAS and MQMAS NMR of spin-3/2 nuclei, Chem. Phys. Lett. 300 (1999) 435–443.

[46] R. Siegel, T.T. Nakashima, R.E. Wasylishen, Signal enhancement of NMR spectra of half-integer quadrupolar nuclei in solids using hyperbolic secant pulses, Chem. Phys. Lett. 388 (2004) 441–445.

[47] K.K. Dey, S. Prasad, J.T. Ash, M. Deschamps, P.J. Grandinetti, Spectral editing in solid state MAS NMR of quadrupolar nuclei using selective satellite inversion, J. Magn. Reson. 185 (2007) 326–330.

[48] K. Wang, J. Yu, G. Zhu, Y. Zou, R. Xu, Synthesis and characterization of a new microporous aluminophosphate $[Al_2P_2O_8][OCH_2CH_2NH_3]$ with an open-framework analogous to $AlPO_4$-D, Microporous Mesoporous Mater. 39 (2000) 281–289.

[49] T. Vosegaard, F.H. Larsen, H.J. Jakobsen, P.D. Ellis, N.C. Nielsen, Sensitivity-enhanced multiple quantum MAS NMR of half-integer quadrupolar nuclei, J. Am. Chem. Soc. 119 (1997) 9055–9056.

[50] R. Lefort, J. W Wiench, M. Pruski, J.P. Amoureux, Optimization of data acquisition and processing in Carr–Purcell–Meiboom–Gill multiple-quantum magic angle spinning nuclear magnetic resonance, J. Chem. Phys. 116 (2002) 2493–2501.

[51] K. Mao, J. Wiench, V.S.Y. Lin, M. Pruski, Indirectly detected through-bond chemical shift correlation NMR spectroscopy in solids under fast MAS: studies of organic-inorganic hybrid materials, J. Magn. Reson. 196 (2009) 92–95.

[52] H.T. Kwak, P. Srinivasan, J. Quine, D. Massiot, Z. Gan, Satellite transition rotational resonance of homonuclear quadrupolar spins: magic-angle effect on spin-echo decay and inversion recovery, Chem. Phys. Lett. 376 (2003) 75–82.

[53] D. Iuga, C. Morais, Z. Gan, D.R. Neuville, L. Cormier, D. Massiot, NMR heteronuclear correlation between quadrupolar nuclei in solids, J. Am. Chem. Soc. 127 (2005) 11540–11541.

[54] L. Frydman, J.S. Harwood, Isotropic spectra of half-integer quadrupolar spins from bidimensional magic-angle spinning NMR, J. Am. Chem. Soc. 117 (1995) 5367–5368.

[55] Z. Gan, Isotropic NMR spectra of half-integer quadrupolar nuclei using satellite transitions and magic-angle spinning, J. Am. Chem. Soc. 122 (2000) 3242–3243.

[56] J. Trebosc, J.P. Amoureux, Z. Gan, Comparison of high-resolution solid-state NMR MQMAS and STMAS methods for half-integer quadrupolar nuclei, Solid State NMR 31 (2007) 1–9.

[57] M. Edén, Determination of absolute quadrupolar tensor orientations by double-quantum NMR on powders, Chem. Phys. Lett. 470 (2009) 318–324.

[58] J. Lin, M.J. Bayro, R.G. Griffin, N. Khaneja, Dipolar recoupling in solid state NMR by phase alternating pulse sequences, J. Magn. Reson. 197 (2009) 145–152.

Chapitre 3

Recouplage dipolaire hétéronucléaire

Les séquences de recouplage dipolaire hétéronucléaire réintroduisent les couplages dipolaires entre des isotopes différents dans les conditions MAS [160]. Ces séquences ont plusieurs finalités, telles que :

- la spectroscopie de corrélation hétéronucléaire (HETCOR) 2D, qui facilite l'attribution des spectres en permettant d'identifier les proximités entre des isotopes différents [161],
- la mesure de distances interatomiques hétéronucléaires [162],
- la détection de noyaux quadripolaires de spin demi-entier (^{27}Al, ^{23}Na...) [163] et entier (^{14}N) [164, 165] par le truchement de noyaux voisins de spin-1/2.

Une séquence de recouplage hétéronucléaire idéale doit satisfaire aux conditions suivantes :

i. Elle doit être robuste au déplacement chimique isotrope et au CSA, notamment pour pouvoir être appliquée à haut champ pour les noyaux ^{13}C, ^{19}F et ^{31}P ;

ii. La robustesse aux inhomogénéités de champ rf doit être élevée ;

iii. Elle doit pouvoir être employée pour des fréquences MAS supérieures à 30 kHz et les champs rf requis doivent être compatibles avec les spécifications de la sonde. L'utilisation de la haute vitesse est particulièrement utile pour la détection indirecte via les noyaux ^{1}H, ^{19}F, ^{13}C et ^{31}P ;

iv. Elle doit être robuste aux fluctuations de vitesse du rotor ;

v. Elle doit être γ-encodée [133, 135], ce qui permet d'obtenir une meilleure efficacité et des plus grandes oscillations dipolaires pour les mesures précises de distances sur des poudres ;

vi. L'hamiltonien de recouplage hétéronucléaire doit avoir la forme de l'hamiltonien d'Ising. Ceci permet d'éviter les problèmes de troncature dipolaire et d'interférences du CSA ;

vii. Elle doit permettre d'atténuer ou même d'éliminer les couplages dipolaires homonucléaires ;

viii. La période de la séquence ne doit pas être trop longue, de façon à pouvoir ajuster au mieux le déphasage sous l'effet du couplage hétéronucléaire ;

ix. La séquence doit pouvoir être employée pour corréler des noyaux de spin-1/2 entre eux, ou les corréler à des noyaux quadripolaires.

Une grande variété de séquences de recouplage ont été développées. Certaines, telles que la polarisation croisée (CP) [160] et les séquences basées sur des symétries duales [166], utilisent des irradiations simultanées sur les deux noyaux recouplés. Cependant, ces séquences souffrent de la troncature dipolaire et ne permettent pas de mesurer des couplages dipolaires à longue distance. En outre, elles sont peu robustes lorsque le recouplage implique un noyau de spin demi-entier et inapplicable pour le recouplage avec l'azote-14.

Heureusement, le recouplage dipolaire peut être réalisé plus simplement en irradiant un seul des noyaux couplés. Cette méthode est particulièrement avantageuse lorsqu'un des noyaux subit l'interaction quadripolaire, puisqu'elle permet de minimiser le nombre d'impulsions appliquées aux noyaux quadripolaires. Cette catégorie de recouplage hétéronucléaire comprend différentes séquences d'impulsions, telles que le recouplage par résonance rotatoire (R^3) [162], le REDOR [167], le SFAM [168], les séquences dérivant des symétries $\mathrm{R}N_n^\nu$ ($\mathrm{R}18_2^5$ [169], $\mathrm{R}12_3^5$ [170], $\mathrm{SR}4_1^2$ [171]). Les séquences R^3 et $\mathrm{R}18_2^5$ sont γ-encodées, mais elles souffrent de la troncature dipolaire et d'interférences entre le couplage dipolaire hétéronucléaire et le CSA. En outre, elles sont sensibles aux inhomogénéités de champ rf.

Les techniques REDOR, SFAM, $\mathrm{R}12_3^5$ et $\mathrm{SR}4_1^2$, si elles sont non-γ-encodées, ont l'avantage, en revanche, d'engendrer un hamiltonien dipolaire recouplé de type Ising. Par conséquent, elles ne sont pas affectées par la troncature dipolaire et les interférences du CSA. Le recouplage REDOR, s'il est très populaire, réintroduit les couplages dipolaires homonucléaires, dès lors que la durée des impulsions n'est pas négligeable par rapport à la période du rotor, ce qui est généralement le cas à haute vitesse [172]. Actuellement, ce sont les séquences SFAM-2, $\mathrm{R}12_3^5$ et $\mathrm{SR}4_1^2$, qui permettent la meilleure suppression des couplages homonucléaires, tout en réintroduisant les couplages hétéronucléaires. Ces séquences nécessitent des champs rf raisonnables ($\nu_{rf} = 2\nu_r$ pour $\mathrm{R}12_3^5$ et $\mathrm{SR}4_1^2$) et sont, de ce fait, compatibles avec la haute vitesse.

En utilisant ces techniques de recouplage performantes, nous avons conçu de nouvelles expériences RMN permettant, d'une part de mesurer des distances hétéronucléaires entre noyaux quadripolaires et noyaux de spin-1/2, et d'autre part, d'obtenir des cartes 2D HETCOR, permettant de corréler les noyaux quadripolaires et les noyaux de spin-1/2.

3.1 Mesures de distances hétéronucléaires

Il existe deux façons de mesurer une distance hétéronucléaire dans les conditions MAS. La première consiste à appliquer le recouplage hétéronucléaire au noyau non observé, une seule fois au cours de la séquence, tandis que le noyau observé est soumis à un écho de spin. Cette stratégie n'est pas applicable pour les mesures de distance ^{13}C–^{14}N. Une autre possibilité consiste à scinder en deux la période de recouplage et à l'appliquer de part et d'autre d'une impulsion 180°. Cette stratégie est employée pour les expériences REDOR [167], REAPDOR [173] et RESPDOR [165]. Ces trois expériences se distinguent par l'impulsion appliquée sur le noyau non observé, afin d'éviter la refocalisation de l'interaction dipolaire hétéronucléaire. Les séquences REDOR, REAPDOR et RESPDOR utilisent respectivement des impulsions 180°, adiabatiques et de saturation.

La méthode REDOR ne convient généralement pas pour la mesure de distances entre noyaux de spin-1/2 et noyaux quadripolaires. En effet, l'allure de la courbe de déphasage dipolaire pour cette expérience dépend à la fois du couplage dipolaire et de l'interaction quadripolaire. Par conséquent, la mesure de la distance nécessite, à la fois, des simulations numériques de la dynamique de spin et des informations préalables sur le tenseur quadripolaire [174]. Pour la séquence REAPDOR, la condition d'adiabaticité doit être satisfaite, ce qui implique l'utilisation de champ rf intenses, notamment à haute vitesse et pour les sites subissant une interaction quadripolaire élevée. En outre, les courbes de déphasage dipolaire REAPDOR dépendent, faiblement, de l'interaction quadripolaire. L'expérience RESPDOR a l'avantage de ne pas être soumise aux contraintes de l'adiabaticité. Par conséquent, elle est applicable à haute vitesse, pour des noyaux subissant des interactions quadripolaires importantes et elle nécessite des champs rf plus faibles que les méthodes REAPDOR.

Notre contribution à ce domaine a consisté à associer la méthode RESPDOR, récemment introduite, avec le recouplage SR4_1^2 [30]. Cette nouvelle expérience, baptisée S-RESPDOR, combine les avantages du SR4_1^2 et du RESPDOR. En particulier, elle permet de mesurer des distances ^{13}C–X, où X est un noyau quadripolaire [31].

Nous avons aussi dérivé une expression analytique exacte décrivant la courbe de déphasage dipolaire S-RESPDOR [30]. Ceci a nécessité le calcul de la moyenne de poudre pour la séquence SR4_1^2, qui est non-γ-encodées et qui recouple la composante d'espace $m = 2$ de l'interaction dipolaire hétéronucléaire. Jusqu'ici, ces moyennes de poudre avaient été calculées pour des séquences non-γ-encodée recouplant la composante $m = 1$ et γ-encodée recouplant la composante $m = 1$ ou 2. Une expression générale des courbes RESPDOR, valable quelle que soit la valeur du spin du noyau quadripolaire, a été proposée [31]. Cette expression montre que la pente initiale et le maximum de la courbe de déphasage augmente lorsque la valeur du spin augmente.

Nous avons établi par des simulations et des expériences que la méthode S-RESPDOR est robuste au CSA, aux inhomogénéités de champ rf, qu'elle permet aussi de supprimer les couplages dipolaires ^{13}C–^{13}C et qu'elle peut être appliquée pour des constantes de couplage quadripolaire élevées. Son principal défaut reste sa sensibilité aux fluctuations de fréquence MAS, en raison de son absence d'encodage-γ [30].

La séquence S-RESPDOR a été, tout d'abord, employée pour mesurer des distances entre les atomes de carbone et d'azote. La mesure de ces distances est cruciale pour la caractérisation des systèmes biologiques. La méthode la plus employée pour mesurer ces distances consiste à estimer les couplages hétéronucléaires entre les noyaux de spin-1/2 ^{13}C–^{15}N. Cependant, comme l'abondance isotopique naturelle de l'azote-15 est de l'ordre de 0,4 %, les systèmes biologiques doivent être marqués en ^{15}N. Une possibilité, pour éviter ce marquage, consiste à utiliser l'isotope ^{14}N, qui a une abondance naturelle de 99,6 %. La méthode S-RESPDOR s'est révélée particulièrement utile pour mesurer les couplages ^{13}C–^{14}N entre des noyaux de spin-1/2 et de spin-1. Elle a, notamment, permis de mesurer des distances ^{13}C–^{14}N jusqu'à 3 Å dans L-[U-^{13}C]-histidine·HCl·H_2O. Les distances obtenues sont en accord avec celles obtenues par diffraction.

L'utilité de la méthode S-RESPDOR a aussi été démontrée pour la mesure de distance ^{13}C–^{17}O [31]. Il a été possible, dans ce cas, de mesurer une distance ^{13}C–^{17}O de 137 pm pour la L-[30 %-^{17}O^{4}]-tyrosine·HCl en abondance naturelle ^{13}C et enrichie à 30 % en ^{17}O. Bien que seul 0,3 % des molécules de L-tyrosine contribue au signal S-RESPDOR, la courbe de déphasage dipolaire a pu être enregistrée en un temps raisonnable (68 h).

3.2 Observations de proximités hétéronucléaires

Si les séquences de recouplage dipolaire hétéronucléaire permettent de mesurer les couplages hétéronucléaires et les distances associées, elles sont aussi très utiles pour réaliser des transferts de cohérence hétéronucléaire et ainsi corréler des isotopes différents. Ces techniques *D*-HETCOR facilitent l'attribution des spectres RMN et permettent d'obtenir des informations sur les proximités interatomiques. En outre, même si elles sont moins sélectives, les expériences *D*-HETCOR sont généralement plus efficaces que les méthodes *J*-HETCOR, puisque les couplages dipolaires sont souvent très supérieurs aux couplages *J*.

Différentes séquences D-HETCOR ont été proposées. Elles peuvent être classées en fonction du nombre de transferts de cohérence. Certaines, telles que la polarisation croisée [160] ou les séquences D-INEPT [175], utilisent un seul transfert de cohérence. Nous parlerons alors de détection directe. D'autres, telles que la double CP [176], la D-HMQC [177] ou la D-HSQC [178], utilisent deux transferts successifs. Nous parlerons alors de détection indirecte. La sensibilité relative des expériences D-HETCOR par détection directe ou indirecte dépend des caractéristiques des noyaux étudiés (rapport gyromagnétique, temps de relaxation T_1, largeur de raie) [176]. Néanmoins, la détection indirecte par l'intermédiaire des protons ou des fluors conduit généralement à des gains de sensibilité à haute vitesse.

Dans ce contexte, nous avons testé et développé de nouvelles méthodes D-HETCOR utilisant la détection indirecte. Ces séquences ont été appliquées pour la détection de noyaux quadripolaires par l'intermédiaire des protons ou des noyaux ^{31}P [29,32]. Nous avons tout d'abord comparé les performances des séquences D-HMQC et D-HSQC sans haute-résolution. L'étape suivante a consisté à obtenir la haute résolution pour le noyau quadripolaire en combinant les séquences D-HMQC et STMAS [32].

3.2.1 Détection indirecte des noyaux quadripolaires sans haute-résolution

Parmi les méthodes D-HETCOR utilisant la détection indirecte, les séquences D-HMQC et D-HSQC ont l'avantage d'employer des recouplages dipolaires basés sur l'irradiation d'un seul des isotopes couplés. Elles sont donc préférables pour la corrélation des noyaux quadripolaires et des noyaux de spin-1/2, puisqu'elles ne nécessitent pas l'application de champ rf pour manipuler les noyaux quadripolaires. Comme nous l'avons rappelé dans l'introduction, les recouplages monocanal les plus performants sont les séquences SFAM et $\mathrm{SR4}_1^2$.

Les méthodes D-HMQC et D-HSQC sélectionnent respectivement les cohérences simple- et multi-quantum durant la période d'évolution, t_1. Ainsi, les spectres 2D D-HSQC bénéficient en principe d'une meilleure résolution dans la dimension indirecte que les spectres 2D D-HMQC, puisque la vitesse de décroissance des cohérences simple-quantum est moins rapide que celle des cohérences multi-quantum. Cependant, la méthode D-HSQC classique nécessite un grand nombre d'impulsions et n'est donc pas adaptée au cas des noyaux quadripolaires. Des variantes de l'expérience HSQC employant un nombre limité d'impulsions ont été proposées pour corréler les noyaux de spin-1/2 et les noyaux quadripolaires [179, 180]. Nous avons comparé l'efficacité et la résolution des méthodes D-HMQC et D-HSQC comprenant un nombre limité d'impulsion. Les séquences de recouplages employées étaient SFAM-2 et $\mathrm{SR4}_1^2$.

Nous avons montré que la séquence D-HMQC conduit à une sensibilité plus élevée que l'expérience D-HSQC [29]. La sensibilité relative dépend de la position du recouplage (sur le canal observé ou indirect), du CSA du noyau détecté et de la position de la porteuse. Dans des conditions défavorables, l'expérience D-HSQC avec un nombre limité d'impulsions peut être jusqu'à deux fois moins sensible que l'expérience D-HMQC. En outre, pour les échantillons étudiés, la résolution des spectres 2D D-HSQC n'était pas supérieure à celle du spectre 2D D-HMQC. Nous recommandons donc l'utilisation de la séquence D-HMQC pour les expériences D-HETCOR impliquant un noyau quadripolaire.

Dans le cas où le noyau detecté est le proton, la séquence de recouplage doit être appliquée au noyau détecté, afin de diminuer l'effet des couplages dipolaires ^{1}H–^{1}H. Si le choix d'un recouplage adapté permet d'éliminer les couplages dipolaires ^{1}H–^{1}H pendant les périodes de recouplage, ces interactions ne sont pas complètement supprimées par le MAS durant les délais t_1 et t_2. Ces couplages résiduels diminuent la résolution spectrale dans les dimensions directe et indirecte du spectre 2D D-HMQC. L'élargissement, dans la dimension indirecte, provient de l'absence de commutation des hamiltoniens correspondant aux couplages homo- et hétéro-nucléaires. Nous avons montré qu'il est possible d'augmenter la résolution d'un facteur trois dans les deux dimensions en appliquant une séquence de découplage homonucléaire pendant les temps t_1 et t_2 [29]. Le découplage homonucléaire employé doit pouvoir s'accommoder de l'impulsion π appliquée également au proton au milieu du délai t_1 de la séquence D-HMQC. Nous avons montré qu'il est possible d'utiliser des séquences de symétrie $\mathrm{C}8_1^4$ dont l'élément cyclique de base, $\mathcal{C}$, correspond à la demi-période d'une fonction cosinus. Il est important toutefois de remarquer que l'utilisation d'une séquence de découplage homonucléaire, pendant le temps t_2, conduit à une diminution de la sensibilité, puisque le signal de précession libre n'est échantillonné que durant des fenêtres de courte durée.

Cette séquence D-HMQC avec découplage homonucléaire dans les deux dimensions spectrales a permis d'enregistrer le spectre 2D D-HECTOR ^{23}Na–^{1}H d'hydrogénophosphate (NaH_2PO_4). Ce spectre a permis l'attribution des signaux ^{23}Na à partir du spectre ^{1}H. Cette attribution a été confirmée par des calculs DFT utilisant le logiciel Quantum-ESPRESSO [181,182]. Si pour les protons, il y a un bon accord entre les déplacements chimiques isotropes calculés et expérimentaux, les calculs DFT pour les sites ^{23}Na sont moins précis. En particulier, les constantes de couplage quadripolaire calculées sont supérieures à celles mesurées expérimentalement. La recherche d'un meilleur accord nécessiterait une optimisation des pseudopotentiels ^{23}Na utilisés par Quantum-ESPRESSO.

3.2.2 Détection indirecte des noyaux quadripolaires avec haute-résolution

Pour les noyaux quadripolaires, les expériences D-HMQC et D-HSQC décrites dans la section 3.2.1 utilisent des impulsions sélectives pour manipuler la polarisation de la transition centrale $1/2 \leftrightarrow -1/2$. Ainsi, les spectres 2D D-HMQC présentent des pics de corrélation entre la fréquence de résonance des spins 1/2 et cette transition centrale, qui est élargie par l'interaction quadripolaire au second ordre. Cet élargissement peut masquer les informations sur les déplacements chimiques isotropes dans la dimension correspondant au noyau quadripolaire.

Pour éliminer cet élargissement quadripolaire du second ordre, il est nécessaire de combiner une technique D-HETCOR avec une séquence, telle que le MQMAS [183] ou le STMAS [165]. Jusqu'à présent, cette stratégie n'a été appliquée que dans le cas de la détection directe, en ajoutant à la fin des séquences MQMAS ou STMAS, un transfert par polarisation croisée [184, 185]. Pour bénéficier à la fois de la haute résolution pour la dimension quadripolaire et de la sensibilité de la détection indirecte par l'intermédiaire des isotopes de spin-1/2, nous avons introduit un filtre STMAS pendant le délai t_1 de la séquence HMQC [32]. Cette méthode, appelée HMQC-ST, permet l'acquisition de spectres 2D HETCOR haute-résolution entre les noyaux de spin-1/2 et de spin-3/2. Elle est applicable, en principe, pour des transferts de cohérences par le couplage J (J-HMQC-ST) ou le couplage dipolaire (D-HMQC-ST).

Le choix de la séquence HMQC s'explique par sa robustesse et son efficacité plus grande pour les noyaux quadripolaires que celle de la méthode HSQC (voir section 3.2.1). La recherche d'une sensibilité maximale pour cette nouvelle méthode a aussi présidé au choix d'un filtre STMAS. En effet, la technique STMAS est plus sensible que la méthode MQMAS, notamment pour les noyaux soumis à de fortes interactions quadripolaires [186]. De plus, les expériences STMAS peuvent fournir des informations sur les mouvements à l'échelle atomique [187].

Des calculs analytiques et numériques pour des spins 1/2 et 3/2 couplés ont permis de prédire les durées optimales des impulsions appliquées aux noyaux quadripolaires et des temps de défocalisation. Nous avons aussi calculé l'efficacité de ces séquences. Nous avons montré ainsi que l'efficacité de la méthode HMQC-ST augmente avec le champ rf appliqué au noyau quadripolaire. Pour des champs rf de 200 kHz, qui sont accessibles grâce aux sondes 1,3 mm, l'efficacité des expériences D-HMQC-ST atteint 76 % de celle de la D-HMQC classique, dépourvue de STMAS. En pratique, pour des sondes 1,3 mm, la sensibilité des expériences D-HMQC-ST est généralement supérieure à celle de la D-HMQC et ce, en raison de la diminution de largeur de raie dans la dimension quadripolaire pour la méthode HMQC-ST. Cette séquence D-HMQC-ST, utilisant des recouplages SFAM-2 ou $SR4_1^2$, a permis l'acquisition de spectres 2D D-HETCOR haute-résolution ^{23}Na–

^{1}Het ^{23}Na–^{31}P pour les composés Na_2HPO_4 et NaH_2PO_4 [32].

3.3 Perspectives

Une limitation générale des recouplages proposés est leur sensibilité aux fluctuations de vitesse du rotor. Ce problème peut être reglé soit en synchronisant la séquence de recouplage sur la détection optique de la rotation, soit en utilisant la vitesse instantanée du rotor pour calculer la durée des différents délais dans la séquence.

D'un point de vue méthodologique, il est aussi important de comparer les performances des séquences $\mathrm{R}12_3^5$, $\mathrm{SR}4_2^1$ et SFAM, et de préconiser dans quels cas, il est préférable de les employer. Les recouplages $\mathrm{R}12_3^5$ et $\mathrm{SR}4_2^1$ ont l'avantage d'être simples à utiliser, puisqu'ils ne comportent pas de paramètre ajustable. À l'inverse, les degrés de liberté supplémentaires offerts par les séquences SFAM, tels que la possibilité de varier le champ rf ou de balayer la fréquence de la porteuse, peuvent permettre d'exciter des noyaux soumis à des déplacements chimiques importants.

De façon plus fondamentale, nous pouvons nous demander quelle est la portée des méthodes de recouplage hétéronucléaire et combien de distances interatomiques, il est possible d'obtenir à partir d'une expérience de type REDOR ou RESPDOR. Les distances maximales mesurables par ces méthodes sont limitée par le temps de relaxation T_2' des noyaux observés durant l'écho de spin. Les couplages dipolaires résiduels ainsi que les couplages J homonucléaires contribuent à raccourcir le temps T_2' et à diminuer la portée de cette technique. En outre, ces interactions « parasites » diminuent la sensibilité de la méthode. Les séquences $\mathrm{R}12_3^5$, $\mathrm{SR}4_2^1$ et SFAM permettent de diminuer les couplages dipolaires homonucléaires. Néanmoins, elles ne les suppriment pas complètement et des recouplages hétéronucléaires plus sélectifs seraient utiles pour les mesures de distances impliquant des protons. Le déphasage dû aux couplages J homonucléaire peut être refocalisé notamment en appliquant une impulsion 180° sélective au noyau observé [188]. Ce type de stratégie peut être employé pour la séquence RESPDOR afin de mesurer des couplages dipolaires hétéronucléaires plus faibles que les couplages J homonucléaires.

Le nombre de distances mesurables par recouplage hétéronucléaire dépend du système de spin. Le cas le plus simple est celui où les noyaux observés, S, ne sont couplés qu'à un noyau non observé, I. Dans ce cas, il est possible de mesurer, a priori, autant de distances qu'il y a de signaux résolus dans le spectre des noyaux S. Un cas plus complexe est celui, où les noyaux S sont couplés à plusieurs noyaux I. Contrairement aux recouplages homonucléaires, les séquences $\mathrm{R}12_3^5$, $\mathrm{SR}4_2^1$ et SFAM ne sont pas soumises à la troncature dipolaire et l'aimantation d'un noyau S évolue sous l'effet de plusieurs couplages homonucléaires, quel que soit l'amplitude relative de ceux-ci. Cependant, malgré l'absence de troncature dipolaire, il n'est pas facile d'extraire, de la courbe de déphasage dipolaire, l'amplitude des différents couplages hétéronucléaires. En effet, l'allure de cette courbe dépend non seulement de l'amplitude des couplages, mais aussi de leur orientation relative. Une conséquence est qu'il n'existe pas de forme analytique pour les courbes de déphasage de ces systèmes de spin de type SI_N avec $N \in \mathbb{N}$ et $N \leq 2$. Différentes méthodes ont été proposées afin de simplifier ces courbes de déphasage [188–190]. Cependant, elles ne sont pas directement transposables pour l'expérience RESPDOR.

Un raisonnement hâtif pourrait laisser penser que des expériences 2D D-HMQC permettraient de séparer les mesures de distances des différentes paires hétéronucléaires. Cependant, ce n'est pas exact. En effet, l'intensité des pics de corrélation dépend de l'orientation relative des couplages dipolaires. Une difficulté supplémentaire pour les noyaux quadripolaires provient de l'utilisation d'impulsions sélectives. Dans ce cas, l'intensité des pics de corrélation dépend de l'interaction quadripolaire et ne peut être calculée que par des simulations numériques. Ainsi, les expériences D-HMQC et D-HMQC-ST ne peuvent fournir que des informations qualitatives sur les proximités interatomiques.

Une autre aspect du développement des recouplages hétéronucléaires consistera à démontrer la généralité des méthodes S-RESPDOR, D-HMQC et D-HMQC-ST en testant ces méthodes pour différents couples de noyaux. Il s'agira, en particulier, de tester les limites de ces séquences en terme de robustesse au CSA, au déplacement chimique et au couplage homonucléaire.

3.4 Articles

View Online

PAPER www.rsc.org/pccp | Physical Chemistry Chemical Physics

Measurement of hetero-nuclear distances using a symmetry-based pulse sequence in solid-state NMR†

Lei Chen,[a] Qiang Wang,[abc] Bingwen Hu,[bd] Olivier Lafon,[b] Julien Trébosc,[b] Feng Deng*[a] and Jean-Paul Amoureux*[b]

Received 15th December 2009, Accepted 12th April 2010
DOI: 10.1039/b926546e

A Symmetry-based Resonance-Echo DOuble-Resonance (S-REDOR) method is proposed for measuring hetero-nuclear dipolar couplings between two different spin-1/2 nuclei, under fast magic-angle spinning. The hetero-nuclear dipolar couplings are restored by employing the $SR4_1^2$ sequence, which requires the rf-field strength to be only twice the spinning frequency. The S-REDOR experiment is extended to S-RESPDOR (Symmetry-based Resonance-Echo Saturation-Pulse DOuble-Resonance) for determining dipolar coupling between a spin-1/2 nucleus (*e.g.* ^{13}C) and ^{14}N. It is demonstrated that S-REDOR and S-RESPDOR methods suppress efficiently the homo-nuclear dipolar interaction of the irradiated nucleus and benefit from high robustness to the rf-field inhomogeneity, chemical shielding and dipolar truncation. Therefore, these methods allow the measurement of ^{13}C/^{14,15}N distances, with ^{13}C observation, in uniformly ^{13}C-labeled samples. Furthermore, we provide analytical solutions for the S-REDOR and S-RESPDOR dephasing curves. These solutions facilitate the measurement of hetero-nuclear distances from experimental data.

I. Introduction

Solid-state nuclear magnetic resonance (NMR) has become an important tool for obtaining structural information on solids. In particular, the measurement of hetero-nuclear dipolar couplings allows determining distances between different isotopes. There are presently numerous recoupling methods for measuring hetero-nuclear dipolar couplings between two different spin-1/2 nuclei under magic-angle spinning (MAS). These methods are widely used for the structural characterization of biological systems.[1] For such applications, the measurement of carbon–nitrogen distances often plays a key role. The proximities between carbon and nitrogen atoms are generally assessed by determining ^{13}C–^{15}N hetero-nuclear couplings since both isotopes are spin-1/2 nuclei. However, the ^{15}N natural abundance is 0.4% and the sample must thus be ^{15}N enriched. An elegant alternative may consist of measuring ^{13}C–^{14}N hetero-nuclear couplings.[2–4] This approach could easily be employed since the ^{14}N natural abundance is 99.6%. However, ^{14}N is a low-gamma spin-1 quadrupolar nucleus.

The determination of hetero-nuclear couplings under MAS requires the use of recoupling techniques. A first possibility to restore the hetero-nuclear dipolar couplings consists of the radio-frequency (rf) irradiation of both isotopes. This approach is employed in cross-polarization (CP) and dual symmetry-based sequences.[5,6] However, these recoupling methods suffer from dipolar truncation and hence long-range inter-nuclear distances cannot be determined.[7] Furthermore, they are not applicable when one of the two isotopes is an integer-spin quadrupolar nucleus, such as ^{14}N.

Therefore, in this article, we will focus on recoupling sequences involving irradiation of only one of the two isotopes. These techniques comprise rotary resonance recoupling (R^3),[4,8–10] Rotational Echo DOuble Resonance (REDOR),[11] SFAM,[12,13] and RN_n^ν symmetry-based sequences,[14–16] such as $R18_2^5$, $R12_3^5$, $R20_5^9$, and $SR4_1^2$. The R^3 and $R18_2^5$ methods benefit from γ-encoding.[17–19] However, they both suffer from dipolar truncation, and the recoupled hetero-nuclear dipolar interactions do not commute with the recoupled chemical shift anisotropy (CSA).[16,20,21] Hence, the CSA interferes with the determination of hetero-nuclear coupling, especially at high-magnetic field (*e.g.* for ^{13}C). Another disadvantage associated with R^3 is its sensitivity to rf inhomogeneity.[13b]

The REDOR, SFAM, $R12_3^5$, $R20_5^9$ and $SR4_1^2$ sequences have the common property of accomplishing longitudinal two-spin order (I_zS_z) recoupling of the dipolar interaction.[6,12–14,16] Consequently, these methods do not suffer from dipolar truncation and CSA interference. However, the REDOR sequence has the disadvantage of recoupling the homo-nuclear dipolar interaction between the irradiated nuclei, especially when the π-pulse length is not negligible with respect to the

---

[a] State Key Laboratory of Magnetic Resonance and Atomic and Molecular Physics, Wuhan Center for Magnetic Resonance, Wuhan Institute of Physics and Mathematics, the Chinese Academy of Sciences, Wuhan 430071, China. E-mail: dengf@wipm.ac.cn; Fax: (86) 27-87199291; Tel: (86) 27-87198820
[b] Unit of Catalysis and Chemistry of Solids-UMR CNRS 8181, Lille-1 University, 59652 Villeneuve d'Ascq cedex, Lille, France. E-mail: jean-paul.amoureux@univ-lille1.fr; Fax: (33)3.20.43.68.14; Tel: (33)3.20.43.41.43
[c] Graduate School of the Chinese Academy of Sciences, Beijing, China
[d] Shanghai Key Laboratory of Magnetic Resonance, East China Normal University, 3663 Northern Zhongshan Road, Shanghai 200062, China

† Electronic supplementary information (ESI) available: Simulated signal fraction data; effect of rf field inhomogeneity; experimental REDOR signals for glycine; simulated REDOR signal fraction *versus* recoupling time; validity of eqn (9). See DOI: 10.1039/b926546e

rotor period, T_R.[22,23] Hence, when estimating ^{13}C–^{15}N distances in uniformly ^{13}C/^{15}N-labeled samples, REDOR pulses must be applied to the ^{15}N non-observed channel, in order to limit the interference of homo-nuclear dipolar couplings with hetero-nuclear distance determination. This is not possible when measuring ^{13}C–^{14}N distances and hence REDOR is definitely not the method of choice for ^{13}C–^{14}N hetero-nuclear recoupling in uniformly ^{13}C-labeled systems. An additional concern is related to the effect of finite π-pulse length on the REDOR dipolar dephasing curve.[21,24] The hetero-nuclear dipolar coupling constants determined by REDOR must be corrected by a scaling factor, which depends on the ratio between finite pulse length and T_R (Fig. S1 of the ESI†).[24]

Conversely, in the windowless recoupling sequences, SFAM, $R12_3^5$, $R20_5^9$ and $SR4_1^2$, the rf field is never turned off and the magnitude of the recoupled dipolar interaction is thus not affected by finite pulse effects. This allows decreasing the number of fitting parameters for the determination of inter-atomic distances. Furthermore, these four methods have the advantage of suppressing homo-nuclear dipolar couplings between the irradiated nuclei. The most efficient suppression of homo-nuclear dipolar coupling is achieved by SFAM$_2$ and $SR4_1^2$.[13b] Moreover, owing to their low rf requirements, both sequences are compatible with ultra-fast MAS. Here, we propose the use of $SR4_1^2$, which has less parameters to be optimized than SFAM$_2$, to recover ^{13}C–^{15}N and ^{13}C–^{14}N dipolar interactions under MAS.

The single-channel recoupling sequences, such as $SR4_1^2$, can be employed in different ways in order to measure hetero-nuclear dipolar couplings. A first possibility consists of applying a single incremented recoupling period to the non-observed nucleus, I.[14,16,25,26] This method cannot be used in the case of ^{13}C–^{14}N recoupling since the number of pulses applied to the ^{14}N quadrupolar nucleus must be minimized. Consequently, this method will not be considered in the following. Another possibility consists of splitting the recoupling sequence into two parts of equal duration.

This strategy is employed in REDOR[11,21,24] as well as in Rotary Resonance-Echo DOuble-Resonance (R-REDOR),[9] and Rotary Resonance-Echo Saturation-Pulse DOuble-Resonance (R-RESPDOR)[4] sequences. R-REDOR and R-RESPDOR methods employ R^3 as a recoupling scheme.

Split recoupling sequences can be applied either to the non-observed, I, or the observed, S, nucleus. Therefore, this implementation can be employed for the measurement of ^{13}C–^{14}N dipolar interactions.[2–4] For split recoupling periods, the S signal is usually observed as a spin-echo. Hence, the refocusing of the recoupled I–S dipolar interaction can be prevented by applying an additional I pulse simultaneously with the S π-pulse of the spin-echo. This additional I pulse is a π-pulse for $I = 1/2$, and either an adiabatic or a saturation pulse for $I = 1$. For instance, the adiabatic and saturation pulses are employed in Rotational-Echo Adiabatic-Passage DOuble-Resonance (REAPDOR)[2] and R-RESPDOR sequences,[4] respectively. A saturation pulse offers several advantages compared to an adiabatic pulse in the frame of ^{13}C–^{14}N recoupling. First, saturation pulses can be employed at high MAS frequencies and require moderate ^{14}N rf field. In contrast, adiabatic pulses are generally more difficult to achieve under fast MAS, especially for low-γ nuclei experiencing large quadrupole interaction, such as ^{14}N, since the adiabaticity condition

$$\alpha = \frac{\nu_1^2}{\nu_Q \nu_R} \gg 1 \qquad (1)$$

has to be fulfilled.[27] In eqn (1), α is the adiabaticity parameter, ν_1 the nutation frequency of the rf field, $\nu_Q = 3C_Q/\{2I(2I-1)\}$ the quadrupolar frequency with $C_Q = e^2qQ$ the quadrupolar coupling constant, and ν_R the MAS frequency. Second, the dipolar dephasing REAPDOR curve depends on the relative orientation between the quadrupolar and dipolar tensors and must thus be calculated in principle using numerical simulations.[3,28,29] Approximate analytical expressions of the REAPDOR curve can be employed for short recoupling times within fixed experimental conditions, but they have an inherent error associated with them.[30] Conversely, for certain recoupling sequences, such as $SR4_1^2$, the dipolar dephasing resulting from the application of a saturation pulse can be expressed by an exact analytical expression, which allows a rapid determination of the inter-nuclear distances (see eqn (11) and (16)).

In this article, we propose two new NMR methods, S-REDOR and S-RESPDOR, for measuring carbon–nitrogen distances in solid-state samples. These methods, which are inspired from R-REDOR[9] and R-RESPDOR,[4] incorporate the symmetry-based $SR4_1^2$ recoupling scheme instead of R^3. We demonstrate that S-REDOR allows the measurement of inter-nuclear distances for pairs of spin-1/2 nuclei. Compared to classical REDOR, the S-REDOR method is not affected by the finite pulse effect, and the suppression of homo-nuclear dipolar interactions by $SR4_1^2$ allows the application of the recoupling sequence to the observed nuclei. We also introduce the S-RESPDOR sequence to measure distances between a spin-1/2 and a ^{14}N nucleus. Compared to R-RESPDOR, the S-RESPDOR is more robust to rf inhomogeneity, does not suffer from dipolar truncation and CSA interferences and can be applied to fully ^{13}C-labelled biological samples. Moreover, we show that the S-REDOR and S-RESPDOR dephasing curves can be expressed by a universal REDOR-type function. This allows a rapid fitting of the experimental data to structural constraints.

II. Pulse sequences and theory

In the present article, the hetero-nuclear dipolar couplings were recovered under MAS by the use of $SR4_1^2$.[14] The basic recoupling block of $SR4_1^2$ consists of consecutive $R4_1^2$ $(\pi_y\pi_{-y}\pi_y\pi_{-y})$ and $R4_1^{-2}$ $(\pi_{-y}\pi_y\pi_{-y}\pi_y)$ blocks, each lasting one rotor-period T_R. This inversion super-cycle achieves the suppression of homo-nuclear dipolar interactions, hetero-nuclear scalar couplings and isotropic chemical shifts to the first order, while reintroducing the space component $m = 2$ of CSA and hetero-nuclear dipolar interactions. To better suppress the unwanted second-order cross-terms, an additional super-cycle can be applied by repeating the combined block $R4_1^2R4_1^{-2}$ three times with overall rf phase shift of 0°, 120° and 240°. When the $SR4_1^2$ sequence is applied to the S spin of an isolated hetero-nuclear *I*–*S* spin-pair, the first-order Average Hamiltonian (AH) is given by:

$$\bar{H}^{(1)} = 2\omega_{D,IS} I_z S_z + \omega_{CSA,S} S_z + \Omega_I^0 I_z + \bar{H}^{(2)}_{Q,I} \qquad (2)$$

where $\omega_{D,IS}$ is the magnitude of the recoupled *I*–*S* dipolar coupling, $\omega_{CSA,S}$ is the magnitude of the recoupled CSA_S of *S* spin, Ω_I^0 is the resonance offset frequency (isotropic chemical shift) of *I*-spin and $\bar{H}^{(2)}_{Q,I}$ is the Hamiltonian of second-order quadrupole interaction averaged by MAS (if its speed is fast enough).[31] This term is null in the case of spin-1/2 nucleus, whereas it produces a second-order shift for quadrupolar nucleus. The frequency $\omega_{D,IS}$ is given by:

$$\omega_{D,IS} = \frac{1}{4} b_{IS} \sin^2(\beta_{PR}^{D,IS}) \cos[2(\gamma_{PR}^{D,IS} + \alpha_{RL}^0 - \omega_R t_0)] \qquad (3)$$

where $\{\alpha_{PR}^{D,IS}, \beta_{PR}^{D,IS}, \gamma_{PR}^{D,IS}\}$ are the Euler angles relating the inter-nuclear vector $\boldsymbol{r}_{IS}$ to the MAS rotor-fixed frame. The dipolar coupling constant is equal to $b_{IS} = -\mu_0\hbar\gamma_S\gamma_I/4\pi(r_{IS})^3$ in SI units. t_0 refers to the starting point of the pulse sequence and α_{RL}^0 denotes the rotor angular position at time $t = 0$, which corresponds to the beginning of signal acquisition. Eqn (3) shows that $SR4_1^2$ sequence is non-γ-encoded since the magnitude of $\omega_{D,IS}$ depends on the Euler angle, $\gamma_{PR}^{D,IS}$.[18,19]

The $SR4_1^2$ sequence requires the rf-field strength to be only twice the spinning frequency: $\nu_1 = 2\nu_R$. This low rf-power requirement is compatible with the dipolar coupling measurement at high MAS frequencies. $SR4_1^2$ fulfills the condition $N = 2\nu$ of RN_n^ν sequences and then is called an "amplitude modulated" sequence, which renders this sequence robust with respect to rf-inhomogeneity.[32]

The properties of $SR4_1^2$ can be compared with those of the classical REDOR recoupling. When applied to the *S* spin of an isolated *I*–*S* spin pair, the REDOR recoupling produces a first-order AH identical to that of eqn (2). However, the REDOR sequence recouples the space component $m = 1$ of hetero-nuclear dipolar coupling and the expression of $\omega_{D,IS}$ differs between $SR4_1^2$ and REDOR. Moreover, for REDOR, the magnitude of recoupled *I*–*S* dipolar interaction depends on the π-pulse length.[21,24] In the limit of infinitely short π-pulses, the frequency $\omega_{D,IS}$ is given by:

$$\omega_{D,IS} = -\frac{\sqrt{2}}{\pi} b_{IS} \sin(2\beta_{PR}^{D,IS}) \cos[\gamma_{PR}^{D,IS} + \alpha_{RL}^0 - \omega_R t_0] \qquad (4)$$

REDOR also differs from $SR4_1^2$ by the fact that it reintroduces the *S*–*S* dipolar interactions for finite π-pulse lengths.

In order to measure inter-atomic distances, the $SR4_1^2$ recoupling must be incorporated in a spin-echo. In Fig. 1a,b, we have represented the S-REDOR pulse sequences for measuring hetero-nuclear dipolar coupling between two different spin-1/2 nuclei. The hetero-nuclear dipolar interaction and the CSA of the irradiated nucleus are recovered during the dipolar evolution period (τ), by applying the $SR4_1^2$ scheme either to the *I* (Fig. 1a) or *S* (Fig. 1b) spins. Because the $SR4_1^2$ sequence is non-γ-encoded, the magnitude of $\omega_{D,IS}$ depends on the initial time point t_0 of the pulse sequence. In the case of S-REDOR sequences displayed in Fig. 1, the first and the second recoupling periods must thus be rotor-synchronized, *i.e.*

$$t_0^{(2)} = t_0^{(1)} + \frac{\tau}{2} + kT_R \qquad (5)$$

where $t_0^{(1)}$ and $t_0^{(2)}$ denote the initial time points of the first and second recoupling periods respectively, τ/2 is a multiple of T_R and *k* is an integer. The relationship of eqn (5) ensures that the magnitude of $\omega_{D,IS}$ frequency is unchanged between the two recoupling periods. Here, we have chosen to separate the two recoupling periods by only two rotor periods ($k = 2$) to limit irreversible losses and J_{I-S} attenuation. The middle π-pulse in the *S* channel refocuses the CSAs by forming an echo at the beginning of data acquisition. When the π-pulse in the *I*-channel is omitted, the *I*–*S* dipolar interaction is refocused and this produces the reference signal (S_0). However, when the *I* π-pulse is applied, the states of *I* spins are reversed. This interrupts the refocusing of the hetero-nuclear dipolar interaction and results in a reduced signal (*S*). The difference signal, $\Delta S = S_0 - S$, is obtained by subtracting the reduced signal from the reference signal. The hetero-nuclear dipolar coupling constant can be extracted from the signal fraction ($\Delta S/S_0$). This fraction, which depends on the dimensionless $\lambda = \tau \cdot b_{IS}/(2\pi)$ parameter, is independent from the irreversible losses.

We derive below an analytical expression of the powder-averaged signal fraction $\Delta S/S_0$ for S-REDOR in the case of an isolated *I*–*S* spin-pair. For rotor-synchronized recoupling

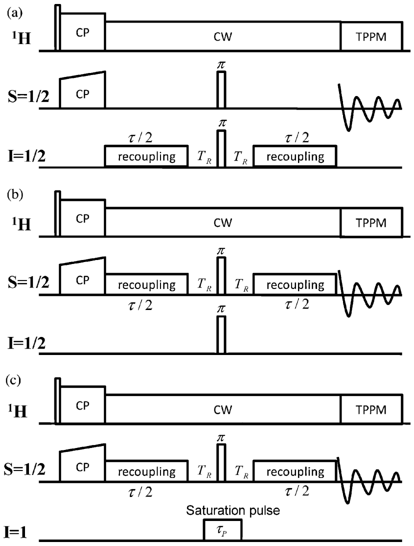

Fig. 1 S-REDOR (a,b) and S-RESPDOR (c) pulse sequences. These methods use $SR4_1^2$ as recoupling scheme. The dipolar evolution periods are rotor-synchronized. The distance determination requires the acquisition of two separate spin-echo signals as function of τ: the dipolar dephased signal, *S*, recorded with the pulse sequences displayed in the Figure, and the reference signal, S_0, recorded by omitting the *I* pulse in the middle of the dipolar evolution period.

periods, $\omega_{D,IS}$ remains the same and the signal fraction $\Delta S/S_0$ for S-REDOR is thus given by

$$\frac{\Delta S}{S_0} = 1 - \langle\cos(\omega_{D,IS}\tau)\rangle \tag{6}$$

where the frequency $\omega_{D,IS}$ is given by eqn (3) and the angular brackets denote an average over all orientations of the internuclear vector $\boldsymbol{r}_{IS}$. This "powder average" may be written explicitly as

$$\begin{aligned}\langle\cos(\omega_{D,IS}\tau)\rangle = \frac{1}{4\pi}\int_0^{2\pi} d\gamma_{PR}^{D,IS} \int_0^{\pi} d\beta_{PR}^{D,IS} \sin[\beta_{PR}^{D,IS}] \\ \times \cos\left\{\frac{\tau}{4} b_{IS}.\sin^2[\beta_{PR}^{D,IS}]\cos[2(\gamma_{PR}^{D,IS}+\xi)]\right\}\end{aligned} \tag{7}$$

where the constant angle ξ is defined by

$$\xi = \alpha_{RL}^0 - \omega_R t_0^{(1)}. \tag{8}$$

Analytical expressions for powder averaged NMR signals were derived for $m = 1$ non-γ-encoded recoupling sequence, such as REDOR[33] and SR26,[34] and for $m = 1$ or 2 γ-encoded recoupling sequences, such as POST-C7 and $R20_2^9$.[19] In the case of $SR4_1^2$, an $m = 2$ non-γ-encoded recoupling sequence, the powder average integral given by eqn (7) differs from those of REDOR and SR26 and cannot be calculated directly. Nevertheless, we show in the ESI,† that

$$\begin{aligned}\int_0^{2\pi} d\gamma \int_0^{\pi} d\beta \sin[\beta]\cos\{\theta\sin^2[\beta]\cos[2(\gamma+\xi)]\} \\ = \int_0^{2\pi} d\gamma \int_0^{\pi} d\beta \sin[\beta]\cos\{\theta\sin[2\beta]\cos[\gamma]\}\end{aligned} \tag{9}$$

Eqn (9) demonstrates that the orientational averages for $m = 1$ and $m = 2$ non-γ-encoded recoupling sequences have identical analytical expressions. To the best of our knowledge, such a result has only been proved in the case of γ-encoded recoupling.[19] Using eqn (9), the integral of eqn (7) can be written as

$$\begin{aligned}\langle\cos(\omega_{D,IS}\tau)\rangle = \frac{1}{4\pi}\int_0^{2\pi} d\gamma_{PR}^{D,IS} \int_0^{\pi} d\beta_{PR}^{D,IS} \sin\left[\beta_{PR}^{D,IS}\right] \\ \times \cos\left\{\frac{\tau}{4} b_{IS}.\sin[2\beta_{PR}^{D,IS}]\cos[\gamma_{PR}^{D,IS}]\right\}\end{aligned} \tag{10}$$

The integral of eqn (10) has been analytically calculated by Mueller using Bessel functions,[33] and the powder-averaged signal fraction $\Delta S/S_0$ for S-REDOR simplifies to the following form

$$\begin{aligned}\frac{\Delta S}{S_0} &= 1 - \frac{\pi\sqrt{2}}{4} J_{1/4}\left(\frac{\pi}{4} b_{IS}\tau\right) J_{-1/4}\left(\frac{\pi}{4} b_{IS}\tau\right) \\ &= 1 - S_d\left(\frac{\pi}{4\sqrt{2}} b_{IS}\tau\right)\end{aligned} \tag{11}$$

where $S_d(b_{IS}\tau)$ is the normalized dipolar-dephased signal intensity for classical REDOR experiment.[33] Eqn (11) establishes that the signal fraction curves of REDOR and S-REDOR are homothetic with a dipolar dephasing $\pi/(4\sqrt{2})$ slower for S-REDOR than for REDOR.

In the pulse sequence of Fig. 1b, the $SR4_1^2$ recoupling is only applied to the observed S spin. Therefore, the method can be easily extended to measure dipolar couplings between the S spin-1/2 and nearby quadrupolar nuclei. When the non-observed nucleus is ^{14}N, the π-pulse applied to the I spin can be replaced by a saturation ^{14}N pulse, as shown in Fig. 1c. A *complete saturation* ^{14}N pulse induces the ^{14}N population transfers indicated in Table 1. These population transfers result from zero-, single- and double-quantum transitions, having $|\Delta m_I| = 0$, 1 or 2, respectively.

In the case of *complete saturation*, all the population transfers reported in Table 1 are equiprobable. If the differences between thermal equilibrium populations of ^{14}N spin-states are neglected, the fractions of ^{14}N nuclei, which experience zero-, single- and double-quantum transitions during the saturation pulse, are thus equal to 1/3, 4/9 and 2/9, respectively. Furthermore, when a saturation pulse is applied to the ^{14}N channel, the ^{13}C transverse magnetization of a given ^{13}C–^{14}N spin-pair is dephased by $\Phi^{(1)} = \omega_{D,IS}\tau\cdot m_I^{\text{before}}$ during the first $\tau/2$ delay and by $\Phi^{(2)} = -\omega_{D,IS}\tau\cdot m_I^{\text{after}}$ during the second $\tau/2$ delay, where the frequency $\omega_{D,IS}$ is given by eqn (3). Therefore, when the ^{14}N nucleus experiences Δm_I transition, the explicit dipolar dephasing is given by:[3]

$$\Delta\Phi = \Delta m_I \omega_{D,IS}\tau\cdot \tag{12}$$

As in the S-REDOR experiment, the signal fraction is measured by two experiments, one with (S) and the other without (S_0) the saturation pulse. The contribution to S signal intensity of a specific ^{13}C–^{14}N spin pair is modulated by $\cos(\Delta\Phi)$, whereas the S_0 signal is not dephased by dipolar coupling. Consequently, in the case of *complete saturation*, the theoretical powder-averaged signal fraction for S-RESPDOR experiment is given by

$$\frac{\Delta S}{S_0} = \frac{2}{3} - \frac{4}{9}\langle\cos(\omega_{D,IS}\tau)\rangle - \frac{2}{9}\langle\cos(2\omega_{D,IS}\tau)\rangle \tag{13}$$

The orientational average in eqn (13) can be calculated as in S-REDOR experiments (eqn (7)–(11)). Finally, in the case of *complete saturation*, the powder-averaged analytical expression for S-RESPDOR experiment is given by:

$$\begin{aligned}\frac{\Delta S}{S_0} = \frac{2}{3} - \frac{\pi\sqrt{2}}{9} J_{1/4}\left(\frac{\pi}{4} b_{IS}\tau\right) J_{-1/4}\left(\frac{\pi}{4} b_{IS}\tau\right) \\ - \frac{\pi\sqrt{2}}{18} J_{1/4}\left(\frac{\pi}{2} b_{IS}\tau\right) J_{-1/4}\left(\frac{\pi}{2} b_{IS}\tau\right)\end{aligned} \tag{14}$$

III. Details of the experiments and simulations

All experiments were carried out on a wide bore 9.4 T Bruker Avance-II spectrometer (^{1}H, ^{13}C, ^{15}N and ^{14}N Larmor frequencies of 400.1, 100.6, 40.5 and 28.9 MHz, respectively) using a 3.2 mm triple resonance MAS probe. The NMR experiments were performed on samples of [2-^{13}C,^{15}N]-glycine and L-[U-^{13}C]-histidine·HCl·H$_2$O with 99% ^{13}C purity. For [2-^{13}C,^{15}N]-glycine, the ^{15}N purity was 98%. All samples were purchased from CortecNet and used without purification.

Table 1 Population transfers among ^{14}N spin states induced by a *complete saturation* ^{14}N pulse

$\|\Delta m_I\|^a$	0	1	2
Population transfers^b	$\|1,1\rangle \rightarrow \|1,1\rangle$ $\|1,0\rangle \rightarrow \|1,0\rangle$ $\|1,-1\rangle \rightarrow \|1,-1\rangle$	$\|1,1\rangle \rightarrow \|1,0\rangle$ $\|1,0\rangle \rightarrow \|1,1\rangle$ $\|1,0\rangle \rightarrow \|1,-1\rangle$ $\|1,-1\rangle \rightarrow \|1,0\rangle$	$\|1,1\rangle \rightarrow \|1,-1\rangle$ $\|1,-1\rangle \rightarrow \|1,1\rangle$
Fraction of nuclei^c	1/3	4/9	2/9

[a] Changes in ^{14}N quantum magnetic numbers are defined as $\Delta m_I = m_I^{\text{after}} - m_I^{\text{before}}$, where m_I^{after} and m_I^{before} are the m_I value after and before the ^{14}N saturation pulse. [b] Population transfers are denoted in the form $|I,m_I^{\text{before}}\rangle \rightarrow |I,m_I^{\text{after}}\rangle$. [c] Fractions of ^{14}N nuclei experiencing $|\Delta m_I|$ transition during the *complete saturation* ^{14}N pulse. These fractions are equal to the vertical sums of possible transfers related to the same change of quantum magnetic numbers Δm_I, divided by $9 = 3^2$.

The pulse sequences shown in Fig. 1 have been combined with a preliminary ramped CP to create the initial ^{13}C transverse magnetization. The CP contact time was 1.5 ms. The ^{13}C nutation frequency during CP was 45 kHz. The power of ^{1}H was optimized with a ramped shape. The rf field strength during the $SR4_1^2$ sequence was set to 32 and 20 kHz at the spinning frequency of ν_R = 16 and 10 kHz, respectively. The $SR4_1^2$ recoupling was applied either to the observed $S = {}^{13}$C or non-observed $I = {}^{15}$N channels. The ^{13}C and ^{15}N π-pulse lengths in the middle of the S-REDOR experiment were equal to 10 μs and 11 μs , *i.e.* rf nutation frequencies of $\nu_{1,\pi}$ (^{13}C) = 50 kHz and $\nu_{1,\pi}$ (^{15}N) = 45 kHz for ^{13}C and ^{15}N π-pulses. In the S-RESPDOR experiments, the duration τ_p of ^{14}N saturation pulse was set to one rotor period with ν_1 (^{14}N) = 50 kHz, and the ^{13}C refocusing π pulse-length was of 6.25 μs, *i.e.* $\nu_{1,\pi}$ (^{13}C) = 80 kHz. Continuous-wave (CW) and two-pulse phase-modulation (TPPM)[35] proton decoupling sequences were used with a ^{1}H rf field strength of 100 and 80 kHz during the dipolar evolution period and signal acquisition, respectively. The recycle delay was 4 s in all experiments. Additional experimental details are given in the Figure captions.

The simulations were performed using SIMPSON software (version 1.1.0).[36] The powder averaging was accomplished using 5760 orientations: 320 $\{\alpha_{MR},\beta_{MR}\}$-pairs × 18 γ_{MR}-angles. The 320 $\{\alpha_{MR},\beta_{MR}\}$-pairs, which relate the molecular and rotor frames, were selected according to the REPULSION algorithm.[37] NMR parameters (rf field and spinning speed) and spin interactions (dipolar and quadrupolar couplings and chemical shielding) of the spin systems are specified in the figure captions. In the simulations, the central π pulse-lengths were either negligible or of 6.25 μs, *i.e.* $\nu_{1,\pi}$ = 80 kHz. However, we have verified that results obtained with finite central π-pulse are quasi-identical to those obtained with ideal ones.

IV. Results and discussion

IV.1 S-REDOR

The properties of S-REDOR are analyzed by numerical simulations and experimental measurement of ^{13}C–^{15}N dipolar coupling. The performances of S-REDOR are compared to those of already reported methods, REDOR and R-REDOR.[9,11] In the R-REDOR experiment, we employ $R^3(n = 1)$ irradiation, where the rf nutation frequency of the irradiated spins is equal to the MAS frequency ($\nu_1 = \nu_R$).[8]

IV.1a Validation of analytical expression. The theoretical signal fraction calculated from eqn (11) was verified by comparison with numerical simulations. Fig. 2 shows the simulated variation of $\Delta S/S_0$ fraction as function of the dimensionless parameter $\lambda = \tau{\cdot}b_{IS}/(2\pi)$ for S-REDOR experiment on a ^{13}C–^{15}N spin-pair. There is an excellent agreement between numerical SIMPSON simulation and analytical expression (eqn (11)). Fig. 2 also shows the simulated signal fraction for REDOR experiment. As expected from eqn (11), the REDOR method requires a dipolar evolution period $\pi/(4\sqrt{2}) \approx 0.56$ shorter than that of S-REDOR in order to obtain an identical signal fraction. The simulated signal fraction curves of S-REDOR and REDOR were also compared to that of R-REDOR employing R^3 irradiation (Fig. S2†). As expected, REDOR and S-REDOR lead to smaller oscillations of the NMR signal *versus* τ than R-REDOR since REDOR and $SR4_1^2$ are non-γ-encoded, whereas R^3 is. More precisely, during R^3 the magnitude of $\omega_{D,IS}$ is independent from the Euler angle, $\gamma_{PR}^{D,IS}$, while the direction of effective field experienced by irradiated nucleus varies with $\gamma_{PR}^{D,IS}$.[21] The R-REDOR signal fraction could be described in terms of Fresnel functions.[19]

The validity of eqn (11) was also confirmed by measuring experimentally the $\Delta S/S_0$ ratio of an isolated ^{13}C–^{15}N spin pair. Fig. 3 shows the experimental signal fraction curves for [2-^{13}C,^{15}N]-glycine obtained by applying the $SR4_1^2$ scheme either to the observed (Fig. 3a) or the non-observed (Fig. 3b) channel. In both cases, the analytical expression fits well the experimental data, whatever the channel location of the $SR4_1^2$ recoupling. A single fit parameter, $b_{13C\alpha-15N}$, is required. For Fig. 3a and b, the best fit curves are obtained for $|b_{13C\alpha-15N}|$ = 909 and 886 Hz, respectively, which corresponds to a ^{13}C$_\alpha$–^{15}N distance of 1.50 and 1.51 Å, respectively. Thus, the $SR4_1^2$ location does not affect the distance measurement significantly. These distances obtained from S-REDOR are consistent with the distance estimate of 1.48 Å obtained by neutron diffraction.[38] These experimental results demonstrate the potential of S-REDOR for hetero-nuclear distance measurement. The validity of eqn (11) leads to a rapid determination of the inter-nuclear distance.

IV.1b Compatibility with high MAS frequency. The required rf field for $SR4_1^2$ recoupling is twice the MAS frequency, $\nu_1 = 2\nu_R$. This low rf requirement is fully compatible with the usual probe specifications, even at ultra-fast MAS (ν_R = 60–70 kHz). Furthermore, eqn (4) shows that the

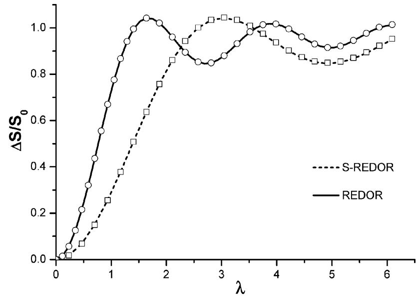

Fig. 2 Signal fraction $\Delta S/S_0$ of S-REDOR and REDOR as function of dimensionless parameter $\lambda = \tau \cdot b_{IS}/(2\pi)$. The dashed line represents the analytical solution, given in eqn (11), for S-REDOR signal fraction. The continuous line describes the analytical solution for REDOR signal fraction according to ref. 33. The SIMPSON simulated signal fraction for S-REDOR (square) and REDOR (circle) were calculated at $\nu_R = 16$ kHz for ^{13}C–^{15}N spin system with $b_{13C\text{–}15N}/(2\pi) = -937$ Hz. This dipolar coupling constant is typical for covalently bonded $^{13}C^{\alpha}$ and ^{15}N nuclei in amino-acids. The anisotropic chemical deshielding constant, δ_{aniso} (^{13}C), is equal to 3 kHz and η_{CSA} (^{13}C) = 0.5. The ^{15}N CSA was disregarded. The orientations of ^{13}C CSA tensor and ^{13}C–^{15}N dipolar interaction are characterized by $\Omega_{PC}^{CSA} = \{50°,20°,10°\}$ and $\Omega_{PC}^{13C\text{–}15N} = \{10°,20°,30°\}$, respectively. All simulations were carried out under a static magnetic field of 9.4 T. In numerical simulations, all REDOR π pulses are ideal, and the ^{13}C S-REDOR refocusing π pulse-length was of 6.25 μs, *i.e.* $\nu_{1,\pi}$ (^{13}C) = 80 kHz. The dipolar recoupling schemes were applied to the observed channel, $S = {}^{13}C$. The ^{13}C rf nutation frequency was 32 kHz during $SR4_1^2$ recoupling.

hetero-nuclear dipolar Hamiltonian restored by $SR4_1^2$ does not depend on the spinning speed and the location of the $SR4_1^2$ recoupling scheme: on the observed or non-observed channel, as can be observed in Fig. S3.†

Conversely, the magnitude of recoupled dipolar interactions during REDOR scheme depends on the π-pulse length.[21,24] Hence, the signal fraction curves depend on the ratio ν_1/ν_R, as illustrated by Fig. S1.† Owing to the limited rf power delivered by NMR probes and the duration of rf pulse transients, the shortest achievable π-pulses last a few μs (2.5 μs for $\nu_1 = 200$ kHz). This represents a significant fraction of the rotor period under ultra-fast MAS ($T_R = 15$ μs at $\nu_R = 65$ kHz). Therefore, at high MAS frequencies, the finite pulse effect is especially important and the ratio ν_1/ν_R must be specified in order to fit the REDOR signal fraction correctly.

IV.1c No CSA interferences. Hetero-nuclear dipolar recoupling sequences may suffer from CSA interferences. For instance, in the case of R-REDOR, the signal fraction curve is strongly affected by the relative orientation of the ^{13}C–^{15}N inter-nuclear direction and the CSA principal axes of the irradiated nucleus, as illustrated by Fig. S4.† Such CSA interferences complicate distance determination, if constraints about relative orientation are not available. These interferences result from the fact that in the effective Hamiltonian, the CSA terms of the irradiated nuclei do not commute with the hetero-nuclear dipolar interaction terms for R^3 recoupling.

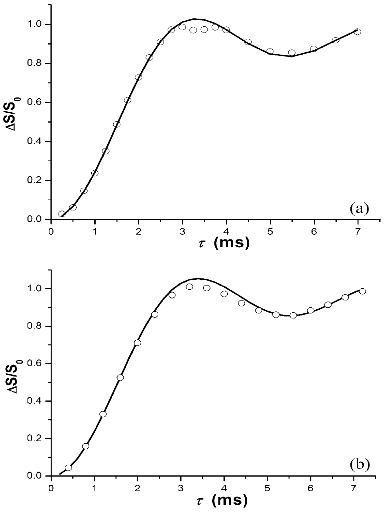

Fig. 3 Experimental signal fraction $\Delta S/S_0$ (○) of S-REDOR as function of τ for [2-^{13}C,^{15}N]-glycine. The lines refer to the best fit curves calculated according to eqn (11). The detected nucleus is $S = {}^{13}C$. The central ^{13}C and ^{15}N π pulse nutation frequencies were: $\nu_{1,\pi}$ (^{13}C) = 50 kHz , $\nu_{1,\pi}$ (^{15}N) = 45 kHz. The $SR4_1^2$ recoupling scheme was applied either (a) to the ^{13}C channel at $\nu_R = 16$ kHz with ν_1 (^{13}C) = 32 kHz, or (b) to the ^{15}N channel at $\nu_R = 10$ kHz with ν_1 (^{15}N) = 20 kHz.

Fig. S5 and S6† show that the CSA interferences are much smaller in the case of S-REDOR and REDOR, respectively. For such recoupling sequences, the hetero-nuclear dipolar interaction and CSA terms in the first-order AH commute since they are respectively proportional to I_zS_z and S_z when the recoupling scheme is applied to the S nucleus.[13,21] Furthermore, the numerically exact simulations of Fig. S5 and S6† demonstrate that S-REDOR is less sensitive to CSA interferences than REDOR. For the same reason, the simulations show that S-REDOR is very little sensitive to offsets, even when the recoupling sequence is applied to the observed nucleus.

IV.1d Suppression of homo-nuclear dipolar interaction. It is well-known that REDOR recouples the homo-nuclear dipolar interactions between the irradiated nuclei as long as the π pulse-length is not negligible with respect to the rotor period. These homo-nuclear dipolar interactions may interfere with the hetero-nuclear dipolar dephasing. For instance, in uniformly labeled ^{13}C biological samples, the largest ^{13}C–^{13}C dipolar coupling constants ($|b_{13C\text{–}13C}|/(2\pi) \approx 2.1$ kHz) exceed the largest ^{13}C–^{15}N ones ($|b_{13C\text{–}15N}|/(2\pi) \approx 1$ kHz). The only approach to avoid these interferences of homo-nuclear dipolar couplings consists of applying the REDOR π-pulses to the non-observed isotopes, usually $I = {}^{15}N$. However, the ^{15}N maximum rf-field is quite limited ($\nu_{1,15N} < 40$–50 kHz) due to low Larmor frequency, thus leading to long π-pulses, and the ^{13}C–^{15}N REDOR experiment is thus often used at small or moderate spinning speed. Conversely, the $SR4_1^2$ sequence suppresses the homo-nuclear dipolar interactions and thus can be applied either to the observed or to the non-observed channel. For instance, the SIMPSON simulations of Fig. S7† show that the signal fraction of S-REDOR is not affected by homo-nuclear dipolar interactions, even if the $SR4_1^2$ recoupling is applied to the observed spin $S = {}^{13}$C. This suppression of homo-nuclear dipolar coupling by $SR4_1^2$ is especially useful in the case of ^{13}C–^{14}N S-RESPDOR, because the ^{13}C–^{13}C interactions are much larger than the ^{13}C–^{14}N interactions.

IV.1e Robustness to rf inhomogeneity. We further investigated the effect of rf inhomogeneity on the S-REDOR experiment. Fig. S8b† shows the simulated signal fraction curves at ν_R = 16 kHz using rf field deviating by ±15% from the nominal $SR4_1^2$ rf nutation frequency, which is equal to $2\nu_R$. Similar numerical simulations at ν_R = 30 and 65 kHz are presented in Fig. S9 and S10, respectively.† Whatever the MAS frequency, the signal fraction shows little dependence on nutation frequency. The rf field variation only slightly affects the accuracy of the estimated dipolar coupling, and as an example, the fitted inter-nuclear distance only changes by 4% when the rf-field amplitude is changed by 15% (see caption of Fig. S8†). This robustness of S-REDOR to rf inhomogeneity results from its amplitude modulation character.[32] Experimentally the slight effect of rf field misadjustement is still weaker, as seen in Fig. S8a.† This may arise from the rf inhomogeneity inside the full rotor sample.

IV.1f Robust to MAS frequency instabilities. As $SR4_1^2$ is non-γ-encoded, the magnitudes of the recoupled dipolar and CSA interactions depend on the starting time point of the recoupling sequence, t_0 (eqn (4)). Therefore, for S-REDOR experiment, the second $SR4_1^2$ scheme must start an integer number of rotor periods after the end of the first one. Such rotor synchronization requires a high stability of the MAS frequency. This effect is very important when REDOR π-pulses are sent in the observed channel.[39] Fig. S11† shows the influence of MAS frequency misadjustment on the S_0 experimental reference signal of [2-^{13}C,^{15}N]-glycine. When the recoupling scheme is applied to the ^{13}C observed nucleus, a change in MAS frequency prevents the refocusing of CSA$_{13C}$ and ^{13}C–^{15}N dipolar coupling by the central ^{13}C π-pulse. This increases the signal damping and reduces the sensitivity of S-REDOR. Fig. S11 demonstrates that the detrimental effect of spinning speed fluctuations can only be reduced by applying the $SR4_1^2$ scheme to the ^{15}N non-observed channel. In that case, the loss of rotor-synchronization reintroduces the ^{13}C–^{15}N dipolar coupling and the CSA$_{15N}$. However, CSA$_{15N}$ does not dephase the ^{13}C single-quantum coherence. Hence, if possible, the recoupling scheme in S-REDOR should be applied to the non-observed channel.[13b] In practice, for S-REDOR, the spinning speed fluctuations must be lower than ±2–3 Hz in order to avoid sensitivity losses. On the contrary, with R-REDOR, the S_0 amplitude evolution is little dependent on these fluctuations, as seen in Fig. S12.† This better robustness results from the γ-encoding property of the R^3 scheme.

However, it is important to note that if the S_0 and S signal-to-noise ratios are strongly affected by spinning frequency fluctuations in S-REDOR experiment, the $\Delta S/S_0$ curve is less dependent on the ν_R value. Fig. S13† shows the signal fraction curves obtained at different spinning frequencies. The position of the first maximum only slightly varies with the MAS frequency, and the fitted inter-nuclear distance only changes by 3% when the spinning speed changes by ±15 Hz (see the caption to Fig. S13†). Therefore, the estimated dipolar coupling is weakly influenced by spinning speed variations, if they remain limited.

IV.2 S-RESPDOR

IV.2a Validation of analytical expression. Eqn (14) assumes a *complete saturation* of ^{14}N nucleus. However, low ^{14}N rf field and large C_Q values lead to incomplete saturation. In that case, the simplest model consists of assuming that the ^{14}N saturation pulse equalizes the ^{14}N energy levels of only a fraction of crystallites, f, whereas the other crystallites are not affected by the ^{14}N saturation pulse. Under such assumption, eqn (13) becomes

$$\frac{\Delta S}{S_0} = 1 - \left\{ f\left[\frac{1}{3} + \frac{4}{9}\langle\cos(\omega_{D,IS}\tau)\rangle + \frac{2}{9}\langle\cos(2\omega_{D,IS}\tau)\rangle\right] + 1 - f\right\} \tag{15}$$

The orientational averages in eqn (15) can then be replaced by their analytical expression and in case of *incomplete saturation* we obtain:

$$\frac{\Delta S}{S_0} = \left\{\frac{2}{3} - \frac{\pi\sqrt{2}}{9}J_{1/4}\left(\frac{\pi}{4}b_{IS}\tau\right)J_{-1/4}\left(\frac{\pi}{4}b_{IS}\tau\right) - \frac{\pi\sqrt{2}}{18}J_{1/4}\left(\frac{\pi}{2}b_{IS}\tau\right)J_{-1/4}\left(\frac{\pi}{2}b_{IS}\tau\right)\right\}f \tag{16}$$

The validity of eqn (16) was tested by SIMPSON simulations. Fig. 4 shows simulated signal fraction curves for the ^{13}C–^{14}N S-RESPDOR experiment. The analytical curves obtained from eqn (16) fit the simulated data quite well. The f fraction of saturated nuclei decreases globally with increasing C_Q value and decreasing ν_1 (^{14}N) rf-field (Table 2 and Table 3).

Besides vertical scaling by the factor f, large C_Q values also induce some deviation of simulated signal fraction from eqn (16). These distortions may affect the accuracy of the estimated dipolar coupling. In Table 3, are reported $b_{13C-14N}$ dipolar coupling constants estimated by fitting the simulated signal fraction of Fig. 4b to eqn (16). Large C_Q values result in the under-estimation of ^{13}C–^{14}N dipolar coupling constants. Nevertheless, the error on the dipolar coupling constant is below 5% and hence the estimated distance is artificially increased by 1.7%. Therefore, ^{13}C–^{14}N S-RESPDOR experiment allows the measurement of accurate carbon–nitrogen distance, even if the ^{14}N nuclei experiences large quadrupolar couplings. Moreover, it must be noted that the C_Q values in biological samples are mainly in the 1–2 MHz range.[40]

IV.2b Suppression of homo-nuclear dipolar interaction. We have performed SIMPSON simulations to compare the S-RESPDOR signal fraction of an isolated ^{14}N–^{13}C system with that of a ^{14}N–^{13}C–^{13}C′ system submitted to a large homo-nuclear

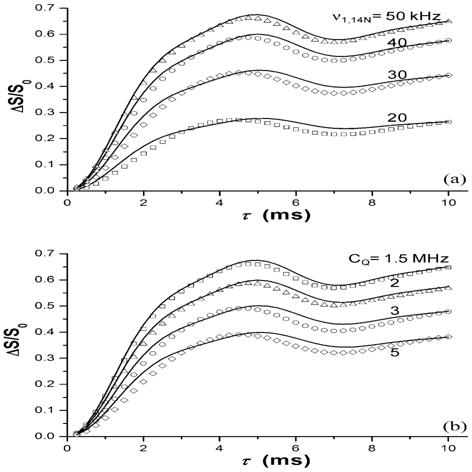

Fig. 4 Simulated ^{13}C–^{14}N S-RESPDOR signal fraction as function of the τ value. The solid lines are the best fits to eqn (16). The curves were calculated at ν_R = 16 kHz for ^{13}C–^{14}N spin system with $b_{13C-14N}/(2\pi)$ = −674 Hz. The ^{14}N asymmetry parameter is η_Q = 0.24. The anisotropic chemical de-shielding constant, δ_{aniso} (^{13}C), is equal to 8 kHz and η_{CSA} (^{13}C) = 0.5. The ^{14}N CSA was disregarded. The orientations of ^{13}C CSA tensor, ^{14}N quadrupolar tensor and ^{13}C–^{14}N dipolar interaction were characterized by the Euler angles, $\Omega_{PC}^{CSA,13C}$ = {50°,20°,10°}, $\Omega_{PC}^{Quadrupolar,14N}$ = {0°,0°,0°} and $\Omega_{PC}^{13C-14N}$ = {10°,20°,30°}, respectively. The $SR4_1^2$ irradiation is applied to the observed channel, S = ^{13}C, with a nutation frequency of 32 kHz. The delay between the two $SR4_1^2$ schemes is two rotor periods. The nutation frequency of the central ^{13}C π pulse is 80 kHz. The saturation ^{14}N pulse lasts one rotor period. (a) Signal fractions using different ^{14}N nutation frequencies, ν_1 (^{14}N) = 20 (□), 30 (◇), 40 (○) and 50 (△) kHz. The C_Q (^{14}N) value is 1.5 MHz. (b) Signal fractions using different ^{14}N quadrupolar coupling constant, C_Q = 1.5 (□), 2.0 (◇), 3.0 (○) and 5.0 (△) MHz. The nutation frequency of ^{14}N saturation pulse is 50 kHz.

Table 2 Influence of the ν_1 (^{14}N) value on the dipolar coupling constant estimated by fitting simulated ^{13}C–^{14}N S-RESPDOR signal fraction to eqn (16) The simulation parameters are those of Fig. 4a

ν_1 (^{14}N)/kHz	$b_{13C-14N,fit}/(2\pi)$/Hz	Error[a]	Distance/Å	f
50	659	2.2%	1.49	0.99
40	651	3.4%	1.50	0.88
30	645	4.2%	1.50	0.68
20	640	5.0%	1.51	0.41

[a] Error = (674 – $b_{13C-14N,fit}/2\pi$)/674.

dipolar interaction ($b_{13C-13C'} \approx 3b_{13C-14N}$) and a moderate ^{14}N quadrupole interaction (C_Q = 1.24 MHz, η_Q = 0.24). In the same way as for S-REDOR (Fig. S7†), both spin systems show similar S-RESPDOR fractions, with only slight deviations over very long evolution times (Fig. 5). This result demonstrates that $SR4_1^2$ recoupling efficiently suppresses ^{13}C–^{13}C dipolar interactions. Conversely to R-RESPDOR, the S-RESPDOR sequence can thus be applied to $^{13}C/^{14}N$ distance measurement in fully ^{13}C-labelled bio-molecules.

Table 3 Influence of the C_Q value on the dipolar coupling constant estimated by fitting the simulated ^{13}C–^{14}N S-RESPDOR signal fraction to eqn (16). Except for the C_Q value, the simulation parameters are identical to those of Fig. 4b

C_Q/MHz	$b_{13C-14N,fit}/(2\pi)$/Hz	Error[a]	Distance/Å	f
1.5	659	2.2%	1.49	0.99
2.0	650	3.6%	1.50	0.88
2.5	653	3.1%	1.50	0.80
3.0	646	4.2%	1.50	0.74
3.5	639	5.2%	1.51	0.64
4.0	642	4.7%	1.50	0.66
4.5	645	4.3%	1.50	0.60
5.0	641	4.9%	1.50	0.59

[a] Error = (674 – $b_{13C-14N,fit}/2\pi$)/674.

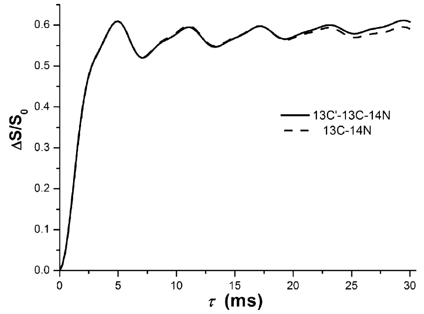

Fig. 5 Simulated ^{13}C–^{14}N S-RESPDOR signal fraction as function of the τ value. The dashed and solid lines correspond to the curves obtained for ^{13}C–^{14}N two-spin and $^{13}C'$–^{13}C–^{14}N three-spin systems. For the two-spin system, the dipolar coupling constant is $b_{13C-14N}/(2\pi)$ = −660 Hz, while for the three-spin system, the additional dipolar coupling constant is $b_{13C-13C'}/(2\pi)$ = −2 kHz. The three nuclei are aligned in the $^{13}C'$–^{13}C–^{14}N system and the dipolar coupling between $^{13}C'$ and ^{14}N is neglected. The C_Q (^{14}N) value is 1.24 MHz. The other simulation parameters are identical to those of Fig. 4. The anisotropic chemical deshielding constant, δ_{aniso} (^{13}C), is equal to 8 kHz and η_{CSA} (^{13}C) = 0.5. The ^{14}N CSA was disregarded. The orientations of ^{13}C CSA tensor, ^{14}N quadrupolar tensor and ^{13}C–^{14}N dipolar interaction were characterized by the Euler angles, $\Omega_{PC}^{CSA,13C}$ = {50°,20°,10°}, $\Omega_{PC}^{Quadrupolar,14N}$ = {0°,0°,0°} and $\Omega_{PC}^{13C-14N}$ = {10°,20°,30°}, respectively. The $SR4_1^2$ irradiation is applied to the observed channel, S = ^{13}C, with a nutation frequency of 32 kHz. The delay between the two $SR4_1^2$ schemes is two rotor periods. The nutation frequency of the central ^{13}C π pulse is 80 kHz. The saturation ^{14}N pulse with ν_1 (^{14}N) = 50 kHz lasts one rotor period.

IV.2c Experimental distance measurement by S-RESPDOR.

Fig. 6 shows experimental $^{13}C/^{14}N$ S-RESPDOR signal fraction for L-[U-^{13}C]-histidine. Owing to the robustness of $SR4_1^2$ to offset, the measurement of hetero-nuclear dipolar couplings between the amide ^{14}N nucleus and the C′ and C$^{\alpha}$ sites can be performed in a single S-RESPDOR experiment. This is advantageous compared to R-RESPDOR method, which requires separate experiments for C′ and C$^{\alpha}$ sites.[4] The experimental data of Fig. 6 can be fitted to eqn (16), neglecting long-range dipolar coupling with the ^{14}N nuclei of the imidazole ring. The best fit curves have the following parameters $b_{13C\alpha-14N}/(2\pi)$ = −635 Hz, $b_{13C'-14N}/(2\pi)$ = −185 Hz and f = 0.98. The high

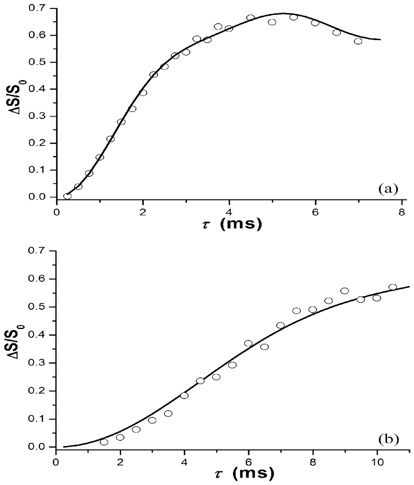

Fig. 6 Experimental $^{13}C/^{14}N$ S-RESPDOR signal fraction (○) for $^{13}C^{\alpha}$ (a) and $^{13}C'$ (b) sites of [U-^{13}C]-histidine·HCl·H_2O at ν_R = 16 kHz. The $SR4_1^2$ scheme with a nutation frequency of 32 kHz is applied to the observed ^{13}C nuclei. The nutation frequency of the central ^{13}C π-pulse is 80 kHz. The saturation ^{14}N pulse with ν_1 (^{14}N) = 50 kHz lasts one rotor period. The delay between the two $SR4_1^2$ schemes is two rotor periods. The solid lines are the best fits to eqn (16).

f value indicates an almost complete saturation in agreement with the moderate ^{14}N quadrupole interaction of amide nitrogen (C_Q = 1.24 MHz).[40] The estimated dipolar couplings lead to a C^{α}–N and C′–N distances of 1.51 and 2.29 Å, respectively. The C^{α}-N distance obtained from S-RESPDOR is close to the distance of 1.49 Å determined by neutron diffraction, whereas the NMR experiment yields a C′–N distance shorter by 0.18 Å compared to neutron diffraction.[41] This slight discrepancy between neutron diffraction and NMR estimate for C′–N distance might arise from long-range C′–N^{π} dipolar coupling. In fact, this coupling should be about 50 Hz, since the shortest C′–N^{π} distance in the crystal structure is 3.49 Å.[41]

V. Conclusion

We have developed two simple and robust double resonance experiments for measuring hetero-nuclear distances, using symmetry-based $SR4_1^2$ recoupling sequence. Our methods combine the $SR4_1^2$ sequence proposed by Brinkmann and Kentgens[14] with the R-REDOR and R-RESPDOR experiments proposed by Gan.[4,9]

The first method has been proposed in a slightly different way, and the $SR4_1^2$ sequence was then applied to the non-observed channel with a constant time experiment.[14] Moreover, the exploitation of the data was performed with ‘numerically exact simulations’ with a SIMPSON-type software.[14] The R-REDOR and R-RESPDOR sequences have been applied in a similar way to our methods.[4,9] However, these sequences are submitted to dipolar truncation, to CSA interferences, and to homo-nuclear dipolar interactions of the observed nucleus.[4,9] The S-REDOR method is similar to the C-REDOR method proposed by Chan and Eckert.[42] The only difference is that C-REDOR uses POST-composite rotor-synchronized symmetry-based recoupling sequence instead of $SR4_1^2$ for S-REDOR. This leads C-REDOR to be insensitive to homo-nuclear dipolar interactions (see Fig. 4 of ref. 42*a*), as S-REDOR. However, C-REDOR is slightly sensitive to rf-field inhomogeneity (see Fig. 4a of ref. 42*c*), more sensitive than S-REDOR to spinning speed fluctuations, and there is no analytical formulae for its signal fraction.

Our methods can be applied not only to pairs of spin-1/2 nuclei (S-REDOR) but also to spin systems including one quadrupolar nucleus (S-RESPDOR). Experiments measured for [2-^{13}C,^{15}N]-L-glycine and [U-^{13}C]-L-histidine·HCl·H_2O have demonstrated that our experimental results are in agreement with diffraction data. S-REDOR and S-RESPDOR sequences have the advantages of not being dipolar truncated, which allows the simultaneous determination of long and short $^{13}C/^{14,15}N$ distances. Moreover, owing to the use of the $SR4_1^2$ scheme, our sequences are little sensitive to rf-field inhomogeneity and homo-nuclear dipolar interactions, both specifications favoring the S/N ratio. The $SR4_1^2$ scheme also benefits from higher robustness to CSA and offset than the R^3 scheme. These advantages thus allow measuring $^{13}C/^{14,15}N$ inter-nuclear distances in fully ^{13}C labeled bio-molecules, even in case of long distances in multiple-spin systems. Moreover, S-REDOR and S-RESPDOR signal fractions only depend on the inter-nuclear distance and they are completely independent from the relative orientation of the inter-nuclear vector with respect to CSA and quadrupolar interactions. One great advantage of our sequences is that inter-nuclear distances, involving one quadrupolar nucleus, can also be determined by using an analytical expression. Moreover, it can be shown that there is a single general common analytical expression that works for all spin pairs, including or not quadrupolar nuclei.[43]

One common limitation of most hetero-nuclear distance measurement methods is related to *S*–*S* scalar couplings, which are not refocused. The *S* and S_0 signals are thus attenuated by these J_{S-S} scalar couplings, hence decreasing their signal to noise ratios, but the signal fraction ($\Delta S/S_0$) is not changed. This limitation, which is obviously important when measuring long hetero-nuclear distances, may be overcome either by using frequency-selective pulses,[44,45] or by combining Hahn and solid echoes.[46] The second common limitation concerns the analysis of multi-spin systems, for which it is difficult to extract quantitative distances. There are two ways to avoid this problem. The first one is to use a phase or amplitude modulated REDOR-type experiment.[47] The second is to use frequency-selective pulses to disentangle the dipolar interactions.[14,48,49] The application of these two types of methods to S-REDOR and S-RESPDOR will be presented in forthcoming articles.

One specific limitation of our methods is related to the spinning speed, which must be relatively well stabilized. When this is not the case, the S/N ratio deteriorates. One way to avoid this limitation may be to trigger all pulses with respect to the sample rotation. Another way is to directly introduce into the pulse sequence the instantaneous actual spinning speed instead of the desired one. The second specific limitation is related to the longer recoupling times of our sequences with respect to REDOR, *e.g.* $4\sqrt{2}/\pi \approx 1.8$ longer with S-REDOR. These longer recoupling times lead to larger losses and thus smaller S/N ratios. This effect decreases with increasing spinning speed and ^{1}H decoupling.

Globally, our combination of the $SR4_1^2$ sequence and double resonance experiments for distance determination complements the sequence proposed by Brinkmann and Kentgens,[14] the REDOR,[11] REAPDOR,[2] R-REDOR,[9] R-RESPDOR[4] and C-REDOR[42] experiments and is anticipated to become a useful tool for structural analysis in biological research. The S-RESPDOR ^{13}C–^{14}N distance determination can be combined with the analysis of the ^{1}H–^{13}C (^{14}N-edited) HETCOR spectrum, which only shows carbons that are close to ^{14}N atoms.[50]

Acknowledgements

The authors are grateful for funding provided by Region Nord/Pas de Calais, Europe (FEDER), CNRS, French Minister of Science, USTL, ENSCL, CortecNet and Bruker BIOSPIN. Financial support from the TGE RMN THC (FR-3050) for conducting the research is gratefully acknowledged. L. C. and F. D. thank the National Natural Science Foundation of China (10804122, 20773159, and 20933009) and the National Basic Research Program of China (2009CB918600) for financial support.

References

1 (*a*) C. P. Jaroniec, J. C. Lansing, B. A. Tounge, M. Belenky, J. Herzfeld and R. G. Griffin, Measurement of dipolar couplings in a uniformly ^{13}C,^{15}N-labeled membrane protein: distances between the Schiff base and aspartic acids in the active site of bacteriorhodopsin, *J. Am. Chem. Soc.*, 2001, **123**, 12929–12930; (*b*) L. M. McDowel, B. Poliks, D. R. Studelska, R. D. O'Connor, D. D. Beusen and J. Schaefer, Rotational-echo double-resonance NMR-restrained model of the ternary complex of 5-enolpyruvylshikimate-3-phosphate synthase, *J. Biomol. Nucl. Magn. Reson.*, 2004, **28**, 11–29; (*c*) A. T. Petkova, W. M. Yau and R. Tycko, Experimental constraints on quaternary structure in Alzheimer's β-amyloid fibrils, *Biochemistry*, 2006, **45**, 498–512; (*d*) S. L. Grace and A. Watts, Applications of REDOR for distance measurements in biological solids, *Annu. Rep. Nucl. Magn. Reson. Spectrosc.*, 2006, **60**, 191–228.

2 T. Gullion, Measurement of dipolar interactions between spin-1/2 and quadrupolar nuclei by rotational-echo adiabatic-passage double-resonance NMR., *Chem. Phys. Lett.*, 1995, **246**, 325–330.

3 (*a*) Y. Ba, H. M. Kao, C. P. Grey, L. Chopin and T. Gullion, Optimizing the ^{13}C–^{14}N REAPDOR NMR experiment: a theoretical and experimental study, *J. Magn. Reson.*, 1998, **133**, 104–114; (*b*) B. Kesling, E. Hughes and T. Gullion, ^{13}C–^{14}N REAPDOR and ^{13}C–^{2}D θ-REDOR NMR on a blend of tri-*p*-tolylamine and bisphenol-A-polycarbonate, *Solid State Nucl. Magn. Reson.*, 2000, **16**, 1–7; (*c*) T. Gullion, Measuring ^{13}C–^{2}D dipolar couplings with a universal REDOR dephasing curve, *J. Magn. Reson.*, 2000, **146**, 220–222; (*d*) E. Hughes, T. Gullion, A. Goldbourt, S. Vega and A. J. Vega, Inter-nuclear distance determination of $S = 1$, $I = 1/2$ spin pairs using REAPDOR NMR, *J. Magn. Reson.*, 2002, **156**, 230–241.

4 Z. Gan, Measuring multiple carbon–nitrogen distances in natural abundant solids using R-RESPDOR NMR., *Chem. Commun.*, 2006, 4712–4714.

5 E. O. Stejskal, J. Schaefer and J. S. Waugh, Magic-angle spinning and polarization transfer in proton-enhanced NMR, *J. Magn. Reson.*, 1977, **28**, 105–112.

6 A. Brinkmann and M. H. Levitt, Symmetry principles in the nuclear magnetic resonance of spinning solids: heteronuclear recoupling by generalized Hartmann–Hahn sequences, *J. Chem. Phys.*, 2001, **115**, 357.

7 M. Baldus and B. H. Meier, Broadband polarization transfer under magic-angle spinning: application to total through-space-correlation NMR spectroscopy, *J. Magn. Reson.*, 1997, **128**, 172–193.

8 T. G. Oas, R. G. Griffin and M. H. Levitt, Rotary resonance recoupling of dipolar interactions in solid-state nuclear magnetic resonance spectroscopy, *J. Chem. Phys.*, 1988, **89**, 692.

9 Z. Gan, Rotary resonance echo double resonance for measuring heteronuclear dipolar coupling under MAS, *J. Magn. Reson.*, 2006, **183**, 235–241.

10 Z. Gan, J. P. Amoureux and J. Trébosc, Proton-detected ^{14}N MAS NMR using homo-nuclear decoupled rotary resonance, *Chem. Phys. Lett.*, 2007, **435**, 163–169.

11 T. Gullion and J. Schaefer, Rotational-echo double-resonance NMR, *J. Magn. Reson.*, 1989, **81**, 196–200.

12 R. Fu, S. A. Smith and G. Bodenhausen, Recoupling of heteronuclear dipolar interactions in solid state magic-angle spinning NMR by simultaneous frequency and amplitude modulation, *Chem. Phys. Lett.*, 1997, **272**, 361–369.

13 (*a*) O. Lafon, Q. Wang, B. Hu, F. Vasconcelos, J. Trébosc, S. Cristol, F. Deng and J. P. Amoureux, Indirect detection via spin-1/2 nuclei in solid-state NMR spectroscopy: application to the observation of proximities between protons and quadrupolar nuclei, *J. Phys. Chem. A*, 2009, **113**, 12864–12878; (*b*) B. Hu, J. Trébosc and J. P. Amoureux, Comparison of several hetero-nuclear dipolar recoupling NMR methods to be used in MAS HMQC/HSQC, *J. Magn. Reson.*, 2008, **192**, 112–122.

14 A. Brinkmann and A. P. M. Kentgens, Proton-selective ^{17}O-^{1}H distance measurements in fast magic-angle-spinning solid-state NMR spectroscopy for the determination of hydrogen bond lengths, *J. Am. Chem. Soc.*, 2006, **128**, 14758–14759.

15 M. Carravetta, M. Eden, X. Zhao, A. Brinkmann and M. H. Levitt, Symmetry principles for the design of radiofrequency pulse sequences in the nuclear magnetic resonance of rotating solids, *Chem. Phys. Lett.*, 2000, **321**, 205–215.

16 A. Brinkmann and A. P. M. Kentgens, Sensitivity enhancement and heteronuclear distance measurements in biological ^{17}O solid-state NMR, *J. Phys. Chem. B*, 2006, **110**, 16089–16101.

17 N. C. Nielsen, H. Bildsoe, H. J. Jakobsen and M. H. Levitt, Double-quantum homo-nuclear rotary resonance: efficient dipolar recovery in magic angle spinning, *J. Chem. Phys.*, 1994, **101**, 1805–1812.

18 M. H. Levitt, Symmetry-based pulse sequences in magic-angle spinning NMR, in *Encyclopedia of Nuclear Magnetic Rresonance*, ed. D.M. Grant and R.K. Harris, John Wiley & Sons, Chichester, 2002, vol. 9.

19 G. Pileio, M. Concistre, N. McLean, A. Gansmüller, R. C. D. Brown and M. H. Levitt, Analytical theory of γ-encoded double-quantum recoupling sequences in solid-state NMR, *J. Magn. Reson.*, 2007, **186**, 65–74.

20 J. D. van Beek, R. Dupree and M. H. Levitt, Symmetry-based recoupling of ^{17}O-^{1}H spin pairs in magic-angle spinning NMR, *J. Magn. Reson.*, 2006, **179**, 38–48.

21 C. P. Jaroniec, Dipolar recoupling: heteronuclear, in *Encyclopedia of Magnetic Resonance*, ed. R. K. Harris and R. E. Wasylishen, John Wiley, Chichester, 2009.

22 J. M. Goetz and J. Schaefer, REDOR dephasing by multiple spins in the presence of molecular motion, *J. Magn. Reson.*, 1997, **127**, 147–154.

23 J. C. C. Chan and H. Eckert, Dipolar coupling information in multi-spin systems: application of a compensated REDOR NMR approach to inorganic phosphates, *J. Magn. Reson.*, 2000, **147**, 170–178.

24 C. P. Jaroniec, B. A. Tounge, C. M. Rienstra, J. Herzfeld and R. G. Griffin, Recoupling of hetero-nuclear dipolar interactions with rotational-echo double-resonance at high magic-angle spinning frequencies, *J. Magn. Reson.*, 2000, **146**, 132–139.

25 X. Zhao, M. Eden and M. H. Levitt, Recoupling of hetero-nuclear dipolar interactions in solid-state NMR using symmetry-based pulse sequences, *Chem. Phys. Lett.*, 2001, **342**, 353–361.

26 X. Zhao, J. L. Sudmeier, W. W. Bachovchin and M. H. Levitt, Measurement of NH bond lengths by fast magic-angle spinning solid-state NMR spectroscopy: a new method for the quantification of hydrogen bonds, *J. Am. Chem. Soc.*, 2001, **123**, 11097–11098.

27 C. P. Grey and A. J. Vega, Determination of quadrupole coupling constant of the invisible aluminium spins in zeolite HY with ^{1}H/^{27}Al TRAPDOR, *J. Am. Chem. Soc.*, 1995, **117**, 8232–8242.

28 (*a*) T. Gullion, Detecting ^{13}C-^{17}O dipolar interactions by rotational-echo adiabatic-passage double-resonance NMR, *J. Magn. Reson., Ser. A*, 1995, **117**, 326–329; (*b*) L. Chopin, S. Vega and T. Gullion, A MAS NMR method for measuring ^{13}C-^{17}O distances, *J. Am. Chem. Soc.*, 1998, **120**, 4406–4409; (*c*) M. Kalwei and H. Koller, Quantitative comparison of REAPDOR and TRAPDOR experiments by numerical simulations and determination of ^{1}H–^{27}Al distances in zeolites, *Solid State Nucl. Magn. Reson.*, 2002, **21**, 145–157; (*d*) S. Ganapathy, R. Kumar, L. Delevoye and J. P. Amoureux, Identification of distinct Brønsted acidic sites in zeolite mordenite by proton localization and ^{27}Al-^{1}H REAPDOR NMR, *Chem. Commun.*, 2003, 2076–2077.

29 A. Goldbourt, S. Vega, T. Gullion and A. J. Vega, Interatomic distance measurement in solid-state NMR between a spin-1/2 and a spin-5/2 using a universal REAPDOR curve, *J. Am. Chem. Soc.*, 2003, **125**, 11194–11195.

30 T. Gullion and A. J. Vega, Measuring dipolar couplings for $I = 1/2$, $S > 1/2$ spin pairs by REDOR and REAPDOR NMR, *Prog. Nucl. Magn. Reson. Spectrosc.*, 2005, **47**, 123–136.

31 A. Jerschow, From nuclear structure to the quadrupolar NMR interaction and high resolution spectroscopy, *Prog. Nucl. Magn. Reson. Spectrosc.*, 2005, **46**, 63–78.

32 M. H. Levitt, Symmetry in the design of NMR multiple-pulse sequences, *J. Chem. Phys.*, 2008, **128**, 052205.

33 (*a*) K. T. Mueller, Analytical solutions for the time evolution of dipolar-dephasing NMR signals, *J. Magn. Reson., Ser. A*, 1995, **113**, 81–93; (*b*) K. T. Mueller, T. P. Jarvie, D. J. Aurentz and B. W. Roberts, The REDOR transform: direct calculation of internuclear couplings from dipolar-dephasing NMR data, *Chem. Phys. Lett.*, 1995, **242**, 535–542.

34 P. E. Kristiansen, M. Carravetta, J. D. van Beek, W. C. Lai and M. H. Levitt, Theory and applications of super-cycled symmetry-based recoupling sequences: in solid-state NMR, *J. Chem. Phys.*, 2006, **124**, 234510–234519.

35 A. E. Bennett, C. M. Rienstra, M. Auger, K. V. Lakshmi and R. G. Griffin, Hetero-nuclear decoupling in rotating solids, *J. Chem. Phys.*, 1995, **103**, 6951–6958.

36 M. Bak, J. T. Rasmussen and N. C. Nielsen, SIMPSON: a general simulation program for solid-state NMR spectroscopy, *J. Magn. Reson.*, 2000, **147**, 296–330.

37 M. Bak and N. C. Nielsen, REPULSION: a novel approach to efficient powder averaging in solid-state NMR, *J. Magn. Reson.*, 1997, **125**, 132–139.

38 P. G. Jönsson and Å. Kvick, Precision neutron diffraction structure determination of protein and nucleic acid components. III. The crystal and molecular structure of the amino acid α-glycine, *Acta Crystallogr., Sect. B: Struct. Crystallogr. Cryst. Chem.*, 1972, **28**, 1827–1833.

39 (*a*) J. R. Garbow and T. Gullion, The importance of precise timing in pulsed, rotor-synchronous MAS NMR, *Chem. Phys. Lett.*, 1992, **192**, 71–76; (*b*) E. Hughes and T. Gullion, A simple, inexpensive, and precise magic angle spinning speed controller, *Solid State Nucl. Magn. Reson.*, 2004, **26**, 16–21.

40 (*a*) T. Giavani, H. Bildsoe, J. Skibsted and H. J. Jakobsen, A solid-state N-14 magic-angle spinning NMR study of some amino acids, *J. Magn. Reson.*, 2004, **166**, 262–272; (*b*) L. A. O'Dell and R. W. Schurko, Static solid-state N-14 NMR and computational studies of nitrogen EFG tensors in some crystalline amino acids, *Phys. Chem. Chem. Phys.*, 2009, **11**, 7069–7077.

41 H. Fuess, D. Hohlwein and S. A. Mason, Neutron diffraction study of L-histidine hydrochloride monohydrate, *Acta Crystallogr., Sect. B: Struct. Crystallogr. Cryst. Chem.*, 1977, **33**, 654–659.

42 (*a*) J. C. C. Chan, C-REDOR: rotational-echo double-resonance under very fast magic-angle spinning, *Chem. Phys. Lett.*, 2001, **335**, 289–297; (*b*) J. C. C. Chan and H. Eckert, C-rotational-echo double-resonance: hetero-nuclear dipolar recoupling with homonuclear dipolar decoupling, *J. Chem. Phys.*, 2001, **115**(13), 6095–6105; (*c*) F. C. Chou, S. J. Huang and J. C. C. Chan, Hetero-nuclear dipolar recoupling in multiple-spin system under fast magic-angle spinning, *J. Magn. Reson.*, 2009, **197**, 96–99.

43 X. Lu, L. Chen, Q. Wang, O. Lafon, J. Trébosc, F. Deng and J. P. Amoureux, Determination of distances between a spin-1/2 and a half-integer quadrupolar nucleus by solid-state NMR with S-RESPDOR method , submitted.

44 C. P. Jaroniec, B. A. Tounge, C. M. Rienstra, J. Herzfeld and R. G. Griffin, Measurement of ^{13}C–^{15}N distances in uniformly ^{13}C labeled biomolecules: J-decoupled REDOR, *J. Am. Chem. Soc.*, 1999, **121**, 10237–10238.

45 V. S. Bajaj, M. L. Mak-Jurkauskas, M. Belenky, J. Herzfeld and R. G. Griffin, DNP enhanced frequency-selective TEDOR experiments in bacteriorhodopsin, *J. Magn. Reson.*, 2010, **202**, 9–13.

46 A. K. Mehta and J. Schaefer, Rotational-echo double resonance of uniformly labeled ^{13}C clusters, *J. Magn. Reson.*, 2003, **163**, 188–191.

47 O. Liivak and D. B. Zax, Rotational-echo double-resonance in IS_N spin networks: deconvolution of multiple dipole–dipole couplings, *J. Chem. Phys.*, 2001, **115**(1), 402–409.

48 C. P. Jaroniec, B. A. Tounge, J. Herzfeld and R. G. Griffin, Frequency selective heteronuclear dipolar recoupling in rotating solids: accurate ^{13}C–^{15}N distance measurements in uniformly ^{13}C,^{15}N-labeled peptides, *J. Am. Chem. Soc.*, 2001, **123**, 3507–3519.

49 J. Trébosc, J. P. Amoureux, J. W. Wiench and M. Pruski, Simultaneous frequency-selective solid-state NMR analysis of internuclear distances and through-bond connectivities in the presence of quadrupolar nuclei, *Chem. Phys. Lett.*, 2003, **374**, 432–438.

50 J. P. Amoureux, Q. Wang, B. Hu, O. Lafon, J. Trébosc and F. Deng, Rapid analysis of isotopically unmodified amino acids by high-resolution ^{14}N-edited ^{1}H–^{13}C correlation NMR spectroscopy, *Chem. Commun.*, 2008, 6525–6527.

J. Phys. Chem. A **2009,** *113,* 12864–12878

Indirect Detection via Spin-1/2 Nuclei in Solid State NMR Spectroscopy: Application to the Observation of Proximities between Protons and Quadrupolar Nuclei

Olivier Lafon,*,† Qiang Wang,†,‡,§ Bingwen Hu,† Filipe Vasconcelos,† Julien Trébosc,† Sylvain Cristol,† Feng Deng,‡ and Jean-Paul Amoureux†

Unité de Catalyse et de Chimie du Solide (UCCS), UMR CNRS 8181, École Nationale Supérieure de Chimie de Lille, Université de Lille 1, Bâtiment C7, B.P. 90108, 59652 Villeneuve d'Ascq Cedex, France, State Key Laboratory of Magnetic Resonance and Atomic and Molecular Physics, Wuhan Center for Magnetic Resonance, Wuhan Institute of Physics and Mathematics, Chinese Academy of Sciences, Wuhan 430071, People's Republic of China, and Graduate School of the Chinese Academy of Sciences, Beijing, People's Republic of China

Received: June 30, 2009; Revised Manuscript Received: August 28, 2009

We present a comprehensive comparison of through-space heteronuclear correlation techniques for solid state NMR, combining indirect detection and single-channel recoupling method. These techniques, named *D*-HMQC and *D*-HSQC, do not suffer from dipolar truncation and can be employed to correlate quadrupolar nuclei with spin-1/2 nuclei. The heteronuclear dipolar couplings are restored under magic-angle spinning by applying supercycled symmetry-based pulse sequences (SR4_1^2) or simultaneous frequency and amplitude modulation (SFAM). The average Hamiltonian theory (AHT) of these recoupling methods is developed. These results are applied to analyze the performances of *D*-HMQC and *D*-HSQC sequences. It is shown that, whatever the magnitude of spin interations, *D*-HMQC experiment offers larger efficiency and higher robustness than *D*-HSQC. Furthermore, the spectral resolution in both dimensions of proton detected two-dimensional *D*-HMQC and *D*-HSQC spectra can be enhanced by applying recently introduced symmetry-based homonuclear dipolar decoupling schemes that cause a *z*-rotation of the spins. This is demonstrated by ^{1}H−^{13}C and ^{1}H−^{23}Na correlation experiments on L-histidine and NaH_2PO_4, respectively. The two-dimensional heteronuclear ^{1}H−^{23}Na correlation spectrum yields the assignment of ^{23}Na resonances of NaH_2PO_4. This assignment is corroborated by first-principles calculations.

1. Introduction

Two-dimensional (2D) heteronuclear correlation (HETCOR) nuclear magnetic resonance (NMR) spectroscopy is a valuable tool for the characterization and structural investigation of solid state compounds under magic-angle spinning (MAS). First, these methods facilitate spectral assignment owing to the improved resolution and information on the *J*-couplings or dipolar couplings. Second, the HETCOR experiments can also be employed to observe indirectly an isotope via a spy nucleus. In particular, such a strategy has been applied for the observation of integer (^{14}N) or half-integer (^{27}Al, ^{23}Na, ...) quadrupolar nuclei, $I > 1/2$, via nearby spin-1/2 spy nuclei.[1−11] Third, the HETCOR experiments allow probing the local environment of atoms, since the *J*-couplings and dipolar couplings reveal the through-bond connectivities and the through-space proximities, respectively. Hence the HETCOR methods using coherence transfers via the dipolar couplings (*D*-HETCOR) or via the *J*-couplings (*J*-HETCOR) are complementary. The *J*-HETCOR techniques help in identifying the molecular entities in solid state compounds, while the *D*-HETCOR methods can be used to establish their three-dimensional structures and to reveal the noncovalent intra- and intermolecular interactions (ionic and hydrogen bonds, π-stacking, ...).

A variety of *J*-HETCOR and *D*-HETCOR pulse sequences have been proposed so far. Figure 1 summarizes their main properties. The sequences are classified according to the mode of detection, direct or indirect, and the order of coherences during the t_1 evolution period. The *J*-HETCOR methods include the directly detected *J*-INEPT experiment[12,13] as well as the indirectly detected *J*-HSQC and *J*-HMQC schemes.[8,14−19] However, *D*-HETCOR experiments are generally more efficient than the *J*-HETCOR.[5−7,10,11] This arises from the large size of dipolar couplings, allowing the use of short recoupling times in *D*-HETCOR experiments. The *D*-HETCOR methods using direct detection comprise cross-polarization (CP)[20,21] or *D*-INEPT sequences.[22,23] The *D*-INEPT methods derives from the *J*-INEPT experiment, but heteronuclear dipolar recoupling techniques are applied during the defocusing and refocusing delays in order to restore the dipolar couplings under MAS. TEDOR sequence is an example of the *D*-INEPT method, where the employed dipolar recoupling method is REDOR.[24,25] However, indirect detection can enhance the sensitivity of *D*-HETCOR experiments, depending on the gyromagnetic ratios, γ, longitudinal relaxation times, T_1, and spectral line widths of the correlated nuclei.[26] In particular, inverse proton detection of ^{13}C and ^{15}N nuclei can become advantageous at high MAS frequency ($\nu_r \geq 30$ kHz).[26−31] The *D*-HETCOR methods employing indirect detection include consecutive CP transfers (denoted double CP),[26−31] heteronuclear multiquantum spectroscopy by dual symmetry-based pulse sequences,[32] and the *D*-HSQC and *D*-HMQC techniques.[5,6,23,33−35] The *D*-HSQC and *D*-HMQC experiments are adapted from *J*-HSQC and *J*-HMQC schemes, which are employed to characterize the chemical bonds in liquids and solids.[8,14−19]

In CP and dual symmetry-based pulse sequences, resonant radio frequency (rf) irradiation is applied to both spin species

---

[†] Université de Lille 1.

[‡] Chinese Academy of Sciences.

[§] Graduate School of the Chinese Academy of Sciences.

10.1021/jp906099k CCC: $40.75

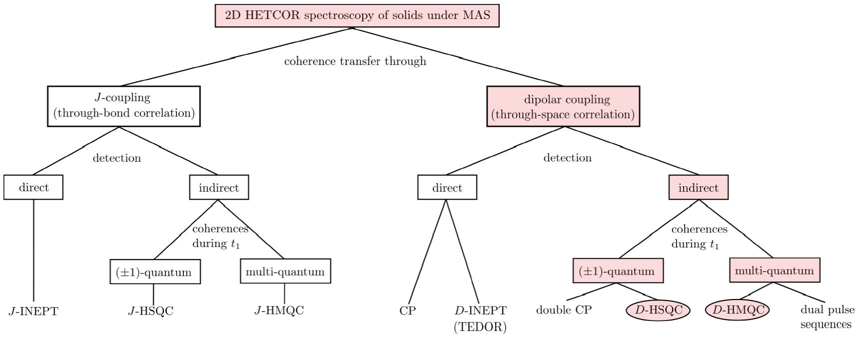

Figure 1. Schematic classification of 2D heteronuclear correlation NMR experiments, which can be employed to characterize solid state compounds under MAS condition. The paths corresponding to *D*-HMQC and *D*-HSQC sequences are highlighted.

I and *S* to achieve heteronuclear dipolar recoupling. However, the recoupled heteronuclear dipolar interactions do not commute for different pairs and these techniques suffer from dipolar truncation.[36,37] Hence the short-range dipolar couplings average the long-range ones, with the consequence that the long-range through-space proximities cannot be observed. Furthermore, CP and dual pulse sequences involving quadrupolar nuclei is a complicated process because of the difficulty to selectively rotate the central-transition polarization.[11,38] For these nuclei, multiple-pulse CP sequences outperform the continuous-wave CP transfer.[39] However, CP involving quadrupolar nuclei yields generally low sensitivity and is not robust to resonance offset and rf inhomogeneity.[40]

D-HSQC and *D*-HMQC methods alleviate these shortcomings. First, the dipolar recoupling sequences in *D*-HSQC and *D*-HMQC accomplish a *longitudinal two-spin-order* (I_zS_z) recoupling of the dipolar interactions.[32,41,42] This recoupled Hamiltonian commutes across different spin pairs and therefore does not suffer from dipolar truncation, allowing the observation of both short- and long-range correlations between heteronuclear spins. Second, longitudinal two-spin-order recoupling can be generated by the application of rf fields to only one of the spin species, which can be either the undetected spins (*I*) or the detected ones (*S*). This is clearly an advantage when using *D*-HMQC or *D*-HSQC experiments to correlate quadrupolar and spin-1/2 nuclei, since the number of pulses sent on the quadrupolar channel can be minimized by applying the heteronuclear recoupling sequences to the spin-1/2 nucleus.

The difference between *D*-HMQC and *D*-HSQC techniques lies in the order of coherences evolving during the t_1 period and in the number of rf pulses. Multiple-quantum (MQ) and single-quantum (1Q) coherences are selected during t_1 by *D*-HMQC and *D*-HSQC, respectively. Thus, in *D*-HSQC, the F_1 spectral dimension is immune to both homogeneous and inhomogeous decays of the coherence of the spy nucleus during the t_1 period. Consequently, the 1Q scheme can provide higher resolution than the MQ scheme.[8,9,17] This possible gain in resolution comes at the expense of a larger number of rf pulses, which may decrease the sensitivity especially in the case of quadrupolar nuclei. Nevertheless, variants of HSQC with limited number of pulses have been proposed in solids.[8,9] They are especially suitable for *D*-HETCOR involving quadrupolar nuclei, since they allow decreasing the number of pulses applied to the quadrupolar spins. The performances of *D*-HMQC and *D*-HSQC also depend on the choice of the heteronuclear recoupling sequence. Different longitudinal two-spin-order recoupling methods with single channel irradiation can be employed, including REDOR,[24,25] rotary resonance recoupling (R^3),[43−46] simultaneous frequency and amplitude modulation (SFAM),[35,47,48] and symmetry-based sequences, e.g., $R12_3^5$, $R20_5^9$, and $SR4_1^2$.[7,32,41,49] We have recently demonstrated that $SR4_1^2$ and SFAM sequences provide higher efficiency and robustness to rf inhomogeneity or maladjustment than the other recoupling schemes.[35] Nevertheless, the robustness to resonance offset and the effect of the position of the recoupling sequence—in the undetected or detected channels—have not been investigated so far.

In this contribution, we will compare the performances of *D*-HMQC and *D*-HSQC experiments in solids, with a view to employing these techniques in order to correlate a quadrupolar nucleus with a spin-1/2 nucleus. Hence, only *D*-HSQC sequences with restricted numbers of pulses will be considered. Furthermore, only $SR4_1^2$ and SFAM sequences will be employed as heteronuclear recoupling methods. In particular, we will analyze in detail how the position of the heteronuclear recoupling sequence affects the efficiency and the robustness of *D*-HMQC and *D*-HSQC. We will also demonstrate that, in the case of inverse proton detection, the spectral resolution in both dimensions F_1 and F_2 can be improved by applying the recently introduced $C8_1^4$(half-cos) homonuclear decoupling scheme.[10,50,51] In the following, the indirectly detected spin is denoted *I* and the detected spy spin *S*. We refer to the *D*-HMQC and *D*-HSQC experiments involving $S \rightarrow I \rightarrow S$ polarization transfers as "*I*−*S*".

This article is organized as follows. Section 2 will introduce the zero-order average Hamiltonian (AH) theory of the *D*-HMQC and *D*-HSQC pulse sequences.[52,53] The analytical predictions will be tested by numerical simulations. In section 3, experimental results will be presented. The dependence of *D*-HMQC and *D*-HSQC sensitivity with offset will be illustrated by experiments on glycine. The properties of *D*-HMQC and *D*-HSQC methods will be also compared in 2D $^{13}C-^{1}H$ and $^{23}Na-^{1}H$ correlation experiments on L-histidine and NaH_2PO_4. We show how *D*-HMQC experiment incorporating the $C8_1^4$(half-cos) decoupling scheme permits the assignment of ^{23}Na resonances of NaH_2PO_4. This assignment will be supported by periodic density functional theory (DFT) calculations.[54]

2. Theory

2.1. *D*-HMQC and *D*-HSQC Pulse Sequences. The basic pulse sequences for *D*-HMQC and *D*-HSQC experiments are shown in Figure 2a and 2b, respectively. The indirectly detected

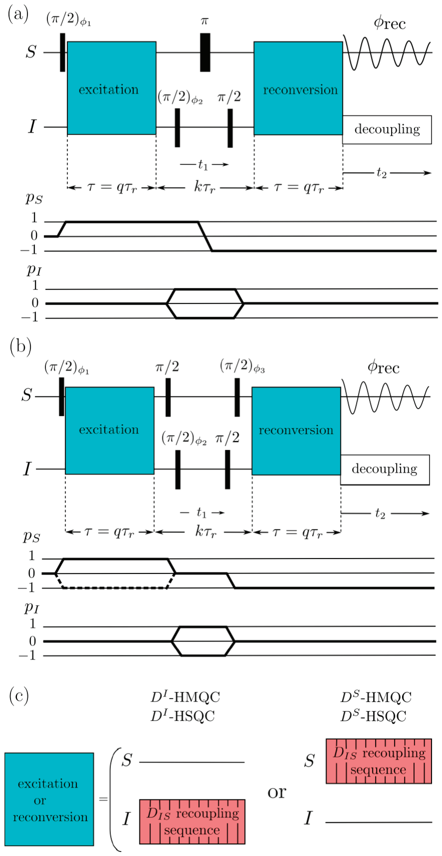

Figure 2. Pulse sequences and coherence transfer pathways for (a) *D*-HMQC and (b) *D*-HSQC experiments. In (b), two coherence transfer pathways are shown during excitation period. *D*-HSQC(±1) experiment allows both pathways, while *D*-HSQC(+1) variant only selects the one shown as a continuous line. Coherence pathways were selected by the following phase cyclings: (i) for *D*-HMQC, $\phi_1 = \pi/2(\text{floor})(m_c/2)$, $\phi_2 = \pi m_c$, and $\phi_{\text{rec}} = -\phi_1 - \phi_2$, where m_c denote the phase cycle counter; (ii) for *D*-HSQC(±1), $\phi_1 = \pi(\text{floor})(m_c/2)$, $\phi_2 = \pi m_c$, $\phi_3 = \pi/2(\text{floor})(m_c/4)$, and $\phi_{\text{rec}} = -\phi_1 - \phi_2 + \phi_3$; (iii) for *D*-HSQC(+1), $\phi_1 = \pi/2(\text{floor})(m_c/2)$, $\phi_2 = \pi m_c$, $\phi_3 = \pi(\text{floor})(m_c/8)$, and $\phi_{\text{rec}} = -\phi_1 - \phi_2 + \phi_3$. Quadrature detection in indirect dimension was achieved using the States-TPPI procedure[56] by incrementing the phase ϕ_2. (c) During τ intervals, heteronuclear dipolar recoupling sequences are used to recover the heteronuclear dipolar interaction. These sequences can be applied to either the undetected (*I*) or detected (*S*) spins.

spin is denoted *I* and the detected spy spin *S*. These experiments exploit *IS* dipolar couplings, D_{IS}, for the transfers of coherence from spin *S* to *I* and back. The heteronuclear D_{IS}-couplings are restored under MAS by applying heteronuclear dipolar recoupling techniques during the excitation and reconversion delays, τ. Thus, during the first τ, the *S*-spin magnetization for a pair of coupled *IS* spins evolves from in-phase (S_x) into antiphase ($2I_zS_y$) coherence with respect to *I*. In the *D*-HMQC experiment [see Figure 2a], this antiphase *S*-spin 1Q coherence is converted into a heteronuclear MQ coherence ($2I_xS_y$) by the $(\pi/2)_{\phi_2}$ pulse on the *I* channel, while in the *D*-HSQC experiment [see Figure 2b] two simultaneous $\pi/2$ pulses applied on both channels transform this antiphase *S*-spin 1Q coherence into an antiphase heteronuclear 1Q *I*-spin coherence ($2I_xS_z$). The isotropic chemical shift, δ^I_{iso}, *I* nucleus is then encoded by allowing these MQ or 1Q coherences to evolve during the indirect evolution time, t_1. For an *I*-spin experiencing quadrupolar interaction, the peak resonance frequency along the indirect dimension is shifted from the δ^I_{iso} value by the quadrupolar isotropic shift, ν^I_{QIS}.[55] In principle, an additional π pulse on the *S* channel can be inserted in the middle of the t_1 period of the *D*-HSQC experiment in order to refocus the isotropic heteronuclear *J*-couplings, J_{IS}, between *S*- and *I*-spins. However, this π *S*-pulse is not always essential in solids, since the J_{IS}-couplings are generally much smaller than the line widths in F_1 dimension.[8,9] This prevails especially for the indirect observation of quadrupolar nuclei.

At the end of t_1, the MQ and 1Q coherences are converted back into antiphase *S*-spin coherences by the $\pi/2$ pulses, and these coherences evolve during the second τ to become observable transverse *S*-spin magnetization. A 2D Fourier transform of the time domain signal provides isotropic shift correlations between pairs of *I* and *S* nuclei.

For half-integer spin quadrupolar nuclei, only correlations involving the central transition (CT) −1/2 ↔ 1/2 are observed in 2D *D*-HMQC and *D*-HSQC spectra. The central transition is not broadened by the first-order quadruprolar interaction. The CT polarizations are excited and rotated by using CT selective rf pulses. When the *S* spin is half-integer and experiences quadrupolar interaction, the anisotropic second-order terms of quadrupolar interaction must be averaged out by combining MAS and rotor synchronization of the delay between the centers of the first and the second *S*-pulses as well as the delay between the center of the last *S*-pulse and the start of the acquisition period, t_2, in both HMQC and HSQC sequences.[23] Integer spin quadrupolar nuclei, such as ^{14}N, are generally indirectly detected. In that case, the t_1 period, defined as the interval between the centers of the two pulses on the *I* channel, must be an integer multiple of the rotor period for the complete averaging of the first-order quadrupolar interaction.[4]

The quadrupolar interaction also affects the *D*-HMQC and *D*-HSQC efficiencies since it complexifies the spin dynamics during the rf pulses. However, for the indirect detection of quadrupolar nuclei via protons, the quadrupolar interaction does not modify the relative efficiency of *D*-HMQC and *D*-HSQC experiments, since the *I*-spins are subjected to the same rf pulses in both sequences [see Figure 2a,b].

2.2. Heteronuclear Dipolar Recoupling. In this work, we applied either SR4_1^2 or SFAM recoupling techniques during the τ delays in order to restore the dipolar D_{IS}-couplings. These rotor-synchronized sequences have common properties. First, they accomplish heteronuclear dipolar recoupling by irradiating only one of the isotopes, either *I*- or *S*-spins. Thus, for correlation between quadrupolar and spin-1/2 nuclei, the SR4_1^2 or SFAM sequences can be applied only to the spin-1/2 nuclei. This allows avoiding interferences between quadrupolar interaction and rf field. Second, these recoupling sequences are not γ-encoded[42,57] and hence the interval between the excitation and reconversion delays must be an integer multiple of the rotor period, $k\tau_r$, as shown in Figure 2a,b. Third, these recoupling sequences applied on a single rf channel recouple the chemical shift anisotropy (CSA) interactions of the irradiated spins at the same time as the heteronuclear D_{IS} interactions, since these terms evolve identically under sample rotation and rf irradiation of a single spin. However, the recoupled terms of the CSA and the heteronuclear D_{IS}-couplings commute. Therefore, the evolution of spin coherences due to the D_{IS}-couplings is not affected by the CSA of irradiated spins. Additional features of these sequences are summarized below.

2.2.1. SR4_1^2 Recoupling. The SR4_1^2 pulse sequence is constructed from the symmetry-based R4_1^2 sequence employing a single 180_0 pulse as a basic element.[49] Here β_ϕ indicates a rectangular, resonant rf pulse with flip angle β and phase ϕ (both in degrees). The basic R4_1^2 sequence, which consists of four 180° pulses, spans one rotor period and requires the rf field strength to be twice the spinning frequency. A nested supercycle is constructed by first forming a phase inversion sequence R4_1^2R4_1^{-2} and subsequently applying a three-step MQ-phase cycling. The SR4_1^2 pulse sequence can be denoted (R4_1^2R4_1^{-2})3^1.

Consider the case where the SR4_1^2 sequence is applied to the I-spins. The symmetry-based selection rules entail that the zero-order AH, $\bar{\mathscr{H}}^{(0)}$, contains D_{IS}-couplings, CSA of the I-spin, CSA$_I$, chemical and quadrupolar isotropic shifts of the S-spin, δ_{iso}^S and ν_{QIS}^S, and homonuclear isotropic J-couplings, J_{II} and J_{SS}, while all the terms of the homonuclear dipolar couplings between I-spins, D_{II}, δ_{iso}^I shifts, and J_{IS}-couplings between I- and S-spins are suppressed to zero order. Thus the $\bar{\mathscr{H}}^{(0)}$ Hamiltonian of a heteronuclear I_2S spin system during R4_1^2R4_1^{-2} or SR4_1^2 irradiation can be written

$$\bar{\mathscr{H}}^{(0)} = \left(\sum_{j=1,2} \omega_{D,jS} I_{jz} S_z + \omega_{\mathrm{CSA},j} I_{jz}\right) + 2\pi J_{II} I_1 I_2 + \Omega_S^0 S_z + \bar{\mathscr{H}}_{\mathrm{Q},S}^{(2)} \quad (1)$$

The $\bar{\mathscr{H}}^{(0)}$ Hamiltonian results from averaging over an even number of rotor periods. In eq 1, $\omega_{D,jS}$ with $j = 1, 2$ is the magnitude of the recoupled D_{IS}-coupling between I_j- and S-spins, $\omega_{\mathrm{CSA},j}$ is the magnitude of the recoupled CSA of I_j-spin, J_{II} is the homonuclear isotropic J-coupling between I-spins, and Ω_S^0 is the resonance offset frequency (isotropic chemical shift) of S-spin. $\bar{\mathscr{H}}_{\mathrm{Q},S}^{(2)}$ is the Hamiltonian of the second-order quadrupolar interaction averaged by MAS.[55] This term is null in the case of spin-1/2 nucleus, whereas it produces ν_{QIS}^S shift for quadrupolar nucleus. The CSA$_S$ and the first-order quadrupolar interaction of S-spin are absent in eq 1 since they are averaged out by MAS over an integer number of rotor period. The magnitude of homonuclear J_{II}-coupling is not scaled by SR4_1^2 irradiation since this interaction is left unchanged by sample rotation and rf irradiation of both I_1- and I_2-spins. When the SR4_1^2 sequence is applied to the S-spins of a IS_2 spin system, $\bar{\mathscr{H}}^{(0)}$ becomes

$$\bar{\mathscr{H}}^{(0)} = \left(\sum_{j=1,2} \omega_{D,Ij} I_z S_{jz} + \omega_{\mathrm{CSA},j} S_{jz}\right) + 2\pi J_{SS} S_1 S_2 + \Omega_I^0 I_z + \bar{\mathscr{H}}_{\mathrm{Q},I}^{(2)} \quad (2)$$

Compared to eq 2, the I and S symbols are simply interchanged. The frequencies ω_Λ with $\Lambda = D, jS$; D, Ij; or CSA, j in eqs 1 and 2 are given by[49]

$$\omega_\Lambda = \kappa\, \mathrm{Re}\{[A_{22}^{\Lambda}]^R \exp[-2\imath(\alpha_{RL}^0 - \omega_r t_0)]\} \quad (3)$$

where the scaling factor is $\kappa = 1/(6^{1/2})$ for SR4_1^2 sequence. t_0 refers to the starting time point of the pulse sequence and α_{RL}^0 denotes the initial rotor position. $[A_{22}^{\Lambda}]^R$ is the space component $m = 2$ of interaction Λ with space rank $l = 2$, expressed in the rotor-fixed frame. The space component of D_{IS}-coupling is given by

$$[A_{22}^{D,jS}]^R = \frac{3}{2} b_{jS} \exp(-2\imath\gamma_{PR}^{D,jS}) \sin^2(\beta_{PR}^{D,jS}) \quad (4)$$

where $\{\alpha_{PR}^{D,jS}, \beta_{PR}^{D,jS}, \gamma_{PR}^{D,jS}\}$ are the Euler angles relating the internuclear vector $\mathbf{r}_{jS}$ to the MAS rotor-fixed frame. The dipolar coupling constant b_{jS} is related to the internuclear distance r_{jS} and the gyromagnetic ratios γ_S and γ_I by $b_{jS} = -(\mu_0/4\pi)\gamma_S\gamma_I\hbar/(r_{jS}{}^3)$ in SI units. The space component of CSA is equal to

$$[A_{22}^{\mathrm{CSA},j}]^R = -\frac{6^{1/2}}{4}\gamma_I B^0 \delta_{\mathrm{aniso}}^j \exp(-2\imath\gamma_{PR}^{\mathrm{CSA},j})\Bigg[\sin^2(\beta_{PR}^{\mathrm{CSA},j}) - \frac{\eta_{\mathrm{CS}}^j}{3}\{[1 + \cos^2(\beta_{PR}^{\mathrm{CSA},j})]\cos(2\alpha_{PR}^{\mathrm{CSA},j}) - 2\imath\cos(\beta_{PR}^{\mathrm{CSA},j})\sin(2\alpha_{PR}^{\mathrm{CSA},j})\}\Bigg] \quad (5)$$

where $\{\alpha_{PR}^{\mathrm{CSA},j}, \beta_{PR}^{\mathrm{CSA},j}, \gamma_{PR}^{\mathrm{CSA},j}\}$ are the Euler angles describing the orientation of the principal axis frame of the CSA $_j$ tensor in the rotor-fixed frame. B^0 is the magnitude of the external static magnetic field, $\delta_{\mathrm{aniso}}^j = \delta_{zz}^j - \delta_{\mathrm{iso}}^j$ is the anisotropic chemical deshielding constant, and $\eta_{\mathrm{CS}}^j = (\delta_{yy}^j - \delta_{xx}^j)/\delta_{\mathrm{aniso}}^j$ is the asymmetry parameter.[58] The isotropic chemical shift is given by $\delta_{\mathrm{iso}}^j = (\delta_{xx}^j + \delta_{yy}^j + \delta_{zz}^j)/3$, and δ_{xx}^j, δ_{yy}^j, and δ_{zz}^j denote the principal values of the chemical shift tensor, labeled such that $|\delta_{zz}^j - \delta_{\mathrm{iso}}^j| \geq |\delta_{xx}^j - \delta_{\mathrm{iso}}^j| \geq |\delta_{yy}^j - \delta_{\mathrm{iso}}^j|$.

2.2.2. SFAM-N Recoupling. The SFAM-N sequences are rotor-synchronized single-channel irradiations employing simultaneous cosinusoidal and sinusoidal time modulations of the carrier frequency and rf field amplitude.[35,47] The angular modulation frequency is N times the angular spinning frequency, ω_r. In the following, we will consider the case where the SFAM-N sequence is applied to the I-spins. When it is applied to the S channel, the I and S symbols must be interchanged. During a SFAM-N scheme, the instantaneous amplitude of the rf field experienced by I-spins is given by

$$\omega_{\mathrm{nut}I}(t) = \omega_{\mathrm{nut}I}^{\max} \sin[N\omega_r(t - t_0)] \quad (6)$$

where $\omega_{\mathrm{nut}I}^{\max}$ is the peak amplitude of the rf field. In a suitably chosen rotating frame, the instantaneous modulation of the carrier frequency is

$$\Delta\omega_{\mathrm{ref}I}(t) = \Delta\omega_{\mathrm{ref}I}^{\max} \cos[N\omega_r(t - t_0)] \quad (7)$$

where $\Delta\omega_{\mathrm{ref}I}^{\max}$ is the peak amplitude of the modulation.

In this rotating frame, the SFAM-N sequences produce an effective field of magnitude

$$\omega_{\mathrm{eff}I}(t) = \left[\omega_{\mathrm{nut}I}(t)^2 + \Delta\omega_{\mathrm{ref}I}(t)^2\right]^{1/2} \quad (8)$$

This effective field revolves around the y-axis with an apparent frequency[47]

$$\omega_{\mathrm{app}I}(t) = \frac{\omega_{\mathrm{nut}I}^{\max}\Delta\omega_{\mathrm{ref}I}^{\max} N\omega_r}{\omega_{\mathrm{eff}I}^2(t)} \quad (9)$$

The $\bar{\mathscr{H}}^{(0)}$ Hamiltonian depends on the relative values of ω_r, $\omega_{\mathrm{nut}I}^{\max}$, and $\Delta\omega_{\mathrm{ref}I}^{\max}$. An analytical expression of $\bar{\mathscr{H}}^{(0)}$ can only be derived in some limit cases, such as $\omega_{\mathrm{eff}I}(t) \gg \omega_{\mathrm{app}I}(t)$ or $\omega_{\mathrm{nut}I}^{\max} \gg \Delta\omega_{\mathrm{ref}I}^{\max}$, which are discussed below.

SFAM-N Sequences When $\omega_{\mathrm{eff}I}(t) \gg \omega_{\mathrm{app}I}(t)$. The fulfillment of this condition requires frequencies $\omega_{\mathrm{nut}I}^{\max}$ and $\Delta\omega_{\mathrm{ref}I}^{\max}$ to be both much larger than $N\omega_r$. This case was treated by Fu et al.[47] However, the D_{II}-couplings were not considered explicitly. Here we specify the analytical expression of the different terms in $\bar{\mathscr{H}}^{(0)}$ when the SFAM-N sequences are applied to spin-1/2 nuclei.

If $\omega_{\mathrm{eff}I}(t) \gg \omega_{\mathrm{app}I}(t)$, the SFAM-1 and SFAM-2 irradiations achieve longitudinal two-spin-order recoupling of the D_{IS}-couplings while suppressing the $\delta_{\mathrm{iso}}^{I}$ shifts of the irradiated spin and the J_{IS}-couplings. The J_{II}-couplings are not affected by the SFAM-N irradiations.

Like the SR4_1^2 sequence, the SFAM-2 irradiation also removes the D_{II}-couplings when $\omega_{\mathrm{eff}I}(t) \gg \omega_{\mathrm{app}I}(t)$. This result is demonstrated in the Supporting Information, section 1.2. Therefore, during SFAM-2 irradiation, the $\bar{\mathscr{H}}^{(0)}$ Hamiltonian of an I_2S spin system is given by eq 1. Furthermore, as SFAM-2 and SR4_1^2 sequences both recouple the space component $m = 2$ of D_{IS}-couplings and CSA$_I$ interactions, the ω_Λ frequency with $\Lambda = D, jS$ or CSA, j is given by eq 3 for the SFAM-2 scheme. Only the scaling factor κ differs between the two recoupling methods. For the SFAM-2 scheme, the D_{IS}-coupling and CSA scaling factor is equal to $\kappa = C_1/6^{1/2}$, where C_1 is the first coefficient in the Fourier cosine series expansion of $\cos\theta(t) = \Delta\omega_{\mathrm{ref}I}(t)/\omega_{\mathrm{nut}I}(t)$, and $\theta(t)$ is the tilt angle between the B^0-axis and the effective rf field of magnitude $\omega_{\mathrm{eff}I}(t)$.[46] The C_1 coefficient is a function of the parameter $\xi = \omega_{\mathrm{nut}I}^{\max}/\Delta\omega_{\mathrm{ref}I}^{\max}$. For $\omega_{\mathrm{nut}I}^{\max} = \Delta\omega_{\mathrm{ref}I}^{\max} \gg N\omega_r$, we have $C_1 = 1$ and SFAM-2 and SR4_1^2 sequences achieve identical heteronuclear dipolar recoupling at zero order.

Contrary to SFAM-2 and SR4_1^2, the SFAM-1 irradiation does not remove the D_{II}-couplings. Therefore, when applied to the I_2S spin system, the SFAM-1 scheme yields the zero-order AH

$$\bar{\mathscr{H}}^{(0)} = \left(\sum_{j=1,2} \omega_{D,jS} I_{jz} S_z + \omega_{\mathrm{CSA},j} I_{jz}\right) + \omega_{D,II}\Big[2I_{1z}I_{2z} - \frac{1}{2}(I_1^{+}I_2^{-} + I_1^{-}I_2^{+})\Big] + 2\pi J_{II} I_1 I_2 + \Omega_S^0 S_z + \bar{\mathscr{H}}_{\mathrm{Q},S}^{(2)} \tag{10}$$

In eq 10, the notations are the same as in eq 1 and $\omega_{D,II}$ is the magnitude of the recoupled homonuclear dipolar coupling between I-spins. The SFAM-1 scheme reintroduces the space component $m = 1$ of D_{IS}-couplings and CSA$_I$. Thus the frequencies ω_Λ with $\Lambda = D, jS$ or CSA,j in eq 10 are equal to

$$\omega_\Lambda = \kappa\, \mathrm{Re}\{[A_{21}^{\Lambda}]^R \exp[-\iota(\alpha_{RL}^0 - \omega_r t_0)]\} \tag{11}$$

using the same notation as in eq 3. The scaling factor of SFAM-1 scheme is equal to $\kappa = -C_1/3^{1/2}$. Its magnitude is multiplied by $2^{1/2}$ compared to that of SFAM-2 in the same conditions. Therefore, SFAM-1 requires a shorter recoupling time than SFAM-2 and SR4_1^2.[35] $[A_{21}^{\Lambda}]^R$ is the space component $m = 1$ of interaction Λ with space rank $l = 2$, expressed in the rotor-fixed frame. For the D_{IS}-coupling, the space component is given by

$$[A_{21}^{D,jS}]^R = \frac{3}{2} b_{jS} \exp(-\iota\gamma_{PR}^{D,jS}) \sin(2\beta_{PR}^{D,jS}) \tag{12}$$

using the same notation as in eq 4. The space component for the CSA is equal to

$$[A_{21}^{\mathrm{CSA},j}]^R = -\frac{6^{1/2}}{2}\gamma_I B^0 \delta_{\mathrm{aniso}}^j \exp(-\iota\gamma_{PR}^{\mathrm{CSA},j}) \sin(\beta_{PR}^{\mathrm{CSA},j}) \left\{\cos(\beta_{PR}^{\mathrm{CSA},j}) + \frac{\eta_{\mathrm{CS}}^j}{3}[\cos(\beta_{PR}^{\mathrm{CSA},j})\cos(2\alpha_{PR}^{\mathrm{CSA},j}) - \iota\sin(2\alpha_{PR}^{\mathrm{CSA},j})]\right\} \tag{13}$$

using the same notation as in eq 5.

Furthermore, the SFAM-1 scheme also recouples the space component $m = 2$ of D_{II}-coupling. Hence, the frequency $\omega_{D,II}$ in eq 10 is given by eq 3 with $\Lambda = D, II$. The component $[A_{22}^{D,II}]^R$ has an analytical expression identical to that of $[A_{22}^{D,jS}]^R$ [see eq 4]. For the SFAM-1 scheme, the scaling factor of D_{II}-coupling is $\kappa = C_1^{D,II}/6^{1/2}$, where $C_1^{D,II}$ is the first coefficient in the Fourier cosine series expansion of the function $\{3\cos^2[\theta(t)] - 1\}/2$ of the tilt angle. The demonstration is given in the Supporting Information, section 1.2. For $\omega_{\mathrm{nut}I}^{\max} = \Delta\omega_{\mathrm{ref}I}^{\max} \gg N\omega_r$, we have $C_1^{D,II} = 0.75$ and $\kappa = 0.75/6^{1/2} = 0.31$.

The above derivation shows that an analytical expression for $\bar{\mathscr{H}}^{(0)}$ during SFAM-N irradiations can be obtained when the magnitude of the effective field is much larger than its apparent revolving frequency around the y-axis. This approximation $\omega_{\mathrm{eff}I}(t) \gg \omega_{\mathrm{app}I}(t)$ is only valid for large modulations of both rf field amplitude and carrier frequency ($\omega_{\mathrm{nut}I}^{\max} \gg N\omega_r$ and $\Delta\omega_{\mathrm{ref}I}^{\max} \gg N\omega_r$). These large modulations can produce significant rf pulse transients, which can affect the recoupling performances.[59] However, the fulfillment of the condition $\omega_{\mathrm{eff}I}(t) \gg \omega_{\mathrm{app}I}(t)$ is not essential to achieve heteronuclear dipolar recoupling with SFAM-N methods and experimentally carrier frequency modulations smaller than $N\omega_r$ were employed.[35,47] We show below that an analytical expression of $\bar{\mathscr{H}}^{(0)}$ can be derived in the regime $\Delta\omega_{\mathrm{ref}I}^{\max} < N\omega_r$, provided the modulation of the rf field amplitude is larger than that of the carrier frequency ($\omega_{\mathrm{nut}I}^{\max} \gg \Delta\omega_{\mathrm{ref}I}^{\max}$). As this regime is mainly advantageous for SFAM-2, we will only consider the case of SFAM-2 in the following.

SFAM-2 Sequence When $\omega_{\mathrm{nut}I}^{\max} \gg \Delta\omega_{\mathrm{ref}I}^{\max}$. When this condition is satisfied during SFAM-2 irradiation, the recoupled D_{IS}-couplings are scaled by the first-order Bessel function of the first kind, $J_1(\psi)$, where $\psi = \omega_{\mathrm{nut}I}^{\max}/(2\omega_r)$. On the contrary, the magnitude of the recoupled D_{II}-couplings depends on $J_1(2\psi)$. The demonstration is given in the Supporting Information, section 1.3. Plots of $J_1(\psi)$ and $J_1(2\psi)$ versus ψ are shown in Figure 3. As seen in the figure, the condition $\omega_{\mathrm{nut}I}^{\max} = 3.82\omega_r$ corresponds to the lowest rf field, allowing suppression of D_{II}-couplings and reintroduction of D_{IS}-couplings. Furthermore, for such conditions, the magnitude of recoupled D_{IS}-coupling is very close to its global maximum.

In addition, when $\omega_{\mathrm{nut}I}^{\max} \gg \Delta\omega_{\mathrm{ref}I}^{\max}$, none of the $\delta_{\mathrm{iso}}^{I}$ and J_{IS} terms in $\bar{\mathscr{H}}^{(0)}$ commutes with the terms arising from D_{IS}-couplings, CSA$_I$, and the modulation of the carrier frequency. Therefore, if the frequencies $\omega_{D,jS}$, $\omega_{\mathrm{CSA},j}$, or $\Delta\omega_{\mathrm{ref}I}^{\max}$ are much larger than the offset of I_j-spin, Ω_j^0, and the $2\pi J_{jS}$ coupling, the $\delta_{\mathrm{iso}}^{I}$ and J_{IS} terms do not contribute to the dephasing of the I_j-spin. Subsequently when (i) $\omega_{\mathrm{nut}I}^{\max} = 3.82\omega_r \gg \Delta\omega_{\mathrm{ref}I}^{\max}$ and (ii) $\sup\{\omega_{D,jS};\omega_{\mathrm{CSA},j};\Delta\omega_{\mathrm{ref}I}^{\max}\} \gg \sup\{\Omega_j^0, 2\pi J_{jS}\}$ with $j = 1, 2$, the $\bar{\mathscr{H}}^{(0)}$ Hamiltonian of the I_2S spin system during SFAM-2 irradiation is given by

$$\bar{\mathscr{H}}^{(0)} = \sum_{j=1,2} \omega_{D,jS} I_{jZ} S_z + (\omega_{\mathrm{CSA},j} - \Delta\omega_{\mathrm{ref}I}^{\max}) I_{jZ} + 2\pi J_{II} I_1 I_2 + \Omega_S^0 S_z + \bar{\mathscr{H}}_{\mathrm{Q},S}^{(2)} \quad (14)$$

The above equation is almost identical to eq 1. The Z-axis is obtained from the B^0-axis by a rotation of $\pi/2 - \psi$ around the x-axis of the usual rotating frame (denoted $\mathscr{F}_a$ in the Supporting Information, section 1.1)

$$I_{jZ} = \sin(\psi) I_{jz} - \cos(\psi) I_{jy} \quad (15)$$

where I_{jz} and I_{jy} are the angular moment operators in the usual rotating frame. The frequencies ω_Λ with $\Lambda = D$, jS or CSA, j in eq 14 are given by eq 3. In that case, the scaling factor κ is equal to $2J_1(\psi)/6^{1/2}$. When $\omega_{\mathrm{nut}I}^{\max} = 3.82\omega_{\mathrm{r}}$, we have $\kappa = 0.47$, which is 16% larger than that of SR4_1^2. Moreover, the angle ψ is equal to 109.8° and hence the Z-axis is tilted by 19.8° from the z-direction. Equation 14 shows that the D_{IS}-coupling terms commute for different spin pairs. Therefore, these sequences do not suffer from dipolar truncation. Furthermore, the terms arising from CSA$_I$ interaction and carrier frequency modulation also commute with the D_{IS}-coupling. Therefore, the evolution of spin coherences due to D_{IS}-coupling is not affected by the CSA and the carrier frequency modulation.

In summary, eq 14 shows that SFAM-2 also achieves longitudinal two-spin-order dipolar recoupling when $\omega_{\mathrm{nut}I}^{\max} \gg \Delta\omega_{\mathrm{ref}I}^{\max}$. This condition allows employing smaller carrier frequency modulation than the regime $\omega_{\mathrm{eff}I}(t) \gg \omega_{\mathrm{app}I}(t)$, and hence reducing rf pulse transients.[59] When $\omega_{\mathrm{nut}I}^{\max} \gg \Delta\omega_{\mathrm{ref}I}^{\max}$, the rf field peak amplitude must be close to $3.82\omega_{\mathrm{r}}$, in order to suppress the D_{II}-couplings. This is consistent with experiments and numerical simulations presented in ref 35. In this regime, the carrier frequency modulation only helps in averaging out the I_j-spin offsets and the J_{IS}-couplings. Therefore, the $\Delta\omega_{\mathrm{ref}I}^{\max}$ frequency must be smaller than $\omega_{\mathrm{nut}I}^{\max}$, but nonzero. Thus, the SFAM-2 recoupling under the condition $\omega_{\mathrm{nut}I}^{\max} \gg \Delta\omega_{\mathrm{ref}I}^{\max}$ and $\Delta\omega_{\mathrm{ref}I}^{\max} \neq 0$ differs from the modulatory resonance (MORE) recoupling, which consists in an amplitude-modulated irradiation at a constant carrier frequency.[60] Owing to the carrier frequency modulation, SFAM-2 displays a higher robustness to resonance offset than MORE. In practice the $\Delta\omega_{\mathrm{ref}I}^{\max}$ frequency must be larger than the maximal resonance offset. This condition ensures that the carrier frequency is swept over all the resonances during SFAM-2 irradiation. For protons, a peak amplitude of $\Delta\nu_{\mathrm{ref}I}^{\max} = \Delta\omega_{\mathrm{ref}I}^{\max}/(2\pi) \approx 15$ kHz is generally sufficient.

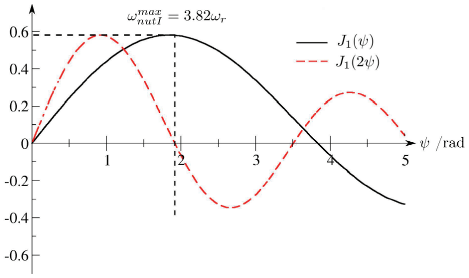

Figure 3. Plots of $J_1(\psi)$ and $J_1(2\psi)$ versus $\psi = \omega_{\mathrm{nut}I}^{\max}/(2\omega_{\mathrm{r}})$. For SFAM-2 irradiation with $\omega_{\mathrm{nut}I}^{\max} \gg \Delta\omega_{\mathrm{ref}I}^{\max}$, the magnitude of D_{IS}- and D_{II}-couplings vary with the parameter ψ, as $J_1(\psi)$ and $J_1(2\psi)$, respectively. The condition $\omega_{\mathrm{nut}I}^{\max} = 3.82\omega_{\mathrm{r}}$ allows a cancelation of D_{II}-couplings, while the magnitude of D_{IS}-coupling is only 0.2% lower than the maximal value, which is obtained for $\omega_{\mathrm{nut}I}^{\max} = 3.68\omega_{\mathrm{r}}$.

2.3. Efficiency versus Offset. The SR4_1^2, SFAM-1, and SFAM-2 recoupling methods can be inserted in either channel of D-HMQC and D-HSQC experiments [see Figure 2c]. In the following, the corresponding pulse sequences are denoted D^I-HMQC and D^I-HSQC, when the heteronuclear recoupling schemes are applied to the undetected spins, and D^S-HMQC and D^S-HSQC, when the recoupling rf field is sent to the detected channel. These sequences lead to different offset dependences of the indirect observation efficiency.

2.3.1. Recoupling Sequence Applied to the Undetected Spins. When the recoupling sequence is applied to the undetected spin-1/2 I nuclei, the S-spin magnetization evolves during the delays τ under the D_{IS}-couplings and the δ_{iso}^S shift, and ν_{QIS}^S shift for S-spins experiencing quadrupolar interactions.

In the D^I-HMQC experiment, the δ_{iso}^S and ν_{QIS}^S evolution during the periods τ (and t_1) is refocused by the π S-spin pulse applied in the middle of the pulse sequence. For an isolated pair of I and S nuclei, the signal intensity observed in D^I-HMQC experiment is

$$s_{D\text{-HMQC}}(\tau) \approx C\left\langle \sin^2\left(\frac{\omega_{D,IS}}{2}\tau\right)\right\rangle \quad (16)$$

where $\langle\ldots\rangle$ denotes the orientational average over all possible molecular orientations in the powder and $\omega_{D,IS}$ frequency is given by eq 3 for SR4_1^2 and SFAM-2 and by eq 11 for SFAM-1. The factor C subsumes different contributions to the signal intensity, such as B^0, γ_S, the relaxation factors owing to saturation and additional losses during τ and t_1 periods, the line width, the losses arising from pulse imperfections, the receiver duty time, and the probe performances (quality factor and geometry of the coil, filling factor, lead loss).[26,61]

In the D^I-HSQC experiment, the δ_{iso}^S and possible ν_{QIS}^S evolution during the recoupling delays can be refocused in two ways: (i) either by applying two simultaneous π pulses to I- and S-spins in the middle of the fixed intervals τ, (ii) or by selecting, by the mean of phase cycling, the coherence order $p_S = +1$ during the excitation interval [see Figure 2b]. The first method is the one usually employed in J-HSQC experiments between spins 1/2 in liquids and solids.[14,16,17] In this contribution, we will focus on the second approach, denoted D^I-HSQC(+1), which allows reducing the number of pulses sent on both channels. Hence it is especially advantageous for correlation experiments involving quadrupolar nuclei, since the number of pulses sent on the quadrupolar channel is minimized. Recently, the HSQC(+1) technique was used for the indirect observation of quadrupolar nuclei with integer spin ($I = {}^{14}$N and $S = {}^{1}$H or ^{13}C).[8,9] The removal of the coherence pathway with $p_S = -1$ during the first τ entails a 2-fold loss of the sensitivity compared to HMQC experiment, hence

$$s_{D\text{-HSQC}(+1)}(\tau) = s_{D\text{-HMQC}}(\tau)/2 \quad (17)$$

Finally, in the case of D^I-HSQC(±1) experiment, which allows both coherence transfer pathways during the first τ and does not comprise π pulses on both channels [see Figure 2b], the real signal intensity is equal to that of HMQC for on-resonance irradiation, but strongly depends on the offset:

$$s^{I}_{D\text{-HSQC}(\pm1)}(\tau) \approx \mathrm{Re}\{\cos[(\Omega_S^0 + 2\pi\nu_{\mathrm{QIS}}^S)\tau]\exp[\imath(\Omega_S^0 + 2\pi\nu_{\mathrm{QIS}}^S)\tau]s_{D\text{-HMQC}}(\tau)\} \quad (18)$$

Equations 16−18 are valid only for an isolated *IS* pair since the homonuclear couplings among *S*-spins are not refocused during the D^I-HMQC and D^I-HSQC pulse sequences. As a result, the sensitivity of these experiments is reduced by the evolution under D_{SS} couplings during the τ intervals.

The above analytical expressions, eqs 16−18, were validated by comparison with accurate numerical simulations of the spin dynamics using realistic parameters. The simulations shown in Figure 4a used the spin system parameters defined in Table 1, which are typical for amino acids.[62] The MAS frequency and the parameters of rf and $\mathbf{B}^0$ magnetic fields are given in Table 2. All simulations were performed using Simpson software.[58] The powder averages were calculated using 2520 orientations (168 $\{\alpha_{\mathrm{MR}}, \beta_{\mathrm{MR}}\}$ pairs × 15 γ_{MR}-angles). The 168 $\{\alpha_{\mathrm{MR}}, \beta_{\mathrm{MR}}\}$ Euler angles, which relate the molecular frame to the rotor frame, were selected according to the repulsion algorithm,[63] while the γ_{MR}-angle was equally stepped from 0 to 2π rad.

In Figure 4a, the simulated indirect observation efficiency of ^{15}N−^{13}C D^I-HMQC, D^I-HSQC(+1), and D^I-HSQC(±1) schemes are plotted as a function of the carrier frequency offset, $\Delta\nu(S) = \Omega_S^0/(2\pi)$, of the detected nucleus (^{13}C). The heteronuclear dipolar couplings were recovered during τ delays by applying SFAM-1 irradiation to the undetected spin, ^{15}N. Efficiencies of indirect observation were determined by dividing the signal integral of the first row of the 2D spectrum by the integral of a signal obtained by a single $\pi/2$ *S*-pulse excitation experiment. The integrations were performed on the real part of the signal. This definition allows a direct comparison of HMQC and HSQC efficiencies. The agreement between the simulated curves and eqs 16−18 is excellent. The efficiency of D^I-HMQC is constant over the range -6 kHz $\leq \Delta\nu(S) \leq 6$ kHz and is 2 times lower than the maximal efficiency, which can be obtained in principle by optimal transfer through the J_{IS}-coupling. This loss originates from the powder average of heteronuclear dipolar coupling evolutions, since $\langle\sin^2(\omega_{D,IS}/2)\rangle \approx 0.5$ when $\tau \gg 2\pi/(\kappa b_{IS})$. Similarly, the efficiency of D^I-HSQC(+1) does not depend on the carrier frequency offset of the detected channel, but is 2 times lower than the one of D^I-HMQC, as expected from eq 17. Finally, the efficiency of D^I-HSQC(±1) varies with the detected channel offset and is perfectly fitted by the function $\cos^2[2\pi\Delta\nu(S)\tau]$, showing the validity of eq 18. Identical simulated curves were obtained when employing SFAM-2 and SR4_1^2 sequence as the recoupling technique (simulations not shown).

2.3.2. Recoupling Sequence Applied to the Detected Spins. When the recoupling sequence is applied to the detected spin-1/2 *S* nuclei, the zero-order AHT predicts that the *S*-spin 1Q coherences evolve during the delays τ under the D_{IS}-couplings and the CSA$_S$. The CSA$_S$ evolution is refocused by the π *S*-pulse in the D^S-HMQC experiment, and by the coherence pathway selection in D^S-HSQC(+1). This refocusing requires identical excitation and reconversion periods. When the CSA$_S$ refocusing is perfect, the signal intensities observed in D^S-HMQC and D^S-HSQC(+1) experiments are given by the analytical expression of eqs 16 and 17, respectively. Thus, in the zero-order approximation, the sensitivity of *D*-HMQC and *D*-HSQC(+1) experiments does not depend on which channel is applied in the recoupling sequence.

In contrast, the sensitivity of D^S-HSQC(±1) differs from that of D^I-HSQC(±1) as the CSA$_S$ evolution is not refocused for the *S*-spin coherence pathway $-1 \rightarrow 0 \rightarrow -1$. The signal intensity of D^S-HSQC(±1) is given by

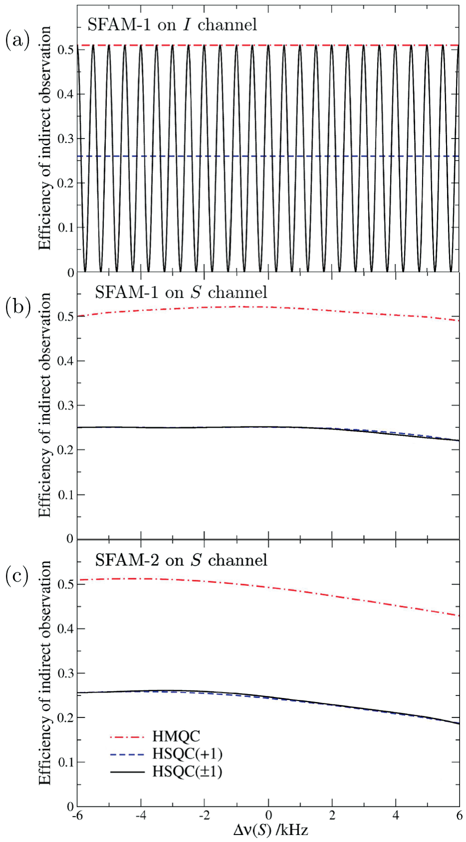

Figure 4. Numerically simulated efficiencies of indirect observation for ^{15}N−^{13}C *D*-HMQC, *D*-HSQC(±1), and *D*-HSQC(+1) sequences as function of the carrier frequency offset, $\Delta\nu(S)$, of the detected ^{13}C nucleus. The ^{15}N carrier was kept on resonance. (a) Numerical simulation for D^I-HMQC, D^I-HSQC(±1), and D^I-HSQC(+1) sequences, with SFAM-1 recoupling applied to the undetected spin, ^{15}N. (b, c) Numerical simulation for D^S-HMQC, D^S-HSQC(±1), and D^S-HSQC(+1) sequences. Two heteronuclear dipolar recoupling schemes were tested: SFAM-1 in (b) and SFAM-2 in (c). The τ intervals were fixed to 1 ms for SFAM-1 and 1.4 ms for SFAM-2, i.e., the least multiple of τ_r leading to maximal efficiency for indirect observation in each case.[34] Additional parameters used in the numerical simulations are given in Tables 1 and 2.

$$s^{S}_{D\text{-HSQC}(\pm1)}(\tau) \approx \frac{C}{2}\left\langle[1 + \exp(2\imath\omega_{\mathrm{CSA},S}\tau)]\sin^2\left(\frac{\omega_{D,IS}}{2}\tau\right)\right\rangle \quad (19)$$

In the above equation, the term $\exp(2\imath\omega_{\mathrm{CSA},S}\tau)$ originates from the *S*-spin coherence pathway $-1 \rightarrow 0 \rightarrow -1$, while the contribution from the coherence pathway $+1 \rightarrow 0 \rightarrow -1$ is independent of CSA$_S$. Equation 19 indicates that the signal intensity of D^S-HSQC(±1) is between those of *D*-HMQC and *D*-HSQC(+1) depending on the magnitude of the CSA$_S$ interaction. For small CSA$_S$ ($\gamma_S B^0 \delta^S_{\mathrm{aniso}}/(2\pi) \ll 1/\tau$), $s^S_{D\text{-HSQC}(\pm1)}(\tau)$ must

TABLE 1: Spin Interaction Parameters Used in the Numerical Simulations[a]

		(I, S)	
parameter	meaning	$(^{15}\mathrm{N}, ^{13}\mathrm{C})^b$	$(^{13}\mathrm{C}, ^{1}\mathrm{H})^c$
$(\delta^I_{\mathrm{aniso}}, \delta^S_{\mathrm{aniso}})$	CSA	(99 ppm, −76 ppm)	(−20 ppm, 5 ppm)
$(\eta^I_{\mathrm{CS}}, \eta^S_{\mathrm{CS}})$	shift tensor asymmetry parameter	(0.19, 0.90)	(0.65, 0.70)
$(\alpha^{\mathrm{CSA},I}_{\mathrm{PM}}, \beta^{\mathrm{CSA},I}_{\mathrm{PM}}, \gamma^{\mathrm{CSA},I}_{\mathrm{PM}})^d$	CSA$_I$ principal axis orientation	(0, −90°, 17°)	(90°, 90°, 0)
$(\alpha^{\mathrm{CSA},S}_{\mathrm{PM}}, \beta^{\mathrm{CSA},S}_{\mathrm{PM}}, \gamma^{\mathrm{CSA},S}_{\mathrm{PM}})^d$	CSA$_S$ principal axis orientation	(0, 0, 94°)	(90°, −90°, 54°)
J_{IS}	isotropic *J*-coupling	0 Hz	0 Hz
$b_{IS}/(2\pi)$	dipole−dipole (DD) coupling	+1 kHz	−23.3 kHz
$(\alpha^{D,IS}_{\mathrm{PM}}, \beta^{D,IS}_{\mathrm{PM}}, \gamma^{D,IS}_{\mathrm{PM}})^e$	D_{IS} principal axis orientation	(0, 90°, 57°)	(0, −36°, 0)

[a] The magnitude and the orientation of the spin interaction tensors were set to typical values reported for amino acids.[62] [b] The parameters of ^{13}C−^{15}N spin system are realistic for ^{13}C′ and ^{15}N nuclei of an amide group. [c] The parameters of ^{13}C−^{1}H spin system are realistic for ^{13}C$^{\alpha}$ and ^{1}H$^{\alpha}$ nuclei of an amino acid. [d] Euler angles (in degrees) relating the principal axis system of the CSA to the molecular reference frame. [e] Euler angles (in degrees) relating the principal axis system of the D_{IS} coupling between nuclei *I* and *S* to the molecular reference frame.

TABLE 2: MAS Frequency and Parameters of External Magnetic Fields Used in the Numerical Simulations

			$\nu^{\max\ d}_{\mathrm{nut}}$ (kHz)		$\Delta\nu^{\max\ e}_{\mathrm{ref}}$ (kHz)	
$\nu_r{}^a$ (kHz)	$\mathbf{B}^{0\ b}$ (T)	$\nu_{\mathrm{nut}}{}^c$ (kHz)	SFAM-1	SFAM-2	SFAM-1	SFAM-2
20	9.4	150	40	56	50	20

[a] MAS frequency. [b] Static magnetic field. [c] rf nutation frequency of $\pi/2$ and π pulses. [d] Peak amplitude of rf field applied during SFAM recoupling, $\nu^{\max}_{\mathrm{nut}} = \omega^{\max}_{\mathrm{nut}}/(2\pi)$. [e] Peak amplitude of carrier frequency modulation for SFAM recoupling, $\Delta\nu^{\max}_{\mathrm{ref}} = \Delta\omega^{\max}_{\mathrm{ref}}/(2\pi)$.

be close to the intensity of *D*-HMQC, while for large CSA$_S$ the contribution from the coherence pathway $-1 \rightarrow 0 \rightarrow -1$ is averaged to zero by CSA$_S$ defocusing and $s^S_{D\text{-HSQC}(\pm1)}(\tau) = s_{D\text{-HSQC}(+1)}(\tau) = s_{D\text{-HMQC}}(\tau)/2$. Furthermore, eq 19 shows that the sensitivity of D^S-HSQC(±1) is offset-independent at zero order.

The SFAM-2 and SR4^2_1 recoupling schemes remove the homonuclear D_{SS}-coupling terms. In consequence, D^S-HMQC and D^S-HSQC pulse sequences have to be preferentially chosen when the *S*-spins experience strong dipolar couplings. The homonuclear J_{SS}-couplings are not suppressed. However, in most of the cases, these couplings are much smaller than the D_{IS}-couplings and, hence, have no influence on the signal intensity.

The indirect observation efficiencies of D^S-HMQC, D^S-HSQC(+1), and D^S-HSQC(±1) were simulated as a function of the offset, $\Delta\nu(S)$, for two different spin systems, a ^{15}N−^{13}C pair and a ^{13}C−^{1}H one. Figure 4b shows the simulated efficiencies for the ^{15}N−^{13}C system described in Table 1, when using SFAM-1 sequence as the recoupling method. The simulation parameters are given in Table 2 and in the caption of Figure 4. They were identical to those used in Figure 4a, except that the SFAM-1 scheme was applied to the detected ^{13}C spins. In this case, the efficiency of D^S-HMQC is 0.50 for on-resonance irradiation ($\Delta\nu(S) = 0$) and hence applying the recoupling schemes to the detected spins does not lead to a loss in signal intensity. Whatever the ^{13}C offset, the efficiencies of D^S-HSQC(+1) and D^S-HSQC(±1) are equal and 2 times lower than that of D^S-HMQC. This indicates that the ^{13}C CSA (10.0 kHz $\gg 1/\tau = 1.7$ kHz) is large enough to eliminate the contribution from the ^{13}C coherence pathway $-1 \rightarrow 0 \rightarrow -1$ to the detected signal. As expected from zero-order AHT [see eqs 16, 17, and 19], the three plots show little dependence on ^{13}C offset. Similar results were obtained when using SR4^2_1 as the recoupling technique (simulations not shown).

Figure 4c is analogous to Figure 4b, but SFAM-2 irradiation was employed to recouple the D_{IS}-couplings. The simulation parameters for SFAM-2 correspond approximately to the case $\omega^{\max}_{\mathrm{nut}S} \gg \Delta\omega^{\max}_{\mathrm{ref}S}$ [see Table 2]. Compared with Figure 4b, Figure 4c exhibits a 5% lower efficiency on resonance. This small sensitivity loss results from the +10° deviation of the *Z*-axis from the B^0-direction since $\psi = 80°$ [see eqs 14 and 15]. The asymmetrical dependence of the efficiency with $\Delta\nu(S)$ agrees with the tilt of the effective field. As seen in Figure 5 and shown in the Supporting Information, section 1.3, the effective field is the sum of the carrier frequency modulation term, $-\Delta\nu^{\max}_{\mathrm{ref}S}J_1(\psi)S_Z$, and the isotropic chemical shift term, $\Delta\nu(S)$ $J_0(\psi)S_Y$, where $J_0(\psi)$ is the zero-order Bessel function of the first kind. Consequently, there is a negative offset value $\Delta\nu(S)$ such that

$$\arccos(\Delta\nu^{\max}_{\mathrm{ref}S}J_1(\psi)/\{[\Delta\nu^{\max}_{\mathrm{ref}S}J_1(\psi)]^2 + [\Delta\nu(S)\,J_0(\psi)]^2\}^{1/2}) = 10° \quad (20)$$

i.e., $\Delta\nu(S) = -3.4$ kHz, where the effective field points in the $(-B^0)$-direction. This condition yields maximal efficiency, as seen in Figure 4c.

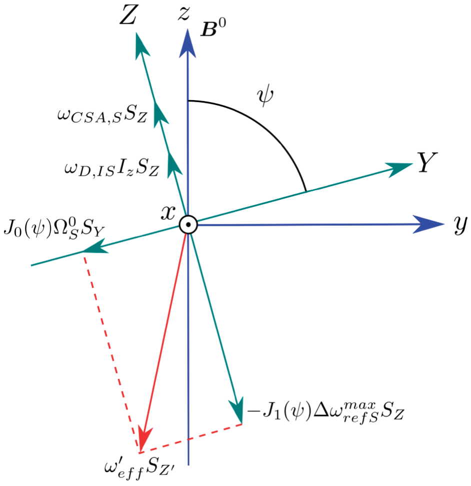

Figure 5. Schematic of the different contributions to $\bar{\mathscr{H}}^{(0)}$ for SFAM-2 irradiation on the *S* channel. The relative magnitudes of the interactions agree with those of the ^{13}C−^{15}N spin system [see Tables 1 and 2]. We assume $\omega^{\max}_{\mathrm{nut}S} \gg \Delta\omega^{\max}_{\mathrm{ref}S}$. The Ω^0_S offset is negative. The frequencies ω_Λ with $\Lambda = D$, *IS* or CSA, *S* are given by eq 3. The effective field, $\omega'_{\mathrm{eff}}S_{Z'}$, is the sum of two fields: the one induced by the offset modulation, $-\Delta\omega^{\max}_{\mathrm{ref}S}J_1(\psi)S_Z$, and the second due to the average offset, $\Omega^0_S J_0(\psi)S_Y$.

Figure 6 illustrates the case where CSA$_S$ is small. The spin system was the ^{13}C−^{1}H pair described in Table 1. In Figure

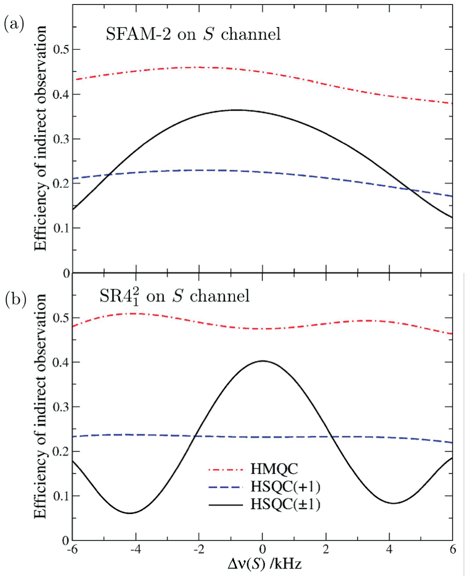

Figure 6. Numerically simulated efficiencies of indirect observation for $^{13}C-^{1}H$ D^S-HMQC, D^S-HSQC(±1), and D^S-HSQC(+1) sequences as function of the carrier frequency offset, $\Delta\nu(S)$, of the detected ^1H nucleus. The ^{13}C $\pi/2$ pulses were applied on resonance. Two different heteronuclear dipolar recoupling schemes were tested: SFAM-2 (a) and $SR4_1^2$ (b). The τ intervals were fixed to 0.3 ms. Additional parameters used in the numerical simulations are given in Tables 1 and 2.

6a, SFAM-2 was employed as the recoupling method. The simulation parameters are given in Table 2. They were identical to those employed in Figure 4c, but a shorter recoupling time was used because of the larger b_{IS} constant. The comparison of Figures 4c and 6a shows that the simulated efficiencies of D^S-HMQC and D^S-HSQC(+1) for the $^{13}C-^{1}H$ pair are similar to those obtained for a $^{15}N-^{13}C$ system. In contrast, the on-resonance efficiency of D^S-HSQC(±1) is higher when ^1H nuclei are detected instead of ^{13}C. This efficiency (0.35) is between those of D^S-HSQC(+1) (0.23) and D^S-HMQC (0.46), because the 1Q proton coherences are only partially defocused during τ periods by the small ^1H CSA (2 kHz $\approx 1/\tau = 3$ kHz). Nevertheless, the signal intensity of D^S-HSQC(±1) varies with the offset. This modulation originates from nonzero-order terms in the AH, which depends on $\Delta\nu(S)$.

Figure 6b shows the results of numerical simulations when using $SR4_1^2$. The recoupling sequences apart, the simulation parameters were the same as those of Figure 6a. The relative efficiencies of D^S-HMQC, D^S-HSQC(+1), and D^S-HSQC(±1) including $SR4_1^2$ recoupling are globally similar to those obtained for SFAM-2 [see Figure 6a]. However, the offset dependence of the signal intensity differs between $SR4_1^2$ and SFAM-2. In particular, the $SR4_1^2$ recoupling leads to a stronger offset dependence of D^S-HSQC(±1) efficiency than SFAM-2. This phenomenon must be related to the different cycle times between SFAM-2 and $SR4_1^2$. Indeed, the isotropic chemical shift terms in $\bar{\mathscr{H}}^{(0)}$ are averaged to zero over one rotor period in the case of SFAM-2, whereas they are only suppressed by the phase inversion supercycle extending over two τ_r in the case of $SR4_1^2$. Furthermore, the SFAM-2 sequence benefits from a better robustness to rf inhomogeneity than the $SR4_1^2$ method.[35]

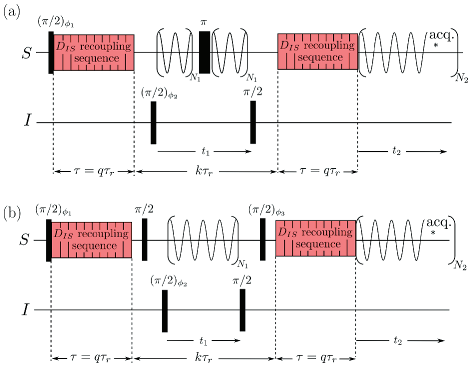

Figure 7. Pulse sequences for (a) D^S-HMQC and (b) D^S-HSQC experiments with $C8_1^4$(half-cos) and $wC8_1^4$(half-cos) irradiations applied during t_1 and t_2 evolution periods, respectively. The phase cyclings were identical to those given in the caption of Figure 2. Homonuclear dipolar recoupling sequences were applied on the detected channel.

2.4. Homonuclear Dipolar Decoupling. The HMQC and HSQC pulse sequences can be applied to observe lower γ nuclei, such as ^{13}C or ^{14}N, through nearby high-γ isotopes, such as ^1H.[5,6,14,16] Proton is an ideal spy nucleus because of its high gyromagnetic ratio and its high isotopic natural abundance. However, this combination generally entails strong homonuclear couplings among the protons. These homogeneous anisotropic interactions[64] are not completely averaged out by the MAS, and hence, the $^1H-^1H$ strong dipolar couplings can reduce the sensitivity of HMQC and HSQC experiments as well as the spectral resolution in both direct (F_2) and indirect (F_1) dimensions. In the case of indirect detection via the protons ($S = {}^1H$), the line broadening in F_1 dimension originates from the noncommutation of Hamiltonians representing D_{SS}- and D_{IS}-couplings.

As explained in subsection 2.3.2, the SS dipolar coupling evolution during the τ delays can be suppressed by applying recoupling sequences, such as $SR4_1^2$ or SFAM-2, to the spy spins. The enhancement of resolution in F_1 and F_2 dimensions requires the use of windowless and windowed homonuclear decoupling sequences in the t_1 and t_2 periods, respectively. So far various decoupling techniques, including frequency switched Lee–Goldberg (FSLG)[17,18,65−67] and DUMBO,[68,69] were used in HSQC and HMQC experiments. However, they were not applied to the detected spin. In this article, we explore the use of $CN_n^{N/2}$ irradiation on the detected channel during t_1 and t_2 times.[10,50,51] A half-cosine pulse was used as the basic C element and the corresponding pulse sequences are denoted $CN_n^{N/2}$(half-cos) in the following. These symmetry-based schemes have the benefit of creating a broad-banded z-rotation of nuclear spins, thus allowing the elimination of zero and image peaks, without the requirement of preparatory pulses. Furthermore, the scaling factor is offset-independent and conventional phase cycling can be employed in multidimensional experiments. Finally these new CRAMPS sequences require lower rf power than PMLG and DUMBO, partly because their rf amplitude can be modulated.[51,70] Applying $CN_n^{N/2}$ schemes to the S-spins suppresses, in the zero-order AH, D_{SS}- and D_{IS}-couplings as well as CSA_S, but preserves δ_{iso}^S chemical shift, J_{IS}-couplings, and J_{SS}-couplings.[51]

Windowless $CN_n^{N/2}$ sequences can be implemented straightforwardly in the indirect dimension of the HSQC variant, devoid of a π S-pulse during t_1 [see Figure 7b], while windowed $CN_n^{N/2}$ decoupling (denoted $wCN_n^{N/2}$ in the following) is required during the acquisition period, t_2.[49] In contrast, only a subgroup of $CN_n^{N/2}$ sequences can be inserted during the t_1 period of HMQC because of the presence of a π S-pulse in the middle of t_1 time [see Figure 7a]. We found that $CN_1^{N/2}$ symmetries, where N is a multiple of 8, can incorporate a short π pulse in their middle, while keeping their decoupling properties. These symmetries are also suitable for HSQC experiments, which employs a π S-pulse during t_1 to refocus the J_{IS}-couplings.[14,16,17]

3. Experimental Demonstrations

3.1. Samples and Experimental Conditions. All the experiments were performed on a wide-bore Bruker AVANCE II 400 MHz NMR spectrometer operating at a magnetic field of 9.4 T, using samples of isotopically substituted α-(2-^{13}C,^{15}N)-glycine,[71] isotopically unmodified L-histidine·HCl, and monosodium dihydrogenophosphate (NaH_2PO_4). The amino acids and NaH_2PO_4 were purchased from Sigma-Aldrich and Prolabo, respectively, and were used without purification. The samples were confined to the middle of the rotor in order to improve the B_1 homogeneity.

The ^{1}H and ^{13}C chemical shifts are referenced to tetramethylsilane (TMS). The ^{23}Na chemical shifts are referenced to a 1 mol·L^{-1} NaCl aqueous solution.[72] For 2D spectra recorded with homonuclear dipolar decoupling [see Figures 9d,e and 10c], the frequency scales of F_2 projections were divided by the experimentally determined scaling factors to restore the actual chemical shift values.

The glycine sample was spun at 20 kHz in a wide-bore triple-resonance 3.2 mm MAS NMR probe. The 1D ^{15}N−^{13}C D-HMQC, D-HSQC(±1), and D-HSQC(+1) spectra with ^{13}C detection [see Figure 8] were obtained with 64 scans and a recycle delay of 1.5 s. The interval between the two $(\pi/2)^I$ pulses, t_1 [see Figure 2], was fixed to τ_r. A rotor-synchronized gap of 100 μs ($k = 2$ in Figure 2) separated the two recoupling intervals. Cross-polarization (CP) transfer from protons to carbons (with $\nu_{1,CP}(^1H) = 75$ kHz, $\nu_{1,CP}(^{13}C) = 55$ kHz, and $\tau_{CP} = 1$ ms) replaced the first $(\pi/2)^S$ pulse in the sequences of Figure 2. During the remaining part of the sequences, a SPINAL-64 decoupling sequence with $\nu_{1,dec}(^1H) = 105$ kHz was applied to the ^{1}H channel. The rf nutation frequencies of the hard pulses were 105 kHz for ^{1}H, 77 kHz for ^{13}C, and 56 kHz for ^{15}N. SFAM-2 recoupling schemes were applied during $\tau = 22\tau_r = 1.1$ ms on either the ^{13}C or ^{15}N channels. In both cases, the peak values of the rf nutation frequency and the maximum offsets were $\nu_{nut}^{max} = 40$ kHz and $\Delta\nu_{ref}^{max} = 25$ kHz, respectively.

The L-histidine·HCl and NaH_2PO_4 samples were spun at 31.746 kHz in a wide-bore triple-resonance 2.5 mm MAS probe. The 2D X−^{1}H through-space correlation spectra were recorded by using D^S-HMQC and D^S-HSQC sequences. $SR4_1^2$ recoupling with a rf nutation frequency of 63.5 kHz was applied to the ^{1}H channel. A rotor-synchronized gap of $k\tau_r$ ($k = t_1/\tau_r + 2$ in Figures 2 and 7) separated the two recoupling intervals. The peak value of the rf nutation frequency for $C8_1^4$(half -cos) and $wC8_1^4$(half-cos) irradiations was 130 kHz.

The 2D ^{13}C−^{1}H D^S-HMQC and D^S-HSQC spectra of L-histidine·HCl with ^{1}H detection [see Figure 9] result from averaging 64 transients for each of 350 t_1 increments with $\Delta t_1 = \tau_r = 31.5$ μs and a recycle delay of 1.5 s. The τ delays were equal to $6\tau_r = 189$ μs. The rf nutation frequencies of the hard pulses were 67 kHz for ^{1}H and 71 kHz for ^{13}C.

The 2D ^{23}Na−^{1}H D^S-HMQC spectra of NaH_2PO_4 with ^{1}H detection [see Figure 10] result from averaging 320 transients for each of 120 t_1 increments with $\Delta t_1 = \tau_r = 31.5$ μs and a recycle delay of 1.5 s. As the ^{1}H T_1 relaxation time of NaH_2PO_4 is 23 s, two rf pulses of 16 ms with orthogonal phases were applied at the beginning of the pulse sequence on the ^{1}H channel in order to ensure equivalent conditions for each transient. The rf nutation frequency of this pulse pair satisfies the rotary resonance recoupling (R^3) condition $\nu_{nut}^H = \nu_r$,[27,28,44] which reintroduces D_{HH} and D_{NaH} couplings as well as CSA_H under MAS condition. Thus these R^3 pulses eliminate any residual ^{1}H coherences remaining after the t_2 period. The τ delays were equal to $\tau = 12\tau_r = 378$ μs. The rf field strengths of ^{1}H hard pulses and ^{23}Na central transition selective pulses were 67 and 9 kHz, respectively.

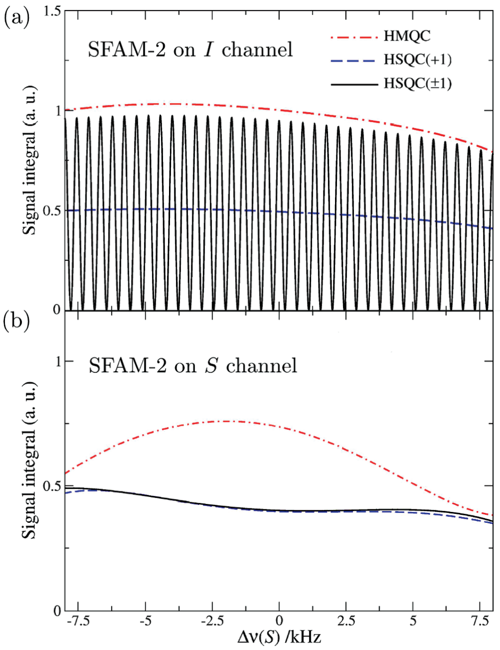

Figure 8. Experimental signal integrals of (2-^{13}C,^{15}N)-glycine measured for 1D ^{15}N−^{13}C D-HMQC, D-HSQC(+1), and D-HSQC(±1) experiments as function of the carrier frequency offset, $\Delta\nu(S)$, of the detected ^{13}C nucleus. The employed pulse sequences are depicted in Figure 2. During τ intervals, heteronuclear dipolar recoupling schemes, SFAM-2, were applied either (a) to the undetected channel, ^{15}N, or (b) to the detected one, ^{13}C. Signal integrals were normalized to the on-resonance signal integral of D^I-HMQC experiment. Additional details are given in the experimental section.

3.2. Efficiency versus Offset. To evaluate the validity of eqs 16−19, the dependence of D-HMQC and D-HSQC signal intensity with the offset of the detected spin was measured experimentally. To that end, several 1D ^{15}N−^{13}C D-HMQC, D-HSQC(+1), and D-HSQC(±1) experiments were performed on (2-^{13}C,^{15}N)-glycine. The heteronuclear recoupling sequences, SFAM-2, were applied either to the undetected spin, $I = {}^{15}$N, or to the detected one, $S = {}^{13}$C.

Figure 8a shows the experimental dependence of signal integral with ^{13}C offset, when ^{15}N nuclei are subjected to SFAM-2 irradiation. The D^I-HMQC experiment yields the highest indirect observation efficiency, whereas the sensitivity of D^I-HSQC(+1) is 2 times lower. The efficiency of these sequences weakly depends on the ^{13}C offset, whereas the D^I-HSQC(±1) signal integral oscillates with $\Delta\nu(S)$ between zero and that of D^I-HMQC.

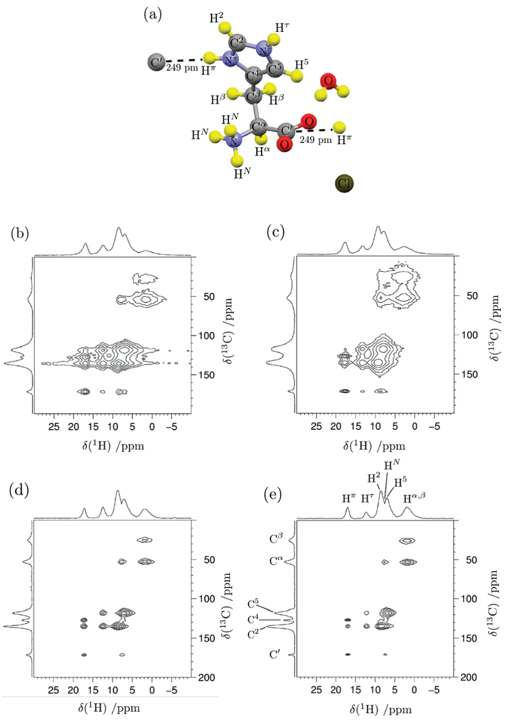

Figure 9. (a) Structure of L-histidine·HCl obtained from neutron diffraction[75] with IUPAC atom labeling.[76] (b−e) Experimental 2D ^{13}C−^{1}H D^S-HMQC (b, d) and D^S-HSQC(±1) (c, e) spectra of isotopically unmodified L-histidine·HCl at $\nu_r = 31.746$ kHz. Spectra b and c were recorded by employing the pulse sequences of Figure 2, whereas spectra d and e were obtained by using the schemes of Figure 7, which include $\mathrm{C8}_1^4$(half-cos) and $\mathrm{wC8}_1^4$(half-cos) irradiations during t_1 and t_2 periods. ^{13}C−^{1}H dipolar couplings were restored by applying $\mathrm{SR4}_1^2$ recoupling to the detected ^{1}H channel. Additional details are given in the experimental section.

These experimental variations of indirect observation efficiency with $\Delta\nu(S)$ are quite similar to those predicted from eqs 16−18, or calculated by numerical simulations [see Figure 4a]. This confirms the validity of the theoretical analysis presented in section 2. The main difference with simulations lies in the weak experimental dependence of D^I-HMQC and D^I-HSQC(+1) efficiencies with $\Delta\nu(S)$. First, this dependence may originate from finite rf power. Second, the variation in ^{13}C offset affects the efficiency of the initial ^{1}H−^{13}C CP transfer, which replaces the first ^{13}C $\pi/2$ pulse.

The insertion of SFAM-2 sequence in the detected channel $S = {}^{13}$C yields different experimental dependences of signal integral with ^{13}C offset, as seen in Figure 8b. The efficiencies of D^S-HSQC(+1) and D^S-HSQC(±1) experiments are almost equal over the range $\Delta\nu(S) = \pm 8$ kHz. Furthermore, on resonance, the sensitivity of D^S-HSQC experiments is 2 times lower than that of D^S-HMQC. These observations agree with simulations shown in Figure 4c and indicate that the CSA of glycine α-carbon atom ($\delta_{\mathrm{aniso}}^{C^\alpha} = -19.4$ ppm)[73,74] is large enough to suppress the contribution from the ^{13}C coherence pathway $-1 \rightarrow 0 \rightarrow -1$ to D^S-HSQC(±1) signal intensity. Compared to the simulations, the experimental efficiency of D^S-HMQC exhibits a stronger dependence with ^{13}C offset. The slight offset dependence owing to the tilt of the Z-axis is enhanced by changes in the efficiency of the initial ^{1}H−^{13}C CP transfer and imperfect refocusing of ^{13}C CSA by the middle π pulse for a large resonance offset.

The comparison of Figure 8a and 8b evidences that, in the case of weak dipolar couplings among the detected spins, it is preferable to apply the heteronuclear recoupling sequences to the undetected nuclei and to employ D^I-HMQC.

3.3. ^{13}C−^{1}H *D*-HMQC and *D*-HSQC 2D Spectra. The *D*-HMQC and *D*-HSQC experiments were also compared in the case of indirect detection via the protons. Figure 9 shows the 2D ^{13}C−^{1}H D^S-HMQC and D^S-HSQC(±1) spectra of isotopically unmodified L-histidine·HCl. The 2D ^{13}C−^{1}H D^S-HSQC(+1) spectra are not shown since the intensities of correlation peaks in this spectra are lower than those of 2D D^S-HSQC(±1) spectra [see Figure 9c,e]. The $\mathrm{SR4}_1^2$ sequences were applied to the detected channel $S = {}^1$H in order to suppress the D_{HH} dephasing during the τ delays. Applying the $\mathrm{SR4}_1^2$ scheme to the undetected channel $I = {}^{13}$C prevents the observation of correlation peaks, C$^\alpha$−H$^\alpha$ and C$^\beta$−H$^\beta$, between aliphatic carbon-13 and proton nuclei.

Figure 9b,c shows the 2D ^{13}C−^{1}H D^S-HMQC and D^S-HSQC(±1) spectra recorded without homonuclear decoupling, while Figure 9d,e displays the 2D D^S-HMQC and D^S-HSQC(±1) spectra obtained when applying $\mathrm{C8}_1^4$(half-cos) and $\mathrm{wC8}_1^4$(half-cos) homonuclear decoupling during t_1 and t_2 periods, respectively. The comparison of Figure 9b and 9d, and 9c and 9e, clearly evidences that $\mathrm{C8}_1^4$ homonuclear decoupling sequences allow improving the spectral resolution in both F_1 and F_2 dimensions. In particular, the C^4 signal is resolved in the F_1 projections of Figure 9d,e, whereas it is hardly visible in the projections of Figure 9b,c. More quantitatively, the use of $\mathrm{C8}_1^4$(half-cos) decoupling yields a 3-fold decrease in line width of the C$^\alpha$ peak, while the scaled-up line width of the H$^\alpha$ peak is divided by a factor of 2 when employing $\mathrm{wC8}_1^4$(half-cos) irradiation during the t_2 period.

The assignment of the 1D ^{13}C and ^{1}H spectra has been previously reported.[71,77] In the 2D spectra of Figure 9, all the protonated carbons are correlated with their attached protons ($d_{\mathrm{CH}} = 103{-}110$ pm and -28.0 kHz $\leq b_{\mathrm{CH}} \leq -23.0$ kHz). For the chosen excitation and reconversion periods, $\tau = 189$ μs, intramolecular two-bond cross-peaks are also observed but they are less intense than the one-bond correlations. The two-bond cross-peaks result from ^{1}H−^{13}C contacts at $d_{\mathrm{CH}} = 207{-}223$ pm (-3.4 kHz $\leq b_{\mathrm{CH}} \leq -2.7$ kHz). Longer range cross-peaks include the intramolecular three-bond correlation, C′−H^N, and the intermolecular correlation, C′−H$^\pi$ ($d_{\mathrm{C'H^\pi}} = 249$ pm and $b_{\mathrm{C'H^\pi}} = -1.9$ kHz).

The relative intensities of D^S-HSQC(±1) and D^S-HMQC cross-peaks, $s^S_{D\text{-HSQC}(\pm1)}/s^S_{D\text{-HMQC}}$, fluctuate between 0.5 and 1 depending on the ^{1}H sites, whereas the intensities of D^S-HSQC(+1) cross-peaks are 2 times lower than those of D^S-HMQC. These results are consistent with the low CSA of protons in organic compounds[78] and the numerical simulations of Figure 6. The fluctuation of $s^S_{D\text{-HSQC}(\pm1)}/s^S_{D\text{-HMQC}}$ between the different protons ensues from the dependence of $s^S_{D\text{-HSQC}(\pm1)}$ with proton CSA and offset, $\Delta\nu(S)$. Anyway, the D^S-HMQC experiment yields the highest signal-to-noise ratio. Furthermore, in this case, no significant differences in the F_1 spectral resolution were observed between D^S-HMQC and D^S-HSQC experiments. In conclusion, the D^S-HMQC experiment outperforms D^S-HSQC(±1) and D^S-HSQC(+1) techniques in this case.

3.4. ^{23}Na−^{1}H *D*-HMQC and *D*-HSQC 2D Spectra. Finally, the *D*-HMQC and *D*-HSQC experiments were employed for

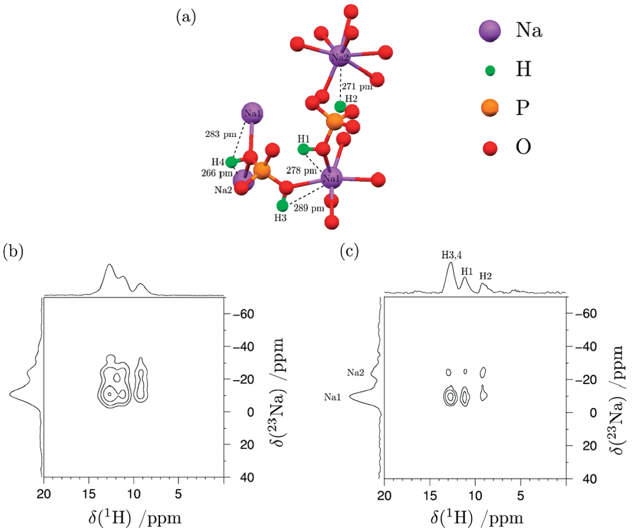

Figure 10. (a) Atomic structure of NaH_2PO_4. The H−Na distances shorter than 2.9 Å are displayed as dashed lines. (b, c) Experimental 2D $^{23}Na-^{1}H$ D^S-HMQC spectra of NaH_2PO_4 at $\nu_r = 31.746$ kHz. Spectrum b was recorded by employing the pulse sequences of Figure 2a, whereas spectrum c was obtained from the scheme displayed Figure 7a; i.e., $C8_1^4$(half-cos) and $wC8_1^4$(half-cos) irradiations were applied during t_1 and t_2 periods, respectively. $^{23}Na-^{1}H$ dipolar couplings were restored by applying $SR4_1^2$ recoupling to the detected ^1H channel. Additional details are given in the experimental section.

TABLE 3: Experimental and Calculated ^1H NMR Parameters of NaH_2PO_4

		experimental	calculated[b]		
site	d_{OO}[a] (pm)	δ_{iso}[c] (ppm)	δ_{iso}[d] (ppm)	δ_{aniso}[e] (ppm)	η_{CS}[e]
H1	257	11.1	11.2	22.7	0.11
H2	263	9.3	9.3	20.2	0.08
H3	255	12.4	12.4	23.4	0.12
H4	249	12.8	12.9	24.6	0.10

[a] The O···H−O distances, d_{OO}, were estimated from the DFT-optimized structure. [b] The calculated parameters result from the DFT-GIPAW calculations on the DFT-optimized structure. [c] The ^1H chemical shifts are referenced to tetramethylsilane (TMS). [d] The calculated chemical shifts are shifted by a constant value to match the calculated value for H2 with the most experimental shielded resonance. [e] The definitions of δ_{aniso} and η_{CS} are given below eq 5.

TABLE 4: Experimental and Calculated ^{23}Na NMR Parameters of NaH_2PO_4

site	method[a]	δ_{iso}[b] (ppm)	C_Q (kHz)	η_Q
Na1	exp	−2.5	1.6	0.5
	calc	−2.5	1.46	0.46
Na2	exp	−6.4	2.4	0.9
	calc	−5.95	1.95	0.88

[a] The experimental (exp) parameters are obtained by fitting the 1D ^{23}Na MAS NMR spectrum with dmfit program,[97] while the calculated (calc) parameters result from the DFT-GIPAW calculations on the DFT-optimized structure. [b] The ^{23}Na chemical shifts are referenced to a 1 mol·L^{-1} NaCl aqueous solution.[72] The calculated chemical shifts are shifted by a constant value to match the calculated value for Na1 with the most experimental deshielded resonance.

the indirect detection of half-integer quadrupolar nuclei, $I = {}^{23}Na$, via the protons, $S = {}^{1}H$. The D_{HH} dephasing during the τ delays was removed by applying the $SR4_1^2$ sequences to the protons. The 2D $^{23}Na-^{1}H$ D^S-HMQC and D^S-HSQC experiments were performed on a model inorganic compound, NaH_2PO_4.

Figure 10c shows the D^S-HMQC spectrum recorded with $^1H-^1H$ decoupling [see Figure 7]. This 2D spectrum correlates through D_{NaH}-couplings the $\delta_{iso}(^1H)$ shifts in the F_2 dimension with the chemical and quadrupolar isotropic shifts of ^{23}Na nuclei in the F_1 dimension. For comparison, the same spectrum recorded without homonuclear decoupling is shown in Figure 10b. The use of $C8_1^4$(half-cos) and $wC8_1^4$(half-cos) sequences improves the spectral resolution in both F_1 and F_2 dimensions, as evidenced by the comparison of the 2D spectrum projections. In particular, the H3,4 and H1 signals are better resolved in Figure 10c than in Figure 10b.

NaH_2PO_4 unit cell contains four nonequivalent protons (denoted H1 to H4) and two distinct sodium sites (Na1 and Na2). The assignment of $\delta_{iso}(^1H)$ shifts has been already reported and is given in Table 3 as well as in Figure 10c.[79] The differences in δ_{iso} between the proton sites result from disparity in hydrogen bond lengths between the phosphate groups.[80−82] The 1D ^{23}Na MAS NMR spectrum consists of two overlapping second-order quadrupolar line shapes. The NMR parameters resulting from deconvolution of the ^{23}Na line shapes are given in Table 4.

The assignment of the ^{23}Na spectrum was derived from the 2D D^S-HMQC spectrum in Figure 10c. We used the fact that the intensity of correlation peaks in D^S-HMQC experiment depends on the size of the effective heteronuclear couplings, and hence on the $^{23}Na-^{1}H$ distance. First, the H2 site exhibits in Figure 10c a much weaker correlation peak with the deshielded ^{23}Na resonance than the other protons. Second, the neutron diffraction structure[83] reveals that the H2 proton is much closer to the Na2 site than to the Na1 site, since the closest Na2−H2 and Na1−H2 distances are 271 and 368 pm, respectively ($b_{Na2H2} = -1.6$ kHz and $b_{Na1H2} = -0.6$ kHz). Third, the other protons are much closer to the Na1 atom than the H2 site is ($d_{Na1H1} = 278$ pm, $d_{Na1H3} = 289$ pm, and $d_{Na1H4} = 283$ pm).

Subsequently, the deshielded and shielded ^{23}Na resonances must stem from Na1 and Na2 nuclei, respectively.

This assignment was corroborated by periodic density functional theory (DFT) calculations, using the Quantum-ESPRESSO code.[84,85] We used the PBE functional for the generalized gradient approximation (GGA) of the exchange-correlation functional.[86] The wave function is expanded on a plane-wave basis set with an energy cutoff of 100 Ry. The potentials due to the ions were represented by norm-conserving Troullier−Martins pseudopotentials.[87] The electronic configurations involved in the construction of the pseudopotentials for the different nuclei Na, P, O, and H are {$2s^2$ $2p^6$ $3d^0$}, {$3s^2$ $3p^3$ $3d^0$}, {$2s^2$ $2p^{3.5}$ $3d^0$}, and {$1s^{0.1}$} with respective core radii (in atomic units) {1.81 1.25 1.8}, {1.63 1.8 1.93}, {1.43 1.43 1.43}, and {1.2}. The electronic structure gives access to the electric field gradient (EFG) tensor through the reconstruction of the all-electron wave function obtained with the projector augmented wave (PAW) approach.[88,89] The parameters describing the quadrupolar interaction, C_Q and η_Q, are related to the principal components (V_{xx},V_{yy},V_{zz}) of the EFG tensor by $C_Q = eQ|V_{zz}|/h$ and $\eta_Q = (V_{xx} - V_{yy})/V_{zz}$, where by convention $|V_{xx}| \leq |V_{yy}| \leq |V_{zz}|$, Q is the nuclear quadrupole moment, h is the Planck constant, and e is the elementary charge.[55] In the present work, we used $Q = 10.4$ fm^2 for ^{23}Na nuclei.[90] As the sign of C_Q is, in most cases, not determined directly from a simple MAS spectrum, absolute values of C_Q have been considered. The calculation of the absolute chemical shielding was performed using GIPAW algorithms developed by Pickard and Mauri.[91] The calculation of NMR parameters requires the accurate knowledge of the structure. Hence the NMR parameters were determined after DFT optimization of the neutron-diffraction structure.[83] We used the VASP code[92,93] for the structure optimization, with GGA-PW91 functional[94] and the PAW scheme[95] to describe the electron−ion interactions and an energy cutoff of 44 Ry for the expansion of the plane-wave basis set.

The calculated ^{1}H $\delta_{\rm iso}$, $\delta_{\rm aniso}$, and $\eta_{\rm CS}$ values are reported in Table 3. There is a remarkable agreement between the calculated and experimental $\delta_{\rm iso}$ differences, while the calculated $\delta_{\rm aniso}$ and $\eta_{\rm CS}$ are consistent with those reported in the literature for P−O···H−O−P hydrogen bonds.[96] The ^{1}H CSA decreases with increasing O···H−O distances.[80−82] The large magnitude of ^{1}H CSA in NaH_2PO_4 is confirmed by the 2-fold lower efficiency of D^S-HSQC(±1) and D^S-HSQC(+1) experiments [not shown] compared to that of D^S-HMQC. These relative experimental efficiencies agree with the numerical simulations of Figure 4c corresponding to the case of large CSA$_S$ of the detected spins. Therefore, the comparison of on-resonance sensitivities between D^S-HSQC(±1), D^S-HSQC(+1), and D^S-HMQC experiments yields a qualitative assessment of CSA$_S$.

^{23}Na NMR parameters resulting from the DFT-GIPAW calculations are given in Table 4. The comparison between the experimental and calculated NMR parameters confirms the assignment of ^{23}Na resonance based on a 2D D^S-HMQC spectrum. Indeed, the isotropic chemical shift of Na2 is computed 3.5 ppm lower than the one of Na1, in excellent agreement with the experimentally observed difference (3.9 ppm). Furthermore, the calculated and experimental η_Q values are close. The η_Q value of Na1 nucleus is smaller than that of Na2, since the primary coordination sphere of the octahedral site Na1 is more symmetrical than that of the Na2 site, which is surrounded by seven oxygen atoms. The relative magnitude of calculated C_Q values is also consistent with the experimental ones, although the agreement between the computed values and the experimental ones is less good: the computed C_Q values are clearly underestimated. Nevertheless, assignment is unambiguous and confirms the attribution resulting from D-HMQC and D-HSQC experiments.

4. Conclusion

We have compared the performances of different D-HMQC and D-HSQC variants. These experiments allow obtaining 2D heteronuclear correlation spectra by using dipolar couplings to transfer the coherences between unlike spins. These sequences do not suffer from dipolar truncation and enable the indirect detection of low-γ isotopes via high-γ nuclei. The indirectly detected spins and the spy nucleus can be either spin-1/2 or quadrupolar nuclei. For correlation between spin-1/2 and quadrupolar nuclei, the heteronuclear recoupling is achieved by irradiating only the spin-1/2 isotope. This prevents any interference between quadrupolar interaction and rf irradiation.

We have shown that the efficiency and the robustness to resonance offset depend on the sequence design as well as on the magnitude of spin interactions. The investigated D-HMQC and D-HSQC versions differ by the heteronuclear recoupling methods (SR4_1^2, SFAM-1, and SFAM-2), the channel in which this recoupling is inserted (detected or undetected), and, for HSQC sequences, the selected coherence pathways during the excitation time.

When the dipolar interactions between the S-spins are weak enough to be averaged out by MAS, the D^I-HMQC version offers the largest efficiency over a broad $\Delta\nu(S)$ range. Furthermore, the SFAM-1 technique must be employed since it requires a shorter recoupling time than SFAM-2 and SR4_1^2, owing to its larger scaling factor.[35] This allows minimizing the irreversible losses of signal during excitation and reconversion delays.

When the dipolar interactions between the S-spins are not averaged out solely by MAS, SFAM-2, or SR4_1^2 recoupling methods must be applied to the S-spins. SFAM-2 sequence requires slightly higher rf power than SR4_1^2, but it has the benefit of decreasing rf pulse transients and is more robust to rf homogeneity. This is advantageous, especially under ultrafast MAS ($\nu_r = 65-70$ kHz). Furthermore, for large D_{SS}-couplings, we have shown that the D^S-HMQC experiment is more sensitive than the D^S-HSQC techniques. In principle, the HSQC scheme can provide an advantage in terms of resolution in the indirect dimension.[8,9,68] However, in the investigated examples, no significant gain was observed when using HSQC. We have demonstrated that the resolution in both spectral dimensions can be enhanced by using windowless and windowed C8_1^4(half-cos) homonuclear decoupling in the t_1 and t_2 periods, respectively.

For NaH_2PO_4 compound, the 2D ^{23}Na−^{1}H D^S-HMQC experiment incorporating C8_1^4(half-cos) decoupling has enabled the assignment of ^{23}Na spectrum from the ^{1}H isotropic chemical shifts. We have circumvented the long ^{1}H relaxation times in such a compound, by using a pair of R^3 pulses at the beginning of the sequence. The resonance assignment was corroborated by periodic DFT calculations of the ^{23}Na and ^{1}H chemical shift tensors and the ^{23}Na quadrupolar coupling tensor.

The D^S-HMQC and D^S-HSQC spectra reported in this paper were carried out on model samples, but these techniques are applicable to a wide variety of crystalline and amorphous compounds. They are expected to become very useful in the structural investigation of solids containing quadrupolar nuclei. When the amount of I nuclei is low (observation of isotopes with low natural abundance in diluted or surface species), dedicated techniques must be employed in order to eliminate the "t_1-noise"[61] contributed by S nuclei that do not participate in polarization transfer to I nuclei.[26,28,29,31,98]

The theoretical aspects of this work extend previous treatments of SFAM sequences by deriving analytical expressions for SFAM-2 irradiation under conditions closer to those used experimentally. In particular, we have demonstrated that SFAM-2 sequence allows the reintroduction of heteronuclear dipolar couplings, even if the carrier frequency modulation is small. Under this condition, the peak amplitude of the rf field must be close to $3.82\omega_r$ in order to suppress the homonuclear dipolar couplings. Furthermore, this theoretical treatment underlines the relationships between SFAM methods and symmetry-based pulse sequences. Hence, the implementation of amplitude and carrier frequency modulations for various symmetry-based sequences may be envisaged.

Acknowledgment. The authors are grateful for funding provided by Region Nord/Pas de Calais, Europe (FEDER), CNRS, French Minister of Science, FR-3050, USTL, ENSCL, Bruker BIOSPIN, and ANR Contract No. NT05-2-41632. We acknowledge the Bruker company and Fabien Aussenac for the lending of a wide-bore 2.5 mm Bruker MAS NMR probe. F.D. thanks the National Natural Science Foundation of China (20773159 and 20673139) and the National Basic Research Program of China (2009CB918600) for financial support.

Supporting Information Available: Derivation of the average Hamiltonian expressions for SFAM sequence. This material is available free of charge via the Internet at http://pubs.acs.org.

References and Notes

(1) Fyfe, C. A.; Grondey, H.; Mueller, K. T.; Wong-Moon, K. C.; Markus, T. *J. Am. Chem. Soc.* **1992**, *114*, 5876–5878.
(2) Fyfe, C. A.; zu Altenschildesche, H. M.; Wong-Moon, K. C.; Grondey, H.; Chezeau, J. M. *Solid State Nucl. Magn. Reson.* **1997**, *9*, 97–106, In Honour of Gunter Engelhardt.
(3) Cavadini, S.; Lupulescu, A.; Antonijevic, S.; Bodenhausen, G. *J. Am. Chem. Soc.* **2006**, *128*, 7706–7707.
(4) Gan, Z. *J. Am. Chem. Soc.* **2006**, *128*, 6040–6041.
(5) Gan, Z. *J. Magn. Reson.* **2007**, *184*, 39–43.
(6) Gan, Z.; Amoureux, J. P.; Trébosc, J. *Chem. Phys. Lett.* **2007**, *435*, 163–169.
(7) Cavadini, S.; Abraham, A.; Bodenhausen, G. *Chem. Phys. Lett.* **2007**, *445*, 1–5.
(8) Cavadini, S.; Abraham, A.; Bodenhausen, G. *J. Magn. Reson.* **2008**, *190*, 160–164.
(9) Antonijevic, S.; Halpern-Manners, N. *Solid State Nucl. Magn. Reson.* **2008**, *33*, 82–87.
(10) Amoureux, J.-P.; Hu, B.; Trébosc, J. *J. Magn. Reson.* **2008**, *193*, 305–307.
(11) Amoureux, J.-P.; Trébosc, J.; Delevoye, L.; Lafon, O.; Hu, B.; Wang, Q. *Solid State Nucl. Magn. Reson.* **2009**, *35*, 12–18.
(12) Burum, D. P.; Ernst, R. R. *J. Magn. Reson.* **1980**, *39*, 163–168.
(13) Morris, G. A. *J. Am. Chem. Soc.* **1980**, *102*, 428–429.
(14) Maudsley, A. A.; Ernst, R. R. *Chem. Phys. Lett.* **1977**, *50*, 368–372.
(15) Müller, L. *J. Am. Chem. Soc.* **1979**, *101*, 4481–4484.
(16) Bodenhausen, G.; Ruben, D. J. *Chem. Phys. Lett.* **1980**, *69*, 185–189.
(17) Lesage, A.; Emsley, L. *J. Magn. Reson.* **2001**, *148*, 449–454.
(18) Lesage, A.; Sakellariou, D.; Steuernagel, S.; Emsley, L. *J. Am. Chem. Soc.* **1998**, *120*, 13194–13201.
(19) Massiot, D.; Fayon, F.; Alonso, B.; Trébosc, J.; Amoureux, J.-P. *J. Magn. Reson.* **2003**, *164*, 160–164.
(20) Stejskal, E. O.; Schaefer, J.; Waugh, J. S. *J. Magn. Reson.* **1977**, *28*, 105–112.
(21) Caravatti, P.; Bodenhausen, G.; Ernst, R. *Chem. Phys. Lett.* **1982**, *89*, 363–367.
(22) Hing, A. W.; Vega, S.; Schaefer, J. *J. Magn. Reson.* **1992**, *96*, 205–209.
(23) Trébosc, J.; Hu, B.; Amoureux, J.; Gan, Z. *J. Magn. Reson.* **2007**, *186*, 220–227.
(24) Gullion, T.; Schaefer, J. *J. Magn. Reson.* **1989**, *81*, 196–200.
(25) Gullion, T.; Vega, A. J. *Prog. Nucl. Magn. Reson. Spectrosc.* **2005**, *47*, 123–136.
(26) Ishii, Y.; Tycko, R. *J. Magn. Reson.* **2000**, *142*, 199–204.
(27) Ishii, Y.; Yesinowski, J. P.; Tycko, R. *J. Am. Chem. Soc.* **2001**, *123*, 2921–2922.
(28) Wiench, J. W.; Bronnimann, C. E.; Lin, V. S.-Y.; Pruski, M. *J. Am. Chem. Soc.* **2007**, *129*, 12076–12077.
(29) Zhou, D. H.; Shah, G.; Comos, M.; Mullen, C.; Sandoz, D.; Rienstra, C. M. *J. Am. Chem. Soc.* **2007**, *129*, 11791–11801.
(30) Zhou, D. H.; Rienstra, C. M. *Angew. Chem., Int. Ed.* **2008**, *47*, 7328–7331.
(31) Mao, K.; Wiench, J. W.; Lin, V. S.-Y.; Pruski, M. *J. Magn. Reson.* **2009**, *196*, 92–95.
(32) Brinkmann, A.; Levitt, M. H. *J. Chem. Phys.* **2001**, *115*, 357–384.
(33) Hong, M.; Griffin, R. G. *J. Am. Chem. Soc.* **1998**, *120*, 7113–7114.
(34) Saalwächter, K.; Spiess, H. W. *J. Chem. Phys.* **2001**, *114*, 5707.
(35) Hu, B.; Trébosc, J.; Amoureux, J. *J. Magn. Reson.* **2008**, *192*, 112–122.
(36) Baldus, M.; Meier, B. H. *J. Magn. Reson.* **1997**, *128*, 172–193.
(37) Hodgkinson, P.; Emsley, L. *J. Magn. Reson.* **1999**, *139*, 46–59.
(38) Vega, A. J. *J. Magn. Reson.* **1992**, *96*, 50–68.
(39) Hu, B.; Amoureux, J.; Trébosc, J.; Hafner, S. *J. Magn. Reson.* **2008**, *192*, 8–16.
(40) Amoureux, J.-P.; Pruski, M. *Mol. Phys.* **2002**, *100*, 1595–1613.
(41) Brinkmann, A.; Kentgens, A. *J. Phys. Chem. B* **2006**, *110*, 16089–16101.
(42) Levitt, M. H. In *Encyclopedia of Nuclear Magnetic Resonance*; Wiley: Chichester, 2002.
(43) Levitt, M. H.; Oas, T. G.; Griffin, R. G. *Isr. J. Chem.* **1988**, *28*, 271.
(44) Oas, T. G.; Griffin, R. G.; Levitt, M. H. *J. Chem. Phys.* **1988**, *89*, 692.
(45) Gan, Z.; Grant, D. M. *Chem. Phys. Lett.* **1990**, *168*, 304–308.
(46) Gan, Z.; Grant, D. M.; Ernst, R. R. *Chem. Phys. Lett.* **1996**, *254*, 349–357.
(47) Fu, R.; Smith, S. A.; Bodenhausen, G. *Chem. Phys. Lett.* **1997**, *272*, 361–369.
(48) Nishimura, K.; Fu, R.; Cross, T. A. *J. Magn. Reson.* **2001**, *152*, 227–233.
(49) Brinkmann, A.; Kentgens, A. *J. Am. Chem. Soc.* **2006**, *128*, 14758–14759.
(50) Amoureux, J.-P.; Hu, B.; Trébosc, J.; Wang, Q.; Lafon, O.; Deng, F. *Solid State Nucl. Magn. Reson.* **2009**, *35* (1), 19–24.
(51) Lafon, O.; Wang, Q.; Hu, B.; Trébosc, J.; Deng, F.; Amoureux, J.-P. *J. Chem. Phys.* **2009**, *130*, 014504.
(52) Haeberlen, U.; Waugh, J. S. *Phys. Rev.* **1968**, *175*, 453–467.
(53) Haeberlen, U. *High-Resolution NMR in Solids: Selective Averaging*; Academic: New York, 1976.
(54) Mauri, F.; Pfrommer, B. G.; Louie, S. G. *Phys. Rev. Lett.* **1996**, *77*, 5300–5303.
(55) Jerschow, A. *Prog. Nucl. Magn. Reson. Spectrosc.* **2005**, *46*, 63–78.
(56) Marion, D.; Ikura, M.; Tschudin, R.; Bax, A. *J. Magn. Reson.* **1989**, *85*, 393–399.
(57) Nielsen, N. C.; Bildsøe, H.; Jakobsen, H. J.; Levitt, M. H. *J. Chem. Phys.* **1994**, *101*, 1805–1812.
(58) Bak, M.; Rasmussen, J. T.; Nielsen, N. C. *J. Magn. Reson.* **2000**, *147*, 296–330.
(59) Vega, A. J. *J. Magn. Reson.* **2004**, *170*, 22–41.
(60) Takegoshi, K.; Takeda, K.; Terao, T. *Chem. Phys. Lett.* **1996**, *260*, 331–335.
(61) Ernst, R. R.; Bodenhausen, G.; Wokaun, A. *Principles of nuclear magnetic resonance in one and two dimensions*; Oxford University Press: Oxford, 1987.
(62) Bak, M.; Schultz, R.; Vosegaard, T.; Nielsen, N. C. *J. Magn. Reson.* **2002**, *154*, 28–45.
(63) Bak, M.; Nielsen, N. C. *J. Magn. Reson.* **1997**, *125*, 132.
(64) Maricq, M. M.; Waugh, J. S. *J. Chem. Phys.* **1979**, *70*, 3300–3316.
(65) Bielecki, A.; Kolbert, A. C.; Levitt, M. H. *Chem. Phys. Lett.* **1989**, *155*, 341–346.
(66) Bielecki, A.; Kolbert, A. C.; Levitt, M. H. *Adv. Magn. Reson.* **1989**, *14*, 111.
(67) Levitt, M. H.; Kolbert, A. C.; Bielecki, A.; Ruben, D. J. *Solid State Nucl. Magn. Reson.* **1993**, *2*, 151–163.
(68) Lesage, A.; Sakellariou, D.; Hediger, S.; Elena, B.; Charmont, P.; Steuernagel, S.; Emsley, L. *J. Magn. Reson.* **2003**, *163*, 105–113.
(69) Sakellariou, D.; Lesage, A.; Hodgkinson, P.; Emsley, L. *Chem. Phys. Lett.* **2000**, *319*, 253–260.
(70) Mafra, L.; Coelho, C.; Siegel, R.; Rocha, J. *J. Magn. Reson.* **2009**, *197*, 20–27.
(71) Kimura, H.; Nakamura, K.; Eguchi, A.; Sugisawa, H.; Deguchi, K.; Ebisawa, K.; Suzuki, E.; Shoji, A. *J. Mol. Struct.* **1998**, *447*, 247–255.
(72) Hayashi, S.; Hayamizu, K. *Bull. Chem. Soc. Jpn.* **1989**, *62*, 2429–2430.

(73) Brinkmann, A.; Schmedt auf der Günne, J.; Levitt, M. H. *J. Magn. Reson.* **2002**, *156*, 79–96.

(74) Haberkorn, R. A.; Stark, R. E.; Van Willigen, H.; Griffin, R. G. *J. Am. Chem. Soc.* **1981**, *103*, 2534–2539.

(75) Fuess, H.; Hohlwein, D.; Mason, S. A. *Acta Crystallogr., Sect. B: Struct. Sci.* **1977**, *33*, 654–659.

(76) IUPAC-IUB Joint Commission on Biochemical Nomenclature. *Pure Appl. Chem.* **1984**, *56*, 595−624.

(77) Madhu, P.; Vinogradov, E.; Vega, S. *Chem. Phys. Lett.* **2004**, *394*, 423–428.

(78) Brouwer, D. H.; Ripmeester, J. A. *J. Magn. Reson.* **2007**, *185*, 173–178.

(79) Mafra, L.; Gomes, J. R. B.; Trébosc, J.; Rocha, J.; Amoureux, J.-P. *J. Magn. Reson.* **2009**, *196*, 88–91.

(80) Ditchfield, R. *J. Chem. Phys.* **1976**, *65*, 3123–3133.

(81) Berglund, B.; Vaughan, R. W. *J. Chem. Phys.* **1980**, *73*, 2037–2043.

(82) Rohlfing, C. M.; Allen, L. C.; Ditchfield, R. *J. Chem. Phys.* **1983**, *79*, 4958–4966.

(83) Choudhary, R. N. P.; Nelmes, R. J.; Rouse, K. D. *Chem. Phys. Lett.* **1981**, *78*, 102–105.

(84) Kohn, W.; Sham, L. J. *Phys. Rev.* **1965**, *140*, 1133.

(85) See http://www.quantum-espresso.org.

(86) Perdew, J. P.; Burke, K.; Ernzerhof, M. *Phys. Rev. Lett.* **1996**, *77*, 3865–3868.

(87) Troullier, N.; Martins, J. L. *Phys. Rev. B* **1991**, *43*, 1993–2006.

(88) Blöchl, P. E. *Phys. Rev. B* **1994**, *50*, 17953–17979.

(89) Profeta, M.; Mauri, F.; Pickard, C. J. *J. Am. Chem. Soc.* **2003**, *125*, 541–548.

(90) Pyykkö, P. *Mol. Phys.* **2008**, *106*, 1965–1974.

(91) Pickard, C. J.; Mauri, F. *Phys. Rev. B* **2001**, *63*, 245101.

(92) Kresse, G.; Furthmüller, J. *Phys. Rev. B* **1996**, *54*, 11169–11186.

(93) Kresse, G.; Hafner, J. *Phys. Rev. B* **1993**, *48*, 13115–13118.

(94) Perdew, J. P.; Burke, K.; Wang, Y. *Phys. Rev. B* **1996**, *54*, 16533–16539.

(95) Kresse, G.; Joubert, D. *Phys. Rev. B* **1999**, *59*, 1758–1775.

(96) Duma, L.; Abergel, D.; Tekely, P.; Bodenhausen, G. *Chem. Commun.* **2008**, 2361–2363.

(97) Massiot, D.; Fayon, F.; Capron, M.; King, I.; Le Calvé, S.; Alonso, B.; Durand, J.-O.; Bujoli, B.; Gan, Z.; Hoatson, G. *Magn. Reson. Chem.* **2002**, *40*, 70–76.

(98) Zhou, D. H.; Rienstra, C. M. *J. Magn. Reson.* **2008**, *192*, 167–172.

JP906099K

Chemical Physics Letters 496 (2010) 201–207

Contents lists available at ScienceDirect

Chemical Physics Letters

journal homepage: www.elsevier.com/locate/cplett

Indirect high-resolution detection for quadrupolar spin-3/2 nuclei in dipolar HMQC solid-state NMR experiments

Julien Trébosc [a,*], Olivier Lafon [a], Bingwen Hu [a,b], Jean-Paul Amoureux [a]

[a] UCCS, Université Nord de France, CNRS UMR-8181, Villeneuve d'Ascq 59652, France
[b] Physics Department and Shanghai Key Laboratory of Magnetic Resonance, East China Normal University, 3663 Northern Zhongshan Road, Shanghai 200062, China

ARTICLE INFO

Article history:
Received 27 April 2010
In final form 13 July 2010
Available online 16 July 2010

ABSTRACT

We present a new kind of NMR pulse sequences to observe heteronuclear correlation (HETCOR) specifically between spin-1/2 and spin-3/2 nuclei with isotropic resolution on the quadrupolar channel. These methods, called HMQC-ST, feature a STMAS filter during the evolution period of the HMQC scheme. Compared to existing HETCOR techniques involving quadrupolar nuclei, the HMQC-ST combines high-resolution and high efficiency and allows indirect detection of spin-3/2 nuclei via sensitive nuclei. We study analytically and using simulations how through-bond and through-space HMQC-ST perform compared to regular HMQC sequence. HMQC-ST potential is demonstrated experimentally by recording through-space HETCOR 2D spectra of Na_2HPO_4 and NaH_2PO_4.

1. Introduction

Half-integer quadrupolar spins represent three-quarters of nucleus isotopes observable by nuclear magnetic resonance (NMR) spectroscopy. Hence, inorganic, organic and biological solids usually contain both spin-1/2 (^{1}H, ^{13}C, ^{31}P...) and half-integer quadrupolar (^{11}B, ^{23}Na, ^{17}O, ^{27}Al...) nuclei. Therefore, the observation of specific proximities or connectivities between spin-1/2 and quadrupolar nuclei is an important step in the structural characterization of solids. Extracting such information requires the use of two-dimensional (2D) heteronuclear correlation (HETCOR) experiments, when there are more than one distinct site for both considered isotopes. More precisely, the HETCOR methods using coherence transfers via *J*-coupling (*J*-HETCOR) or dipolar coupling (*D*-HETCOR) reveal the through-bond connectivities and the through-space proximities, respectively.

For quadrupolar nuclei, *J*- and *D*-HETCOR sequences, initially designed to observe spin-1/2–spin-1/2 heteronuclear correlations in the solid state, can suffer of lack of resolution and/or sensitivity. Nevertheless, several of them were successfully used to correlate spin-1/2 with half-integer quadrupolar isotopes. They differ by their spectral resolution as well as the number of coherence transfers (one or two). The first proposed HETCOR experiments involving half-integer quadrupolar nuclei were not endowed with isotropic resolution for the quadrupolar nuclei and employed a single coherence transfer [1–4]. *J*-HETCOR experiments were performed using *J*-INEPT sequence [3], whereas *D*-HETCOR were achieved by using either cross-polarization (CP) transfer [1] or *D*-INEPT methods like TEDOR [2]. The absence of isotropic resolution stems from the observation of the central transition (CT) coherence $-1/2 \leftrightarrow +1/2$ of quadrupolar nuclei. Although not affected by first-order quadrupolar interaction, the CT is still broadened to the second-order. Even if the spectral resolution in 2D HETCOR experiment, compared to one-dimensional (1D) spectra, is enhanced by the use of a second spectral dimension, this broadening may obscure the chemical shift information. Finally, the robustness of *D*-HETCOR experiment depends on the nature of the coherence transfer. Continuous-wave CP transfers between quadrupolar and spin-1/2 nuclei are sensitive to offset and radio-frequency (rf) inhomogeneity [5]. Such limitation is partly alleviated by employing multiple-pulse CP sequence [6]. A better option to enhance the robustness consists in recoupling the dipolar interaction by applying the rf field to the spin-1/2 isotope only. This single channel dipolar recoupling was first used in *D*-INEPT experiments [2,4].

An alternative method to design *J*- and *D*-HETCOR methods involving half-integer quadrupolar nuclei consists in the use of double quantum coherences as in *J*-HMQC [7], *D*-HMQC [4] and *D*-HSQC [8] experiments. One advantage of this approach is the possibility to do indirect detection through a sensitive isotope with large gyromagnetic ratio γ. The indirect detection may enhance the sensitivity of HETCOR experiment depending on the longitudinal relaxation times, T_1, γ and the line widths of correlated nuclei [9]. This can be most beneficial when the spy nuclei are spin-1/2 isotopes, such as ^{1}H or ^{31}P.

The combination of high-resolution pulse sequences, such as MQMAS [10–12] or STMAS [13], with HETCOR [14–17] allowed recording high-resolution HETCOR 2D spectra under magic-angle spinning (MAS). Nevertheless, this strategy was only applied to the case of HETCOR experiment using single coherence transfer,

---

[*] Corresponding author. Fax: +33 320 43 68 14.
E-mail address: julien.trebosc@univ-lille1.fr (J. Trébosc).

0009-2614/$ - see front matter © 2010 Elsevier B.V. All rights reserved.
doi:10.1016/j.cplett.2010.07.037

such as CP [18,16] or INEPT [15]. Typically, such experiment begins with a MQMAS/STMAS block on the quadrupolar nucleus channel in order to refocus the second-order quadrupolar interaction. Then, the resulting CT single quantum (1Q) coherence is transferred by CP or INEPT to the spin-1/2 nucleus, which is detected during the acquisition. Unfortunately, these high-resolution HETCOR methods are incompatible with indirect detection since the excited nucleus must be the quadrupolar nucleus. Although MQMAS sequence was also combined with *J*-HMQC [17], getting isotropic resolution for such MQ-*J*-HMQC experiment requires a prohibitively long 3D acquisition and the excitation and detection of the quadrupolar nucleus, which is incompatible with indirect detection via ^{1}H or ^{31}P.

To combine isotropic resolution for spin-3/2 quadrupolar nuclei with indirect detection via spin-1/2 isotope, we introduce a STMAS filter during the evolution period of HMQC technique. This 2D correlation method, called HMQC-ST, benefits from STMAS high resolution and high efficiency transfers in addition to indirect detection via high-γ isotope. First, we describe the HMQC-ST pulse sequences. Second, analytical and numerical density matrix calculations are presented for HMQC-ST experiments using coherence transfers either via *J*-coupling (*J*-HMQC-ST) or dipolar coupling (*D*-HMQC-ST). These calculations permit to assess the efficiency of the methods and to rationalize the choice of delays and pulses for *J*- and *D*-HMQC-ST. In the following the indirectly detected spin-3/2 nucleus is denoted *I* and the detected spin-1/2 spy nucleus *S*. We refer to the HMQC and HMQC-ST experiments involving $S \rightarrow I \rightarrow S$ polarization transfer as '*I*–*S*'. Finally, experimental ^{23}Na-^{31}P and ^{23}Na-^{1}H *D*-HMQC-ST 2D spectra are presented for Na_2HPO_4 and NaH_2PO_4.

We describe both the basic HMQC scheme [7,4] devoid of STMAS filter and the HMQC-ST pulse sequence since these two strategies are compared in the next section.

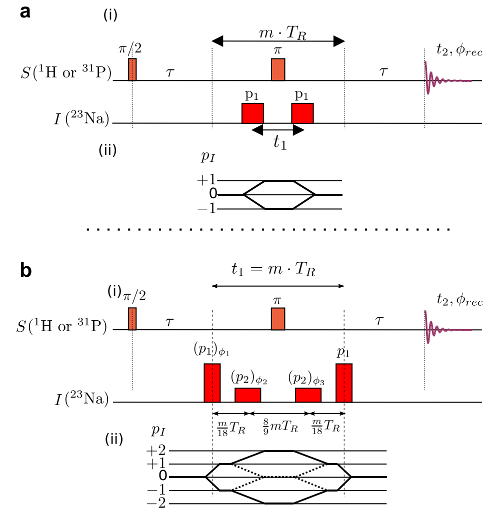

Fig. 1. Basic HMQC (a) and HMQC-ST (b) pulse sequences (i) and coherence pathways (ii) for the *I* nucleus. The coherence order for *I* nucleus is denoted p_I. For *J*-HMQC and *J*-HMQC-ST, no rf field is applied on the *S* and *I* nuclei during the defocusing and refocusing delays, τ, whereas for *D*-HMQC and *D*-HMQC-ST, dipolar recoupling irradiation, such as $SR4_1^2$ or $SFAM_2$, is sent on the *S* channel during τ delays. For basic HMQC, the evolution time, t_1, does not require being rotor-synchronized and the pulses on ^{23}Na should be 90° CT-selective pulses. For HMQC-ST, t_1 must be rotor-synchronized. Note that the delays during the symmetrical t_1-split STMAS are not depicted at scale. The desired coherence pathway for *I* channel, $p_I = 0 \rightarrow \pm 1 \rightarrow \pm 2 \rightarrow \pm 1 \rightarrow 0$, is shown as full lines, while the dashed lines represent the undesired pathways that would also be selected if both desired pathways are recorded together in a States hypercomplex acquisition. For ^{23}N–^{31}P *D*-HMQC-ST experiment on Na_2HPO_4 (see Fig. 6b), $^1\mathrm{H} \rightarrow {}^{31}\mathrm{P}$ CP replaces the first $\pi/2$ pulse applied on the *S* channel. This allows enhancing the sensitivity by benefiting from shorter T_1 and higher γ for the excited nuclei. In addition, ^{1}H decoupling was applied during the HMQC and acquisition parts.

1.1. Basic HMQC

The regular HMQC is presented in Fig. 1a. This sequence allows the observation of *I*–*S* heteronuclear correlation involving the CT of quadrupolar *I* nuclei. Therefore, the two pulses sent on the quadrupolar channel of the regular HMQC sequence should be both CT-selective $\pi/2$-pulses [4]. By CT-selective pulses, one means pulses that act only on ±1/2 spin-states by using rf-fields of the order of the second-order quadrupole interaction. A phase cycling over four steps is usually sufficient [7,4]. For *D*-HMQC, we sent $SFAM_2$ [19] or $SR4_1^2$ [20] recoupling on the *S* nuclei in order to reintroduce the heteronuclear dipolar coupling. These sequences are advantageous since (i) they suppress ^{1}H–^{1}H or ^{31}P–^{31}P homonuclear dipolar interaction, (ii) they are robust to offset and rf inhomogeneity [19,8] and (iii) they have same dipolar scaling factor. As $SFAM_2$ and $SR4_1^2$ are not γ-encoded, they must be rotor-synchronized, i.e. the delay between the τ periods must a multiple of the rotor period, T_R. Such condition does not have to be fulfilled for *J*-HMQC or *D*-HMQC using γ-encoded dipolar recoupling methods.

1.2. HMQC-ST sequence

The HMQC-ST derives from HMQC by the introduction of a t_1-split-STMAS sequence [21] during the evolution period of HMQC (see Fig. 1b). Therefore it cannot be used for spin higher than 3/2. We employed $SR4_1^2$ or $SFAM_2$ as dipolar recoupling. The choice of STMAS as high-resolution technique was motivated by the larger sensivity of STMAS compared to MQMAS, especially for *I*-spin sites displaying large quadrupolar constant, C_Q [22]. Furthermore, the sensitivity of STMAS to atom dynamics can provide additional information [23]. STMAS doubles the isotropic spectral width for rotor synchronized t_1 acquisition compared to MQMAS [24]. It needs precise setting of the magic angle (within a few millidegrees) as well as high stability of the MAS frequency, but these requirements can be met by equipping the probes with Hall effect sensor [25] and by triggering the pulses on the rotor position when necessary.

The HMQC-ST pulse sequence is depicted in Fig. 1b. Note that the evolution time t_1 in Fig. 1b is a composite delay that corresponds to the isotropic dimension of STMAS experiment. The first p_1 pulse applied to the *I* spin creates CT and satellite transition (ST) 1Q coherences ($\frac{1}{2} \leftrightarrow -\frac{1}{2}$ and $\pm\frac{3}{2} \leftrightarrow \pm\frac{1}{2}$, respectively). Then a CT-selective π pulse applied to the *I* spin exchanges ±1/2 spin-states and converts the ST 1Q coherences into the double-quantum (2Q) coherences $\frac{3}{2} \leftrightarrow -\frac{1}{2}$ and $\frac{1}{2} \leftrightarrow -\frac{3}{2}$. Selection of 2Q coherences suppresses the unwanted CT–CT signal [26]. A second CT-selective π pulse converts back the 2Q coherences into ST 1Q coherences. The t_1 time must be perfectly rotor-synchronized, and the magic-angle perfectly adjusted, to cancel the first-order quadrupole interaction. Furthermore, in the case of $I = 3/2$, the second-order quadrupolar interaction can be suppressed if the time spent on 2Q coherences is eight times longer than that on 1Q coherences. This symmetrical t_1-split STMAS sequence was also used in STARTMAS experiment [27]. After double Fourier transform, the HMQC-ST 2D spectrum displays an isotropic dimension, which can be compared to that of t_1-split STMAS or sheared MQMAS/STMAS spectra by using universal scaling [24].

The phase cycling of HMQC-ST is described below. The pulse phases for the spin-1/2 channel are cycled as in basic HMQC. The design of the phase cycling for *I* channel requires specific attention. It is usually possible to produce pure absorption 2D spectra using

TPPI, States or Echo-Antiecho methods. States (or States-TPPI) method leads to a short 8-step phase cycling that consists in changing independently the phase of the three first pulses on the I channel between x and $\bar{x}$ in a nested manner. Unfortunately, it does not suppress the $0 \rightarrow \pm1 \rightarrow 0 \rightarrow \mp1 \rightarrow 0$ pathways. In practice, such undesired pathways lead to an artifact on the carrier frequency in the indirect dimension (see Fig. 6a). This artifact can only be suppressed using an Echo-Antiecho method that selects the $0 \rightarrow 1 \rightarrow 2 \rightarrow 1 \rightarrow 0$ and $0 \rightarrow -1 \rightarrow -2 \rightarrow -1 \rightarrow 0$ pathways separately at the cost of a longer 32-phase cycling scheme on the quadrupolar channel. We managed to shorten this cycling to only 16 phases by recording an hypercomplex point in a multiplex fashion [28]. We used phases listed in Eq. 1 to record the first row signal, $s(t_1, t_2)$, and ϕ_1 and ϕ_{rec} incremented by 90° to record the second row signal $s'(t_1, t_2)$. From these two datasets one can reconstruct the echo signal by $s(t_1, t_2) + s'(t_1, t_2)$, and the anti-echo by $s(t_1, t_2) - s'(t_1, t_2)$. Then the spectrum can be processed in the regular Echo-Antiecho manner.

$$\begin{aligned}
\phi_1 &= [x\,\bar{x}\,x\,\bar{x}\,x\,\bar{x}\,x\,\bar{x}\,y\,\bar{y}\,y\,\bar{y}\,y\,\bar{y}\,y\,\bar{y}] \\
\phi_2 &= [x\,x\,\bar{x}\,\bar{x}\,x\,x\,\bar{x}\,\bar{x}\,y\,y\,\bar{y}\,\bar{y}\,y\,y\,\bar{y}\,\bar{y}] \\
\phi_3 &= [x\,x\,x\,x\,\bar{x}\,\bar{x}\,\bar{x}\,\bar{x}\,x\,x\,x\,x\,\bar{x}\,\bar{x}\,\bar{x}\,\bar{x}] \\
\phi_{rec} &= [x\,\bar{x}\,\bar{x}\,x\,\bar{x}\,x\,x\,\bar{x}\,\bar{x}\,x\,x\,\bar{x}\,x\,\bar{x}\,\bar{x}\,x]
\end{aligned} \tag{1}$$

2. Theory for a 1/2 – 3/2 spin-pair

Here, analytical and numerical density matrix calculations are performed in order to understand the coherence transfers in HMQC and HMQC-ST. These calculations also permit to predict the optimal length of p_1 pulses and τ delays. We consider coherence transfer via J- or dipolar couplings. To shorten the equations, we introduce the following notation:

$$S_{n\theta} = \sin(n\theta), \quad S_{n\lambda} = \sin(\pi n\lambda), \quad C_{n\lambda} = \cos(\pi n\lambda) \tag{2}$$

with

$$\lambda = \tau F_{IS} \quad \text{and} \quad \theta = 2\pi\tau_p \nu_{1I} \tag{3}$$

The dimensionless λ parameter is related to the F_{IS} re-introduced interaction, which can either be the isotropic J_{IS} scalar-coupling, or the d_{IS} recoupled dipolar value for J- and D-HMQC, respectively. The $d_{IS}(\alpha, \beta)$ value depends on the used sequence and on the crystallite orientation. θ is the flip-angle of pulse p_1 on the quadrupolar channel, with τ_p and ν_{1I} the pulse duration and rf-field amplitude, respectively. The two pulses on the S spin-1/2 channel are assumed to be ideal. When considering the quadrupole interaction, the transfer efficiency of HMQC experiments can only be calculated analytically in two cases: $\nu_{1I} \ll C_Q$ or $\nu_{1I} \gg C_Q$. In the following, signals s^X going through quadrupolar nucleus coherences X are calculated at $t_1 = t_2 = 0$ and are always normalized with respect to an optimized J-HMQC signal obtained with two CT-selective 90°-pulses (see Eq. (4) and Fig. 2a).

2.1. J-HMQC

2.1.1. Weak rf-field ($\nu_{1I} \ll C_Q$)

For I nuclei experiencing large quadrupole interaction, the basic J-HMQC of Fig. 1a can be applied using CT-selective pulses. In that case, the transfer efficiency is the same for all crystallites and is then equal to:

$$s^{CT}_{sel} = S^2_{(I+\frac{1}{2})\theta} \cdot S^2_{\lambda} \tag{4}$$

This evolution of the signal is identical to that observed with a pair of spin-1/2 nuclei, except its optimum flip-angle is $(I + 1/2)$ smaller corresponding to the so-called CT-selective 90°-pulse (Fig. 2a):

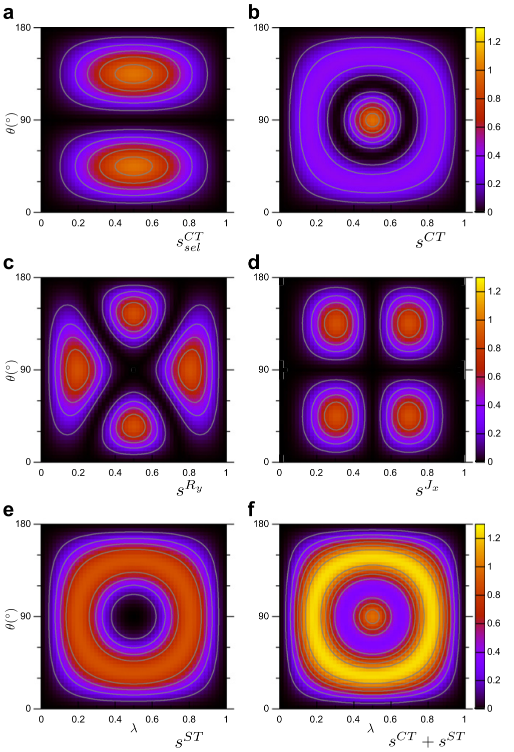

Fig. 2. J-HMQC transfer efficiency calculated from Eqs. (4), (7)–(9) versus the dimensionless $\lambda = \tau J_{IS}$ parameter and the θ pulse flip-angle on the quadrupolar channel. The two pulses on the spin-1/2 channel are assumed ideal. The two pulses on the quadrupolar channel are either CT-selective (a) or ideal (b–f). In the latter case, figures correspond to: (b) s^{CT}, (c) s^{R_y}, (d) s^{J_x}, (e) $s^{ST} = s^{R_y} + s^{J_x}$, (f) total signal: $s^{CT} + s^{ST}$. Contour lines start from 0.1 with 0.2 increment. These curves derived from analytical expressions agree with numerical simulations performed with SIMPSON software (not shown).

$$\theta_{opt} = \frac{\pi}{2I + 1} \tag{5}$$

This condition cannot be employed for the p_1 pulses of J-HMQC-ST since the signal originating from CT coherences is suppressed by the 2Q filter.

For J-HMQC experiments, the interaction frequency is independent from the crystallite orientation, $F_{IS} = J_{IS}$, and the maximum signal is thus always observed for:

$$\tau_{opt} = \frac{1}{2J_{IS}}. \tag{6}$$

2.1.2. Ideal hard-pulses ($\nu_{1I} \gg C_Q$)

This condition is ideal for the p_1 pulses of J-HMQC-ST. However, for solid samples, this condition is usually difficult to fulfill, even if rf-fields with nutation frequencies of several MHz can be produced inside micro-coils [29]. Under such condition, the first p_1 pulse creates both CT and ST 1Q coherences. The CT and ST evolve differently under J-coupling and rf field. Nevertheless, the HMQC transfer efficiency for spin-3/2 nuclei can be calculated analytically using the same formalism as that used previously for INEPT experiments [30]. In particular, we use the same set of $S = 3/2$ spin operators. For the HMQC pulse sequence of Fig. 1a, the final in-phase signal originating from CT coherence during t_1 is equal to:

$$s^{CT} = \left\{S_\lambda^2(5S_\theta + 9S_{3\theta})^2 + 9S_{3\lambda}^2(3S_\theta - S_{3\theta})^2 + 6S_\lambda S_{3\lambda}(5S_\theta + 9S_{3\theta})(3S_\theta - S_{3\theta})\right\}\frac{1}{256} \quad (7)$$

For the same experiment, there are two final in-phase signals originating from ST coherences during t_1, one resulting from in-phase ST coherences (R_y) and the other from anti-phase ST coherences (J_x):

$$s^{R_y} = \left\{S_\lambda^2(S_\theta - 3S_{3\theta})^2 + S_{3\lambda}^2(5S_\theta + S_{3\theta})^2 + 2S_\lambda S_{3\lambda}(S_\theta - 3S_{3\theta})(5S_\theta + S_{3\theta})\right\}\frac{3}{128} \quad (8)$$

$$s^{J_x} = \frac{3}{8}(C_{3\lambda} - C_\lambda)S_{2\theta}^2 \quad (9)$$

The behavior of these in-phase signals, versus the flip-angle θ and the λ parameter, is displayed in Fig. 2b–f in the case of *J*-HMQC.

On powder samples, if the two pulses on the quadrupolar channel are not rotor-synchronized ($t_1 \neq mT_R$), one only observes the CT signal (Eq. 7), as the ST signals are spread across the indirect spectral-width and are thus unobservable. The s^{CT} maximum signal, observed for $(\theta, \lambda) = (90°, 1/2)$, reaches 100% of that observed with CT-selective pulses for $(\theta, \lambda) = (45°$ or $135°, 1/2)$ (compare Fig. 2a and b). This can appear contrary to the case of direct excitation for which the signal is $n + \frac{1}{2}$ larger using hard pulses instead of CT selective pulse. But one has to remind that in HMQC, CT coherences are excited from a state different from I_z.

The s^{R_y} and s^{J_x} signals are represented in Fig. 2c and d, respectively. They are characterized by four maxima of ca. 90%. As they contribute to the same resonance in the 2D *J*-HMQC spectrum, these two terms must be added, giving the circle shaped optimum region shown in Fig. 2e. If the quadrupole interaction is weak, as in the liquid state, there is no second-order quadrupolar effect and one cannot distinguish CT and ST resonances. The total signal, $s^{CT} + s^{R_y} + s^{J_x}$, is shown in Fig. 2f. In this case, the maximum signal is 25% larger than with CT-selective pulses. This optimum signal is observed on a circled region in the (θ, λ) plane. However, when taking into account T_2 losses, the maximum signal will be observed in the left region of this plane $(\theta, \lambda) \approx (90°, 0.2)$, which corresponds to the shortest $\tau \approx \frac{1}{5J_{IS}}$ recoupling time. It must be noted that the central local maximum, $(\theta, \lambda) = (90°, 1/2)$, is only related to a transfer through the CT during t_1.

In Eqs. (7)–(9), we only consider the in-phase signals along F2 dimension. This is justified by the fact that the anti-phase quadruplet patterns along F2 are usually hardly visible in solid-state where inhomogeneous line-width is often much larger than *J*-coupling or can be decoupled [31].

For *J*-HMQC-ST, the signal resulting from CT (Eq. 7) is canceled out by the double-quantum filter. Furthermore, if we assume that the CT-selective π-pulses produce $1Q \leftrightarrow 2Q$ transfers with 100% efficiency, the transfer efficiency of *J*-HMQC-ST is equal to $s^{R_y} + s^{J_x}$ (see Fig. 2e). Hence, the maximal transfer efficiency of *J*-HMQC-ST is 90% of that of *J*-HMQC using CT-selective pulses.

2.1.3. Real hard-pulses ($\nu_{1I} \lesssim C_Q$)

In the case of real hard-pulses and non-negligible quadrupole interactions, numerical simulations are required. These simulations were performed with SIMPSON [32] and a large quadrupole interaction ($C_Q = 3$ MHz). In analogy to the case of ideal hard pulse, the transfer efficiency of *J*-HMQC-ST can be derived from the in-phase *J*-HMQC signal originating from ST coherence during t_1. Therefore, numerical simulations were performed for ^{23}Na–^{31}P ST-filtered *J*-HMQC experiment comprising two real hard-pulses of identical amplitude. The result are presented in Fig. 3 and should be compared to those in Fig. 2e. Compared to ideal hard pulses, the use of real hard pulses results in a significant decrease of the efficiency and only short pulses ($\theta \approx 30$—$45°$) remain effective. At low rf-fields (around 50–80 kHz), usually used with triple resonance probes, only ca. 10–30% of the signal remains for these short pulses. Nevertheless, close to 60% efficiency can be reached at rf-field of 200 kHz, which is achievable on 1.3 mm probe for example (Fig. 3c).

2.2. D-HMQC

For *D*-HMQC experiments, it must be reminded that the reintroduced interaction depends on the crystallite orientation: $F_{IS} = d_{IS}(\alpha, \beta)$. On powder samples, with respect to *J*-HMQC, this leads to a decrease of the maximum signal and to an optimum recoupling time that depends on the recoupling sequence scaling factor. *D*-HMQC sequences were simulated with SIMPSON using $SR4_1^2$ [20] technique and direct matrix selection of CT or ST coherences during t_1. We have not differentiated R_y and J_x evolutions, and intensities in Figs. 4 and 5 are reported to the same scale as *J*-HMQC results.

2.2.1. Weak rf-field ($\nu_{1I} \ll C_Q$)

The regular *D*-HMQC experiment displays a maximal transfer efficiency 50% lower than that of regular *J*-HMQC (see Fig. 4a). This is expected for non-γ-encoded recoupling sequences such as $SR4_1^2$. The maximal transfer efficiency is found at delay $\tau \approx 2.0$ ms and $\theta = 45°$ or $135°$ flip-angles corresponding to the expected 90 or 270° CT-selective pulse.

2.2.2. Ideal hard-pulses ($\nu_{1I} \gg C_Q$)

Unlike the *J*-coupling case, ideal pulses do not excite well CT since the transfer efficiency for signal arising from CT only reaches 33% and is lower than that obtained with CT-selective pulses. We have observed experimentally this fact (not shown). In Fig. 4b,

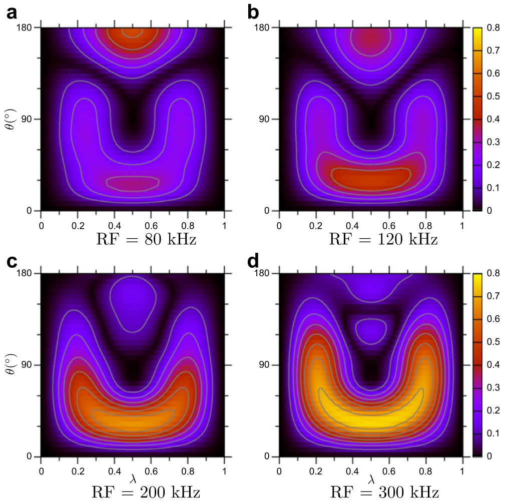

Fig. 3. Simulated ST-filtered ^{23}Na–^{31}P *J*-HMQC transfer efficiency versus λ and θ parameters at $B_0 = 9.4$ T and $\nu_R = 10$ kHz. The ^{23}Na nucleus experiences quadrupolar interaction with $C_Q = 3$ MHz and a quadrupolar asymmetry parameter $\eta_Q = 0.1$. Contour lines start from 0.1 with 0.1 increment. Plots show the magnitude of magnetization as this latter can spread along *X* and *Y* components. Figures correspond to: $\nu_{1I} = 80$ (a), 120 (b), 200 (c), and 300 kHz (d).

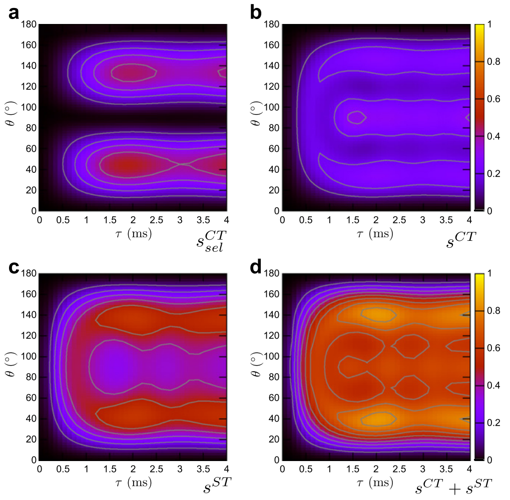

Fig. 4. Simulated ^{23}Na–^{31}P *D*-HMQC efficiency versus θ flip angle and τ delay with SR4^2_1 recoupling sequence. The two pulses on the spin-1/2 channel are assumed ideal. The two pulses on the quadrupolar channel are either CT-selective (a) or ideal (b–d). In the latter case, figures correspond to: (b) s^{CT}, (c) s^{ST}, (d) total signal: $s^{CT} + s^{ST}$. The dipolar coupling constant is 800 Hz and the interatomic vector is collinear with the main axis of the quadrupole tensor. Other parameters are those of Fig. 3.

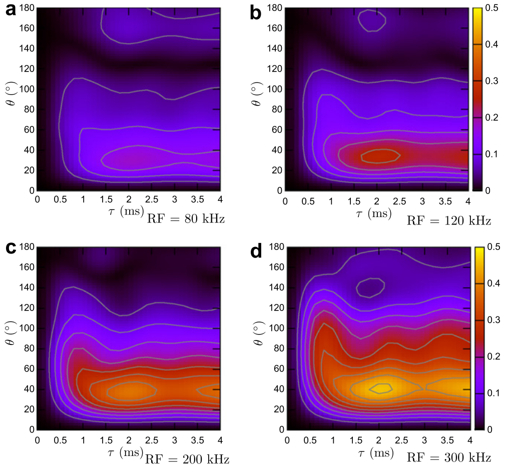

Fig. 5. Simulated ST-filtered ^{23}Na–^{31}P *D*-HMQC transfer efficiency versus θ and τ parameters. The two pulses on the spin-1/2 channel are assumed ideal. Figures correspond to: $\nu_{1I} = 80$ (a), 120 (b), 200 (c), and 300 kHz (d). The dipolar interaction is identical to that of Fig. 4. Contour levels start from 0.05 with 0.05 increments. Other parameters are those of Fig. 3.

overall maximum occurs at $\tau \approx 1.5$ ms and $\theta = 90^\circ$. However, a bit like in *J*-HMQC, a smaller plateau about half as high (16%) is observed at shorter and longer pulse-length ($\theta \approx 35^\circ$ and 145°).

STs are better excited than the CT. In Fig. 4c, one notes again a $\subset$ shape with slightly higher efficiency (62%) for $\tau \approx 2$ ms ($\theta = 45^\circ$ or 135°) than for short mix time: 45% for $\tau \approx 0.8$ ms and $\theta = 90^\circ$. The theoretical transfer efficiency of *D*-HMQC-ST using ideal hard p_1 pulses is displayed in Fig. 4c. Finally, in Fig. 4d, when all transitions cannot be discriminated (small C_Q) one obtains 88% efficiency of a CT-selective *J*-HMQC for $\tau \approx 2$ ms and $\theta = 40^\circ$ or 140°.

2.2.3. *Real hard-pulses* ($\nu_{1I} \lesssim C_Q$)

The transfer efficiency of a ST-filtered *D*-HMQC experiment simulated with two identical real hard-pulses is plotted in Fig. 5 for several rf-fields. Although the dipolar recoupling pattern is different from that corresponding to *J*-coupling (compare Figs. 3 and 5), qualitative conclusions are similar and they show that only short $\theta = 30$–45° flip-angles are relatively efficient. The optimal defocusing and refocusing times are about $\tau \approx 2$ ms corresponding to the optimum observed for CT-selective *D*-HMQC whatever the nutation frequency of the p_1 pulses. Conversely, maximum efficiency increases significantly with rf-field: 18%, 27%, 38% and 46% for 80, 120, 200 and 300 kHz, respectively.

D-HMQC-ST is obtained from the ST-filtered *D*-HMQC experiment (Fig. 5) by adding two CT-selective π-pulses. The overall transfer efficiency of these two pulses is about 65–80% and hence *D*-HMQC-ST is able to achieve very good S/N ratio compared to the classical *D*-HMQC experiment. On a 1.3 mm probe for example, using a 200 kHz rf-field in *D*-HMQC-ST sequence, one gets around 76% of the efficiency of a *D*-HMQC experiment performed with CT-selective pulses (compare Figs. 4a and 5c). This is in line with the experimental observation of spectrum in Fig. 7 for which the transfer efficiency reached more than 50% of that of regular *D*-HMQC. Given that isotropic lines of *D*-HMQC-ST spectrum are much narrower than those observed with *D*-HMQC, S/N becomes significantly higher in *D*-HMQC-ST. Finally, it must be noted that for small C_Q values, the simulated patterns in Figs. 3 and 5 look the same, but with a shift to lower rf-strength as a weaker rf-field will be able to better excite STs.

3. Experimental section

The HMQC-ST experiment was tested experimentally in the case of coherence transfer via the dipolar coupling (*D*-HMQC-ST) between ^{23}Na and ^{1}H or ^{23}Na and ^{31}P. Spectra presented in Figs. 6,7 were recorded on Bruker spectrometers operating at 9.4 or 18.8 T. Additional details are given in the figure captions.

3.1. *Sample description*

We have chosen to demonstrate our new sequence on NaH_2PO_4 and anhydrous Na_2HPO_4 that were both purchased from CortecNet and used without further purification. These samples have well-known crystal structures and several ^{23}Na sites well-suited to STMAS with C_Q values larger than 1.5 MHz.

3.1.1. *Na_2HPO_4*

Anhydrous Na_2HPO_4 has three sodium, one phosphorous and one proton sites. Protons are rather dilute as the two first-neighbors are at 340 pm, while second-neighbors are farther than 500 pm. This compound is highly crystalline and has long longitudinal relaxation times, which lead to very narrow isotropic lineshapes in MQMAS/STMAS. Therefore, this sample allows adjusting accurately the magic-angle within a few millidegrees. From the slices of this spectrum, we have extracted the chemical shift and quadrupolar parameters: $(\delta_{CS}\,(\text{ppm}), C_Q\,(\text{MHz}), \eta_Q) = (4.9, 1.4, 0.17), (3.9, 2.1, 0.68), (6.2, 3.7, 0.26)$ for Na_1, Na_2 and Na_3, respectively. They are in good agreement with previous measures [33].

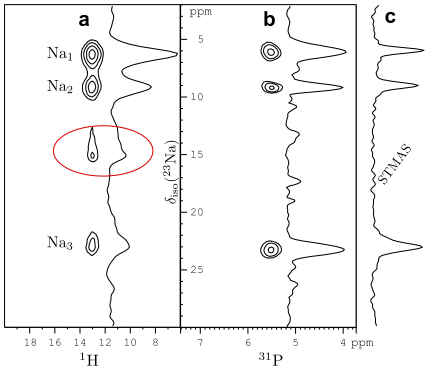

Fig. 6. 2D *D*–HMQC-ST spectra of Na_2HPO_4 recorded at 9.4 T. (a) ^{23}Na–^1H spectrum recorded at $\nu_R = 20$ kHz using 3.2 mm HXY probe and States-TPPI procedure. The carrier artifact (circled resonance) is related to unwanted $0 \rightarrow \pm1 \rightarrow 0 \rightarrow \pm1 \rightarrow 0$ pathways. The dipolar recoupling used $SR4_1^2$ sequence with $\tau = 600$ µs. The hard- and soft-pulses on the ^{23}Na channel had nutation frequencies and pulse length of (100 kHz, 1.25 µs) and (17 kHz, 15 µs), respectively. An rf-field of 40 kHz was used on the ^1H channel. The 2D spectrum results from the average of 16 transients and 57 pairs of rows with t_1 increments of 100 µs and a recycling delay of 40 s, leading to 20 h total experimental time. (b) ^{23}Na–^{31}P spectrum recorded at $\nu_R = 12.5$ kHz using 4 mm HXY probe and special echo/antiecho acquisition (see Eq. (1)). No carrier artifact is observable. Dipolar recoupling used $SFAM_2$ sequence in the ^{31}P channel with $\tau = 2$ ms, an rf-amplitude of 50 kHz and an offset-amplitude of 80 kHz. The hard- and soft-pulses on the ^{23}Na channel had nutation frequencies and pulse length of (85 kHz, 1 µs) and (11 kHz, 22 µs), respectively. The 2D spectrum results from the average of 32 transients and 54 pairs of rows with t_1 increments of 160 µs and a recycling delay of 40 s, totalizing 20 h of experimental time. After $^1H \rightarrow {}^{31}P$ CP, proton decoupling using PISSARRO [37] with pulse-length of 0.9 T_R and rf-field of 60 kHz was applied during the remaining part of the sequence. (c) Sum projection of t_1-split STMAS.

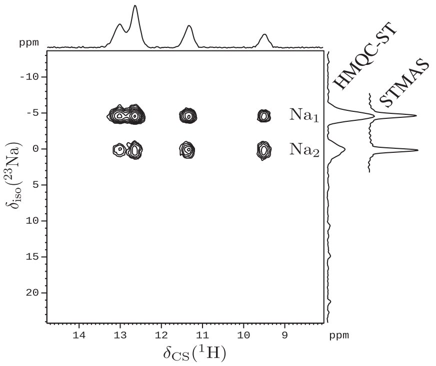

Fig. 7. ^{23}Na–^1H *D*-HMQC-ST spectrum of NaH_2PO_4 recorded at 18.8 T and $\nu_R = 64$ kHz using 1.3 mm probe and special echo/antiecho acquisition (see Eq. (1)). No carrier artifact is observable. Dipolar recoupling used $SFAM_2$ sequence on the ^1H channel with $\tau = 500$ µs, an rf-amplitude of 180 kHz and an offset-amplitude of 20 kHz. The hard- and soft-pulses on the ^{23}Na channel had nutation frequencies and pulse length of (210 kHz, 1.5 µs) and (11 kHz, 22 µs), respectively. The 2D spectrum results from the average of 32 transients and 80 pairs of rows with t_1 increments of 125 µs and a recycling delay of 10 s, totalizing 7 h of experimental time. The *D*-HMQC-ST and STMAS projections are shown on the right-side.

3.1.2. NaH_2PO_4

This compound has two sodium, one phosphorous and four proton sites [34]. Quadrupolar parameters, fitted from 1D spectra, are $(C_Q(\text{MHz}), \eta_Q) = (2.38, 0.96)$, and (1.56, 0.45) for Na_1 and Na_2, respectively.

3.2. Optimizing a D-HMQC-ST experiment

Optimization of *D*-HMQC-ST experiment is pretty straightforward as parameters only depend on three independent basic block elements. First, if required, $^1H \rightarrow$ spin-1/2 CP conditions should be optimized. Then, the *D*-HMQC experiment should be optimized, which means adjustment of the spin-1/2 pulse-lengths, the dipolar recoupling conditions (rf-field amplitude and mix-time) and possibly the decoupling parameters. Third, simulations show that the ST hard-pulses should be around 30–45° flip-angle for optimum recoupling time. They get closer to 90° if mix-times are shorter than the optimum theoretical value without losses (see Fig. 5). Alternatively, for moderate hard-pulse rf-fields (50–80 kHz), we have noticed that pulse-lengths correspond roughly to the optimal first hard-pulse of a separate t_1-split STMAS experiment. Finally, one can directly refine the optimal pulse on *D*-HMQC-ST experiment itself.

4. Experimental results

Na_2HPO_4 spectra were recorded at 9.4 T with 3.2 mm (Fig. 6a) and 4 mm (Fig. 6b) HXY probes. STMAS hard-pulses were optimized to $\theta \approx 30 - 45^\circ$ flip-angle, in agreement with our simulations, although direct comparison must be done with care as the spin system is more complex than an isolated pair. Fig. 6a displays the ^{23}Na-^1H *D*-HMQC-ST 2D spectrum recorded by using a regular States-TPPI 2D complex acquisition mode with 8-steps phase-cycling. One can observe an artifact at the carrier frequency (circled resonance) due to the unwanted pathways $0 \rightarrow \pm1 \rightarrow 0 \rightarrow \pm1 \rightarrow 0$, as discussed in Section 1.2. The recoupling time was $\tau = 600$ µs, which must be optimal for the closest H-Na distances.

Fig. 6b displays the ^{23}Na–^{31}P *D*-HMQC-ST 2D spectrum recorded using the multiplexed echo-antiecho acquisition (Eq. 1), therefore the artifact on the carrier frequency is absent. The recoupling time is $\tau = 2$ ms, which is optimal for the closest P–Na distances. Since dipolar recoupling is sent on ^{31}P channel, it is mandatory to decouple protons. We tested several hetero-nuclear decoupling sequences: CW, TPPM [35], and SPINAL-64 [36]. However, PISSARRO [37] exhibited a much improved efficiency compared to the three other methods.

In Fig. 7, the ^{23}Na–^1H spectrum of NaH_2PO_4, recorded at 18.8 T with multiplexed echo/antiecho acquisition does not exhibit artifact at the ^{23}Na carrier frequency. The four proton and the two sodium sites are fully resolved in this figure. The spectrum demonstrates that all protons correlate with both sodium sites as expected from crystal structure. The structure of NaH_2PO_4 shows that closest H–Na distances are between 270 and 370 pm, corresponding to 600–1600 Hz dipolar coupling constants in absolute value. Optimal recoupling time should be larger than 1 ms, but relaxation processes shortened it to 500 µs. In this case, it is not surprising to use a $\theta \approx 76^\circ$ flip-angle, as it would correspond to points situated around 500 µs in Fig. 5. A comparison of simulated and experimental optimization of p_1 pulse can be found in electronic Supplemetary material online. The observed transfer efficiency is 50% to 60% of that of a CT-selective HMQC, in line with simulations of Fig. 5. It must be emphasized that it is dangerous to compare proximities using the *D*-HMQC-ST method as cross-peak intensities depend on C_Q values, distances and the recoupling time. In comparison with the STMAS projections, one observes along the ^{23}Na dimension larger resonances in Fig. 6a than in Fig. 6b. This extra-broadening is due to residual ^1H–^1H dipolar couplings.

5. Conclusions

We have shown that a through-space hetero-nuclear multiple-quantum coherence (*D*-HMQC) experiment in between spin-1/2 and quadrupolar nuclei can be combined with a t_1-split STMAS block, if this nucleus has a spin-3/2. It produces HETCOR spectra with isotropic resolution with a very good efficiency. The optimum conditions have been given and explained.

If such *D*-HETCOR experiment could also have been obtained with a STMAS-INEPT experiment, the great advantage of *D*-HMQC-ST is that it may allow the inverse detection under high-resolution of spin-3/2 low-gamma nuclei such as ^{35}Cl or ^{39}K. This may lead to a large S/N gain, with respect to direct detection, especially when the spin-1/2 nucleus is a high-gamma nucleus, such as ^{1}H or ^{19}F. Another application of such technique may be to obtain through-space HETCOR spectra, with semi high-resolution, where two quadrupolar nuclei are involved [38], as long as there is a spin-3/2 nucleus in the indirect dimension. We have verified that the same principle can also be applied to *D*-HSQC experiments. However, as recently shown, HMQC experiments are more robust than HSQC when dealing with quadrupolar nuclei [8].

Acknowledgments

Authors are grateful for funding provided by Region Nord/Pas de Calais, Europe (FEDER), CNRS, French Minister of Science, USTL, ENSCL, Bruker BIOSPIN and CortecNet. Financial support from the TGE RMN THC (FR-3050) for conducting the research is gratefully acknowledged. The authors also thank Zhehong Gan for fruitful discussions.

Appendix A. Supplementary data

Supplementary data associated with this article can be found, in the online version, at doi:10.1016/j.cplett.2010.07.037.

References

[1] C.A. Fyfe, H. Grondey, K.T. Mueller, K.C. Wong-Moon, T. Markus, J. Am. Chem. Soc. 114 (1992) 5876.
[2] C. Fyfe, K. Mueller, H. Grondey, K. Wong-Moon, Chem. Phys. Lett. 199 (1992) 198.
[3] C.A. Fyfe, H.M. zu Altenschildesche, K.C. Wong-Moon, H. Grondey, J.M. Chezeau, Solid State Nucl. Magn. Reson. 9 (1997) 97.
[4] J. Trebosc, B. Hu, J.P. Amoureux, Z. Gan, J. Magn. Reson. 186 (2007) 220.
[5] J.-P. Amoureux, M. Pruski, Mol. Phys. 100 (2002) 1595.
[6] B. Hu, J.P. Amoureux, J. Trébosc, S. Hafner, J. Magn. Reson. 192 (2008) 8.
[7] D. Massiot, F. Fayon, B. Alonso, J. Trebosc, J.-P. Amoureux, J. Magn. Reson. 164 (2003) 160.
[8] O. Lafon, Q. Wang, B. Hu, F. Vasconcelos, J. Trébosc, S. Cristol, F. Deng, J.-P. Amoureux, J. Phys. Chem. A 113 (2009) 12864.
[9] Y. Ishii, R. Tycko, J. Magn. Reson. 142 (2000) 199.
[10] L. Frydman, J.S. Harwood, J. Am. Chem. Soc. 117 (1995) 5367.
[11] J.-P. Amoureux, C. Fernandez, S. Steuernagel, J. Magn. Reson. Ser A 123 (1996) 116.
[12] J.P. Amoureux, C. Fernandez, Solid State Nucl. Magn. Reson. 10 (1998) 211.
[13] Z. Gan, J. Am. Chem. Soc. 122 (2000) 3242.
[14] S.H. Wang, S.M. De Paul, L.M. Bull, J. Magn. Reson. 125 (1997) 364.
[15] J.W. Wiench, M. Pruski, Solid State Nucl. Magn. Reson. 26 (2004) 51.
[16] R. Siegel, J. Rocha, L. Mafra, Chem. Phys. Lett. 470 (2009) 337.
[17] C.M. Morais, V. Montouillout, M. Deschamps, D. Iuga, F. Fayon, F.A.A. Paz, J. Rocha, C. Fernandez, D. Massiot, Magn. Reson. Chem. 47 (2009) 942.
[18] S. Steuernagel, Solid State Nucl. Magn. Reson. 11 (1998) 197.
[19] B. Hu, J. Trébosc, J.P. Amoureux, J. Magn. Reson. 192 (2008) 112.
[20] A. Brinkmann, A. Kentgens, J. Am. Chem. Soc. 128 (2006) 14758.
[21] J. Trebosc, J.-P. Amoureux, Z. Gan, Solid State Nucl. Magn. Reson. 31 (2007) 1.
[22] S.E. Ashbrook, S. Wimperis, J. Magn. Reson. 156 (2002) 269.
[23] S. Antonijevic, S.E. Ashbrook, S. Biedasek, R.I. Walton, S. Wimperis, H. Yang, J. Am. Chem. Soc. 128 (2006) 8054.
[24] J.-P. Amoureux, C. Huguenard, F. Engelke, F. Taulelle, Chem. Phys. Lett. 356 (2002) 497.
[25] S. Mamone, A. Dorsch, O.G. Johannessen, M.V. Naik, P.K. Madhu, M.H. Levitt, J. Magn. Reson. 190 (2008) 135.
[26] H.-T. Kwak, Z. Gan, J. Magn. Reson. 164 (2003) 369.
[27] M.J. Thrippleton, T.J. Ball, S. Steuernagel, S.E. Ashbrook, S. Wimperis, Chem. Phys. Lett. 431 (2006) 390.
[28] N. Ivchenko, C.E. Hughes, M.H. Levitt, J. Magn. Reson. 160 (2003) 52.
[29] A.P.M. Kentgens, J. Bart, P.J.M. van Bentum, A. Brinkmann, E.R.H. van Eck, J.G.E. Gardeniers, J.W.G. Janssen, P. Knijn, S. Vasa, M.H.W. Verkuijlen, J. Chem. Phys. 128 (2008) 052202.
[30] H.-M. Kao, C.P. Grey, J. Magn. Reson. 133 (1998) 313.
[31] L. Delevoye, J. Trébosc, Z. Gan, L. Montagne, J.-P. Amoureux, J. Magn. Reson. 186 (2007) 94.
[32] M. Bak, J.T. Rasmussen, N.C. Nielsen, J. Magn. Reson. 147 (2000) 296.
[33] M. Baldus, B.H. Meier, R.R. Ernst, A.P.M. Kentgens, H. Meyer zu Altenschildesche, R. Nesper, J. Am. Chem. Soc. 117 (1995) 5141.
[34] R.N.P. Choudhary, R.J. Nelmes, K.D. Rouse, Chem. Phys. Lett. 78 (1981) 102.
[35] A.E. Bennett, C.M. Rienstra, M. Auger, K.V. Lakshmi, R.G. Griffin, J. Chem. Phys. 103 (1995) 6951.
[36] B.M. Fung, A.K. Khitrin, K. Ermolaev, J. Magn. Reson. 142 (2000) 97.
[37] M. Weingarth, P. Tekely, G. Bodenhausen, Chem. Phys. Lett. 466 (2008) 247.
[38] D. Iuga, C. Morais, Z. Gan, D.R. Neuville, L. Cormier, D. Massiot, J. Am. Chem. Soc. 127 (2005) 11540.

Chapitre 4

Découplage dipolaire homonucléaire

L'hydrogène est l'élément le plus abondant dans l'univers, dont il constitue plus de 75 % de la masse. Il est présent dans de nombreux composés chimiques. Citons, au risque d'un inventaire « à la Prévert » : l'eau, les molécules organiques et biologiques, les polymères, les matériaux hybrides, les catalyseurs supportés, les conducteurs protoniques ou les hydrures utilisés pour le stockage de l'hydrogène. Toutefois, l'importance des atomes d'hydrogène ne se limite pas à leur ubiquité. Ils jouent aussi un rôle majeur en termes de structure et de réactivité :

i. Les atomes d'hydrogène peuvent être engagés dans des liaisons hydrogènes [191]. Ces liaisons non covalentes gouvernent la structure de nombreux composés, tels que l'eau ou les macromolécules biologiques, et sont impliquées dans les phénomènes d'agrégation ou de reconnaissance moléculaire ;

ii. L'échange de cations d'hydrogène est à la base des réactions acido-basiques au sens de Brønsted-Lowry, ce qui constituent un mode fondamental de réactivité en chimie.

La détermination de la position des atomes d'hydrogènes dans les composés chimiques est donc capitale pour comprendre leur structure, leur stabilité et leur réactivité. Cependant, les atomes d'hydrogène sont difficilement observables en diffraction des rayons X du fait de leur faible nombre d'électrons. À l'inverse, les protons sont facilement détectables par RMN. En effet, cet isotope bénéficie de propriétés RMN favorables, telles qu'un spin $I = 1/2$, une abondance naturelle de 99,985% et un rapport gyromagnétique élevé (le deuxième en valeur absolue après celui du tritium). Ces caractéristiques conduisent à une sensibilité élevée et à la possibilité de sonder les proximités ^{1}H–^{1}H en abondance naturelle. Cette possibilité, utilisée depuis longtemps en RMN des solutions, est une des voies prometteuse pour la cristallographie par RMN en abondance naturelle [105, 106].

Cependant, pour les solides, l'utilisation de la RMN des protons est limitée par la faible gamme des déplacements chimiques, et les largeurs de raies importantes, résultant du réseau étendu des couplages dipolaires ^{1}H–^{1}H. En effet, il suffit de comparer le spectre RMN ^{1}H d'un même composé en solution et à l'état solide pour comprendre la richesse des informations chimiques masquées par les couplages dipolaires.

La suppression des couplages dipolaires homonucléaires est une opération relativement délicate. La solution la plus simple consiste à manipuler la partie spatiale de l'interaction, en utilisant la rotation à l'angle magique. Cependant, comme les interactions dipolaires sont homogènes pour des noyaux non alignés, la largeur de raie ne décroît que comme l'inverse de la fréquence MAS [37–39]. Ainsi, même à $\nu_r = 80$ kHz, les couplages dipolaires ne sont pas complètement éliminés. Une alternative consiste à moyenner la partie de spin de l'interaction dipolaire à l'aide d'un champ rf [40]. En effet, les fréquences de nutation rf accessibles sont largement supérieures aux fréquences MAS, ce qui permet d'éliminer plus efficacement l'interaction dipolaire.

Les séquences de découplage dipolaire doivent, cependant, pouvoir être utilisées dans les conditions MAS, car la rotation à l'angle magique est nécessaire pour supprimer le CSA des protons tout en préservant les déplacements chimiques isotropes. La suppression du CSA des protons peut nécessiter l'utilisation de fréquences MAS non négligeables, puisque l'amplitude de cette interaction peut être supérieure à 25 ppm pour certaines liaisons hydrogène [192, 193]. Les fréquences MAS requises sont proportionnelles à la norme du champ $\boldsymbol{B}^0$. En outre, les séquences de découplage homonucléaire doivent pouvoir être insérées dans des expériences de corrélation hétéronucléaire entre les protons et des noyaux soumis à des CSA élevés, tels que ^{13}C ou ^{31}P. Pour ces noyaux, l'utilisation de fréquences MAS élevées est nécessaire, en particulier à haut champ.

Ces séquences, combinant rotation à l'angle magique et séquence d'impulsion, sont appelées CRAMPS. Durant une expérience CRAMPS, les termes d'espace et de spin sont modulés de façon simultanée et les interférences entre ces deux modulations temporelles peuvent réintroduire les couplages dipolaires ^{1}H–^{1}H. À l'origine, ces interférences ont été évitées en utilisant des fréquences MAS faibles ($\nu_r < 10$ kHz) [194–196]. Dans ces conditions, il est possible d'utiliser des supercyclages, dont le temps de cycle est long, afin d'éliminer au mieux l'interaction dipolaire. Plus récemment, il a été montré que des séquences d'impulsion désynchronisées avec la période de rotor et utilisant des temps de cycle court, telles que FSLG [197, 198], PMLG [199] et DUMBO [200], peuvent être utilisées dans la gamme 10 kHz $\leq \nu_r \leq$ 25 kHz. En parallèle, une autre stratégie pour éviter les interférences entre la rotation de l'échantillon et le champ rf a été proposée. Elle consiste à utiliser des séquences de découplage basées sur la symétrie pour éliminer les couplages dipolaires et le CSA, tout en conservant les déplacements chimiques isotropes [201, 202]. Ces méthodes basées sur la symétrie ont été introduites, elles aussi, pour des fréquences MAS comprises entre 10 et 25 kHz.

C'est dans ce contexte qu'en 2008, nous avons abordé le problème du découplage homonucléaire. À cette date, aucune expérience de découplage n'avait été effectuée à $\nu_r > 25$ kHz. Il y avait, cependant, un besoin de méthodes de découplages homonucléaires compatibles avec cette gamme de fréquence. Leur absence empêchait notamment l'enregistrement, à haut champ, de spectres 2D de corrélation ^{1}H–^{13}C et ^{1}H–^{31}P présentant une résolution élevée en dimension ^{1}H. Le groupe de méthodologie RMN de Lille a comblé cette lacune en introduisant de nouvelles méthodes basées sur les symétries $\mathrm{C}N_n^{N/2}$ et en montrant qu'elles fonctionnent à $\nu_r = 65$ kHz [33, 34, 41]. Ceci a stimulé fortement la recherche de séquences de découplage homonucléaire fonctionnant pour des fréquences MAS élevées. Plusieurs groupes ont alors montré que les séquences PMLG et DUMBO pouvaient aussi être employées à $\nu_r = 65$ kHz [203–205]. Cependant, les méthodes PMLG et DUMBO ont été conçues pour des fréquences MAS faibles. De ce fait, elles ne sont pas forcément optimales à haute vitesse. C'est la raison pour laquelle nous avons proposé récemment, en collaboration avec Z. Gan et P. K. Madhu, une méthode de découplage désynchronisée, baptisée TIMES. Cette méthode produit des spectres ^{1}H à $\nu_r = 80$ kHz, dont la résolution est supérieure à celle obtenue avec PMLG, tandis que la puissance rf utilisée est plus faible [35].

Au vu de notre expérience du découplage homonucléaire, une séquence idéale dans ce domaine doit posséder les caractéristiques suivantes :

i. Elle doit conduire à une résolution élevée ;

ii. Les spectres obtenus doivent présenter peu d'artefacts ;

iii. Elle doit nécessiter des champs rf modérés, surtout dans le cas des applications pour les molécules biologiques sensibles à la chaleur ;

iv. Elle doit être robuste aux inhomogénéités de champ rf et aux transitoires ;

v. Elle doit être robuste aux déplacements chimiques isotropes et au CSA. En particulier, le facteur de réduction des déplacements chimiques doit être constant sur une large gamme de fréquence, afin d'éviter les déformations des spectres. Cette condition n'est, cependant, pas très critique pour les protons, étant donné leur faible écrantage électronique ;

vi. Elle doit être utilisable dans différents types d'expériences, qu'il s'agisse d'acquisition 1D, des délais de défocalisation ou de refocalisation dans les expériences basées sur le couplage J ou des périodes d'évolution t_1 de séquence HMQC ou d'expériences de corrélation homonucléaire 2Q–1Q ;

vii. Elle doit être utilisable pour une large gamme de fréquences MAS.

4.1 Méthodes basées sur la symétrie

Les séquences basées sur la symétrie consistent à combiner astucieusement les modulations dues au MAS et au champ rf, de façon à éliminer les couplages dipolaires, tout en conservant les déplacements chimiques isotropes. Ces séquences sont, en principe, synchronisées avec la période du rotor et elles sont généralement plus simples à mettre en oeuvre que les séquences non-synchronisées, en particulier pour des fréquences MAS élevées. En effet, il n'est pas nécessaire d'éviter les interférences entre la séquence d'impulsion et la rotation de l'échantillon, puisqu'au contraire, ces séquences tirent parti de ces phénomènes d'interférence. Dans la pratique, la période de la séquence d'impulsion n'a pas à être optimisée et elle est fixée par la période du rotor et la symétrie choisies. Les séquences basées sur la symétrie comportent donc un paramètre de moins à optimiser, que les séquences non-synchronisées. Un autre désavantage des séquences non-synchronisées est le nombre élevé de conditions d'interférence Rotor-RF (RRF) entre la rotation et le champ rf. Le recouvrement entre un pic et une fréquence d'interférence RRF provoque un élargissement de raie [206]. En revanche, pour les séquences synchronisées, nous avons montré que les fréquences RRF sont uniquement situées au centre et aux bords du spectre [34]. Ce faible nombre de conditions RRF facilite le choix de la position de la porteuse.

Les premières séquences de découplage homonucléaire, basées sur la symétrie, utilisaient les symétries $\mathrm{C}4_1^0$ et $\mathrm{R}N_n^{N/2}$ [201,202]. Cependant, pour ces séquences, le champ magnétique effectif résultant des déplacements chimiques isotropes n'est pas dirigé selon l'axe z, l'axe du champ magnétique $\boldsymbol{B}^0$. Par conséquent, ces techniques de découplage produisent des pics images et des pics à la fréquence de la porteuse (pic zéro).

Notre contribution, à ce domaine, a consisté à montrer que les séquences basées sur les symétries $\mathrm{C}N_n^{N/2}$ permettaient de découpler les interactions dipolaires ^{1}H–^{1}H aux fréquences MAS élevées, tout en produisant un champ effectif suivant l'axe z pour les déplacements chimiques [33, 34, 41]. En effet, pendant longtemps, les séquences $\mathrm{C}N_n^{N/2}$ avaient été délaissées, car l'utilisation d'impulsion 360_0 ou $90_0 360_{180} 270_0$ comme élément de base conduisait à annuler les déplacements chimiques isotropes. La notation ξ_ϕ désigne, ici, une impulsion rf résonante, de forme rectangulaire, dont l'angle de nutation est ξ et la phase est ϕ. Nous avons montré qu'à l'inverse, les éléments de base $\mathcal{C} = \alpha_0 \alpha_{180}$, ou leurs versions lissées, n'éliminent pas complètement les déplacements chimiques et peuvent être utilisées pour le découplage homonucléaire. En outre, les séquences $\mathrm{C}N_n^{N/2}$ produisent une rotation autour de l'axe z sous l'effet des déplacements chimiques. Ceci a été démontré dans le cadre de la théorie de l'hamiltonien moyen et a été vérifié par des simulations et des expériences. Cette propriété offre plusieurs avantages. Premièrement, elle permet de s'affranchir des artefacts, tels que les pics zéro et images. Deuxièmement, elle autorise l'emploi des cyclages de phase usuels pour les expériences multidimensionnelles.

Cependant, les éléments de base $\mathcal{C} = \alpha_0\alpha_{180}$, ou leurs versions lissées, n'éliminent pas complètement l'interaction dipolaire homonucléaire. Ils se contentent de la réduire. Ce sont les propriétés de symétrie de la séquence qui assurent la suppression des couplages dipolaires dans l'hamiltonien moyen à l'ordre zéro. Les termes d'ordre supérieur impliquant les couplages dipolaires sont, eux, réduits par la rotation de l'échantillon. C'est la raison pour laquelle la résolution offerte par les séquences $\mathrm{C}N_n^{N/2}$ augmente avec la fréquence MAS. Cette constatation est générale pour toutes les séquences basées sur la symétrie, qui sont essentiellement intéressantes à haute vitesse.

En outre, aux fréquences MAS élevées, les séquences $\mathrm{C}N_n^{N/2}$, lissées en amplitude, nécessitent des puissances rf plus faibles que les séquences DUMBO et PMLG. Par exemple, à $\nu_r = 65$ kHz, les séquences $\mathrm{C}N_n^{N/2}$ lissées et DUMBO nécessitent des champs rf efficaces respectivement de 150 et 170 kHz [41,204]. En outre, le lissage de l'amplitude permet de diminuer les transitoires.

Les séquences $\mathrm{C}N_n^{N/2}$ ne comportent, en principe, pas de fenêtre et ne sont donc pas compatibles avec l'acquisition du signal pendant le découplage. Cependant, nous avons démontré que l'insertion de fenêtres d'acquisition entre les trains d'impulsion $\mathrm{C}N_n^{N/2}$ permet l'enregistrement de spectres 1D ^{1}H [33]. La présence de ces fenêtres d'acquisition désynchronise les trains d'impulsion $\mathrm{C}N_n^{N/2}$ sans pour autant compromettre la résolution spectrale. Comme les séquences $\mathrm{C}N_n^{N/2}$ correspondent à une rotation autour de l'axe z, il n'est pas nécessaire d'utiliser des impulsions auxiliaires pour basculer la direction du champ effectif. À l'inverse, les séquences $\mathrm{R}N_n^{N/2}$, qui produisent une rotation autour de l'axe x, n'ont pas été employées pour l'acquisition de spectre 1D.

4.2 Méthodes désynchronisées ajustables

Les techniques de découplage homonucléaire désynchronisées, telles que PMLG ou DUMBO, sont, jusqu'à présent, les méthodes, qui ont permis d'obtenir la meilleure résolution spectrale. Cependant, elles ne sont pas parfaites, et ce pour deux raisons :

i. elles ont été conçues ou optimisées sans fenêtre d'acquisition. Par conséquent, l'insertion de fenêtres d'acquisition dans les expériences 1D diminue l'efficacité du découplage et la résolution spectrale ;

ii. elles ont été développées dans les conditions statiques ou pour des fréquences MAS modérées [199,200,207]. De ce fait, elles ne tirent pas forcément profit de la rotation MAS, qui élimine partiellement l'interaction dipolaire.

Une première possibilité pour surmonter ces limitations consiste à optimiser expérimentalement les séquences DUMBO à $\nu_r = 65$ kHz à partir d'expériences 1D ^{1}H comportant des fenêtres. Cette stratégie a conduit à l'introduction des séquences e-DUMBO-PLUS [208].

En parallèle, nous avons proposé une autre stratégie. Elle consiste à employer une séquence de découplage désynchronisée, baptisée TIMES, ajustable suivant la fréquence MAS et dont l'élément de base comporte des fenêtres pour l'acquisition. Dans cette séquence, l'utilisation d'une rampe de phase de pente variable permet d'optimiser l'inclinaison, θ, du champ effectif dû aux déplacements chimiques par rapport à l'axe z. En jouant sur la valeur de θ et sur la longueur des fenêtres, la méthode TIMES peut être équivalente à l'enregistrement de spectres MAS sans champ rf ($\theta = 0°$), en présence de découplages FSLG ou PMLG ($\theta = 54,7°$), ou encore MSHOT [194] ($\theta = 90°$). Nous avons montré expérimentalement qu'à $\nu_r = 10$, 65 ou 80 kHz, la séquence TIMES conduit à des spectres ^{1}H mieux résolus que PMLG, MSHOT ou le simple MAS.

Cette meilleure résolution de TIMES s'explique par la possibilité d'ajuster l'orientation du champ effectif en fonction de la fréquence MAS. En effet, la résolution spectrale pour les expériences de découplage homonucléaire résulte d'un compromis entre la réduction des couplages dipolaires et celle des déplacements chimiques. Il y a donc différents régimes pour les expériences de découplage homonucléaire. Pour des fréquences MAS faibles, la rotation de l'échantillon n'est pas suffisamment rapide pour éliminer les couplages dipolaires. La réduction des couplages dipolaires repose donc uniquement sur le champ rf et il faut choisir θ proche de 90°. En revanche, à haute vitesse ($\nu_r \geq 30$kHz), le MAS moyenne en grande partie les couplages dipolaires ^{1}H–^{1}H. Le champ rf n'a donc pas besoin d'éliminer complètement l'interaction dipolaire. Il est préférable pour obtenir une résolution spectrale optimale, d'utiliser un champ rf effectif incliné d'environ 20° à 40° par rapport à $\boldsymbol{B}^0$. Ce champ élimine moins les couplages dipolaires qu'un champ orthogonal à $\boldsymbol{B}^0$, mais il réduit également moins fortement les déplacements chimiques isotropes. Ce champ proche de $\boldsymbol{B}^0$ permet d'obtenir, à haute-vitesse, une meilleure résolution spectrale qu'un champ orthogonal à $\boldsymbol{B}^0$. Ce régime de découplage homonucléaire haute-vitesse est comparable à celui employé pour les séquences $\mathrm{C}N_n^{N/2}$ [34] et e-DUMBO-PLUS [208].

4.3 Perspectives

Un point important est aujourd'hui de mieux comprendre le fonctionnement des découplages homonucléaires $\mathrm{C}N_n^{N/2}$ et TIMES. Pour les séquences $\mathrm{C}N_n^{N/2}$ dépourvues de fenêtre, la théorie de l'hamiltonien moyen prenant en compte les termes, d'ordres zéro et un, est suffisante [209], tandis que pour les méthodes

$\mathrm{C}N_n^{N/2}$ avec fenêtres et TIMES, il est nécessaire de recourir à la théorie de Floquet [210]. Ces outils théoriques peuvent permettre de comparer l'efficacité des différentes méthodes de découplage en terme de résolution et de prévoir les champs rf optimaux pour chaque technique.

Il est aussi utile d'évaluer l'effet des transitoires pour les séquences $\mathrm{C}N_n^{N/2}$ et TIMES. Ceci passe par la détection des transitoires lors du découplage homonucléaire ainsi que la réalisation de simulations numériques [211]. Nous pouvons prévoir que l'effet des transitoires doit être particulièrement marqué à haute vitesse, où les durées d'impulsion sont courtes. Pour diminuer ces transitoires, une solution consiste, en théorie, à lisser les impulsions, comme nous l'avons proposé pour les séquences $\mathrm{C}N_n^{N/2}$. Cette méthode nécessite, cependant, de disposer de spectromètres RMN dont l'électronique soit suffisamment rapide.

De façon pratique, il est nécessaire de comparer les performances des différentes séquences de découplage homonucléaire utilisables pour $\nu_r \geq 10$ kHz. Ces séquences comprennent les méthodes $\mathrm{C}N_n^{N/2}$, $\mathrm{R}N_n^{N/2}$, PMLG et DUMBO. Cette comparaison doit être effectuée pour différentes applications, telles que l'accroissement de la résolution des spectres ^{1}H ou l'augmentation de l'efficacité des transferts via les couplages J hétéronucléaires. Dans tous les cas, les performances des découplage ne doivent pas uniquement être évaluées en terme de résolution spectrale. Il est important d'inclure des critères tels que la puissance rf nécessaire, la robustesse de la séquence et sa facilité de mise en œuvre.

Signalons, enfin, que l'intérêt du découplage homonucléaire ne se limite pas, en principe, à la RMN du ^{1}H. Cette stratégie pourrait aussi être appliquée pour les noyaux ^{19}F, qui subissent souvent des couplages dipolaires homonucléaires élevés. Cependant, la conception du découplage homonucléaire ^{19}F représente un défi pour la méthodologie RMN autrement plus difficile que le découplage ^{1}H–^{1}H en raison de l'amplitude élevée de l'écrantage électronique. Seules quelques tentatives ont été réalisées dans ce domaine à ce jour [212].

4.4 Articles

THE JOURNAL OF CHEMICAL PHYSICS **130**, 014504 (2009)

Proton-proton homonuclear dipolar decoupling in solid-state NMR using rotor-synchronized *z*-rotation pulse sequences

Olivier Lafon,[1,a)] Qiang Wang,[1,2,3] Bingwen Hu,[1] Julien Trébosc,[1] Feng Deng,[2] and
Jean-Paul Amoureux[1]
[1]*Unité de Catalyse et de Chimie du Solide (UCCS), UMR CNRS 8181, École Nationale Supérieure de Chimie de Lille, Université de Lille 1, Bât. C7, B.P. 90108, 59652 Villeneuve d'Ascq Cedex, France*
[2]*Wuhan Institute of Physics and Mathematics, Chinese Academy of Sciences, Wuhan 430071, People's Republic of China*
[3]*Graduate School of the Chinese Academy of Sciences, Beijing 100049, People's Republic of China*

(Received 2 October 2008; accepted 20 November 2008; published online 6 January 2009)

We present a theoretical analysis of rotor-synchronized homonuclear dipolar decoupling schemes that cause a *z*-rotation of the spins. These pulse sequences applicable at high spinning rates ($\nu_r \geq 30$ kHz) yield high-resolution proton NMR spectra that are free of artifacts, such as zero lines and image peaks. We show that the scaled isotropic chemical-shift positions of proton lines can be calculated from the zero-order average Hamiltonian and that the scaling factor does not depend on offset. The effects of different adjustable parameters (rf field, spinning rate, pulse shape, offset) on the decoupling performance are analyzed by numerical simulations of proton spectra and by ^{1}H solid-state NMR experiments on NaH$_2$PO$_4$ and glycine. © *2009 American Institute of Physics*. [DOI: 10.1063/1.3046479]

I. INTRODUCTION

The high gyromagnetic ratio of proton as well as its 99.985% isotopic natural abundance renders this nucleus the ideal candidate for NMR detection.[1,2] If ^{1}H NMR is routinely used in solution state, ^{1}H signal detection and ^{1}H–^{1}H NMR constraints have only been exploited recently in the solid state, for characterizing materials,[3–7] small molecules,[6,8] and biological macromolecular systems.[9–11]

Up to now, the main limitation of proton solid-state NMR remains its small chemical-shift range and the spectral resolution of each resonance. Actually the extensive network of dipole-dipole (DD) couplings among the protons leads to broad spectral lines, thus obscuring the chemical-shift information.[12] Moreover, as the homonuclear DD couplings are homogeneous interactions,[13] the individual ^{1}H linewidths only decrease as the inverse magic-angle spinning (MAS) frequency.[14–16] As a consequence, rotation of the sample at the magic angle alone does not generally achieve very high resolution, even when spinning rates as high as ν_r=60 kHz are employed.[17]

The resolution can be further enhanced by combining MAS with radio-frequency (rf) irradiation schemes that manipulate the spin part of the ^{1}H–^{1}H dipolar interaction. Such combined rotation and multiple-pulse spectroscopy (CRAMPS) was originally designed for the quasistatic limit, in which low spinning frequencies ensure an approximately static sample on the time scale of the rf pulse sequence.[18] Recently these schemes were modified to be applicable at spinning speeds in the range of 10–25 kHz.[6] A remaining challenge is the development of homonuclear decoupling sequences at high MAS frequencies ($\nu_r \geq 30$ kHz). High MAS rates can lead to substantial benefits in terms of resolution and sensitivity not only for ^{1}H but also for nuclei, such as ^{13}C and ^{31}P, which experience large chemical-shift anisotropy (CSA) at high magnetic fields. In practice, correlation NMR experiments of these nuclei with ^{1}H are crucial for analyzing structural properties. Furthermore, fast spinning speed decreases the irreversible losses and increases the spectral width in the indirect dimension of rotor-synchronized two-dimensional (2D) experiments.

Very recently, the phase-modulated Lee–Goldburg[19,20] (PMLG) and decoupling using mind-boggling optimization[21–23] (DUMBO) experiments have been shown to perform well at high MAS rates up to ν_r=65 kHz.[24] However, PMLG and DUMBO schemes were derived, respectively, from quasistatic Lee–Goldburg[25] and BLEW12 (Ref. 26) experiments, and these decoupling schemes may not be optimal at high spinning frequencies. In particular, as the sample is spun faster, the resolution is not improved and higher rf field strength are required.[24,27] Furthermore, the scaling factors of the chemical shifts under PMLG and DUMBO irradiations are lower than $1/\sqrt{3}$, which limits the achievable resolution.[22,24] At last, as these sequences are nonsynchronized with the period of the sample rotation, several rotor-radio-frequency (RRF) lines appear in the NMR spectra and can cause line broadening.

To develop homonuclear decoupling at high MAS rates, an alternative approach consists in applying rf pulse sequences that are rotor synchronized. In this way, pulse sequences can be designed from scratch by explicitly taking into account the sample rotation. Symmetry arguments can be used to help in the construction of these pulse sequences.[28,29] Pulse sequences with $C4_1^0$ and $RN_n^{N/2}$ symmetries have been shown to be efficient in yielding highly resolved ^{1}H spectra.[30–34] However, for these pulse schemes,

---

[a)] Electronic mail: olivier.lafon@ensc-lille.fr.

the effective field resulting from isotropic chemical-shift points away from the $\boldsymbol{B}^0$ axis (also called z axis). This creates undesirable zero and image peaks.

In this publication we will explore the properties of recently introduced broad-banded z-rotation $CN_n^{N/2}$ decoupling schemes.[35,36] As already shown in the case of PMLG, an effective z-rotation sequence leads to favorable properties of homonuclear decoupling: (i) cleaner ^{1}H spectra with lesser artifacts, such as zero and image peaks, (ii) improved resolution, and (iii) possible use of conventional phase-cycling schemes in multidimensional experiments.[27,37–39] These $CN_n^{N/2}$ pulse sequences have been implemented in the indirect dimension of 2D experiments[35] as well as in a one-dimensional (1D) fashion after insertion of acquisition windows.[36] Moreover, they have been shown to yield highly resolved ^{1}H double-quantum spectra.[40]

The basic $\mathcal{C}$ element of $CN_n^{N/2}$ sequences can be either a composite 0° rectangular pulse or its smoothly amplitude-modulated (SAM) version. The SAM sequence allows reducing rf pulse transients, which can affect the decoupling performances.[37,41] This is especially important for homonuclear decoupling sequences at high MAS frequencies, since they can involve short rf pulses, not much longer than the duration of pulse transients.

This article is organized as follows. Section II introduces zero-order average Hamiltonian theory (AHT)[12,42] of $CN_n^{N/2}$ schemes and derives analytical expressions for the scaling factors of isotropic chemical shifts. Section III presents numerical simulations that demonstrate the validity of the theoretical predictions and analyzes the effects of different parameters (rf field, spinning rates, pulse shape, offset) on the decoupling performance. In Sec. IV, results of 2D ^{1}H $CN_n^{N/2}$ experiments for NaH$_2$PO$_4$ and glycine are presented and compared with the theoretical predictions and numerical simulations.

II. ZERO-ORDER AHT

A. Spin interactions and average Hamiltonian

In order to describe the evolution of a proton spin system that rotates at the magic angle and is subjected to rf irradiation close to resonance, a convenient representation of its spin Hamiltonian must first be introduced. The Hamiltonian $\mathcal{H}^\Lambda$ of a spin interaction Λ is characterized by its space rank l and its spin rank λ. Each spin interaction may therefore be regarded as a superposition of $(2l+1)\times(2\lambda+1)$ components, with component indexes m and μ running, respectively, from $-l$ to $+l$ and $-\lambda$ to λ in integer steps,

$$\mathcal{H}^\Lambda = \sum_{m=-l}^{+l} \sum_{\mu=-\lambda}^{+\lambda} \mathcal{H}^\Lambda_{lm\lambda\mu}. \tag{1}$$

The various nuclear spin interactions are distinguished by the values of l and λ. For instance, the pair $\{l,\lambda\}$ is equal to {2, 2} for homonuclear DD interaction, {0, 1} for isotropic chemical shifts, and {2, 1} for CSA. A summary of the spin interaction components, in the case of exact MAS, is given in Ref. 43.

When the rf irradiation is synchronized with the sample rotation, as in $CN_n^{N/2}$ sequences, the dynamics of nuclear spins can be described in the framework of AHT.[12,42,43] This leads to a time-independent average Hamiltonian (AH), which may be approximated using the Magnus expansion. In this work, the theoretical analysis is restricted to the zero-order term of AH. As in Eq. (1), the zero-order AH in the interaction frame, $\overline{\mathcal{H}}^{(0)}$, can be expressed as a sum of many rotational components, $\overline{\mathcal{H}}^{\Lambda,(0)}_{lm\lambda\mu}$,[29,43,44]

$$\overline{\mathcal{H}}^{(0)} = \sum_{\Lambda lm\lambda\mu} \overline{\mathcal{H}}^{\Lambda,(0)}_{lm\lambda\mu}. \tag{2}$$

B. Symmetry classes and zero-order selection rules

Setting up periodic symmetry relationships between the mechanical and the rf rotations facilitates the design of homonuclear decoupling sequences, since these symmetry arguments allow generating a zero-order AH containing desired rotational components in Eq. (2) while other components are suppressed. There are two major classes of symmetry-based decoupling sequences, denoted CN_n^ν (Refs. 43 and 45–47) and RN_n^ν.[29,43,48] They are both composed of N elements $\{\epsilon_0\epsilon_1\cdots\epsilon_{N-1}\}$, each of which has the same duration $\tau_E = n\tau_r/N$, where $\tau_r = 1/\nu_r$ is a period of the magic sample rotation. In the case of CN_n^ν sequences, the elements are derived from a basic element $\mathcal{C}$ by an incremental phase shift,

$$\epsilon_q = \mathcal{C}_{2\pi q\nu/N}. \tag{3}$$

In the case of RN_n^ν sequences, the phases alternate between two values,

$$\epsilon_q = \begin{cases} \mathcal{R}_{\pi\nu/N} & (q \ \text{even}) \\ \mathcal{R}'_{-\pi\nu/N} & (q \ \text{odd}), \end{cases} \tag{4}$$

where the prime indicates a change in the sign of all phases internal to the basic element $\mathcal{R}$. For CN_n^ν symmetry, the basic $\mathcal{C}$ element must be a rf cycle, meaning that in the absence of other spin interactions, the rf pulses of $\mathcal{C}$ induce a rotation of the nuclear spins through an integer multiple of 360° (*including* 0°). In other words, the rf propagator of the completed $\mathcal{C}$ element is proportional to the identity operator. The RN_n^ν schemes are built from the basic inversion element $\mathcal{R}$, which rotates the nuclear spins through an odd multiple of 180° about the rotating-frame x-axis.

The symmetry properties of CN_n^ν and RN_n^ν pulse sequences lead to the following selection rules on the zero-order AH:[43,46]

$$\overline{\mathcal{H}}^{\Lambda,(0)}_{lm\lambda\mu}(CN_n^\nu) = 0 \quad \text{if} \ \ mn - \mu\nu \neq NZ, \tag{5}$$

where Z is any integer, including zero, and

$$\overline{\mathcal{H}}^{\Lambda,(0)}_{lm\lambda\mu}(RN_n^\nu) = 0 \quad \text{if} \ \ mn - \mu\nu \neq \frac{NZ_\lambda}{2}, \tag{6}$$

where Z_λ is an integer with the same parity as λ. If $\overline{\mathcal{H}}^{\Lambda,(0)}_{lm\lambda\mu}$ is zero, the term (l,m,λ,μ) is said to be *symmetry forbidden* in the zero-order AH, otherwise the term (l,m,λ,μ) is *symmetry allowed*.

C. Selection of isotropic chemical shifts

High-resolution isotropic shift spectra may be obtained in solids if all DD couplings and CSA terms are suppressed, while isotropic chemical shifts are preserved. In the absence of rf irradiation, the DD coupling and CSA terms in the zero-order AH are zero due to sample spinning. In contrast, the rf irradiation can interfere with MAS in a destructive manner and may reintroduce the undesired interactions at zero order. CN_n^ν and RN_n^ν sequences offer the advantage that the zero-order selection rules given by Eq. (5) and (6) prevent these interferences, whatever the spinning and rf nutation frequencies. Nevertheless, the symmetry numbers N, n, and ν must be carefully chosen.

The DD couplings and CSA terms have a space rank $l=2$, while isotropic chemical shifts have $l=0$. Therefore, the suitable CN_n^ν and RN_n^ν sequences must have symmetry numbers N, n, and ν such that some terms of the form $(l,m,\lambda,\mu)=(0,0,1,\mu)$ with $\mu=-1,0,+1$ are symmetry allowed, while all terms of the form $(2,m,\lambda,\mu)$, with $m\neq 0$, are symmetry forbidden. Sequences satisfying these conditions produce a zero-order AH containing only isotropic chemical shifts and hetero- and homonuclear J-couplings.

A list of CN_n^ν and RN_n^ν symmetries suitable for high-resolution ^{1}H spectroscopy in the solid state was given in Ref. 33. The RN_n^ν sequences belong to the series $RN_n^{N/2}$ and thus only involve phase shifts of 180° between subsequent elements. The suitable CN_n^ν sequences include not only $CN_n^{N/2}$ series, with phase shifts of 180°, but also CN_n^0 sequences, with no phase shift, and CN_n^ν sequences (e.g., $C9_1^3$ and $C10_1^3$), with phase shifts lower than 180°.

D. Effective *z*-rotation sequences

As explained in Sec. I, it is highly favorable that isotropic chemical-shift interaction leads to effective rotation of the spins around the $\boldsymbol{B}^0$ axis. For the different suitable CN_n^ν and RN_n^ν pulse sequences, it is thus important to determine the effective field resulting from isotropic chemical shift. In first approximation, this effective field can be calculated from the terms of isotropic chemical shift in the zero-order AH. For instance, all $RN_n^{N/2}$ sequences select terms $(l,m,\lambda,\mu)=(0,0,1,\pm 1)$ of isotropic chemical shift, thus generating an effective field along the x-axis.[33,34] Conversely CN_n^ν sequences with $\nu\neq 0$ only allow terms $(l,m,\lambda,\mu)=(0,0,1,0)$ and the effective field points in the z-direction. At last, the zero-order AH during CN_n^0 sequences contains terms $(l,m,\lambda,\mu)=(0,0,1,0)$ and $(0,0,1,\pm 1)$. In this case, the zero-order selection rules do not restrain the direction of the effective field.

In this article, we focus on $CN_n^{N/2}$ symmetries [see Fig. 1(a)], which cause a z-rotation of the spins. Furthermore, they only involve phase shifts of 180° between subsequent cycles, and hence can be implemented as amplitude-modulated sequences, if the basic element $\mathcal{C}$ corresponds itself to an amplitude modulation. In this article, we employ as basic $\mathcal{C}$ element either a composite 0° rectangular pulse, $\alpha_0\alpha_{180}$, or one of its SAM version, a half-cosine pulse, denoted half-cos in the text. Here the standard notation for rf pulses is used: ξ_ϕ indicates a rectangular, resonant rf pulse with flip angle ξ and phase ϕ, and the angles are written in degrees. To unify the notations of this article, the $CN_n^{N/2}$ sequences built from either basic elements are denoted $CN_n^{N/2}(\alpha_0\alpha_{180})$ and $CN_n^{N/2}$(half-cos) (instead of SAM). These two types of homonuclear decoupling sequences are exemplified by $C6_1^3(\alpha_0\alpha_{180})$ and $C6_1^3$(half-cos) pulse sequences shown in Figs. 1(b) and 1(c).

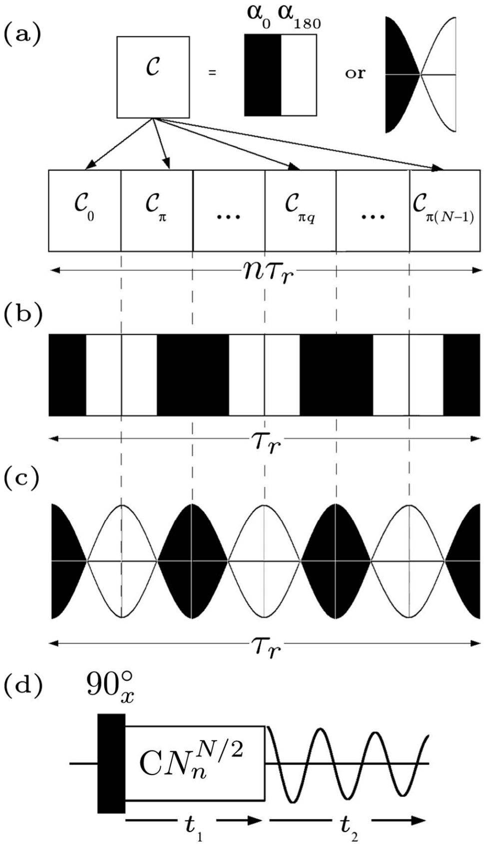

FIG. 1. (a) Implementation of $CN_n^{N/2}$ sequences. This pulse schemes are built of N phase shifted elements, which all derive from a cyclic basic element $\mathcal{C}$. Here the used $\mathcal{C}$ pulse trains are either an amplitude-modulated composite 0° pulse, $\alpha_0\alpha_{180}$, or one of its smoothly modulated version, a half-cosine pulse. As an example, $C6_1^3$ pulse sequences built from $\mathcal{C}=\alpha_0\alpha_{180}$ or half-cosine pulses are shown, respectively, in (b) and (c). (d) Pulse scheme for 2D ^{1}H–^{1}H experiment incorporating a $CN_n^{N/2}$ sequence for the indirect observation of high-resolution proton spectra.

As the $CN_n^{N/2}$ sequences are windowless decoupling sequences, they should ideally be applied in the indirect dimension of a multidimensional homo- or heteronuclear correlation experiment. Figure 1(d) shows the 2D ^{1}H–^{1}H experiment allowing the indirect observation of high-resolution $CN_n^{N/2}$ decoupled proton spectrum. However, these homonuclear decoupling sequences can also be used in 1D experiments if acquisition windows are inserted between $CN_n^{N/2}$ pulse trains. This has been presented elsewhere.[36]

E. Scaling factor

The selection rules provide information on which terms are symmetry forbidden. However, they provide no information on the magnitude of the symmetry-allowed terms. In general, the form of a symmetry-allowed zero-order term is as follows:

$$\overline{\mathcal{H}}^{\Lambda,(0)}_{lm\lambda\mu} = \kappa_{lm\lambda\mu}[A^{\Lambda}_{lm}]^{R}\exp\{-\imath m(\alpha^{0}_{RL} - \omega_r t^{0})\}T^{\Lambda}_{\lambda\mu}, \tag{7}$$

where $[A^{\Lambda}_{lm}]^{R}$ is a component of the spatial tensor of interaction Λ, expressed in the rotor-fixed frame R, $T^{\Lambda}_{\lambda\mu}$ is a component of the spin tensor of interaction Λ, expressed in the laboratory frame, α^{0}_{RL} denotes the initial rotor position, and t^0 refers to the starting time point of the sequence. The factor $\kappa_{lm\lambda\mu}$ is called the *scaling factor* of the pulse sequence and depends on the symmetry class, as well as the detailed structure of the basic element upon which the pulse sequence is built. The calculation of $\kappa_{lm\lambda\mu}$ for arbitrary basic elements is discussed in Ref. 43.

High-resolution ^{1}H spectroscopy requires large scaling factors of isotropic chemical shift. Therefore, we express the zero-order AH and the scaling factors for $CN_n^{N/2}$ and $RN_n^{N/2}$ pulse sequences introduced above and built from different basic elements.

In the case of I_2S spin system with $RN_n^{N/2}$ irradiation of the I-spins, the zero-order AH in natural units is

$$\begin{aligned}\overline{\mathcal{H}}^{(0)} = \kappa^{\mathcal{R}}_{Ix}(&\Omega^{0}_{I1}I_{1,x} + \Omega^{0}_{I2}I_{2,x} + 2\pi J_{I1S}I_{1,x}S_z + 2\pi J_{I2S}I_{2,x}S_z)\\ &+ 2\pi J_{I1I2}\boldsymbol{I}_1 \cdot \boldsymbol{I}_2 + \Omega^{0}_{S}S_z,\end{aligned} \tag{8}$$

where

$$\kappa^{\mathcal{R}}_{Ix} = -\frac{1}{\sqrt{2}}(\kappa^{\mathcal{R}}_{0,0,1,1} + \kappa^{\mathcal{R}}_{0,0,1,-1}). \tag{9}$$

In Eq. (8), Ω^{0}_{Ii} and J_{IiS} with $i=1,2$ denote, respectively, the isotropic chemical-shift (off-resonance) values of I-spins and heteronuclear isotropic J-coupling, J_{I1I2} is the homonuclear isotropic J-coupling, and Ω^{0}_{S} the isotropic chemical shift of S-spin. If the basic element $\mathcal{R}$ is a 180_0 pulse, the scaling factor $\kappa^{\mathcal{R}}_{Ix}$ is equal to $-2/\pi \approx -0.64$. Equation (8) shows that the effective field related to isotropic chemical shift is along the x-axis. This prevents the use of $RN_n^{N/2}$ homonuclear decoupling in 1D experiment.[33,34]

Conversely, the CN_n^{ν} irradiation (with $\nu \neq 0$), and, in particular, $CN_n^{N/2}$ sequences, generates a zero-order AH that can be written

$$\begin{aligned}\overline{\mathcal{H}}^{(0)} = \kappa^{\mathcal{C}}_{0,0,1,0}(&\Omega^{0}_{I1}I_{1,z} + \Omega^{0}_{I2}I_{2,z} + 2\pi J_{I1S}I_{1,z}S_z\\ &+ 2\pi J_{I2S}I_{2,z}S_z) + 2\pi J_{I1I2}\boldsymbol{I}_1 \cdot \boldsymbol{I}_2 + \Omega^{0}_{S}S_z\end{aligned} \tag{10}$$

using the same notation as above. This equation confirms that for these sequences, the isotropic chemical-shift terms can be described as an effective field along the z-axis. The scaling factor $\kappa^{\mathcal{C}}_{0,0,1,0}$ of term $(l,m,\lambda,\mu)=(0,0,1,0)$ depends on the basic element $\mathcal{C}$. If $\mathcal{C}=360_0$ or $90_0 360_{180} 270_0$, $\kappa^{\mathcal{C}}_{0,0,1,0}$ is equal to zero. Such basic elements are thus unsuitable to obtain high-resolution proton spectra. Conversely, the basic elements $\mathcal{C}=\alpha_0\alpha_{180}$ and $\mathcal{C}=$half-cos lead to nonzero scaling factor,

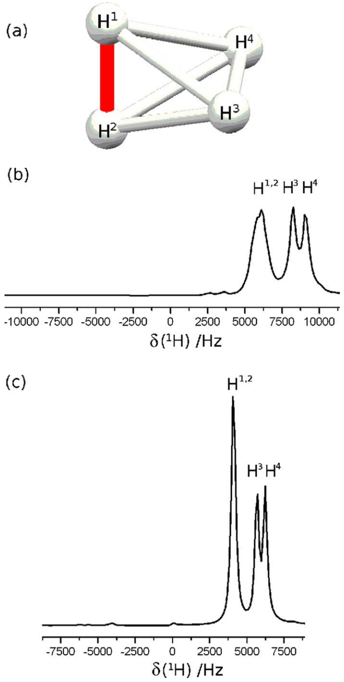

FIG. 2. (Color online) (a) Schematic representation of the four proton spin system used for numerical simulations. The off-resonance frequencies of the protons were $\Delta\nu^{1,2}=6$ kHz, $\Delta\nu^{3}=8.2$ kHz, and $\Delta\nu^{4}=9$ kHz, whereas the DD coupling constants were $b_{12}/(2\pi)=-30$ kHz and $b_{13}/(2\pi)=b_{14}/(2\pi)=b_{23}/(2\pi)=b_{24}/(2\pi)=b_{34}/(2\pi)=-10$ kHz. Additional parameters are given in Table I. [(b) and (c)] Simulated ^{1}H spectra of the model spin system in a powder sample at $\nu_r=65$ kHz. The proton Larmor frequency was 400 MHz. (b) corresponds to the 1D MAS spectrum, whereas (c) is the projection along the indirect dimension of the 2D experiment [Fig. 1(d)] calculated under $C6_1^3$(half-cos) irradiation with $\nu_{1,\mathrm{peak}}=225$ kHz.

$$\kappa^{\mathcal{C}}_{0,0,1,0} = \begin{cases} \mathrm{sinc}(\alpha) & \mathcal{C} = \alpha_0\alpha_{180} \\ J_0\left(2\dfrac{\alpha}{\pi}\right) & \mathcal{C} = \text{half-cos}, \end{cases} \tag{11}$$

where $\mathrm{sinc}(\alpha)=\sin(\alpha)/\alpha$, J_0 is the zero-order Bessel function of the first kind, and the angle α in radians is defined as

$$\alpha = 2\pi\nu_{1,\mathrm{peak}}\frac{\tau_E}{2} = \pi\frac{n}{N} \times \frac{\nu_{1,\mathrm{peak}}}{\nu_r}, \tag{12}$$

where $\nu_{1,\mathrm{peak}}$ denotes the maximal value of rf nutation frequency. Note that using the same $\nu_{1,\mathrm{peak}}$ value ($\nu_{1,\mathrm{peak}}=N\nu_r/(2n)$), the $CN_n^{N/2}(90_0 90_{180})$ and the $RN_n^{N/2}$ sequences with $\mathcal{R}=180_0$ have the same scaling factor in absolute value: $2/\pi \approx 0.64$. These two pulse sequences only differ by the direction of the effective field, which is, respectively, along x- and z-axes for $RN_n^{N/2}$ and $CN_n^{N/2}$ sequences. For the same *rms value* of rf nutation frequency ($\nu_{1,\mathrm{rms}}=N\nu_r/(2n)$), the scaling factor of CN_n^{ν}(half-cos) sequences is slightly lower: about 0.56.

TABLE I. Parameters of the four proton spin system used for numerical simulations. The proton coordinates are given in an arbitrary molecular reference frame.

Label	x (Å)	y (Å)	z (Å)	$\Delta\nu$ (kHz)	δ_{aniso} (ppm)	η_{CS}
H^1	0.00	0.00	0.79	6.0	5	0.8
H^2	0.00	0.00	−0.79	6.0	5	0.8
H^3	1.14	1.81	0.00	8.2	10	0.2
H^4	−1.14	1.81	0.00	9.0	10	0.2

III. NUMERICAL SIMULATIONS

To assess the performance of $CN_n^{N/2}$ sequences, we performed a variety of numerical simulations by using SIMPSON program.[49]

A. Scaling factor

The analytical expressions of scaling factor $\kappa_{0,0,1,0}^{\mathcal{C}}$ [Eq. (11)] were derived from zero-order AHT. To verify the validity of this approximation, the analytical expressions were compared to scaling factor values calculated from numerically exact simulation. To this end, proton spectra under $CN_n^{N/2}$ irradiation were simulated for a model system containing four protons, as shown in Fig. 2(a). The relative positions and chemical-shift parameters of these protons are given in Table I. The propagators were evaluated by small-step time integration of the spin evolution. The time step over which the spin Hamiltonian may be considered time independent was 0.2 μs. The powder averaging was accomplished using 320 orientations, selected according to REPULSION algorithm.[50] The free induction decays were simulated by sampling 512 points in the time domain. The proton spectra were simulated, at a ^{1}H Larmor frequency of 400 MHz, for different $CN_n^{N/2}$ symmetries and rf nutation frequencies. In Figs. 2(b) and 2(c), compared are the two spectra of the model compound at ultrafast MAS, ν_r=65 kHz. Spectrum b was calculated without homonuclear decoupling, whereas spectrum c was obtained using $C6_1^3$(half-cos) sequence. The lower line frequencies in spectrum c compared to spectrum b indicate a scale down of isotropic chemical shift under $C6_1^3$(half-cos) irradiation.

The numerically exact scaling factors were calculated from simulated proton spectra as

$$\kappa = \frac{\Delta\mathcal{N}(\Delta\nu) - \Delta\mathcal{N}(0)}{\Delta\nu}, \qquad (13)$$

where $\Delta\nu$ is the off-resonance frequency and $\Delta\mathcal{N}(\Delta\nu)$ and $\Delta\mathcal{N}(0)$ are the observed line positions for, respectively, off- and on-resonance irradiations. In the simulated NMR spectra, whatever the DD coupling values, the $\Delta\mathcal{N}(0)$ values were found to be exactly zero for $CN_n^{N/2}(\alpha_0\alpha_{180})$ and $CN_n^{N/2}$(half-cos) sequences [see Fig. 7(a)]. In Fig. 3, the κ values at a moderate spinning frequency, ν_r=30 kHz, are plotted as function of the angle α, defined in Eq. (12). Whatever the pulse sequence symmetry [i.e., the ratio $N/(2n)$] and the basic element ($\mathcal{C}=\alpha_0\alpha_{180}$ or half-cos), there is a decrease in κ for increasing α, i.e., increasing rf nutation frequency.

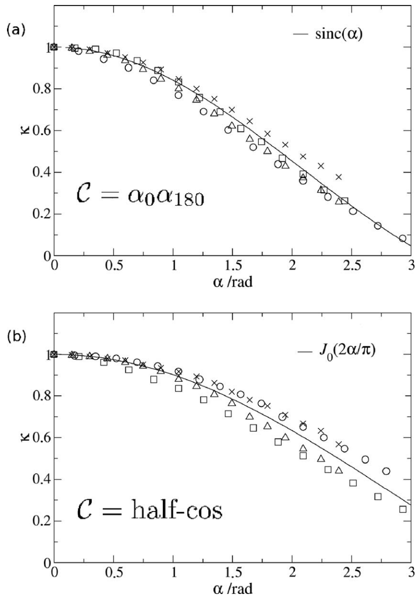

FIG. 3. The scaling factor values κ as function of the pulse angle α for $CN_n^{N/2}$ sequences with basic element (a) $\mathcal{C}=\alpha_0\alpha_{180}$ and (b) $\mathcal{C}$=half-cos. In both cases, α is defined by Eq. (12). The scaling factor values were calculated by numerical simulation at ν_r=30 kHz for the $H^{1,2}$ resonance. The spin system parameters are given in Table I and in the caption of Fig. 2. The curves are plotted for four $N/(2n)$ ratios, 2.5 (circle), 3 (square), 3.5 (triangle), and 4 (cross), corresponding, respectively, to the symmetry numbers $(N,n)=(10,2)$, (6,1), (14,2), and (8,1). The continuous lines represent the corresponding scaling factor values $\kappa_{0,0,1,0}^{\mathcal{C}}$ derived from zero-order AHT [Eq. (11)].

Furthermore, for comparison, the scaling factors derived from zero-order AHT, $\kappa_{0,0,1,0}^{\mathcal{C}}$ [see Eq. (11)], are also represented as a continuous line. For all symmetries and basic elements, there is a good fit between numerically exact scaling factors and $\kappa_{0,0,1,0}^{\mathcal{C}}$, showing the validity of truncating the Magnus expansion at zero order. Similar agreement was obtained at ν_r=65 kHz (data not shown).

B. Optimal rf field

The use of symmetry-based sequences insures the suppression of homonuclear DD couplings to zero order. However, the higher order AH terms involving homonuclear DD couplings may remain and significantly contribute to linewidths in proton spectra. The calculation of higher order AH terms is out of the scope of the present paper and will be given elsewhere. Instead here, numerical simulations were performed to assess the decoupling efficiency of $CN_n^{N/2}$ sequences. From an "ideal" homonuclear decoupling sequence, we demand (i) a high spectral resolution, (ii) an efficient decoupling over a large range of isotropic chemical shifts and spinning frequencies, (iii) a required rf power that matches easily the probe specifications, (iv) a scaling factor constant over a large range of off-resonance irradiation, (v) minimized artifacts (zero and image peaks, RRF lines), and

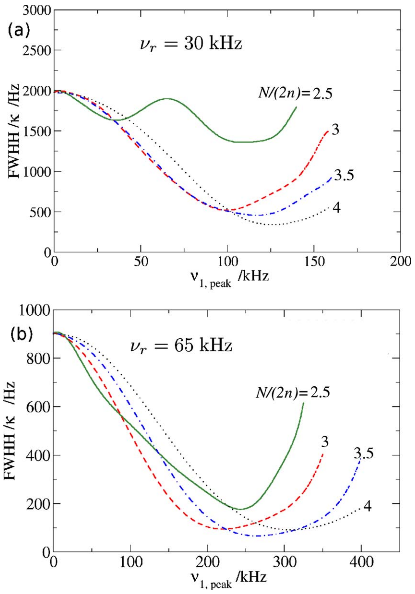

FIG. 4. (Color online) The scaled up linewidths of the $H^{1,2}$ resonance obtained during $CN_n^{N/2}$(half-cos) sequence at (a) ν_r=30 kHz and (b) ν_r=65 kHz are plotted as function of the rf nutation frequency peak value $\nu_{1,\text{peak}}$. The spin system parameters were identical to the ones of Fig. 2. The proton Larmor frequency was 400 MHz. The curves are plotted for four $N/(2n)$ values, 2.5, 3, 3.5, and 4, corresponding, respectively, to the symmetry numbers $(N,n)=(10,2)$, (6,1), (14,2), and (8,1).

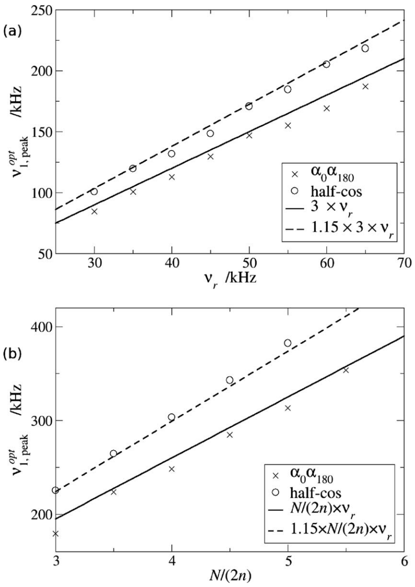

FIG. 5. The optimal peak values $\nu_{1,\text{peak}}^{\text{opt}}$ of the rf nutation frequency, leading to the best spectral resolution, are plotted, for $CN_n^{N/2}(\alpha_0\alpha_{180})$ (cross) and $CN_n^{N/2}$(half-cos) (circle) sequences, as function of (a) ν_r with $N/(2n)$=3 or (b) $N/(2n)$ with ν_r=65 kHz. The n symmetry number is equal to 1 for integer $N/(2n)$ ratios and to 2 for half-integer $N/(2n)$ ratios. In figures (a) and (b), the continuous and dashed lines represent, respectively, the linear functions $\nu_{1,\text{peak}}^{\text{opt}}=N/(2n)\times\nu_r$ and $\nu_{1,\text{peak}}^{\text{opt}}=1.15\times N/(2n)\times\nu_r$.

(vi) a pulse block that can be applied both in direct and indirect dimensions using conventional phase-cycling schemes. Requirements (i)–(iii) are addressed in this subsection, while the points (iv)–(vi) will be discussed in the Sec. III D.

Spectral resolution can be characterized by the scaled up linewidths, i.e., the full width at half height (FWHH) given in Hertz units and divided by the numerically exact scaling factor. In Fig. 4 the scaled up linewidths of the $H^{1,2}$ resonance are plotted for two spinning frequencies, ν_r=30 and 65 kHz, as function of rf nutation frequency peak value, $\nu_{1,\text{peak}}$. As we have used only 320 crystallite orientations, the simulated line shapes were not smooth. To facilitate the linewidth determination, the simulated spectra were apodized with a Lorentzian weighting function causing an extra line broadening of 300 Hz, which was then subtracted before plotting the curves of Fig. 4. The values of symmetry numbers N and n are indicated in the figure caption.

For each $CN_n^{N/2}$ sequence, Fig. 4 evidences the existence of a minimum in scaled up linewidths at a given rf nutation frequency, $\nu_{1,\text{peak}}^{\text{opt}}$. Such an optimum results from a competition between the simultaneous decreases in FWHH and κ with increasing $\nu_{1,\text{peak}}$ value. Inspection of Fig. 5 shows that the $\nu_{1,\text{peak}}^{\text{opt}}$ value linearly depends on spinning frequency and symmetry number ratio $N/(2n)$ over the ranges $3\leq N/(2n)\leq 5$ and 30 kHz$\leq\nu_r\leq$65 kHz. When a half-cosine pulse is used as basic $\mathcal{C}$ element, the optimal resolution is obtained when

$$\nu_{1,\text{peak}}^{\text{opt}}(\text{half-cos}) = 1.15\frac{N}{2n}\nu_r. \tag{14}$$

For such condition, the angle α, defined in Eq. (12), is equal to 103.5° and, hence, the zero-order scaling factor is equal to $\kappa_{0,0,1,0}^{\mathcal{C}}$=0.70. The minima in the scaled up linewidths observed in Fig. 4 are broad. Therefore, the rf field amplitude must not fulfill stringent conditions and the $CN_n^{N/2}$(half-cos) sequences are robust with respect to rf power miscalibration. Nevertheless, even if the rf field amplitude is close to $\nu_{1,\text{peak}}^{\text{opt}}$, the spectral resolution can be sensitive to rf inhomogeneity.[51] Actually, neglecting $\Delta\mathcal{N}(0)$, the observed line position, $\Delta\mathcal{N}(\Delta\nu)$, is equal to $\kappa\Delta\nu$ [see Eq. (13)], and as seen in Fig. 3, around $\nu_{1,\text{peak}}^{\text{opt}}$, the scaling factor strongly depends on the rf field amplitude. Hence, for off-resonance irradiation, the rf field distribution over the sample volume can lead to a distribution in line position, and hence to a decrease in resolution.

Considering Eq. (14), the practicable $CN_n^{N/2}$ decoupling sequences are limited by the spinning frequency and the maximal admissible rf power, which is related to the maximal admissible rms rf frequency $\nu_{1,\text{rms}}^{\text{max}}$ for decoupling time lasting several milliseconds. For instance, if ν_r=30 kHz and

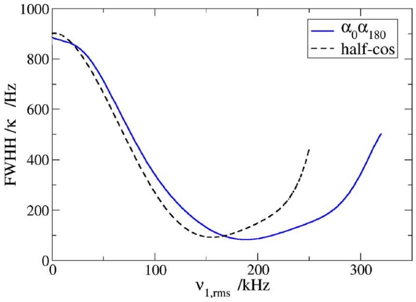

FIG. 6. (Color online) Comparison of the scaled up linewidths of $H^{1,2}$ peak at ν_r=65 kHz using $C6_1^3(\alpha_0\alpha_{180})$ (continuous line) and $C6_1^3$(half-cos) (dashed line) sequences. The linewidths were plotted as function of the rms value of rf nutation frequency $\nu_{1,rms}$. Indeed, the rf nutation frequency is experimentally limited by the maximal admissible electric power, which is proportional to $(\nu_{1,\mathrm{rms}}^{\max})^2$.

$\nu_{1,\mathrm{rms}}^{\max}=135$ kHz, the optimal rf nutation frequency $\nu_{1,\mathrm{peak}}^{\mathrm{opt}}$(half-cos) can only be reached for symmetry numbers such that $N/(2n)\leq 5.5$.

Figure 4(a) shows that $C10_2^5$(half-cos) sequence corresponding to ratio $N/(2n)=2.5$ provides lower spectral resolution than $CN_n^{N/2}$ sequences with $N/(2n)\geq 3$. Low resolution was also obtained for all $CN_n^{N/2}$ sequences with $0<N/(2n)<2.66$. This arises from an increase in first-order AH terms related to homonuclear dipolar couplings, when $N/(2n)$ ratio is close to 1 and 2. Indeed Brinkman and Edén showed that the magnitude of first-order AH terms is often increased in the vicinity of conditions which lead to finite zero-order terms.[44] As $C2_1^1$ and $C4_1^2$ sequences recouple homonuclear dipolar couplings to zero order, $CN_n^{N/2}$ sequences with $N/(2n)$ close to 1 or 2 are likely to provide large first-order terms, even if the zero-order terms disappear under particular conditions. This phenomenon is less important at ν_r=65 kHz, as the ultrafast MAS speed mostly cancels the homonuclear dipolar couplings [see Fig. 4(b)].

The comparison of Figs. 4(a) and 4(b) shows that the spectral resolution is improved as the sample is spun faster. This is the opposite of PMLG experiments where the scaled up linewidths stay constant as the spinning speed is increased.[24,27] These simulations indicate that $CN_n^{N/2}$ sequences are suitable for homonuclear decoupling at high ν_r. In Ref. 35, the SAM_3 decoupling, which corresponds to a $C6_1^3$(half-cos) experiment, was demonstrated at ν_r=65 kHz. The spectral resolution is improved by faster spinning whatever the (N,n) symmetry numbers. Nevertheless, the $CN_n^{N/2}$ sequences leading to the best spectral resolution differ between ν_r=30 kHz and 65 kHz.

Curves similar to those of Fig. 4 were obtained when using $\mathcal{C}=\alpha_0\alpha_{180}$ as basic element. The main difference lies in the position of the minimum in scaled up linewidths. In this case, Fig. 5 shows that the optimal resolution is obtained when

$$\nu_{1,\mathrm{peak}}^{\mathrm{opt}}(\alpha_0\alpha_{180})=\frac{N}{2n}\nu_r. \tag{15}$$

Such condition corresponds to $\alpha=90°$ and $\kappa_{0,0,1,0}=0.64$.

C. Comparison of $CN_n^{N/2}$ sequences with $\mathcal{C}=\alpha_0\alpha_{180}$ or half-cos

Figure 6 compares the spectral resolution obtained using $C6_1^3$ sequences built from either $\mathcal{C}=\alpha_0\alpha_{180}$ or $\mathcal{C}$=half-cos. The minimal values of scaled up linewidths are similar whatever the basic element. Nevertheless, the rms value of rf nutation frequency leading to optimal resolution is lower for smoothly modulated half-cosine pulses [$\nu_{1,\mathrm{rms}}^{\mathrm{opt}}(\alpha_0\alpha_{180})\approx 190$ kHz and $\nu_{1,\mathrm{rms}}^{\mathrm{opt}}$(half-cos)$\approx 158$ kHz]. This is in agreement with Eqs. (14) and (15). Furthermore, the use of smoothly modulated pulses allows reducing pulse transients, the size of which scales with the amplitude and phase changes.[41]

D. Direction of the effective field

The magnitude and the direction of the effective field generated by $C6_1^3$ irradiation were determined as a function of the off-resonance irradiation frequency $\Delta\nu$. To that end, the propagators of a single proton were evaluated by small-step time numerical integration of the following equation:

$$\frac{d}{dt}U(t,t^0)=-\imath\mathcal{H}(t)U(t,t^0), \tag{16}$$

where the Hamiltonian $\mathcal{H}(t)$ contains isotropic chemical shift and interaction with rf fields. In practice the numerical evaluation of U was performed by using SIMPSON simulation program.[49] In the case of $C6_1^3$ irradiation, $\mathcal{H}(t)$ is periodic with the rotor period, implying that the effective field can be calculated from the one-rotor period propagator $U(\tau_r,0)$. Because the Hamiltonian $\mathcal{H}(t)$ contains only terms linear in the angular moment operators, I_χ with $\chi=(x,y,z)$, the propagator $U(\tau_r,0)$ must take the form of a rotation operator, which can be parametrized by its axis and an angle,[52]

$$U(\tau_r,0)=\exp[-\imath 2\pi(-\Delta\mathcal{N})\tau_r I_{\theta,\phi}]. \tag{17}$$

This equation shows that the magnetization of the proton precesses around an effective field in the rotating frame, with a Hamiltonian of the form $-\Delta\mathcal{N}I_{\theta,\phi}$. The amplitude of the effective field corresponds to the observed line position, $\Delta\mathcal{N}=\mathcal{N}-\nu_{\mathrm{ref}}$, where the observed line frequency $\mathcal{N}$ and the spectrometer reference frequency ν_{ref} are positive, whereas the proton Larmor frequency is negative. Here $I_{\theta,\phi}$ is an angular moment operator aligned along the effective field, the direction of which is described by the zenith and azimuth angles (θ,ϕ) with $0\leq\theta\leq\pi$ and $0\leq\phi\leq 2\pi$,

$$I_{\theta,\phi}=XI_zX^{-1}=\cos(\theta)I_z+\sin(\theta)[\cos(\phi)I_x+\sin(\phi)I_y], \tag{18}$$

where X is a unitary operator and X^{-1} its inverse. For a single proton, $U(\tau_r,0)$ is represented by a 2×2 complex unitary matrix. By inserting Eq. (18) into Eq. (17), we obtain

$$U(\tau_r,0)=X\begin{pmatrix}\exp(\imath\pi\Delta\mathcal{N}\tau_r) & 0\\ 0 & \exp(-\imath\pi\Delta\mathcal{N}\tau_r)\end{pmatrix}X^{-1}. \tag{19}$$

The matrix representation of X can be determined by

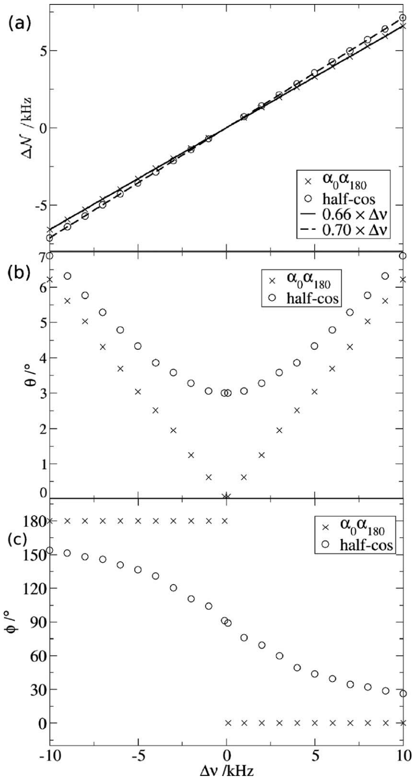

FIG. 7. (a) Effective rotation frequency $\Delta\mathcal{N}$ and [(b) and (c)] the direction angles (θ,ϕ) of the effective field are plotted as function of the off-resonance frequency $\Delta\nu$ for $C6_1^3$ sequences at $\nu_r=30$ kHz. $\nu_{1,\mathrm{peak}}$ values of 86 and 100 kHz were, respectively, chosen for $\mathcal{C}=\alpha_0\alpha_{180}$ (cross) and $\mathcal{C}$=half-cos (circle). The effective rotation frequencies behave linearly over a very broad offset range and are perfectly fitted by the continuous and dashed straight lines, the slopes of which are equal to the scaling factors $\kappa_{0,0,1,0}^{\mathcal{C}}$ derived from zero-order AHT.

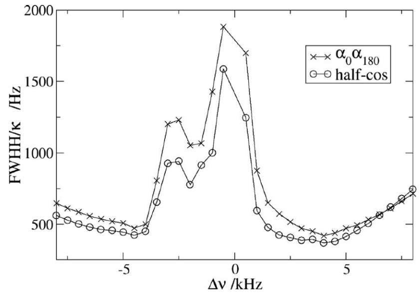

FIG. 8. The scaled up linewidth of $\mathrm{H}^{1,2}$ resonance at $\nu_r=30$ kHz is plotted as function of the off-resonance frequency $\Delta\nu$ for $C6_1^3$ sequences. The $\nu_{1,\mathrm{peak}}$ values were equal to the ones leading to optimal spectral resolution, viz. 86 kHz for $\mathcal{C}=\alpha_0\alpha_{180}$ (cross) and 100 kHz for $\mathcal{C}$=half-cos (circle).

diagonalizing numerically $U(\tau_r,0)$. As $U(\tau_r,0)$ is unitary, it can be decomposed into

$$U(\tau_r,0)=XDX^{-1}, \tag{20}$$

where D is a diagonal matrix with diagonal elements, d_{11} and d_{22}, equal to the eigenvalues of $U(\tau_r,0)$ and the columns of X are the eigenvectors of $U(\tau_r,0)$. The effective rotation frequency $\Delta\mathcal{N}$ and (θ,ϕ) angles can then be calculated using

$$\Delta\mathcal{N}=\frac{\arg(d_{11})}{\pi\tau_r},$$
$$\theta=\arccos(c_z), \tag{21}$$
$$\phi=\frac{\arg(c_x+\imath c_y)}{\sin(\theta)},$$

where c_χ with $\chi=(x,y,z)$ are the projections of $I_{\theta,\phi}$ onto I_χ operator

$$c_\chi=(I_\chi|I_{\theta,\phi})=\frac{\mathrm{Tr}(I_\chi^\dagger XI_zX^{-1})}{\mathrm{Tr}(I_\chi^\dagger I_\chi)} \tag{22}$$

and $I_\chi^\dagger$ denotes the adjoint of I_χ operator. However, an indetermination remains since the effective rotation can be described either as a rotation of $-2\pi\Delta\mathcal{N}\tau_r$ around an axis (θ,ϕ) or as a rotation of $2\pi\Delta\mathcal{N}\tau_r$ around an axis $(\pi-\theta,\phi+\pi)$. We chose the solution that was closest to the isotropic chemical-shift term of the zero-order AH [see Eq. (10)].

The values of $\Delta\mathcal{N}$, θ, and ϕ were plotted in Fig. 7 as function of $\Delta\nu$ for $C6_1^3(\alpha_0\alpha_{180})$ and $C6_1^3$(half-cos) sequences. As expected from zero-order AHT [see Eq. (10)], the effective field direction is close to the z-axis. On resonance $(\Delta\nu=0)$, the effective field generated by the sequence with $\mathcal{C}=\alpha_0\alpha_{180}$ perfectly aligns along the $\boldsymbol{B}^0$ field, whereas in the case of half-cosine basic element, it is tilted by an angle $\theta=3°$. For larger $\Delta\nu$, the deviation from the z-axis slightly increases, but whatever the basic element, it remains below 7° in the off-resonance range of ±10 kHz. The ϕ values also differs between the two basic elements. The effective field projection onto the xy plane always points in the x direction in the case of $\mathcal{C}=\alpha_0\alpha_{180}$, whereas it is aligned along the y direction only when $\Delta\nu=0$ Hz in the case of $\mathcal{C}$=half-cos. However, the effective field projection onto the xy plane is always small $(\leq 12\%)$ compared to its projection onto the z-axis. The small deviation of θ from zero and its off-resonance dependence originate from the nonzero-order terms of AH.

Given the definition of the scaling factor κ [see Eq. (13)], the off-resonance frequency measured in the spectrum, $\Delta\mathcal{N}$, is equal to $\kappa\Delta\nu+\Delta\mathcal{N}(0)$. Whatever the basic element, Fig. 7 shows a linear dependence of $\Delta\mathcal{N}$ versus $\Delta\nu$. Hence, as expected from Eq. (11), the scaling factor κ is constant over the off-resonance range of ±10 kHz. This allows avoiding spectral distortions arising from nonconstant scaling factor.[37–39] Furthermore, the linear fits intercept the plot origin, and hence $\Delta\mathcal{N}(0)=0$ in Eq. (13).

E. Resolution versus offset

After discussing the positions of the lines in the decoupled spectrum, we now determine the line-narrowing efficiency of the $CN_n^{N/2}$ sequences as function of the off-resonance frequency. To do so we simulated the NMR spectra resulting from $C6_1^3$ irradiation on the four spin system described in Fig. 2 and Table I. The off-resonance dependence of scaled up $H^{1,2}$ linewidth is shown in Fig. 8. The linewidth weakly depends on the offset over the intervals $[-8;-4\ \text{kHz}]$ and $[1;8\ \text{kHz}]$, while severe line broadenings are observed between -4 and 1 kHz. This phenomenon is not related to rf pulse imperfections, since the simulation was performed for perfect irradiation schemes, without including any transient or pulse distortion. Additionally, this decrease in spectral resolution does not originate from the tilt of effective field away from the z-direction. Indeed in the simulated spectrum of Fig. 2(c), the zero and image peaks are very small and almost not noticeable. Furthermore, the broadening is observed for both basic elements $\mathcal{C}=\alpha_0\alpha_{180}$ and $\mathcal{C}$=half-cos, whereas for $\mathcal{C}=\alpha_0\alpha_{180}$, the tilt angles θ were smaller and exactly equal to zero for on-resonance irradiation (see Fig. 7).

As the effects of pulse transient and tilted effective field can be disregarded, the line broadening around $\Delta\nu=0$ Hz must stem from the proximity between the $H^{1,2}$ spectral line and the RRF condition at $\Delta\mathcal{N}=0$ kHz. Broadening due to RRF conditions has been described extensively in the case of PMLG sequences using bimodal Floquet theory[20,27,39] but it is still valid in the case of rotor-synchronized pulse sequences. In the general case, the effective positions of the RRF lines in the decoupled spectra are

$$\Delta\mathcal{N}=p\nu_r+k\nu_c, \tag{23}$$

where ν_c is the repeating frequency of rf decoupling sequence unit and p and k are two integers including zero. For $CN_n^{N/2}$ sequences, the characteristic frequency ν_c is equal to $N\nu_r/(2n)$, and hence Eq. (23) simplifies into

$$\Delta\mathcal{N}=j\frac{\nu_r}{2n}, \tag{24}$$

where $j=2np+Nk$ is an integer. As the t_1 increment of $CN_n^{N/2}$ sequence is usually an integer multiple of n rotor periods, the observed spectral width is a submultiple of ν_r/n, and RRF conditions are fulfilled only when $\Delta\mathcal{N}=0$ and $\pm\nu_r/(2n)$ (on both edges of the F_1 projection).

An additional broadening is observed around $\Delta\nu=-2.5$ kHz. This results from the fact that H^3 and H^4 spectral lines get in the vicinity of the RRF line at 0 kHz (Ref. 39) since $\Delta\nu^{1,2}-\Delta\nu^3=-2.2$ kHz and $\Delta\nu^{1,2}-\Delta\nu^4=-3$ kHz.

In order to accommodate a proton chemical-shift range of 15 ppm on a 400 MHz spectrometer, a spectral width of 4.2 kHz is required, assuming a scaling factor of 0.70. Despite of the broadening near the zero RRF line, such a region can always be found by setting the carrier frequency either in the middle of the spectrum or on one of its sides. Actually the required $\Delta\mathcal{N}$ frequency range is generally much lower than half of the available spectral width, $\nu_r/(2n)$.

IV. EXPERIMENTAL DEMONSTRATIONS

A. Samples and experimental conditions

All the experiments were performed on a Bruker AVANCE II 400 MHz NMR spectrometer operating at a magnetic field of 9.4 T and equipped with a wide-bore double-resonance 2.5 mm MAS NMR probe. The spinning frequency in all experiment was 31.746 kHz. Such MAS speed allows achieving perfect rotor synchronization of the decoupling sequences given the 50 ns spectrometer resolution time. However, it has been shown in Ref. 36 that the synchronization condition of $CN_n^{N/2}$ schemes is not stringent and the spinning frequency can vary within a range of ± 1 kHz.

The rf nutation frequencies were calibrated by nutation experiments on adamantane. NMR experiments were performed on samples of monosodium dihydrogenophosphate (NaH_2PO_4) and α-glycine[53] purchased, respectively, from Prolabo and Sigma-Aldrich and used without purification. NaH_2PO_4, and glycine was confined to the middle of the rotor by two spacers in order to improve the B_1 homogeneity. The ^1H chemical shifts are referenced to tetramethylsilane (TMS) using the resonance of adamantane (1.74 ppm) in ^1H MAS NMR spectrum as a secondary reference. For 2D experiments shown in Fig. 1(d), the frequency scales of all F_1 projections were divided by the experimentally determined scaling factors to restore the actual chemical-shift values.

For NaH_2PO_4, the recycle delay was 4 s and the indirect dimension t_1 was acquired with 200 points each obtained with four scans. The t_1 increment was equal to four rotor periods. For α-glycine, we employed presaturation pulses consisting of ten 90° pulses separated by 10 ms prior to a recycle delay of 1.5 s. 200 points in t_1 dimensions were acquired, each obtained with four scans and a t_1 dwell time of two rotor periods.

B. Scaling factor

To evaluate the validity of Eq. (11), the dependence of scaling factor with pulse angle α was measured experimentally. Therefore several 2D $C6_1^3$(half-cos) experiments with different nutation frequencies were performed on NaH_2PO_4. This compound is a model inorganic material, which is used in metal paint undercoats and as a food additive. The ^1H MAS NMR spectrum shown in Fig. 9(a) consists of three overlapping resonances, which were assigned to protons involved in $O-H\cdots O$ hydrogen bonds between phosphate groups.[40] The distinct ^1H chemical shifts arise from differences in hydrogen bond lengths between the four nonequivalent crystallographic sites. Two of them, H3 and H4, have very close chemical shifts.

Experimentally an off-resonance independent contribution $\Delta\mathcal{N}(0)$ to the actual line positions was observed [see Fig. 12(a)] and hence the scaling factor cannot be simply determined as the ratio $\Delta\mathcal{N}/\Delta\nu$ [see Eq. (13)]. However, since κ for $C6_1^3$(half-cos) experiment is constant over a broad offset range (see Sec. IV E), the scaling factor was calculated from the ratio $(\Delta\mathcal{N}_{H1}-\Delta\mathcal{N}_{H2})/(\Delta\nu_{H1}-\Delta\nu_{H2})$.

The scaling factor dependence versus α is shown in Fig. 10(a) in the case of $C6_1^3$(half-cos) experiment. The experi-

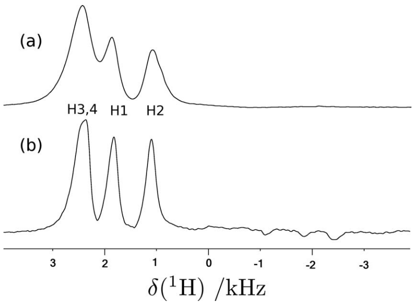

FIG. 9. Proton MAS spectra of NaH_2PO_4 (a) 1D MAS spectrum. (b) The scaled up F_1 projection from the 2D $C6_1^3$(half-cos) experiment [displayed in Fig. 1(d)]. The peak value of the rf nutation frequency was 103 kHz. The numbering of ^{1}H resonances is in agreement with the assignment given in Ref. 40.

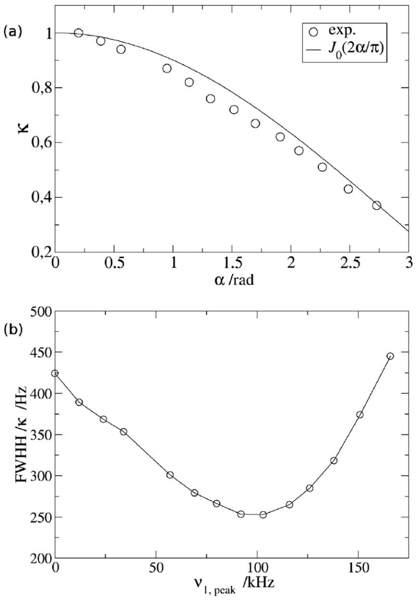

FIG. 10. (a) The experimental scaling factor values κ (circle) during $C6_1^3$(half-cos) experiment are plotted as function of the angle α [defined in Eq. (12)]. The offset of H2 resonance (+0.7 kHz) was kept constant. The continuous line represents scaling factor values $\kappa^{\mathcal{C}}_{0,0,1,0}$ derived from zero-order AHT [see Eq. (11)]. (b) In the same experimental conditions, the scaled up linewidths of the NaH_2PO_4 protons were measured as function of the peak value of rf nutation frequency. No apodization was used.

mental scaling factor monotonously decreases with increasing rf nutation frequency and its evolution is very similar to those obtained from either simulations (see Fig. 3) or Eq. (11). The agreement between experimental scaling factors and Eq. (11) shows the validity of zero-order AHT for predicting the isotropic chemical-shift scaling factor. Therefore, the isotropic chemical-shift interaction can be legitimately approximated by its zero-order term in Eq. (10) and the corresponding effective field must point in a direction close to the z-axis (see Sec. IV E).

The slight deviation between κ and $\kappa^{\mathcal{C}}_{0,0,1,0}$ can arise from higher order terms in the AH, inaccuracy on line positions due to finite linewidth, and pulse imperfections.

C. Optimal rf field

In order to verify the existence of an optimal rf field for $C6_1^3$(half-cos) homonuclear decoupling, we followed the scaled up linewidth as function of $\nu_{1,\mathrm{peak}}$ for the H2 line of a NaH_2PO_4 powder. The offset value was chosen so that no ^{1}H resonance of NaH_2PO_4 got into the vicinity of the zero RRF condition. The experimental dependence of scaled up linewidth with rf nutation frequency is shown in Fig. 10(b). It agrees with numerical simulation results shown in Fig. 4. The antagonistic decreases of linewidth and scaling factor with $\nu_{1,\mathrm{peak}}$ lead to an optimum in spectral resolution at $\nu^{\mathrm{opt}}_{1,\mathrm{peak}} \approx 103$ kHz. This value is close to the theoretical $\nu^{\mathrm{opt}}_{1,\mathrm{peak}}$ frequency predicted from Eq. (14) $(1.15 \times 6/2 \times 30.746 = 109$ kHz), and its rms value ($\nu^{\mathrm{opt}}_{1,\mathrm{rms}} \approx 73$ kHz) is much lower than the maximal admissible rf frequency $\nu^{\max}_{1,\mathrm{rms}}$, which was about 135 kHz for the used 2.5 mm probe. The remaining linewidth is related to nonaveraged homonuclear dipolar interactions and distribution of surroundings. At the minimum of scaled up linewidth, an increase in spectral resolution by a factor of 1.7 is achieved compared to MAS spectrum recorded. The best resolved F_1 projection of 2D $C6_1^3$(half-cos) experiments is displayed in Fig. 9(b).

Nonetheless, the optimum in spectral resolution is broad, since a 10% variation in $\nu_{1,\mathrm{peak}}$ about its optimal value produces only a 5% decrease in spectral resolution. Therefore, $CN_n^{N/2}$ experiments are robust with respect to changes in the rf field amplitude.

D. Comparison of $CN_n^{N/2}$ sequences with $\mathcal{C}=\alpha_0\alpha_{180}$ or half-cos

To evaluate the influence of the shape of basic element pulses, 2D CN_n^{ν} experiments built from either $\mathcal{C}=\alpha_0\alpha_{180}$ or $\mathcal{C}$=half-cos were performed on glycine. An offset value was chosen so that no spectral line appeared on resonance, and for each decoupling sequence, the rf nutation frequency was optimized to achieve maximal resolution. Experimentally at $\nu_r = 31.746$ kHz, the best spectral resolution was obtained when using $C14_2^7$ homonuclear decoupling, whatever the basic element.

As seen in Fig. 11, these homonuclear decouplings allow resolving the signals of two crystallographically nonequivalent methylene protons in α-glycine.[53] These methylene resonances exhibit different linewidths and intensities, since these nonequivalent ^{1}H sites experience distinct ^{1}H–^{1}H dipolar couplings. Such a difference in intensity was already observed in previously reported ^{1}H CRAMPS spectra of α-glycine obtained using other homonuclear decoupling techniques.[27,38,39,53] $C14_2^7(\alpha_0\alpha_{180})$ and $C14_2^7$(half-cos) F_1 projections show the same spectral resolution in agreement

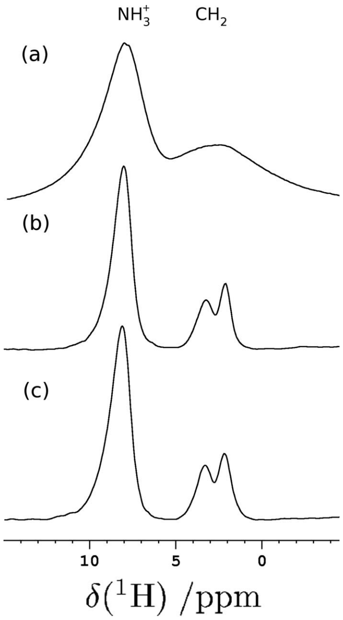

FIG. 11. Proton MAS spectra of glycine. (a) 1D MAS spectrum. [(b) and (c)] The F_1 projections from the 2D $C14_2^7(\alpha_0\alpha_{180})$ (b) and $C14_2^7$(half-cos) (c) experiments. The peak values of the rf nutation frequency were, respectively, 103 and 120 kHz for b and c spectra. The offset frequency of the most shielded methylene ^1H resonance was +1.5 kHz.

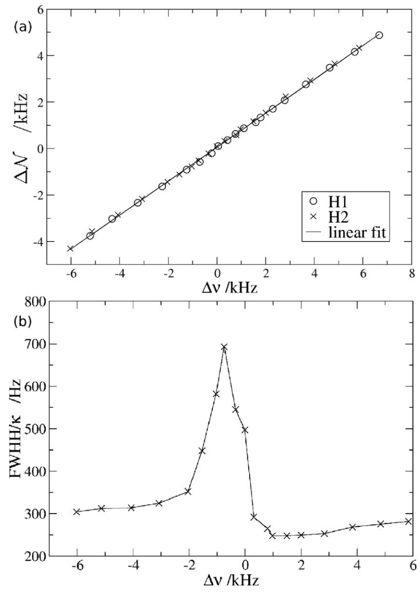

FIG. 12. (a) The dependence of the line positions $\Delta\mathcal{N}$ with the offset $\Delta\nu$ in the case of $C6_1^3$(half-cos) decoupling. This experimental dependence is shown for H1 and H2 peaks of NaH_2PO_4. The $\nu_{1,\text{peak}}$ value was 103 kHz. The continuous line is the linear fit of H1 and H2 experimental points. Its equation is $\Delta\mathcal{N}=0.73\times\Delta\nu+0.05$ kHz. (b) In the same experimental conditions, the scaled up linewidths of H2 proton line are plotted as function of $\Delta\nu$. The continuous line is only a guide for the eyes.

with numerical simulation results shown in Fig. 6. Consequently, at $\nu_r=31.746$ kHz, the pulse transients do not affect the spectral resolution. In $C14_2^7(\alpha_0\alpha_{180})$ and $C14_2^7$(half-cos) spectra, the scaled up linewidth of NH_3^+ peak is divided by a factor of 3.3 compared to MAS spectra. This spectral resolution is similar to the one achieved by PMLG$5_{pp}^{x\bar{x}}$ decoupling.[36]

If the spectral resolution is the same for both basic elements, smoothly modulated decoupling requires less rf power than its square pulse version. Indeed the optimized rms frequencies $\nu_{1,\text{rms}}^{\text{opt}}$ were, respectively, 103 and 85 kHz for $C14_2^7(\alpha_0\alpha_{180})$ and $C14_2^7$(half-cos) sequences. These values agree with Eqs. (14) and (15).

E. Effective field and resolution versus offset

To measure the experimental dependence $\Delta\mathcal{N}(\Delta\nu)$, 2D $C6_1^3$(half-cos) experiments were performed on NaH_2PO_4 for various rf offset values.

In Fig. 12(a), the H1 and H2 line positions, $\Delta\mathcal{N}$, are plotted as function of the offset, $\Delta\nu$. $\Delta\mathcal{N}$ and $\Delta\nu$ values were measured, respectively, in the F_1 and F_2 dimensions of the 2D $C6_1^3$(half-cos) spectra. The line positions of both peaks vary linearly with offset according to $(0.73\times\Delta\nu+0.05)$ kHz. This indicates a constant scaling factor over the range of ±6 kHz in agreement with zero-order AHT and numerical simulation [see Eq. (11) and Fig. 7(a)]. Furthermore, the experimental κ and α values (0.73 and 97°) completely agree with Eqs. (11) and (12). Contrary to simulated spectra, a small offset independent line shift, $\Delta\mathcal{N}(0)=50$ Hz, is observed, which arises from the z-component of the effective field due to pulse imperfections. Finally, whatever the offset, the zero and image peaks were small, as can be seen in Fig. 9(b). This confirms that $CN_n^{N/2}$ irradiation causes a broad-banded effective z-rotation.

In order to verify the offset dependence of spectral resolution, the scaled up H2 linewidth is plotted in Fig. 12(b) as function of $\Delta\nu$. As explained in Sec. III D, line broadening is expected when one of the resonances gets in the vicinity of zero RRF condition. Thus the H2 line can experience a broadening not only when $\Delta\nu=0$ but also when the H1 or H3,4 peaks reach the same position, i.e., $\Delta\nu=-0.8$ and -1.4 kHz. Inspection of Fig. 12(b) indeed reveals a important loss of resolution around these conditions.

Outside of the interval [−2;0.3 kHz], the zero RRF condition falls outside of the NaH_2PO_4 ^1H spectrum and the scaled up linewidth is about 300 Hz. Such offsets allow a gain in spectral resolution over the whole NaH_2PO_4 ^1H spectrum, as seen in Fig. 9(b).

V. CONCLUSIONS

We have presented here a theoretical description of the various facets of $CN_n^{N/2}$ sequences, which were used recently to obtain high-resolution ^{1}H spectra in 1D and 2D solid-state NMR experiments at $\nu_r > 25$ kHz.[35,36,40] Contrary to earlier $RN_n^{N/2}$ schemes, they have the benefit of creating a broad-banded z-rotation of nuclear spins resulting in clean spectra with near elimination of zero and image peaks. Another advantage is its offset-independent scaling factor, which simplifies chemical-shift analysis. Furthermore, a spectral region free from artifacts can easily be found.

The $CN_n^{N/2}$ sequences can be set up and optimized easily via the following steps. First a $CN_n^{N/2}$ symmetry must be selected. Generally $C6_1^3$, $C14_2^7$, and $C8_1^4$ sequences combine the highest spectral resolution with spectral windows large enough to accommodate proton chemical-shift range. Second, the choice of the basic $\mathcal{C}$ element mainly depends on the used NMR spectrometer. $CN_n^{N/2}$ sequences built from $\mathcal{C}=\alpha_0\alpha_{180}$ can be implemented on all spectrometers, while its smoothly modulated version requires fast electronics in order to define the cosine line shape. Both basic elements lead to similar spectral resolution, but $CN_n^{N/2}$(half-cos) has the benefit of requiring less rf power and decreasing rf transients. Third, an offset value has to be chosen so that the zero RRF condition is not fulfilled. Fourth, the rf power must be optimized to achieve maximal resolution. By means of numerical simulations and experiments, we have demonstrated that the optimal resolution is obtained when the pulse angles α are about 90° for $\mathcal{C}=\alpha_0\alpha_{180}$ and 103° for $\mathcal{C}$=half-cos.

From a theoretical point of view, the zero-order AHT has enabled us to calculate the scaling factor value, which defines the scaled isotropic chemical-shift positions of the lines in a proton powder spectrum. The line broadening arises from higher order terms of the AH. Extended first and second order AHT treatments will be presented elsewhere. Furthermore, in the case of windowed 1D $CN_n^{N/2}$ experiments,[36] the insertion of acquisition windows results in nonrotor-synchronized decoupling blocks, thus preventing an AHT approach. In such conditions, bimodal Floquet theoretical treatment is required.

ACKNOWLEDGMENTS

The authors are grateful for funding provided by Region Nord/Pas de Calais, Europe (FEDER), CNRS, French Ministry of Higher Education and Research, FR-3050, USTL, ENSCL, Bruker BIOSPIN, and ANR Contract No. NT05-2-41632. We acknowledge the Bruker company and Fabien Aussenac for the lending of a wide-bore 2.5 mm Bruker MAS NMR probe.

[1] Y. Ishii and R. Tycko, J. Magn. Reson. **142**, 199 (2000).

[2] Y. Ishii, J. P. Yesinowski, and R. Tycko, J. Am. Chem. Soc. **123**, 2921 (2001).

[3] I. Schnell, S. P. Brown, H. Y. Low, H. Ishida, and H. W. Spiess, J. Am. Chem. Soc. **120**, 11784 (1998).

[4] S. P. Brown, I. Schnell, J. D. Brand, K. Müllen, and H. W. Spiess, J. Am. Chem. Soc. **121**, 6712 (1999).

[5] S. P. Brown, T. Schaller, U. P. Seelbach, F. Koziol, C. Ochsenfeld, F.-G. Klärner, and H. W. Spiess, Angew. Chem., Int. Ed. **40**, 717 (2001).

[6] S. P. Brown, Prog. Nucl. Magn. Reson. Spectrosc. **50**, 199 (2007) and references therein.

[7] J. Wiench, C. Bronnimann, V.-Y. Lin, and M. Pruski, J. Am. Chem. Soc. **129**, 12076 (2007).

[8] D. H. Zhou and C. M. Rienstra, Angew. Chem., Int. Ed. **47**, 7328 (2008).

[9] E. K. Paulson, C. R. Morcombe, V. Gaponenko, B. Dancheck, R. A. Byrd, and K. W. Zilm, J. Am. Chem. Soc. **125**, 14222 (2003).

[10] V. Agarwal, A. Diehl, N. Skrynnikov, and B. Reif, J. Am. Chem. Soc. **128**, 12620 (2006).

[11] D. H. Zhou, G. Shah, M. Comos, C. Mullen, D. Sandoz, and C. M. Rienstra, J. Am. Chem. Soc. **129**, 11791 (2007).

[12] M. Mehring, *Principles of High Resolution NMR in Solids* (Springer-Verlag, Berlin, 1983).

[13] M. M. Maricq and J. S. Waugh, J. Chem. Phys. **70**, 3300 (1979).

[14] E. Brunner, D. Freude, B. C. Gerstein, and H. Pfeifer, J. Magn. Reson. (1969-1992) **90**, 90 (1990).

[15] C. Filip, S. Hafner, I. Schnell, D. E. Demco, and H. W. Spiess, J. Chem. Phys. **110**, 423 (1999).

[16] V. E. Zorin, S. P. Brown, and P. Hodgkinson, J. Chem. Phys. **125**, 144508 (2006).

[17] J. W. Traer, E. Montoneri, A. Samoson, J. Past, T. Tuherm, and G. R. Goward, Chem. Mater. **18**, 4747 (2006).

[18] B. C. Gerstein, R. G. Pembleton, R. C. Wilson, and L. M. Ryan, J. Chem. Phys. **66**, 361 (1977).

[19] E. Vinogradov, P. K. Madhu, and S. Vega, Chem. Phys. Lett. **314**, 443 (1999).

[20] E. Vinogradov, P. K. Madhu, and S. Vega, J. Chem. Phys. **115**, 8983 (2001).

[21] D. Sakellariou, A. Lesage, P. Hodgkinson, and L. Emsley, Chem. Phys. Lett. **319**, 253 (2000).

[22] A. Lesage, D. Sakellariou, S. Hediger, B. Elena, P. Charmont, S. Steuernagel, and L. Emsley, J. Magn. Reson. **163**, 105 (2003).

[23] B. Elena, G. de Paëpe, and L. Emsley, Chem. Phys. Lett. **398**, 532 (2004).

[24] M. Leskes, S. Steuernagel, D. Schneider, P. K. Madhu, and S. Vega, Chem. Phys. Lett. **466**, 95 (2008).

[25] M. Lee and W. I. Goldburg, Phys. Rev. **140**, A1261 (1965).

[26] D. P. Burum, M. Linder, and R. R. Ernst, J. Magn. Reson. (1969-1992) **44**, 173 (1981).

[27] M. Leskes, P. K. Madhu, and S. Vega, J. Chem. Phys. **128**, 052309 (2008).

[28] M. H. Levitt, J. Chem. Phys. **128**, 052205 (2008).

[29] M. H. Levitt, *Encyclopedia of Nuclear Magnetic Resonance* (Wiley, Chichester, 2002), pp. 165–196.

[30] D. E. Demco, S. Hafner, and H. W. Spiess, J. Magn. Reson., Ser. A **116**, 36 (1995).

[31] S. Hafner and H. W. Spiess, Solid State Nucl. Magn. Reson. **8**, 17 (1997).

[32] S. Hafner and H. W. Spiess, J. Magn. Reson., Ser. A **121**, 160 (1996).

[33] P. K. Madhu, X. Zhao, and M. H. Levitt, Chem. Phys. Lett. **346**, 142 (2001).

[34] S. Paul, R. J. Thakur, and P. K. Madhu, Chem. Phys. Lett. **456**, 253 (2008).

[35] J.-P. Amoureux, B. Hu, and J. Trébosc, J. Magn. Reson. **193**, 305 (2008).

[36] J.-P. Amoureux, B. Hu, J. Trébosc, O. Lafon, Q. Wang, and F. Deng, "Homonuclear dipolar decoupling schemes for fast MAS," Solid State Nucl. Magn. Reson. (in press).

[37] L. Bosman, P. K. Madhu, S. Vega, and E. Vinogradov, J. Magn. Reson. **169**, 39 (2004).

[38] M. Leskes, P. K. Madhu, and S. Vega, Chem. Phys. Lett. **447**, 370 (2007).

[39] M. Leskes, P. K. Madhu, and S. Vega, J. Chem. Phys. **125**, 124506 (2006).

[40] L. Mafra, J. R. B. Gomes, J. Trébosc, J. Rocha, and J.-P. Amoureux, J. Magn. Reson. **196**, 88 (2009).

[41] A. J. Vega, J. Magn. Reson. **170**, 22 (2004).

[42] U. Haeberlen and J. S. Waugh, Phys. Rev. **175**, 453 (1968).

[43] A. Brinkmann and M. H. Levitt, J. Chem. Phys. **115**, 357 (2001).

[44] A. Brinkmann and M. Edén, J. Chem. Phys. **120**, 11726 (2004).

[45] Y. K. Lee, N. D. Kurur, M. Helmle, O. G. Johannessen, N. C. Nielsen, and M. H. Levitt, Chem. Phys. Lett. **242**, 304 (1995).

[46] M. Edén and M. H. Levitt, J. Chem. Phys. **111**, 1511 (1999).

[47] A. Brinkmann, M. Edén, and M. H. Levitt, J. Chem. Phys. **112**, 8539 (2000).
[48] M. Carravetta, M. Edén, X. Zhao, A. Brinkmann, and M. H. Levitt, Chem. Phys. Lett. **321**, 205 (2000).
[49] M. Bak, J. T. Rasmussen, and N. C. Nielsen, J. Magn. Reson. **147**, 296 (2000).
[50] M. Bak and N. C. Nielsen, J. Magn. Reson. **125**, 132 (1997).
[51] P. Charmont, D. Sakellariou, and L. Emsley, J. Magn. Reson. **154**, 136 (2002).
[52] J. Zhou, C. Ye, and B. C. Sanctuary, J. Chem. Phys. **101**, 6424 (1994).
[53] H. Kimura, K. Nakamura, A. Eguchi, H. Sugisawa, K. Deguchi, K. Ebisawa, E. Suzuki, and A. Shoji, J. Mol. Struct. **447**, 247 (1998).

A tilted magic-echo homonuclear dipolar decoupling scheme for high-resolution proton nuclear magnetic resonance of solids

Zhehong Gan [a]*, P. K. Madhu [b]*, Jean-Paul Amoureux [c], Julien Trébosc[c], Olivier Lafon[c]

[a] *Center of Interdisciplinary Magnetic Resonance, National High Magnetic Field Laboratory, 1800 East Paul Dirac Drive, Tallahassee, FL 32310, USA*

[b] *Department of Chemical Sciences, Tata Institute of Fundamental Research, Homi Bhabha Road, Colaba, Mumbai 400 005, India*

[c] *UCCS (CNRS-8181), University of Lille-1, 59652 Villeneuve d'Ascq Cedex, France*

[*] Corresponding authors. Fax +1 850 644 1366.
E-mail address: gan@magnet.fsu.edu (Z. Gan).
madhu@tifr.res.in (P. K. Madhu)

ABSTRACT

A homonuclear dipolar decoupling scheme is introduced for obtaining proton high-resolution spectra of solids under slow to fast magic-angle spinning (MAS). The basic unit is a magic-echo sequence with its effective field tilted in the rotating frame, bracketed by two sandwich pulses. The angle of the tilt can be varied for obtaining optimal spectral resolution according to the spinning frequency. Improved resolution has been obtained using this tunable sequence on a sample of glycine at 10 and 60 kHz of MAS and compared with windowed phase-modulated Lee-Goldburg and magic-echo sandwich schemes.

Keywords: ^{1}H, homonuclear decoupling, MAS, ultra fast MAS, Lee-Goldburg, magic-echo, magic-sandwich, FSLG, *w*PMLG, MSHOT, *z*-rotation

1. Introduction

Proton nucleus is widely used in nuclear magnetic resonance (NMR), especially in liquid state, for its high sensitivity and abundance [1]. In the solid state, the strong homonuclear interactions among the protons must be removed for obtaining high spectral resolution. Homonuclear dipolar decoupling can be achieved by magic-angle spinning (MAS) and multiple-pulse decoupling [2-6] that average the spatial and the spin parts of the dipolar Hamiltonian, respectively. MAS is also necessary to remove the broadening from proton chemical-shift anisotropy for obtaining high-resolution spectra of powder samples [5-9]. The goal of high-resolution for proton solid-state NMR has driven the development of numerous homonuclear dipolar decoupling sequences [2-39] and of ultra-fast MAS probes that can deliver spinning frequencies up to 65 kHz [32,34,36,38-40]. High magnetic fields [40] and the use of selectively deuterated samples [41,42] have been also shown to help obtaining proton spectral resolution.

Although acquiring spectra using only MAS has the advantages of simplicity, high sensitivity, and artifact-free spectra over windowed multiple-pulse experiments, averaging in spin space with *rf* fields far above the mechanical spinning frequency still outperforms MAS in terms of spectral resolution. However, under combined rotation and multiple-pulse spectroscopy (CRAMPS), both the spatial and spin parts of the dipolar Hamiltonian are modulated and hence can interfere with each other depending on their time scales [3]. In the early days of static or slow MAS quasi-static sample conditions, the two time scales were far away from interference. Long and nested super cycles could then be applied to eliminate high-order terms of the average dipolar Hamiltonian that led to efficient pulse sequences such as BR-24 [7,8] and MSHOT [21,22]. However, with increasing MAS frequency the cycle time of the *rf* pulses (τ_c) got closer to the rotor period (τ_r) and the benefit of high-order averaging of these sequences started to diminish. Windowless sequences like the frequency-switched Lee-Goldburg [15,17], PMLG [24], and DUMBO [26] then became more favorable with their short cycle times for uses in heteronuclear-detected proton NMR [43] and *J*-spectroscopy [44,45]. Direct acquisition of high-resolution proton spectra requires insertion of a short but finite window period into these windowless sequences. As the spinning frequency further increased, the total cycle time which is limited by the finite acquisition window and *rf* field strength got close to the rotor period leading to interference regimes causing severe resonant broadening, a phenomenon with the same origin as in many recoupling experiments under MAS [46]. The resonant phenomenon and its conditions can be understood with average Hamiltonian [2] and bimodal Floquet theory [3]. With spinning frequencies up to 65 kHz, the fast MAS leaves enough room for obtaining high-resolution proton spectra with certain τ_r/τ_c ratios that avoid the resonant conditions [36,38,39]. It has also been shown recently that two rotor-synchronized sequences, namely RN_n^{ν} [27,31] and SAM [34,35,37], can yield good proton resolution. However, both sequences mainly work at fast MAS frequencies as they scale only the spin part of the dipolar Hamiltonian and rely on MAS to average the whole dipolar Hamiltonian.

In this communication, we introduce a new type of homonuclear dipolar decoupling sequence that can be tuned considering the interplay between the *rf* and the mechanical averaging of the dipolar Hamiltonian from slow to fast MAS conditions. The pulse sequence is a magic-echo sandwich [14,21,22], shown in Figure 1, where the 2π pulses rotate the nuclear spins about an effective *rf* field. The rotations are sandwiched by a pair of toggling pulses and followed by a blank period for windowed acquisition. The key feature of the sequence is that the angle of the effective field with respect to the *z* axis (θ) and the ratio between the *rf* and the windowed periods (η) can be varied covering three commonly used experiments for obtaining high-resolution proton NMR spectra: MAS-only (θ = 0°), the frequency-switched or phase-modulated Lee-Goldburg (θ = 54.7°), and the magic-echo (θ = 90°) experiment with the effective field close to the *z*-axis, the magic-angle, or the *x*-axis, respectively. Thus, the tunable *ti*lted *m*agic-*e*cho *s*andwich sequence, which we denote as TIMES, should perform at least no worse and possibly better than the best of these three experiments. We will show experimentally that the sequence can be indeed tuned for improved performances at ultra high (60 kHz) and moderate (10 kHz) spinning frequencies using a 1.3 mm ultra-fast MAS probe. The mechanism of the improved resolution under these two conditions will be explained.

2. Theory

We present here the theory in the static limit to describe the mechanism of the TIMES sequence. A full theory considering the fast MAS requires the bi-model Floquet treatment [3]. The spin Hamiltonians can be expressed in the irreducible representation

$$H_{\text{int}} = \sum_{\lambda}\sum_{l} A^{\lambda}_{l,0} T^{\lambda}_{l,0} \qquad (1)$$

Here λ is an index for chemical shift and homonuclear dipolar interactions. The spatial part of the Hamiltonian is modulated by sample rotation, with the isotropic ($l_\lambda = 0$) and the anisotropic ($l_\lambda = 2$) parts of the spin interactions, as

$$A^{\lambda}_{l,0} = \sum_{m=-l_\lambda}^{l_\lambda} \tilde{A}^{\lambda}_{l,m} D^{l_\lambda}_{0,m}(0,\theta_M,\omega_r t) \qquad (2)$$

$D^{l_\lambda}_{0,m}(0,\theta_M,\omega_r t)$ are the Wigner rotation matrix elements from the rotor to lab-frame and $\tilde{A}^{\lambda}_{l,m}$ are the spatial tensor components in the rotor frame. θ_M is the magic angle and ω_r is the angular MAS frequency. The spin part of the Hamiltonian is modulated by the *rf* pulse sequence as

$$U_{rf}^{-1}(t)T_{l,0}^{\lambda}U_{rf}(t)=\sum_{m=-l'_{\lambda}}^{l'_{\lambda}}\tilde{T}_{l,m}^{\lambda}D_{0,m}^{l'_{\lambda}}(\Omega_{rf}) \qquad (3)$$

Here $U_{RF}(t)$ is the time propagator of the *rf* Hamiltonian and $\tilde{T}_{l,m}^{\lambda}$ are the spin tensor operators in the *rf* rotating frame described by the Euler angles Ω_{rf} . The spin-tensor rank for the homonuclear dipolar coupling is $l'_{\lambda}=2$, but the rotation for chemical shift spin tensors behaves as $l'_{\lambda}=1$. For a constant effective *rf* field, $\Omega_{rf}=(0,\theta,\omega_{eff}t)$, where θ is the orientation of the effective field ω_{eff} with respect to the magnetic field B_0. A 2π rotation about the effective field averages all $m\neq 0$ terms leaving only a single scaled $\tilde{T}_{l'_{\lambda},0}^{\lambda}$ term,

$$\left\langle T_{l,0}^{\lambda}\right\rangle = P_{l'_{\lambda}}(\cos\theta)\tilde{T}_{l'_{\lambda},0}^{\lambda} \qquad (4)$$

Under such a *rf* rotation, the homonuclear dipolar interaction ($l'_{\lambda}=2$) scales as $P_2(\cos\theta)$ just like magic-angle spinning and the chemical shift ($l'_{\lambda}=1$) scales as $\cos\theta$. It is important to note that the spin tensor operators $\tilde{T}_{l,m}^{\lambda}$ are defined in the tilted frame with its *z'*-axis along the effective *rf* field, and are thus different from the tensor operators in the lab frame $T_{l,m}^{\lambda}$.

Figure 1 shows the schematic of the TIMES pulse sequence with two elements added to the basic tilted magic-echo unit of a rotation about the tilted *rf* field $2\pi_{\theta x}$ and a sandwich pulse θ_y. The first combines a mirror image of the pulses with a phase

$$\varphi(\tau-t)=\varphi(t)-\pi \qquad (5)$$

where $\tau = 2(\tau_p + \tau_\theta)$ is the length of the R block in Figure 1. This ensures the pulse sequence to be cyclic, $U_{rf}(n\tau)=1$, and the Hamiltonian in the *rf* rotating frame then satisfies the so-called time-reversal symmetry, $H(t)=H(\tau-t)$ [2]. This property makes all even terms in the average Hamiltonian equal to zero in the static limit. The second element is a super cycle that consists of

N units ($N \geq 2$) with $2\pi / N$ phase increment. Each unit consists of a small rotation about the effective chemical shift field that may tilt off the *z*-axis. The average of the *N* super cycle makes the sum a pure *z*-rotation for the chemical shift that eliminates mirror image peaks. Modulations by the super cycle can cause sidebands if signal is acquired during every window within the super cycle. For the two-step super cycle ($N = 2$) used in Figure 1, the sidebands are at the edges of the spectral window.

In the magic-echo experiment the *rf* rotating frame must be switched to the original *z*-axis using the sandwich pulses so that the spin operators are the same between the *rf* rotation and the window periods. The average Hamiltonian can be simply obtained by adding the scaling factors weighted by their durations which, respectively for the dipolar and chemical-shift interactions, are given by

$$\kappa_D \approx \frac{2P_2(\cos\theta)+\eta}{2+\eta}, \qquad \kappa_{CS} \approx \frac{2\cos\theta+\eta}{2+\eta} \qquad (6)$$

The finite length of the sandwich toggling pulses is neglected here. Two well-known cases to average the homonuclear dipolar interaction ($\kappa_D = 0$) are $\theta = \theta_M$, $\eta = 0$ (FSLG/PMLG) and $\theta = \pi/2$, $\eta = 1$ (magic-echo). However, as there are two parameters in κ_D, the combinations of θ and η leading to an averaging of the dipolar interactions are in principle infinite, but only those with finite window acquisition period and short cycle time are practically useful and preferred.

As mentioned before, the toggling pulses make the scaled dipolar Hamiltonian of windowless sequence to have the same spin operators during the blank period. This is a simple way of incorporating a blank period into a windowless sequence. The average Hamiltonian can then be tuned to zero by varying the tilt angle θ and the ratio η between the window and pulsed period in Eq. (6).

It should be noted that the *z*-rotation super cycle projects every rotation to the *z*-axis causing an additional $\cos\theta$ weighting in the chemical-shift scaling during the $2\pi\, rf$ rotation. This additional scaling leads to the following chemical-shift scaling factor for supercycled TIMES sequence

$$\chi_{\mathrm{CS}} \approx \frac{2\cos^2\theta + \eta}{2+\eta} \qquad (7)$$

Incidentally, the super-cycled FSLG/PMLG and MSHOT, have the same theoretical chemical shift scaling factor of 1/3. Equation (7) shows that the chemical shift scaling increases with the tilted *rf* field approaching the *z*-axis.

3. Results and Discussions

Figure 2 shows the results at a MAS frequency of 60 kHz. The resolution of the MAS-only spectrum in Figure 2a is already good with resolved peaks between the two diastereotopic CH_2 resonances. Direct window-detected *w*PMLG and TIMES multiple-pulse sequences yield better resolution in Figure 2b and 2c. At this high MAS frequency *w*PMLG was found performing better than the two-step supercycled magic-echo or MSHOT-2 (not shown). A comparison between Figure 2b and 2c shows that TIMES is better than *w*PMLG in terms of both spectral resolution and line shape using a lower *rf* field. The experimentally optimized TIMES spectrum was found with a τ_p = 3.84 μs linearly ramped ($\phi_{\mathrm{last}} = 320^0$) pulse using 134 kHz *rf* field. The phase ramp in τ_p is equivalent to $\phi_{\mathrm{last}} / 2\pi\tau_p \approx 261$ kHz frequency offset and an effective field of 267 kHz tilted at ~ 30^o to the *z*-axis. This pulse make ~370^0 rotation at an angle far above the magic-angle. The 0.48 μs sandwich pulse corresponds to 28^o rotation. Both the rotation and tilt angles are in a good agreement with the theoretically expected values.

The TIMES sequence gains spectral resolution from a net increase in the chemical-shift scaling over a lesser line broadening from the scaled homonuclear dipolar coupling under this fast MAS condition. This kind of resolution enhancement occurs only at ultra-fast MAS that can average the remaining homonuclear interaction efficiently. The experimentally optimized *w*PMLG actually already has this kind of resolution enhancement mechanism in it. The *w*PMLG optimized effective *rf* field was found at about $\theta \approx 42^\circ$, closer to the z-axis than the Lee-Goldburg condition. This mechanism can also be found in experimentally optimized DUMBO sequence under fast MAS, which has an effective chemical shift rotation closer to the *z*-axis and a scaling factor larger than the regular DUMBO sequence [29,38].

With respect to *w*PMLG, the TIMES sequence uses shorter *rf* pulses (8.64 vs 9.5 μs), lower *rf* field (134 vs 190 kHz), and has a larger scaling factor (0.705 vs 0.538). For *w*PMLG, the higher *rf* field was necessary to avoid resonant broadening at the 60 kHz spinning frequency. Short cycle time provides flexibilities when going to high MAS frequencies to avoid the τ_r/τ_c ratios that can cause resonant broadening. To the best of our knowledge this TIMES condition has a shorter cycle time than other pulse sequences. The other feature in comparison with *w*PMLG is the line shape distortion. The wiggles in the *w*PMLG spectrum are not truncation artifacts but likely from the *rf* field inhomogeneity, which can be sizable for the high-frequency 900 MHz probe using a solenoid coil and a full rotor sample. In this aspect, the TIMES sequence has an advantage because the chemical-shift evolution occurs more during the window period and the effective chemical-shift rotation is closer the z-axis during the pulse period than the *w*PMLG. The *rf* inhomogeneity is inactive during the blank period and has less effects during the 2π rotation being closer to the *z*-axis. Thus, the TIMES sequence is less susceptible to possible spectral broadening and intensity modulation from an inhomogeneous *rf* field. The property of having *rf* rotations closer to the *z*-axis is also favorable when used with the *z*-rotation super cycle. It makes the projection onto the *z*-axis with a less reduction on the chemical-shift scaling factor. The TIMES sequence has the largest super-cycled chemical shift scaling so far besides the MAS-only experiment with $\chi_{cs} \approx 0.705$ and a pure *z*-rotation for obtaining quadrature detected spectra without mirror image peaks.

Figure 3 shows the results at 10 kHz MAS frequency. The broad spectrum of an MAS-only experiment in Figure 3a indicates that this spinning frequency alone is insufficient for averaging out the homonuclear dipolar coupling. Therefore the homonuclear decoupling relies mostly on a carefully designed and optimized pulse sequence to average out the spin part of the dipolar Hamiltonian for high spectral resolution. Figure 3b and 3c show the glycine spectra under 10 kHz MAS using optimized MSHOT-2 and TIMES sequences. The MSHOT-2 sequence performed better than the *w*PMLG at this MAS frequency and 170 kHz *rf* field (not shown). Indeed, the window period is fairly close to the on-resonance 2π rotation of the magic-echo sequence (4.8 vs 5.6 μs). The homonuclear dipolar scaling is close to, but not exactly, zero for the whole MSHOT-2 sequence including the window period. Figure 3c shows a significant improvement on spectral resolution by the TIMES sequence with a slightly tilted *rf* effective field. The spectrum was obtained using $\phi_{last} = 16^0$ phase ramp for the τ_p pulse with an experimental optimization that led to $\tau_\theta = 1.65$ μs and $\tau_p = 5.28$ μs. These pulse lengths correspond to 101^o and 323^o rotations with the 170 kHz *rf* field and are fairly close to the conditions of magic-echo sequence. Under these conditions, the phase ramp is equivalent to a mere 8.4 kHz offset during the 2π rotation that tilts the effective field only about 3^o from the *x*-axis. Such a small tilt changes very little the chemical-shift scaling factor (the experimentally measured factor remains the same at 0.35), but it apparently does lead to a more complete suppression of the homonuclear coupling for the improved spectral resolution. In principle, the MSHOT sequence can be tuned by lengthening the windowed detection period. However, an increase of the basic cycle time usually degrades the decoupling performance. An experimental optimization was made by lengthening the window period but it did not yield better resolution (not shown). With the TIMES sequence, a tuning of the effective field off the transverse plane is apparently a better way with a shorter cycle than lengthening the window period for complete decoupling of the homonuclear dipolar interactions.

4. Conclusion

We have introduced a new type of homonuclear dipolar decoupling pulse sequence with tilted-magic-echo pulse. Changing the tilt angle and window detection period allows the tuning of the scaling factors of homonuclear dipolar coupling and chemical shift. Under ultra-fast MAS, the dipolar scaling part can be relaxed for a larger chemical shift scaling and fast MAS is efficient to average the remaining homonuclear coupling for a net gain in resolution. Optimization usually leads to *rf* rotation axes between the magic-angle and the *z*-axis. The TIMES multiple-pulse decoupling under this condition requires low *rf* fields and has short cycles and small artifacts. Under slow MAS, the tunable pulse sequence can be adjusted for complete suppression of the homonuclear coupling including the dipolar evolution during the finite detection window. The optimization then leads to pulse sequences with effective *rf* fields between the magic angle and the *x*-axis. The TIMES sequence at the slow MAS condition gains spectral resolution through line narrowing with better suppression of the homonuclear coupling. The concept of tunable pulse sequences has been demonstrated here with a constant *rf* effective field but the principle can be extended to other basic decoupling units for rational optimization of homonuclear decoupling sequences for high-resolution proton NMR of solids at various MAS conditions.

Acknowledgements

ZG acknowledges support by the National High Magnetic Field Laboratory through National Science Foundation Cooperative Agreement (DMR-0084173) and by the State of Florida. ZG and PKM acknowledge support from the Erasmus Mundus Master of Science on Advanced Spectroscopy in Chemistry during their stay at the University of Lille. JPA, OL, and JT are grateful for funding provided by Region Nord/Pas de Calais, Europe (FEDER), CNRS, French Minister of Science, USTL, ENSCL, CortecNet, and Bruker BIOSPIN. They also acknowledge the financial support from the TGIR RMN THC (FR-3050) for conducting the research.

Figure Captions

Figure 1: (a) *Ti*lted-*m*agic-*e*cho *s*andwich (TIMES) sequence for proton homonuclear dipolar decoupling under MAS. The $2\pi_{\theta x}$ rotation is about an effective *rf* field tilted at an angle θ with respect to the *z*-axis that can be programmed by a phase ramp from 0 to ϕ_{last}, as indicated in the plot. The phase ramp for the second 2π rotation ($\overline{2\pi}_{\theta x}$) is from ϕ_{last} -π to -π. The θ_y and $\overline{\theta}_y$ are the sandwich pulses. A two-step super cycle, R and $\overline{R}$, is applied for a pure *z*-rotation for chemical shift but the signal is acquired during every window. The excitation pulse phase and the receiver phase are cycled as Ψ = 0°, 90°, 180°, 270°.

Figure 2: ^{1}H NMR spectra of glycine at 60 kHz of MAS acquired using a Bruker 1.3 mm CPMAS double-resonance probe with a full rotor sample on a 900 MHz Avance III NMR spectrometer. 16 scans with a 5 s recycle delay were acquired for each spectrum. The off-resonance *rf* pulses were programmed by a 32-step shape pulse with a phase ramp from 0 to ϕ_{last} with the carrier frequency set at $\Delta\omega_0$. The pulse sequence parameters are listed against the plots. The acquisition window was w = 4.8 μs and the ^{1}H chemical shift was referenced by setting the mean of the two CH_2 peaks to 3.55 ppm.

Figure 3: ^{1}H NMR spectra of glycine at 10 kHz of MAS with the rest of the experimental details the same as in Fig. 2. The pulse sequence parameters are listed against the plots.

References

1. R. R. Ernst, G. Bodenhausen, A. Wokaun, Principles of NMR in one and two dimensions, Oxford Science Publication, London, 1991.
2. U. Haeberlen, High resolution NMR in solids-selective averaging, Supplement 1, Adv. Magn. Reson. Academic Press, New York, (1976).
3. E. Vinogradov, P. K. Madhu, S. Vega, Topics Curr. Chem. 246 (2005) 33.
4. B. C. Gerstein, Encyc. of Magn. Reson. Ed. R. K. Harris, John Wiley (2009).
5. B. C. Gerstein, C. Clor, R. G. Pembleton, R. C. Wilson, J. Phys. Chem. 81 (1977) 565.
6. R. E. Taylor, R. G. Pembleton, L. M. Ryan, B. C. Gerstein, J. Chem. Phys. 71 (1979) 4541.
7. D. P. Burum, W. K. Rhim, J. Chem. Phys. 71 (1979) 94.
8. D. P. Burum, W. K. Rhim, J. Chem. Phys. 70 (1979) 3553
9. C. E. Bronnimann, B. L. Hawkings, M. Zhang, G. E. Maciel, Anal. Chem. 60 (1988) 1743.
10. J. S. Waugh, L. M. Huber, U. Haeberlen, Phys. Rev. Lett. 20 (1968) 180.
11. P. Mansfield, J. Phys. C. 4 (1971) 1444.
12. M. Mehring, J. S. Waugh, Phys. Rev. B. 5 (1972) 3459.
13. D. P. Burum, M. Linder, R. R. Ernst, J. Magn. Reson. 44 (1981) 173.
14. K. Takegoshi, C. A. McDowell, Chem. Phys. Lett. 116 (1985) 100.
15. A. Bielecki, A. C. Kolbert, M. H. Levitt, Chem. Phys. Lett. 155 (1989) 341.
16. D. G. Cory, J. Magn. Reson. 94 (1991) 526.

17. M. H. Levitt, A. Bielecki, A. C. Kolbert, D. J. Ruben, Solid State Nucl. Magn. Reson. 2 (1991) 151.
18. M. L. Buszko, C. E. Bronnimann, G. E. Maciel, J. Magn. Reson. A. 103 (1993) 183 (1997) 7571.
19. D. Demco, S. Hafner, H. W. Spiess, J. Magn. Reson. A 116 (1995) 36.
20. S. Hafner, H. W. Spiess, J. Magn. Reson. A 121 (1996) 160.
21. M. Howhy, P. V. Bower, H. J. Jakobsen, N. C. Nielsen, Chem. Phys. Lett. 273 (1997) 5.
22. M. Hohwy, N. C. Nielsen, J. Chem. Phys. 106 (1997) 7571.
23. H. Cho, J. Magn. Reson. 141 (1999) 164.
24. E. Vinogradov, P. K. Madhu, S. Vega, Chem. Phys. Lett. 314 (1999) 443.
25. E. Vinogradov, P. K. Madhu, S. Vega, Chem. Phys. Lett. 329 (2000) 207.
26. D. Sakellariou, A. Lesage, P. Hodgkinson, L. Emsley, Chem. Phys. Lett. 319 (2000) 253.
27. P. K. Madhu, X. Zhao, M. H. Levitt, Chem. Phys. Lett. 346 (2001) 142.
28. E. Vinogradov, P. K. Madhu, S. Vega, J. Chem. Phys. 115 (2001) 8983.
29. A. Lesage, D. Sakellariou, S. Hediger, B. Eléna, P. Charmont, S. Steuernagel, L. Emsley, J. Magn. Reson. 163 (2003) 105.
30. B. Eléna, G. de Paepe, L. Emsley, Chem. Phys. Lett. 398 (2004) 532.
31. S. Paul, R. S. Thakur, P. K. Madhu, Chem. Phys. Lett. 456 (2008) 253.
32. M. Leskes, S. Steuernagel, D. Schneider, P. K. Madhu, S. Vega, Chem. Phys. Lett. 466 (2008) 95.
33. M. Leskes, P. K. Madhu, S. Vega, J. Chem. Phys. 128 (2008) 052309.
34. J. P. Amoureux, B. Hu. J. Trebosc, J. Magn. Reson. 193 (2008) 305.
35. J. P. Amoureux, B. Hu. J. Trebosc, F. Deng, Solid State Nucl. Magn. Reson. 35 (2009) 19.

36. M. Leskes, P. K. Madhu, S. Vega, J. Magn. Reson. 199 (2009) 208.

37. O. Lafon, Q. Wang, B. Hu, J. Trébosc, F. Deng, J. P. Amoureux, J. Chem. Phys. 130 (2009) 014504.

38. E. Salager, R. S. Stein, S. Steuernagel, A. Lesage, B. Eléna, L. Emsley, Chem. Phys. Lett. 469 (2009) 336.

39. K. Mao, M. Pruski, J. Magn. Reson. 203 (2010) 144.

40. A. Samoson, T. Tuherm, Z. Gan, Solid State Nucl. Magn. Reson. 20 (2001) 130.

41. R. Linser, U. Fink, B. Reif, J. Biomol. NMR. 47 (2010) 1.

42. D. H. Zhou, G. Shah, M. Cormos, C. Mullen, D. Sandoz, C. M. Rienstra, J. Am. Chem. Soc. 129 (2007) 11791.

43. B.-J. van Rossum, H. Foerster, H. J. M. de Groot. J. Magn. Reson. 124 (1997) 516.

44. S. Cavadini, V. Vitzthum, S. Ulzega, A. Abraham, G. Bodenhausen, J. Magn. Reson. 202 (2010) 57.

45. O. Lafon, Qiang Wang, B. Hu, F. Vasconcelos, J. Trébosc, S. Cristol, F. Deng, J.-P. Amoureux, J. Phys. Chem. A113 (2009) 12864.

46. M. H. Levitt, Symmetry-based pulse sequences in magic-angle spinning solid-state NMR, Encyc. of NMR (D.M. Grant, R.K. Harris, Eds.), John Wiley & Sons, Chichester, 2002.

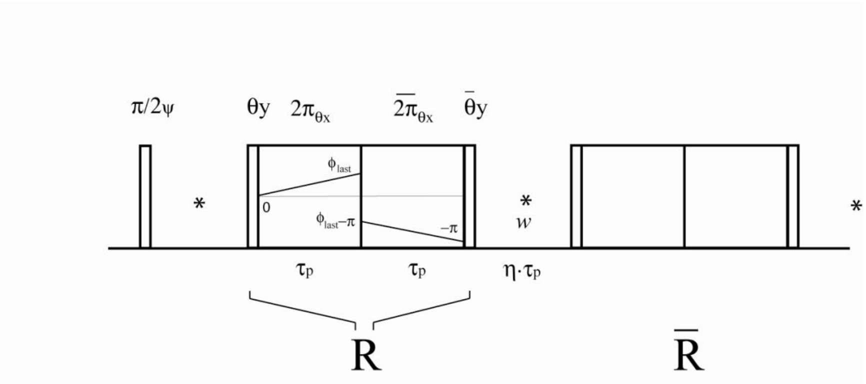
$\pi/2\psi$
θy
$2\pi_{\theta x}$
$\overline{2\pi}_{\theta x}$
$\bar{\theta} y$
*
ϕ_{last}
0
$\phi_{last}-\pi$
$-\pi$
*
w
*
τ_p
τ_p
$\eta\cdot\tau_p$
R
$\overline{R}$

Figure 1

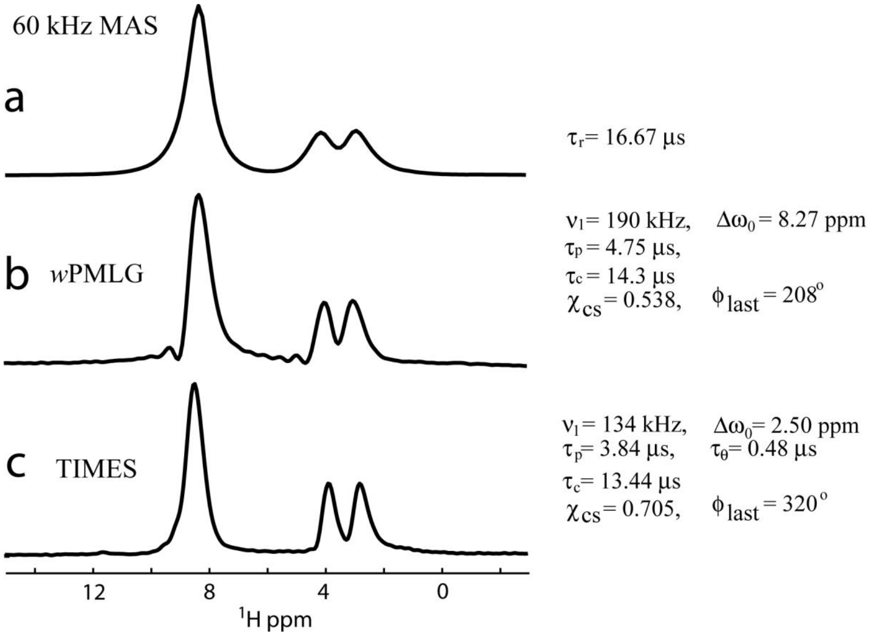
60 kHz MAS
a
τr= 16.67 µs
b wPMLG
ν1= 190 kHz, Δω0= 8.27 ppm
τp = 4.75 µs,
τc = 14.3 µs
χcs= 0.538, ϕlast = 208°
c TIMES
ν1= 134 kHz, Δω0= 2.50 ppm
τp= 3.84 µs, τθ= 0.48 µs
τc= 13.44 µs
χcs= 0.705, ϕlast = 320°
12
8
4
0
1H ppm

Figure 2

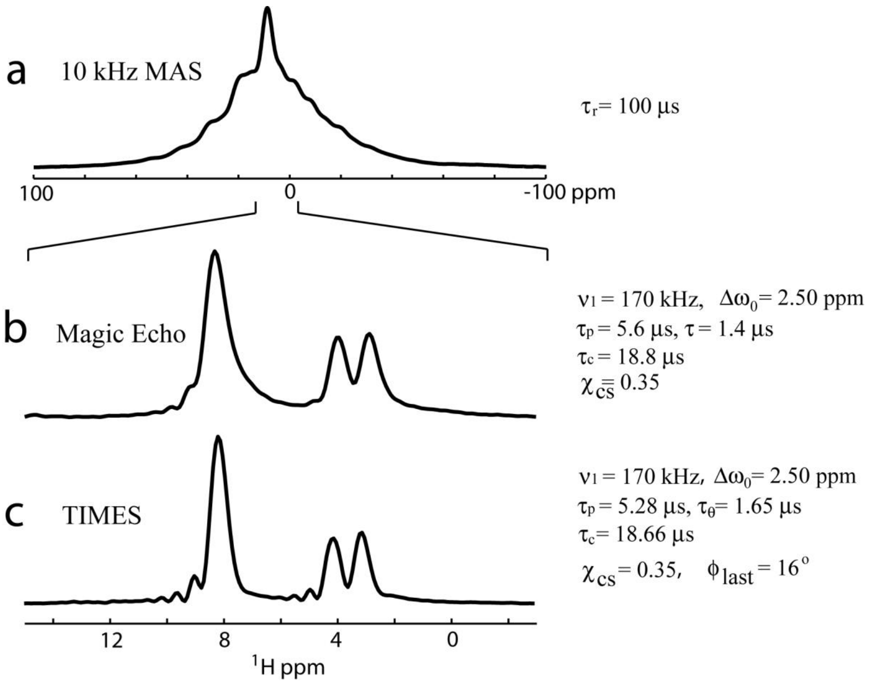
a
10 kHz MAS
τ_r= 100 μs
100
0
-100 ppm
b
Magic Echo
ν1 = 170 kHz, Δω_0= 2.50 ppm
τp = 5.6 μs, τ = 1.4 μs
τc = 18.8 μs
χ_cs= 0.35
c
TIMES
ν1 = 170 kHz, Δω_0= 2.50 ppm
τp = 5.28 μs, τ_θ= 1.65 μs
τc= 18.66 μs
χ_cs= 0.35, ϕ_last = 16°
12
8
4
0
1H ppm

Figure 3

Chapitre 5

Projets de recherche

Mes projets de recherche actuels comprennent, à la fois, le développement de la polarisation nucléaire dynamique à haut champ pour les matériaux et l'enregistrement rapide d'expériences multidimensionnelles en RMN du solide. Ces deux projets sont complémentaires. L'objectif du premier est d'accroître la sensibilité de la RMN, tandis que le deuxième vise à réduire la durée des expériences multidimensionnelles, dès lors que la sensibilité est suffisante. Le projet sur la DNP des matériaux a été classé premier, en 2010, sur la liste complémentaire de l'appel à projet ANR Jeunes Chercheuses et Jeunes Chercheurs.

5.1 Polarisation nucléaire dynamique des matériaux

Si la RMN des solides est actuellement l'une des rares techniques permettant de sonder la structure et la dynamique, à l'échelle atomique, au sein des matériaux non-cristallins (verres, polymères, catalyseurs, protéines membranaires, matériaux de batterie...), elle souffre d'un manque cruel de sensibilité dû à la faiblesse des moments magnétiques nucléaires. Ainsi, même à haut champ, l'interaction Zeeman conduit à des faibles différences d'énergie entre les niveaux de spin nucléaire, ne dépassant pas la gamme des radiofréquences. De ce fait, la polarisation nucléaire à l'équilibre est faible, elle aussi, et difficile à détecter, notamment pour les noyaux de faible rapport gyromagnétique (^{17}O, ^{25}Mg, ^{67}Zn, ^{33}S, ^{95}Mo...).

Cette sensibilité limitée empêche l'étude de problèmes de chimie des matériaux importants, tels que :

- la détermination de la structure et de la dynamique aux interfaces dans les catalyseurs, les matériaux poreux, les électrodes ou les nanomatériaux ;
- la détection d'espèces peu abondantes, comme les intermédiaires réaction-

TAB. 5.1 – Comparaison des gains en sensibilité pour différentes techniques RMN.

Technique	Gain en sensibilité[a]
TF[b]	10 à 100
CP[c]	10
Doublement B^0	2,8
cryosonde	4
DNP haut-champ[d]	60

[a] Pour l'azote-15. [b] Transformée de Fourier. [c] Polarisation croisée $^1H \rightarrow ^{15}N$. [d] Résultats expérimentaux obtenus à $9,4$ T et $T = 100$ K avec un système DNP Bruker.

nels en catalyse ou les défauts au sein des matériaux ;
- l'observation de noyaux de faible moment magnétique ou de faible abondance naturelle.

Ainsi, différentes méthodes ont été proposées pour augmenter la sensibilité. Ces méthodes peuvent être classées en deux catégories :

- celles visant à augmenter la sensibilité de la détection (micro-bobine [213], cryosonde [214], SQUID [215, 216], magnétomètre atomique optique [217], RMN par détection optique [218] ou mécanique [219, 220]...) ;
- celles basées sur l'accroissement de la polarisation nucléaire (utilisation de champs magnétiques élevés, expériences à basse température [221], polarisation nucléaire dynamique [42, 222–224], utilisation de ^{129}Xe hyperpolarisé [225] ou d'hydrogène para [226]...).

Certaines de ces techniques ne sont, cependant, pas matures pour une utilisation en chimie structurale ou ne sont applicables que pour un petit nombre de systèmes. Ainsi, la détection mécanique ne permet, pour le moment, de détecter l'aimantation de quelques milliers de spins nucléaires, mais pas d'un spin nucléaire unique [220]. Elle n'offre donc pas une résolution atomique. L'intérêt des SQUID ou d'autres magnétomètres très sensibles n'a été démontré qu'à bas champ magnétique, ce qui limite la résolution spectrale [215–217]. La RMN par détection optique a été utilisée essentiellement pour les semi-conducteurs ou les éléments lourds, tels que ^{141}Pr [218]. D'autres méthodes visant à augmenter la sensibilité ont l'avantage d'être plus générales, mais elles permettent d'espérer des gains en sensibilité limités (voir tableau 5.1). Ainsi, le doublement du champ magnétique B^0 ne conduit qu'à un gain de sensibilité d'un facteur 2,8. En outre, actuellement, la technologie des aimants utilisant des supraconducteurs refroidis à l'hélium liquide atteint ses limites. Le gain en sensibilité offert par les cryosondes est, lui aussi, limité en RMN des solides (de l'ordre de 4) [214]. Les microbobines permettent d'augmenter la sensibilité par spin, mais pas la sensibilité totale. Elle sont surtout utiles pour les échantillons de volume limité.

Dans ce contexte, les méthodes utilisant le ^{129}Xe hyperpolarisé, l'hydrogène para ou la polarisation dynamique nucléaire (DNP) présentent plusieurs avantages. Elles conduisent à des gains de sensibilité élevés et elles sont compatibles avec l'utilisation de haut champ et d'expériences RMN multidimensionnelles. Parmi ces méthodes conduisant à des gains de sensibilité élevés, la DNP est la technique la plus générale. En effet, l'utilisation du ^{129}Xe hyperpolarisé ou d'hydrogène para est limitée par le faible temps de vie de ces espèces hyperpolarisées, ce qui nécessite de préparer l'échantillon juste avant l'expérience RMN [225,226]. En outre, le transfert de polarisation des noyaux hyperpolarisés vers les autres isotopes est difficile dans le cas du ^{129}Xe. Dans le cas de l'hydrogène para, ce transfert nécessite une réaction chimique, qui modifie le système étudié. La DNP a l'avantage de permettre la répétition d'expériences RMN à plusieurs mois d'intervalle, puisque la source de la polarisation nucléaire est la polarisation électronique, à l'équilibre, de radicaux chimiquement stables. Si la présence d'espèces radicalaires est nécessaire, la DNP peut être réalisée pour des concentrations en radical relativement faibles (5 à 40 mmol.ℓ^{-1}) et le radical ne doit pas être couplé par l'interaction dipolaire aux noyaux observés. Ainsi, nous observons, en général, en DNP, des régions de l'échantillon, dont la structure chimique n'est pas modifiée par la présence d'un radical.

La DNP est basée sur le transfert de polarisation d'un électron, non apparié, vers les noyaux de l'échantillon. Ce transfert comprend en réalité deux étapes. Dans un premier temps, la saturation d'une transition RPE transfère une partie de la polarisation électronique vers les noyaux environnants, couplés aux électrons par l'interaction hyperfine. Dans un deuxième temps, la polarisation nucléaire élevée autour des centres paramagnétiques s'étend à l'ensemble de l'échantillon par diffusion de spin. Bien entendu, dans la pratique, ces deux étapes sont réalisées simultanément. Le phénomène de DNP a été démontré, tout d'abord, dans les années 1950-1960, pour des échantillons statiques à bas champ magnétique [222], puis dans les années 1980, pour des échantillons dans les conditions MAS toujours à faible champ ($<$ 1,5 T) [227]. À cette époque, l'absence de sources micro-ondes de puissance et de fréquences élevées empêchait la réalisation d'expériences DNP dans des champs magnétiques élevés. Le développement de sources micro-ondes à haute-fréquence, telles que les gyrotrons, et d'agents paramagnétiques adaptés, tels que les biradicaux nitroxides, a ouvert la voie à la DNP à haut champ (jusqu'à 14,1 T) dans les conditions MAS [42, 223, 224, 228]. Ces avancées ont permis l'observation d'intermédaires réactionnels de la bactériorhodopsine, ce qui aurait été pratiquement impossible sans l'utilisation de la DNP [229].

Cependant, en 2009, la DNP/RMN haut-champ n'avait été appliquée que pour des noyaux ^{13}C et ^{15}N de molécules organiques ou biologiques au sein de solutions gelées. Le fait que les échantillons soient liquides à température ambiante permettait une incorporation aisée des agents paramagnétiques. Dans ce contexte,

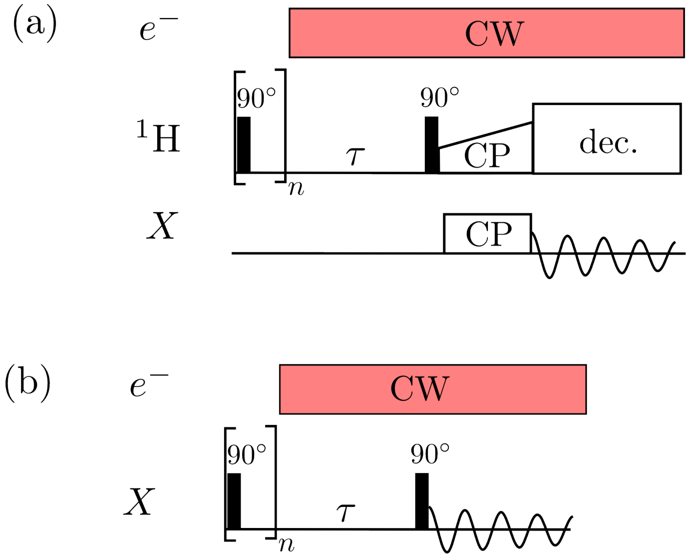

Fig. 5.1 – Séquences d'impulsions rf utilisées pour la polarisation des noyaux X par (a) DNP indirecte via les protons et (b) par DNP directe. Les deux séquences débutent par une période de présaturation, qui détruit l'aimantation nucléaire existante. Cette présaturation est suivie par un délai de polarisation, τ, durant lequel les transitions RPE des électrons (e^-) sont saturées, ce qui permet de polariser par DNP (a) les protons ou (b) directement l'isotope X. Dans le cas de la DNP indirecte, l'aimantation des protons est transférée vers les noyaux X par une étape de CP.

nous nous sommes proposés de tester les possibilités de la DNP/RMN haut-champ pour des matériaux solides à température ambiante et pour d'autres isotopes de spins $I = 1/2$ (^{29}Si…) ou $I > 1/2$ (^{27}Al, ^{95}Mo…). Pour pouvoir réaliser ce projet, nous avons initié une collaboration avec la société Bruker, qui a développé un instrument DNP/RMN haut-champ (9.4 T) dédié aux solides, et nous avons déposé une ANR Jeunes Chercheurs en janvier 2010. Ce projet vise notamment à répondre aux questions suivantes :

- Quels sont les agents paramagnétiques (endogènes, exogènes) utilisables pour la DNP/RMN des matériaux ?
- Pour quels types d'échantillon cette méthodologie peut-elle être employée et quelles sont les meilleurs procédés pour incorporer les agents paramagnétiques au sein de l'échantillon (incorporation du radical lors d'une synthèse sol-gel, imprégnation d'un matériaux poreux, dispersion de nanoparticules au sein d'une solution…) ?
- Pour quels isotopes, la DNP/RMN peut-elle être employée et quelles sont les méthodes de polarisation les plus adaptées, directes ou indirectes via les ^{1}H (voir figure 5.1) ?

Pour tester la faisabilité du projet, nous avons commencé par étudier un système modèle, des verres poreux utilisés pour la photonique. Ces verres poreux sont préparés par procédé sol-gel reposant sur les réactions d'hydrolyse et de condensation du tétraméthoxysilane (TMOS). Le volume des pores est de l'ordre de 0,7 $cm^3.g^{-1}$. Cet échantillon solide ne contient pas de radicaux endogènes. Cependant, comme il est poreux, des radicaux organiques, tels que le TOTAPOL [230], peuvent être facilement introduits au sein de l'échantillon par imprégnation (voir figures 5.2a et b). En utilisant ce procédé, nous avons pu appliquer la DNP à ces échantillons et augmenter le signal RMN ^{29}Si de ces solides d'un facteur 30, sans dégrader la résolution spectrale (voir figure 5.2c). La dépendance du gain en sensibilité avec le champ B^0 (voir figure 5.2d) est caractéristique d'un processus DNP utilisant l'aimantation des radicaux nitroxides [231]. Pour cet échantillon, des gains de sensibilité plus élevés ont été obtenus par DNP directe que par DNP indirecte via les protons. La DNP directe ^{29}Si nécessite des temps de polarisation longs (voir figure 5.2e) en raison de la faible diffusion de spin ^{29}Si–^{29}Si.

Nous avons aussi pu appliquer la DNP/RMN ^{29}Si à haut champ pour des catalyseurs hétérogènes, les zéolites H_nZSM-5, qui sont utilisées pour la conversion méthanol-carburant [232]. Ceci nous a permis d'explorer l'utilisation d'autres radicaux organiques que le TOTAPOL et d'autres méthodes d'incorporation des radicaux que l'imprégnation. En effet, les zéolites ont la propriété étonnante d'être capable d'ioniser les molécules qui s'adsorbent à la surface [233]. Tirant profit de cette spécificité, des molécules de *trans*-stilbène ont été adsorbées par sublimation au sein de la zéolite, où elles s'ionisent spontanément. Il a ensuite été possible par DNP/RMN de transférer l'aimantation de ces radicaux organiques vers les noyaux ^{29}Si de l'échantillon. Le gain en sensibilité dû à la DNP est de 13 (voir figure 5.3c). Ce gain est plus faible que celui obtenu pour les verres poreux contenant le biradical TOTAPOL. Ceci s'explique par le fait que le mécanisme DNP d'effet croisé [234] est plus efficace pour les biradicaux que les monoradicaux. La dépendance du gain en sensibilité avec le champ B^0 (voir figure 5.3d) confirme que ce gain résulte d'un phénomène de DNP. En outre, là encore, la méthode DNP directe s'est révélée plus efficace que la DNP via les protons.

Nous avons obtenu les premiers résultats significatifs DNP ^{29}Si sur des échantillons solides à haut champ en mai 2010. Ils ont permis de démontrer, tout d'abord, l'intérêt de la DNP/RMN pour l'étude des échantillons poreux. Il est certain que cette méthodologie pourra être transposée dans le cas d'autres échantillons poreux, tels que les catalyseurs ou les matériaux utilisés pour le stockage de gaz. Peu de temps après, des spectres DNP/RMN ^{13}C et ^{29}Si pour des systèmes hybrides nanoporeux ont été présenté à la conférence Euromar en juillet 2010 en utilisant la méthode DNP indirecte.

Ces résultats démontrent aussi la possibilité d'augmenter le signal RMN ^{29}Si dans les conditions MAS en utilisant la DNP. Jusqu'ici, la DNP/RMN ^{29}Si n'avait été démontrée que pour des semi-conducteurs, immobiles et plongés dans un faible

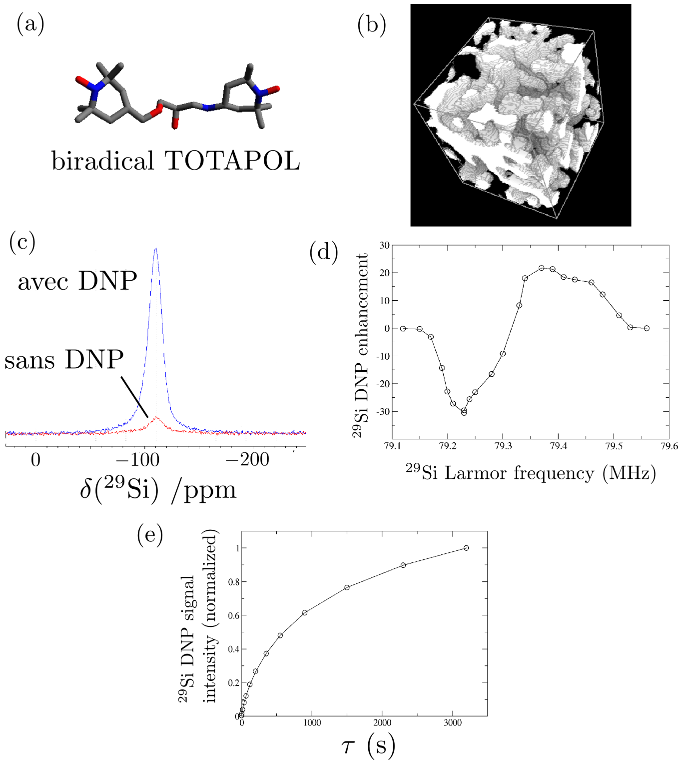

FIG. 5.2 – (a) Structure du biradical TOTAPOL. (b) Verres poreux obtenus par procédé sol-gel. Ces verres poreux peuvent être dopés par des ions lanthanides ou des nanoparticules semi-conductrices, afin de contrôler leurs propriétés optiques. Dans notre cas, le radical TOTAPOL est introduit dans les canaux d'un verre poreux par imprégnation. La solution utilisée pour l'imprégnation est une solution de TOTAPOL de concentration 20 mmol.ℓ^{-1} dans un mélange [$^2H_6$]-DMSO/^2H_2O et H_2O. (c) Spectres RMN MAS ^{29}Si du verre poreux imprégnés à 9,4 T avec et sans irradiation micro-onde. La fréquence MAS est de 10 kHz, la température de l'échantillon 100 K et le délai entre deux acquisitions successives est de 240 s. La polarisation des noyaux ^{29}Si est créée par DNP directe (voir figure 5.1b). (d) Dépendance du gain en sensibilité dû à la DNP avec le champ magnétique. Le champ de l'aimant utilisé pour la RMN est balayé, alors que la fréquence des micro-ondes délivrées par le gyrotron est fixe. En dehors du champ, les autres conditions expérimentales sont identiques à celles utilisées pour enregistrer les spectres de la figure (c). (e) Courbe de création de la polarisation ^{29}Si en fonction du délai τ. Les autres conditions expérimentales sont identiques à celles utilisées pour enregistrer les spectres de la figure (c).

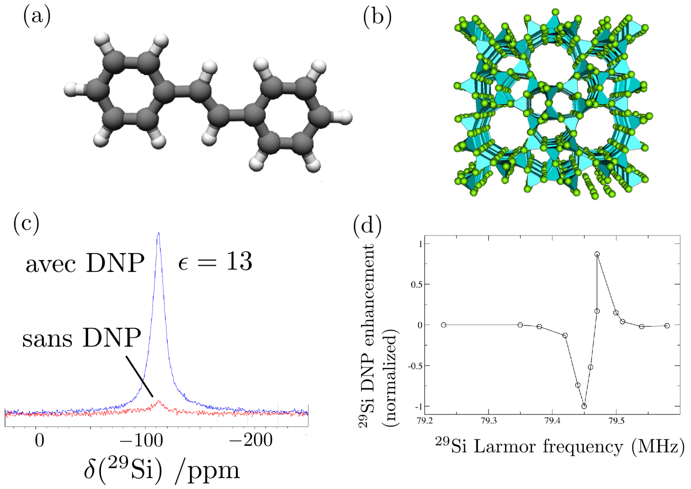

FIG. 5.3 – (a) Structure du radical *trans*-stilbène (*E*-1,2-diphenylethene). Cette molécule combine une faible énergie d'ionisation et des dimensions appropriées pour entrer dans les canaux contenant 10 atomes d'oxygène des zéolites H_nZSM-5. (b) Structure de la zéolite H_nZSM-5. Des études RPE ont permis de montrer que le cation *trans*-stilbène s'ionise les canaux des zéolites H_nZSM-5 [233]. (c) Spectres RMN MAS ^{29}Si de imprégnés à 9,4 T avec et sans irradiation micro-onde. L'accroissement du signal dû à la DNP est de 13. La fréquence MAS est de 10 kHz, la température de l'échantillon 100 K et le délai entre deux acquisitions successives est de 20 s. La polarisation des noyaux ^{29}Si est créée par DNP directe (voir figure 5.1). (d) Dépendance du gain en sensibilité dû à la DNP avec le champ magnétique. Le champ de l'aimant utilisé pour la RMN est balayé, alors que la fréquence des micro-ondes délivrées par le gyrotron est fixe. En dehors du champ, les autres conditions expérimentales sont identiques à celles utilisées pour enregistrer les spectres de la figure (c).

champ magnétique [235–240]. Enfin, les résultats obtenus avec le radical *trans*-stilbène montre que la DNP à haut champ ne nécessite pas forcément l'utilisation de radicaux nitroxides, mais que d'autres radicaux organiques peuvent être employés.

Concernant la DNP, nos projets de recherche visent à mieux comprendre les gains en sensibilité ^{29}Si obtenus par DNP directe. Il serait, en particulier, intéressant d'estimer les temps de relaxation $T_1(^{29}\text{Si})$ à 100 K et de les comparer au temps de diffusion de spin ^{29}Si–^{29}Si. De façon plus quantitative, des simulations de la dynamique des spins pour un grand nombre de noyaux pourront être réalisées [155]. Une autre particularité des systèmes poreux étudiés est que l'avantage de la méthode directe en terme de sensibilité est beaucoup plus marqué que pour les solutions gelées de molécules organiques [241]. Cette spécificité peut être due à la faible concentration en protons ou à la localisation de ces noyaux le long des canaux du verre ou de la zéolite. Ceci pourra être testé en faisant varier la concentration en protons et en étudiant des échantillons avec différentes tailles de canaux.

La concentration en radical est aussi un paramètre sur lequel il est important de jouer afin d'obtenir le meilleur gain en sensibilité possible pour ces systèmes. En outre, les zéolites sont des systèmes de choix pour tester différents radicaux organiques, puisqu'elles favorisent l'autoionisation et la formation spontanée d'ions radicalaires. Remarquons en particulier que pour la DNP ^{29}Si directe, les radicaux nitroxides ne sont pas les radicaux les plus adaptés. En effet, compte tenue de la faible fréquence de Larmor de cet isotope, il serait préférable d'utiliser des biradicaux présentant des spectres RPE étroits [242].

En dépit de ces avancées récentes, de nombreuses questions restent posées. L'une d'elle est la possibilité d'appliquer la DNP pour les noyaux quadripolaires, qui représentent environ 75 % des noyaux magnétiquement actifs. Récemment, il a été montré que la DNP indirecte pouvait être utilisée pour augmenter la sensibilité d'expériences D-HETCOR ^{13}C–^{14}N [243]. La DNP directe a aussi pu être appliquée pour les noyaux ^{2}H, qui subissent de faibles interactions quadripolaires (de l'ordre de 170 kHz) [242]. Il serait, bien sûr, souhaitable de pouvoir appliquer la DNP pour des noyaux quadripolaires de spin demi-entier, tels que ^{27}Al, ^{17}O, ^{95}Mo... Pour ces noyaux, la méthode la plus simple consiste à combiner la DNP indirecte et les séquences HMQC permettant la détection indirecte via les noyaux de spin 1/2, comme pour les expériences DNP/RMN ^{14}N [243]. Cependant, les matériaux inorganiques ne contiennent pas tous des protons. Une alternative serait, dans ce cas, d'utiliser la DNP directe pour les noyaux quadripolaires de spin demi-entier. La diffusion de spin entre noyaux quadripolaires, tels que ^{23}Na, ^{27}Al et ^{11}B, existe et a été utilisée pour établir des corrélations homonucléaires [146,149]. Elle pourrait donc être mise à profit en DNP pour transférer la polarisation nucléaire au sein de l'échantillon. Une des questions est de savoir quel gain en sensibilité, il est possible d'atteindre par cette méthode. L'efficacité de la DNP directe pour les noyaux quadripolaires peut notamment être limitée par la relaxation rapide de ces isotopes. Il est donc important d'estimer les vitesses de diffusion de spin et de relaxation longitudinale pour les noyaux quadripolaires à basse température.

Une deuxième phase du projet consistera à montrer que le gain en sensibilité offert par la DNP permet d'obtenir des informations structurales et dynamiques nouvelles sur les matériaux. Ce gain en sensibilité peut, par exemple, permettre d'observer les sites actifs faiblement concentrés au sein des catalyseurs hétérogènes. L'usage de la DNP est d'autant plus nécessaire que les sites actifs comprennent généralement des isotopes de faible réceptivité RMN, tels que ^{95}Mo, difficiles à observer par les méthodes RMN existantes. Nous envisageons donc d'utiliser la DNP pour des catalyseurs hétérogènes réels. Une autre application de la DNP est l'observation par RMN des intermédiaires réactionnels et des conformères. En effet, pour augmenter les temps de relaxation T_1 nucléaires et électroniques, les expériences DNP sont réalisées à environ 100 K. Cette basse température permet de geler la cinétique de nombreuses réactions chimiques ou de changements de conformations. Ainsi, la DNP/RMN pourrait permettre de préciser les mécanismes réactionnels lors des procédés catalytiques.

Si ces premiers résultats sur la DNP/RMN des matériaux sont prometteurs, il est certain que le domaine d'application de cette méthode s'élargira au rythme des innovations techniques. En particulier, à l'heure actuelle, la fréquence MAS maximale utilisable à 100 K est inférieure à 15 kHz. L'utilisation de fréquences MAS plus élevées est notamment nécessaire pour l'enregistrement de spectres ^{1}H. Une solution pour surmonter cette limitation est d'utiliser un gaz moins visqueux, comme l'hélium, pour mettre en rotation le rotor [221]. L'utilisation d'hélium peut permettre, en outre, de diminuer la température des expériences DNP/RMN et ainsi d'accroître l'efficacité de la DNP. Une deuxième limitation est que l'efficacité des méthodes DNP à ondes continues diminue avec le champ magnétique. C'est une des raisons pour lesquelles les expériences DNP/RMN ont été réalisées, jusqu'à présent, à des champs $B^0 \leq 9,4$ T. Une alternative intéressante consiste à utiliser la DNP par impulsion et à transférer, de façon cohérente, la polarisation des électrons vers les noyaux voisins [244].

5.2 Enregistrer plus rapidement les expériences RMN multidimensionnelles

Un autre projet, en cours, vise à diminuer les temps d'acquisition pour les expériences multidimensionnelles en RMN des solides. Nous nous proposons, pour cela, d'appliquer de nouvelles méthodes d'acquisition et de traitement des données. Rappelons que le temps d'acquisition des spectres RMN multidimensionnels dépend notamment de deux contraintes indépendantes : la résolution et la sensibilité. Ici, la sensibilité est entendue dans son acception statistique et désigne la capacité à distinguer un signal du bruit. Habituellement, en RMN par transformée de Fourier, le terme de sensibilité est employé pour désigner la sensibilité temporelle, définie comme le rapport signal sur bruit divisé par la racine carrée du temps d'expérience. Dans de nombreux cas, la sensibilité n'est pas le facteur limitant et les signaux recherchés sont déjà observables en enregistrant uniquement un faible nombre de points. Cette constatation est d'autant plus vraie qu'il existe aujourd'hui des méthodes (détection indirecte) et des appareillages RMN (DNP, aimants haut-champ) sensibles. Dans cette situation, la méthode standard, combinant échantillonnage sur un maillage cartésien et TF multidimensionnelle, ne conduit pas à un temps d'expérience minimal. En effet, la majorité du temps d'expérience ne sert qu'à échantillonner tous les points du maillage dans les différentes dimensions spectrales, et ce, afin d'obtenir une résolution spectrale suffisante, sans violer la condition de Nyquist-Shannon. Cette dernière condition est particulièrement contraignante à haut champ, puisque la largeur spectrale est proportionnelle au champ B^0. Ainsi, pour maintenir une résolution constante, le nombre de points collectés dans chaque dimension spectrale doit être proportionnel à la valeur de B^0 et la durée des expériences croît linéairement avec la valeur du champ. Ceci rend difficile l'enregistrement à haut champ de spectres multidimensionnels pour les noyaux relaxant lentement (^{29}Si. . .).

Pour diminuer le temps d'expérience, une solution consiste à échantillonner moins de points que nécessaire pour appliquer la transformée de Fourier. Ce type d'échantillonnage est qualifié de lâche (*sparse* en anglais). Différents types d'échantillonnage lâche ont été proposés :

- des échantillonnages uniformes à la fréquence de Nyquist tronqués ou retardés,
- des sous-échantillonnages uniformes à une fréquence inférieure à la fréquence de Nyquist,
- des échantillonnages non-uniformes de type exponentiel [245–247] ou radial [248, 249].

La première méthode est la plus simple et la plus couramment utilisée. Cependant, cet échantillonnage conduit forcément à une résolution spectrale plus faible que les autres échantillonnages, puisque deux sinusoïdes oscillant avec des fréquences proches sont difficiles à distinguer aux temps courts. Lorsque la résolution est un facteur limitant, il est donc préférable d'utiliser un échantillonnage non-uniforme.

Si l'utilisation d'un échantillonnage lâche permet de diminuer le temps d'expérience, les jeux de données obtenus sont difficiles à analyser par TF. Par exemple, le traitement par TF d'un signal RMN tronqué convolue les pics par une fonction sinus cardinal. Certes, une solution pour minimiser ces artefacts de troncature consiste à utiliser une fenêtre d'apodisation, mais cette méthode conduit toujours à une perte de résolution. L'utilisation d'échantillonnage lâche a ainsi stimulé le développement d'une multitude de méthodes de traitement des données RMN autres que la TF. Citons, sans être exhaustif, la reconstruction par maximisation d'entropie [44, 45], la prédiction linéaire [250, 251], les méthodes d'ajustement à un modèle, telles que ANAFOR [252,253], les méthodes de transformée de Fourier non uniforme [248, 249, 254], la FDM [255, 256], les méthodes de dimensionnalités réduites, telles que la transformée de Fourier utilisant des matrices G (GFT) [257] ou les techniques de projection-reconstruction [258], la décomposition multidimensionnelle [46, 47] et la covariance [48, 49]. Nous n'avons pas la place ici de détailler le principe de ces différentes méthodes de même que leurs avantages et leurs inconvénients. Nous pouvons néanmoins remarquer que la plupart de ces méthodes ont été introduites et testées en RMN des liquides. Il est important d'évaluer leurs performances dans le cas de la RMN des solides.

Une méthode de traitement idéale pour la RMN des solides doit remplir le cahier des charges suivant :

i. Elle doit conduire à une résolution élevée, si possible comparable à celle obtenue par un échantillonnage cartésien complet ;
ii. Elle doit être compatible avec l'échantillonnage le plus lâche possible de façon à minimiser le temps d'acquisition ;
iii. Elle doit être applicable pour des expériences RMN de dimension supérieure ou égale à 2, puisqu'en RMN des solides, le temps d'acquisition de certaines expériences 2D peut être rédhibitoire ;
iv. Son utilisation doit être la plus générale possible, c'est-à-dire qu'elle doit, par exemple, pouvoir être employée pour des expériences HOMCOR 1Q–1Q, 2Q–1Q ou HETCOR ;
v. Elle ne doit pas conduire à une dégradation de la sensibilité par rapport au jeu de données dans le domaine temporelle, c'est-à-dire qu'elle doit être applicable même lorsque le rapport signal sur bruit est faible dans le domaine temporel ;
vi. Elle doit être quantitative ;
vii. Le nombre d'artefacts et de faux positifs doit être minimisé.

Au vu de ces spécifications, nous avons écarté les techniques GFT [257], de projection-reconstruction [258], de TF avec échantillonnage radial [248, 249], qui ne sont pertinentes que pour des expériences de dimensions supérieures ou égales à 3. Les méthodes de prédiction linéaire et FDM sont, elles, utilisables pour des formes de raies lorentziennes, ce qui limite leur emploi en RMN des solides. La reconstruction par maximisation d'entropie est une méthode générale, mais elle modifie l'intensité relative des pics. La quantification nécessite alors une calibration empirique, ce qui rend plus complexe l'analyse du spectre [259]. Les méthodes, telles que ANAFOR, ne sont applicables que lorsque le nombre de signaux est limité. En outre, elles nécessitent d'exhiber un minimum global lors de l'ajustement des données. Dans ce contexte, la covariance apparaît comme une méthode pratique pour le traitement des expériences RMN sur des solides. En effet, elle ne fait pas d'hypothèse sur la forme de raies et est applicable pour les expériences RMN 2D. L'utilisation de méthode de régularisation permet de rendre cette méthode quantitative [260]. L'intérêt de la covariance a d'ores et déjà été démontré en RMN des solides [261–263]. Elle permet généralement de réduire d'un facteur trois le temps d'expérience.

Cependant, jusqu'à présent, la covariance n'avait été appliquée que dans le cas d'échantillonnage cartésien uniforme [264]. Cette limitation résultait notamment de la procédure de régularisation utilisée, qui n'était applicable que dans le domaine fréquenciel. Pour remedier à ce problème, nous avons introduit une méthode de régularisation dans le domaine temporel. Grâce à cette méthode, il a été possible de traiter des données par covariance obtenues par échantillonnage non uniforme. Ceci est illustré, dans la figure 5.4, par le traitement d'expériences Q-COSY avec filtre z. L'utilisation de l'échantillonnage non uniforme permet de réduire le nombre d'artefacts observés pour les spectres traités par covariance (comparer les figures 5.4 h et k). Il est ainsi possible de réduire d'un facteur 2 le temps d'expérience par rapport à la covariance avec échantillonnage uniforme aux temps courts. Globalement, la covariance avec échantillonnage non uniforme permet de réduire d'un facteur 6 le temps d'expérience par rapport à la méthode standard (échantillonnage uniforme et transformée de Fourier 2D).

En outre, l'échantillonnage non uniforme exponentiel peut permettre d'accroître la sensibilité temporelle, puisque le signal RMN est échantillonné plus fréquemment aux temps courts, où le signal est important, qu'aux temps longs, où il est faible [247]. Cependant, comme la covariance n'est pas une méthode linéaire, le rapport signal sur bruit n'est pas un bon indicateur de la sensibilité [267]. Des travaux complémentaires seront donc nécessaires pour préciser le gain en sensibilité dû à la covariance avec échantillonnage exponentiel. Il est aussi important de déterminer la plage dynamique et le rapport signal sur bruit minimal pour lesquels la covariance est utilisable.

Une limitation du traitement par covariance est que le spectre 2D obtenu est symétrique. Ainsi, le traitement par covariance d'expériences 2D HOMCOR 2Q–1Q engendre des spectres HOMCOR 1Q–1Q comportant des signaux diagonaux, n'apportant aucune information sur les connectivités ou les proximités interatomiques [268]. Ceci est gênant en RMN des solides, où il est important de pouvoir observer des corrélations entre des sites ayant des fréquences de résonance proches ou identiques.

Pour résoudre ce problème, il est important de trouver des alternatives au traitement par covariance. Nous pouvons tout d'abord remarquer que parmi l'ensemble des points d'un spectre RMN 2D, la majorité d'entre eux est superflue. Ainsi, un spectre 2D décrit par un million de points ne contient au plus que des centaines de signaux, qui peuvent, chacun, être caractérisés par quelques dizaines de points. En d'autres termes, la proportion de points utiles au sein du spectre 2D est généralement inférieur à 1 %. En outre, pour la plupart des expériences RMN 2D, les fréquences de résonance possibles pour les pics en dimension indirecte peuvent être calculées, avant même de réaliser l'expérience 2D, à partir de l'analyse des spectres 1D. Par exemple, pour une expérience 2D HOMCOR 2Q–1Q, les fréquences de résonance en dimension indirecte sont la somme des fréquences de résonance présentes dans le spectre 1D de cet isotope. Cette connaissance préalable permet d'éliminer un grand nombre d'artefacts de troncature et de faciliter l'analyse du spectre. Ceci est illustré par la figure 5.5. En utilisant les méthodes standard d'échantillonnage et de traitement, plus de 5 heures sont nécessaires

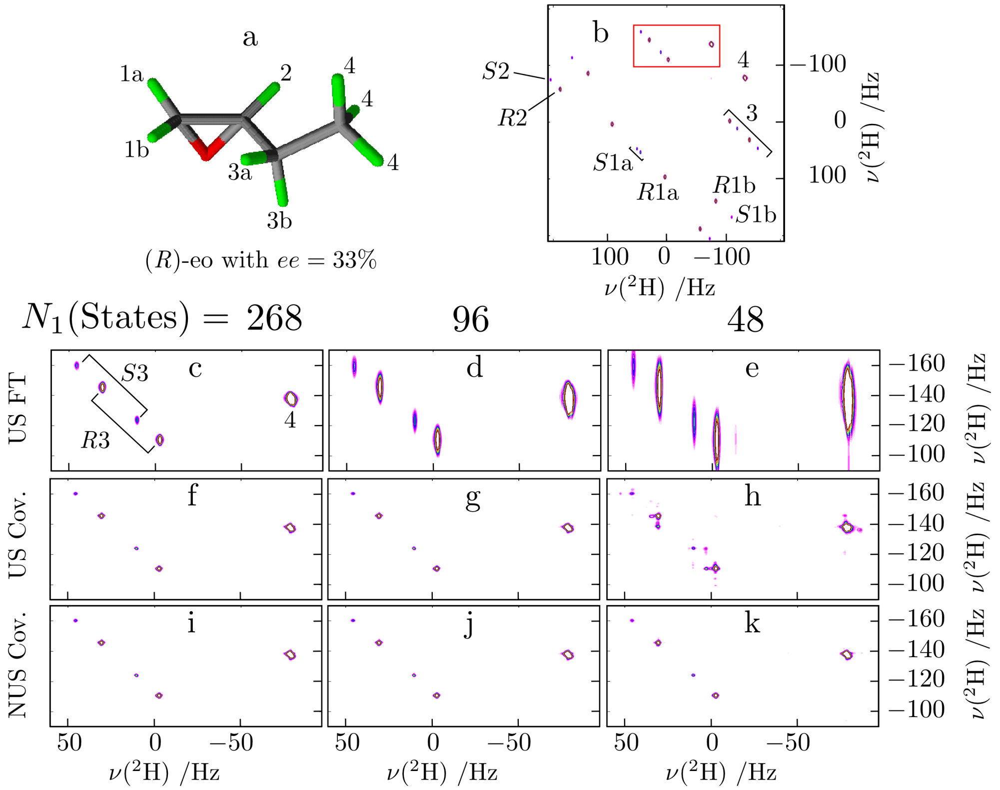

FIG. 5.4 – (a) Structure du (R)-éthyloxirane (eo) comportant la numérotation des atomes. (b) Spectre 2D Q-COSY avec filtre z ^{2}H en abondance naturelle du eo enrichi en énantiomère R et dissous dans un cristal liquide chiral PBLG/CHCl$_3$. Le spectre a été enregistré avec une cryosonde ^{2}H placée dans un champ de 14.1 T. La température de l'échantillon est régulé à $300{,}0 \pm 0{,}1$ K. Le spectre 2D a été enregistré en mode States [265] avec 64 *scans* en utilisant respectivement 1024 et 268 points complexes dans les dimensions t_2 et t_1. Les apodisations appliquées en dimensions t_2 et t_1 sont respectivement une fenêtre exponentielle de constante 1 Hz et de Hamming. La fenêtre de Hamming permet de minimiser les artefacts de troncature pour une largeur de raie donnée [266]. Le spectre 2D a ensuite été traité en utilisant la transformée de Fourier standard. Un agrandissement de la région encadrée dans le spectre b est présenté dans la figure c. L'attribution des signaux RMN est indiquée sur les sous-figures b et c. (c-k) Région du spectre Q-COSY obtenu en utilisant différents échantillonnages et différentes méthodes de traitement : (c-e) échantillonnage uniforme aux temps courts et TF 2D ; (f-h) échantillonnage uniforme aux temps courts et covariance régularisée ; (j-k) échantillonnage non uniforme exponentiel et covariance régularisée. Les spectres (c,f,i), (d,g,j) et (e,h,k) utilisent respectivement 268, 96 et 48 incréments dans la dimension t_1.

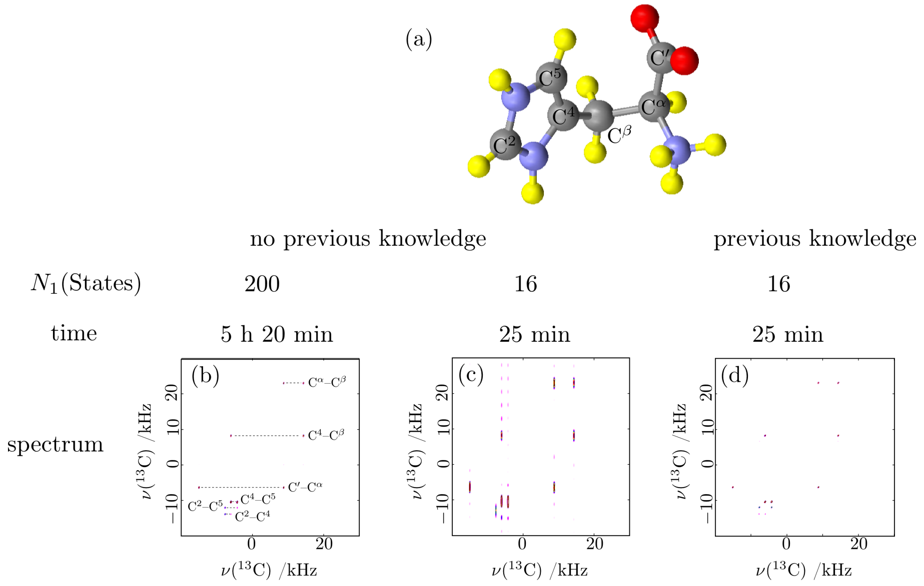

FIG. 5.5 – (a) Structure de [U-^{13}C]-L-histidine·HCl (his) avec la numérotation des atomes selon la nomenclature IUPAC. (b-d) Spectres 2D HOMCOR 2Q–1Q ^{13}C de his enregistrés dans un champ de 18,8 T à $\nu_r = 64$ kHz en utilisant la séquence de recouplage BR2_2^1 sans fenêtre. L'attribution des signaux RMN est donnée sur le spectre b. Les spectres 2D ont été enregistrés en mode States [265] avec 32 *scans* en utilisant 1024 points complexes dans la dimension t_2. Les spectres 2D sont traités en utilisant la double transformée de Fourier. (b) Spectre 2D sans connaissance préalable obtenu avec un échantillonnage uniforme de 200 points complexes, aux temps courts, dans la dimension t_1. (c) Spectre 2D sans connaissance préalable obtenu avec un échantillonnage uniforme de 16 points complexes, aux temps courts, dans la dimension t_1. (d) Spectre 2D avec connaissance préalable dans la dimension F_1 obtenu avec un échantillonnage uniforme de 16 points complexes, aux temps courts, dans la dimension t_1.

pour obtenir un spectre 2D HOMCOR 2Q–1Q ^{13}C dépourvu d'artefacts de troncature (voir figure 5.5b). La connaissance préalable des fréquences en dimension F_1 permet d'obtenir un spectre 2D comparable en seulement 25 min (voir figure 5.5d). Ainsi, la connaissance préalable permet, dans ce cas, une réduction du temps d'expérience d'un facteur 13.

Pour le moment, la connaissance préalable en dimension F_1 n'a été appliquée que pour un échantillonnage uniforme et en combinaison avec la transformée de Fourier. Un de nos objectifs est de tester l'application de cette méthode en combinaison avec des échantillonnages non uniformes et des méthodes de traitement plus adaptées aux échantillonnages lâches.

Conclusion

> Oui, la bêtise consiste à vouloir conclure.
>
> Gustave Flaubert, Lettre du 4 septembre 1850 à Louis Bouilhet

L'écriture de ce document a été l'occasion de faire le point sur mes travaux de recherche et sur certains hasards de la vie. En effet, c'est en voulant faire de la synthèse organique puis de la diffraction des rayons X que je me suis finalement orienté vers la RMN et notamment celles des solides. Mon goût pour les belles formules mathématiques et mes expériences infructeuses dans le domaine de la synthèse d'oligosaccharides m'ont conduit du côté de la méthodologie. Aujourd'hui, la ligne directrice de mes activités de recherche est le développement de nouvelles méthodes RMN dans les solides et la matière molle. J'apprécie particulièrement la possibilité qu'offre la spectroscopie RMN de collaborer avec des chimistes de différents horizons et de pouvoir appliquer cette technique aussi en bien en chimie organique qu'en chimie des matériaux.

Durant ma thèse, je me suis intéressé à l'analyse stéréochimique des molécules organiques dans les milieux orientés chiraux. Nous avons introduit des techniques RMN originales pour l'attribution des spectres ^{2}H en milieu anisotrope. Certaines d'entre elles ont notamment pu être appliquées en abondance naturelle deutérium. Ces nouvelles méthodes ont permis de discriminer plusieurs énantiomères, notamment les énantiomères de chiralité isotopique. La mise au point de techniques d'attribution performantes pour les spectres ^{2}H a permis d'envisager l'étude de molécules chirales et prochirales plus complexes, comprenant un grand nombre de sites deutérium. Ces études nous ont conduit à mieux comprendre l'origine des énantiodiscriminations pour les molécules flexibles de chiralité isotopique et les molécules prochirales. Nous avons aussi montré que la RMN dans les cristaux liquides chiraux permet d'observer des mouvements intramoléculaires non détectables en milieu achiral.

Suite à la transition de phase thèse-post-doctoctorat, mes activités de recherche se sont tournées vers le développement de nouvelles méthodes RMN pour l'étude structurale des poudres solides. Nous avons introduit différentes techniques qui peuvent être classées en trois catégories :

i. Les méthodes de découplage dipolaire visent à améliorer la résolution des spectres ^{1}H de façon à distinguer le maximum d'environnements chimiques différents pour les atomes d'hydrogène. Nous avons en particulier introduit des méthodes compatibles avec les fréquences MAS élevées (jusqu'à 80 kHz) ;

ii. Les méthodes de recouplage dipolaire homo- et hétéro-nucléaire pour une paire de noyaux isolés permettent de mesurer des distances internucléaires précises. La détermination des couplages dipolaires ^{3}H–^{3}H nous a permis, par exemple, de mesurer une distance entre atomes d'hydrogène de 14,4 Å. Des distances internucléaires aussi élevées n'avaient jamais pu être mesurées auparavant. Nous avons aussi introduit des méthodes permettant de mesurer, à des fréquences MAS élevées, la distance entre un noyau quadripolaire et un isotope de spin-1/2.

iii. Les méthodes de recouplage dipolaire homo- et hétéro-nucléaire pour des systèmes comprenant au moins trois noyaux couplés permettent de sonder les proximités internucléaires. Nous avons cherché à rendre ces méthodes compatibles avec les fréquences MAS élevées et robustes à la fois aux différences de déplacement chimique, au CSA et éventuellement à l'interaction quadripolaire. Nous avons notamment proposé des méthodes de recouplage dipolaire entre noyaux ^{27}Al au moins deux fois plus efficaces que les techniques existantes.

Ces différentes méthodes ont été appliquées, pour l'instant, à la fois pour des petites molécules organiques ou des matériaux inorganiques. La méthode de recouplage dipolaire, SPIP, a notamment permis d'attribuer les signaux ^{19}F de composé aluminophosphate, caractérisés par une large gamme de déplacement chimique isotrope. Sa variante, $BR2_2^1$, a permis d'obtenir des informations nouvelles sur les proximités ^{27}Al–^{27}Al dans les zéolites HY et les processus de déalumination de ces composés.

De façon générale, ces développements méthodologiques ont été menés en lien avec les avancées technologiques (cryosonde ^{2}H, sonde haute-vitesse, aimant haut champ), l'objectif étant d'augmenter autant que possible la sensibilité et la résolution de la technique RMN.

Suivant l'épigraphe flaubertienne, la conclusion d'une habilitation à diriger des recherches ne saurait être que provisoire. De ce fait, je me suis efforcé dans ce document de présenter les questions non résolues concernant d'une part, la RMN en milieu anisotrope chiral, et d'autre part, le recouplage et le découplage dipolaire au sein des échantillons solides. J'espère, dans les années à venir, pouvoir apporter des éléments de réponses à ces questions. En outre, j'ai initié récemment deux projets : l'un sur l'enregistrement rapide d'expériences multidimensionnelles en RMN des solides et l'autre sur la DNP/RMN des matériaux à haut champ. L'enregistrement rapide est aujourd'hui nécessaire avec l'utilisation d'aimants haut champ. Elle devrait permettre de réduire de plus d'un facteur trois le temps d'expérience. La DNP/RMN à haut champ devrait, quant à elle, permettre d'augmenter, d'au moins un ordre de grandeur, la sensibilité de la RMN pour des matériaux largement utilisés, tels que les catalyseurs, les solides poreux, les matériaux de batterie, les nanomatériaux, les verres ou les semi-conducteurs. Ce gain en sensibilité devrait permettre d'obtenir des informations structurales et dynamiques nouvelles (observation de noyaux peu sensibles, de défauts, d'intermédiaires réactionnels). Au niveau international, de plus en plus de groupes initient des actions autour de cette thématique.

Bibliographie

[1] I. Canet, J. Courtieu, A. Loewenstein, A. Meddour et J.-M. Péchiné : Enantiomeric analysis in a polypeptide lyotropic liquid crystal by deuterium NMR. *J. Am. Chem. Soc.*, 117:6520–6526, 1995.

[2] E. E. Sackman, S. Meiboom et L. C. Snyder : The nuclear magnetic resonance spectra of enantiomers in optically active liquid crystals. *J. Am. Chem. Soc.*, 90:2183–2184, 1968.

[3] M. Sarfati, J. Courtieu et P. Lesot : First successful enantiomeric discrimination of chiral alkanes using NMR spectroscopy. *Chem. Commun.*, pages 1113–1114, 2000.

[4] P. Lesot, M. Sarfati et J. Courtieu : Natural abundance deuterium NMR spectroscopy in polypeptide liquid crystals as a new and incisive means for the enantiodifferentiation of chiral hydrocarbons. *Chem. Eur. J.*, 9:1724–1745, 2003.

[5] A. Meddour, I. Canet, A. Loewenstein, J.-M. Péchiné et J. Courtieu : Observation of enantiomers, chiral by virtue of isotopic substitution, through deuterium NMR in a polypeptide liquid crystal. *J. Am. Chem. Soc.*, 116:9652–9656, 1994.

[6] P. Lesot, O. Lafon, J. Courtieu et P. Berdagué : Analysis of the ^{13}C NMR spectra of molecules, chiral by isotopic substitution, dissolved in a chiral oriented environment : towards the absolute assignment of the *pro-R*/*pro-S* character of enantiotopic ligands in prochiral molecules. *Chem. Eur. J.*, 10:3741–3746, 2004.

[7] Olivier Lafon, Philippe Lesot, Herbert Zimmermann, Raphy Poupko et Zeev Luz : Chiral discrimination in the ^{13}C and ^{2}H NMR of the crown and saddle isomers of nonamethoxy-cyclotriveratrylene in chiral liquid-crystalline solutions. *J. Phys. Chem. B*, 111(32):9453–9467, 2007.

[8] Philippe Lesot, Olivier Lafon, Herbert Zimmermann et Zeev Luz : Enantiodiscrimination in deuterium NMR spectra of flexible chiral molecules with average axial symmetry dissolved in chiral liquid crystals : The case of tridioxyethylenetriphenylene. *J. Am. Chem. Soc.*, 130(27):8754–8761, 2008.

[9] Chun-An Fan, Benoît Ferber, Henri B. Kagan, Olivier Lafon et Philippe Lesot : Two aspects of the desymmetrization of selected prochiral aromatic or vinylic dihalides : enantioselective halogen-lithium exchange and prochiral recognition in chiral liquid crystals. *Tetrahedron : Asymmetry*, 19(23):2666 – 2677, 2008.

[10] Christie Aroulanda, Olivier Lafon et Philippe Lesot : Enantiodiscrimination of flexible cyclic solutes using NMR spectroscopy in polypeptide chiral mesophases : Investigation of cis-decalin and THF. *J. Phys. Chem. B*, 113(31):10628–10640, 2009.

[11] O. Lafon, P. Lesot, C.-A. Fan et H. B. Kagan : Analysis of intramolecular dynamics processes and determination of activation parameters in enantiomeric biaryl atropoisomers and prochiral analogous derivatives through deuterium NMR in polypeptide liquid crystals. *Chem. Eur. J.*, 13:3772, 2006.

[12] P. Lesot, O. Lafon, H. B. Kagan et C.-A. Fan : Study of molecular rotational isomerism using deuterium NMR in chiral oriented solvents. *Chem. Commun.*, pages 389–391, 2006.

[13] O. Lafon, P. Lesot, D. Merlet et J. Courtieu : Modified z-gradient filtering as a mean to obtain phased deuterium autocorrelation 2D NMR spectra in oriented solvents. *J. Magn. Reson.*, 171:135–142, 2004.

[14] O. Lafon et P. Lesot : Deuterium 3D NMR experiments for analysing weakly aligned, isotopically enriched solutes. *Chem. Phys. Lett.*, 404:90–94, 2005.

[15] Philippe Lesot et Olivier Lafon : Enantiomeric analysis using natural abundance deuterium 3d NMR spectroscopy in polypeptide chiral oriented media. *Chem. Phys. Lett.*, 458(1-3):219 – 222, 2008.

[16] P. Lesot, M. Sarfati, D. Merlet, B. Ancian, J. W. Emsley et B. A. Timimi : 2D NMR strategy dedicated to the analysis of weakly ordered, fully deuterated enantiomers in chiral liquid crystals. *J. Am. Chem. Soc.*, 125:7689–7695, 2003.

[17] O. Lafon, P. Berdagué et P. Lesot : Use of two-dimensional correlation between ^{2}H quadrupolar splittings and ^{13}C CSA's for assignment of NMR spectra in chiral nematics. *Phys. Chem. Chem. Phys.*, 6:1080–1084, 2004.

[18] H. Villar, F. Guibe, C. Aroulanda et P. Lesot : Investigation of SmI_2 mediated cyclisation process of δ-iodo-α,β-unsaturated esters by deuterium 2D NMR in oriented solvents. *Tetrahedron : Asymmetry*, 13:1465–1475, 2002.

[19] O. LAFON et P. LESOT : Theoretical and experimental investigation of ^{13}C relayed ^{2}H–^{2}H–COSY 2D experiments : application to the analysis of weakly aligned solutes. *J. Magn. Reson.*, 174:254–264, 2005.

[20] Karim Ben ALI, Olivier LAFON, Herbert ZIMMERMANN, Eric GUITTET et Philippe LESOT : Homo- and heteronuclear 2D NMR approaches to analyse a mixture of deuterated unlike/like stereoisomers using weakly ordering chiral liquid crystals. *J. Magn. Reson.*, 187(2):205 – 215, 2007.

[21] B. HU, L. DELEVOYE, O. LAFON, J. TRÉBOSC et J.P. AMOUREUX : Double-quantum NMR spectroscopy of ^{31}P species submitted to very large csas. *J. Magn. Reson.*, 200(2):178 – 188, 2009.

[22] B. HU, Q. WANG, O. LAFON, J. TRÉBOSC, F. DENG et J.P. AMOUREUX : Robust and efficient spin-locked symmetry-based double-quantum homonuclear dipolar recoupling for probing ^{1}H-^{1}H proximity in the solid-state. *J. Magn. Reson.*, 198(1):41 – 48, 2009.

[23] Qiang WANG, Bingwen HU, Franck FAYON, Julien TRÉBOSC, Christophe LEGEIN, Olivier LAFON, Feng DENG et Jean-Paul AMOUREUX : Double-quantum ^{19}F—^{19}F dipolar recoupling at ultra-fast magic angle spinning NMR : application to the assignment of ^{19}F NMR spectra of inorganic fluorides. *Phys. Chem. Chem. Phys.*, 11(44):10391–10395, 2009.

[24] J.P. AMOUREUX, J. TRÉBOSC, L. DELEVOYE, O. LAFON, B. HU et Q. WANG : Correlation nmr spectroscopy involving quadrupolar nuclei. *Solid State Nucl. Magn. Reson.*, 35(1):12 – 18, 2009.

[25] Q. WANG, B. HU, O. LAFON, J. TR ?BOSC, F. DENG et J.P. AMOUREUX : Double-quantum homonuclear NMR correlation spectroscopy of quadrupolar nuclei subjected to magic-angle spinning and high magnetic field. *J. Magn. Reson.*, 200(2):251 – 260, 2009.

[26] Qiang WANG, Bingwen HU, Olivier LAFON, Julien TRÉBOSC, Feng DENG et Jean-Paul AMOUREUX : Homonuclear dipolar recoupling under ultra-fast magic-angle spinning : Probing ^{19}F–^{19}F proximities by solid-state NMR. *J. Magn. Reson.*, 203(1):113 – 128, 2010.

[27] Alexander K. L. YUEN, Olivier LAFON, Thibault CHARPENTIER, Myriam ROY, Francine BRUNET, Patrick BERTHAULT, Dimitrios SAKELLARIOU, Bruno ROBERT, Sylvie RIMSKY, Florence PILLON, Jean-Christophe CINTRAT et Bernard ROUSSEAU : Measurement of long-range interatomic distances by solid-state tritium-NMR spectroscopy. *J. Am. Chem. Soc.*, 132(6):1734–1735, 2010.

[28] Jean-Paul AMOUREUX, Qiang WANG, Bingwen HU, Olivier LAFON, Julien TRÉBOSC et Feng DENG : Rapid analysis of isotopically unmodified amino

acids by high-resolution ^{14}N-edited ^{1}H-–^{13}C correlation NMR spectroscopy. *Chem. Commun.*, (48):6525–6527, 2008.

[29] Olivier Lafon, Qiang Wang, Bingwen Hu, Filipe Vasconcelos, Julien Trébosc, Sylvain Cristol, Feng Deng et Jean-Paul Amoureux : Indirect detection via spin-1/2 nuclei in solid state NMR spectroscopy : Application to the observation of proximities between protons and quadrupolar nuclei. *J. Phys. Chem. A*, 113(46):12864–12878, 2009.

[30] Lei Chen, Qiang Wang, Bingwen Hu, Olivier Lafon, Julien Trébosc, Feng Deng et Jean-Paul Amoureux : Measurement of hetero-nuclear distances using a symmetry-based pulse sequence in solid-state NMR. *Phys. Chem. Chem. Phys.*, In Press, Accepted Manuscript:–, 2010.

[31] Lei Chen, Xingyu Lu, Qiang Wang, Olivier Lafon, Julien Trébosc, Feng Deng et Jean-Paul Amoureux : Distance measurement between a spin-1/2 and a half-integer quadrupolar nuclei by solid-state NMR using exact analytical expressions. *J. Magn. Reson.*, In Press, Accepted Manuscript:–, 2010.

[32] Julien Trébosc, Olivier Lafon, Bingwen Hu et Jean-Paul Amoureux : Indirect high-resolution detection for quadrupolar spin-3/2 nuclei in dipolar hmqc solid-state NMR experiments. *Chem. Phys. Lett.*, 496(1-3):201–207, 2010.

[33] Jean-Paul Amoureux, Bingwen Hu, Julien Trébosc, Qiang Wang, Olivier Lafon et Feng Deng : Homonuclear dipolar decoupling schemes for fast MAS. *Solid State Nucl. Magn. Reson.*, 35(1):19 – 24, 2009.

[34] Olivier Lafon, Qiang Wang, Bingwen Hu, Julien Trebosc, Feng Deng et Jean-Paul Amoureux : Proton-proton homonuclear dipolar decoupling in solid-state NMR using rotor-synchronized z-rotation pulse sequences. *J. Chem. Phys.*, 130(1):014504, 2009.

[35] Z. Gan, P. K. Madhu, J.-P. Amoureux, J. Trébosc et O. Lafon : A tilted magic-echo homonuclear dipolar decoupling scheme for high-resolution proton nuclear magnetic resonance of solids. *Chem. Phys. Lett.*, 2010. soumise.

[36] M. M. Maricq et J. S. Waugh : NMR in rotating solids. *J. Chem. Phys.*, 70:3300–3316, 1979.

[37] E. Brunner, D. Freude, B. C. Gerstein et H. Pfeifer : Residual linewidths of NMR spectra of systems under magic-angle spinning. *J. Magn. Reson.*, 90(1):90–99, octobre 1990.

[38] C. Filip, S. Hafner, I. Schnell, D. E. Demco et H. W. Spiess : Solid-state nuclear magnetic resonance spectra of dipolar-coupled multi-spin systems under fast magic angle spinning. *J. Chem. Phys.*, 110:423–440, 1999.

[39] V. E. Zorin, S. P. Brown et P. Hodgkinson : Origins of linewidth in ^{1}H magic-angle spinning NMR. *J. Chem. Phys.*, 125:144508, 2006.

[40] J. W. Traer, E. Montoneri, A. Samoson, J. Past, T. Tuherm et G. R. Goward : Unraveling the complex hydrogen bonding of a dual-functionality proton conductor using ultrafast magic angle spinning NMR. *Chem. Mater.*, 18:4747–4754, 2006.

[41] J.-P. Amoureux, B. Hu et J. Trébosc : Enhanced-resolution in proton solid-state NMR with very-fast MAS experiments. *J. Magn. Reson.*, 193: 305–307, 2008.

[42] Thorsten Maly, Galia T. Debelouchina, Vikram S. Bajaj, Kan-Nian Hu, Chan-Gyu Joo, Melody L. MakJurkauskas, Jagadishwar R. Sirigiri, Patrick C. A. van der Wel, Judith Herzfeld, Richard J. Temkin et Robert G. Griffin : Dynamic nuclear polarization at high magnetic fields. *J. Chem. Phys.*, 128(5):052211, 2008.

[43] A. B. Barnes, G. De Paëpe, P. C. A. van der Wel, K.-N. Hu, C.-G. Joo, V. S. Bajaj, M. L. Mak-Jurkauskas, J. R. Sirigiri, J. Herzfeld, R. J. Temkin et R. G. Griffin : High-field dynamic nuclear polarization for solid and solution biological NMR. *Applied Magnetic Resonance*, 34(3):237–263, août 2008.

[44] S.J. Wernecke et L.R. D'Addario : Maximum entropy image reconstruction. *IEEE T. Comput.*, 26:351–364, 1977.

[45] Joel F. Martin : The maximum entropy method in NMR. *J. Magn. Reson.*, 65(2):291 – 297, 1985.

[46] Vladislav Yu. Orekhov, Ilghiz Ibraghimov et Martin Billeter : Munin : A new approach to multi-dimensional NMR spectra interpretation. *J. Biomol. NMR*, 20(1):49–60, 2001.

[47] Vladislav Yu. Orekhov, Ilghiz Ibraghimov et Martin Billeter : Optimizing resolution in multidimensional NMR by three-way decomposition. *J. Biomol. NMR*, 27:165–173, 2003.

[48] Charles D. Eads et Isao Noda : Generalized correlation NMR spectroscopy. *J. Am. Chem. Soc.*, 124(6):1111–1118, 2002.

[49] Rafael Bruschweiler et Fengli Zhang : Covariance nuclear magnetic resonance spectroscopy. *J. Chem. Phys.*, 120(11):5253–5260, 2004.

[50] E. Lafontaine, J.-M. Péchiné, J. Courtieu et C. L. Maynes : Visualization of enantiomers in cholesteric solvents through deuterium NMR. *Liq. Cryst.*, 7:293–298, 1990.

[51] I. Canet, J. Løvschall et J. Courtieu : Visualization of enantiomers through deuterium NMR in cholesterics. Optimization of the chiral liquid crystal solvent. *Liq. Cryst.*, 16:405–412, 1994.

[52] E. T. Samulski et A. V. Tobolsky : Properties of poly(γ-benzyl-L-glutamate) films cast in strong magnetic fields. *Macromolecules*, 1:555–557, 1968.

[53] C. Aroulanda, M. Sarfati, J. Courtieu et P. Lesot : Investigation of the enantioselectivity of three polypeptide liquid-crystalline solvents using NMR spectroscopy. *Enantiomer*, 6:281–287, 2001.

[54] L. Arnold, A. Marx, C. Thiele et M. Reggelin : Polyguanidines as chiral orienting media for organic compounds. *Chem. Eur. J.*, 16(34):10342–10346, 2010.

[55] O. Lafon, P. Lesot, , M. Rivard, M. Chavarot, F. Rose-Munch et E. Rose : Enantiomeric analysis of planar chiral (η^6-arene)chromium tricarbonyl complexes using NMR in oriented solvents. *Organometallics*, 24:4021–4028, 2005.

[56] Alain Horeau, Andrée Nouaille et Kurt Mislow : Secondary deuterium isotope effects in asymmetric syntheses and kinetic resolutions. *J. Am. Chem. Soc.*, 87(21):4957–4958, 1965.

[57] H. Pracejus : Bin sterischer isotopeneffekt als ursache einer katalytisch-asymmetrischen synthese. *Tetrahedron Lett.*, 7(32):3809 – 3813, 1966.

[58] Itaru Sato, Daisuke Omiya, Takahiro Saito et Kenso Soai : Highly enantioselective synthesis induced by chiral primary alcohols due to deuterium substitution. *J. Am. Chem. Soc.*, 122(47):11739–11740, 2000.

[59] Tsuneomi Kawasaki, Yukari Matsumura, Takashi Tsutsumi, Kenta Suzuki, Masateru Ito et Kenso Soai : Asymmetric Autocatalysis Triggered by Carbon Isotope ($^{13}C/^{12}C$) Chirality. *Science*, 324(5926):492–495, 2009.

[60] D. Arigoni et E. L. Eliel : *Chirality Due to the Presence of Hydrogen Isotopes at Noncyclic Positions.* Top. Stereochem. John Wiley & Sons, Inc., 1969.

[61] David O'Hagan, Rebecca J. M. Goss, Abdelkrim Meddour et Jacques Courtieu : Assay for the enantiomeric analysis of [$^2H_1$]-fluoroacetic acid :insight into the stereochemical course of fluorination during fluorometabolite biosynthesis in streptomyces cattleya. *J. Am. Chem. Soc.*, 125(2):379–387, 2003.

[62] G. J. Martin et M. L. Martin : Deuterium labelling at the natural abundance level as studied by high field quantitative 2h nmr. *Tetrahedron Lett.*, 22(36):3525 – 3528, 1981.

[63] Philippe Lesot, Christie Aroulanda et Isabelle Billault : Exploring the analytical potential of nmr spectroscopy in chiral anisotropic media for the study of the natural abundance deuterium distribution in organic molecules. *Anal. Chem.*, 76(10):2827–2835, 2004.

[64] Philippe LESOT, Vincent BAILLIF et Isabelle BILLAULT : Combined analysis of C-18 unsaturated fatty acids using natural abundance deuterium 2D NMR spectroscopy in chiral oriented solvents. *Anal. Chem.*, 80(8):2963–2972, 2008.

[65] Gérard J. MARTIN, Maryvonne L. MARTIN et Gérald REMAUD : Snif-nmr—part 3 : From mechanistic affiliation to origin inference. *In* Graham A. WEBB, éditeur : *Modern Magnetic Resonance*, pages 1669–1680. Springer Netherlands, 2006.

[66] Eric JAMIN et Gérard J. MARTIN : Snif-nmr—part 4 : Applications in an economic context : The example of wines, spirits, and juices. *In* Graham A. WEBB, éditeur : *Modern Magnetic Resonance*, pages 1681–1687. Springer Netherlands, 2006.

[67] William H. PIRKLE et Kevin Z. GAN : A direct chromatographic separation of enantiomers chiral by virtue of isotopic substitution. *Tetrahedron : Asymmetry*, 8(6):811 – 814, 1997.

[68] D. PARKER : NMR determination of enantiomeric purity. *Chem. Rev.*, 91:1441–1457, 1991.

[69] Morton RABAN et Kurt MISLOW : The determination of optical purity by nuclear magnetic resonance spectroscopy. ii. compounds which owe their dissymmetry to deuterium substitution. *Tetrahedron Lett.*, 7(33):3961 – 3966, 1966.

[70] D. MERLET, J. W. EMSLEY, P. LESOT et J. COURTIEU : The relationship between molecular symmetry and second-rank orientational order parameters for molecules in chiral liquid crystalline solvents. *J. Chem. Phys.*, 111:6890–6896, 1999.

[71] C. AROULANDA, D. MERLET, J. COURTIEU et P. LESOT : NMR experimental evidence of the differentiation of enantiotopic directions in C_s and $C_{2\mathrm{v}}$ molecules using partially oriented, chiral media. *J. Am. Chem. Soc.*, 123:12059–12066, 2001.

[72] Philippe LESOT, Christie AROULANDA et Zeev LUZ : Analysis of enantiotopic discrimination in the nmr spectra of prochiral solutes in chiral liquid crystals by symmetry factorization of the saupe ordering matrix. *J. Chem. Phys.*, 131(10):104501, 2009.

[73] P. LESOT, D. MERLET, M. SARFATI, J. COURTIEU, H. ZIMMERMANN et Z. LUZ : Enantiomeric and enantiotopic analysis of cone-shaped compounds with C_3 and $C_{3\mathrm{v}}$ symmetry using NMR spectroscopy in chiral anisotropic solvents. *J. Am. Chem. Soc.*, 124:10071–10082, 2002.

[74] J. W. EMSLEY, P. LESOT, J. COURTIEU et D. MERLET : The effect of a chiral nematic solvent on the orientational order and conformational distri-

bution of a flexible prochiral molecule. *Phys. Chem. Chem. Phys.*, 6:5331–5337, 2004.

[75] A. L. Eliel : On the concept of isomerism. *Israel J. Chem.*, 15:7–11, 1977.

[76] P. Lesot, D. Merlet, A. Loewenstein et J. Courtieu : Enantiomeric visualization using proton-decoupled natural abundance deuterium in poly-γ-benzyl-L-glutamate liquid crystalline solutions. *Tetrahedron : Asym.*, 9: 1871–1881, 1998.

[77] Philippe Lesot et Jacques Courtieu : Natural abundance deuterium nmr spectroscopy : Developments and analytical applications in liquids, liquid crystals and solid phases. 55(2):128–159, 2009.

[78] D. Merlet, B. Ancian, J. Courtieu et P. Lesot : Two-dimensional deuterium NMR spectroscopy of chiral molecules oriented in a polypeptide liquid crystal : applications for the enantiomeric analysis through natural abundance deuterium NMR. *J. Am. Chem. Soc.*, 121:5249–5258, 1999.

[79] S. Vega, T. W. Shattuck et A. Pines : Double-quantum cross-polarization NMR in solids. *Phys. Rev. A*, 22:638–661, 1980.

[80] C. Auger, A. Lesage, S. Caldarelli, P. Hodgkinson et L. Emsley : Deuterium-carbon NMR correlation spectroscopy in oriented materials. *J. Am. Chem. Soc.*, 119:12000–12001, 1997.

[81] D. Sandström et H. Zimmermann : Correlation of deuterium quadrupolar couplings and carbon-13 chemical shifts in ordered media by multiple-quantum NMR. *J. Phys. Chem. B*, 104:1490–1493, 2000.

[82] K. Schmidt, K. Saalwächter, S.-F. Liu et M. Hong : High-sensivity ^{2}H nmr in solids by ^{1}H detection. *J. Am. Chem. Soc.*, 123:7168–7169, 2001.

[83] J. W. Emsley : *Nuclear Magnetic Resonance of liquid crystals*, pages 379–412. Reidel, Dordrecht, 1985.

[84] K. Kobzar, H. Kessler et B. Luy : Stretched gelatin gels as chiral alignment media for the discrimination of enantiomers by nmr spectroscopy. *Angew. Chem. Int. Ed. Engl.*, 44:3145–3147, 2005.

[85] C. Naumann et P. W. Kuchel : Nmr (pro)chiral discrimination using polysaccharide gels. *Chem. Eur. J.*, 15:12189–12191, 2009.

[86] S. P. Sau et K. V. Ramanathan : Visualization of enantiomers in the liquid-crystalline phase of a fragmented dna solution. *J. Phys. Chem. B*, 113:1530–1532, 2009.

[87] P. Lesot, D. Merlet, A. Meddour et J. Courtieu : Visualization of enantiomers in a polypeptide liquid-crystal solvent through carbon-13 NMR spectroscopy. *J. Chem. Soc. Faraday Trans.*, 91:1371–1375, 1995.

[88] P. Lesot, D. Merlet, T. P. Rantala, J. Jokisaari, J. W. Emsley et J. Courtieu : Calculation of the molecular ordering parameters of (±)-3-butyn-2-ol dissolved in a organic solution of poly(γ-benzyl-L-glutamate). *J. Phys. Chem. A*, 101:5719–5724, 1997.

[89] J. Farjon, D. Merlet, P. Lesot et J. Courtieu : Enantiomeric excess measurements in weakly oriented chiral liquid crystal solvents through 2D ^{1}H selective refocusing experiments. *J. Magn. Reson.*, 158:169–172, 2002.

[90] B. Baishya, U. R. Prabhu et N. Suryaprakash : Enantiomeric discrimination by double quantum excited selective refocusing (DQ-SERF) experiment. *J. Phys. Chem. B*, 111:12403–12410, 2007.

[91] J. Farjon, J.-P. Baltaze, P. Lesot, D. Merlet et J. Courtieu : Heteronuclear selective refocusing 2D NMR experiments for the spectral analysis of enantiomers in chiral oriented solvents. *Magn. Reson. Chem.*, 42:594–599, 2004.

[92] Latifa Ziani, Philippe Lesot, Abdelkhrim Meddour et Jacques Courtieu : Empirical determination of the absolute configuration of small chiral molecules using natural abundance ^{2}H nmr in chiral liquid crystals. *Chem. Commun.*, (45):4737–4739, 2007.

[93] J. Helfrich et R. Hentschke : Molecular dynamics simulation of macromolecular interactions in solution : Poly(γ-benzyl glutamate) in dimethylformamide and tetrahydrofuran. *Macromolecules*, 28(11):3831–3841, 1995.

[94] E. E. Burnell et C. A. de Lange : Prediction from molecular shape of solute orientational order in liquid crystals. *Chemical Reviews*, 98(6):2359–2388, 1998.

[95] P. Diehl, P. M. Henrichs et W. Niederberger : A study of the molecular structure and of the barrier to methyl rotation in *o*-chlorotoluene partially oriented in the nematic phase. *Molecular Physics : An International Journal at the Interface Between Chemistry and Physics*, 20(1):139–145, 1971.

[96] Nico Tjandra et Ad Bax : Direct Measurement of Distances and Angles in Biomolecules by NMR in a Dilute Liquid Crystalline Medium. *Science*, 278(5340):1111–1114, 1997.

[97] Martin Karplus : Contact electron-spin coupling of nuclear magnetic moments. *J. Chem. Phys.*, 30(1):11–15, 1959.

[98] F. A. L. Anet et A. J. R. Bourn : Nuclear magnetic resonance spectral assignments from nuclear overhauser effects1. *J. Am. Chem. Soc.*, 87(22):5250–5251, 1965.

[99] Bernd REIF, Mirko HENNIG et Christian GRIESINGER : Direct Measurement of Angles Between Bond Vectors in High-Resolution NMR. *Science*, 276(5316):1230–1233, 1997.

[100] Christina M. THIELE et Stefan BERGER : Probing the diastereotopicity of methylene protons in strychnine using residual dipolar couplings. *Org. Lett.*, 5(5):705–708, 2003.

[101] C. AROULANDA, V. BOUCARD, F. GUIBÉ, J. COURTIEU et D. MERLET : Weakly oriented liquid-crystal nmr solvents as a general tool to determine relative configurations. *Chem. Eur. J.*, 9(18):4536–4539, 2003.

[102] E. E. BURNELL et C. A. de LANGE : Effects of interaction between molecular internal motion and reorientation on nmr of anisotropic liquids. *J. Magn. Reson.*, 39(3):461 – 480, 1980.

[103] Judit A. LOSONCZI, Michael ANDREC, Mark W. F. FISCHER et James H. PRESTEGARD : Order matrix analysis of residual dipolar couplings using singular value decomposition. *J. Magn. Reson.*, 138(2):334 – 342, 1999.

[104] Christina M. THIELE, Arnold MALINIAK et Baltzar STEVENSSON : Use of local alignment tensors for the determination of relative configurations in organic compounds. *J. Am. Chem. Soc.*, 131(36):12878–12879, 2009.

[105] Bénédicte ELENA et Lyndon EMSLEY : Powder crystallography by proton solid-state nmr spectroscopy. *J. Am. Chem. Soc.*, 127(25):9140–9146, 2005.

[106] Elodie SALAGER, Robin S. STEIN, Chris J. PICKARD, Benedicte ELENA et Lyndon EMSLEY : Powder NMR crystallography of thymol. *Phys. Chem. Chem. Phys.*, 11(15):2610–2621, 2009.

[107] A. L. ELIEL et A. H. WILEN : *Stereochemistry of organic compounds*. Wiley, New York, 1994.

[108] Howard D. W. HILL, A. P. ZENS et John JACOBUS : Solid-state nmr spectroscopy. distinction of diastereomers and determination of optical purity. *J. Am. Chem. Soc.*, 101(23):7090–7091, 1979.

[109] M. J. POTRZEBOWSKI, E. TADEUSIAK, K. MISIURA, W. CIESIELSKI, G. BUJACZ et P. TEKELY : A new method for distinguishing between enantiomers and racemates and assignment of enantiomeric purity by means of solid-state nmr. examples from oxazaphosphorinanes. *Chem. Eur. J.*, 8(21):5007–5011, 2002.

[110] B. H. MEIER et William L. EARL : Excitation of multiple quantum transitions under magic angle spinning conditions : Adamantane. *J. Chem. Phys.*, 85(9):4905–4911, 1986.

[111] Robert TYCKO et Gary DABBAGH : Measurement of nuclear magnetic dipole–dipole couplings in magic angle spinning NMR. *Chem. Phys. Lett.*, 173(5-6):461 – 465, 1990.

[112] B. H. MEIER et William L. EARL : Double-quantum filter for rotating solids. *J. Am. Chem. Soc.*, 109(26):7937–7942, 1987.

[113] Robert TYCKO et Gary DABBAGH : Double-quantum filtering in magic-angle-spinning NMR spectroscopy : an approach to spectral simplification and molecular structure determination. *J. Am. Chem. Soc.*, 113(25):9444–9448, 1991.

[114] Helen GEEN, Jeremy J. TITMAN, Johannes GOTTWALD et Hans W. SPIESS : Solid-state proton multiple-quantum NMR spectroscopy with fast magic angle spinning. *Chem. Phys. Lett.*, 227(1-2):79 – 86, 1994.

[115] Helen GEEN, Johannes GOTTWALD, Robert GRAF, Ingo SCHNELL, Hans W. SPIESS et Jeremy J. TITMAN : Elucidation of dipolar coupling networks under magic-angle spinning. *J. Magn. Reson.*, 125(1):224 – 227, 1997.

[116] X. FENG, Y. K. LEE, D. SANDSTROM, M. EDÉN, H. MAISEL, A. SEBALD et M. H. LEVITT : Direct determination of a molecular torsional angle by solid-state NMR. *Chem. Phys. Lett.*, 257(3-4):314 – 320, 1996.

[117] K. SCHMIDT-ROHR : Torsion angle determination in solid ^{13}C-labeled amino acids and peptides by separated-local-field double-quantum NMR. *J. Am. Chem. Soc.*, 118(32):7601–7603, 1996.

[118] Stéphane BALAYSSAC, Ivano BERTINI, Moreno LELLI, Claudio LUCHINAT et Massimiliano MALETTA : Paramagnetic ions provide structural restraints in solid-state NMR of proteins. *J. Am. Chem. Soc.*, 129(8):2218–2219, 2007.

[119] Philippe S. NADAUD, Jonathan J. HELMUS, Nicole HÖFER et Christopher P. JARONIEC : Long-range structural restraints in spin-labeled proteins probed by solid-state nuclear magnetic resonance spectroscopy. *J. Am. Chem. Soc.*, 129(24):7502–7503, 2007.

[120] Edina BALOGH, Dong WU, Guangyan ZHOU et Miriam GOCHIN : NMR second site screening for structure determination of ligands bound in the hydrophobic pocket of hiv-1 gp41. *J. Am. Chem. Soc.*, 131(8):2821–2823, 2009.

[121] David A. MIDDLETON, Saffron RANKIN, Mikael ESMANN et Anthony WATTS : Structural insights into the binding of cardiac glycosides to the digitalis receptor revealed by solid-state NMR. *Proc. Natl. Acad. Sci. U. S. A.*, 97(25):13602–13607, 2000.

[122] M. Lane GILCHRIST, Kenji MONDE, York TOMITA, Takashi IWASHITA, Koji NAKANISHI et Ann E. MCDERMOTT : Measurement of interfluorine distances in solids. *J. Magn. Reson.*, 152(1):1 – 6, 2001.

[123] Anthony Watts : Solid-state NMR in drug design and discovery for membrane-embedded targets. *Nat Rev Drug Discov*, 4(7):555–568, juillet 2005.

[124] Younkee Paik, Chao Yang, Belhu Metaferia, Shoubin Tang, Susan Bane, Rudravajhala Ravindra, Natasha Shanker, Ana A. Alcaraz, Scott A. Johnson, Jacob Schaefer, Robert D. O'Connor, Lynette Cegelski, James P. Snyder et David G. I. Kingston : Rotational-echo double-resonance NMR distance measurements for the tubulin-bound paclitaxel conformation. *J. Am. Chem. Soc.*, 129(2):361–370, 2007.

[125] M. Baldus et B. H. Meier : Broadband polarization transfer under magic-angle spinning : Application to total through-space-correlation NMR spectroscopy. *J. Magn. Reson.*, 128(2):172–193, octobre 1997.

[126] Paul Hodgkinson et Lyndon Emsley : The accuracy of distance measurements in solid-state NMR. *J. Magn. Reson.*, 139(1):46 – 59, 1999.

[127] Marvin J. Bayro, Matthias Huber, Ramesh Ramachandran, Timothy C. Davenport, Beat H. Meier, Matthias Ernst et Robert G. Griffin : Dipolar truncation in magic-angle spinning NMR recoupling experiments. *J. Chem. Phys.*, 130(11):114506, 2009.

[128] G. V. D. Tiers, C. A. Brown, R. A. Jackson et T. N. Lahr : Tritium nuclear magnetic resonance spectroscopy. i. observation of high-resolution signals from the methyl and methylene groups of ethylbenzene. the nonradiochemical use of tritium as a tracer. *J. Am. Chem. Soc.*, 86(12):2526–2527, 1964.

[129] Jasim M. A. Al-Rawi, John A. Elvidge, Devendra K. Jaiswal, John R. Jones et Robert Thomas : Use of tritium nuclear magnetic resonance for the direct location of 3h in biosynthetically-labelled penicillic acid. *J. Chem. Soc., Chem. Commun.*, (6):220–221, 1974.

[130] M. G. Kubinec et P. G. Williams : *Encyclopedia of Nuclear Magnetic Resonance*, chapitre Tritium NMR in Biology. Wiley, 1996.

[131] M. G. Kubinec et P. G. Williams : *Encyclopedia of Nuclear Magnetic Resonance*, chapitre Tritium NMR. Wiley, 1996.

[132] P. C. Souers, R. T. Tsugawa, E. M. Fearon et G. W. Collins : NMR lineshapes in solid tritium and deuterium-tritium. *J. Low Temp. Phys.*, 100(1):21–43, 1995.

[133] N. C. Nielsen, H. Bildsoe, H. J. Jakobsen et M. H. Levitt : Double-quantum homonuclear rotary resonance : Efficient dipolar recovery in magic-angle spinning nuclear magnetic resonance. *J. Chem. Phys.*, 101(3): 1805–1812, 1994.

[134] Ingo Schnell : Dipolar recoupling in fast-MAS solid-state NMR spectroscopy. *Prog. Nucl. Magn. Reson. Spectrosc.*, 45(1-2):145 – 207, 2004.

[135] M. H. Levitt : *Encyclopedia of Nuclear Magnetic Resonance*, chapitre Symmetry-Based Pulse Sequences in Magic-Angle Spinning Solid-State NMR, pages 165–196. Wiley, Chichester, 2002.

[136] Y. K. Lee, N. D. Kurur, M. Helmle, O. G. Johannessen, N. C. Nielsen et M. H. Levitt : Efficient dipolar recoupling in the NMR of rotating solids. a sevenfold symmetric radiofrequency pulse sequence. *Chem. Phys. Lett.*, 242(3):304 – 309, 1995.

[137] M. Hohwy, H. J. Jakobsen, M. Eden, M. H. Levitt et N. C. Nielsen : Broadband dipolar recoupling in the nuclear magnetic resonance of rotating solids : A compensated C7 pulse sequence. *J. Chem. Phys.*, 108(7):2686–2694, 1998.

[138] Marina Carravetta, Mattias Edén, Xin Zhao, Andreas Brinkmann et Malcolm H. Levitt : Symmetry principles for the design of radiofrequency pulse sequences in the nuclear magnetic resonance of rotating solids. *Chem. Phys. Lett.*, 321(3-4):205 – 215, 2000.

[139] W. Sommer, J. Gottwald, D.E. Demco et H.W. Spiess : Dipolar heteronuclear multiple-quantum NMR spectroscopy in rotating solids. *J. Magn. Reson. A*, 113(1):131 – 134, 1995.

[140] M. Feike, D. E. Demco, R. Graf, J. Gottwald, S. Hafner et H. W. Spiess : Broadband multiple-quantum NMR spectroscopy. *J. Magn. Reson. A*, 122(2):214 – 221, 1996.

[141] Francisco J. Blanco et Robert Tycko : Determination of polypeptide backbone dihedral angles in solid state NMR by double quantum ^{13}C chemical shift anisotropy measurements. *J. Magn. Reson.*, 149(1):131 – 138, 2001.

[142] Yoshitaka Ishii : ^{13}C–^{13}C dipolar recoupling under very fast magic angle spinning in solid-state nuclear magnetic resonance : Applications to distance measurements, spectral assignments, and high-throughput secondary-structure determination. *J. Chem. Phys.*, 114(19):8473–8483, 2001.

[143] Luis Mafra, Renée Siegel, Christian Fernandez, Denis Schneider, Fabien Aussenac et J. Rocha : High-resolution ^{1}H homonuclear dipolar recoupling NMR spectra of biological solids at MAS rates up to 67 kHz. *J. Magn. Reson.*, 199(1):111 – 114, 2009.

[144] Jean-Baptiste d'Espinose de Lacaillerie, Benjamin Jarry, Ovidiu Pascui et Detlef Reichert : Cooking the sample : Radiofrequency induced heating during solid-state NMR experiments. *Solid State Nucl. Magn. Re-*

son., 28(2-4):225 – 232, 2005. Special issue in honor of Prof. Jerzy Blicharski.

[145] Seth A. McNeill, Peter L. Gor'kov, Kiran Shetty, William W. Brey et Joanna R. Long : A low-E magic angle spinning probe for biological solid state NMR at 750 MHz. *J. Magn. Reson.*, 197(2):135 – 144, 2009.

[146] M. J. Duer : Determination of structural data from multiple-quantum magic-angle spinning NMR experiments. *Chem. Phys. Lett.*, 277(1-3):167 – 174, 1997.

[147] Shangwu Ding et Charles A. McDowell : Spectral spin diffusion of a spin-3/2 system in rotating solids. *Mol. Phys.*, 85(2):283–298, 1995.

[148] M. Nijman, M. Ernst, A. P. M. Kentgens et B. H. Meier : Rotational-resonance NMR experiments in half-integer quadrupolar spin systems. *Mol. Phys.*, 98(3):161–178, 2000.

[149] Mattias Eden et Lucio Frydman : Homonuclear NMR correlations between half-integer quadrupolar nuclei undergoing magic-angle spinning. *J. Phys. Chem. B*, 107(51):14598–14611, décembre 2003.

[150] A. James Painter et Melinda J. Duer : Double-quantum-filtered nuclear magnetic resonance spectroscopy applied to quadrupolar nuclei in solids. *J. Chem. Phys.*, 116(2):710–722, 2002.

[151] Gregor Mali, Gerhard Fink et Francis Taulelle : Double-quantum homonuclear correlation magic angle sample spinning nuclear magnetic resonance spectroscopy of dipolar-coupled quadrupolar nuclei. *J. Chem. Phys.*, 120(6):2835–2845, 2004.

[152] Mattias Ed'en, Hans Annersten et Asa Zazzi : Pulse-assisted homonuclear dipolar recoupling of half-integer quadrupolar spins in magic-angle spinning NMR. *Chem. Phys. Lett.*, 410(1-3):24–30, juillet 2005.

[153] Z. Yu, A. Zheng, Q. Wang, L. Chen, J. Xu, J.-P. Amoureux et F. Deng : New insights into the dealumination of zeolite hy revealed by sensitivity-enhanced ^{27}Al DQ MAS NMR spectroscopy at high field. *Angew. Chem. Int. Ed. Engl.*, in press, 2010.

[154] Jonathan P. Bradley, Carmen Tripon, Claudiu Filip et Steven P. Brown : Determining relative proton–proton proximities from the build-up of two-dimensional correlation peaks in ^{1}H double-quantum MAS NMR : insight from multi-spin density-matrix simulations. *Phys. Chem. Chem. Phys.*, 11(32):6941–6952, 2009.

[155] Mark C. Butler, Jean-Nicolas Dumez et Lyndon Emsley : Dynamics of large nuclear-spin systems from low-order correlations in liouville space. *Chem. Phys. Lett.*, 477(4-6):377 – 381, 2009.

[156] D. P. Raleigh, M. H. Levitt et R. G. Griffin : Rotational resonance in solid state NMR. *Chem. Phys. Lett.*, 146(1-2):71 – 76, 1988.

[157] Yun Mou et Jerry C.C. Chan : Frequency selective polarization transfer based on multiple chemical shift precession. *Chem. Phys. Lett.*, 419(1-3):144 – 148, 2006.

[158] Anant K. Paravastu et Robert Tycko : Frequency-selective homonuclear dipolar recoupling in solid state NMR. *J. Chem. Phys.*, 124(19):194303, 2006.

[159] Robert Tycko : Theory of stochastic dipolar recoupling in solid-state nuclear magnetic resonance†. *J. Phys. Chem. B*, 112(19):6114–6121, mai 2008.

[160] E. O. Stejskal, Jacob Schaefer et J. S. Waugh : Magic-angle spinning and polarization transfer in proton-enhanced NMR. *J. Magn. Reson.*, 28(1): 105 – 112, 1977.

[161] P. Caravatti, G. Bodenhausen et R.R. Ernst : Heteronuclear solid-state correlation spectroscopy. *Chem. Phys. Lett.*, 89(5):363 – 367, 1982.

[162] T. G. Oas, R. G. Griffin et M. H. Levitt : Rotary resonance recoupling of dipolar interactions in solid-state nuclear magnetic resonance spectroscopy. *J. Chem. Phys.*, 89:692, 1988.

[163] C. A. Fyfe, H. Grondey, K. T. Mueller, K. C. Wong-Moon et T. Markus : *J. Am. Chem. Soc.*, 114(14):5876–5878, 1992.

[164] Simone Cavadini, Adonis Lupulescu, Sasa Antonijevic et Geoffrey Bodenhausen : Nitrogen-14 NMR spectroscopy using residual dipolar splittings in solids. *J. Am. Chem. Soc.*, 128(24):7706–7707, 2006.

[165] Zhehong Gan : Measuring amide nitrogen quadrupolar coupling by high-resolution ^{14}N/^{13}C NMR correlation under magic-angle spinning. *J. Am. Chem. Soc.*, 128(18):6040–6041, 2006.

[166] A. Brinkmann et M. H. Levitt : Symmetry principles in the nuclear magnetic resonance of spinning solids : Heteronuclear recoupling by generalized Hartmann-Hahn sequences. *J. Chem. Phys.*, 115:357–384, 2001.

[167] Terry Gullion et Jacob Schaefer : Rotational-echo double-resonance NMR. *J. Magn. Reson.*, 81(1):196–200, janvier 1989.

[168] Riqiang Fu, Scott A. Smith et Geoffrey Bodenhausen : Recoupling of heteronuclear dipolar interactions in solid state magic-angle spinning NMR by simultaneous frequency and amplitude modulation. *Chem. Phys. Lett.*, 272(5-6):361–369, juillet 1997.

[169] Xin Zhao, Mattias Edén et Malcolm H. Levitt : Recoupling of heteronuclear dipolar interactions in solid-state NMR using symmetry-based pulse sequences. *Chem. Phys. Lett.*, 342(3-4):353 – 361, 2001.

[170] A. Brinkmann et A.P.M. Kentgens : Sensitivity enhancement and heteronuclear distance measurements in biological ^{17}O solid-state NMR. *J. Phys. Chem. B*, 110(32):16089–16101, 2006.

[171] A. Brinkmann et A.P.M. Kentgens : Proton-selective ^{17}O-^{1}H distance measurements in fast magic-angle-spinning solid-state NMR spectroscopy for the determination of hydrogen bond lengths. *J. Am. Chem. Soc.*, 128(46):14758–14759, 2006.

[172] Jon M. Goetz et Jacob Schaefer : REDOR dephasing by multiple spins in the presence of molecular motion. *J. Magn. Reson.*, 127(2):147 – 154, 1997.

[173] Terry Gullion : Measurement of dipolar interactions between spin-1/2 and quadrupolar nuclei by rotational-echo, adiabatic-passage, double-resonance NMR. *Chem. Phys. Lett.*, 246(3):325 – 330, 1995.

[174] Terry Gullion et Alexander J. Vega : Measuring heteronuclear dipolar couplings for $i=1/2$, $s>1/2$ spin pairs by REDOR and REAPDOR NMR. *Prog. Nucl. Magn. Reson. Spectrosc.*, 47(3-4):123 – 136, 2005.

[175] Andrew W. Hing, Shimon Vega et Jacob Schaefer : Transferred-echo double-resonance NMR. *J. Magn. Reson.*, 96(1):205 – 209, 1992.

[176] Yoshitaka Ishii et Robert Tycko : Sensitivity enhancement in solid state ^{15}n NMR by indirect detection with high-speed magic angle spinning. *J. Magn. Reson.*, 142(1):199–204, janvier 2000.

[177] K. Saalwächter et H. W. Spiess : Heteronuclear ^{1}H–^{13}C multiple-spin correlation in solid-state nuclear magnetic resonance : Combining rotational-echo double-resonance recoupling and multiple-quantum spectroscopy. *J. Chem. Phys.*, 114:5707, 2001.

[178] Mei Hong et Robert G. Griffin : Resonance assignments for solid peptides by dipolar-mediated ^{13}C/^{15}N correlation solid-state NMR. *J. Am. Chem. Soc.*, 120(28):7113–7114, 1998.

[179] Sasa Antonijevic et Nicholas Halpern-Manners : Probing amide bond nitrogens in solids using ^{14}N NMR spectroscopy. *Solid State Nucl. Magn. Reson.*, 33(4):82–87, 2008.

[180] Simone Cavadini, Anuji Abraham et Geoffrey Bodenhausen : Coherence transfer between spy nuclei and nitrogen-14 in solids. *J. Magn. Reson.*, 190(1):160–164, 2008.

[181] W. Kohn et L. J. Sham : Self-consistent equations including exchange and correlation effects. *Phys. Rev.*, 140(4A):1133, 1965.

[182]

[183] Lucio FRYDMAN et John S. HARWOOD : Isotropic spectra of half-integer quadrupolar spins from bidimensional magic-angle spinning NMR. *J. Am. Chem. Soc.*, 117(19):5367–5368, 1995.

[184] S. H. WANG, S. M. De PAUL et L. M. BULL : High-resolution heteronuclear correlation between quadrupolar and spin- nuclei using multiple-quantum magic-angle spinning. *J. Magn. Reson.*, 125(2):364 – 368, 1997.

[185] Renée SIEGEL, Joao ROCHA et Luis MAFRA : Combining STMAS and CRAMPS NMR spectroscopy : High-resolution hetcor NMR spectra of quadrupolar and ^{1}H nuclei in solids. *Chem. Phys. Lett.*, 470(4-6):337 – 341, 2009.

[186] Sharon E. ASHBROOK et Stephen WIMPERIS : Satellite-transition MAS NMR of spin I=3/2, 5/2, 7/2, and 9/2 nuclei : Sensitivity, resolution, and practical implementation. *J. Magn. Reson.*, 156(2):269 – 281, 2002.

[187] Sasa ANTONIJEVIC, Sharon E. ASHBROOK, Silke BIEDASEK, Richard I. WALTON, Stephen WIMPERIS et Huaixin YANG : Dynamics on the microsecond timescale in microporous aluminophosphate AlPO-14 as evidenced by ^{27}Al mqMAS and STMAS NMR spectroscopy. *J. Am. Chem. Soc.*, 128(24):8054–8062, 2006.

[188] Christopher P. JARONIEC, Brett A. TOUNGE, Judith HERZFELD et Robert G. GRIFFIN : Frequency selective heteronuclear dipolar recoupling in rotating solids : accurate ^{13}C-^{15}N distance measurements in uniformly ^{13}C,^{15}N-labeled peptides. *J. Am. Chem. Soc.*, 123(15):3507–3519, 2001.

[189] Terry GULLION et Charles H. PENNINGTON : [theta]-REDOR : an MAS NMR method to simplify multiple coupled heteronuclear spin systems. *Chem. Phys. Lett.*, 290(1-3):88 – 93, 1998.

[190] Oskar LIIVAK et David B. ZAX : Rotational echo double resonance in is[sub n] spin networks : Deconvolution of multiple dipole–dipole couplings. *J. Chem. Phys.*, 115(1):402–409, 2001.

[191] T. STEINER : The hydrogen bond in the solid state. *Angewandte Chemie International Edition*, 41(1):48–76, 2002.

[192] Darren H. BROUWER et John A. RIPMEESTER : Symmetry-based recoupling of proton chemical shift anisotropies in ultrahigh-field solid-state NMR. *J. Magn. Reson.*, 185(1):173 – 178, 2007.

[193] Luminita DUMA, Daniel ABERGEL, Piotr TEKELY et Geoffrey BODENHAUSEN : Proton chemical shift anisotropy measurements of hydrogen-bonded functional groups by fast magic-angle spinning solid-state NMR spectroscopy. *Chem. Commun.*, pages 2361–2363, 2008.

[194] M. Hohwy, P. V. Bower, H. J. Jakobsen et N. C. Nielsen : A high-order and broadband CRAMPS experiment using z-rotational decoupling. *Chem. Phys. Lett.*, 273(5-6):297 – 303, 1997.

[195] D. P. Burum et W. K. Rhim : Analysis of multiple pulse NMR in solids. iii. *J. Chem. Phys.*, 71(2):944–956, 1979.

[196] M. Hohwy et N. C. Nielsen : Elimination of high order terms in multiple pulse nuclear magnetic resonance spectroscopy : Application to homonuclear decoupling in solids. *J. Chem. Phys.*, 106(18):7571–7586, 1997.

[197] A. Bielecki, A.C. Kolbert et M.H. Levitt : Frequency-switched pulse sequences : Homonuclear decoupling and dilute spin NMR in solids. *Chem. Phys. Lett.*, 155(4-5):341 – 346, 1989.

[198] M. H. Levitt, A. Bielecki, A. C. Kolbert et D. J. Ruben : High-resolution ^{1}H NMR in solids with frequency-switched multiple-pulse sequences. *Solid State Nucl. Magn. Reson.*, 2:151–163, 1993.

[199] E. Vinogradov, P. K. Madhu et S. Vega : High-resolution proton solid-state NMR spectroscopy by phase-modulated Lee-Goldburg experiment. *Chem. Phys. Lett.*, 314:443–450, 1999.

[200] Dimitris Sakellariou, Anne Lesage, Paul Hodgkinson et Lyndon Emsley : Homonuclear dipolar decoupling in solid-state NMR using continuous phase modulation. *Chem. Phys. Lett.*, 319(3-4):253–260, mars 2000.

[201] D. E. Demco, S. Hafner et H. W. Spiess : Rotation-synchronized homonuclear decoupling. *J. Magn. Reson. A*, 116:36–45, 1995.

[202] P. K. Madhu, X. Zhao et M. H. Levitt : High-resolution ^{1}H NMR in the solid state using symmetry-based pulse sequences. *Chem. Phys. Lett.*, 346:142–148, 2001.

[203] Michal Leskes, Stefan Steuernagel, Denis Schneider, P.K. Madhu et Shimon Vega : Homonuclear dipolar decoupling at magic-angle spinning frequencies up to 65 kHz in solid-state nuclear magnetic resonance. *Chem. Phys. Lett.*, 466(1-3):95 – 99, 2008.

[204] Elodie Salager, Robin S. Stein, Stefan Steuernagel, Anne Lesage, Bénédicte Elena et Lyndon Emsley : Enhanced sensitivity in high-resolution ^{1}H solid-state NMR spectroscopy with DUMBO dipolar decoupling under ultra-fast MAS. *Chem. Phys. Lett.*, 469(4-6):336 – 341, 2009.

[205] Michal Leskes, P.K. Madhu et Shimon Vega : Why does pmlg proton decoupling work at 65 kHz MAS ? *J. Magn. Reson.*, 199(2):208 – 213, 2009.

[206] E. Vinogradov, P. K. Madhu et S. Vega : Phase modulated Lee-Goldburg magic angle spinning proton nuclear magnetic resonance experiments in the solid state : A bimodal Floquet theoretical treatment. *J. Chem. Phys.*, 115:8983–9000, 2001.

[207] Bénédicte Elena, Gaël de Paëpe et Lyndon Emsley : Direct spectral optimisation of proton-proton homonuclear dipolar decoupling in solid-state NMR. *Chem. Phys. Lett.*, 398(4-6):532–538, 2004.

[208] E. Salager, J.-N. Dumez, R. Stein, S. Steuernagel, A. Lesage, B. Elena-Hermann et L. Emsley : Homonuclear dipolar decoupling with very large scaling factors for high-resolution ultra-fast magic angle spinning ^{1}H solid-state NMR spectroscopy. *Chem. Phys. Lett.*, in press, 2010.

[209] A. Brinkmann et M. Edén : Second order average Hamiltonian theory of symmetry-based pulse schemes in the nuclear magnetic resonance of rotating solids : Application to triple-quantum dipolar recoupling. *J. Chem. Phys.*, 120:11726–11745, 2004.

[210] Michal Leskes, P.K. Madhu et Shimon Vega : Floquet theory in solid-state nuclear magnetic resonance. *Prog. Nucl. Magn. Reson. Spectrosc.*, In Press, Corrected Proof:–, 2010.

[211] L. Bosman, P. K. Madhu, S. Vega et E. Vinogradov : Improvement of homonuclear dipolar decoupling sequences in solid-state nuclear magnetic resonance utilising radiofrequency imperfections. *J. Magn. Reson.*, 169:39–48, 2004.

[212] Shinji Ando, Robin K. Harris, Jérôme Hirschinger, Stefan A. Reinsberg et Ulrich Scheler : Solid-state ^{19}F MAS, ^{19}F CRAMPS, and ^{19}F $\rightarrow$ ^{13}C CP/MAS NMR study of an amorphous perfluoropolymer. *Macromolecules*, 34(1):66–75, 2001.

[213] D. Sakellariou, G. Le Goff et J.-F. Jacquinot : High-resolution, high-sensitivity NMR of nanolitre anisotropic samples by coil spinning. *Nature*, 447(7145):694–697, 2007.

[214] Takashi Mizuno et K. Takegoshi : Development of a cryogenic duplexer for solid-state nuclear magnetic resonance. *Rev. Sci. Instrum.*, 80(12):124702, 2009.

[215] N.Q. Fan, M.B. Heaney, J. Clarke, D. Newitt, L.L. Wald, E.L. Hahn, A. Bielecki et A. Pines : Nuclear magnetic resonance with dc squid preamplifiers. *IEEE T. Magn.*, 25(2):1193–1199, 1989.

[216] Ya. S. Greenberg : Application of superconducting quantum interference devices to nuclear magnetic resonance. *Rev. Mod. Phys.*, 70(1):175–222, 1998.

[217] I. M. Savukov et M. V. Romalis : NMR detection with an atomic magnetometer. *Phys. Rev. Lett.*, 94(12):123001, 2005.

[218] D. Suter et R. Klieber : Spins as probes of different electronic states. *Concepts Magn. Reson.*, 30A(2):116–126, 2007.

[219] D. RUGAR, C. S. YANNONI et J. A. SIDLES : Mechanical detection of magnetic resonance. *Nature*, 360(6404):563–566, 1992.

[220] A. SUTER : The magnetic resonance force microscope. *Prog. Nucl. Magn. Reson. Spectrosc.*, 45(3-4):239 – 274, 2004.

[221] M. CARRAVETTA, O. G. JOHANNESSEN, M. H. LEVITT, I. HEINMAA, R. STERN, A. SAMOSON, A. J. HORSEWILL, Y. MURATA et K. KOMATSU : Cryogenic NMR spectroscopy of endohedral hydrogen-fullerene complexes. *J. Chem. Phys.*, 124(10):104507, 2006.

[222] T. R. CARVER et C. P. SLICHTER : Polarization of nuclear spins in metals. *Phys. Rev.*, 92(1):212–213, 1953.

[223] Lino R. BECERRA, Gary J. GERFEN, Richard J. TEMKIN, David J. SINGEL et Robert G. GRIFFIN : Dynamic nuclear polarization with a cyclotron resonance maser at 5 t. *Phys. Rev. Lett.*, 71(21):3561–3564, 1993.

[224] Dennis A. HALL, Douglas C. MAUS, Gary J. GERFEN, Souheil J. INATI, Lino R. BECERRA, Frederick W. DAHLQUIST et Robert G. GRIFFIN : Polarization-enhanced NMR spectroscopy of biomolecules in frozen solution. *Science*, 276(5314):930–932, 1997.

[225] Boyd M. GOODSON : Nuclear magnetic resonance of laser-polarized noble gases in molecules, materials, and organisms. *J. Magn. Reson.*, 155(2):157 – 216, 2002.

[226] Simon B. DUCKETT et Christopher J. SLEIGH : Applications of the parahydrogen phenomenon : A chemical perspective. *Prog. Nucl. Magn. Reson. Spectrosc.*, 34(1):71 – 92, 1999.

[227] R.A. WIND, M.J. DUIJVESTIJN, C. van der LUGT, A. MANENSCHIJN et J. VRIEND : Applications of dynamic nuclear polarization in ^{13}C NMR in solids. *Prog. Nucl. Magn. Reson. Spectrosc.*, 17:33 – 67, 1985.

[228] Yoh MATSUKI, Hiroki TAKAHASHI, Keisuke UEDA, Toshitaka IDEHARA, Isamu OGAWA, Mitsuru TODA, Hideo AKUTSU et Toshimichi FUJIWARA : Dynamic nuclear polarization experiments at 14.1 t for solid-state NMR. *Phys. Chem. Chem. Phys.*, 12(22):5799–5803, 2010.

[229] Vikram S. BAJAJ, Melody L. MAK-JURKAUSKAS, Marina BELENKY, Judith HERZFELD et Robert G. GRIFFIN : Functional and shunt states of bacteriorhodopsin resolved by 250 GHz dynamic nuclear polarization–enhanced solid-state NMR. *Proc. Natl. Acad. Sci. U. S. A.*, 106(23):9244–9249, 2009.

[230] Changsik SONG, Kan-Nian HU, Chan-Gyu JOO, Timothy M. SWAGER et Robert G. GRIFFIN : Totapol : A biradical polarizing agent for dynamic nuclear polarization experiments in aqueous media. *J. Am. Chem. Soc.*, 128(35):11385–11390, 2006.

[231] Kan-Nian Hu, Changsik Song, Hsiao hua Yu, Timothy M. Swager et Robert G. Griffin : High-frequency dynamic nuclear polarization using biradicals : A multifrequency EPR lineshape analysis. *J. Chem. Phys.*, 128(5):052302, 2008.

[232] R. J. Argauer et G. R. Landolt, 1972.

[233] H. Vezin, A. Moissette, M. Hureau et C. Brémard : trans-stilbene incorporation in acidic medium-pore ZSM-5 zeolite : A pulsed EPR study. *Chem. Eur. J. of Chem. Phys.*, 7(12):2474–2477, 2006.

[234] A. V. Kessenikh, V. I. Lushchikov, A. A. Manenkov et Y. V. Taran : On explanation of experimental data on dynamic polarization of protons in irradiated polyethylenes. *Sov. Phys. Solid State*, 5:321, 1963.

[235] A. Abragam, J. Combrisson et I. Solomon : Polarisation dynamique des noyaux du silicium 29 dans le silicium. *C. R. Acad. Sci.*, 246:1035, 1958.

[236] A. Abragam, J. Combrisson et I. Solomon : Polarisation dynamique des noyaux du silicium 29 dans le silicium à 4.2 k. *C. R. Acad. Sci.*, 247:2337, 1958.

[237] A. E. Dementyev, D. G. Cory et C. Ramanathan : Dynamic nuclear polarization in silicon microparticles. *Phys. Rev. Lett.*, 100(12):127601–, mars 2008.

[238] Hiroshi Hayashi, Kohei M. Itoh et Leonid S. Vlasenko : Nuclear magnetic resonance linewidth and spin diffusion in s 29 i isotopically controlled silicon. *Phys. Rev. B*, 78(15):153201–, octobre 2008.

[239] A. Henstra, P. Dirksen et W. Th. Wenckebach : Enhanced dynamic nuclear polarization by the integrated solid effect. *Phys. Lett. A*, 134(2): 134–136, décembre 1988.

[240] T. Itahashi, H. Hayashi, K.M. Itoh, D.S. Poloskin, L.S. Vlasenko et M.P. Vlasenko : Dynamic nuclear polarization of ^{29}Si via spin s=1 centers in isotopically controlled silicon. *Physica B : Condensed Matter*, 404(23-24):5054–5056, décembre 2009.

[241] T. Maly, A.-F. Miller et R. G. Griffin : In situ high-field dynamic nuclear polarization—direct and indirect polarization of ^{13}C nuclei. *Chem. Eur. J. of Chem. Phys.*, 11(5):999–1001, 2010.

[242] Thorsten Maly, Loren B. Andreas, Albert A. Smith et Robert G. Griffin : ^{2}H-DNP-enhanced ^{2}H-^{13}C solid-state NMR correlation spectroscopy. *Phys. Chem. Chem. Phys.*, 12(22):5872–5878, 2010.

[243] Veronika Vitzthum, Marc A. Caporini et Geoffrey Bodenhausen : Solid-state nitrogen-14 nuclear magnetic resonance enhanced by dynamic nuclear polarization using a gyrotron. *J. Magn. Reson.*, 205(1):177 – 179, 2010.

[244] V. Weis et R.G. Griffin : Electron-nuclear cross polarization. *Solid State Nucl. Magn. Reson.*, 29(1-3):66 – 78, 2006. Special Issue honouring Prof. Alexander Pines on his 60th birthday.

[245] J. C. J. Barna, E. D. Laue, M. R. Mayger, J. Skilling et S. J. P. Worrall : Exponential sampling, an alternative method for sampling in two-dimensional NMR experiments. *J. Magn. Reson.*, 73(1):69 – 77, 1987.

[246] Peter Schmieder, Alan S. Stern, Gerhard Wagner et Jeffrey C. Hoch : Application of nonlinear sampling schemes to COSY-type spectra. *J. Biomol. NMR*, 3:569–576, 1993.

[247] Alan S. Stern, Kuo-Bin Li et Jeffrey C. Hoch : Modern spectrum analysis in multidimensional NMR spectroscopy : ? comparison of linear-prediction extrapolation and maximum-entropy reconstruction. *J. Am. Chem. Soc.*, 124(9):1982–1993, 2002.

[248] Krzysztof Kazimierczuk, Wiktor Kozminski et Igor Zhukov : Two-dimensional fourier transform of arbitrarily sampled NMR data sets. *J. Magn. Reson.*, 179(2):323 – 328, 2006.

[249] Dominique Marion : Processing of ND NMR spectra sampled in polar coordinates : a simple fourier transform instead of a reconstruction. *J. Biomol. NMR*, 36:45–54, 2006.

[250] H. Barkhuijsen, R. de Beer, W. M. M. J. Bovee et D. van Ormondt : Retrieval of frequencies, amplitudes, damping factors, and phases from time-domain signals using a linear least-squares procedure. *J. Magn. Reson.*, 61(3):465 – 481, 1985.

[251] Henrik Gesmar, Jens J. Led et Frits Abildgaard : Improved methods for quantitative spectral analysis of NMR data. *Prog. Nucl. Magn. Reson. Spectrosc.*, 22(3):255 – 288, 1990.

[252] Yishay Manassen, Gil Navon et C. T. W. Moonen : Reduced multidimensional NMR experiments using a linear least-squares procedure. *J. Magn. Reson.*, 72(3):551 – 555, 1987.

[253] Philippe R. Bodart, Jean Paul Amoureux et Franis Taulelle : Anafor : Application of a restricted linear least squares procedure to NMR data processing. *Solid State Nucl. Magn. Reson.*, 21(1-2):1 – 20, 2002.

[254] Jennifer C. J. Barna, Sze M. Tan et Ernest D. Lade : Use of CLEAN in conjunction with selective data sampling for 2D NMR experiments. *J. Magn. Reson.*, 78(2):327 – 332, 1988.

[255] Vladimir A. Mandelshtam, Howard S. Taylor et A. J. Shaka : Application of the filter diagonalization method to one- and two-dimensional NMR spectra. *J. Magn. Reson.*, 133(2):304 – 312, 1998.

[256] V. A. Mandelshtam : Fdm : the filter diagonalization method for data processing in NMR experiments. *Prog. Nucl. Magn. Reson. Spectrosc.*, 38(2):159 – 196, 2001.

[257] Seho Kim et Thomas Szyperski : GFT NMR, a new approach to rapidly obtain precise high-dimensional NMR spectral information. *J. Am. Chem. Soc.*, 125(5):1385–1393, 2003.

[258] Eriks Kupce et Ray Freeman : Projection-reconstruction of three-dimensional NMR spectra. *J. Am. Chem. Soc.*, 125(46):13958–13959, 2003.

[259] Peter Schmieder, Alan S. Stern, Gerhard Wagner et Jeffrey C. Hoch : Quantification of maximum-entropy spectrum reconstructions. *J. Magn. Reson.*, 125(2):332 – 339, 1997.

[260] Yanbin Chen, Fengli Zhang, David Snyder, Zhehong Gan, Lei Bruschweiler-Li et Rafael Brüschweiler : Quantitative covariance NMR by regularization. *J. Biomol. NMR*, 38:73–77, 2007. 10.1007/s10858-007-9148-8.

[261] Christoph Kaiser, Jakob J. Lopez, Wolfgang Bermel et Clemens Glaubitz : Dual transformation of homonuclear solid-state NMR spectra–an option to decrease measuring time. *Biochim. Biophys. Acta*, 1768(12):3107 – 3115, 2007. NMR Structural Studies on Membrane Proteins.

[262] Bingwen Hu, Jean-Paul Amoureux, Julien Trebosc, Michael Deschamps et Gregory Tricot : Solid-state NMR covariance of homonuclear correlation spectra. *J. Chem. Phys.*, 128(13):134502, 2008.

[263] Markus Weingarth, Piotr Tekely, Rafael Bruschweiler et Geoffrey Bodenhausen : Improving the quality of 2D solid-state NMR spectra of microcrystalline proteins by covariance analysis. *Chem. Commun.*, 46(6): 952–954, 2010.

[264] Yanbin Chen, Fengli Zhang, Wolfgang Bermel et Rafael Brüschweiler : Enhanced covariance spectroscopy from minimal datasets. *J. Am. Chem. Soc.*, 128(49):15564–15565, 2006.

[265] D. J. States, R. A. Haberkorn et D. J. Ruben : A two-dimensional nuclear overhauser experiment with pure absorption phase in four quadrants. *J. Magn. Reson.*, 48:286, 1982.

[266] R. R. Ernst, G. Bodenhausen et A. Wokaun : *Principles of Nuclear Magnetic Resonance in one and two dimensions.* Clarendon Press, Oxford, 1987.

[267] D L Donoho, I M Johnstone, A S Stern et J C Hoch : Does the maximum entropy method improve sensitivity ? *Proc. Natl. Acad. Sci. U. S. A.*, 87(13):5066–5068, 1990.

[268] Fengli ZHANG, Nikola TRBOVIC, Jinbu WANG et Rafael BRÜSCHWEILER : Double-quantum biased covariance spectroscopy : Application to the 2D inadequate experiment. *J. Magn. Reson.*, 174(2):219 – 222, 2005.

Curriculum Vitae

UNITE DE CATALYSE ET DE CHIMIE DU SOLIDE (UCCS), UMR CNRS 8181, ÉCOLE NATIONALE SUPERIEURE DE CHIMIE DE LILLE, UNIVERSITE DE LILLE 1, BAT. C7, B.P. 90108, 59652 VILLENEUVE D'ASCQ CEDEX,
MEL:OLIVIER.LAFON@ENSC-LILLE.FR,
SITE WEB : HTTP://UCCS.UNIV-LILLE1.FR/SPIP.PHP?ARTICLE199

Dr OLIVIER LAFON

PARCOURS DE RECHERCHE

2007 – **École Nationale Supérieure de Chimie de Lille** Villeneuve d'Ascq

Maître de conférences, section C.N.U. 33 : chimie des matériaux

Groupe « Verres et méthodologie RMN » dirigé par les professeurs Jean-Paul Amoureux et Lionel Montagne

2006 – 2007 **Commissariat à l'énergie atomique** Saclay

Post-doctorant

Laboratoire structure et dynamique par résonance magnétique.

Encadrants : Dr Thibault Charpentier et Dr Dimitris Sakellariou

2002 – 2006 **Université Paris-Sud** Orsay

Thèse et DEA: « Du développement de la RMN multidimensionnelle ^{2}H à l'étude des phénomènes de discriminations énantiomériques »

Directeurs de thèse : Dr Philippe Lesot et Prof. Jacques Courtieu

2001 **Imperial College** Londres

Stage de recherche : « Étude par RMN du solide du comportement de phases de molécules amphiphiles, les monoglycérides »

Encadrant : Dr Robert V. Law

FORMATION

2002 – 2006 **Université Paris-Sud** Orsay

Doctorat en chimie

DEA de physico-chimie moléculaire

3e année de *Magistère* de science de la matière, option chimie

1999 – 2002 **École Normale Supérieure de Lyon** Lyon

Élève de l'École Normale Supérieure de Lyon

Reçu au concours de l'*agrégation* de sciences physiques, option chimie

1ère et 2e années de *Magistère* de science de la matière, option chimie

Licence et *Maîtrise* de chimie physique

1997 – 1999 **Lycée Pierre de Fermat** Toulouse

Élève en PCSI et PC*

THÈMES DE RECHERCHE

- Développement de la spectroscopie de résonance magnétique nucléaire (**RMN**) à l'état solide et pour la matière molle
- Application de la **DNP/RMN haut-champ** pour l'étude des matériaux
- **Enregistrement rapide** d'expériences multidimensionnelles en RMN des solides
- **Découplage** des interactions RMN : enregistrement de spectres ^{1}H haute-résolution à l'état solide
- **Recouplage** des interactions RMN : mesure de distances et observation des proximités interatomiques
- Détection des **noyaux quadripolaires** (^{23}Na, ^{27}Al, ^{14}N…) à l'état solide
- **Discrimination chirale** dans les solvants orientés polypeptidiques

ENCADREMENT

2010 – **Université de Lille 1** Villeneuve d'Ascq

Co-encadrement de la thèse de Aany Sofia Lilly Thankamony (taux d'encadrement : 50 %)

2010 – **Université de Lille 1** Villeneuve d'Ascq

Co-encadrement de la thèse de Xingyu Lu (taux d'encadrement : 50 %)

2007 – 2010 **Université de Lille 1** Villeneuve d'Ascq

Co-encadrement de la thèse de Qiang Wang (taux d'encadrement : 50 %)

2005 **Université Paris-Sud** Orsay

Co-encadrement d'un stage de 3 mois de M1 de chimie physique de l'université Paris-Sud

INDICES BIBLIOMETRIQUES

- Nombre de **publications** : 33 (29 publiées, 4 soumises)
- Facteur h : 6
- Nombre de citations : 66

PRINCIPALES COLLABORATIONS

- **Zhehong Gan**, National High Magnetic Field Laboratory, Tallahassee, États-Unis
- **P. K. Madhu**, Tata Institute of Fundamental Research, Mumbai, Inde
- **Feng Deng**, Académie des sciences de Chine, Wuhan, République populaire de Chine
- **Zeev Luz**, Institut Weizmann, Rehovot, Israël
- **Henri B. Kagan**, Université Paris-Sud, Orsay, France
- **Philippe Lesot,** Université Paris-Sud, Orsay, France

RESPONSABILITÉS COLLECTIVES

2010 **École Nationale Supérieure de Chimie de Lille** Villeneuve d'Ascq

Coordinateur du projet « Caractérisation des matériaux micro- et nano-structurés par RMN : augmentation de la sensibilité par transferts de cohérences électron-noyau »

1er sur liste complémentaire du programme **ANR jeunes chercheurs**, SIMI 8.

Financé en tant que projet émergent par l'institut Chevreul dans le cadre du CPER 2007-2013

2010 **École Nationale Supérieure de Chimie de Lille** Villeneuve d'Ascq

Responsable de l'enseignement de physique en cycle préparatoire intégré à l'ENSCL

2008 **Université de Nantes** Nantes

Membre du **comité de sélection** pour le poste de maître de conférences 0533

2008 **École Nationale Supérieure de Chimie de Lille** Villeneuve d'Ascq

En charge du recrutement d'un technicien pour les travaux pratiques de physique et chimie du cycle préparatoire intégré

2008 – **École Nationale Supérieure de Chimie de Lille** Villeneuve d'Asc

Représentation de la fédération Gay-Lussac et de l'ENSCL lors de salons événementiels

RAYONNEMENT

- Nombre de séminaires invités : 7
- Nombre de communications orales : 10
- Nombre de communications par affiche : 19

2010 **Universität Leipzig** Oppurg

Cours durant l'International Summer School on Molecular Spectroscopy

2009 **National Chemistry Laboratory** Pune

Séjour de trois semaines au National Chemistry Laboratory (NCL) dans le cadre du laboratoire international associé (LIA) UCCS-NCL

2009 **Université de Lille 1** Lille

Encadrement de la « formation pratique RMN liquide et solide » organisée par le centre commun de mesures RMN de l'université de Lille 1

ACTIVITÉS PÉDAGOGIQUES

2010 – **École Nationale Supérieure de Chimie de Lille** Villeneuve d’Ascq

Cours sur les applications de la RMN des solides en deuxième année de cycle ingénieur à l’ENSCL

2010 – **École Nationale Supérieure de Chimie de Lille** Villeneuve d’Ascq

Tuteur pédagogique de deux moniteurs de physique à l’ENSCL

2009 – **Université de Lille 1** Villeneuve d’Ascq

Cours en anglais *Solid-state NMR* en M2 *Advanced Spectroscopy for Chemistry*

2007 – **École Nationale Supérieure de Chimie de Lille** Villeneuve d’Ascq

Cours d’électricité et d’électromagnétisme en première année de cycle préparatoire intégré de la fédération Gay-Lussac

Travaux dirigés et pratiques de physique (métrologie, mécanique, thermodynamique, électricité, électromagnétisme) en première année de cycle préparatoire intégré de la fédération Gay-Lussac

2007 – **École Nationale Supérieure de Chimie de Lille** Villeneuve d’Ascq

Tuteur des projets professionnels et personnels des élèves du cycle ingénieur de l’ENSCL

2003 – 2006 **Université Paris-Sud** Orsay

Moniteur en chimie

Travaux dirigés de chimie générale et organique en PCEM

Travaux pratiques de chimie analytique en M1 de chimie

2003 – 2006 **Lycée Blaise Pascal** Orsay

Colleur de chimie en PC et PC*

Publications et communications

PUBLICATIONS DANS DES REVUES DE RANG A

1. “Rapid two-dimensional NMR spectroscopy by combining non-uniform sampling and covariance: application to stereochemical analysis by ^{2}H NMR at natural abundance”
   O. Lafon, Z. Sehran, J.-P. Amoureux, P. Lesot *J. Am. Chem. Soc.* soumis
2. “Measurement of ^{13}C-^{1}H dipolar couplings in solids by using ultra-fast magic-angle spinning NMR spectroscopy and symmetry-based recoupling”
   Q. Wang, X. Lu, O. Lafon, J. Trébosc, J.-P. Amoureux, F. Deng, B. Hu, Q. Chen *Phys. Chem. Chem. Phys.* soumis
3. “Observing ^{13}C-^{13}C proximities in biomolecules at very high fields and ultra-fast MAS”
   O. Lafon, J. Trébosc, B. Hu, J.-P. Amoureux *J. Magn. Reson.* soumis
4. “A tunable titlted magic-echo homonuclear dipolar decoupling scheme for high-resolution proton nuclear magnetic resonance of solids”
   Z. Gan, P. K. Madhu, J.-P. Amoureux, J. Trébosc, O. Lafon *Chem. Phys. Lett.* soumis
5. “Distance measurement between a spin-1/2 and a half-integer quadrupolar nuclei by solid-state NMR using exact analytical expressions”
   L. Chen, X. Lu, Q. Wang, O. Lafon, J. Trébosc, F. Deng, J.-P. Amoureux *J. Magn. Reson.* 206, 269 (2010)
6. “Indirect high-resolution detection for quadrupolar spin-3/2 nuclei in dipolar HMQC solid-state NMR experiments”
   J. Trébosc O. Lafon, B. Hu, J.-P. Amoureux *Chem. Phys. Lett.* 496, 201 (2010)
7. “Measurement of hetero-nuclear distances using symmetry-based pulse sequence in solid-state NMR”
   L. Chen, Q. Wang, B. Hu, O. Lafon, J. Trébosc, F. Deng, J.-P. Amoureux *Phys. Chem. Chem. Phys.* 12, 9395 (2010)
8. “Measurement of long-range interatomic distances by solid-state tritium NMR spectroscopy”
   A. K. L. Yuen, O. Lafon, T. Charpentier, M. Roy, F. Brunet, P. Berthault, D. Sakellariou, B. Robert, S. Rimsky, F. Pillon, J.-C. Cintrat, B. Rousseau *J. Am. Chem. Soc.* 132, 1734 (2010)
9. “Homonuclear dipolar recoupling under ultra-fast magic-angle spinning: probing ^{19}F-^{19}F proximities by solid-state NMR”
   Q. Wang, B. Hu, O. Lafon, J. Trébosc, F. Deng, J.-P. Amoureux *J. Magn. Reson.* 203, 113 (2010)
10. “Indirect Detection via Spin-1/2 Nuclei in Solid State NMR Spectroscopy: Application to the Observation of Proximities between Protons and Quadrupolar Nuclei”
    O. Lafon, Q. Wang, B. Hu, F.Vasconcelos, J. Trébosc, S. Cristol, F. Deng**,** J.-P. Amoureux *J Phys. Chem. A* 113, 12864 (2009)
11. “Double-quantum ^{19}F–^{19}F dipolar recoupling at ultra-fast magic angle spinning NMR: application to the assignment of ^{19}F NMR spectra of inorganic fluorides”
    Q. Wang, B. Hu, F. Fayon, J. Trébosc, C. Legein, O. Lafon, F. Deng**,** J.-P. Amoureux *Phys. Chem. Chem. Phys.* 11, 10391 (2009)
12. “Double-quantum NMR spectroscopy of ^{31}P species submitted to very large CSAs”

B. Hu, L. Delevoye, O. Lafon, J. Trébosc**,** J.-P. Amoureux *J. Magn. Reson.* 200, 178 (2009)

13. “Enantiodiscrimination of flexible cyclic solutes using NMR spectroscopy in polypeptide chiral mesophases: Investigation of cis-decalin and THF”
C. Aroulanda, O. Lafon, P. Lesot *J. Phys. Chem. B* 113, 10628 (2009)

14. “Double-quantum homonuclear NMR correlation spectroscopy of quadrupolar nuclei subjected to magic-angle spinning and high magnetic field”
Q. Wang, B. Hu, O. Lafon, J. Trébosc**,** F. Deng**,** J.-P. Amoureux *J. Magn. Reson.* 200, 251 (2009)

15. “Robust and efficient spin-locked symmetry-based double-quantum homonuclear dipolar recoupling for probing ^{1}H-^{1}H proximity in the solid-state”
B. Hu, Q. Wang**,** O. Lafon**,** J. Trébosc**,** F. Deng**,** J.-P. Amoureux *J. Magn. Reson.* 198, 41 (2009)

16. “Proton-proton homonuclear dipolar decoupling in solid-state NMR using rotor-synchronized *z*-rotation pulse sequences”
O. Lafon, Q. Wang, B. Hu, J. Trébosc, F. Deng, J.-P. Amoureux, *J. Chem. Phys.* 130, 014504 (2009)

17. “Correlation NMR spectroscopy involving quadrupolar nuclei”
J.-P. Amoureux, J. Trébosc, L. Delevoye, O. Lafon, B. Hu, Q. Wang, *Solid State Nucl. Magn. Reson.* 35, 12 (2009)

18. “Homonuclear dipolar decoupling schemes for fast MAS”
J.-P. Amoureux, B. Hu, J. Trébosc, Q. Wang, O. Lafon, F. Deng *Solid State Nucl. Magn. Reson.* 35, 19 (2009)

19. “Rapid analysis of isotopically unmodified amino acids by high-resolution ^{14}N-edited ^{1}H-^{13}C correlation NMR spectroscopy”
J.-P. Amoureux, Q. Wang, B. Hu, O. Lafon, J. , F. Deng *Chem. Commun.* 6525-6527 (2008)

20. “Enantiodiscrimination in deuterium NMR spectra of flexible chiral molecules with average axial symmetry dissolved in chiral liquid crystals: the case of tridioxyethylenetriphenylene”
P. Lesot, O. Lafon, H. Zimmermann and Z. Luz *J. Am. Chem. Soc.* 130, 8754-8761 (2008)

21. “Two aspects of the desymmetrization of selected prochiral aromatic or vinylic dihalides: enantioselective halogen-lithium exchange and prochiral recognition in chiral liquid crystals”
C.-A. Fan, B. Ferber, H. B. Kagan, O. Lafon, P. Lesot *Tetrahedron Asymmetry* 19, 2666 (2008)

22. “^{2}H NMR studies of two-homopolypeptide lyotropic enantiodiscriminating mesophases: experimental quantification of solute-fiber affinities”
P. Lesot, O. Lafon, C. Aroulanda and R. Y. Dong *Chem. Eur. J.* 14, 4082-4092 (2008)

23. “Enantiomeric analysis using natural abundance 3D NMR spectroscopy in polypeptide chiral oriented media”
P. Lesot, O. Lafon *Chem. Phys. Lett.* 458, 219-222 (2008)

24. “Analysis of intramolecular processes in enantiomeric diaryl atropoisomers and

related derivatives through ^{2}H NMR in polypeptide liquid crystals"
O. Lafon, P. Lesot, C.-A. Fan, H. B. Kagan *Chem. Eur. J.* 13, 3772-3786 (2007)

25. "Chiral discrimination in the ^{13}C and ^{2}H NMR of the crown and saddle isomers of nonamethoxy-cyclotriveratrylene"
O. Lafon, P. Lesot, H. Zimmermann, R. Poupko and Z. Luz *J. Phys. Chem. B* 111, 9453-9467 (2007)

26. "Homo- and heteronuclear 2D NMR approaches to analyse a mixture of deuterated unlike/like stereoisomers using weakly ordering chiral liquid crystals"
K. Ben Ali, O. Lafon, H. Zimmermann, E. Guittet and P. Lesot *J. Magn. Reson.* 187, 205-215 (2007)

27. "Study of molecular rotational isomerism using deuterium NMR in chiral oriented solvents"
P. Lesot, O. Lafon, H. B. Kagan and C.-A. Fan *Chem. Commun.*, 389-391 (2006) accepted as "hot paper"

28. "Enantiomeric Analysis of Planar Chiral (η^6-Arene)chromium Tricarbonyl Complexes using NMR in Oriented Solvents"
O. Lafon, P. Lesot, M. Rivard, M. Chavarot, F. Rose-Munch, E. Rose *Organometallics*, 24, 4021-4028 (2005)

29. "Theoretical and Experimental Investigation of ^{13}C Relayed ^{2}H-^{2}H-COSY 2D Experiments: Application to the Analysis of Weakly Aligned Solutes"
O. Lafon, P. Lesot *J. Magn. Reson.* 174, 254-264 (2005)

30. "Deuterium 3D NMR Experiments for Analyzing Weakly Aligned, Isotopically Enriched Solutes"
O. Lafon, P. Lesot *Chem. Phys. Lett.* 404, 90-94 (2005)

31. "Modified z-Gradient Filtering as a Mean to Obtain Phased Deuterium Autocorrelation 2D NMR Spectra in Oriented Solvents"
O. Lafon, P. Lesot, D. Merlet, J. Courtieu *J. Magn. Reson.* 171, 135-142 (2004)

32. "Analysis of the ^{13}C NMR Spectra of Molecules, Chiral by Isotopic Substitution, Dissolved in a Chiral Oriented Environment: Towards the Absolute Assignment of the pro-*R*/pro-*S* Character of Enantiopic Ligands in Prochiral Molecules"
P. Lesot, O. Lafon, J. Courtieu, P. Berdagué *Chem. Eur. J.* 10, 3741-3746 (2004)

33. "Use of Two-Dimensional Correlation between ^{2}H Quadrupolar Splittings and ^{13}C CSA's for Assignment of NMR Spectra in Chiral Nematics"
O. Lafon, P. Berdagué, P. Lesot *Phys. Chem. Chem. Phys.* 6, 1080-1084 (2004)

SÉMINAIRES INVITÉS

1- "Dipolar decoupling and recoupling in solid-state NMR in high magnetic field and at high MAS frequency"
O. Lafon, *Indian Institute of Science*, Bangalore (Inde), aout, 2009

2- "NMR spectroscopy in solids and mesophases: the golconda of anisotropic interactions interactions "
O. Lafon, *TIFR*, Mumbai (Inde), aout 2009

3- "NMR in chiral mesophases: a powerful tool for stereochemical analysis"
O. Lafon, *Indian Institute of Science*, Bangalore (Inde), aout, 2009

4- "The challenge of sensitivity and resolution in solid-state NMR spectroscopy"

O. Lafon, *National chemistry laboratory*, Pune (Inde), aout, 2009

5- "Solid-state NMR spectroscopy: an efficient tool for material chemistry"
O. Lafon, *NITT*, Tiruchirapalli (Inde), aout 2009

6- "^{2}H and ^{3}H NMR in oriented and solid phases"
O. Lafon, *Stony Brook University*, New-York (USA), novembre 2007

7- "From chiral discriminations to long-range distance measurements"
O. Lafon, *New-York University*, New-York (USA), novembre, 2007

COMMUNICATIONS ORALES

1- "Recouplage homonucléaire à très haut-champ magnétique avec MAS ultra-rapide : analyse des proximités ^{1}H-^{1}H et ^{19}F-^{19}F"
J.-P. Amoureux, Q. Wang, B. Hu, O. Lafon, J. Trébosc, F. Deng, *RMN structurale dans le bassin parisien*, Paris (France), janvier, 2010

2- "Measurement of distances including a ^{14}N nucleus"
L. Chen, O. Lafon, J. Trébosc, J.-P. Amoureux, *RMN structurale dans le bassin parisien*, Caen (France), juin, 2009

3- "Nouvelles méthodes DQ-SQ adaptées aux très hauts champs magnétiques et très hautes vitesses de rotation ^{1}H, ^{13}C, ^{19}F"
Q. Wang, O. Lafon, B. Hu, J. Trébosc, J.-P. Amoureux, *RMN structurale dans le bassin parisien*, Caen (France), juin, 2009

4- "Proton-proton dipolar decoupling at high magic angle spinning frequencies"
O. Lafon, B. Hu, J. Trébosc, J.-P. Amoureux, *RMN structurale dans le bassin parisien*, Paris (France), février, 2009

5- "From the development of multidimensional ^{2}H NMR to the study of enantiomeric discriminations"
O. Lafon, P. Lesot *High-resolution NMR in solids*, Aix-en-Provence (France), novembre, 2006

6- "New applications of NMR in chiral oriented solvents dedicated to stereochemical analysis"
O. Lafon, P. Lesot *SECO 43*, Fréjus (France), mai, 2006

7- "New deuterium NMR experiments for analysing weakly aligned solutes"
O. Lafon, P. Lesot *NMR in oriented phase*, Tropea (Italie), octobre, 2005

8- "Enantiomeric analysis of chiral (η^{6}-arene)chromium tricarbonyl complexes using NMR in oriented solvents"
O. Lafon, P. Lesot, M. Rivard, M. Chavarot *Journée de l'école doctorale : du matériau à l'interface chimie-biologie*, Orsay (France), septembre, 2005

9- "Homo- and heteronuclear 2D NMR involving deuterium-carbon coherence transfer dedicated to analysis in liquid crystal media"
O. Lafon, P. Lesot *Réunion du réseau de RMN structurale dans le grand bassin parisien*, Paris (France), janvier, 2005

10- "NMR : from prion to quantum computing"
O. Lafon *Séminaire d'intérêt général de l'ENS Lyon*, Lyon (France), mars, 2004

COMMUNICATIONS PAR AFFICHE

1- "Homonuclear dipolar recoupling under ultra-fast MAS: what are the best options?"

O. Lafon, J. Trébosc, Q. Wang, B. Hu, F. Deng, J.-P. Amoureux, 51th ENC conference, Asilomar (USA) avril 2010

2- "Isotropic resolution for spin-3/2 quadrupolar nuclei by inverse detection of spin-1/2"
J. Trébosc, J.-P. Amoureux, O. Lafon, B. Hu, Q. Wang, 51th ENC conference, Asilomar (USA) avril 2010

3- **"**Indirect Detection via Spin-1/2 Nuclei in Solid State NMR Spectroscopy: Observing Proximities between Protons and Quadrupolar Nuclei**"**
O. Lafon, J. Trébosc, S. Cristol, Q. Wang, B. Hu, F. Vasconcelos, F. Deng, J.-P. Amoureux, 51th ENC conference, Asilomar (USA) avril 2010

4- "Measurement of hetero-nuclear distances using a symmetry-based pulse sequence in solid-state NMR"
J.-P. Amoureux, L. Chen, B. Hu, O. Lafon, J. Trébosc, F. Deng, Q. Wang, 51th ENC conference, Asilomar (USA) avril 2010

5- "Proton Line Narrowing in Solid-state NMR at high MAS frequencies using symmetry-based z-rotation pule sequences"
O. Lafon, J.-P. Amoureux, F. Aussenac, Q. Wang,.Hu, J. Trébosc, F. Deng, 50th ENC conference, Asilomar (USA) mars 2009

6- "Rapid analysis of isotopically unmodified amino-acids by high-resolution ^{14}N-edited ^{1}H–^{13}C correlation NMR spectroscopy"
J.-P. Amoureux, O. Lafon, Q. Wang, B. Hu, J. Trébosc, F. Deng, 50th ENC conference, Asilomar (USA) mars 2009

7- "Application of spin-locked symmetry-based pulse sequence for robust and efficient double-quantum homonuclear dipolar recoupling for probing ^{1}H-^{1}H proximity"
J.-P. Amoureux, O. Lafon, B. Hu, Q. Wang, J. Trébosc, F. Deng, S. Ganapathy, 50th ENC conference, Asilomar (USA) mars 2009

8- "Double-quantum NMR correlation under magic-angle spinning: a method dedicated to quadrupolar nuclei and high-field spectrometers"
J.-P. Amoureux, Q. Wang, B. Hu, O. Lafon, J. Trébosc, F. Deng, P. Corcos, 50th ENC conference, Asilomar (USA) mars 2009

9- "Tritium MAS NMR: Toward long range distance measurements and more"
T. Charpentier, A. Yuen, O. Lafon, F. Brunet, P. Berthault, D. Sakellariou, J.-C. Cintrat, 50th ENC conference, Asilomar (USA) mars 2009

10- "Double-quantum experiments dedicated to ultra-fast MAS on high-field spectrometers and applied to protons, spin-1/2 nuclei submitted to very large CSAs, and quadrupolar nuclei"
J.-P. Amoureux, Q. Wang, B. Hu, O. Lafon, J. Trébosc, L. Delevoye, F. Deng, 6th Alpine conference on solid-state NMR, Chamonix (France), septembre 2009

11- "Isotropic resolution for 3/2 spin quadrupolar nuclei by inverse detection of spin ½"
J. Trébosc, J.-P. Amoureux, O. Lafon, B. Hu, Q. Wang, EUROMAR 2009, Göteborg (Suède) Juillet 2009

12- "Tritium solid-state NMR: towards long range distance measurement in biological complexes"
O. Lafon, T. Charpentier, D. Sakellariou, P. Berthault, A. Yuen, J.-C. Cintrat, B. Rousseau, *5th Alpine conference*, Chamonix (France), septembre, 2007

13- "Study of conformational dynamics using deuterium NMR in polypeptide oriented

solvents”
O. Lafon, P. Lesot, C.-A. Fan et H. B. Kagan *Spectroscopy and dynamics of molecular coils and aggregates*, Göttingen (Allemagne), mars, 2006

14- “Analysis of intramolecular dynamic processes in diaryl derivatives through deuterium NMR in polypeptide liquid crystals”
P. Lesot, O. Lafon, H. B. Kagan et C.-A. Fan *Groupement français d’Etude de Résonance Magnétique*, Blankenberge (Belgique), mars, 2006

15- “New deuterium multi-dimensional NMR experiments in chiral anisotropic solvents”
P. Lesot, O. Lafon *4th Alpine Conference on Solid-State NMR*, Chamonix (France), septembre, 2005

16- “First asymmetric SmI_2-induced cross-coupling of $Cr(CO)_3$ aromatic nitrone complexes with carbonyl compounds”
M. Chavarot, M. Rivard, F. Rose-Munch, E. Rose, S. Py, O. Lafon, P. Lesot *Congrès SFC-Eurochem,* Nancy (France), août, 2005

17- “Deuterium tridimensional NMR experiment dedicated to stereochemical analysis of deuterated solutes”
O. Lafon, P. Lesot *3ème RCO*, Palaiseau (France), mars, 2005

18- “Chiral imines and microwaves : alkylation of ter-butyl acrylate and determination of stereoselectivity using chiral liquid crystals”
K. Jean-Charles, F. Dumas, A. Loupy, P. Lesot, O. Lafon *Microwaves in Chemistry Conference*, Londres (Royaume-Uni), septembre, 2004

19- “Contribution of ^{13}C Nuclear Magnetic Resonance in chiral liquid crystals for assignment of pro-*R*/pro-*S* descriptors to enantiotopic ligands ”
O. Lafon, P. Lesot, J. Courtieu *Journées de Chimie Organique*, Palaiseau (France), septembre, 2004